GL00594

A Compendium of Reports on the Salton Sea Scientific Drilling Project

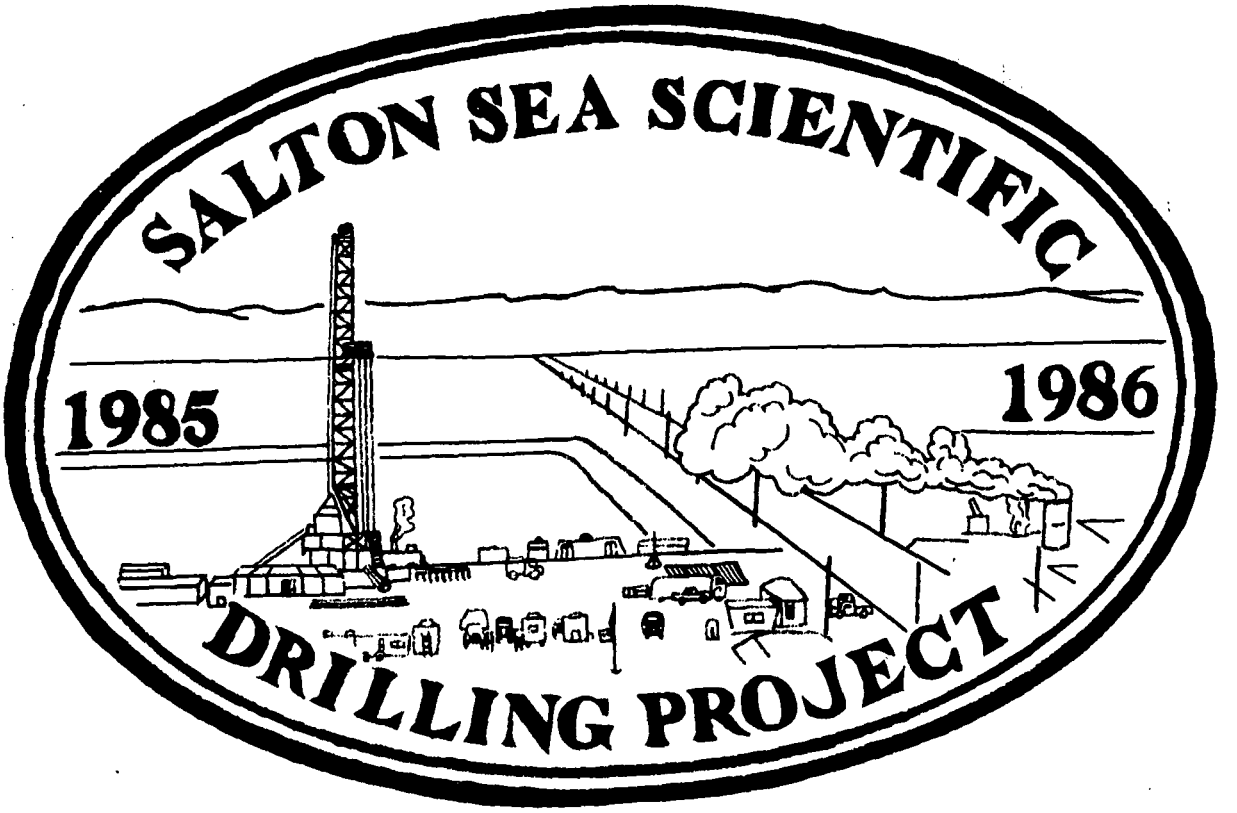

NATIONAL SCIENCE FOUNDATION

DEPARTMENT OF ENERGY · UNITED STATES OF AMERICA

DEPARTMENT OF THE INTERIOR · U.S. GEOLOGICAL SURVEY

A COMPENDIUM OF REPORTS ON THE SALTON SEA SCIENTIFIC DRILLING PROJECT

FOREWORD

The SALTON SEA SCIENTIFIC DRILLING PROJECT (SSSDP) was an investigation of a hot, hypersaline, active geothermal system, on the delta of the Colorado River in Southern California. It was one of the first major scientific drilling projects of the U.S. National Continental Scientific Drilling Program. Funding for the drilling and engineering came from the Geothermal Technology Division of the U.S. Department of Energy and the major funding for the scientific program from the National Science Foundation, the Office of Basic Sciences of the Department of Energy, and the United States Geological Survey.

Symposia reporting the results of the SSSDP were held at the annual meeting of the American Geophysical Union in Baltimore in May 1987, and the annual meetings of the Geothermal Resources Council, in Palm Springs in September 1986, and in San Diego in October 1988. This compendium contains reprints of selected articles arising from these symposia, which originally appeared in the "Journal of Geophysical Research", the "Transactions of the Geothermal Resources Council", and (in one case) the journal "Economic Geology". We thank respectively the American Geophysical Union, the Geothermal Resources Council, and the Society of Economic Geologists for permission to use their copyrighted material.

The reports included were selected and compiled by:-

Wilfred A. Elders,
Chief Scientist of the SSSDP,
Center for Geothermal Research,
Institute of Geophysics and Planetary Physics,
University of California,
Riverside, California, 92521, U.S.A.

Distribution of this compendium was made possible by funds provided under National Science Foundation Grant EAR-8618703.

TABLE OF CONTENTS

The reports reprinted here are presented in four sections with the original pagination maintained as follows:

Tarif, P.A., Wilkens, R.H., Cheng, C.H., and Paillet, F.L., "Laboratory Studies of the Acoustic Properties of Samples From the Salton Sea Scientific Drilling Project and Their Relation to Microstructure and Field Measurements," pp 13,057-13,068.

Herzig, C.T., and Elders, W.A., "Nature and Significance of Igneous Rocks Cored in the State 2-14 Research Borehole: Salton Sea Scientific Drilling Project, California," pp 13,069-13,080.

Cho, M., Liou, J.G., and Bird, D.K., "Prograde Phase Relations in the State 2-14 Well Metasandstones, Salton Sea Geothermal Field, California," pp 13,081-13,103.

Shearer, C.K., Papike, J.J., Simon, S.B., Davis, B.L., and Laul, J.C., "Mineral Reactions in Altered Sediments From the California State 2-14 Well: Variations in the Modal Mineralogy, Mineral Chemistry, and Bulk Composition of the Salton Sea Scientific Drilling Project Core," pp 13,104-13,122.

Caruso, L.J., Bird, D.K., Cho, M., and Liou, J.G., "Epidote-Bearing Veins in the State 2-14 Drill Hole: Implications for Hydrothermal Fluid Composition," pp 13,123-13,134.

Bird, D.K., Cho, M., Janik, C.J., Liou, J.G., and Caruso, L.J., "Compositional, Order/Disorder, and Stable Isotope Characteristics of Al-Fe Epidote, State 2-14 Drill Hole, Salton Sea Geothermal System," pp 13,135-13,144.

Charles, R.W., Janecky, D.R., Goff, F., and McKibben, M.A., "Chemographic and Thermodynamic Analysis of the Paragenesis of the Major Phases in the Vicinity of the 6120-Foot (1866 m) Flow Zone, California State Well 2-14," pp 13,145-13,158.

Roedder, E., and Howard, K.W., "Fluid Inclusions in Salton Sea Drilling Project Core: Preliminary Results," pp 13,159-13,164.

Thompson, J.M., and Fournier, R.O., "Chemistry and Geothermometry of Brine Projects From the Salton Sea Scientific Drill Hole, Imperial Valley, California," pp 13,165-13,174.

Hammond, D.E., Zukin, J.G., and Ku, T.L., "The Kinetics of Radioisotope Exchange Between Brine and Rock in a Geothermal System," pp 13,175-13,186.

Section C

Reprint from ECONOMIC GEOLOGY, VOLUME 83, 1988.

McKibben, M.A., Andes, J.P., and Williams, A.E., "Active Ore Formation at a Brine Interface in Metamophosed Deltaic Lacustrine Sediments: The Salton Sea Geothermal System, California," pp 511-523.

Section D

Reprints selected from GEOTHERMAL RESOURCES COUNCIL TRANSACTIONS, VOLUME 12, 1988.

Herzig, C.T., and Elders, W.A., "Probable Occurrence of the Bishop Tuff in the Salton Sea Scientific Drilling Project Borehole, Salton Sea Geothermal System, California," pp 115-120.

McKibben, M.A., Eldridge, C.S., and Williams, A.E., "Sulfur and Base Metal Transport in the Salton Sea Geothermal System," pp 121-125.

Williams, A.E., "Delineation of a Brine Interface in the Salton Sea Geothermal System, California," pp 151-157.

SECTION A

Reprints selected from the GEOTHERMAL RESOURCES COUNCIL TRANSACTIONS, VOLUME 10, 1986.

Aducci, A.J., Klick, D.W. and Wallace, R.H., "Management of the Salton Sea Scientific Drilling Program," pp 445-448.

Harper, C.A., and Rabb, D.T., "The Salton Sea Scientific Drilling Project: Drilling Program Summary," pp 455-459.

Michels, D.E., "SSSDP Fluid Compositions at the First Flow Test of State 2-14," pp 461-465.

Sass, J.H., and Elders, W.A., "Salton Sea Scientific Drilling Project: Scientific Program," pp 473-478.

MANAGEMENT OF THE SALTON SEA SCIENTIFIC DRILLING PROGRAM

Anthony J. Adducci[1] Donald W. Klick[2] and Raymond H. Wallace, Jr.[3]

(1) DOE-SFO, 1333 Broadway, Oakland, CA 94612
(2) U.S. Geological Survey, 905 National Center, Reston, VA 22092
(3) U.S. Geological Survey, 905 National Center, Reston, VA 22092, on detail to Department of Energy (GTD), 1000 Independence Avenue, SW, Washington, DC 20585

ABSTRACT

The Salton Sea Scientific Drilling Program was undertaken by the Department of Energy, the National Science Foundation, and the U.S. Geological Survey in order to investigate, by drilling a well and conducting scientific experiments, the roots of the Salton Sea hydrothermal system. A two-element organizational structure was established to focus on integration of the drilling and engineering operations with the scientific activities. This management plan, the delegation of site-operational authority to an on-site coordinating group, and the cooperative spirit of the participants have resulted in achievement of the drilling, engineering, and scientific objectives of the program.

INTRODUCTION

The Salton Sea Scientific Drilling Program (SSSDP) was undertaken by the Department of Energy (DOE), the National Science Foundation (NSF), and the U.S. Geological Survey (USGS) in order to investigate, by drilling a well and conducting scientific experiments, the roots of the Salton Sea hydrothermal system. The program had its official start in Fiscal Year 1984 when Congress added $5.9 million to DOE's Geothermal and Hydropower Technologies Division (now Geothermal Technology Division - DOE/GTD) budget. Although the proposal for a deep scientific drillhole in the Salton Sea area had been received enthusiastically by the NSF, the USGS and DOE's Office of Basic Energy Sciences (DOE/OBES), these organizations had no direct appropriations for the program.

In January 1984, the Director of DOE/GTD established an interagency steering group in order to obtain advice and consultation from the other participating agencies and to coordinate their involvement. Thus began the formal management of this multi-million dollar, multi-agency program.

GOALS AND PRIORITIES

The goals of the program are to study the thermal, physical, chemical, and mineralogical conditions within the deeper parts of the Salton Sea hydrothermal system in order to:

1) better define the geological and hydrological nature of the Salton Sea hydrothermal system and its geothermal reservoirs, and test for extension of this system to greater depths,
2) refine geothermal energy resource estimates for the Salton Sea area,
3) develop a better understanding of the genesis of hydrothermal ore deposits,
4) improve understanding of crustal formation processes in a continental spreading zone, and
5) investigate the possibility of the occurrence of "superconvection."

These goals were to be accomplished by:

1) drilling a scientific well to a target depth of 10,000 feet,
2) obtaining core and drill cuttings for the entire depth of the well,
3) conducting flow tests of selected fluid production zones,
4) collecting fluid and gas samples during flow tests,
5) measuring temperature, pressure, and flow rate at appropriate depths,
6) obtaining comprehensive suites of geophysical logs, and
7) conducting geological, geophysical, and geochemical scientific experiments downhole.

Highest program priority was given by management during the drilling phase to data collection and sampling of rocks and fluids. However, a stark reality faced early in the program was the need to obtain high-temperature cable and instrumentation to test, measure, and sample the hostile subsurface thermal and chemical environment to be penetrated; otherwise, several major program goals could not be achieved. Another important program requirement was the release of all information obtained to the public domain.

MANAGEMENT STRATEGY AND FUNCTIONS

In order to effectively manage this complex, multi-agency, multi-discipline program, a two-element organizational structure (Figure 1) was established among the participants to focus on integration of the drilling and engineering operations with the scientific activities. This structure was based on a SSSDP Management Plan, accepted by each participating agency, that was designed to place critical scientific and technical decision-making at the appropriate level, including on-site field managers. The strategy was to encourage cohesive and timely decision-making.

Figure 1. Management Plan for the Salton Sea Scientific Drilling Program.

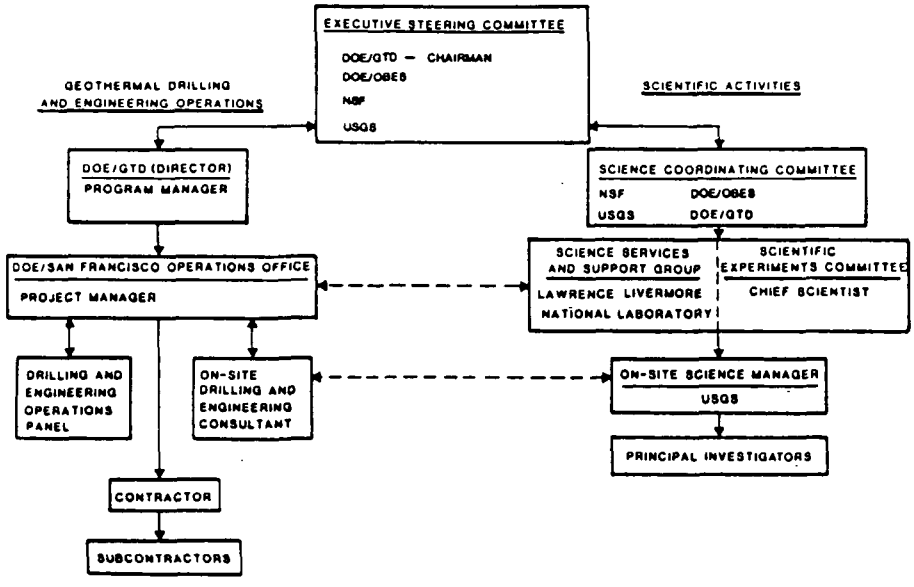

Those associated with the program are pleased to report that most of these objectives have been achieved. Some have been exceeded. There are two important factors that explain this high degree of success. First is the cooperative spirit with which the key individuals entered into program activities. Opportunities for achieving maximum benefit from the total program were pursued, rather than focusing participation on specific interests of the individuals or their agencies. Second is the policy decision of the Executive Steering Committee (ESC) to delegate site-operational authority to the field, ie., to the group of individuals responsible for program success at the well site.

Overall planning, integration, and evaluation of the program, and the resolution of policy issues, were achieved through the Executive Steering Committee. This Committee consisted of policy-level individuals from the three funding agencies, with the member from the organization responsible for well drilling operations, the Director of DOE/GTD, as Chairman.

Drilling and engineering program activities were managed by a Program Manager representing DOE/GTD. The GTD delegated responsibility for conducting drilling and engineering project activities to DOE's San Francisco Operations Office (DOE/SAN), under the leadership of a Project Manager. These responsibilities consisted of pre-drilling and site preparation activities; drilling and completing the scientific well to a target depth of 10,000 feet; recovering the maximum amount of core and drill cuttings; conducting flow tests and collecting fluid and gas samples at the surface; providing instrumentation systems for measuring temperature, pressure, and flow rate, and for downhole fluid and gas sampling; providing maximum time during drilling for scientific experiments and geophysical logging; integrating scientific experiments into drilling operations, while preserving well integrity and avoiding environmental risk and hazards to personnel and equipment; and providing a six-month well-access period after completion of drilling for scientific experiments.

DOE/SAN conducted a solicitation for procurement of a contractor to perform the drilling and engineering operations in the field. The procurement process led to the selection of Bechtel National, Inc. as prime contractor for the scientific well to be drilled on California State lands in the Salton Sea Geothermal Field for which Kennecott Corporation had acquired geothermal prospecting permits. In addition, DOE/SAN contracted Well Production Testing, Inc. as their on-site drilling and engineering consultant. DOE/SAN also established a panel of geothermal industry experts and government representatives for consultation and advice on well construction and on drilling and engineering operations in the Imperial Valley area.

Scientific activities were managed by the Science Coordinating Committee (SCC) comprised of individuals from the three funding agencies. The Scientific Experiments Committee (SEC), under chairmanship of the Chief Scientist, aided the SCC in establishing the scientific content of the program. The On-Site Science Manager was responsible for the interests of the SSSDP scientific community at the well-site. Technical, logistical, and administrative assistance was provided to the SEC by a Science Services and Support Group. This Group also provided the SSSDP scientific community with a regular and continuing interface with the Project Manager at DOE/SAN.

To develop the scientific content of the program, the SCC published a notice of opportunity for submission of proposals to carry out scientific experiments and analyses. NSF, DOE/OBES, and USGS had no funding specifically appropriated for SSSDP science; therefore, each of these agencies allocated an amount, nominally $500,000, from existing appropriations to support selected proposals. The SEC reviewed these proposals for technical feasibility and relevance, and made recommendations to the SCC. The SCC, with assistance of a joint peer review panel established by NSF and DOE/OBES, and with consideration of SEC recommendations, evaluated the proposals and made funding recommendations to the appropriate agencies (in the case of NSF and DOE/OBES, with external programs) or endorsements (in the case of USGS, with only an internal program). Final selection of proposals for SSSDP projects remained the responsibility of each agency, but was coordinated among the agencies.

ON-SITE COORDINATION

The on-site coordinating group to whom the ESC delegated site-operational authority was not included in the SSSDP Management Plan or on the chart of the SSSDP management structure. It was formed at the well-site to provide immediate response to problems affecting the success of program activities, health, and safety. Daily meetings of this group were extremely critical to successfully conducting drilling and engineering operations and scientific activities on-site.

DISCUSSION

Management of this program has been characterized as an exercise in, "how to manage an over-scoped, under-funded program--champagne plans with a beer budget." As more accurate cost estimates were acquired early in 1985, it became evident that the $5.9 million appropriated was significantly less than the revised cost estimates for the drilling and engineering operations originally designed. An ad hoc task force consisting of DOE/SAN management, contractor, landholder, and scientific program representatives was established by the ESC to develop a fundable scope of work. Initial program objectives of a target well depth of 10,000 feet and gathering maximum scientific data were to be retained. The task force made major program revisions, including elimination of long-term flow tests, related surface facilities, and an injection well, in favor of several short-term flow tests using simple test facilities and a brine holding pond.

When the dust subsided from the painful efforts to reduce scope and increase funding, costs for the SSSDP from FY84 through FY86 totalled more than $9.3 million (Table 1). About 75% of this amount was required for drilling and engineering operations. A major element was the inclusion of coring costs as a maximum funded amount ($1 million), rather than as a specific plan and schedule of work.

Table 1. Summary of Drilling and Engineering, and Scientific Program Funding.

	FUNDING BY AGENCY (in $ 000's)				
CATEGORY	NSF	GTD	USGS	OBES	TOTAL
DRILLING & ENGINEERING	25	6,605	25	25	6,680
GEOCHEMISTRY	168	-	165	103	436
PETROLOGY	280		-	150	430
GEOPHYSICS (LAB)	-	55	15	132	202
GEOPHYSICS (SITE)	-		180	170	350
BIO-ORGANIC	-	-	70	-	70
INSTRUMENTATION	-	597	120	-	717
SCIENCE SUPPORT & MANAGEMENT	-	-	300	146	446
TOTAL FUNDING	473	7,352	875	726	9,331
TOTAL ACTIVITIES	7	10	13	11	41

The usefulness of this management structure has been demonstrated not only by the successful achievement of most of the drilling, engineering, and scientific objectives, but also by the quick response that it provided to resolve urgent issues needing immediate attention and response from

all participants. An example of the latter was the provision of $135,000 of additional funding from DOE/GTD, DOE/OBES, NSF, and USGS in the last few days of drilling in order to properly complete and test the well at its total depth.

CONCLUSIONS

The success of this program can be credited to the melding together of the key participants into a single-minded team. This was accomplished by open and frank communications between these participants and by their employment of lateral coordination with their counterparts, rather than resolving issues through their respective management channels. Although much knowledge has been gained from the SSSDP, the roots of the Salton Sea hydrothermal system were not fully penetrated. However, it has been shown to extend at least to 10,564 feet beneath the SSSDP well site. Additional drilling and scientific activities at the well-site are being considered.

Geothermal Resources Council, TRANSACTIONS, Vol. 10, September 1986

THE SALTON SEA SCIENTIFIC DRILLING PROJECT: DRILLING PROGRAM SUMMARY

Charles A. Harper and David T. Rabb

Bechtel National, Inc., P.O. Box 3965, San Francisco, CA 94119

ABSTRACT

Drilling, coring, logging, and flow testing of well "State 2-14" was completed in March 1986. In the 160 days following spud-in, all the major operational objectives of the Salton Sea Scientific Drilling Project (SSSDP) were met or exceeded. A review of the project costs is presented with an emphasis on unusual or unexpected problems encountered on this scientific/exploratory well. A discussion of the flow test procedures and basic results of commercial interest are also discussed.

INTRODUCTION

Spud-in of the Salton Sea Scientific Drilling Project well took place on October 23, 1985. In the following 160 days, the well was drilled to 10,564 ft, exceeding the target depth objective of 10,000 ft. Thirty-six spot cores were taken, with a total of approximately 725 ft recovered. Two flow tests were conducted, providing fluid samples for scientific study and estimates of productivity from an upper zone at 6,120 ft and a lower interval with mixed flow, primarily from zones at 8,600 ft and 10,475 ft. Downhole logging suites and fluid sampling were performed by researchers (about 425 hrs) and service companies (about 60 hrs), providing additional data to be used in the study of the Salton Sea geothermal resource and the factors that have influenced the geological evolution of the basin.

This paper presents an overview of the management approach, and some of the technical and cost results unique to the project. A brief summary of the flow tests and results is also included. Preliminary reports on the science portion of the program and core drilling are the subject of separate papers being presented at the Conference.

MANAGEMENT SUMMARY

Bechtel, under a contract with the U.S. Department of Energy,* had overall responsibility for design, procurement, and supervision of operations at the site, near Niland, California. The site was made available to the project by Kennecott, holder of an exploration permit from the State Lands Commission. More than 65 competitively bid subcontracts and purchase orders were activated to provide the support services, equipment, materials, and personnel necessary to carry out the complete program.

Consequently, a critical element in project control was the development and use of an accrual system for daily accounting of costs. Suppliers were required to submit work and delivery tickets at the site, as services were performed, that showed estimated actual costs. These, along with estimates for labor, equipment rental, and all other costs, were processed daily to produce a current expenditure report. Individual estimates were cross-checked with bid prices and actual billings at frequent intervals and adjustments made accordingly. The availability of "real time" cost information at the drill site was invaluable in planning and prioritizing engineering and science objectives.

The overall project costs are summarized in Table 1. Prespud activities included a major

Table 1. Summary of Salton Sea Scientific Drilling Program Costs (Does not include the science experiments budget.)

Activity	Period of Performance	Estimated Cost ($1000s)
Prespud	Sept 1984 through Oct 1985	1,720
Drilling and completion	Oct 1985 through Mar 1986	2,975
Coring and Logging	Oct 1985 through Mar 1986	930
Flow Test Facility and Two Flow Tests	Dec 1985 and Mar 1986	680
Standby and Restoration	Apr 1986 through Nov 1986	400
Total Budget		$6,705

*Contract Number DE-AC03-84SF12194

rescoping of the project to eliminate installation of an injection well and high-pressure separator from the flow test facility. Other prespud activities included well design, site layout and preparation, and the negotiation and award of the majority of the subcontracts. The drilling and completion costs were higher than might be expected due to three major problem areas, summarized in Table 2 and discussed in more detail below. Nearly $1 million was spent on directional drilling and lost circulation and well control problems. The estimated net cost of coring was $550,000, for an average cost per ft recovered of about $755. The combined estimated cost of scientific and commercial logging was $380,000.

Table 2. Problem Areas and Estimated Costs Incurred During Drilling and Completion

Activity	Approximate Cumulative Duration	Estimated Cost ($1000s)
Lost Circulation and Well Control	20 days	640
Directional Drilling	18 days	390
Fishing and Stuck Pipe	8 days	275

The project schedule, spanning 26 months, is summarized in Figure 1. The current phase of the project is scheduled for completion in November 1986.

PROBLEM ANALYSIS

The drilling of State 2-14 resulted in some unexpected problems and costs, largely to meet the overriding science objectives. A commercial well typically would be drilled with few, if any, cores taken and would be completed at the highest zone(s) believed capable of commercial production. Few wells in the Salton Sea Geothermal Field have been drilled deeper than 8,000 ft. State 2-14, on the other hand, was to be drilled to at least 10,000 ft, if technically and economically feasible, and to be spot cored at intervals of about every 200 ft, or more frequently if interest dictated. The result was that:

- Fifteen of the 61 drill bits used had up to half of their potential drilling life remaining, when they were tripped out of the hole so a core could be taken. These bits were discarded rather than rerun, to avoid the risk of bit failure and a fishing job or premature tripping for bit replacement before the next coring point was reached.
- All cores taken above 6,000 ft required a followup reaming run to open the borehole to gauge. Loss of roller cone bit gauge and bearing failure was accelerated considerably, especially in the deeper, harder formations.
- Every fluid loss zone encountered as the well was deepened, contributed to a continuing problem. Lost circulation control methods, including setting

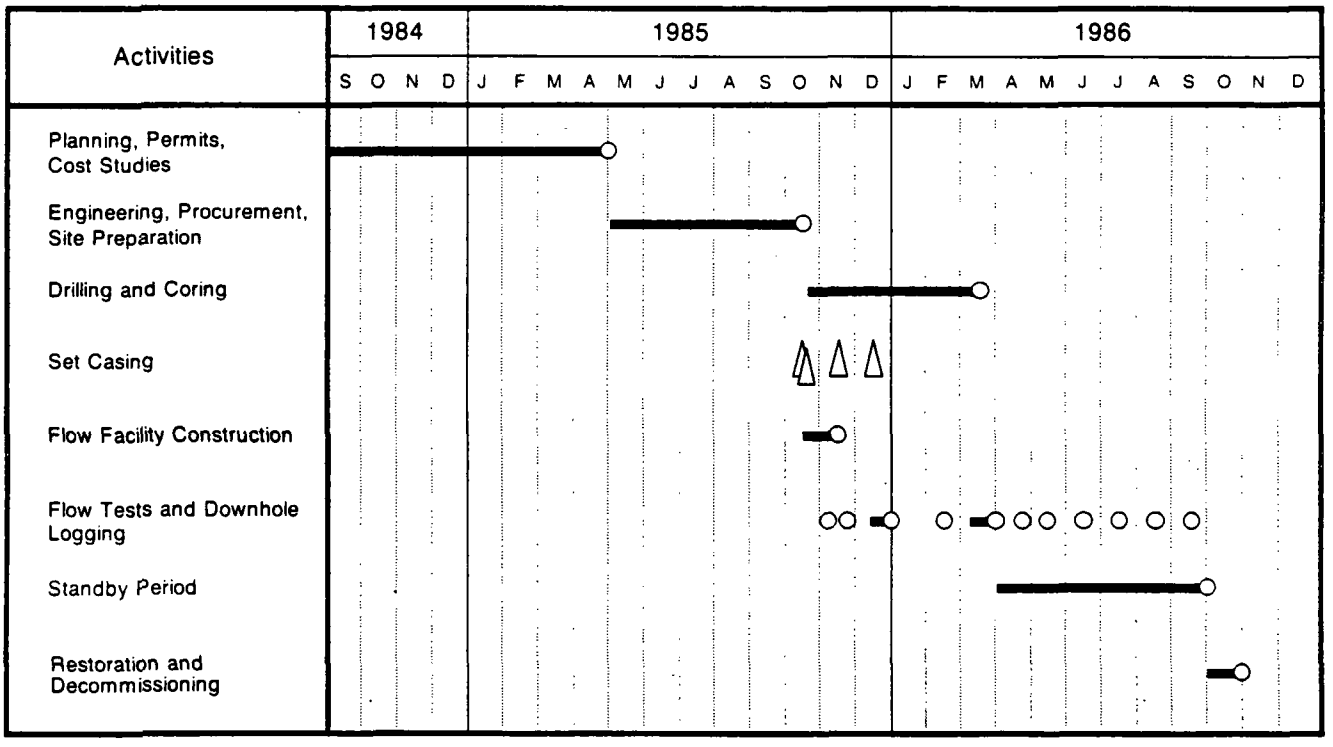

Figure 1. Salton Sea Scientific Drilling Project Schedule

cement plugs, proved to be only temporarily effective. Very high costs were incurred for control materials and lost time to reestablish circulation.

Directional drilling, not included in the original project plan or budget, was required when the path of the borehole deviated several times, approaching the easterly property boundary. Although the final multishot survey failed because of high bottomhole temperatures, the best available information is that the borehole remained on the Kennecott lease.

Drill Bit Usage

A summary of bit usage and cost is presented in Table 3. Average hourly penetration rates when drilling are summarized in Table 4. The average penetration rate was relatively constant at an approximate 25 ft/hr from 3,000 to 8,000 ft, including approximately 550 ft directionally drilled at an average penetration rate of 15 ft/hr. From approximately 9,500 ft, where intrusive igneous dikes were encountered, to total depth (T.D.), drilling became progressively slower. The formation showed complete metamorphosis of the siltstones, mudstones, and sandstones encountered higher in the well, to harder hornsfelsic and quartsitic forms.

Table 3. Bit Usage and Cost Summary

Overall Size	Type	Quantity	Depth Used (feet)
17-1/2	Mill Tooth	6	Surface to 3,500
12-1/4	Mill Tooth	7	3,500 to 6,000
	Carbide Insert	6	
8-1/2	Mill tooth	6	6,000 to 10,475
	Carbide Insert	34	
	Stratapak	1	
6-1/8	Carbide Insert	1	10,475 to 10,564

Total estimated bit cost = $215,000

Table 4. Drill Rate versus Depth

Depth (ft)	Drill Rate (ft/hr) Range	Approximate Average
0 to 1,000	60 to 1,000	100
1,000 to 2,000	15 to 300	75
2,000 to 3,000	15 to 125	50
3,000 to 8,000	5 to 100	25
8,000 to 9,000	5 to 75	20
9,000 to 10,000	5 to 75	15
10,000 to 10,564	5 to 18	10

Seventeen bits were used during directional drilling (turbodrilling) operations. Bit life averaged about 6 hours. Total footage averaged only about 30 ft per bit, rather than the 150 to 240 ft expected in normal service.

Lost Circulation and Flow Control

Lost circulation zones in the Salton Sea Geothermal Field, as observed in State 2-14, typically result from seismic fracturing that has created a network of vertical and horizontal channels for fluid transport. Between 6,000 ft and T.D., nine major fluid loss zones were encountered, as summarized in Table 5. As each zone was penetrated, conventional lost circulation materials (LCM) and control techniques were tried to regain circulation. Zones which were not kept in check by this method were eventually covered with a cement plug. As an intermediate solution, LCM/cement pills consisting of a 50 bbl LCM pill mixed with 50 or 100 sacks of Portland cement were tried. Pills were placed across each loss zone, allowed to set up, and then squeezed to 200 to 300 psi. While this procedure was often successful, the plugs usually broke down within a week. As the well was deepened and more and more zones were exposed, the time required to mix and place LCM pills and the cost of the materials became excessive. As shown in Table 6, the situation became critical between 9,000 and 10,000 ft when the average ft/day drilled dropped below 50 ft and the average cost/ft rose above $500. Core bit damage from inadequate circulation and differential sticking were additional concerns.

Table 5. Major Fluid Loss Zones in State 2-14

Approximate Depth (ft)	Maximum Loss Rate (bbl/hr)	Treatment*	Flowed During Second Flow Test
6,120**	66	CEM	Yes?
6,360	45	LCM, CEM	No
6,635	Total	LCM, CEM	Yes?
6,340	35	LCM, CEM	No
8,095 through 8,160	Total	LCM, CEM	No
8,560 through 8,620	Total	LCM, CEM	Yes
8,950	Total	LCM, CEM	No
9,220	80	LCM, CEM	No
10,475	Total	SAND, CEM, Drillout	Yes

* LCM = Lost circulation material with Portland cement
CEM = Full cement plug
SAND = Sand plug

** First flow test flow zone; cemented after first flow test.

Table 6. Drilling and Coring Performance Trends*

Depth Interval	Days to Complete	Average Cost/Day	Average Ft/Day	Average Cost/Ft	Delays
Surface to 3,500	21	$15,500	165	$ 95	One day setting conductor; one day fishing
3,500 to 6,000	23	$17,000	110	$155	Two days fishing; two days injectivity testing
6,000 to 7,000	20	$19,500	50	$390	Six days directional drilling; two days fishing
7,000 to 8,000	10	$19,500	100	$195	Two days directional drilling; two days lost circulation control
8,000 to 9,000	11	$26,000	90	$290	Five days lost circulation control
9,000 to 10,000	27	$24,500	35	$660	Damaged core bits; seven days lost circulation control and cementing; two days stuck pipe; two days well control
10,000 to 10,460	5	$23,000	90	$250	Two days well control; one day stuck pipe

* Excludes casing, flow tests, and logging activities.

At a depth of 9,450 ft, the decision was made to set full cement plugs across all the open zones. Several of these plugs broke down during subsequent drilling to T.D. and lost circulation and well control problems continued to plague the drilling operation. By the time the well was T.D.'d, daily mud and chemical costs were averaging over $5,000. A partial summary of mud and chemical usage and overall costs are shown in Table 7.

Table 7. Most Frequently Used Mud and Chemicals* and Total Estimated Cost

Product Type	Purpose	Approximate Total Used
Bentonite clay	Viscosifier	1,945 sacks
Sepiolite	Viscosifier	9,130 sacks
Barite	Weight control	3,885 sacks
NaOH	pH control	370 sacks
Cotton seed hulls/ pellets	LCM**	1,220 sacks
Wood chips/ nut hulls	LCM	1,050 sacks
Vegetable/ other fiber	LCM	900 sacks
Polymer	LCM	800 gallons
Granular battery casings	LCM	85 sacks
Diesel fuel	Free stuck pipe	400 barrels

Total estimated mud and chemical cost = $460,000

* A total of forty different products were used.
** Lost circulation material.

WELL COMPLETION AND FLOW TESTING

First Flow Test Configuration

After drilling out of the 9-5/8 inch casing set at 6,000 ft, a 66 bbl/hr fluid loss zone was encountered at 6,120 ft. After drilling a 100 ft rat hole, the borehole fluid was replaced with water and the wellhead was installed and tied into the flow test facility. Wellhead pressure built to 160 psi after being shut in for about 24 hours. However, nitrogen stimulation was finally required to induce flow.

A James' tube was used to estimate the potential productivity of the zone. The extremely high total dissolved solids (250,000 to 300,000 ppm), presented both a physical challenge, in contending with deposition rates that sealed over the lip pressure port in 10 to 20 minutes, and an analytical challenge, in mathematically compensating for salinity effects.

Second Flow Test Configuration

No major fluid loss zones were encountered between about 9,200 and 10,450 ft. The loss of circulation at 10,475 ft led to speculation that a new, possibly lower salinity reservoir might have been discovered. The well completion design was modified, within the limitations of available funding, to increase the chances of flowing the well solely from this lowest zone. The approach taken was as follows:

1. Temporarily plug the bottom flow zone. Several 50 bbl LCM pills (without cement), 86 sacks of #20 silica sand, and approximately 400 cu ft of cement disappeared into this fracture system before a cement plug held.

2. Hang down a 7-inch liner from 5,700 to 10,136 ft to cover over all of the upper zones. It was hoped that any upper zones that started to flow during testing would bridge off, preventing flow down around the liner into the borehole. Installing the liner was a delicate operation because the well was alternately taking fluid or flowing, over a period of a few hours. The well would begin flowing by the time the drill string was tripped out after a cooling run.

3. Drill out the cement plug and make a 100 ft rat hole. The cement plug was less than two feet thick!

The flow test facility was basically identical to that used on the first test. Wellhead pressure rose to 250 psi during the 24 hour shut-in period and the well flowed spontaneously.

Flow Test Results

The results are summarized in Table 8. The well flowed from a single zone on the first test, and drilling fluid contamination was flushed out after about 6 hours of flow, producing good quality fluid and gas samples for science analysis. The well was flowed for about 48 hours.

The second flow test was too brief to allow uncontaminated fluid production. It was concluded when the storage pit was full after 36 hours of flow. Continuous temperature measurements made after brine reinjection indicated that flow occurred behind the liner from the zones identified in Table 5. The percent contribution of each of the zones is unknown, but a major portion of the reinjected brine appears to have entered the zone at 8,560 to 8,620 ft. This zone would appear to have significant commercial potential.

CONCLUSIONS

The heart of the Salton Sea Geothermal Field appears to contain previously undiscovered, deep hydrothermal zones that may be of commercial, as well as scientific interest. An extended flow test of the isolated deeper flow zones in State 2-14 will be required to provide clean fluid samples for scientific study and to more fully assess their commercial potential. Deepening the well might also lead to further discoveries of mutual value to science and industry. The SSSDP has demonstrated that difficult technical problems can be managed, to meet the objectives of scientific investigators. The key is working together to achieve a mutual understanding and balancing of the scientific objectives and the technical limitations.

Table 8. Preliminary Flow Test Results*

	Well Depth (ft)	Estimated Flow Zone(s) (ft)	Approximate Duration (hr)	Flow Rate (lb/hr)	Wellhead Temperature (°F)	Wellhead Pressure (psig)	Estimated Enthalpy** (Btu/lb)
First Test	6,227	6,120	4	600,000	400	200	400
			12	80,000	460	440	400
			2	430,000	410	220	400
			9	150,000	460	450	400
Second Test	10,564	[6,100	3	475,000	445	310	520
		6,600	24	280,000	475	450	~480
		8,800	1	700,000	460	380	480
		10,475]	4	300,000	490	485	450

* Analysis by GeothermEx, Inc.

** Based on James' correlation with TDS correction.

Geothermal Resources Council, TRANSACTIONS, Vol. 10, September 1986

SSSDP FLUID COMPOSITIONS AT FIRST FLOW TEST OF STATE 2-14

Donald E. Michels

Don Michels Associates
P.O. Box 895
Whittier, California 90608

ABSTRACT

Brine and steam were sampled on December 29 and 30, 1985. A four-step temperature cascade was established in a test section of the flowline. In this way, enthalpy data could be obtained from the chemical data.

Brine compositions, on a basis of total flow, are computed separately for Dec. 29 and 30; total dissolved solids were 25.54+0.23 and 25.47+0.036 weight percent. Carbon dioxide and hydrogen sulfide were 1664+20 and 7.01 ppm, respectively, on Dec. 30. CO_2 and H_2S comprised about 98.5 mole percent of the suite of non-condensable gases. Data on other components are tabulated.

Effective pre-flash enthalpys were 335 and 349 Btu/lb on December 29 and 30, respectively. These correspond to temperatures of 548 and 567°F. The greatest observed steam yield was 18.5 weight percent at 328°F on Dec 30.

INTRODUCTION

The Salton Sea Scientific Drilling Project (SSSDP) well, State 2-14, was test flowed on December 28-30 from the interval 6000-6227 feet. The surface facility consisted mainly of 10-inch diameter flowline. It was equipped with a four step temperature cascade, with access ports for sampling liquids and gases at each step, and terminated with a James tube and a silencer. More than 20 geochemists participated in sampling and/or analysis of the brine, steam, and related materials. This report provides the reference composition of the fluids.

The general layout of the test sections is shown in a companion paper (1) which also describes the chemical method used to determine steam fractions in the temperature cascade.

Four insulated zones in a test section were separated by orifice plates in order to set up a cascade of temperature-pressure conditions. The full flow of the geothermal fluid passed through this test section. Individual steps in the cascade involved increments in steam yields of about 1 to 8 weight percent (total flow basis). This corresponds to about 7 to 70 relative percent on a basis of steam.

One objective of sampling was to follow tracers in the steam and brine phases with enough precision to quantify those steam increments. Key tracers were natural carbon dioxide in the steam and natural chloride in the brine. Another major objective was to characterize the brine composition in terms of major and minor elemental components.

STEAM FRACTIONS AT THE SAMPLING PORTS

For Dec 30, the steam fractions at the sampling ports were determined by a chemical method (1). Results are shown here without further explanation. In addition, that method yielded thermodynamic data for the mixed-salt brines. However, the totally chemical approach could not be used for the Dec 29 situation -- no data were obtained for CO_2 in steam. Instead, the steam fractions for December 29 were computed by combining the measured chloride values with the enthalpy relationships determined in (1). The principle is similar to the description in (2).

Results are shown in Table 1. The numbering of ports is retained from field designation. Port 3 was in the first test spool, Port 6 was in the fourth. Although brine and steam sampling points were physically different on each test spool, they are given the same port numbers.

In addition to the flash fraction results, estimates of the pre-flash brine

enthalpy are obtained. In the case for Dec 29, a preflash chlorinity of 153,688 ppm, obtained in (1) for December 30, is used to derive a pre-flash enthalpy value of 335 Btu/lb. This corresponds to an effective flash temperature of 548°F. This is lower than the estimate of 567°F for Dec 30, but not unreasonable considering that the well was still in the early warming stages on Dec 29.

The flash-temperature relationships for Dec 29 and 30 are given in Figure 1. Enthalpy-temperature-composition relationships found in this work show the mixed-salt hypersaline brines have significantly smaller enthalpies than pure NaCl brines (3) of comparable concentrations and temperatures.

TABLE 1:

STEAM FRACTIONS AT SAMPLING PORTS

Dec 29, enthalpy 335 Btu/lb				
Port	3	4	5	6
°F	431	373	327	309
Flash	.10700	.14621	.17288	.18166
Dec 30, enthalpy 349 Btu/lb				
°F	455	395	346	328
Flash	.10513	.15474	.17781	.18522

BRINE SAMPLING AND PREPARATION

Two kinds of brine samples were taken, one for the chloride tracer and the other for general composition. Both were taken with the same port equipment but differed in sample handling procedures.

Brine sampling equipment is diagrammed in Figure 2. Welded to the 10-inch test spools and fully open to the two-phase flow inside, were downcomers of 4-inch diameter pipe which terminated in a system of access valves. The brine in the downcomer tends to deposit scale, so operating the blowdown valve assures that sampled liquid is relatively fresh.

A 1/4-inch (heavy wall) stainless steel tubing was passed through an access valve to tap the one-phase liquid that collected in the downcomer. The probe was integral with a section of 1/8-inch diameter stainless tubing, shaped into a coil and cooled in a water bath. Ice was used to prevent the cooling water from getting hot, but ice temperatures were avoided. A collection temperature of 100 to 140 F is considered ideal. Flow through the probe system was controlled by a valve on the cool end of the 1/8-inch tubing. Brine exited the probe system as a jet into the atmosphere. Samples were collected by directing the jet into polyethylene bottles that contained pre-weighd amounts of diluents.

Samples for general composition were collected into 50-ml bottles that contained about 30 g of 0.1N nitric acid. Enough brine was collected to make the acid:brine ratio about 5:2. The brine stream from the valve spigot was caught directly in the sample bottle without pre-measuring the brine. This technique delivers the brine from hot flowline to sample bottle in just the few seconds of travel time through the tubing. The quick dilution and acidification are considered advantageous, especially for silica. Samples of hypersaline brines are stable for many months when collected in this way.

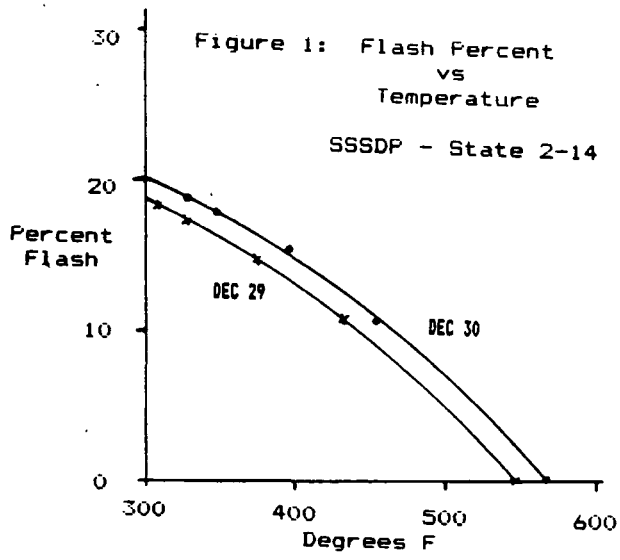

Figure 1: Flash Percent vs Temperature

SSSDP - State 2-14

Dilution factors are determined by weighings to the nearest milligram on an analytical balance. They are accurate to better than +0.0001(relative).

The acidified brine samples were reweighed in the DMA laboratory. Aliquots were taken and diluted further into 20 percent nitric acid. Subsequent analysis was by a commercial laboratory, mainly using inductively coupled plasma (ICP). Chloride was determined (independently from the oceanographic method) by titration, sulfate by turdidimetry, and ammonia by specific ion electrode.

The commercial lab results were based on volumetric standards (ppm = mg/l). These were converted to a weight basis (ppm = mg/kg) through density measurement of the 20 percent nitric acid carrier (1.145 g/ml) and the use of

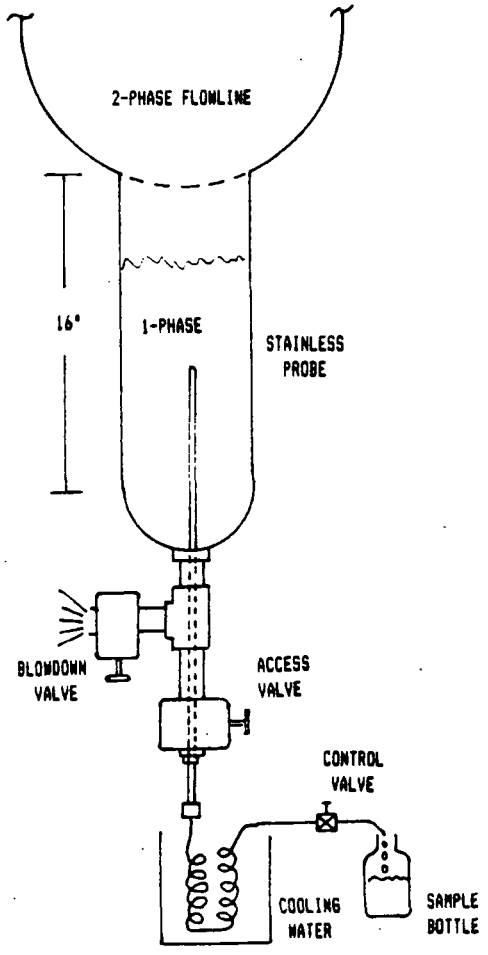

FIGURE 2: BRINE SAMPLING ARRANGEMENT

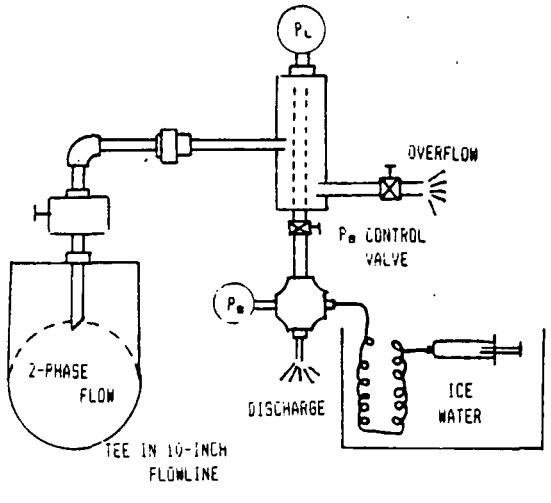

FIGURE 3: STEAM SAMPLING ARANGEMENT

P_L = Line Pressure (to 450 psig)
P_s = Syringe Pressure (12 psig)

weighings to determine the other dilution factors. Density of whole brine is near 1.2 g/ml, thus the distinction between mg/l and mg/kg is important. All concentrations referred to in this paper are on weight basis.

Samples for determination of the chloride tracer were collected similarly, except that about 100 g of distilled water was used and brine was collected to bring the mixture into the range of seawater chlorinity. (Chlorinity and chloride content are used synonymously in this report).

The mixture was reweighed and titrated immediately in a field laboratory by an oceanographic method that involved standardization by standard mean ocean water (4). Subsequently, in the home laboratory, (MIT), the titrant was restandardized and other acidified samples were analyzed. The final selected results are believed accurate to about +0.002 (relative), for single analyses. Replicate analyses yield proportionally better values.

GAS SAMPLING AND ANALYSIS

Brine-free steam samples were obtained through in-line separator devices built into the test spools. Because brine carryover occurred at some ports, a portable centrifugal separator was attached in series between the in-line separator and the gas sampling equipment. This arrangement (Figure 3) provided high quality steam samples and was used at all steam sampling ports.

Surging of pressure (and temperature) in the two-phase flowline was prominent, but steamside pressure was leveled by manual control of the steamside control valve. In principle, the surging is concommitant with incremental differences in flash fraction and hence composition of steam inside the separator. Cycle frequency in this case was about 4/minute, thus, the collections, which take 3 to 7 minutes, provided considerable averaging about the mid-range conditions.

Sampling and analysis for non-condensible gases in steam was done by a syringe method (5) modified to improve precision. A syringe clamp was used that set the working volume of the syringe to be the same for all samplings. The volume was standardized in the laboratory by weighing and calculating the temperature correction. Condensate was recovered into pre-weighed vials for re-weighing.

The principle of the syringe method (5) for CO_2 assay is to establish the pressure and volume of the gas and condensate at ice temperature. Then the amount of CO_2 in the condensate is given by the Bunsen coefficent (STP ml of gas per ml of liquid at 1 atm. gas pressure) and the gas equation is applied to the gas phase and the Bunsen volume to compute the total amount of CO_2. Calculation requires the absolute pressure of CO_2.

The non-CO_2 gases (nitrogen, methane, hydrogen, etc.) are normally determined with the CO_2 assay as an undifferentiated group. This provides data to compute a molar ratio of CO_2/non-CO_2 gases which in turn permits calculating the CO_2 pressure fractions in the other collections.

An alternative was provided by an independently determined composition of the gas mixture (6). Both compositions were used to compute CO_2 assays and each result was within the error limits of the other. The assay computations based on (6) are preferred and reported here.

Ammonia, present in the steam, is suspected to be dissolved in condensate upon formation of NH_4^+ and HCO_3^- by reaction with CO_2. It involves no significant vapor pressure in the assay and the CO_2 consumed by ammonia is disregarded.

Hydrogen sulfide was determined in the mixture of condensate and NaOH obtained from the collection regarding the other non-CO_2 gases. The mixture is stabilized in the field with zinc acetate solution and analyzed in a lab by iodometry.

TABLE 2:

SUMMARY OF GAS CONTENTS

Port	3	4	5	6
Temp	455	395	346	328
Steam Fraction	.10513	.15474	.17781	.18522
CO_2 (ppm)				
Steam	15524	10521	9462	8988
Total Flow	1662	1638	1687	1668
H_2S (ppm)				
Steam		46.2	38.3	
Total Flow		7.15	6.86	

Averages on a total flow bases:
CO_2 1664±20; H_2S 7.01

ADJUSTMENTS TO BRINE CONCENTRATIONS

Analysis by ICP in a commercial laboratory provided the basic data for cations. Lab results are adjusted by the dilution factors and carrier densities to yield gross concentrations of field samples. These gross concentrations are susceptible to further adjustments that relate to electrical charge balance.

Chloride accounts for more than 99.9 percent of the negative charge in the brine composition. The precisions and accuracys of the oceanographic chloride values are the best in the entire data set. They are also considered to be unbiased. Thus, rather than simply reporting the size of the charge imbalance between cations and anions, the cation concentrations are adjusted to match the charge of the chloride. These adjusted values are considered to be the best available representation of the brine composition.

The overall bias of the cation analysis is given by summing the cation charges and comparing the result with the chloride. For ten samples, the average bias is +0.0262 of the chloride value and the standard deviation is 0.0106. No samples show a negative bias. Thus, the gross precision of the ICP data is better than the bias and an upward adjustment is warranted.

In making the charge balance, the relative precision of each individual cation was determined from replicate analyses. These relative precision values were multiplied by nominal concentrations of the respective cations to obtain an index. The total balancing charge needed was then assigned to each cation in proportion to its index. In this way, the more abundant components carried most of the charge adjustment and no adjustment of a single cation exceeded its own analytical precision. For example, sodium carried 0.427 of the charge adjustments and five components, Na, K, Ca, Fe, and NH_4^+, collectively carried more than 0.94 of the adjustment.

FIELD COMPOSITION OF BRINES

The field compositions reported in Table 3 include the charge balancing procedure described above. Dilution factors, described earlier, are also incorporated. Averages are used where replicates were available (Ports 3, 4, and 6 on Dec 30).

There was no sample for Port 6 on Dec 29. The listing in Table 3 is based on the average of the other ports on Dec 29, with conversions made through the flash

fraction values as appropriate.

Sulfate determinations were made on two samples; Dec 30, Ports 3 and 4. Values are 136 and 117 ppm, respectively. Analytical detection limit was about 50 ppm, considering dilutions of the samples.

Silica concentrations show marked reductions through the test system. The implied deposition rate is much greater than indicated by thicknesses of scale deposits. Reasons for the mismatch deserve study.

TABLE 3:
FIELD COMPOSITIONS OF BRINE AT SAMPLE PORTS

DAY	DECEMBER 29				DECEMBER 30			
HOUR	1750	1755	1755		1215	1341	1430	1255
PORT	3	4	5	6	3	4	5	6
CODE	B	I	J	CALC	G	C	A	E
FLASH	.10700	.14621	.17288	.18166	.10513	.15474	.17781	.18522
SODIUM	58658	61988	64348	64574	58756	62405	63794	64753
CALCIUM	29939	31435	33331	33052	29428	30995	32614	32967
POTASSIUM	18357	19823	20419	20451	18398	19488	20109	20316
IRON	1682	1834	1906	1892	1697	1774	1857	1897
MANGANESE	1533	1654	1704	1707	1531	1651	1688	1702
ZINC	571	604	626	628	559	603	616	624
SILICA	511	470	342	465	530	466	434	380
STRONTIUM	453	482	499	500	450	480	496	498
AMMONIUM	389	364	383	397	382	413	361	415
BORON	282	304	314	314	281	300	309	311
BARIUM	220	236	251	246	218	224	237	243
LITHIUM	212	226	237	236	211	222	232	235
LEAD	108	114	119	119	105	108	115	122
MAGNESIUM	41	45	43	45	41	40	45	48
OCEAN CL	170930	179160	186890	188589	171720	181800	186900	188600
SUM	283936	298736	311414	313215	284307	300968	309808	313109

TABLE 4:

	ELEMENT/LITHIUM RATIOS				ELEMENT CONCENTRATIONS			
	DEC 29		DEC 30		DEC 29		DEC 30	
	AVG	U.M.	AVG	U.M.	AVG	U.M.	AVG	U.M.
SODIUM	274.15	1.96	277.86	.97	52843	299.11	52661	50.94
CALCIUM	140.31	.90	139.89	.17	27048	277.91	26515	119.20
POTASSIUM	86.82	.62	87.07	.21	16736	231.68	16502	17.82
IRON	8.03	.07	8.03	.02	1548	29.81	1522	7.25
MANGANESE	7.25	.05	7.31	.04	1397	18.55	1385	6.00
ZINC	2.67	.02	2.67	.01	514	3.10	506	1.61
SILICA	1.98	.31	2.05	.14	330	56.07	387	25.90
STRONTIUM	2.12	.01	2.14	.01	409	3.28	405	.79
AMMONIUM	1.69	.10	1.78	.05	325	15.48	336	8.56
BORON	1.33	.01	1.34	0.00	257	3.25	253	.44
BARIUM	1.05	.01	1.02	.01	202	3.62	194	1.49
LITHIUM	1.00		1.00		193	2.44	190	.63
LEAD	.51	0.00	.50	.01	98	.65	95	1.36
MAGNESIUM	.19	.01	.19	0.00	37	1.06	36	1.00
OCEAN CL	795.91	7.43	810.82	2.71	153410	1087	153668	0
SUM					255396	2257	254654	351

PRE-FLASH BRINE COMPOSITION

The pre-flash compositions for the two sampling days are given in the right half of Table 4, in terms of averages and uncertainties of the mean (U.M.). Table 4 is derived from the Table 3 values multiplied by (1-f) and averaged over each days samples. The averages are different by amounts that approach significance in terms of the U.M. values.

An alternative comparison of the brine compositions on the different days can be made through ratios of components. Specifically, lithium determinations are the most reproducible, based on the replicate samples. Thus, the ratio of element concentration to the lithium concentration is a sensitive indicator of variation between samples.

The averages and U.M. values for element/lithium ratios are given in the left half of Table 4. The differences in the U.M. values, vis-s-vis the two sampling days, are relatively less than their concentration counterparts in the other side, as expected.

ACKNOWLEDGEMENTS

I am indebted to Andy Campbell and Chris Measures for the oceanographic chloride analyses, to Al Truesdell for sharing equipment and data, and to Wilfred Elders for continued motivation. This work was performed through the University of California, Riverside and supported by National Science Foundation Grant EAR 8303557.

REFERENCES

1. Michels, D. E., 1986, A chemical method for measuring steam quality in two-phase flowlines: Geoth. Res. Coun., Transactions, this volume.
2. Ellis, A.J. and W.A.J. Mahon, 1977, Geochemistry and geothermal systems: Academic Press, New York, p. 230.
3. Haas, J.L., 1976, Thermodynamic properties of the coexisting phases and thermochemical properties of the NaCl component in boiling NaCl solutions: U.S. Geol. Surv. Bul. 1421-B Revised, 71 pp.
4. Campbell, Andy, and Chris Measures, 1986, MIT Department of Oceanography, personal communication.
5. Michels, D. E., 1978, CO_2 in geothermal steam - a rapid, precise, and accurate field assay technique: Geoth. Res. Coun. Trans, v. 2, p. 445-8.
6. Alfred Truesdell, 1986, personal communication.

Geothermal Resources Council, TRANSACTIONS, Vol. 10, September 1986

SALTON SEA SCIENTIFIC DRILLING PROJECT: SCIENTIFIC PROGRAM

J. H. Sass[1] and W. A. Elders[2]

(1) On-Site Science Manager, U.S. Geological Survey, Flagstaff, AZ 86001
(2) Chief Scientist, University of California, Riverside, CA 92521

ABSTRACT

State 2-14, the Salton Sea Scientific Drilling Project, was spudded on October 24, 1985, and reached a total depth of 10,564 ft (3.2 km) on March 17, 1986. There followed a period of logging, a flow test, and downhole scientific measurements. The scientific goals were integrated smoothly with the engineering and economic objectives of the program and the ideal of "science driving the drill" in continental scientific drilling projects was achieved in large measure. The principal scientific goals of the project were to study the physical and chemical processes involved in an active, magmatically driven hydrothermal system. To facilitate these studies we attached high priority to four areas of sample and data collection, namely: (1) core and cuttings, (2) formation fluids, (3) geophysical logging, and (4) downhole physical measurements, particularly temperatures and pressures. In all four areas, the results obtained were sufficient to meet the stated scientific goals.

INTRODUCTION

The first deep well of the U.S. Continental Scientific Drilling program was drilled to a depth of 3.22 km in the Salton Sea Geothermal Field of the Imperial Valley near Calipatria, California (Figure 1). The well is located near the southeast end of the Salton Sea (Figure 1) in the Salton Trough, a tectonic depression within the transition zone between the spreading centers of the Gulf of California and the San Andreas transform fault (Elders et al., 1972). The trough is a fluvial sedimentary basin with associated evaporitic and lacustrine deposits. Within the trough and adjacent crystalline basement, heat flow is very high, averaging about 140 mW m^{-2} (Lachenbruch et al., 1985). Within the region of high heat flow are zones of extraordinarily high heat flow like the Salton Sea Geothermal Field, where heat flow averages about 400 mW m^{-2} (Sass et al., 1984) and temperatures as high as 370°C have been encountered at only 2 km depth. The Salton Sea Field is also characterized by brines with total dissolved solids in excess of 200,000 ppm (Muffler and White, 1969).

The well was drilled using standard oilfield technology, modified to take account of the high temperatures; however, the philosophy was quite different from that employed in conventional exploration drilling, chiefly in that scientific objectives had priority over economic and engineering concerns where safety and well integrity were not compromised. This was accomplished through a unique grouping of specialists termed the "Site Coordination Committee" consisting of the site manager, drilling supervisor, toolpusher, DOE technical representative, on-site science manager, and chief scientist, with input from coring engineers, mud chemists, and others as deemed appropriate.

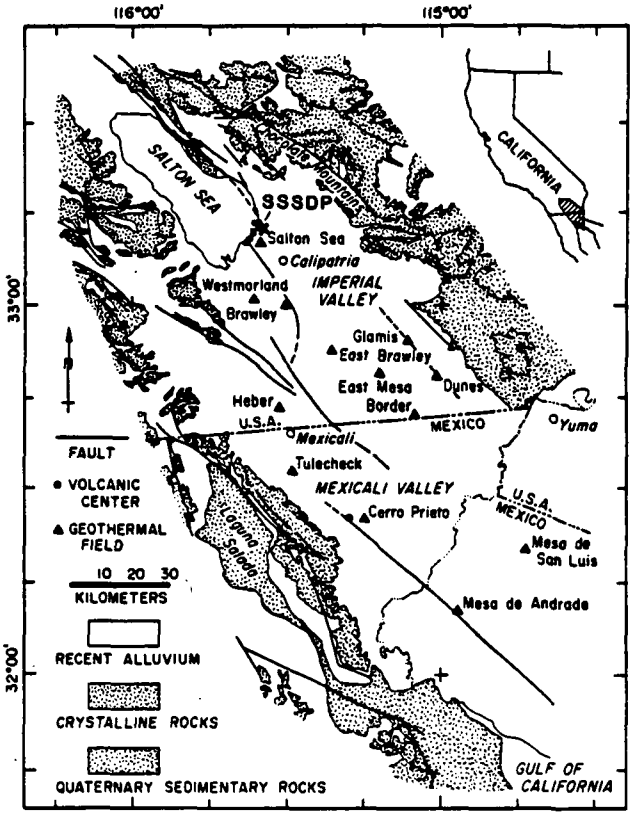

Figure 1. Major faults and geothermal fields of the Salton Trough.

The primary scientific goals of the Salton Sea Scientific Drilling Project (SSSDP) were to study active physical and chemical processes in a magmatically driven hydrothermal system. As the well is twice as deep as typical production wells in the field, the temperatures, pressures, salinities, and flow rates encountered also provided an opportunity for a preliminary study of the deeper reservoir characteristics and geothermal energy potential.

Forty proposals were approved by the Science Coordinating Committee of the SSSDP. Of these, nearly half were concerned with geochemical studies of rock, fluid, and gas including the organic chemistry of fluids. Twenty-five percent of the proposals involved petrologic and geophysical studies of core and cuttings. The remaining proposals were concerned with downhole sampling, geophysical logging, other geophysical measurements, and technology development involving the downhole deployment of geophysical instruments like seismometers, temperature-pressure sensors, flowmeters, and gravimeters.

Given this program, the recovery of core, cuttings, fluid, and gas samples had the highest priority. To maximize the interpretation of data obtained from these samples, and to allow interpretation in zones where samples could not be obtained, high priority was also assigned to the collection of an integrated set of downhole data including geophysical logs, temperature measurements, and downhole fluid samples. A time-depth plot (Figure 2) summarizes the amount of time devoted to the various scientific and engineering activities. A preliminary progress report of these activities by the USGS on-site science management team (which coordinated and supervised all science activities during the drilling phase) has been published (Sass et al., 1986).

CORE AND CUTTINGS

At least 1 kg of cuttings was retained at 6- to 9-m intervals to about 900 m and at 3-m intervals below that depth. Each sample consisted of one 500 mL cup of washed sample and three cups of unwashed samples containing drilling mud and additives as well as rock cuttings. Cuttings were not recovered in zones of complete loss of drilling fluid between 2022 and 2097 m, 2616 and 2682 m, 2719 and 2750 m, and between 3193 and 3220 m (total depth). In some zones of partial fluid loss, cuttings samples were contaminated by

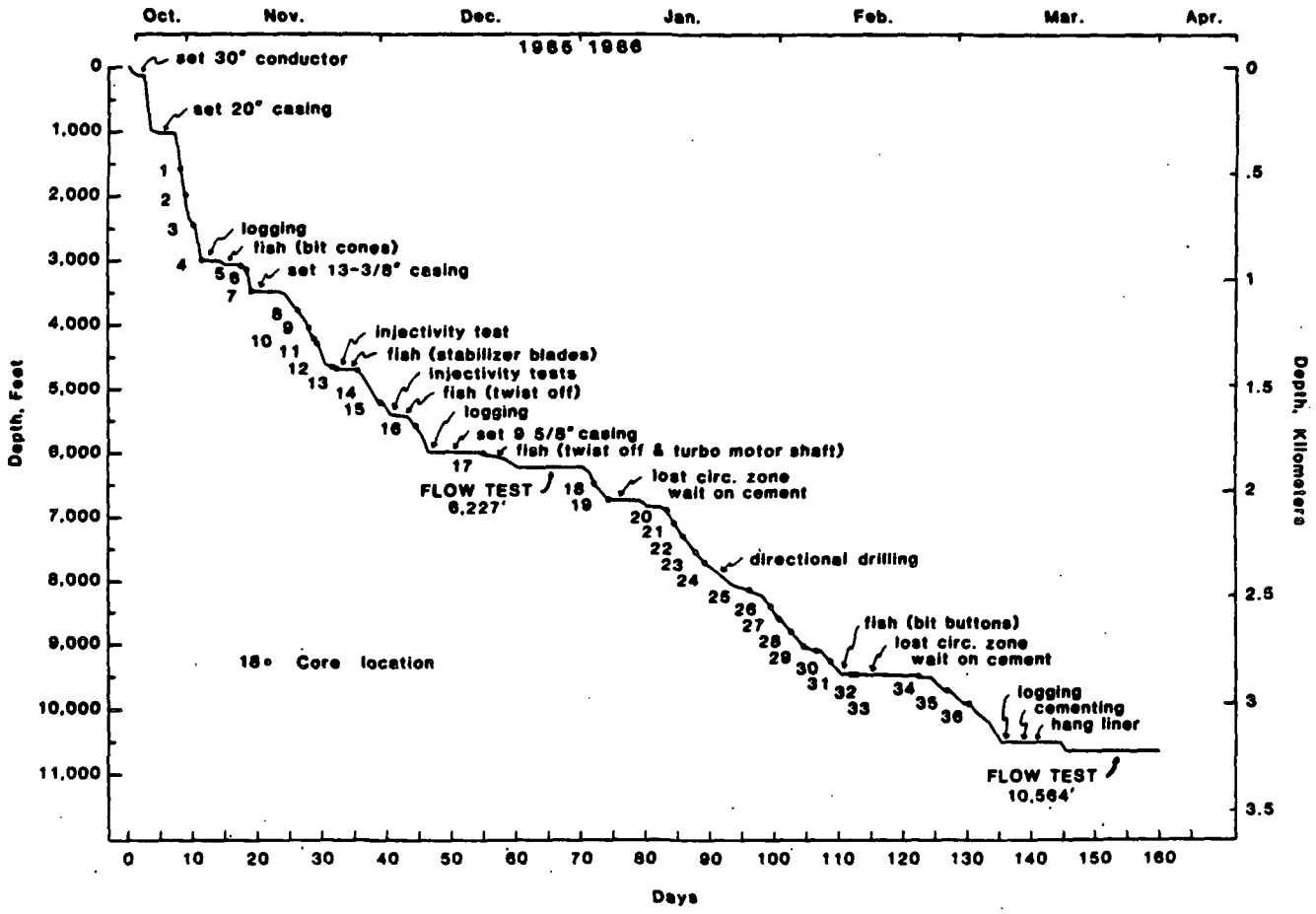

Figure 2. SSSDP depth/progress chart. Core numbers correspond to those in Table 1.

lost circulation material and rock material flowing back into the well from partially plugged lost circulation zones above the bit.

The coring plan developed before drilling envisaged 43 coring attempts between 1700 and 10,000 ft (518 and 3048 m) with an average interval of 200 ft between cores in the depth range 3,000 to 10,000 ft. We hoped to recover 1,200 to 1,500 ft (366 to 460 m), depending on the number of 30-ft core runs as opposed to 60-ft runs. A total of 36 cores were attempted, of which 2 (marked "N/A" in the footage/recovery columns of Table 1) were obtained in junk baskets or junk subs during fishing operations. Percentage recovery was reasonable over the entire depth, but the footage drilled declined precipitously below 5,000 ft (1,500 m) primarily because the rock was fractured either in situ or by the release of stress by the core bit with the result that the barrel jammed frequently, often after only a few feet had been cored. In addition, some cores were drilled "blind" (no circulation) which made coring even more difficult.

Table 1. History of coring attempts and recovery, SSSDP

Date	Core	Ft. drilled	Marked core interval	% recovery
10/31/85	1	25	1553-1577.6	98.4
11/01/85	2	30	1983-2012.2	97.3
11/02/85	3	30	2448-2478.0	100.0
11/04/85	4	60	2970-3028.4	97.3
11/08-09/85	5	N/A	3083-3087.0	N/A
11/11/85	6	60	3107-3161.7	91.2
11/12/85	7	35	3470-3504.0	97.1
11/19/85	8	60	3790-3846.6	94.3
11/20/85	9	60	4007-4069.9	100.0
11/21/85	10	40	4241-4300.4	99.0
11/22/85	11	36	4301-4338.6	100.0
11/25/85	12	38	4643-4680.5	98.6
11/26/85	13	5	4681-4683.0	40.0
11/27-28/85	14	N/A	4718-4718.5	N/A
12/02/85	15	30	5188-5219.2	100.0
12/07/85	16	17.5	5574-5591.5	100.0
12/19/85	17	18	6026-6040.8	82.2
01/03/86	18	11	6506-6517.0	100.0
01/06/86	19	13	6758-6766.0	61.5
01/14/86	20	9	6880-6889.0	100.0
01/16/86	21	9	7100-7107.0	77.7
01/18/86	22	13	7300-7311.5	88.5
01/19/86	23	30	7547-7574.5	91.6
01/20/86	24	30	7708-7738.0	100.0
01/28/86	25	29	8133-8161.0	96.5
01/31/86	26	6	8395-8400.0	83.3
02/01/86	27	19	8585-8597.0	63.2
02/03/86	28	7	8800-8804.5	64.3
02/05/86	29	23	9004-9009.5	23.9
02/07/86	30	3	9095-9098.0	100.0
02/10/86	31	6	9248-9251.5	58.3
02/13/86	32	5	9453-9455.3	46.0
02/14/86	33	15	9458-9463.0	33.3
02/23/86	34	4	9473-9475.0	50.0
02/28/86	35	4	9694-9697.5	87.5
03/02/86	36	5	9907-9908.0	20.0

Even though there were problems, we are satisified with the total recovery of about 730 ft (224 m) in terms of its utility in characterizing the stratigraphy of the well and in satisfying the requirements of the principal investigators interested in physical properties, petrology, and geochemistry of solid rock samples. In view of the difficulties experienced here using the best in off-the-shelf technolgy and experienced coring personnel, it would seem that coring in ultra-deep and/or ultra-hot wells will require considerable research and redesign of conventional coring hardware.

FLOW TESTS

The fluid sampling plan envisaged two or even three discrete flow tests at shallow (1 km), intermediate (2 km), and total depth to allow estimates of salinity and other concentration gradients within the brines. Only one minor (15 bbl/hr) loss zone was encountered above 1 km. Injectivity tests were performed at depths of 4,684 and 5,418 ft (1,428 and 1,651 m), but no significant potential for flow was detected. At that stage, it was decided not to attempt a shallow flow test and 9 5/8" casing was set at 6,000 ft (1,829 m) (Figure 3). A loss zone associated with abundant epidote was encountered slighly below the casing (6,119 to 6,135 ft), and the first flow test was run in late December of 1985 (Figure 2). Only a few hundred barrels of fluid had been lost to the formation, and the fluids cleaned up very rapidly, resulting in very satisfactory samples and confident estimates of total dissolved solids, temperature, enthalpy, and other important parameters. The observed flow rate and enthalpy demonstrated the commercial potential of this well.

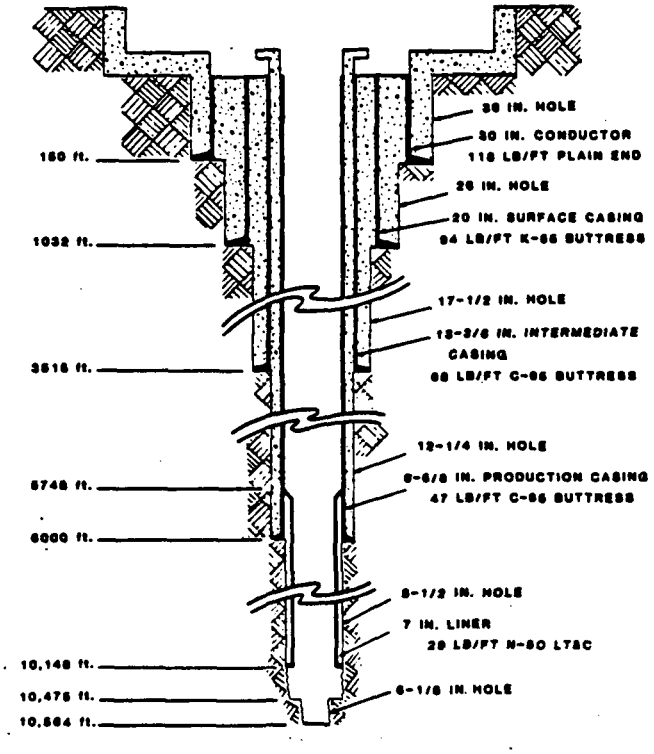

Figure 3. Casing configuration, SSSDP.

From 6,637 to 9,500 ft (2 to 2.9 km), a succession of loss zones (reflecting fracture permeability) was encountered. Enormous quantities of fluid (several tens of thousands of barrels) were lost and a large amount of lost circulation material and cement were used to regain circulation and control losses. When circulation was again lost near total depth (10,475 ft), temperature logs indicated that fluid loss was occurring at the bottom of the well. The zone was then plugged off with cement, a liner was set (but not cemented) at 10,135 ft (3,089 m), the cement plug was drilled out, and an additional 89 ft of hole was drilled with no returns. Following this, the well was flowed, but the brine produced was contaminated, not only by the fluid lost in the bottom zone but probably by inflow around the liner from a depth of about 8,600 ft (2,621 m); the results were considerably less satisfactory than those obtained during the first flow test. The duration of the flow test was limited by the 36,000-bbl (5.7×10^6 L) capacity of the brine pond.

GEOPHYSICAL LOGGING

No open-hole geophysical logs were attempted in the 26-inch (0.66 m)-diameter hole, which was 1,032 ft deep (Figure 3) and into which the 20-inch (0.51 m)-diameter surface casing was set. Because of the large hole diameter, we thought that record quality would be poor, and that if open-hole data in the upper 300 m were needed, a slim hole could be drilled to this depth easily and inexpensively. Complementary and, in some cases, redundant sets of logs were run at the 3,000 to 3,500 ft casing point and 6,000 ft casing point (Figure 3) by both Schlumberger and USGS Water Resources Division's Research Logging Unit (Tables 2 and 3). The Schlumberger logs allowed a comparison and correlation with commercial logs from other wells in the Salton Sea Field. The USGS logs provided both a comparison and confirmation of such things as depth registration (gamma-ray logs) and an extension of the commercial logs. Lawrence Livermore National Laboratory (LLNL) provided at the site a system capable of reading and displaying digital data from both USGS and commercial logs. This proved useful for real-time analysis and interpretation. A second commercial company ((Dialog) carried out a casing caliper log on March 30, 1986, to assess the condition of the 9 5/8-inch casing (Figure 3). Several attempts were made by the USGS (Table 3) to obtain televiewer logs, particularly in loss zones and flow zones. At the 6,000-ft casing point (Figure 3) the televiewers were bedeviled by mechanical and electrical problems. Below 6,000 ft, televiewer records were obtained, but because of deleterious effects of viscous mud, lost circulation material, and cement, a large percentage of the energy was absorbed, resulting in poor record quality. The same comment applies to the acoustic logs made by both Schlumberger and USGS, although useful data were obtained in both cases.

Table 2. Dates, intervals, and types of Schlumberger logs, SSSDP

Date	Logged Interval (ft.)	Logs[a]
11/04/85	1,032 to 3,008	1-6
11/13/85	2,900 to 3,525	1-6
11/17/85	30-3,523	7
12/09/85	3,520 to 5,988	1-6
12/18/85	50-5,670	8
12/18/85	190-5,696	7
03/10/86	6,020-8,813	9

[a]
1) Dual Induction
2) Compensated Neutron-Formation Density
3) Borehole Compensated Sonic
4) Sonic Waveforms
5) Gamma Ray
6) 4-arm Caliper
7) Cement bond
8) Temperature
9) Deep Induction

Table 3. History of USGS geophysical logs, SSSDP.

Date	Log	Interval (ft.)	Comments/Results
11/05/85	Temp	100-2,998	Before circulation.
11/05/85	Nat Gamma	9-3,000	Two second time constant.
11/06/85	Temp/Caliper	100-2,998	After circulation.
11/06/85	Televiewer	N/A	No useful logs due to mud density & problems with tools.
11/06/85	Temp	100-3,000	Many stationary readings.
11/06/85	Caliper	983-2,950	
11/06/85	Acoustic DT	1,000-2,950	2 and 3 ft. spacing.
11/07/85	Waveform		2 microsecond sampling.
11/07/85	Temp	2,500-3,000	Stationary readings temperature vs. time.
11/07/85	Nat Gamma	1,000-2,980	
11/07/85	Gamma Spec	1,000-2,980	
11/07/85	Temp	2,500-2,998	Stationary readings at bottom.
12/04/85	Temp		Stationary readings at bottom.
12/09/85	Temp	2,700-5,984	Build up, stationary readings on bottom.
12/10/85	Temp/Caliper	3,375-6,000	
12/10/85	Televiewer		Both televiewers failed.
12/11/85	Nat Gamma	3,400-6,000	Tool did not work.
12/11/85	Gamma Spec		Analyzer failed after one spectrum.
12/11/85	Single Point Resistivity		Burned up tool.
12/11/85	Acoustic DT		Data marginal due to mud density.
12/11/85	Acoustic Full Wave		Total waveforms.
12/11/85	Temp/Caliper	3,400-5,120	Tool hung up.
12/12/85	Caliper	3,500-6,000	
12/12/85	Neutron	2,900-5,980	
12/23-24/85	Temp	3,500-6,230	
12/26/85	Temp	300-6,240	
02/15/86	Temp	6,000-10,400	
03/08/86	Temp	0-10,500	Pre-flow test.
03/12/86	Temp	0-10,500	Pre-flow test.
03/12/86	Televiewer	6,000-6,500	Log through first flow zone, marginal pictures.
03/13/86	Sonic	6,000-8,000	Several passes.
03/27/86	Temp	0-10,220	After 1st phase of reinjection.
03/29-30/86	Gamma Ray	5,690-10,000	
03/29-30/86	Neutron	5,770-10,000	
03/31-04/1	Temp	0-10,200	
04/07/86	Temp	0-9,660	Insulation resistance declining, Run terminated.

Because of financial constraints, the commercial loggers could only be brought in on specific occasions like casing points. On the other hand, the USGS Water Resources Division committed its geothermal research logging truck for the duration of the period from 3,000 ft to total depth. This gave us the flexibility to run logs, particularly temperature logs, when drilling was suspended (e.g., while waiting for fishing tools). This capability was enhanced by the fact that the on-site science managers were trained in running the logging unit and could do so literally on a moment's notice.

Apart from the lack of useful televiewer data and sonic data of questionable quality, the chief gap in the SSSDP logging program was caused by the failure of a motor in the USGS high-temperature 3-arm caliper. Because of repeated trips below 6,000 ft (Figure 2), the wellbore was doubtless over bit gauge over much of that interval, contributing to the loss of acoustic energy from both the televiewer and sonic velocity tools. Although records of excellent quality were obtained to nearly total depth with both passive gamma and neutron tools, their interpretation will be hampered by the lack of a caliper log. The time series of temperature logs is continuing throughout the six-month shut-in period. By the date of this meeting, a joint USGS/LLNL report is expected to be released, including hard copies of all geophysical logs, comparisons of USGS and Schlumberger logs, and some interpretive comments on the logs. A separate report will be issued on the post-drilling temperature logs.

DOWNHOLE EXPERIMENTS

Other downhole experiments included temperature-pressure measurements during and after flow and an attempt at measuring differential flow rates using a spinner-flow meter (Table 4). These measurements were made with developmental "slickline" type tools commissioned by Sandia Corporation (see C. C. Carson, this volume) and assembled by the Kuster Company. They were essentially conventional slickline tools with modified transducers and with recorders housed in dewars with a design operating period of 10 to 12 hours at 400°C. With the exception of the spinner, these tools functioned well and produced useful data on temperature and pressure. An electronic slickline tool which measures both temperature and pressure was built by Service Systems Engineering and is being used primarily for the time series of temperature logs to establish formation temperature over the entire length of the well.

Another category or downhole experiment involved fluid sampling. This proved exceptionally difficult under the hostile conditions encountered in the well. In fact, out of a total of 11 attempts using three different samplers only one was completely successful and an additional run obtained a liquid sample but no gas (Table 4). An attempt to retrieve fluid inclusions by annealing fractured quartz crystals in the brine within the lowermost producing zone was frustrated when the wireline broke because of corrosion, leaving the sample buried in fill near the bottom of the well.

Other experiments involving downhole instruments included a vertical seismic profile experiment using both shear- and compressional-wave vibrators and a downhole gravity experiment (Table 4). Both experiments yielded useful data.

Table 4. Downhole Experiments, SSSDP.

Date	Depth (ft)	Experiment	Comments/Results
a) 1st Flow Test - 6,220 ft.			
12/30/85	6200	Kuster T/P	Log during flow and buildup after shutin. Well bottom hole temp. (BHT) 305 ±5°C.
12/31/85	6200	LANL/Sandia downhole fluid sampler	Two attempts: 1st failed due to brine flashing upon entry into sample bottle and clogging port. 2nd failed due to malfunction of battery system.
(b) 2nd Flow Test - 10,564 ft.			
03/21/86	0-5,000	Kuster spinner/ pressure	Spinner failed at 5,000 ft.
03/21/86	0-10,000	Kuster T/P	Baseline error on temp chart.
03/22/86	0-10,400	Kuster T/P	BHT 350 ±10°C.
03/22-23/86	10,400	1st LANL downhole fluid sampler	No sample due to seal failure causing motor to flood and short out.
03/23/86	10,400	2nd LANL	No sample due to seal failure.
03/23/86	10,400	1st Leutert downhole fluid sampler	Failure due to LCM clogging bullnose.
03/23/86	10,200	2nd Leutert	Clock stopped so canister did not close.
03/23/86	10,200	3rd Leutert	O-rings on sampler bottle failed.
03/23-24/86		USGS Bethke fluid inclusion	Wireline broke leaving tool in bottom of hole. One fishing attempt with no recovery.
03/25/86	10,200	3rd LANL	Sample bottle returns empty.
03/25/86	10,200	4th LANL	Recovered 1.5 liters liquid and .5 liter gas sample.
03/25/86	10,200	5th LANL	Bottle did not open.
03/25/86	10,200	LBL fluid sampler	Recovered 1 liter unpressurized fluid.
03/27-29/86	50-5,650	LBL- Vertical Seismic Profile	Two good data sets with vibrators on drill pad and 1/2 mile off pad. 3rd data set with tool in liner produced too much noise. 4th run tool shorted out.
03/30-31/86	6,000	LLNL downhole gravity	Recovered good data with gravimeter ascending hole from 6000'.
(c) Shut in Period, April-September, 1986			
04/08/86	10,080	Digital T/P	Calibration off on temp tool.
04/22/86	10,080	Kuster T	Stops at 2,016, 4,032, 6,048, 8,064, 10,080.
04/22/86	10,080	Digital T/P	Same stops as above.

*T, temperature; P, pressure

SUMMARY AND CONCLUSIONS

The SSSDP well exceeded target depth, and a comprehensive set of cuttings, cores, and downhole logs was obtained. Two flow tests of different depth were successfully completed, although interferences between different producing horizons will make the data from the second test difficult to interpret. Temperature logging to establish the equilibrium profile will be completed by September 1986. A proposal for further long-term flow tests and to deepen the well a further 1,000 m is now under consideration. If successful, these activities would greatly increase the scientific yield of the SSSDP.

In an early memo (March 8, 1985), the Science Experiments Committee stated that "The SSSDP will be a success if we obtain and release to the public domain drill cuttings, cores, fluid samples, temperature measurements, and a limited suite of wireline logs from a temperature regime that has not previously been adequately sampled and tested." There is a wealth of data and samples, in some instances exceeding our early expectations, and by the standards enunciated in March of 1985, the SSSDP has been a resounding success.

ACKNOWLEDGMENTS

The work described herein could not have been accomplished without the wholehearted cooperation and dedication of all the scientific investigators involved. We thank the management, technical, and drilling staff for their conscientiousness and their sensitivity to the needs of the scientific program. James Mehegan and his assistants at U.C. Riverside played a valuable role in logging, cataloging, and describing core and cuttings samples.

We are especially indebted to our colleagues, John Hendricks, Susan Priest, and Lori Robison, who obtained many of the data and helped to coordinate and facilitate the collection of the remainder.

We thank Arthur Lachenbruch and Robert Nicholson for constructive comments.

W. A. Elders acknowledges support by NSF grant No. EAR 8303557.

REFERENCES

Elders, W. A., Rex, R. W., Meidav, T., Robinson, P. T., and Biehler, S., 1972. Crustal spreading in Southern California. The Imperial Valley and Gulf of California formed by rifting apart of a continental plate. Science, v. 178, no. 4056, p. 15-24.

Lachenbruch, A. H., Sass, J. H., and Galanis, S. P., Jr., 1985. Heat flow in southernmost California and the origin of the Salton trough. Jour. of Geophys. Res. v. 90, no. B8, p. 6709-6736.

Muffler, L. J. P., and White, D. H., 1969. Active metamorphism of upper Cenozoic sediments in the Salton Sea Geothermal Field and the Salton trough, southeastern California. Geol. Soc. Am. Bull., v. 80, p. 157-182.

Sass, J. H., Galanis, S. P., Jr., Lachenbruch, A. H., Marshall, B. V., and Munroe R. J., 1984. Temperature, thermal conductivity, heat flow, and radiogenic heat production from unconsolidated sediments of the Imperial Valley, California. U.S.G.S. Open-File Report 84-490, 38 pp.

Sass, J. H., Hendricks, J. D., Priest, S. S., and Robison, L. C., 1986. The Salton Sea Scientific Drilling Program--A progress report. 1986 McKelvey Forum, U.S.G.S. Circular 974, p. 60-61.

A COMPENDIUM OF REPORTS ON THE SALTON SEA SCIENTIFIC DRILLING PROJECT

FOREWORD

The SALTON SEA SCIENTIFIC DRILLING PROJECT (SSSDP) was an investigation of a hot, hypersaline, active geothermal system, on the delta of the Colorado River in Southern California. It was one of the first major scientific drilling projects of the U.S. National Continental Scientific Drilling Program. Funding for the drilling and engineering came from the Geothermal Technology Division of the U.S. Department of Energy and the major funding for the scientific program from the National Science Foundation, the Office of Basic Sciences of the Department of Energy, and the United States Geological Survey.

Symposia reporting the results of the SSSDP were held at the annual meeting of the American Geophysical Union in Baltimore in May 1987, and the annual meetings of the Geothermal Resources Council, in Palm Springs in September 1986, and in San Diego in October 1988. This compendium contains reprints of selected articles arising from these symposia, which originally appeared in the "Journal of Geophysical Research", the "Transactions of the Geothermal Resources Council", and (in one case) the journal "Economic Geology". We thank respectively the American Geophysical Union, the Geothermal Resources Council, and the Society of Economic Geologists for permission to use their copyrighted material.

The reports included were selected and compiled by:-

Wilfred A. Elders,
Chief Scientist of the SSSDP,
Center for Geothermal Research,
Institute of Geophysics and Planetary Physics,
University of California,
Riverside, California, 92521, U.S.A.

Distribution of this compendium was made possible by funds provided under National Science Foundation Grant EAR-8618703.

TABLE OF CONTENTS

The reports reprinted here are presented in four sections with the original pagination maintained as follows:

Tarif, P.A., Wilkens, R.H., Cheng, C.H., and Paillet, F.L., "Laboratory Studies of the Acoustic Properties of Samples From the Salton Sea Scientific Drilling Project and Their Relation to Microstructure and Field Measurements," pp 13,057-13,068.

Herzig, C.T., and Elders, W.A., "Nature and Significance of Igneous Rocks Cored in the State 2-14 Research Borehole: Salton Sea Scientific Drilling Project, California," pp 13,069-13,080.

Cho, M., Liou, J.G., and Bird, D.K., "Prograde Phase Relations in the State 2-14 Well Metasandstones, Salton Sea Geothermal Field, California," pp 13,081-13,103.

Shearer, C.K., Papike, J.J., Simon, S.B., Davis, B.L., and Laul, J.C., "Mineral Reactions in Altered Sediments From the California State 2-14 Well: Variations in the Modal Mineralogy, Mineral Chemistry, and Bulk Composition of the Salton Sea Scientific Drilling Project Core," pp 13,104-13,122.

Caruso, L.J., Bird, D.K., Cho, M., and Liou, J.G., "Epidote-Bearing Veins in the State 2-14 Drill Hole: Implications for Hydrothermal Fluid Composition," pp 13,123-13,134.

Bird, D.K., Cho, M., Janik, C.J., Liou, J.G., and Caruso, L.J., "Compositional, Order/Disorder, and Stable Isotope Characteristics of Al-Fe Epidote, State 2-14 Drill Hole, Salton Sea Geothermal System," pp 13,135-13,144.

Charles, R.W., Janecky, D.R., Goff, F., and McKibben, M.A., "Chemographic and Thermodynamic Analysis of the Paragenesis of the Major Phases in the Vicinity of the 6120-Foot (1866 m) Flow Zone, California State Well 2-14," pp 13,145-13,158.

Roedder, E., and Howard, K.W., "Fluid Inclusions in Salton Sea Drilling Project Core: Preliminary Results," pp 13,159-13,164.

Thompson, J.M., and Fournier, R.O., "Chemistry and Geothermometry of Brine Projects From the Salton Sea Scientific Drill Hole, Imperial Valley, California," pp 13,165-13,174.

Hammond, D.E., Zukin, J.G., and Ku, T.L., "The Kinetics of Radioisotope Exchange Between Brine and Rock in a Geothermal System," pp 13,175-13,186.

Section C

Reprint from ECONOMIC GEOLOGY, VOLUME 83, 1988.

McKibben, M.A., Andes, J.P., and Williams, A.E., "Active Ore Formation at a Brine Interface in Metamophosed Deltaic Lacustrine Sediments: The Salton Sea Geothermal System, California," pp 511-523.

Section D

Reprints selected from GEOTHERMAL RESOURCES COUNCIL TRANSACTIONS, VOLUME 12, 1988.

Herzig, C.T., and Elders, W.A., "Probable Occurrence of the Bishop Tuff in the Salton Sea Scientific Drilling Project Borehole, Salton Sea Geothermal System, California," pp 115-120.

McKibben, M.A., Eldridge, C.S., and Williams, A.E., "Sulfur and Base Metal Transport in the Salton Sea Geothermal System," pp 121-125.

Williams, A.E., "Delineation of a Brine Interface in the Salton Sea Geothermal System, California," pp 151-157.

SECTION A

Reprints selected from the GEOTHERMAL RESOURCES COUNCIL TRANSACTIONS, VOLUME 10, 1986.

Aducci, A.J., Klick, D.W. and Wallace, R.H., "Management of the Salton Sea Scientific Drilling Program," pp 445-448.

Harper, C.A., and Rabb, D.T., "The Salton Sea Scientific Drilling Project: Drilling Program Summary," pp 455-459.

Michels, D.E., "SSSDP Fluid Compositions at the First Flow Test of State 2-14," pp 461-465.

Sass, J.H., and Elders, W.A., "Salton Sea Scientific Drilling Project: Scientific Program," pp 473-478.

MANAGEMENT OF THE SALTON SEA SCIENTIFIC DRILLING PROGRAM

Anthony J. Adducci[1] Donald W. Klick[2] and Raymond H. Wallace, Jr.[3]

(1) DOE-SFO, 1333 Broadway, Oakland, CA 94612
(2) U.S. Geological Survey, 905 National Center, Reston, VA 22092
(3) U.S. Geological Survey, 905 National Center, Reston, VA 22092, on detail to Department of Energy (GTD), 1000 Independence Avenue, SW, Washington, DC 20585

ABSTRACT

The Salton Sea Scientific Drilling Program was undertaken by the Department of Energy, the National Science Foundation, and the U.S. Geological Survey in order to investigate, by drilling a well and conducting scientific experiments, the roots of the Salton Sea hydrothermal system. A two-element organizational structure was established to focus on integration of the drilling and engineering operations with the scientific activities. This management plan, the delegation of site-operational authority to an on-site coordinating group, and the cooperative spirit of the participants have resulted in achievement of the drilling, engineering, and scientific objectives of the program.

INTRODUCTION

The Salton Sea Scientific Drilling Program (SSSDP) was undertaken by the Department of Energy (DOE), the National Science Foundation (NSF), and the U.S. Geological Survey (USGS) in order to investigate, by drilling a well and conducting scientific experiments, the roots of the Salton Sea hydrothermal system. The program had its official start in Fiscal Year 1984 when Congress added $5.9 million to DOE's Geothermal and Hydropower Technologies Division (now Geothermal Technology Division - DOE/GTD) budget. Although the proposal for a deep scientific drillhole in the Salton Sea area had been received enthusiastically by the NSF, the USGS and DOE's Office of Basic Energy Sciences (DOE/OBES), these organizations had no direct appropriations for the program.

In January 1984, the Director of DOE/GTD established an interagency steering group in order to obtain advice and consultation from the other participating agencies and to coordinate their involvement. Thus began the formal management of this multi-million dollar, multi-agency program.

GOALS AND PRIORITIES

The goals of the program are to study the thermal, physical, chemical, and mineralogical conditions within the deeper parts of the Salton Sea hydrothermal system in order to:

1) better define the geological and hydrological nature of the Salton Sea hydrothermal system and its geothermal reservoirs, and test for extension of this system to greater depths,
2) refine geothermal energy resource estimates for the Salton Sea area,
3) develop a better understanding of the genesis of hydrothermal ore deposits,
4) improve understanding of crustal formation processes in a continental spreading zone, and
5) investigate the possibility of the occurrence of "superconvection."

These goals were to be accomplished by:

1) drilling a scientific well to a target depth of 10,000 feet,
2) obtaining core and drill cuttings for the entire depth of the well,
3) conducting flow tests of selected fluid production zones,
4) collecting fluid and gas samples during flow tests,
5) measuring temperature, pressure, and flow rate at appropriate depths,
6) obtaining comprehensive suites of geophysical logs, and
7) conducting geological, geophysical, and geochemical scientific experiments downhole.

Highest program priority was given by management during the drilling phase to data collection and sampling of rocks and fluids. However, a stark reality faced early in the program was the need to obtain high-temperature cable and instrumentation to test, measure, and sample the hostile subsurface thermal and chemical environment to be penetrated; otherwise, several major program goals could not be achieved. Another important program requirement was the release of all information obtained to the public domain.

MANAGEMENT STRATEGY AND FUNCTIONS

In order to effectively manage this complex, multi-agency, multi-discipline program, a two-element organizational structure (Figure 1) was established among the participants to focus on integration of the drilling and engineering operations with the scientific activities. This structure was based on a SSSDP Management Plan, accepted by each participating agency, that was designed to place critical scientific and technical decision-making at the appropriate level, including on-site field managers. The strategy was to encourage cohesive and timely decision-making.

Figure 1. Management Plan for the Salton Sea Scientific Drilling Program.

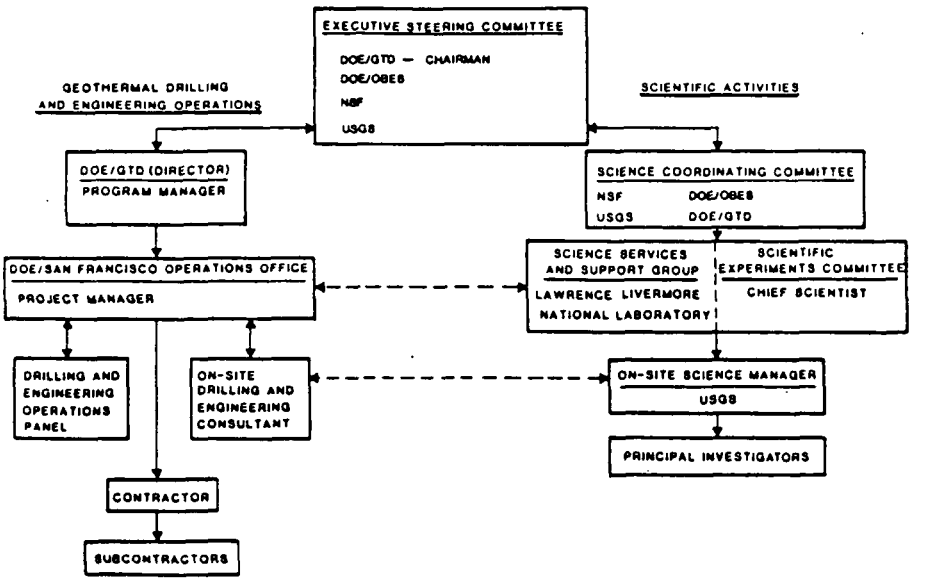

Those associated with the program are pleased to report that most of these objectives have been achieved. Some have been exceeded. There are two important factors that explain this high degree of success. First is the cooperative spirit with which the key individuals entered into program activities. Opportunities for achieving maximum benefit from the total program were pursued, rather than focusing participation on specific interests of the individuals or their agencies. Second is the policy decision of the Executive Steering Committee (ESC) to delegate site-operational authority to the field, ie., to the group of individuals responsible for program success at the well site.

Overall planning, integration, and evaluation of the program, and the resolution of policy issues, were achieved through the Executive Steering Committee. This Committee consisted of policy-level individuals from the three funding agencies, with the member from the organization responsible for well drilling operations, the Director of DOE/GTD, as Chairman.

Drilling and engineering program activities were managed by a Program Manager representing DOE/GTD. The GTD delegated responsibility for conducting drilling and engineering project activities to DOE's San Francisco Operations Office (DOE/SAN), under the leadership of a Project Manager. These responsibilities consisted of pre-drilling and site preparation activities; drilling and completing the scientific well to a target depth of 10,000 feet; recovering the maximum amount of core and drill cuttings; conducting flow tests and collecting fluid and gas samples at the surface; providing instrumentation systems for measuring temperature, pressure, and flow rate, and for downhole fluid and gas sampling; providing maximum time during drilling for scientific experiments and geophysical logging; integrating scientific experiments into drilling operations, while preserving well integrity and avoiding environmental risk and hazards to personnel and equipment; and providing a six-month well-access period after completion of drilling for scientific experiments.

DOE/SAN conducted a solicitation for procurement of a contractor to perform the drilling and engineering operations in the field. The procurement process led to the selection of Bechtel National, Inc. as prime contractor for the scientific well to be drilled on California State lands in the Salton Sea Geothermal Field for which Kennecott Corporation had acquired geothermal prospecting permits. In addition, DOE/SAN contracted Well Production Testing, Inc. as their on-site drilling and engineering consultant. DOE/SAN also established a panel of geothermal industry experts and government representatives for consultation and advice on well construction and on drilling and engineering operations in the Imperial Valley area.

Scientific activities were managed by the Science Coordinating Committee (SCC) comprised of individuals from the three funding agencies. The Scientific Experiments Committee (SEC), under chairmanship of the Chief Scientist, aided the SCC in establishing the scientific content of the program. The On-Site Science Manager was responsible for the interests of the SSSDP scientific community at the well-site. Technical, logistical, and administrative assistance was provided to the SEC by a Science Services and Support Group. This Group also provided the SSSDP scientific community with a regular and continuing interface with the Project Manager at DOE/SAN.

To develop the scientific content of the program, the SCC published a notice of opportunity for submission of proposals to carry out scientific experiments and analyses. NSF, DOE/OBES, and USGS had no funding specifically appropriated for SSSDP science; therefore, each of these agencies allocated an amount, nominally $500,000, from existing appropriations to support selected proposals. The SEC reviewed these proposals for technical feasibility and relevance, and made recommendations to the SCC. The SCC, with assistance of a joint peer review panel established by NSF and DOE/OBES, and with consideration of SEC recommendations, evaluated the proposals and made funding recommendations to the appropriate agencies (in the case of NSF and DOE/OBES, with external programs) or endorsements (in the case of USGS, with only an internal program). Final selection of proposals for SSSDP projects remained the responsibility of each agency, but was coordinated among the agencies.

ON-SITE COORDINATION

The on-site coordinating group to whom the ESC delegated site-operational authority was not included in the SSSDP Management Plan or on the chart of the SSSDP management structure. It was formed at the well-site to provide immediate response to problems affecting the success of program activities, health, and safety. Daily meetings of this group were extremely critical to successfully conducting drilling and engineering operations and scientific activities on-site.

DISCUSSION

Management of this program has been characterized as an exercise in, "how to manage an over-scoped, under-funded program--champagne plans with a beer budget." As more accurate cost estimates were acquired early in 1985, it became evident that the $5.9 million appropriated was significantly less than the revised cost estimates for the drilling and engineering operations originally designed. An ad hoc task force consisting of DOE/SAN management, contractor, landholder, and scientific program representatives was established by the ESC to develop a fundable scope of work. Initial program objectives of a target well depth of 10,000 feet and gathering maximum scientific data were to be retained. The task force made major program revisions, including elimination of long-term flow tests, related surface facilities, and an injection well, in favor of several short-term flow tests using simple test facilities and a brine holding pond.

When the dust subsided from the painful efforts to reduce scope and increase funding, costs for the SSSDP from FY84 through FY86 totalled more than $9.3 million (Table 1). About 75% of this amount was required for drilling and engineering operations. A major element was the inclusion of coring costs as a maximum funded amount ($1 million), rather than as a specific plan and schedule of work.

Table 1. Summary of Drilling and Engineering, and Scientific Program Funding.

	FUNDING BY AGENCY (IN $ 000's)				
CATEGORY	NSF	GTD	USGS	OBES	TOTAL
DRILLING & ENGINEERING	25	6,605	25	25	6,680
GEOCHEMISTRY	168	-	165	103	436
PETROLOGY	280		-	150	430
GEOPHYSICS (LAB)	-	55	15	132	202
GEOPHYSICS (SITE)	-		180	170	350
BIO-ORGANIC	-	-	70	-	70
INSTRUMENTATION	-	597	120	-	717
SCIENCE SUPPORT & MANAGEMENT	-	-	100	146	446
TOTAL FUNDING	473	7,332	875	726	9,331
TOTAL ACTIVITIES	7	10	13	11	41

The usefulness of this management structure has been demonstrated not only by the successful achievement of most of the drilling, engineering, and scientific objectives, but also by the quick response that it provided to resolve urgent issues needing immediate attention and response from

all participants. An example of the latter was the provision of $135,000 of additional funding from DOE/GTD, DOE/OBES, NSF, and USGS in the last few days of drilling in order to properly complete and test the well at its total depth.

CONCLUSIONS

The success of this program can be credited to the melding together of the key participants into a single-minded team. This was accomplished by open and frank communications between these participants and by their employment of lateral coordination with their counterparts, rather than resolving issues through their respective management channels. Although much knowledge has been gained from the SSSDP, the roots of the Salton Sea hydrothermal system were not fully penetrated. However, it has been shown to extend at least to 10,564 feet beneath the SSSDP well site. Additional drilling and scientific activities at the well-site are being considered.

THE SALTON SEA SCIENTIFIC DRILLING PROJECT: DRILLING PROGRAM SUMMARY

Charles A. Harper and David T. Rabb

Bechtel National, Inc., P.O. Box 3965, San Francisco, CA 94119

ABSTRACT

Drilling, coring, logging, and flow testing of well "State 2-14" was completed in March 1986. In the 160 days following spud-in, all the major operational objectives of the Salton Sea Scientific Drilling Project (SSSDP) were met or exceeded. A review of the project costs is presented with an emphasis on unusual or unexpected problems encountered on this scientific/exploratory well. A discussion of the flow test procedures and basic results of commercial interest are also discussed.

INTRODUCTION

Spud-in of the Salton Sea Scientific Drilling Project well took place on October 23, 1985. In the following 160 days, the well was drilled to 10,564 ft, exceeding the target depth objective of 10,000 ft. Thirty-six spot cores were taken, with a total of approximately 725 ft recovered. Two flow tests were conducted, providing fluid samples for scientific study and estimates of productivity from an upper zone at 6,120 ft and a lower interval with mixed flow, primarily from zones at 8,600 ft and 10,475 ft. Downhole logging suites and fluid sampling were performed by researchers (about 425 hrs) and service companies (about 60 hrs), providing additional data to be used in the study of the Salton Sea geothermal resource and the factors that have influenced the geological evolution of the basin.

This paper presents an overview of the management approach, and some of the technical and cost results unique to the project. A brief summary of the flow tests and results is also included. Preliminary reports on the science portion of the program and core drilling are the subject of separate papers being presented at the Conference.

MANAGEMENT SUMMARY

Bechtel, under a contract with the U.S. Department of Energy,* had overall responsibility for design, procurement, and supervision of operations at the site, near Niland, California. The site was made available to the project by Kennecott, holder of an exploration permit from the State Lands Commission. More than 65 competitively bid subcontracts and purchase orders were activated to provide the support services, equipment, materials, and personnel necessary to carry out the complete program.

Consequently, a critical element in project control was the development and use of an accrual system for daily accounting of costs. Suppliers were required to submit work and delivery tickets at the site, as services were performed, that showed estimated actual costs. These, along with estimates for labor, equipment rental, and all other costs, were processed daily to produce a current expenditure report. Individual estimates were cross-checked with bid prices and actual billings at frequent intervals and adjustments made accordingly. The availability of "real time" cost information at the drill site was invaluable in planning and prioritizing engineering and science objectives.

The overall project costs are summarized in Table 1. Prespud activities included a major

Table 1. Summary of Salton Sea Scientific Drilling Program Costs (Does not include the science experiments budget.)

Activity	Period of Performance	Estimated Cost ($1000s)
Prespud	Sept 1984 through Oct 1985	1,720
Drilling and completion	Oct 1985 through Mar 1986	2,975
Coring and Logging	Oct 1985 through Mar 1986	930
Flow Test Facility and Two Flow Tests	Dec 1985 and Mar 1986	680
Standby and Restoration	Apr 1986 through Nov 1986	400
Total Budget		**$6,705**

*Contract Number DE-AC03-84SF12194

rescoping of the project to eliminate installation of an injection well and high-pressure separator from the flow test facility. Other prespud activities included well design, site layout and preparation, and the negotiation and award of the majority of the subcontracts. The drilling and completion costs were higher than might be expected due to three major problem areas, summarized in Table 2 and discussed in more detail below. Nearly $1 million was spent on directional drilling and lost circulation and well control problems. The estimated net cost of coring was $550,000, for an average cost per ft recovered of about $755. The combined estimated cost of scientific and commercial logging was $380,000.

Table 2. Problem Areas and Estimated Costs Incurred During Drilling and Completion

Activity	Approximate Cumulative Duration	Estimated Cost ($1000s)
Lost Circulation and Well Control	20 days	640
Directional Drilling	18 days	390
Fishing and Stuck Pipe	8 days	275

The project schedule, spanning 26 months, is summarized in Figure 1. The current phase of the project is scheduled for completion in November 1986.

PROBLEM ANALYSIS

The drilling of State 2-14 resulted in some unexpected problems and costs, largely to meet the overriding science objectives. A commercial well typically would be drilled with few, if any, cores taken and would be completed at the highest zone(s) believed capable of commercial production. Few wells in the Salton Sea Geothermal Field have been drilled deeper than 8,000 ft. State 2-14, on the other hand, was to be drilled to at least 10,000 ft, if technically and economically feasible, and to be spot cored at intervals of about every 200 ft, or more frequently if interest dictated. The result was that:

- Fifteen of the 61 drill bits used had up to half of their potential drilling life remaining, when they were tripped out of the hole so a core could be taken. These bits were discarded rather than rerun, to avoid the risk of bit failure and a fishing job or premature tripping for bit replacement before the next coring point was reached.
- All cores taken above 6,000 ft required a followup reaming run to open the borehole to gauge. Loss of roller cone bit gauge and bearing failure was accelerated considerably, especially in the deeper, harder formations.
- Every fluid loss zone encountered as the well was deepened, contributed to a continuing problem. Lost circulation control methods, including setting

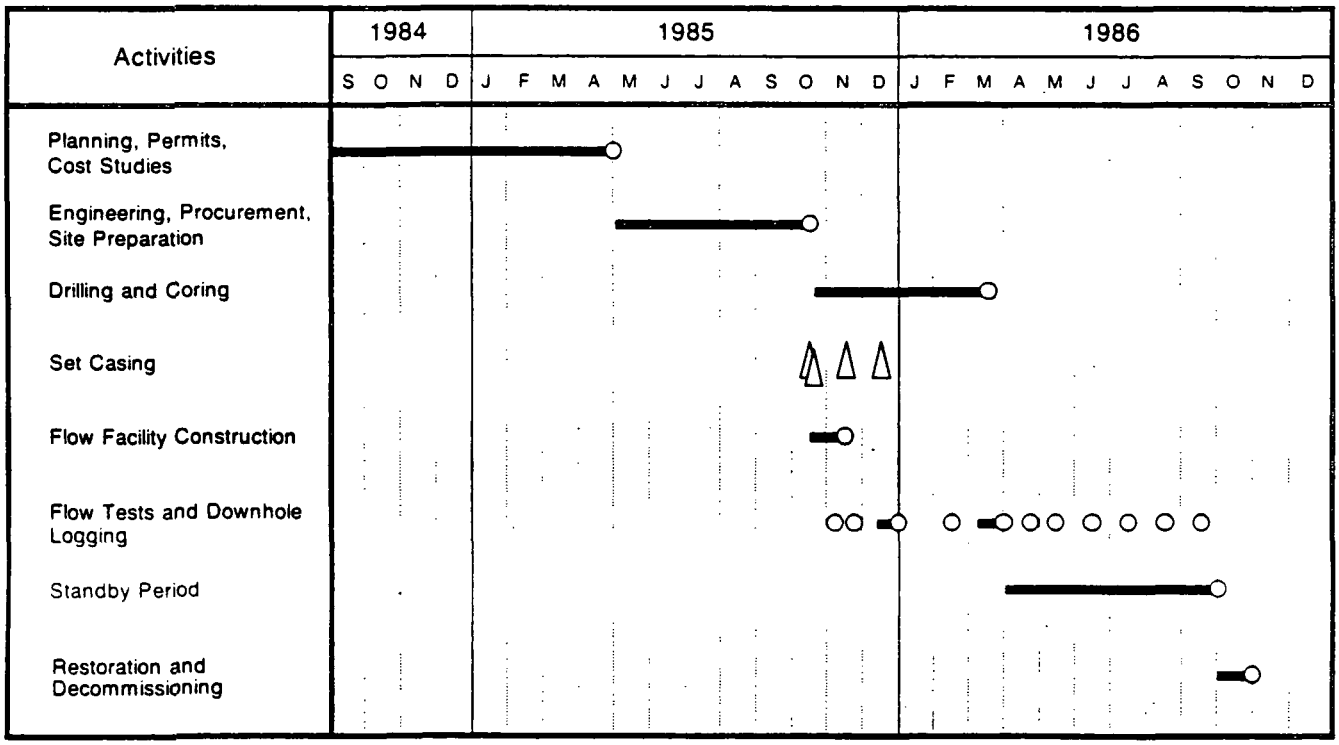

Figure 1. Salton Sea Scientific Drilling Project Schedule

cement plugs, proved to be only temporarily effective. Very high costs were incurred for control materials and lost time to reestablish circulation.

Directional drilling, not included in the original project plan or budget, was required when the path of the borehole deviated several times, approaching the easterly property boundary. Although the final multishot survey failed because of high bottomhole temperatures, the best available information is that the borehole remained on the Kennecott lease.

Drill Bit Usage

A summary of bit usage and cost is presented in Table 3. Average hourly penetration rates when drilling are summarized in Table 4. The average penetration rate was relatively constant at an approximate 25 ft/hr from 3,000 to 8,000 ft, including approximately 550 ft directionally drilled at an average penetration rate of 15 ft/hr. From approximately 9,500 ft, where intrusive igneous dikes were encountered, to total depth (T.D.), drilling became progressively slower. The formation showed complete metamorphosis of the siltstones, mudstones, and sandstones encountered higher in the well, to harder hornsfelsic and quartsitic forms.

Table 3. Bit Usage and Cost Summary

Overall Size	Type	Quantity	Depth Used (feet)
17-1/2	Mill Tooth	6	Surface to 3,500
12-1/4	Mill Tooth	7	3,500 to 6,000
	Carbide Insert	6	
8-1/2	Mill tooth	6	6,000 to 10,475
	Carbide Insert	34	
	Stratapak	1	
6-1/8	Carbide Insert	1	10,475 to 10,564

Total estimated bit cost = $215,000

Table 4. Drill Rate versus Depth

Depth (ft)	Drill Rate (ft/hr) Range	Approximate Average
0 to 1,000	60 to 1,000	100
1,000 to 2,000	15 to 300	75
2,000 to 3,000	15 to 125	50
3,000 to 8,000	5 to 100	25
8,000 to 9,000	5 to 75	20
9,000 to 10,000	5 to 75	15
10,000 to 10,564	5 to 18	10

Seventeen bits were used during directional drilling (turbodrilling) operations. Bit life averaged about 6 hours. Total footage averaged only about 30 ft per bit, rather than the 150 to 240 ft expected in normal service.

Lost Circulation and Flow Control

Lost circulation zones in the Salton Sea Geothermal Field, as observed in State 2-14, typically result from seismic fracturing that has created a network of vertical and horizontal channels for fluid transport. Between 6,000 ft and T.D., nine major fluid loss zones were encountered, as summarized in Table 5. As each zone was penetrated, conventional lost circulation materials (LCM) and control techniques were tried to regain circulation. Zones which were not kept in check by this method were eventually covered with a cement plug. As an intermediate solution, LCM/cement pills consisting of a 50 bbl LCM pill mixed with 50 or 100 sacks of Portland cement were tried. Pills were placed across each loss zone, allowed to set up, and then squeezed to 200 to 300 psi. While this procedure was often successful, the plugs usually broke down within a week. As the well was deepened and more and more zones were exposed, the time required to mix and place LCM pills and the cost of the materials became excessive. As shown in Table 6, the situation became critical between 9,000 and 10,000 ft when the average ft/day drilled dropped below 50 ft and the average cost/ft rose above $500. Core bit damage from inadequate circulation and differential sticking were additional concerns.

Table 5. Major Fluid Loss Zones in State 2-14

Approximate Depth (ft)	Maximum Loss Rate (bbl/hr)	Treatment*	Flowed During Second Flow Test
6,120**	66	CEM	Yes?
6,360	45	LCM, CEM	No
6,635	Total	LCM, CEM	Yes?
6,340	35	LCM, CEM	No
8,095 through 8,160	Total	LCM, CEM	No
8,560 through 8,620	Total	LCM, CEM	Yes
8,950	Total	LCM, CEM	No
9,220	80	LCM, CEM	No
10,475	Total	SAND, CEM, Drillout	Yes

* LCM = Lost circulation material with Portland cement
CEM = Full cement plug
SAND = Sand plug

** First flow test flow zone; cemented after first flow test.

Table 6. Drilling and Coring Performance Trends*

Depth Interval	Days to Complete	Average Cost/Day	Average Ft/Day	Average Cost/Ft	Delays
Surface to 3,500	21	$15,500	165	$ 95	One day setting conductor; one day fishing
3,500 to 6,000	23	$17,000	110	$155	Two days fishing; two days injectivity testing
6,000 to 7,000	20	$19,500	50	$390	Six days directional drilling; two days fishing
7,000 to 8,000	10	$19,500	100	$195	Two days directional drilling; two days lost circulation control
8,000 to 9,000	11	$26,000	90	$290	Five days lost circulation control
9,000 to 10,000	27	$24,500	35	$660	Damaged core bits; seven days lost circulation control and cementing; two days stuck pipe; two days well control
10,000 to 10,460	5	$23,000	90	$250	Two days well control; one day stuck pipe

* Excludes casing, flow tests, and logging activities.

At a depth of 9,450 ft, the decision was made to set full cement plugs across all the open zones. Several of these plugs broke down during subsequent drilling to T.D. and lost circulation and well control problems continued to plague the drilling operation. By the time the well was T.D.'d, daily mud and chemical costs were averaging over $5,000. A partial summary of mud and chemical usage and overall costs are shown in Table 7.

Table 7. Most Frequently Used Mud and Chemicals* and Total Estimated Cost

Product Type	Purpose	Approximate Total Used
Bentonite clay	Viscosifier	1,945 sacks
Sepiolite	Viscosifier	9,130 sacks
Barite	Weight control	3,885 sacks
NaOH	pH control	370 sacks
Cotton seed hulls/ pellets	LCM**	1,220 sacks
Wood chips/ nut hulls	LCM	1,050 sacks
Vegetable/ other fiber	LCM	900 sacks
Polymer	LCM	800 gallons
Granular battery casings	LCM	85 sacks
Diesel fuel	Free stuck pipe	400 barrels

Total estimated mud and chemical cost = $460,000

* A total of forty different products were used.
** Lost circulation material.

WELL COMPLETION AND FLOW TESTING

First Flow Test Configuration

After drilling out of the 9-5/8 inch casing set at 6,000 ft, a 66 bbl/hr fluid loss zone was encountered at 6,120 ft. After drilling a 100 ft rat hole, the borehole fluid was replaced with water and the wellhead was installed and tied into the flow test facility. Wellhead pressure built to 160 psi after being shut in for about 24 hours. However, nitrogen stimulation was finally required to induce flow.

A James' tube was used to estimate the potential productivity of the zone. The extremely high total dissolved solids (250,000 to 300,000 ppm), presented both a physical challenge, in contending with deposition rates that sealed over the lip pressure port in 10 to 20 minutes, and an analytical challenge, in mathematically compensating for salinity effects.

Second Flow Test Configuration

No major fluid loss zones were encountered between about 9,200 and 10,450 ft. The loss of circulation at 10,475 ft led to speculation that a new, possibly lower salinity reservoir might have been discovered. The well completion design was modified, within the limitations of available funding, to increase the chances of flowing the well solely from this lowest zone. The approach taken was as follows:

1. Temporarily plug the bottom flow zone. Several 50 bbl LCM pills (without cement), 86 sacks of #20 silica sand, and approximately 400 cu ft of cement disappeared into this fracture system before a cement plug held.

2. Hang down a 7-inch liner from 5,700 to 10,136 ft to cover over all of the upper zones. It was hoped that any upper zones that started to flow during testing would bridge off, preventing flow down around the liner into the borehole. Installing the liner was a delicate operation because the well was alternately taking fluid or flowing, over a period of a few hours. The well would begin flowing by the time the drill string was tripped out after a cooling run.

3. Drill out the cement plug and make a 100 ft rat hole. The cement plug was less than two feet thick!

The flow test facility was basically identical to that used on the first test. Wellhead pressure rose to 250 psi during the 24 hour shut-in period and the well flowed spontaneously.

Flow Test Results

The results are summarized in Table 8. The well flowed from a single zone on the first test, and drilling fluid contamination was flushed out after about 6 hours of flow, producing good quality fluid and gas samples for science analysis. The well was flowed for about 48 hours.

The second flow test was too brief to allow uncontaminated fluid production. It was concluded when the storage pit was full after 36 hours of flow. Continuous temperature measurements made after brine reinjection indicated that flow occurred behind the liner from the zones identified in Table 5. The percent contribution of each of the zones is unknown, but a major portion of the reinjected brine appears to have entered the zone at 8,560 to 8,620 ft. This zone would appear to have significant commercial potential.

CONCLUSIONS

The heart of the Salton Sea Geothermal Field appears to contain previously undiscovered, deep hydrothermal zones that may be of commercial, as well as scientific interest. An extended flow test of the isolated deeper flow zones in State 2-14 will be required to provide clean fluid samples for scientific study and to more fully assess their commercial potential. Deepening the well might also lead to further discoveries of mutual value to science and industry. The SSSDP has demonstrated that difficult technical problems can be managed, to meet the objectives of scientific investigators. The key is working together to achieve a mutual understanding and balancing of the scientific objectives and the technical limitations.

Table 8. Preliminary Flow Test Results*

	Well Depth (ft)	Estimated Flow Zone(s) (ft)	Approximate Duration (hr)	Flow Rate (lb/hr)	Wellhead Temperature (°F)	Wellhead Pressure (psig)	Estimated Enthalpy** (Btu/lb)
First Test	6,227	6,120	4	600,000	400	200	400
			12	80,000	460	440	400
			2	430,000	410	220	400
			9	150,000	460	450	400
Second Test	10,564	[6,100 6,600 8,800 10,475]	3	475,000	445	310	520
			24	280,000	475	450	~480
			1	700,000	460	380	480
			4	300,000	490	485	450

* Analysis by GeothermEx, Inc.

** Based on James' correlation with TDS correction.

Geothermal Resources Council, TRANSACTIONS, Vol. 10, September 1986

SSSDP FLUID COMPOSITIONS AT FIRST FLOW TEST OF STATE 2-14

Donald E. Michels

Don Michels Associates
P.O. Box 895
Whittier, California 90608

ABSTRACT

Brine and steam were sampled on December 29 and 30, 1985. A four-step temperature cascade was established in a test section of the flowline. In this way, enthalpy data could be obtained from the chemical data.

Brine compositions, on a basis of total flow, are computed separately for Dec. 29 and 30; total dissolved solids were 25.54+0.23 and 25.47+0.036 weight percent. Carbon dioxide and hydrogen sulfide were 1664+20 and 7.01 ppm, respectively, on Dec. 30. CO_2 and H_2S comprised about 98.5 mole percent of the suite of non-condensable gases. Data on other components are tabulated.

Effective pre-flash enthalpys were 335 and 349 Btu/lb on December 29 and 30, respectively. These correspond to temperatures of 548 and 567°F. The greatest observed steam yield was 18.5 weight percent at 328°F on Dec 30.

INTRODUCTION

The Salton Sea Scientific Drilling Project (SSSDP) well, State 2-14, was test flowed on December 28-30 from the interval 6000-6227 feet. The surface facility consisted mainly of 10-inch diameter flowline. It was equipped with a four step temperature cascade, with access ports for sampling liquids and gases at each step, and terminated with a James tube and a silencer. More than 20 geochemists participated in sampling and/or analysis of the brine, steam, and related materials. This report provides the reference composition of the fluids.

The general layout of the test sections is shown in a companion paper (1) which also describes the chemical method used to determine steam fractions in the temperature cascade.

Four insulated zones in a test section were separated by orifice plates in order to set up a cascade of temperature-pressure conditions. The full flow of the geothermal fluid passed through this test section. Individual steps in the cascade involved increments in steam yields of about 1 to 8 weight percent (total flow basis). This corresponds to about 7 to 70 relative percent on a basis of steam.

One objective of sampling was to follow tracers in the steam and brine phases with enough precision to quantify those steam increments. Key tracers were natural carbon dioxide in the steam and natural chloride in the brine. Another major objective was to characterize the brine composition in terms of major and minor elemental components.

STEAM FRACTIONS AT THE SAMPLING PORTS

For Dec 30, the steam fractions at the sampling ports were determined by a chemical method (1). Results are shown here without further explanation. In addition, that method yielded thermodynamic data for the mixed-salt brines. However, the totally chemical approach could not be used for the Dec 29 situation -- no data were obtained for CO_2 in steam. Instead, the steam fractions for December 29 were computed by combining the measured chloride values with the enthalpy relationships determined in (1). The principle is similar to the description in (2).

Results are shown in Table 1. The numbering of ports is retained from field designation. Port 3 was in the first test spool, Port 6 was in the fourth. Although brine and steam sampling points were physically different on each test spool, they are given the same port numbers.

In addition to the flash fraction results, estimates of the pre-flash brine

enthalpy are obtained. In the case for Dec 29, a preflash chlorinity of 153,688 ppm, obtained in (1) for December 30, is used to derive a pre-flash enthalpy value of 335 Btu/lb. This corresponds to an effective flash temperature of 548°F. This is lower than the estimate of 567°F for Dec 30, but not unreasonable considering that the well was still in the early warming stages on Dec 29.

The flash-temperature relationships for Dec 29 and 30 are given in Figure 1. Enthalpy-temperature-composition relationships found in this work show the mixed-salt hypersaline brines have significantly smaller enthalpies than pure NaCl brines (3) of comparable concentrations and temperatures.

TABLE 1:

STEAM FRACTIONS AT SAMPLING PORTS

Dec 29, enthalpy 335 Btu/lb				
Port	3	4	5	6
°F	431	373	327	309
Flash	.10700	.14621	.17288	.18166
Dec 30, enthalpy 349 Btu/lb				
°F	455	395	346	328
Flash	.10513	.15474	.17781	.18522

BRINE SAMPLING AND PREPARATION

Two kinds of brine samples were taken, one for the chloride tracer and the other for general composition. Both were taken with the same port equipment but differed in sample handling procedures.

Brine sampling equipment is diagrammed in Figure 2. Welded to the 10-inch test spools and fully open to the two-phase flow inside, were downcomers of 4-inch diameter pipe which terminated in a system of access valves. The brine in the downcomer tends to deposit scale, so operating the blowdown valve assures that sampled liquid is relatively fresh.

A 1/4-inch (heavy wall) stainless steel tubing was passed through an access valve to tap the one-phase liquid that collected in the downcomer. The probe was integral with a section of 1/8-inch diameter stainless tubing, shaped into a coil and cooled in a water bath. Ice was used to prevent the cooling water from getting hot, but ice temperatures were avoided. A collection temperature of 100 to 140 F is considered ideal. Flow through the probe system was controlled by a valve on the cool end of the 1/8-inch tubing. Brine exited the probe system as a jet into the atmosphere. Samples were collected by directing the jet into polyethylene bottles that contained pre-weighd amounts of diluents.

Samples for general composition were collected into 50-ml bottles that contained about 30 g of 0.1N nitric acid. Enough brine was collected to make the acid:brine ratio about 5:2. The brine stream from the valve spigot was caught directly in the sample bottle without pre-measuring the brine. This technique delivers the brine from hot flowline to sample bottle in just the few seconds of travel time through the tubing. The quick dilution and acidification are considered advantageous, especially for silica. Samples of hypersaline brines are stable for many months when collected in this way.

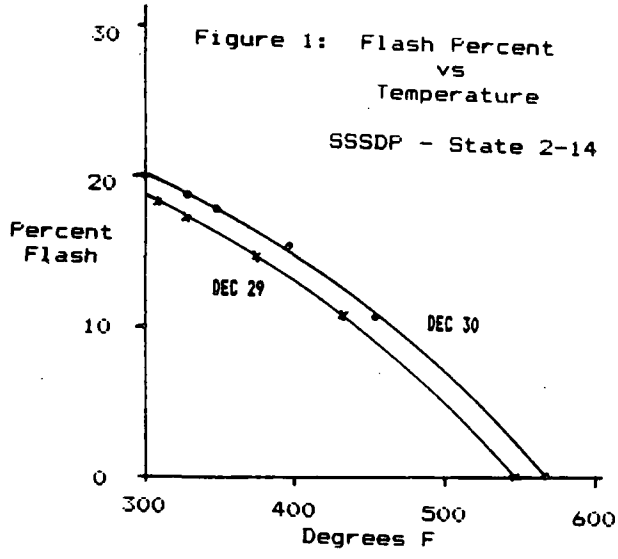

Figure 1: Flash Percent vs Temperature

SSSDP - State 2-14

Dilution factors are determined by weighings to the nearest milligram on an analytical balance. They are accurate to better than +0.0001(relative).

The acidified brine samples were reweighed in the DMA laboratory. Aliquots were taken and diluted further into 20 percent nitric acid. Subsequent analysis was by a commercial laboratory, mainly using inductively coupled plasma (ICP). Chloride was determined (independently from the oceanographic method) by titration, sulfate by turdidimetry, and ammonia by specific ion electrode.

The commercial lab results were based on volumetric standards (ppm = mg/l). These were converted to a weight basis (ppm = mg/kg) through density measurement of the 20 percent nitric acid carrier (1.145 g/ml) and the use of

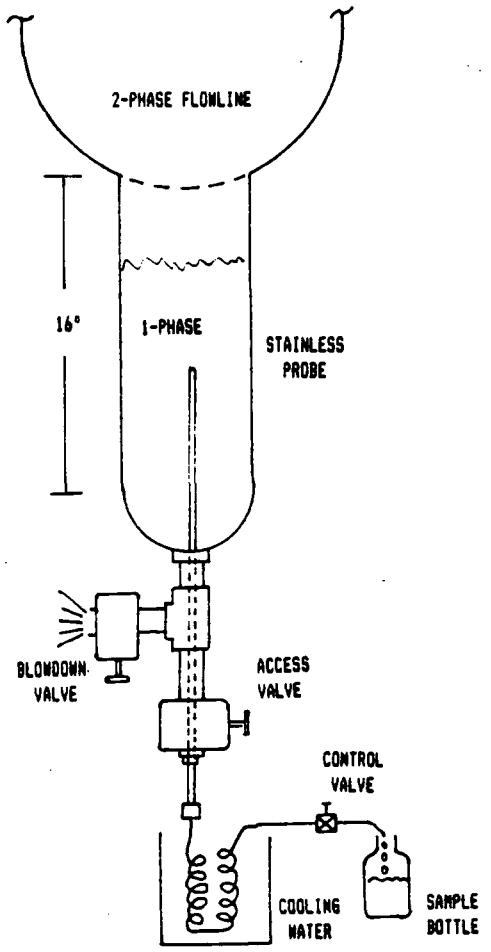

FIGURE 2: BRINE SAMPLING ARRANGEMENT

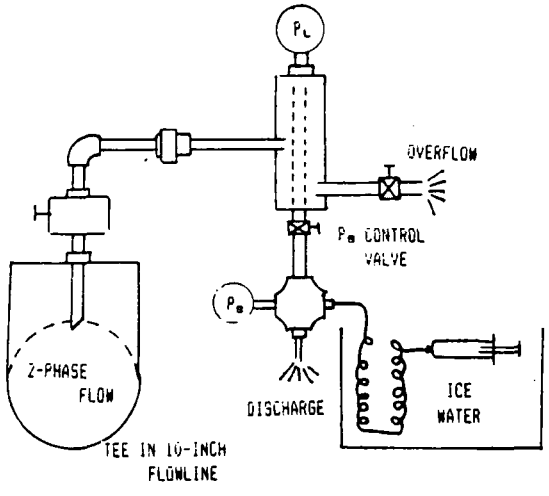

FIGURE 3: STEAM SAMPLING ARANGEMENT

P_L = Line Pressure (to 450 psig)
P_s = Syringe Pressure (12 psig)

weighings to determine the other dilution factors. Density of whole brine is near 1.2 g/ml, thus the distinction between mg/l and mg/kg is important. All concentrations referred to in this paper are on weight basis.

Samples for determination of the chloride tracer were collected similarly, except that about 100 g of distilled water was used and brine was collected to bring the mixture into the range of seawater chlorinity. (Chlorinity and chloride content are used synonymously in this report).

The mixture was reweighed and titrated immediately in a field laboratory by an oceanographic method that involved standardization by standard mean ocean water (4). Subsequently, in the home laboratory, (MIT), the titrant was restandardized and other acidified samples were analyzed. The final selected results are believed accurate to about +0.002 (relative), for single analyses. Replicate analyses yield proportionally better values.

GAS SAMPLING AND ANALYSIS

Brine-free steam samples were obtained through in-line separator devices built into the test spools. Because brine carryover occurred at some ports, a portable centrifugal separator was attached in series between the in-line separator and the gas sampling equipment. This arrangement (Figure 3) provided high quality steam samples and was used at all steam sampling ports.

Surging of pressure (and temperature) in the two-phase flowline was prominent, but steamside pressure was leveled by manual control of the steamside control valve. In principle, the surging is concommitant with incremental differences in flash fraction and hence composition of steam inside the separator. Cycle frequency in this case was about 4/minute, thus, the collections, which take 3 to 7 minutes, provided considerable averaging about the mid-range conditions.

Sampling and analysis for non-condensible gases in steam was done by a syringe method (5) modified to improve precision. A syringe clamp was used that set the working volume of the syringe to be the same for all samplings. The volume was standardized in the laboratory by weighing and calculating the temperature correction. Condensate was recovered into pre-weighed vials for re-weighing.

The principle of the syringe method (5) for CO_2 assay is to establish the pressure and volume of the gas and condensate at ice temperature. Then the amount of CO_2 in the condensate is given by the Bunsen coefficent (STP ml of gas per ml of liquid at 1 atm. gas pressure) and the gas equation is applied to the gas phase and the Bunsen volume to compute the total amount of CO_2. Calculation requires the absolute pressure of CO_2.

The non-CO_2 gases (nitrogen, methane, hydrogen, etc.) are normally determined with the CO_2 assay as an undifferentiated group. This provides data to compute a molar ratio of CO_2/non-CO_2 gases which in turn permits calculating the CO_2 pressure fractions in the other collections.

An alternative was provided by an independently determined composition of the gas mixture (6). Both compositions were used to compute CO_2 assays and each result was within the error limits of the other. The assay computations based on (6) are preferred and reported here.

Ammonia, present in the steam, is suspected to be dissolved in condensate upon formation of NH_4^+ and HCO_3^- by reaction with CO_2. It involves no significant vapor pressure in the assay and the CO_2 consumed by ammonia is disregarded.

Hydrogen sulfide was determined in the mixture of condensate and NaOH obtained from the collection regarding the other non-CO_2 gases. The mixture is stabilized in the field with zinc acetate solution and analyzed in a lab by iodometry.

TABLE 2:

SUMMARY OF GAS CONTENTS

Port	3	4	5	6
Temp	455	395	346	328
Steam Fraction	.10513	.15474	.17781	.18522
CO_2 (ppm)				
Steam	15524	10521	9462	8988
Total Flow	1662	1638	1687	1668
H_2S (ppm)				
Steam		46.2	38.3	
Total Flow		7.15	6.86	

Averages on a total flow bases:
CO_2 1664±20; H_2S 7.01

ADJUSTMENTS TO BRINE CONCENTRATIONS

Analysis by ICP in a commercial laboratory provided the basic data for cations. Lab results are adjusted by the dilution factors and carrier densities to yield gross concentrations of field samples. These gross concentrations are susceptible to further adjustments that relate to electrical charge balance.

Chloride accounts for more than 99.9 percent of the negative charge in the brine composition. The precisions and accuracys of the oceanographic chloride values are the best in the entire data set. They are also considered to be unbiased. Thus, rather than simply reporting the size of the charge imbalance between cations and anions, the cation concentrations are adjusted to match the charge of the chloride. These adjusted values are considered to be the best available representation of the brine composition.

The overall bias of the cation analysis is given by summing the cation charges and comparing the result with the chloride. For ten samples, the average bias is +0.0262 of the chloride value and the standard deviation is 0.0106. No samples show a negative bias. Thus, the gross precision of the ICP data is better than the bias and an upward adjustment is warranted.

In making the charge balance, the relative precision of each individual cation was determined from replicate analyses. These relative precision values were multiplied by nominal concentrations of the respective cations to obtain an index. The total balancing charge needed was then assigned to each cation in proportion to its index. In this way, the more abundant components carried most of the charge adjustment and no adjustment of a single cation exceeded its own analytical precision. For example, sodium carried 0.427 of the charge adjustments and five components, Na, K, Ca, Fe, and NH_4^+, collectively carried more than 0.94 of the adjustment.

FIELD COMPOSITION OF BRINES

The field compositions reported in Table 3 include the charge balancing procedure described above. Dilution factors, described earlier, are also incorporated. Averages are used where replicates were available (Ports 3, 4, and 6 on Dec 30).

There was no sample for Port 6 on Dec 29. The listing in Table 3 is based on the average of the other ports on Dec 29, with conversions made through the flash

fraction values as appropriate.

Sulfate determinations were made on two samples; Dec 30, Ports 3 and 4. Values are 136 and 117 ppm, respectively. Analytical detection limit was about 50 ppm, considering dilutions of the samples.

Silica concentrations show marked reductions through the test system. The implied deposition rate is much greater than indicated by thicknesses of scale deposits. Reasons for the mismatch deserve study.

TABLE 3:
FIELD COMPOSITIONS OF BRINE AT SAMPLE PORTS

DAY	DECEMBER 29				DECEMBER 30			
HOUR	1750	1755	1755		1215	1341	1430	1255
PORT	3	4	5	6	3	4	5	6
CODE	B	I	J	CALC	G	C	A	E
FLASH	.10700	.14621	.17288	.18166	.10513	.15474	.17781	.18522
SODIUM	58658	61988	64348	64574	58756	62405	63794	64753
CALCIUM	29939	31435	33331	33052	29428	30995	32614	32967
POTASSIUM	18357	19823	20419	20451	18398	19488	20109	20316
IRON	1682	1834	1906	1892	1697	1774	1857	1897
MANGANESE	1533	1654	1704	1707	1531	1651	1688	1702
ZINC	571	604	626	628	559	603	616	624
SILICA	511	470	342	465	530	466	434	380
STRONTIUM	453	482	499	500	450	480	496	498
AMMONIUM	389	364	383	397	382	413	361	415
BORON	282	304	314	314	281	300	309	311
BARIUM	220	236	251	246	218	224	237	243
LITHIUM	212	226	237	236	211	222	232	235
LEAD	108	114	119	119	105	108	115	122
MAGNESIUM	41	45	43	45	41	40	45	48
OCEAN CL	170930	179160	186890	188589	171720	181800	186900	188600
SUM	283936	298736	311414	313215	284307	300968	309808	313109

TABLE 4:

	ELEMENT/LITHIUM RATIOS				ELEMENT CONCENTRATIONS			
	DEC 29		DEC 30		DEC 29		DEC 30	
	AVG	U.M.	AVG	U.M.	AVG	U.M.	AVG	U.M.
SODIUM	274.15	1.96	277.86	.97	52843	299.11	52661	50.94
CALCIUM	140.31	.90	139.89	.17	27048	277.91	26515	119.20
POTASSIUM	86.82	.62	87.07	.21	16736	231.68	16502	17.82
IRON	8.03	.07	8.03	.02	1548	29.81	1522	7.25
MANGANESE	7.25	.05	7.31	.04	1397	18.55	1385	6.00
ZINC	2.67	.02	2.67	.01	514	3.10	506	1.61
SILICA	1.98	.31	2.05	.14	380	56.07	387	25.90
STRONTIUM	2.12	.01	2.14	.01	409	3.28	405	.79
AMMONIUM	1.69	.10	1.78	.05	325	15.48	336	8.56
BORON	1.33	.01	1.34	0.00	257	3.25	253	.44
BARIUM	1.05	.01	1.02	.01	202	3.62	194	1.49
LITHIUM	1.00		1.00		193	2.44	190	.63
LEAD	.51	0.00	.50	.01	98	.65	95	1.36
MAGNESIUM	.19	.01	.19	0.00	37	1.06	36	1.00
OCEAN CL	795.91	7.43	810.82	2.71	153410	1087	153668	0
SUM					255396	2257	254654	351

PRE-FLASH BRINE COMPOSITION

The pre-flash compositions for the two sampling days are given in the right half of Table 4, in terms of averages and uncertainties of the mean (U.M.). Table 4 is derived from the Table 3 values multiplied by (1-f) and averaged over each days samples. The averages are different by amounts that approach significance in terms of the U.M. values.

An alternative comparison of the brine compositions on the different days can be made through ratios of components. Specifically, lithium determinations are the most reproducible, based on the replicate samples. Thus, the ratio of element concentration to the lithium concentration is a sensitive indicator of variation between samples.

The averages and U.M. values for element/lithium ratios are given in the left half of Table 4. The differences in the U.M. values, vis-s-vis the two sampling days, are relatively less than their concentration counterparts in the other side, as expected.

ACKNOWLEDGEMENTS

I am indebted to Andy Campbell and Chris Measures for the oceanographic chloride analyses, to Al Truesdell for sharing equipment and data, and to Wilfred Elders for continued motivation. This work was performed through the University of California, Riverside and supported by National Science Foundation Grant EAR 8303557.

REFERENCES

1. Michels, D. E., 1986, A chemical method for measuring steam quality in two-phase flowlines: Geoth. Res. Coun., Transactions, this volume.
2. Ellis, A.J. and W.A.J. Mahon, 1977, Geochemistry and geothermal systems: Academic Press, New York, p. 230.
3. Haas, J.L., 1976, Thermodynamic properties of the coexisting phases and thermochemical properties of the NaCl component in boiling NaCl solutions: U.S. Geol. Surv. Bul. 1421-B Revised, 71 pp.
4. Campbell, Andy, and Chris Measures, 1986, MIT Department of Oceanography, personal communication.
5. Michels, D. E., 1978, CO_2 in geothermal steam - a rapid, precise, and accurate field assay technique: Geoth. Res. Coun. Trans, v. 2, p. 445-8.
6. Alfred Truesdell, 1986, personal communication.

Geothermal Resources Council, TRANSACTIONS, Vol. 10, September 1986

SALTON SEA SCIENTIFIC DRILLING PROJECT: SCIENTIFIC PROGRAM

J. H. Sass[1] and W. A. Elders[2]

(1) On-Site Science Manager, U.S. Geological Survey, Flagstaff, AZ 86001
(2) Chief Scientist, University of California, Riverside, CA 92521

ABSTRACT

State 2-14, the Salton Sea Scientific Drilling Project, was spudded on October 24, 1985, and reached a total depth of 10,564 ft (3.2 km) on March 17, 1986. There followed a period of logging, a flow test, and downhole scientific measurements. The scientific goals were integrated smoothly with the engineering and economic objectives of the program and the ideal of "science driving the drill" in continental scientific drilling projects was achieved in large measure. The principal scientific goals of the project were to study the physical and chemical processes involved in an active, magmatically driven hydrothermal system. To facilitate these studies we attached high priority to four areas of sample and data collection, namely: (1) core and cuttings, (2) formation fluids, (3) geophysical logging, and (4) downhole physical measurements, particularly temperatures and pressures. In all four areas, the results obtained were sufficient to meet the stated scientific goals.

INTRODUCTION

The first deep well of the U.S. Continental Scientific Drilling program was drilled to a depth of 3.22 km in the Salton Sea Geothermal Field of the Imperial Valley near Calipatria, California (Figure 1). The well is located near the southeast end of the Salton Sea (Figure 1) in the Salton Trough, a tectonic depression within the transition zone between the spreading centers of the Gulf of California and the San Andreas transform fault (Elders et al., 1972). The trough is a fluvial sedimentary basin with associated evaporitic and lacustrine deposits. Within the trough and adjacent crystalline basement, heat flow is very high, averaging about 140 mW m^{-2} (Lachenbruch et al., 1985). Within the region of high heat flow are zones of extraordinarily high heat flow like the Salton Sea Geothermal Field, where heat flow averages about 400 mW m^{-2} (Sass et al., 1984) and temperatures as high as 370°C have been encountered at only 2 km depth. The Salton Sea Field is also characterized by brines with total dissolved solids in excess of 200,000 ppm (Muffler and White, 1969).

The well was drilled using standard oilfield technology, modified to take account of the high temperatures; however, the philosophy was quite different from that employed in conventional exploration drilling, chiefly in that scientific objectives had priority over economic and engineering concerns where safety and well integrity were not compromised. This was accomplished through a unique grouping of specialists termed the "Site Coordination Committee" consisting of the site manager, drilling supervisor, toolpusher, DOE technical representative, on-site science manager, and chief scientist, with input from coring engineers, mud chemists, and others as deemed appropriate.

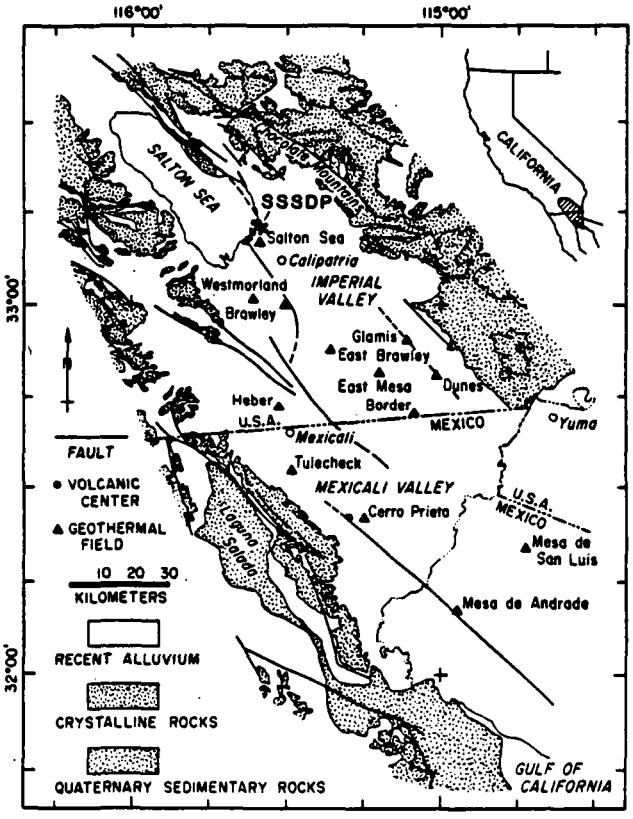

Figure 1. Major faults and geothermal fields of the Salton Trough.

The primary scientific goals of the Salton Sea Scientific Drilling Project (SSSDP) were to study active physical and chemical processes in a magmatically driven hydrothermal system. As the well is twice as deep as typical production wells in the field, the temperatures, pressures, salinities, and flow rates encountered also provided an opportunity for a preliminary study of the deeper reservoir characteristics and geothermal energy potential.

Forty proposals were approved by the Science Coordinating Committee of the SSSDP. Of these, nearly half were concerned with geochemical studies of rock, fluid, and gas including the organic chemistry of fluids. Twenty-five percent of the proposals involved petrologic and geophysical studies of core and cuttings. The remaining proposals were concerned with downhole sampling, geophysical logging, other geophysical measurements, and technology development involving the downhole deployment of geophysical instruments like seismometers, temperature-pressure sensors, flowmeters, and gravimeters.

Given this program, the recovery of core, cuttings, fluid, and gas samples had the highest priority. To maximize the interpretation of data obtained from these samples, and to allow interpretation in zones where samples could not be obtained, high priority was also assigned to the collection of an integrated set of downhole data including geophysical logs, temperature measurements, and downhole fluid samples. A time-depth plot (Figure 2) summarizes the amount of time devoted to the various scientific and engineering activities. A preliminary progress report of these activities by the USGS on-site science management team (which coordinated and supervised all science activities during the drilling phase) has been published (Sass et al., 1986).

CORE AND CUTTINGS

At least 1 kg of cuttings was retained at 6- to 9-m intervals to about 900 m and at 3-m intervals below that depth. Each sample consisted of one 500 mL cup of washed sample and three cups of unwashed samples containing drilling mud and additives as well as rock cuttings. Cuttings were not recovered in zones of complete loss of drilling fluid between 2022 and 2097 m, 2616 and 2682 m, 2719 and 2750 m, and between 3193 and 3220 m (total depth). In some zones of partial fluid loss, cuttings samples were contaminated by

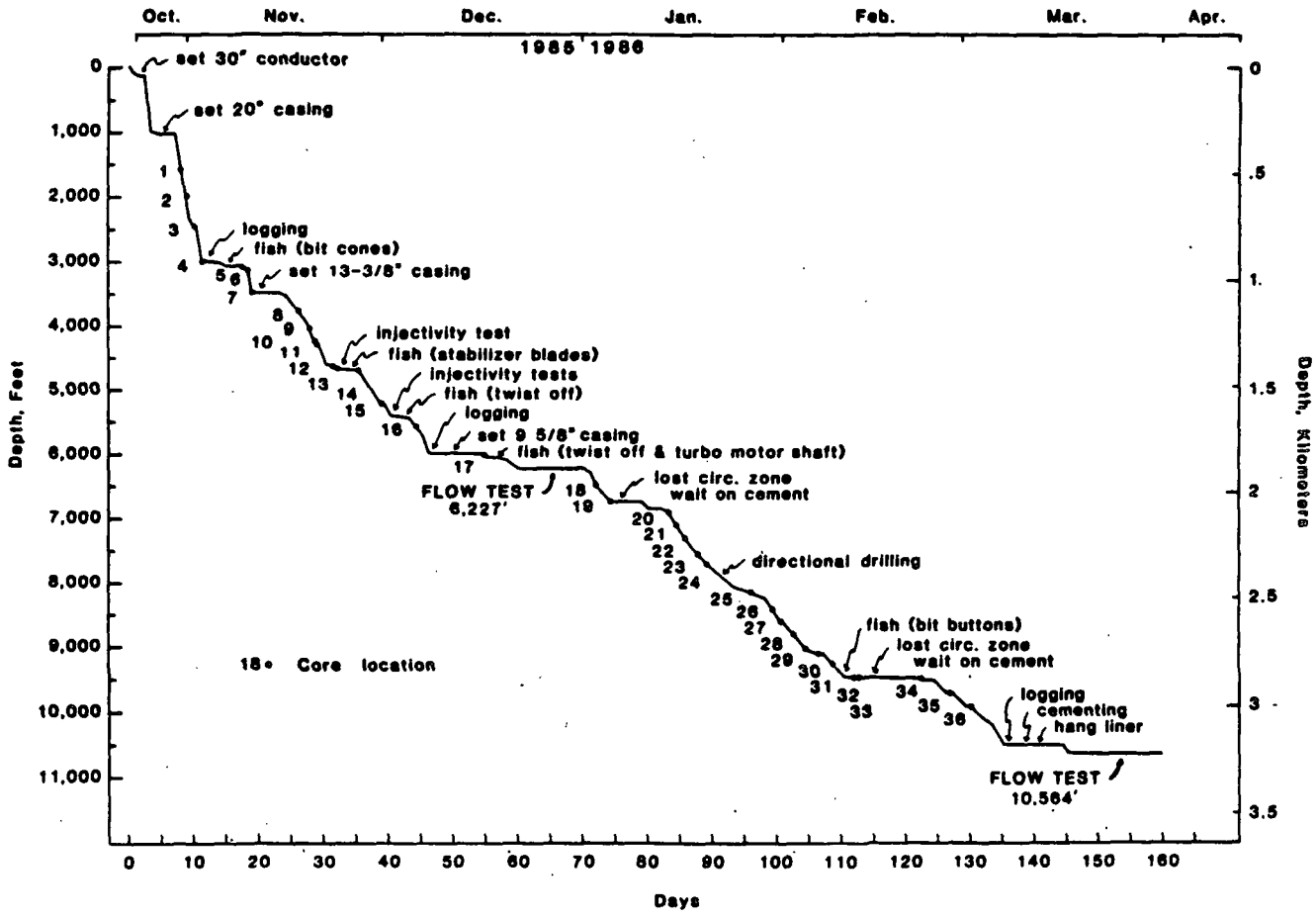

Figure 2. SSSDP depth/progress chart. Core numbers correspond to those in Table 1.

lost circulation material and rock material flowing back into the well from partially plugged lost circulation zones above the bit.

The coring plan developed before drilling envisaged 43 coring attempts between 1700 and 10,000 ft (518 and 3048 m) with an average interval of 200 ft between cores in the depth range 3,000 to 10,000 ft. We hoped to recover 1,200 to 1,500 ft (366 to 460 m), depending on the number of 30-ft core runs as opposed to 60-ft runs. A total of 36 cores were attempted, of which 2 (marked "N/A" in the footage/recovery columns of Table 1) were obtained in junk baskets or junk subs during fishing operations. Percentage recovery was reasonable over the entire depth, but the footage drilled declined precipitously below 5,000 ft (1,500 m) primarily because the rock was fractured either in situ or by the release of stress by the core bit with the result that the barrel jammed frequently, often after only a few feet had been cored. In addition, some cores were drilled "blind" (no circulation) which made coring even more difficult.

Table 1. History of coring attempts and recovery, SSSDP

Date	Core	Ft. drilled	Marked core interval	% recovery
10/31/85	1	25	1553-1577.6	98.4
11/01/85	2	30	1983-2012.2	97.3
11/02/85	3	30	2448-2478.0	100.0
11/04/85	4	60	2970-3028.4	97.3
11/08-09/85	5	N/A	3083-3087.0	N/A
11/11/85	6	60	3107-3161.7	91.2
11/12/85	7	35	3470-3504.0	97.1
11/19/85	8	60	3790-3846.6	94.3
11/20/85	9	60	4007-4069.9	100.0
11/21/85	10	40	4241-4300.4	99.0
11/22/85	11	36	4301-4338.6	100.0
11/25/85	12	38	4643-4680.5	98.6
11/26/85	13	5	4681-4683.0	40.0
11/27-28/85	14	N/A	4718-4718.5	N/A
12/02/85	15	30	5188-5219.2	100.0
12/07/85	16	17.5	5574-5591.5	100.0
12/19/85	17	18	6026-6040.8	82.2
01/03/86	18	11	6506-6517.0	100.0
01/06/86	19	13	6758-6766.0	61.5
01/14/86	20	9	6880-6889.0	100.0
01/16/86	21	9	7100-7107.0	77.7
01/18/86	22	13	7300-7311.5	88.5
01/19/86	23	30	7547-7574.5	91.6
01/20/86	24	30	7708-7738.0	100.0
01/28/86	25	29	8133-8161.0	96.5
01/31/86	26	6	8395-8400.0	83.3
02/01/86	27	19	8585-8597.0	63.2
02/03/86	28	7	8800-8804.5	64.3
02/05/86	29	23	9004-9009.5	23.9
02/07/86	30	3	9095-9098.0	100.0
02/10/86	31	6	9248-9251.5	58.3
02/13/86	32	5	9453-9455.3	46.0
02/14/86	33	15	9458-9463.0	33.3
02/23/86	34	4	9473-9475.0	50.0
02/28/86	35	4	9694-9697.5	87.5
03/02/86	36	5	9907-9908.0	20.0

Even though there were problems, we are satisified with the total recovery of about 730 ft (224 m) in terms of its utility in characterizing the stratigraphy of the well and in satisfying the requirements of the principal investigators interested in physical properties, petrology, and geochemistry of solid rock samples. In view of the difficulties experienced here using the best in off-the-shelf technolgy and experienced coring personnel, it would seem that coring in ultra-deep and/or ultra-hot wells will require considerable research and redesign of conventional coring hardware.

FLOW TESTS

The fluid sampling plan envisaged two or even three discrete flow tests at shallow (1 km), intermediate (2 km), and total depth to allow estimates of salinity and other concentration gradients within the brines. Only one minor (15 bbl/hr) loss zone was encountered above 1 km. Injectivity tests were performed at depths of 4,684 and 5,418 ft (1,428 and 1,651 m), but no significant potential for flow was detected. At that stage, it was decided not to attempt a shallow flow test and 9 5/8" casing was set at 6,000 ft (1,829 m) (Figure 3). A loss zone associated with abundant epidote was encountered slighly below the casing (6,119 to 6,135 ft), and the first flow test was run in late December of 1985 (Figure 2). Only a few hundred barrels of fluid had been lost to the formation, and the fluids cleaned up very rapidly, resulting in very satisfactory samples and confident estimates of total dissolved solids, temperature, enthalpy, and other important parameters. The observed flow rate and enthalpy demonstrated the commercial potential of this well.

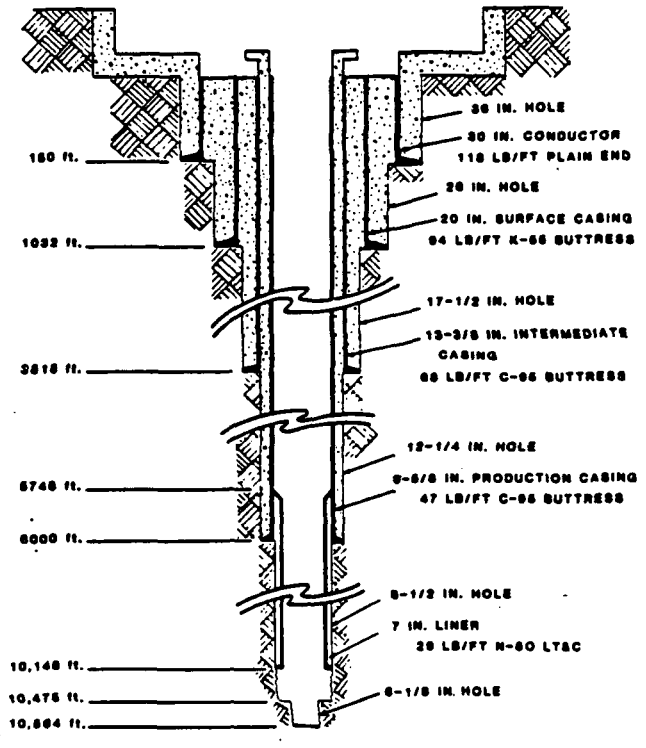

Figure 3. Casing configuration, SSSDP.

From 6,637 to 9,500 ft (2 to 2.9 km), a succession of loss zones (reflecting fracture permeability) was encountered. Enormous quantities of fluid (several tens of thousands of barrels) were lost and a large amount of lost circulation material and cement were used to regain circulation and control losses. When circulation was again lost near total depth (10,475 ft), temperature logs indicated that fluid loss was occurring at the bottom of the well. The zone was then plugged off with cement, a liner was set (but not cemented) at 10,135 ft (3,089 m), the cement plug was drilled out, and an additional 89 ft of hole was drilled with no returns. Following this, the well was flowed, but the brine produced was contaminated, not only by the fluid lost in the bottom zone but probably by inflow around the liner from a depth of about 8,600 ft (2,621 m); the results were considerably less satisfactory than those obtained during the first flow test. The duration of the flow test was limited by the 36,000-bbl (5.7×10^6 L) capacity of the brine pond.

GEOPHYSICAL LOGGING

No open-hole geophysical logs were attempted in the 26-inch (0.66 m)-diameter hole, which was 1,032 ft deep (Figure 3) and into which the 20-inch (0.51 m)-diameter surface casing was set. Because of the large hole diameter, we thought that record quality would be poor, and that if open-hole data in the upper 300 m were needed, a slim hole could be drilled to this depth easily and inexpensively. Complementary and, in some cases, redundant sets of logs were run at the 3,000 to 3,500 ft casing point and 6,000 ft casing point (Figure 3) by both Schlumberger and USGS Water Resources Division's Research Logging Unit (Tables 2 and 3). The Schlumberger logs allowed a comparison and correlation with commercial logs from other wells in the Salton Sea Field. The USGS logs provided both a comparison and confirmation of such things as depth registration (gamma-ray logs) and an extension of the commercial logs. Lawrence Livermore National Laboratory (LLNL) provided at the site a system capable of reading and displaying digital data from both USGS and commercial logs. This proved useful for real-time analysis and interpretation. A second commercial company ((Dialog) carried out a casing caliper log on March 30, 1986, to assess the condition of the 9 5/8-inch casing (Figure 3). Several attempts were made by the USGS (Table 3) to obtain televiewer logs, particularly in loss zones and flow zones. At the 6,000-ft casing point (Figure 3) the televiewers were bedeviled by mechanical and electrical problems. Below 6,000 ft, televiewer records were obtained, but because of deleterious effects of viscous mud, lost circulation material, and cement, a large percentage of the energy was absorbed, resulting in poor record quality. The same comment applies to the acoustic logs made by both Schlumberger and USGS, although useful data were obtained in both cases.

Table 2. Dates, intervals, and types of Schlumberger logs, SSSDP

Date	Logged Interval (ft.)	Logs[a]
11/04/85	1,032 to 3,008	1-6
11/13/85	2,900 to 3,525	1-6
11/17/85	30-3,523	7
12/09/85	3,520 to 5,988	1-6
12/18/85	50-5,670	8
12/18/85	190-5,696	7
03/10/86	6,020-8,813	9

[a]
1) Dual Induction
2) Compensated Neutron-Formation Density
3) Borehole Compensated Sonic
4) Sonic Waveforms
5) Gamma Ray
6) 4-arm Caliper
7) Cement bond
8) Temperature
9) Deep Induction

Table 3. History of USGS geophysical logs, SSSDP.

Date	Log	Interval (ft.)	Comments/Results
11/05/85	Temp	100-2,998	Before circulation.
11/05/85	Nat Gamma	9-3,000	Two second time constant.
11/06/85	Temp/Caliper	100-2,998	After circulation.
11/06/85	Televiewer	N/A	No useful logs due to mud density & problems with tools.
11/06/85	Temp	100-3,000	Many stationary readings.
11/06/85	Caliper	983-2,950	
11/06/85	Acoustic DT	1,000-2,950	2 and 3 ft. spacing.
11/07/85	Waveform		2 microsecond sampling.
11/07/85	Temp	2,500-3,000	Stationary readings temperature vs. time.
11/07/85	Nat Gamma	1,000-2,980	
11/07/85	Gamma Spec	1,000-2,980	
11/07/85	Temp	2,500-2,998	Stationary readings at bottom.
12/04/85	Temp		Stationary readings at bottom.
12/09/85	Temp	2,700-5,984	Build up, stationary readings on bottom.
12/10/85	Temp/Caliper	3,375-6,000	
12/10/85	Televiewer		Both televiewers failed.
12/11/85	Nat Gamma	3,400-6,000	Tool did not work.
12/11/85	Gamma Spec		Analyzer failed after one spectrum.
12/11/85	Single Point Resistivity		Burned up tool.
12/11/85	Acoustic DT		Data marginal due to mud density.
12/11/85	Acoustic Full Wave		Total waveforms.
12/11/85	Temp/Caliper	3,400-5,120	Tool hung up.
12/12/85	Caliper	3,500-6,000	
12/12/85	Neutron	2,900-5,980	
12/23-24/85	Temp	3,500-6,230	
12/28/85	Temp	300-6,240	
02/15/86	Temp	6,000-10,400	
03/08/86	Temp	0-10,500	Pre-flow test.
03/12/86	Temp	0-10,500	Pre-flow test.
03/12/86	Televiewer	6,000-6,500	Log through first flow zone, marginal pictures.
03/13/86	Sonic	6,000-8,000	Several passes.
03/27/86	Temp	0-10,220	After 1st phase of reinjection.
03/29-30/86	Gamma Ray	5,690-10,000	
03/29-30/86	Neutron	5,770-10,000	
03/31-04/1	Temp	0-10,200	
04/07/86	Temp	0-9,660	Insulation resistance declining, Run terminated.

Because of financial constraints, the commercial loggers could only be brought in on specific occasions like casing points. On the other hand, the USGS Water Resources Division committed its geothermal research logging truck for the duration of the period from 3,000 ft to total depth. This gave us the flexibility to run logs, particularly temperature logs, when drilling was suspended (e.g., while waiting for fishing tools). This capability was enhanced by the fact that the on-site science managers were trained in running the logging unit and could do so literally on a moment's notice.

Apart from the lack of useful televiewer data and sonic data of questionable quality, the chief gap in the SSSDP logging program was caused by the failure of a motor in the USGS high-temperature 3-arm caliper. Because of repeated trips below 6,000 ft (Figure 2), the wellbore was doubtless over bit gauge over much of that interval, contributing to the loss of acoustic energy from both the televiewer and sonic velocity tools. Although records of excellent quality were obtained to nearly total depth with both passive gamma and neutron tools, their interpretation will be hampered by the lack of a caliper log. The time series of temperature logs is continuing throughout the six-month shut-in period. By the date of this meeting, a joint USGS/LLNL report is expected to be released, including hard copies of all geophysical logs, comparisons of USGS and Schlumberger logs, and some interpretive comments on the logs. A separate report will be issued on the post-drilling temperature logs.

DOWNHOLE EXPERIMENTS

Other downhole experiments included temperature-pressure measurements during and after flow and an attempt at measuring differential flow rates using a spinner-flow meter (Table 4). These measurements were made with developmental "slickline" type tools commissioned by Sandia Corporation (see C. C. Carson, this volume) and assembled by the Kuster Company. They were essentially conventional slickline tools with modified transducers and with recorders housed in dewars with a design operating period of 10 to 12 hours at 400°C. With the exception of the spinner, these tools functioned well and produced useful data on temperature and pressure. An electronic slickline tool which measures both temperature and pressure was built by Service Systems Engineering and is being used primarily for the time series of temperature logs to establish formation temperature over the entire length of the well.

Another category or downhole experiment involved fluid sampling. This proved exceptionally difficult under the hostile conditions encountered in the well. In fact, out of a total of 11 attempts using three different samplers only one was completely successful and an additional run obtained a liquid sample but no gas (Table 4). An attempt to retrieve fluid inclusions by annealing fractured quartz crystals in the brine within the lowermost producing zone was frustrated when the wireline broke because of corrosion, leaving the sample buried in fill near the bottom of the well.

Other experiments involving downhole instruments included a vertical seismic profile experiment using both shear- and compressional-wave vibrators and a downhole gravity experiment (Table 4). Both experiments yielded useful data.

Table 4. Downhole Experiments, SSSDP.

Date	Depth (ft)	Experiment	Comments/Results
a) 1st Flow Test - 6,220 ft.			
12/30/85	6200	Kuster T/P	Log during flow and buildup after shutin. Well bottom hole temp. (BHT) 305 ±5°C.
12/31/85	6200	LANL/Sandia downhole fluid sampler	Two attempts: 1st failed due to brine flashing upon entry into sample bottle and clogging port. 2nd failed due to malfunction of battery system.
(b) 2nd Flow Test - 10,564 ft.			
03/21/86	0-5,000	Kuster spinner/ pressure	Spinner failed at 5,000 ft.
03/21/86	0-10,000	Kuster T/P	Baseline error on temp chart.
03/22/86	0-10,400	Kuster T/P	BHT 350 ±10°C.
03/22-23/86	10,400	1st LANL downhole fluid sampler	No sample due to seal failure causing motor to flood and short out.
03/23/86	10,400	2nd LANL	No sample due to seal failure.
03/23/86	10,400	1st Leutert downhole fluid sampler	Failure due to LCM clogging bullnose.
03/23/86	10,200	2nd Leutert	Clock stopped so canister did not close.
03/23/86	10,200	3rd Leutert	O-rings on sampler bottle failed.
03/23-24/86		USGS Bethke fluid inclusion	Wireline broke leaving tool in bottom of hole. One fishing attempt with no recovery.
03/25/86	10,200	3rd LANL	Sample bottle returns empty.
03/25/86	10,200	4th LANL	Recovered 1.5 liters liquid and .5 liter gas sample.
03/25/86	10,200	5th LANL	Bottle did not open.
03/25/86	10,200	LBL fluid sampler	Recovered 1 liter unpressurized fluid.
03/27-29/86	50-5,650	LBL- Vertical Seismic Profile	Two good data sets with vibrators on drill pad and 1/2 mile off pad. 3rd data set with tool in liner produced too much noise. 4th run tool shorted out.
03/30-31/86	6,000	LLNL downhole gravity	Recovered good data with gravimeter ascending hole from 6000'.
(c) Shut in Period, April-September, 1986			
04/08/86	10,080	Digital T/P	Calibration off on temp tool.
04/22/86	10,080	Kuster T	Stops at 2,016, 4,032, 6,048, 8,064, 10,080.
04/22/86	10,080	Digital T/P	Same stops as above.

*T, temperature; P, pressure

SUMMARY AND CONCLUSIONS

The SSSDP well exceeded target depth, and a comprehensive set of cuttings, cores, and downhole logs was obtained. Two flow tests of different depth were successfully completed, although interferences between different producing horizons will make the data from the second test difficult to interpret. Temperature logging to establish the equilibrium profile will be completed by September 1986. A proposal for further long-term flow tests and to deepen the well a further 1,000 m is now under consideration. If successful, these activities would greatly increase the scientific yield of the SSSDP.

In an early memo (March 8, 1985), the Science Experiments Committee stated that "The SSSDP will be a success if we obtain and release to the public domain drill cuttings, cores, fluid samples, temperature measurements, and a limited suite of wireline logs from a temperature regime that has not previously been adequately sampled and tested." There is a wealth of data and samples, in some instances exceeding our early expectations, and by the standards enunciated in March of 1985, the SSSDP has been a resounding success.

ACKNOWLEDGMENTS

The work described herein could not have been accomplished without the wholehearted cooperation and dedication of all the scientific investigators involved. We thank the management, technical, and drilling staff for their conscientiousness and their sensitivity to the needs of the scientific program. James Mehegan and his assistants at U.C. Riverside played a valuable role in logging, cataloging, and describing core and cuttings samples.

We are especially indebted to our colleagues, John Hendricks, Susan Priest, and Lori Robison, who obtained many of the data and helped to coordinate and facilitate the collection of the remainder.

We thank Arthur Lachenbruch and Robert Nicholson for constructive comments.

W. A. Elders acknowledges support by NSF grant No. EAR 8303557.

REFERENCES

Elders, W. A., Rex, R. W., Meidav, T., Robinson, P. T., and Biehler, S., 1972. Crustal spreading in Southern California. The Imperial Valley and Gulf of California formed by rifting apart of a continental plate. Science, v. 178, no. 4056, p. 15-24.

Lachenbruch, A. H., Sass, J. H., and Galanis, S. P., Jr., 1985. Heat flow in southernmost California and the origin of the Salton trough. Jour. of Geophys. Res. v. 90, no. B8, p. 6709-6736.

Muffler, L. J. P., and White, D. H., 1969. Active metamorphism of upper Cenozoic sediments in the Salton Sea Geothermal Field and the Salton trough, southeastern California. Geol. Soc. Am. Bull., v. 80, p. 157-182.

Sass, J. H., Galanis, S. P., Jr., Lachenbruch, A. H., Marshall, B. V., and Munroe R. J., 1984. Temperature, thermal conductivity, heat flow, and radiogenic heat production from unconsolidated sediments of the Imperial Valley, California. U.S.G.S. Open-File Report 84-490, 38 pp.

Sass, J. H., Hendricks, J. D., Priest, S. S., and Robison, L. C., 1986. The Salton Sea Scientific Drilling Program--A progress report. 1986 McKelvey Forum, U.S.G.S. Circular 974, p. 60-61.

SECTION B

Reprints from the JOURNAL OF GEOPHYSICAL RESEARCH, VOLUME 93, No. B11, 1988

Elders, W.A., and Sass, J.H., "The Salton Sea Scientific Drilling Project," pp 12,953-12,969.

Herzig, C.T., Mehegan, J.M., and Stelting, C.E., "Lithostratigraphy of the State 2-14 Borehole: Salton Sea Scientific Drilling Project," pp 12,969-12,980.

Paillet, F.L. and Morin, R.H., "Analysis of Geophysical Well Logs Obtained in the State 2-14 Borehole, Salton Sea Geothermal Area, California," pp 12,981-12,994.

Sass, J.H., Priest, S.S., Duda, L.E., Carson, C.C., Hendricks, J.D., and Robison, L.C., "Thermal Regime of the State 2-14 Well, Salton Sea Scientific Drilling Project," pp 12,995-13,004.

Newmark, R.L., Kasameyer, P.W., and Younker, L.W., "Shallow Drilling in the Salton Sea Region: The Thermal Anomaly," pp 13,005-13,024.

Daley, T.M., McEvilly, T.V., and Majer, E.L., "Analysis of P and S Wave Vertical Seismic Profile Data From the Salton Sea Scientific Drilling Project," pp 13,025-13,036.

Kasameyer, P.W., and Hearst, J.R., "Borehole Gravity Measurements in the Salton Sea Scientific Drilling Project," pp 13,037-13,046.

Lin, W. and Daily, W., "Laboratory-Determined Transport Properties of Core From the Salton Sea Scientific Drilling Project," pp 13,047-13,056.

Tarif, P.A., Wilkens, R.H., Cheng, C.H., and Paillet, F.L., "Laboratory Studies of the Acoustic Properties of Samples From the Salton Sea Scientific Drilling Project and Their Relation to Microstructure and Field Measurements," pp 13,057-13,068.

Herzig, C.T., and Elders, W.A., "Nature and Significance of Igneous Rocks Cored in the State 2-14 Research Borehole: Salton Sea Scientific Drilling Project, California," pp 13,069-13,080.

Cho, M., Liou, J.G., and Bird, D.K., "Prograde Phase Relations in the State 2-14 Well Metasandstones, Salton Sea Geothermal Field, California," pp 13,081-13,103.

Shearer, C.K., Papike, J.J., Simon, S.B., Davis, B.L., and Laul, J.C., "Mineral Reactions in Altered Sediments From the California State 2-14 Well: Variations in the Modal Mineralogy, Mineral Chemistry, and Bulk Composition of the Salton Sea Scientific Drilling Project Core," pp 13,104-13,122.

Caruso, L.J., Bird, D.K., Cho, M., and Liou, J.G., "Epidote-Bearing Veins in the State 2-14 Drill Hole: Implications for Hydrothermal Fluid Composition," pp 13,123-13,134.

SECTION B (continued)

JOURNAL OF GEOPHYSICAL RESEARCH, VOL. 93, NO. B11, PAGES 12,953-12,968, NOVEMBER 10, 1988

THE SALTON SEA SCIENTIFIC DRILLING PROJECT

Wilfred A. Elders

Institute of Geophysics and Planetary Physics, University of California, Riverside

John H. Sass

U. S. Geological Survey, Flagstaff, Arizona

Abstract. In March 1986 a research borehole, called the "State 2-14," reached a depth of 3.22 km in the Salton Sea geothermal system of southern California. This was part of the Salton Sea Scientific Drilling Project (SSSDP), the first major (i.e., multimillion dollar) research drilling project in the U.S. Continental Scientific Drilling Program. The principal goals of the project were to investigate the physical and chemical processes of a high-temperature, high-salinity, magmatically driven hydrothermal system. The borehole encountered temperatures of up to 355°C and produced metal-rich, alkali chloride brines containing 25 wt% of total dissolved solids. The rocks penetrated exhibit metamorphism and ore genesis in action. They show a progressive transition from unconsolidated lacustrine and deltaic sediments to hornfelses, with lower amphibolite facies mineralogy, accompanied by pervasive veins containing iron, copper, lead, and zinc ore minerals. The SSSDP included an intensive program of rock and fluid sampling, flow testing, and downhole logging and scientific measurement. The purpose of this paper is to introduce this special section of the Journal of Geophysical Research on the SSSDP, to describe briefly the background of the project and the drilling and testing of the borehole, to summarize the initial scientific results, and to discuss how the lessons learned are applicable to future scientific drilling projects.

Introduction

The Salton Sea Scientific Drilling Project (SSSDP) was born in frustration, a frustration common to most proponents of scientific drilling. Although the results of past geological processes are available for study at outcrops, drilling is the best practical method of studying the active processes shaping the outer few kilometers of the Earth's crust. Hydrothermal processes largely occur in this domain. Scientists studying hydrothermal phenomena can only measure the temperatures and sample the fluids and rocks in place by drilling into hot zones. However, drilling is frustratingly expensive. The frustration of scientists is compounded by the fact that although many geothermal wells are drilled by industry, in this country at least, many of the data and samples produced are kept proprietary.

Paper number 7B7195.
0148-0227/88/007B-7195$05.00

Meanwhile, in the United States the concept of drilling the continents for scientific purposes has been debated for decades [e.g., Shoemaker, 1974]. However, it was not until 1984, with the adoption of the "Interagency Accord on Continental Scientific Drilling" by the National Science Foundation (NSF), U. S. Geological Survey (USGS), and Department of Energy (DOE) that much progress was made toward implementing a national program [Stehli and Andrews, 1987]. Frustration with this lengthy gestation, and with the difficulty of obtaining samples and data from geothermal systems, stimulated W. A. Elders, in the fall of 1982, to make a proposal to the National Academy of Sciences to drill a series of research boreholes in the Salton Sea geothermal system of California (SSGS), one of the largest, and hottest geothermal fields in the world (Figure 1). However, there seemed to be no practical way to implement the plan. Discussions with the NSF, USGS, and DOE made it clear that these agencies did not have sufficient funding for this proposal, even though it was receiving widespread support from fellow scientists. Consequently, Elders took the funding request for the Salton Sea Scientific Drilling Project directly to the U.S. Congress, which responded by adding $5.9 million for Phase 1 of the SSSDP to the 1984 budget of the Geothermal Technology Division of DOE. The history of these negotiations, and the subsequent organization which developed, has been described elsewhere [Elders, 1985]. In May 1984 the DOE selected a major engineering company, Bechtel National, Inc. to drill on a site offered by Kennecott, Inc., a resource company holding leases in the SSGS. The borehole was successfully drilled between October 1985 and March 1986. Eventually, the budget for the drilling, engineering, and management of the SSSDP grew to be $6.7 million. A further $2.65 million of scientific studies was funded jointly by the USGS, NSF, and DOE [Aducci et al., 1986]. In all, some 40 different science and technology development projects were involved [Sass and Elders, 1986].

Our aims in the SSSDP were to probe the roots of a very hot geothermal system, a unique hypersaline environment never before thoroughly investigated scientifically. By drilling and testing a deep and very hot research borehole, we also expected to advance the basic science and technology underlying development of geothermal resources. Highlights of Phase 1 of the SSSDP included the following: (1) a depth of 3220 m and temperatures of 355±10°C were reached; (2) the commercial potential of deeper geothermal resources in the SSGS, with high flow rates measured at 350 tonnes/h, was proved; (3) 224 m

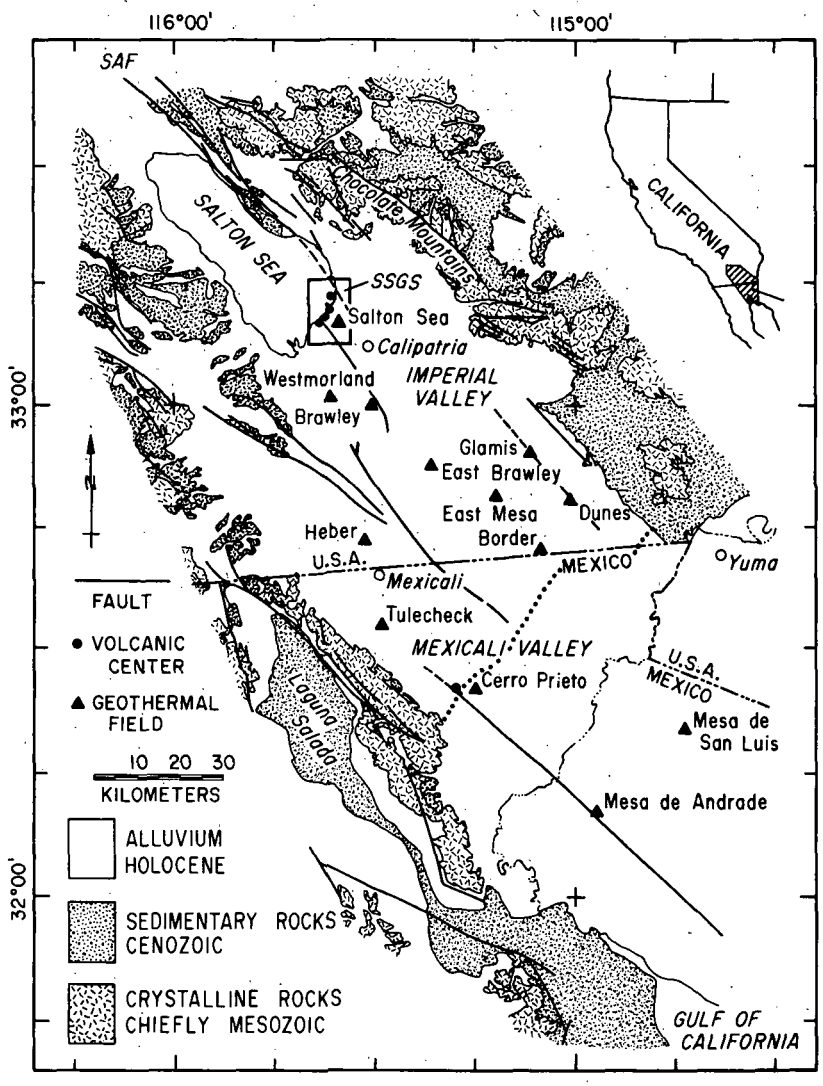

Fig. 1. Geology of the Salton Trough and the location of its geothermal fields. The Salton Sea Geothermal System (SSGS) is the largest and most saline high-temperature hydrothermal system in the Trough. The rectangle marked "SSGS" shows the location of the maps shown in Figures 3 and 4. The dotted line marks the approximate position of the apex of the delta.

of rock core were obtained, demonstrating transitions from unconsolidated lake sediments to highly metamorphosed rocks of lower amphibolite facies, with locally abundant ore minerals; (4) igneous intrusions were penetrated, apparently related to a nearby heat source; (5) samples of steam and of brine containing 25 wt% TDS (total dissolved solids) of metal-rich salts were obtained from two different levels; (6) a comprehensive and technologically sophisticated series of downhole experiments and measurements was successfully concluded, and advanced systems for logging and sampling hot environments were tested; (7) several hundred scientists and engineers from more than 40 different laboratories participated in the overall project; and (8) after initial interinstitutional problems, an excellent collaboration of government, industry, and university agencies was forged, which overcame challenging organizational, technical, and scientific problems.

Geologic Setting

Among the active hydrothermal systems available for study in the United States, the SSGS, in southern California (Figure 1), was selected at an early date as a prime target for research drilling [U.S. Geodynamics Committee, 1979]. Students of hydrothermal processes first became aware of the SSGS through the pioneering publications of White et al. [1963], and Helgeson [1968]. Muffler and White [1969] described greenschist metamorphism occurring at temperatures above 300°C, at only 2-3 km depth.

The SSGS lies on the southeastern shore of the Salton Sea, a lake whose surface is 68 m below sea level, maintained by irrigation runoff in the arid lower desert of California. The Salton Sea is the lowest part of the Salton Trough, a tectonic depression partially filled by detritus deposited by the Colorado River (Figure 1). During the past 4 m.y. the prograding delta of

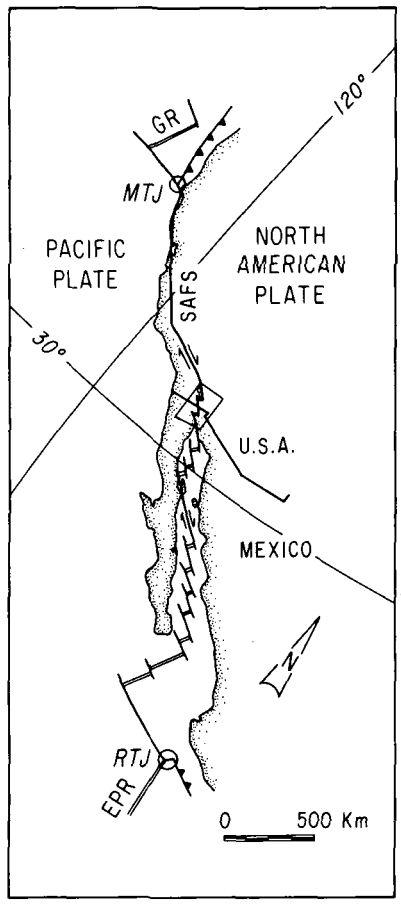

Fig. 2. The boundary between the Pacific and North American plates. The rectangle shows the location of the Salton Trough at the head of the Gulf of California, a tectonic regime transitional between the East Pacific Rise (EPR) and the San Andreas fault system (SAFS). Other abbreviations are GR, Gorda Rise; MJT, Mendocino Triple Junction; RTJ, Rivera Triple Junction (modified after Lachenbruch et al. [1985, (Figure 1)].

the river has isolated this depression from the Gulf of California, to the south, forming a closed basin, containing mainly Pliocene and Pleistocene fluvial and lacustrine deposits [Merriam and Bandy, 1965; Muffler and Doe, 1968; Van de Kamp, 1973; Winker, 1987] (see also Herzig et al. [this issue]). Lesser amounts of basin-margin fan deposits are derived from surrounding mountain ranges. The latter consist largely of Mesozoic crystalline rocks with minor Tertiary volcanic and sedimentary rocks [Dibblee, 1954].

The Salton Trough, consisting of the Imperial Valley north of the international border and the Mexicali Valley south of it, is an area of vigorous tectonic deformation, one of the few regions existing today where a continent is actively rifting and being replaced by oceanic crust. This roughly triangular basin is some 350 km long and 120 km wide at its southern extremity. In location, gross structure, and size it belongs to the Gulf of California tectonic regime (Figure 2). Both the gulf and the Salton Trough have patterns of rapid geodetic deformation, high heat flow, frequent seismicity, and volcanism that reflect the transition from the divergent tectonics of the East Pacific Rise, to the south, to the transform tectonics of the San Andreas fault system, to the north [Elders et al., 1972; Moore, 1973]. Both the Salton Trough and the Gulf of California are dominated by "leaky" transform faulting, with numerous tensional zones developed at the ends of right-stepping, en echelon strike-slip faults. These "pull-apart" structures are the loci of high-temperature geothermal systems [Elders and Biehler, 1975].

The trough has steep, step-faulted margins and a broad, relatively flat basement floor, beneath a cover of sedimentary rocks, apparently 6-10 km thick in the center of the Imperial Valley [Fuis et al., 1982, 1984]. In spite of the thick sedimentary fill, the trough is characterized by a positive gravity anomaly [Biehler et al., 1964; Elders et al., 1972]. Seismic refraction studies are consistent with the hypothesis that the young sediments are being transformed into a metasedimentary basement by high ambient temperatures at 5-6 km depth. This metasedimentary "upper basement" persists to a depth of 10-16 km in the Imperial Valley and is underlain by a "lower basement" with seismic properties and densities similar to those of oceanic crust [Fuis et al., 1982, 1984].

This century, including the two greater than M_L 6.0 earthquakes that occurred in November 1987, there have been 14 earthquakes of modified Mercalli intensity greater than VIII in the Salton Trough. Two distinct types of seismicity occur. Main shock/aftershock sequences produce mainly right-lateral strike-slip faulting. Frequent earthquake swarms also occur with as many as a thousand events in a few days [Johnson and Hill, 1982]. Regional variations in the focal depth of earthquakes occur with the deepest seismicity associated with regions of lowest heat flow. In the trough, which is characterized by high heat flows of more than 100 mW m^{-2} [Lachenbruch et al., 1985], the maximum frequency of depths of hypocenters occurs at only 7 km. In contrast, the maximum occurs at 11 km beneath the Peninsular Ranges, to the west, where heat flows average less than 80 mW m^{-2} [Doser and Kanamori, 1986].

The numerous geothermal fields in the Salton Trough are further manifestations of the high heat flow of the region. Lachenbruch et al. [1985] suggest that the average extensional strain rate in the trough has been about 20-50%/m.y. and that extensional strain must have been distributed over a spreading region about 150 km wide. Consequently, the present seismic pattern must be short-lived on the time scale of the formation of the trough.

The Salton Sea Geothermal System

The SSGS itself has heat flow in excess of 200 mW m^{-2} [Lachenbruch et al., 1985] (see also Figure 9 of Sass et al., [this issue]). In addition, it exhibits a residual Bouguer gravity anomaly of +23 mGal [Biehler, 1974], presumably due to both the densification of the sediments and the presence of igneous intrusions (Figure 3a). A positive magnetic anomaly of 10^{-6} T, 5-8 km wide, extends 28 km northwesterly from

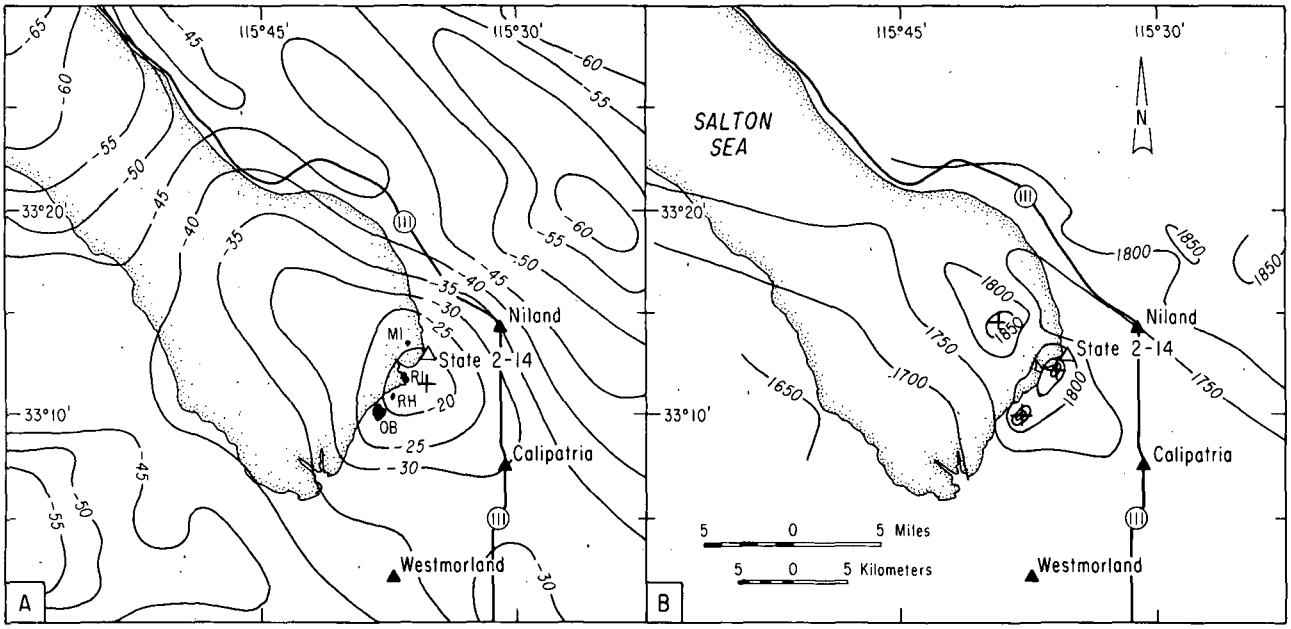

Fig. 3. Geophysical anomalies in the area surrounding the State 2-14 borehole and the Salton Sea geothermal geothermal field. The Quaternary volcanoes (OB, Obsidian Butte; RH, Rock Hill; RI, Red Island (two domes); and MI, Mullet Island) are also shown. (a) Bouguer gravity map; the contour interval is 5 mGal. The plus sign marks the center of a +23 mGal residual anomaly (modified from Biehler, 1974). (b) Aeromagnetic map of total intensity magnetic field; the contour interval is 50 nT (50 gammas). The pluses show locations of local positive magnetic anomalies of $1x10^{-8}$ to $1x10^{-7}$ T, some of which coincide with the Quaternary rhyolite domes [modified after Griscom and Muffler 1971].

Calipatria over the southern part of the Salton Sea (see Figure 3b). Griscom and Muffler [1971] suggest that this is due to the presence of mafic dike swarms at depths greater than 2.25 km. In addition, several small positive magnetic anomalies of 10^{-8} to 10^{-7} T are apparently associated with five small rhyolite domes of Quaternary age. Muffler and White [1969] report a K-Ar date of less than 55,000 years, with a best estimate of 16,000 years, for one of these (Obsidian Butte, see Figure 4). The petrology and petrogenesis of these volcanoes was described by Robinson et al. [1976]. The SSGS is also the locus of low electrical resistivity and high microseismicity. These phenomena and other aspects of the geophysics of the SSGS were reviewed by Younker et al., [1982] and by Elders and Cohen [1983].

The existence of the SSGS has been known for a long time. In 1540, only 48 years after Columbus' epic voyage, Melchor Dias followed the Gulf of California northward and penetrated overland into the delta of the Colorado until turned back by "fields of boiling mud" [Pourade, 1971]. This must have been either the boiling springs, fumaroles, and mud volcanoes at Cerro Prieto or those that formerly existed near Mullet Island, one of the five rhyolite domes in the SSGS (Figure 4). The SSGS hot springs were inundated in 1905-1906 by the rising lake that now forms the modern Salton Sea. These hydrothermal manifestations persuaded the Pioneer Development Company in 1927 to drill three exploratory wells, up to 450 m deep, near Mullet Island [Lande, 1979]. Although steam was encountered, these wells were never exploited for electrical power, and geothermal drilling was not resumed until 1957. Since then more than 50 commercial geothermal wells have been drilled. Although at present only two small geothermal electric power plants are operating in the SSGS, several more are under construction or planned. The slow pace of commercial development stems largely from the high costs of handling brines which after steam separation may have concentrations of up to 35 wt% TDS.

In spite of this long history of development, resource assessments for the SSGS were, until recently, poorly constrained. At the lower end, Towes [1976] calculated the recoverable heat to be $11.7x10^{18}$ J, roughly equivalent to 50 MW electrical for 30 years. At the higher end, Meidav and Howard [1979] estimated the recoverable heat as $586x10^{18}$ J, equivalent to about 20,000 MW electrical for 30 years. In the light of newly acquired data from this project and from the numerous recently completed commercial wells, these estimates can now be refined and ideas on the hydrology of the SSGS improved.

Different investigators have proposed conflicting hydrothermal models for fluid flow in the SSGS. These models can be grouped as follows: (1) influx of cool groundwater from the southeast [Loeltz et al., 1975; Riney et al., 1978; Olson and Matlick, 1978]; (2) influx of cool groundwater from northwest [Rex, 1983]; and (3) outflow of hot water southeast from the center of the SSGS [Kasameyer et al., 1984].

The major uncertainty in developing these models was that the data used were derived almost

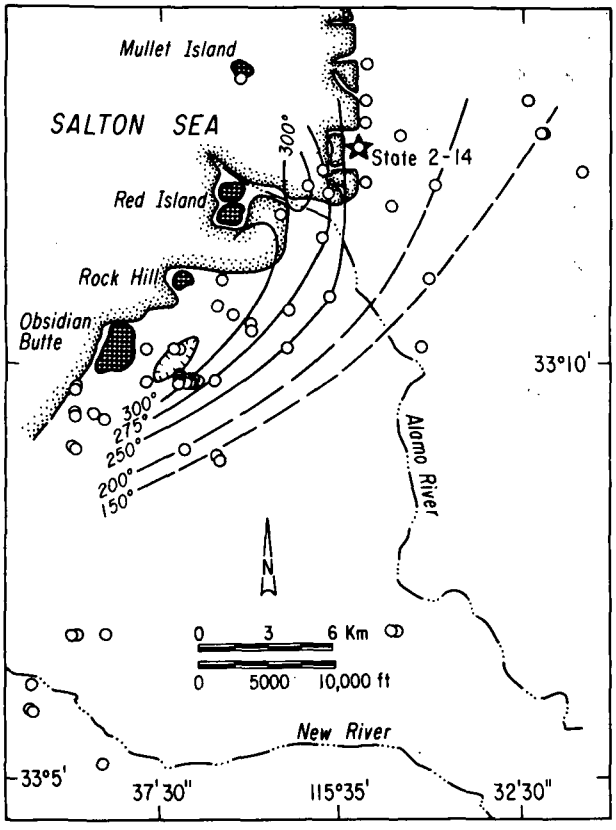

Fig. 4. Location of the borehole State 2-14 in the SSGS (star), and other geothermal wells (open circles). Cross-hatched areas are the Quaternary rhyolite domes. The contours are isotherms in degrees centigrade measured in geothermal wells at 914 m (3000 ft) depth.

entirely from the landward portion of the SSGS; there were no significant drilling data for those parts of the gravity and magnetic anomalies now covered by the Salton Sea. This omission has since been remedied by the work of Newmark et al. [1986; this issue] whose new shallow temperature gradient measurements now cover both the onshore and offshore parts of the system. They indicate a smaller area for the hottest part of the thermal anomaly than previously thought, with a region of shallow, high thermal gradients forming an arcuate band 4 km wide and 12 km long, roughly paralleling the arc of the volcanic domes shown in Figure 4. Within this zone, heat flow exceeds 600 mW m^{-2} and there are heat flow maxima, at each end of the arc, with values exceeding 1200 mW m^{-2}. This intense, high-temperature axial anomaly is surrounded by a broad region of elevated conductive heat flow, with an area of at least 150 km^2, in which bottom-hole temperatures in wells drilled to 2500 m might be expected to be more than 250°C [Newmark et al., this issue]. The location of this shallow heat flow anomaly coincides with the temperature anomaly measured in deep geothermal wells (Figure 4). This suggests that in the zone of highest heat flow, lateral flow of fluids is minor and that at greater depth the SSGS is dominated by vertical fluid flow [Yi, 1987].

These data provide a context in which to discuss the temperature gradient and heat flow measurements in the SSSDP borehole [Sass et al., this issue]. They also suggest that the thermal budget of local "hot spots" such as the SSGS may be large enough to account for the rate of heat flux for the entire Salton Trough and that these intense local thermal anomalies are short-lived [Newmark et al., this issue]. These results also confirm the inferences made by Kasameyer et al., [1984] that the SSGS is about 10^4 years old.

The SSSDP

Borehole State 2-14

The specific location of the SSSDP borehole, called "State 2-14" (S/2-14) because it was sited on land belonging to the State of California, was not dictated by scientific criteria, but was chosen by DOE's requesting competitive proposals from geothermal leaseholders, in accordance with U.S. Government procurement policies. It lies slightly east of the main thermal anomaly, in a zone where some horizontal fluid flow might be expected (Figure 4). Drilling began on October 24, 1985, and took 160 days using a rotary drill rig and standard oilfield technology, modified for high temperatures. It was completed as shown in Table 1.

Figure 5 is a time-depth plot summarizing drilling progress and showing the amount of time allotted to various scientific activities [Sass and Elders, 1986]. Because the primary goals of the SSSDP were scientific rather than commercial, research and development were given priority over engineering, to the extent that safety and borehole integrity were not compromised. However, problems were encountered that caused us to modify the science plan in practice. Attempts to mitigate these problems used up $1.3 million of the budget for drilling and testing. These

TABLE 1. Hole Diameters and Casing Configuration

Depth, meters	Hole Diameter Millimeters	(Inches)	Casing Type	Outside Diameter of Casing Millimeters	(Inches)
0-46	914	(36)	conductor	762	(30)
0-315	660	(26)	surface casing	508	(20)
0-1071	445	(17.5)	intermediate	340	(13.375)
0-1829	311	(12.25)	production	244	(9.625)
1752-3093	216	(8.5)	hung liner	178	(7)
3093-3193	216	(8.5)	open hole	(uncased)	
3193-3220	156	(6.125)	open hole	(uncased)	

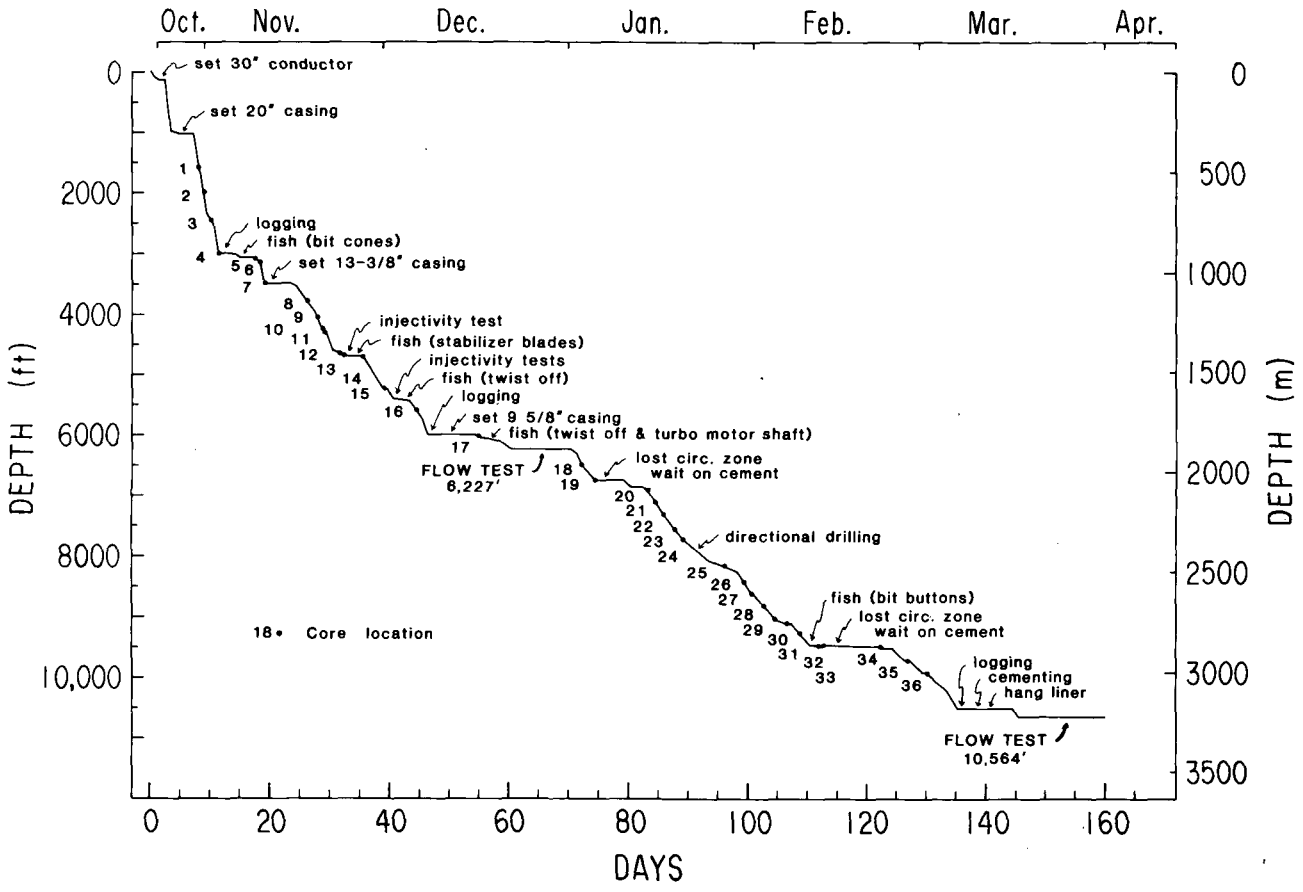

Fig. 5. Depth progress chart for the State 2-14 research borehole. The numbered dots record the locations of the drill cores. Note the large amount of time devoted to logging and testing (6227 ft = 1898 m; 10564 ft = 3220 m).

activities included fishing and stuck pipe (8 days), directional drilling (18 days), and lost circulation and well control (20 days) [Harper and Rabb, 1986]. The highly fractured formations drilled caused directional problems below 1071 m. At 1829 m depth the borehole had deviated to the east at an angle of over 8° from vertical. This required directional drilling between 1853 and 1926 m, which reduced the angle to an acceptible value of 3° [Nicholson, 1986]. Between 1829 m and total depth, nine major fluid loss zones, presumably fracture zones, caused slow progress (Table 2). While the drill string was being removed to change bits, these zones tended to

TABLE 2. Flow Test Results, State 2-14

Well Depth, meters	Depths of Flow, meters	Duration, hours	Flow rate, t/h*	Wellhead Temperature °C	Wellhead Pressure MPa	Enthalpy, kJ/kg
			First Test			
1898	1865	4	273	205	14.0	930
		12	36	240	31.0	930
		2	195	210	15.5	930
		9	68	240	31.5	930
			Second Test			
3220	[1865] **	3	216	230	21.8	1210
	[2012]	24	127	245	31.5	1115
	[2682]	1	318	240	27.0	1115
	[3193]	4	136	255	34.0	1050

Adapted from Harper and Rabb, [1986].
* Tonnes per hour.
** Multiple flow zones.

allow brine to flow vigorously into the borehole and boil. Aggressive treatment was necessary to quench the well and restore borehole integrity, using lost circulation materials and cement.

Cuttings and Core

At least 1 kg of cuttings was collected at 6- to 9-m intervals down to 900 m and at 3-m intervals below that depth (except, of course, from zones of total circulation loss). Because the technology of continuous coring in large diameter wells was not available to us, it was decided to allocate $1,000,000 to spot coring. In practice, only $550,000 was spent on actual coring operations. The funds released were needed to address the problems mentioned above and on additional rig time for wireline logging. In 36 core runs, 241 m of the hole were cored, and 224 m (93%) of core were recovered. At depths greater than 1500 m, the intervals that could be cored successfully declined precipitously due to the increased tendency of fractured rocks to jam the core barrel. Counting the 402-m length of core barrels run, the 224 m of core obtained represent only 56% of the potential core recovery [Nicholson, 1986]. In view of the difficulties encountered here, using the best available oil field technology and experienced personnel, we believe improvements are necessary in coring hot and fractured formations, particularly in large-diameter boreholes.

Fluid Sampling

Because variations of salinity were expected, fluid sampling was planned at 1 km, at 2 km, and at total depth. Unfortunately, no significant permeability was recognized between the casing points at 1071 and 1829 m. However, a major zone of circulation loss, associated with abundant vein-filling epidote, occurred at 1865 m. Accordingly, the brine was stimulated to boil in the well bore and was allowed to discharge to a surface holding pond. A downhole temperature of 305°C±5°C was measured at 1890 m during this flow (Table 2). Cost considerations precluded using a full-flow steam/brine separator or drilling a disposal well for the brine output.

When free of contamination by drilling fluid, the stable brine flow was expanded through a series of four orifice plates and then flashed to the atmosphere [Michels, 1986a]. Table 2 shows well head conditions during flow, and Table 3 shows an average chemical analysis of fluids sampled at the well head during the first flow test, corrected to preflash conditions. Attempts were also made to collect unflashed samples using downhole samplers [Goff et al., 1987]. When the brine storage pit, of approximately 7 x 10^6 L capacity, filled after 1.5 days, the flow test was terminated. The brine was disposed of by injecting it back into the well before drilling resumed.

Budgetary limitations also prevented testing the numerous zones of lost circulation encountered below 1865 m. More than a million liters of drilling fluid were lost to these fractures. However, when circulation was again lost near the planned total depth and temperature logs indicated the loss was occurring at the bottom of the borehole, a 178-mm (7 in) liner was hung to 3079 m, without being cemented in place. The lack of cement in the annulus probably contributed to problems which occurred during the ensuing flow test and to the eventual failure of the liner itself (see below). The borehole was then deepened to a total depth of 3220 m to test the deeper part of the reservoir. During this second flow test a temperature of 355°C±10°C was measured at 3170 m. Tables 2 and 3 show the results of the test. Once more, downhole fluid sampling was attempted. This flow test also had to end after 2 days when the storage pit filled. Unfortunately, this occurred before the produced fluids were completely free of contamination by mud and diesel oil used in drilling. Subsequently, temperature logs indicated that much of the flow came from behind the liner (see the discussion on temperature logging below).

The extent of residual contamination in the brine can be estimated from the hydrogen and oxygen isotopic analyses of A.E. Williams (personal communication, 1987) shown in Figure 6. Coplen et al., [1975] had pointed out that the δD and δO^{18} of surface and shallow groundwaters in the Salton Trough plot to the right of the meteoric water line and define an evaporation line connecting waters from the Colorado River to those from the Salton Sea. The averaged analyses for the second flow test lie on a mixing line between the averaged analyses for the first flow test and those of the drilling mud. The mud was mixed using local canal water, which plots close to Coplen's evaporation line. The isotopic data

TABLE 3. Average Composition of Produced Fluids From State 2-14

Element	Parts Per Million (Weight)	
	December, 1985*	March, 1986**
Na	52,661	52,200
Ca	26,515	27,100
K	16,502	16,900
Fe	1,522	1,630
Mn	1,385	1,430
Zn	506	483
Si	387	560
Sr	405	401
NH_4	336	314
B	253	258
Ba	194	336
Li	190	199
Pb	95	97
Mg	36	47
Cl	153,668	150,000
SO_4	110	50
TDS***	254,849	252,005
CO_2	1,664	1,500
H_2S	7	-

* First flow test analysis, adapted from Michels [1986b].

** Second flow test, A.E. Williams (unpublished data, 1986).

*** TDS, total dissolved solids.

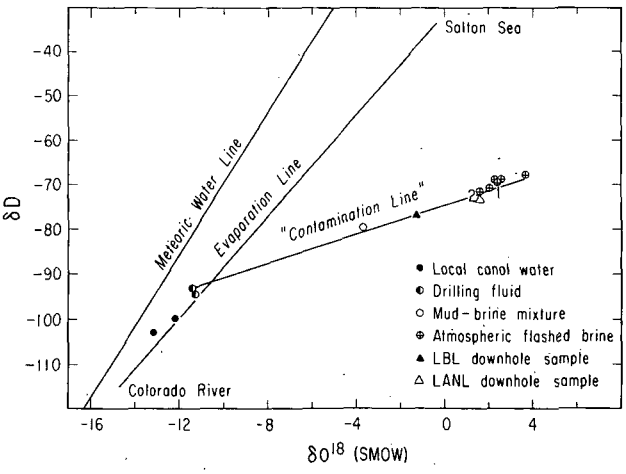

Fig. 6. Hydrogen and oxygen isotopic ratios for fluids produced from the State 2-14 and related samples, relative to the meteoric water line and the evaporation line for groundwaters in the Salton Trough [Coplen et al., 1975], connecting Colorado River waters to Salton Sea waters (see text). The drilling mud was made up using local canal water. The "1" and "2" mark the average isotopic values of fluids produced from the first and second flow tests, respectively, calculated back to downhole conditions before boiling. The "atmospheric flashed brine" samples were collected at the wellhead during the second flow test and have been made isotopically heavier by steam separation. Also shown are two samples collected by downhole samplers during the second flow test (LANL sample SS-21 and LBL sample SS-23), and a sample of mud-brine mixture from the initial flow of the well during this test. These data define a mixing or "contamination line" with fluids from the first flow test having negligible contamination (A.E. Williams, unpublished data, 1986).

suggest that brine from the second test was 5-8% contaminated by drilling fluid.

Downhole Logging and Geophysical Measurements

More than 450 hours of rig time were devoted to downhole logging and measurement. At each casing point below 315 m, a commercial logging company (Schlumberger, Inc.) ran dual induction, natural gamma, compensated neutron formation density, four-arm caliper, and sonic waveform logs. However, at temperatures above 300°C, problems were severe. The only successful log deeper than 1829 m was a deep induction log, which returned data down to 2686 m. A much more extensive logging program was performed by the Borehole Research Logging Project of the USGS. The USGS logging truck was equipped with prototype tools and a Teflon-insulated, seven conductor cable, armored with a corrosion-resistant nonferrous alloy (MP35N), rated to 315°C (specially manufactured for the SSSDP at a cost of $360,000). The USGS unit was stationed at the site so that logs could be run during interruptions of drilling. The USGS logs obtained were temperature, three-arm caliper, natural gamma, gamma spectral, epithermal neutron, acoustic velocity, full waveform, and acoustic televiewer [Sass and Elders, 1986; Paillet, 1986]. Some of the USGS tools were successfully deployed below 1829 m depth. However, the sonic and borehole televiewer logs were of poor quality so that fracture characterization was not possible. At temperatures above 300°C, the best results were obtained from passive gamma and neutron tools, but the USGS three-arm caliper tool failed. The logs obtained have already been published by Paillet [1986] and their interpretation is discussed by Paillet and Morin [this issue].

As part of the technology development program sponsored by DOE, other high-temperature devices which used downhole recording systems were designed for the SSSDP. These included temperature, pressure, and flow meter tools, with mechanical transducers and recorders housed in double-walled vacuum heat shields (Dewars), designed to operate for up to 10 hours at temperatures up to 400°C. In addition, a new continuously recording, digital pressure-temperature tool, built around a heat-shielded downhole electronic memory, was also deployed. This tool has considerable advantages over mechanical recording systems previously used at temperatures greater than 300°C [Carson, 1986; Sass et al., this issue].

Three different kinds of downhole fluid samplers, one mechanical, one powered by an electrical conductor cable, and one using a downhole battery pack as a power source, were deployed during flow tests [Solbau et al., 1986; Wolfenbarger, 1986]. Out of 12 attempts, only one was completely and four partially successful in returning samples [Goff et al., 1987; Grigsby et al., 1987]. The techniques of downhole sampling also require further development to sample fluids hotter than 300°C. Other downhole experiments could only be carried out after cooling the well by injecting cold water. These included vertical seismic profiling and experiments using a down-downhole gravity meter [Daley et al., this issue; Kasameyer and Hearst, 1987].

Temperature Logs

Temperature logs were run during pauses in drilling operations and during flow tests primarily for engineering purposes. After the borehole was shut in, a series of temperature profiles was measured to monitor the return to thermal equilibrium [Sass et al., this issue]. The April 1, 1986, log records the situation immediately after injecting cooled brine from the second flow test (Figure 7). This unexpected temperature profile is the key to understanding problems encountered during that test. The temperature inflections at 1.9, 2.6, and 3.1 km show where cold brine entered the formation. However, the uncemented liner did not isolate the lost circulation zones penetrated during drilling and most of the injected brine flowed up behind the liner, some even reaching the zone at 1865 m that flowed in the first flow test. Apparently, the lack of cement in the annulus of the liner compromised the second flow test so that these permeable zones contributed most of the flow produced in the second flow test (Table 2).

The latest logs show data only shallower than

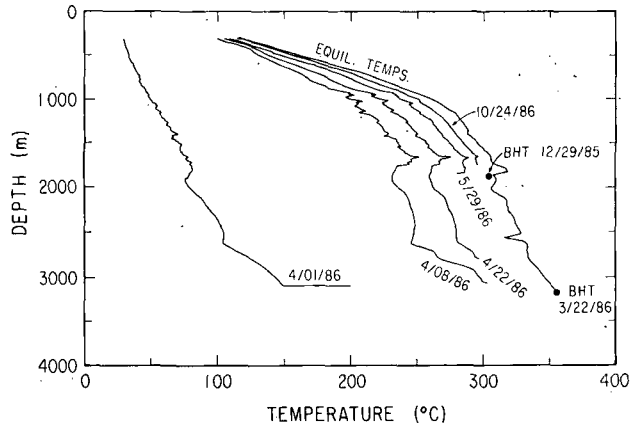

Fig. 7. Temperature profiles measured on various dates in the borehole State 2-14. "BHT" represents bottom hole temperatures measured during flow tests on the two dates shown. The profile marked "Equil. Temps" was extrapolated from the four previous temperature logs to the approximate equilibrium values by Sass et al. (this issue).

1.8 km (Figure 7). On May 29, 1986, it was found that the liner was blocked at about 1.9 km. In June 1986 diagnostic logging revealed that the liner had corroded and parted at 1883 m. It appears that the type of liner chosen and the lack of cement in the annulus made it unsuitable for these hostile conditions. Below 1883 m, the best data are the bottom-hole temperatures measured during the flow tests, i.e., 305°C±5°C at 1890 m and 355°C±10°C at 3170 m. The curve marked "Equil. Temps." in Figure 7 represents an equilibrium temperature profile, estimated by Sass et al. [this issue]. The extrapolated curve gives good agreement with the two bottom-hole measurements (the short sections showing sharp excursions are computational artifacts in zones perturbed by brine injection).

Remedial Actions and Further Work

When the 7-inch (178 mm-) diameter liner parted, only nine joints (82 m, i.e., 270 ft) remained suspended from the production casing. When removed in August 1986, the collars on these joints were found to be moderately to severely cracked due to stress corrosion. Budgetary considerations caused further remedial work to be delayed until August 1987. Because the fallen liner could not be retrieved, the borehole was cemented off at 1860 m and redrilling commenced, using downhole turbine motors to sidetrack past the old liner. Numerous technical difficulties caused this redrilling to be abandoned at only 2188 m depth. In the summer of 1988, DOE carried out a 30-day-long reservoir technology flow test of the open section of the redrilled borehole. Brine disposal was by injection into a nearby well which was drilled by Kennecott, Inc. in September 1987.

Scientific Results

Initial results of the intensive studies of samples and data recovered were reported in a symposium at the annual meeting of the American Geophysical Union in May 1987. Important findings from the resulting papers (including some not submitted to this special section) are briefly summarized here.

Lithostratigraphy

The borehole penetrated Pleistocene strata of the Borrego and Brawley formations [Tarbet and Holman, 1944; Dibblee, 1954] with 70% lacustrine mudstones and siltstones, and minor amounts of sandstones, deposited in lake margin, channel fill, and lacustrine delta environments [Herzig et al., this issue]. To the depth of about 335 m these strata are unconsolidated; at greater depth they become progressively indurated and mineralized. Sandstone compositions indicate a provenance from the Colorado River. Steep bedding, minor faults, and liquefaction features are common, as expected in an area of high seismicity. Anhydrite is abundant as nodules, concretions, and thin beds, the product of an evaporitic environment.

Igneous Rocks

A 0.25-m-long core of the lower contact of a silicic volcanic tuff was recovered from 1704 m. Based on geophysical logs, its thickness may be between 1 and 2 m. As far as we are aware, this is the first published report of a subsurface pyroclastic rock from the Salton Trough. Diabasic sills at 2880-2883 and 2895-2905 m depth have brecciated chilled contacts with the hydrothermally altered shales. Chemical data suggest that the silicic tuff is correlative with a tuff cropping out 25 km NW in the Durmid Hills. This in turn is apparently derived from the Bishop tuff erupted 0.7 m.y. ago from the Long Valley caldera, California [Herzig and Elders, this issue]. It may prove to be a useful marker bed to correlate between geothermal wells. However, the diabase intrusions seen in the S/2-14 borehole are part of a bimodal rhyolite-basalt assemblage, previously observed in the Salton Butte volcanoes in the SSGS [Robinson et al., 1976]. The diabases appear to be representatives of larger basaltic intrusions that are the probable source of the large magnetic anomaly; rhyolites have much too low magnetic susceptibility [Griscom and Muffler, 1971]. Such basaltic intrusions are the most likely heat source for the SSGS. The diabases, although somewhat enriched in light rare earth elements relative to the basalts of the East Pacific Rise, probably had a mantle-derived parent magma, appropriate for a rift system [Herzig and Elders, this issue].

Metamorphism

With increasing depth, the sediments become progressively more metamorphosed and exhibit hornfelsic textures. Earlier workers had described this progressive metamorphism of up to greenschist facies in the SSGS, in samples recovered from geothermal wells [Muffler and White, 1969; McDowell and Elders, 1980, 1983]. This earlier work was based almost entirely on study of drill chips. Thus it was difficult to

elucidate paragenetic sequences and sometimes even to distinguish between detrital, authigenic, and vein minerals. Study of cores from the borehole S/2-14 has reduced many of these uncertainties. The sequence of prograde mineral reactions in the cores has also clearly demonstrated a transition into amphibolite facies at temperatures and pressures much lower than generally accepted for that degree of metamorphism [Turner, 1986].

In the sandstones, metamorphic zones observed with increasing grade include a chlorite-calcite zone (610-2480 m); a biotite zone (2480-3000 m); and a clinopyroxene zone (3000-3180 m) [Cho et al., this issue]. Authigenic epidote, quartz, and albite are ubiquitous below 900 m. In the clinopyroxene zone the coexistence of authigenic actinolite, actinolitic hornblende, and oligoclase demonstrates the transition from greenschist to amphibolite facies. In the mudstones, progressive changes in the phyllosilicates include authigenic illite/smectite mixed layers being replaced by illite at 1222 m, illite-chlorite appearing at 1582 m, chlorite-biotite at 2480 m, and biotite at 3175 m [Donaghe and Peacor, 1987]. Extensive reactions between brines and carbonates in both sandstones and mudstones release CO_2 by reactions forming epidote, actinolite, and diopside. Such extensive chemical interaction is also indicated by progressive leaching of Cu, Zn, and Mn and enrichment of Sr in these rocks [Shearer et al., this issue].

The S/2-14 borehole occupies a flank position in the geothermal field (Figure 4). As might be expected therefore, its petrology shows transitional characteristics relative to that of geothermal wells in the center of the field. Cuttings from geothermal wells in the center of the SSGS show similar metamorphic zonation but at shallower depth and exhibit higher degrees of leaching of Mn, Cu, and Zn and other metals, particularly in the biotite zone. These differences suggest that hydrothermal alteration in the central portion of the SSGS has been more extensive (involving a higher water/rock ratio), has been of longer duration, or both [McDowell, 1987].

Rock fragments ejected from the borehole during the first flow test, when compared with cores above and below the production zone at 1865 m, demonstrate an intense epidote enrichment in the vicinity of open fractures. The fracture-filling minerals consist of an open framework of acicular epidote with pyrite, or acicular epidote with specular hematite. Thermodynamic analyses of solid phases and brine from the first flow zone are generally consistent with the major mineral assemblages in the flow zone at 300°C [Charles et al., this issue]. However, the fluid is not in equilibrium with the pyrite-bearing assemblages. Oxidation of pyrite-bearing meta-metasediments seems to have leached sulfur from these rocks, stabilizing the hematite-bearing assemblages.

Origin of the Brine

The origin of the salt in the SSGS brines has been attributed to dissolution of lacustrine evaporites, formed from evaporated Colorado River water, by percolating groundwater [White, 1968; Rex, 1983]. Studies of newly available drill cores now provide the first direct physical evidence for dissolution of nonmarine evaporites. These cores contain recrystallized, metamorphosed, bedded anhydrite, and anhydrite-cemented shale breccias, which appear to have formed by solution collapse. Some fluid inclusions within these anhydrites contain up to 50% of crystals of halite, sylvite, and carbonates in a Na-Ca-K-Cl brine, and have homogenization temperatures of 300°C [McKibben et al., 1988b]. These observations are consistent with trapping of salt-saturated brines during dissolution of evaporites by hydrothermal fluids.

Comparison of the data from the S/2-14 with that from other wells in the SSGS have led Williams and McKibben [1987] and McKibben et al. [1987] to point out the bimodal character of the SSGS fluids. The hot, hypersaline brine of the type described in Table 3 is overlain by a cooler (less than 250°C), metal-poor fluid of lower salinity (less than 12 wt% TDS). A sharp interface between these two fluid types exists over much of the field. This interface has a domal structure roughly paralleling the isotherms but transgressing the bedding and other structures. Williams and McKibben [1987], and Williams [1988] suggest that this dome formed by advective rise of heated hypersaline brine as a brine diapir. Furthermore, chemical reactions between brines and rocks, especially those involved in ore formation are, to a large degree, controlled by this abrupt brine interface [McKibben et al., 1987]. These conclusions are complemented by extensive geochemical investigations of the brines [Campbell et al., 1987; Thompson and Fournier, this issue; Michels, 1988].

Ore Formation

Active ore formation had earlier been described in the SSGS in studies based primarily on drill cuttings [Skinner et al., 1967; McKibben and Elders, 1985]. The cores from the S/2-14 show that ore minerals are almost entirely restricted to mineralized fractures and the adjacent rocks. These samples have greatly clarified the mineral parageneses [Caruso et al., this issue; McKibben et al., 1987]. An earlier carbonate-sulfide vein set contains minor epidote, adularia, and ankerite together with abundant calcite, sphalerite, pyrite, chalcopyrite, galena, and pyrrhotite. A later, more open, silicate-hematite-sulfide vein set consists of epidote, quartz, chlorite, and abundant hematite, together with chalcopyrite, pyrite, sphalerite, and galena. The later set is apparrently forming today. Further insight into this mineralization comes from fluid inclusion studies [Andes, 1987; Roedder and Howard, this issue] and light stable isotopic studies [Sturtevant and Williams, 1987]. These indicate a complex thermal history in the S/2-14, with somewhat higher paleotemperatures and much lower paleosalinities in the upper 1 km than those observed today at greater depths. This complex history included fracturing and infiltration by fluids of varying composition and temperature that sealed the fractures by mineral precipitation. The vein mineral assemblages observed suggest that cooler, oxidized fluids

have displaced hotter, reduced fluids as brines derived from different sources mixed [McKibben et al., 1988a].

Earlier isotopic studies of Sr and Pb suggested that the source of these components in the brines of the SSGS was leaching from the host rocks [Doe et al., 1966]. Whole rock chemical analyses of the S/2-14 cores lead to the conclusion that the other metals in the brine are also leached from the sediments [Shearer et al., this issue]. Earlier studies of the base metal sulfide ores in the SSGS, using available drill cuttings, suggested that the source of their sulfur was replacement of diagenetic stratabound pyrite by Cu, Pb, and Zn from the metal-rich brines [McKibben and Elders, 1985]. Petrographic studies of the S/2-14 cores and analyses of sulfur isotopes now indicate that the source of sulfur in the hydrothermal sulfides of the SSGS is sedimentary. However, the reduced sulfur is derived by reduction of sulfates in the host evaporites [McKibben and Eldridge, 1988].

Radiochemistry

Study of strong disequilibria of daughter products in the ^{238}U, ^{235}U, and ^{232}Th radioactive decay chains is providing new insights into the mechanisms controlling radioisotope exchange and permits estimation of the rates of brine-rock interaction [Hammond et al., this issue; Zukin et al., 1987]. In the case of the short-lived isotopes $^{228}Ac/^{228}Ra$, the data indicate that the mean lifetime of relatively insoluble actinides in solution, before removal from the brine by sorption on solid surfaces, is about 2 hours. The $^{212}Pb/^{224}Ra$ and $^{210}Pb/^{226}Ra$ ratios in the brine are comparable to ratios predicted from a simple recoil model. The mean residence times of lead and radium in solution are both only about 30 years, whereas the corresponding residence time of radium in associated solid phases is about 2000 years [Hammond et al., this issue]. The implications of these observations are that the SSGS is very young and that chemical exchange rates are very rapid.

Geophysics

Apart from the temperature measurements already discussed, geophysical studies stressed the variation of physical properties within the borehole, both from downhole measurements [Paillet and Morin, this issue; Daley et al., 1988, this issue; Kasameyer and Hearst, 1987] and from laboratory measurements [Lin and Dailey, this issue; Tarif et al., this issue). Downhole estimates of porosity, density, and seismic velocity were in reasonable agreement with laboratory determinations. The downhole gravimetric measurements of density [Kasameyer and Hearst, 1987] are in good agreement with the well log values [Paillet and Morin, this issue] but are slightly higher. Vertical seismic profiling [Daley et al., this issue] provided a compressional wave velocity profile comparable to that obtained from full waveform velocity logs by Paillet and Morin (this issue). They also inferred at this site anisotropy in shear wave velocity of the order of about 1%. A fracture zone at depths of between 2.0 and 2.1 km provided a strong reflector and other fracture zones were detected on the basis of P wave scattering.

Depth-smoothed trends in electrical, acoustic, and gamma attenuation logs recorded changes in the properties of clay minerals with temperature [Paillet, 1986; Lei, 1988; Paillet and Morin, this issue]. Local departures from this trend occur due to brine conduction in porous sands which overwhelm clay mineral conductivity. Below 1.8 km the induction and epithermal neutron logs confirmed the nearly uniformly impermeable nature of the altered sediments due to reduced porosity. However, the frequent lost circulation zones indicate increasing fracture permeability with depth. Neither passive gamma logs nor electrical resistivity logs could be interpreted with great confidence below 1.8 km because of a generally low level of radioactivity, high salinity, and low porosity. Televiewer logs were also of limited value in fracture mapping, owing primarily to the fact that the hole was greatly enlarged and contained significant amounts of cement and lost circulation material in the zones of greatest interest [Paillet, 1986; Paillet and Morin, this issue].

Ongoing Studies

Many of the studies reported in this special section will continue for some time. It seems appropriate, however, to mention some of the things that are not underway and which should be done or that have not yet been sufficiently applied. Perhaps the most significant omission are the areas of sedimentology, stratigraphy, and paleontology. While the cores are a treasure trove for petrologists and economic mineralogists, much more could be done, building on the work of Herzig et al. [this issue], to develop sedimentological information in terms of the source and provenance of the sediments, the depositional environment, the soft-sediment deformation, and the earthquake-induced clastic dikes. More could be done to correlate the sedimentological, petrological, and wireline log properties of the altered sediments.

As yet, we know of no attempts to provide age control on these sediments. Are there hardy microfossils that survive above 200°C and are there hardy micropaleontologists willing to look for them? However, work is underway to attempt radiometric dating of the S/2-14 tuff and the Pleistocene tuff in the Durmid Hills, which Merriam and Bischoff [1975] correlated with the Bishop Tuff erupted from Long Valley caldera, California, 0.72 m.y. ago.

Similarly, it would be highly desirable to extend and improve attempts at dating the hydrothermal system and its igneous rocks by radiometric or other means. Comparisons with the Cerro Prieto geothermal system (Figure 1), which has similar lithology to the SSGS, would be also worthwhile. Whereas the Cerro Prieto system has comparable temperatures and similar hydrothermal minerals to those of the SSGS, there are striking differences [Schiffman et al, 1984]. In contrast to the SSGS, the occurrence of hydrothermal minerals at Cerro Prieto is incipient, and the rocks largely retain their sedimentary textures. In addition, ore minerals and mineralized veins are scarce at Cerro Prieto. Determining the

cause of the differences would improve our understanding of both systems. The detailed information from the S/2-14 should also be correlated with the information available from the other wells in the area, to generate three-dimensional, quantitative models for the origin and evolution of the SSGS, such as has been done for Cerro Prieto [e.g., Elders et al., 1984]. In future phases of the SSSDP, deeper research wells should be sited in the center of the thermal zone closer to the heat sources responsible for the geothermal system and perhaps even to reach molten rock.

Conclusions

Phase 1 of the SSSDP met or exceeded almost all of its initial objectives. The fruitful collaboration that occurred among several government agencies and researchers from various universities and organizations augurs well for the future of continental scientific drilling in the United States. Although organizational and technical problems were encountered, we produced a wealth of new data, under hostile conditions, concerning a dramatic example of active metamorphism and ore genesis. We also showed that although the rocks in the SSGS become increasingly indurated with depth and lose porosity, permeability increases due to fracturing. This suggests that the resource potential of the SSGS may be increased by drilling deeper wells.

We also learned some lessons applicable to other scientific drilling projects. One lesson, as the new shallow temperature gradient data from the SSGS have shown, is the utility of combining both shallow and deep drilling. In a scientific drilling investigation we should not become wedded to any specific depth as the key to success.

A lesson specifically applicable to study of hydrothermal systems is the importance of arranging long-term flow tests of specific production zones. The very successful 2-day flow test at 1859 m sampled brine relatively free of drilling-fluid contamination. Several conditions contributed to this success: there were no major losses of circulation higher in the well; drilling was discontinued soon after encountering the loss zone at 1859 m; and the volume of the holding pond volume was adequate to allow the flow to clean up. However, the short duration of the test meant that the well was always in a transient stage of flow. The flow test of the deepest producing horizon at 3193 m encountered numerous problems because none of the conditions mentioned above were met. We believe therefore that it is desirable, in testing geothermal systems, to (1) isolate specific permeable zones; (2) flow the well long enough to remove contamination; (3) sample successively larger volumes of the reservoir; and (4) establish stable conditions for adequate reservoir characterization. This requires that a disposal well should be available and also suggests the need to develop high-temperature packers and drill stem test equipment. Another lesson was the difficulty of dealing with zones of massive loss of circulation. Normally, in drilling commercial wells we look for permeability rather than try to overcome it.

Perhaps the most important lesson learned from the SSSDP is to obtain as much core as possible. Due to the fractured nature of the rocks, the 7% of the well which was cored was less than the 10% called for in initial planning. The amount of core recovered was, however, comparable to that obtained by other recent Continental Scientific Drilling Projects using rotary rigs. These cores have provided unprecedented research opportunities relative to what is normally available from commercial geothermal wells. They allowed us to (1) make petrophysical measurements, (2) identify sedimentary and evaporitic facies, (3) determine some of the structural relations, (4) distinguish among igneous tephras, sills, and flows, and (5) resolve mineral parageneses and vein sequences, and study the birth of an ore body. Better coring systems obviously need to be developed, especially for deep hot wells and fractured formations.

In spite of the large investments in equipment and rig time, the results of the wireline logging program were disappointing for depths greater than 1.8 km. The tools deployed by the USGS were prototypes, developed some years ago, that were pushed beyond their temperature limits. Hole conditions precluded optimum tool performance in the most interesting depth intervals. Because of the need to obtain good quality wireline logs in deep boreholes which are not continuously cored, the present generation of logging tools and cables need to be upgraded as regards temperature, performance, and reliability for future research drilling projects.

As mentioned earlier, the DOE sponsored the development of several downhole recording ("slickline") tools that provided useful data for the SSSDP. The downhole samplers, although plagued initially with component failures attributable to the hostile environment, demonstrated that they could work at 355°C. Similarly, the heat-shielded, mechanical-recording, pressure-temperature tools operated without the failures associated with conventional mechanical tools above 300°C. However, the most significant advance in logging technology was the heat-shielded digital temperature tool. This has higher accuracy and more rapid response than a mechanical tool (10 s versus 10 m), thus providing a much higher data density. Such digital tools seem to offer a great potential for future development and do not require expensive conductor cables.

Probing deeper into the roots of hydrothermal systems will require more cost effective solutions to the kinds of problems that we faced in drilling, sampling, and logging than were available to us. We have learned that drilling and testing at high temperatures is just as much a technical and scientific frontier as drilling at very great depths. However, as the Continental Scientific Drilling Program drills deeper, even in areas of moderate geothermal gradient, conditions comparable to those at lesser depths in geothermal systems will inevitably be encountered. Thus the accumulated experience of drilling and testing by the world wide geothermal industry will become more generally applicable.

The science of geology developed in the nineteenth century by painstaking mapping of the

surface of the continents. In the first half of this century, geophysical methods began to play an increasing role in our understanding of the crust of the Earth. Twenty years ago geology was revolutionized by the new systematic study of the ocean floors by the Deep Sea Drilling Project. In retrospect, it seems paradoxical to us that although continental geology is inherently more complex, in the United States we have had, until recently, no scientific drilling program on land comparable to the ocean drilling program. Our experience with the Salton Sea Scientific Drilling Project has convinced us of the importance of such a program in the United States.

Acknowledgments. This project, which was funded by DOE, USGS, and NSF, succeeded by the wholehearted cooperation of many individuals too numerous to mention here. We are particularly grateful to John Hendricks, Sue Priest, and Lori Robison, whose efforts as on-site science managers always exhibited the highest degree of professionalism and congeniality. We are also appreciative of the support of colleagues at UCR and USGS. We are indebted to A.E. Williams for providing unpublished data on fluid chemistry and to F.L. Goff, J. Eichelberger, L.J.P. Muffler, and R.H. Wallace, Jr. for penetrating reviews of earlier drafts of this manuscript. The Chief Scientist position for the SSSDP was funded by NSF grant EAR 8303557. The on-site science management team was supported by the Office of the Chief Geologist, USGS. This is IGPP/UCR Report 88-1.

References

Adduci, A.J., D.W. Klick, and R.H. Wallace, Jr., Management of the Salton Sea Scientific Drilling Program, Trans. Geotherm. Resour. Counc., 445-448, 1986.

Andes, J.P., Jr., Mineralogic and fluid inclusion study of ore-mineralized fractures in drillhole State 2-14, Salton Sea Scientific Drilling Project, Imperial Valley, California, UCR-IGPP Rep. 87/17, 136 pp., Inst. of Geophys. and Planet. Phys., Univ. of Calif., Riverside, 1987.

Biehler, S., Bouguer gravity map of California, Salton Sea sheet, Calif. Div. of Mines and Geology, Sacramento, 1974.

Biehler, S.S., R.L. Kovach, and C.R. Allen, Geophysical framework of the northern end of the Gulf of California structural province, Mem. Am. Assoc. Pet. Geol., 3, 126-143, 1964.

Campbell, A.C., J.M. Edmond, T.S. Bowers, C.I. Measures, M.R. Palmer, and E.T. Brown, Geochemistry of Salton Sea Scientific Drilling Project hydrothermal fluids in comparison to Red Sea brines. (Abstract), Eos Trans. AGU, 68, 439, 1987.

Carson, C.C., Development of downhole instruments for use in the Salton Sea Scientific Drilling Project, Trans. Geotherm. Resour. Counc., 10, 449-454, 1986.

Caruso, L.J., D.K. Bird, M. Cho, and J.G. Liou, Epidote-bearing veins in the State 2-14 drillhole: Implications on hydrothermal fluid composition, J. Geophys. Res., this issue.

Charles, R.W., D.R. Janecky , F.E. Goff, and M.A. McKibben, Chemographic and thermodynamic analysis of the paragenesis of the major phases in the vicinity of the 1866 m flow zone, California State 2-14, J. Geophys. Res., this issue.

Cho, M., J.F. Liou, and D.K. Bird, Prograde phase relations in the State 2-14 well metasandstones, Salton Sea geothermal field, California. J. Geophys. Res., this issue.

Coplen, T.B., P. Kolesar, R.E. Taylor, C. Kendall, and C. Mooser, Investigations of the Dunes geothermal anomaly , Imperial Valley, California, part IV, Geochemical studies of water, calcite, and silicates, UCR-IGPP Rep. 75/20, 43 pp., Inst. of Geophys. and Planet. Phys., Univ. of Calif., Riverside, 1975.

Daley, T.M., T.M. McEvilly, and E.L. Majer, Analysis of P and S wave vertical seismic profile data from Salton Sea Scientific Drilling Project, J. Geophys. Res., this issue.

Dibblee, T.W., Jr., Geology of the Imperial Valley region, California, Geology of the natural provinces, chapter 2, Geology of southern California, edited by R.H. Jahns, Bull. Calif. Div. Mines Geol., 170, 21-28, 1954.

Doe, B.R., C.E. Hedge, and D.E. White, Preliminary investigation of the source of lead and strontium in deep geothermal brines underlying the Salton Sea geothermal area, Econ. Geol., 61, 462-483, 1966.

Donaghe, L.L., and D.R. Peacor, Textural and mineralogic transitions in SSSDP argillaceous sediments (1987) (Abstract), Eos Trans. AGU, 68, 454, 1987.

Doser, D.I., and H. Kanamori, Depth of seismicity in the Imperial Valley region (1977-1983) and its relationship to heat flow, crustal structure, and the October 15, 1979, earthquake, J. Geophys. Res., 91, 675-688, 1986.

Elders, W.A., Continental Scientific Drilling in California: The saga of the Salton Sea Scientific Drilling Project (SSSDP), Trans. Geotherm. Resour. Counc., 9, 107-112. 1985.

Elders, W.A., and S. Biehler, Gulf of California Rift System and its Implications for the Tectonics of Western North America, Geology, 3, 85, 1975.

Elders, W.A., and L.H. Cohen, The Salton Sea Geothermal Field, California as a near-field natural analog of a radioactive waste repository in salt, Rep. BMI/ONWI-513, 138 pp., Office of Nucl. Waste Isolation, Battelle Memorial Insitute, Columbus, Ohio, 1983.

Elders, W.A., R.W. Rex, T. Meidav, P.T. Robinson, and S. Biehler, Crustal spreading in southern California: The Imperial Valley and the Gulf of California formed by rifting apart of a continental plate, Science, 178, 15-24, 1972.

Elders, W.A., A.E. Williams, D.K. Bird, and P. Schiffman, Hydrothermal flow regime and magmatic heat source of the Cerro Prieto geothermal system, Baja California, Mexico, Geothermics, 13, 27-47, 1984.

Fuis, G.S., W.D. Mooney, J.H. Healey, G.A. McMechan, and W.J. Lutter, Crustal structure of the Imperial Valley, U.S. Geol. Surv. Prof. Pap., 1254, 25-49,1982.

Fuis, G.S., W.D. Mooney, J.H. Healey, G.A. McMechan, and W.J. Lutter, A seismic refraction survey of the Imperial Valley region, California, J. Geophys. Res., 89, 1165-1189, 1984.

Goff, F., L. Shevnall, C.O. Grigsby, and B. Dennis, Downhole fluid sampling at the SSSDP California State 2-14 well, Salton Sea, California, Los Alamos Nat. Lab., Rep. LA-11052-OBES, 32 pp., 1987.

Grigsby, C.O., F. Goff, L. Shevenell, J. Archuleta, J. Cruz, P.E. Trujillo, D. Counce, and G .K. Bayhurst, Downhole fluid sampling and analytical data for the SSSDP well, Salton Sea, California (Abstract), Eos Trans. AGU, 68, 454, 1987.

Griscom, A., and L.P.J. Muffler, Aeromagnetic map and interpretation of the Salton Sea geothermal area, California, U.S. Geol. Surv. Geophys. Invest. Map, GP 754, 1971.

Hammond, D.E., J.G. Zukin, and T.-L. Ku, The kinetics of radioisotope exchange between brine and rock in a geothermal system, J. Geophys. Res., this issue.

Harper, C.A., and D.T. Rabb, The Salton Sea Scientific Drilling Project, Drilling summary, Trans. Geotherm. Resour. Counc., 10, 455-460, 1986.

Helgeson, H.C., Geologic and thermodynamic characteristics of the Salton Sea geothermal system, Am. J. Sci., 266, 129-166, 1968.

Herzig, C.T. and W.A. Elders, The nature and significance of igneous rocks cored in the State 2-14 research borehole, Salton Sea Scientific Drilling Project, California, J. Geophys. Res., this issue.

Herzig, C.T., J.M. Mehegan, and C.E. Stelting, Lithostratigraphy of the State 2-14 borehole; Salton Sea Scientific Drilling Project, J. Geophys. Res., this issue.

Johnson, C.E., and D.P. Hill, Seismicity in the Imperial Valley, U.S. Geol. Surv. Prof. Pap., 1254, 15-24, 1982.

Kasameyer, P.W., and J.R. Hearst, Bore-hole gravity measurements in the SSSDP hole (Abstract), Eos. Trans. AGU, 68, 445, 1987.

Kasameyer, P.W., L.W. Younker, and J.M. Hanson, Development and application of a hydrothermal model for the Salton Sea geothermal field, California, Geol. Soc. Am. Bull., 95, 1242-1252, 1984.

Lachenbruch, A.J., J.H. Sass, and S.P. Galanis, Heat flow in southernmost California and the origin of the Salton trough, J. Geophys. Res., 90, 6709-6736, 1985.

Lande, D., History of Drilling in the Imperial Valley, in Geology and Geothermics of the Salton Trough, edited by W.A. Elders, Campus Mus. Contrib. 5, pp. 45-46, Univ. of California, Riverside, 1979.

Lei, H.-Y., Porosity and hydrothermal alteration determined from wireline logs from the Salton Sea geothermal field, California, U.S.A, UCR-IGPP Rep. 88/5, 168 pp., Inst. of Geophys. and Planet. Phys., Univ. of Calif. Riverside, 1988.

Lin, W., and W. Dailey, Laboratory-determined transport properties of core from the Salton Sea Scientific Drilling Project, J. Geophys. Res., this issue.

Loeltz, O.J., B. Irelan, J.H. Robison, and F.H. Olmsted, Geohydrologic Reconnaissance of the Imperial Valley, California, U.S. Geol. Surv. Prof. Pap., 486-K, 1975.

McDowell, S.D., The Salton Sea Scientific Drill Hole in context (Abstract), Eos Trans. AGU, 68, 44, 1987.

McDowell, S.D., and W.A. Elders, Authigenic layer silicate minerals in borehole Elmore #1, Salton Sea Geothermal Field, California, U.S.A., Contrib. Mineral. Petrol., 74, 293-310, 1980.

McDowell, S.D., and W.A. Elders, Allogenic layer silicate minerals in borehole Elmore #1, Salton Sea Geothermal Field, California, Am. Mineral., 1146-1159, 1983.

McKibben, M.A., J.P. Andes, Jr., and A.E. Williams, Active ore-formation at a brine interface in metamorphosed deltaic-lacustrine sediments: The Salton Sea geothermal system, California, Econ. Geol., 83, 511-523, 1988a.

McKibben, M.A., and W.A. Elders, Fe-Zn-Cu-Pb mineralization in the Salton Sea geothermal system, Imperial Valley, California, Econ. Geol. 80, 539-559, 1985.

McKibben, M.A., and C.S. Eldridge, Sulfur isotope variations among minerals and aqueous species in the Salton Sea geothermal system: a SHRIMP ion microprobe and conventional study, Am. Jour. Sci. in press, 1988.

McKibben, M.A., A.E. Williams, W.A. Elders, and C.S. Eldridge, Saline brines and metallogenesis in a modern sediment-filled rift: The Salton Sea geothermal system, California, U.S.A, Appl. Geochem., 2, 563-578, 1987.

McKibben, M.A., A.E. Williams, and S. Okubo, Metamorphosed Plio-Pleistocene evaporites and the origins of hypersaline brines in the Salton Sea geothermal system, California, Fluid inclusion evidence, Geochim. Cosmochim. Acta, 52, 1047-1056, 1988b.

Meidav, T., and J.H. Howard, An update of Tectonics and Geothermal Resource Magnitude of the Salton Sea Geothermal Field, Trans. Geotherm. Resour. Counc., 3, 445-448, 1979.

Merriam, R., and O.L. Bandy, Source of the upper Cenozoic sediments in Colorado River Delta Region, J. Sediment. Petrol., 35, 911-916, 1965.

Merriam R., and J.L. Bischoff, Bishop Ash: A widespread volcanic ash extended to southern California, J. Sediment. Petrol., 45, 207-211, 1975.

Michels, D.E., A chemical method for measuring steam quality in two-phase flowlines, Trans. Geotherm. Resourc. Counc., 10, 443-445, 1986a.

Michels, D.E., SSSDP fluid compositions at first flow test of State 2-14, Trans. Geotherm. Resourc. Counc., 10, 461-466, 1988b.

Michels, D.E., Salinity Stabilization for non-advecting brine in a temperature gradient, Trans. Geotherm. Resourc. Counc., 12, in press, 1988.

Moore, D.G., Plate edge deformation and crustal growth, Gulf of California structural province, Geol. Soc. Am. Bull., 84, 1883-1906, 1973.

Muffler, L.J.P., and B.R. Doe, Composition and mean age of detritus of the Colorado River delta in the Salton Trough, southeastern

California, J. Sediment. Petrol., 38, 384-399, 1968.

Muffler, L.J.P., and D.E. White, Active metamorphism of upper cenozoic sediments in the Salton Sea Geothermal Field and the Salton Trough, southeastern California, Geol. Soc. Am. Bull., 80, 157-182, 1969.

Newmark, R.L., P.W. Kasameyer, L.W. Younker, and P.C. Lysne, Research drilling at the Salton Sea geothermal field, California: The shallow thermal gradient project, Eos Trans. AGU, 67, 698-707, 1986.

Newmark, R.L., P.W. Kasameyer, and L.W. Younker, Shallow drilling in the Salton Sea region: The thermal anomaly, J. Geophys. Res., this issue.

Nicholson, R.W., Extensive coring in deep hot geothermal wells, Trans. Geotherm. Resourc. Counc., 10, 467-472, 1986.

Olson, E.R., and J.S. Matlick III, A flow through model for the Westmoreland geothermal system, Imperial Valley, California, UCR-IGPP Rep. 78/7, 41 pp., Inst. of Geophys. and Planet. Phys., Univ. of Calif., Riverside, 1978.

Paillet, F.L. (Ed.), Preliminary report on geophysical well-logging activity on the Salton Sea Scientific Drilling Project, Imperial Valley, California, U.S. Geol. Surv. Open File Rep., 86-544, 99 pp., 1986.

Paillet, F.L. and R.H. Morin, Analysis of geophysical well logs obtained in the State 2-14 borehole, Salton Sea geothermal area, California, J. Geophys. Res., this issue.

Pourade, R.F., Anza Conquers the Desert, 216 pp., Copley Press, San Diego, Calif., 1971.

Rex, R.W., The origin of the brines of the Imperial Valley, California, Trans. Geotherm. Resourc. Counc., 7, 321, 1983.

Riney, T.D., J.W. Pritchett, and S.K. Garg, Salton Sea geothermal field reservoir simulations, Trans. Geotherm. Resourc. Counc., 2, 2571-574, 1978.

Robinson, P.T., W.A. Elders, and L.J.P. Muffler, Quaternary volcanism in the Salton Sea geothermal field, Imperial Valley, Geol. Soc. Am. Bull., 80, 347-360, 1976.

Roedder, E., and K.W. Howard, Fluid inclusions in Salton Sea Scientific Drilling Project core: Preliminary results, J. Geophys. Res., this issue.

Sass, J.H., and W.A. Elders, Salton Sea Scientific Drilling Project: Scientific program, Trans. Geotherm. Resourc. Counc., 10, 473-478, 1986.

Sass, J.H., S.S. Priest, L.E. Duda, C.C. Carson, J.D. Hendricks, and L.C. Robison, Thermal regime of the State 2-14 well, Salton Sea Scientific Drilling Project, J. Geophys. Res., this issue.

Schiffman, P., W.A. Elders, A.E. Williams, S.D. McDowell, and D.K. Bird, Active metasomatism in the Cerro Prieto geothermal system, Baja California, Mexico: A telescoped low P/T metamorphic facies series, Geology, 12, 12-15, 1984.

Shearer, C.K., J.J. Papike, S.B. Simon, B.L. Davis, F.J. Rich and J.C. Laul, Mineral reactions in altered sediments from the California State 2-14 Well: Variations in the modal mineralogy, mineral chemistry, and bulk composition of the Salton Sea Scientific Drilling Project core, J. Geophys. Res., this issue.

Shoemaker, E. (Ed.) Continental drilling, 56 pp, Carnegie Inst. of Washington, D.C., 1974.

Skinner, B.J., D.E. White, H.J. Rose, and R.E. Mays, Sulfides associated with the Salton Sea geothermal brine, Econ. Geol., 62, 316-330, 1967.

Solbau, R., O. Weres, L. Hansen, and B. Dudak, Description of a high temperature downhole fluid sampler, Trans. Geotherm. Resourc. Counc., 10, 479-484, 1986.

Stehli, F.G., and R.S. Andrews, The United States Continental Scientific Drilling Program, in Observations of the Continental Crust Through Drilling II, edited by H.-J. Behr, and F.G. Stehli, 229 pp., Springer-Verlag, New York, 1987.

Sturtevant, R.G., and A.E. Williams, Oxygen isotopic profiles of the State 2-14 geothermal well: Evidence for a complex thermal history, Eos Trans. AGU, 68, 445, 1987.

Tarbet, L.A., and W.H. Holman, Stratigraphy and micropaleontology of the west side of the Imperial Valley, California, Am. Assoc. Pet. Geol. Bull., 28, 1781-1782, 1944.

Tarif, P.A., R.H. Wilkens, C.H. Cheng, and F.L. Paillet, Laboratory studies of the acoustic properties of samples from the Salton Sea Scientific Drilling Project and their relation to microstructure and field measurements, J. Geophys Res., this issue.

Thompson , J.M., and R.D. Fournier, Chemistry and geothermometry of brine produced from the Salton Sea Scientific drill hole, Imperial Valley, California, J. Geophys. Res. this issue.

Towes, D., An estimation of the geothermal energy resource in the Salton Trough, Rep. UCRL-51851, Lawrence Livermore Natl. Lab., Univ. of Calif. Livermore, 1976.

Turner, F.J., Metamorphic Petrology: Mineralogical and Field Aspects, 2nd ed., 403 pp., McGraw-Hill, New York, 1986.

U.S. Geodynamics Committee, Continental Scientific Drilling Program, 150 pp., National Academy of Sciences, Washington, D. C., 1979.

White, D.E., Environments of generation of some base-metal ore deposits, Econ. Geol. 63., 301-335, 1968.

White, D.E., E.T. Anderson, and D.K. Grubbs, Geothermal brine well: Mile deep hole may tap ore-bearing magmatic water and rocks undergoing metamorphism, Science, 130, 919-922, 1963.

Williams, A.E., Delineation of a brine interface in the Salton Sea geothermal system, California, Trans. Geotherm. Resour. Counc., in press, 1988.

Williams, A.E., and M.A. McKibben, A brine interface in the Salton Sea geothermal system, California: Fluid geochemical and isotopic distribution, UCR-IGPP Rep. 87/31, 66 pp., Inst. of Geophys. and Planet. Phys., Univ. of Calif., Riverside, 1987.

Winker, C.D., Neogene stratigraphy of the Fish Creek-Vallecito Section, southern California: Implications for early history of the northern Gulf of California and Colorado Delta, Ph.D. dissertation, Univ. of Ariz., Tucson, 1987.

Wolfenbarger, F.M., Battery pack/controller for

high temperature applications, Trans. Geotherm. Resour. Counc., 10, 485-489, 1986.

Van de Kamp, P.C., Holocene continental sedimentation in the Salton basin, California: A reconnaissance, Geol. Soc. Am. Bull., 84, 827-848, 1973.

Yi, Z., On the shallow hydrothermal regime of the Salton Sea geothermal Field, California, UCR-IGPP Rep. 87/45, 265 pp., Inst. of Geophys. and Planet. Phys., Univ. of Calif., Riverside, 1987.

Younker, L., P.W. Kasameyer, and J.D. Tewhey, Geological, geophysical and thermal characteristics of the Salton Sea geothermal field, California, J. Volcanol. Geotherm. Res., 12, 221-258, 1982.

Zukin, J.G., D.E. Hammond, T.-L. Ku, and W.A. Elders, Uranium-thorium series radionuclides in brines and reservoir rocks from two deep geothermal boreholes in the Salton Sea geothermal field, southeastern California, Geochim. Cosmochim. Acta, 51, 2719-2731, 1987.

W. A. Elders, Institute of Geophysics and Planetary Physics, Univerity of California, Riverside, CA 92521

J. H. Sass, U. S. Geological Survey, 2255 N. Gemini Drive, Flagstaff, AZ 86001.

(Received February 9, 1988;
accepted April 8, 1988.)

JOURNAL OF GEOPHYSICAL RESEARCH, VOL. 93, NO. B11, PAGES 12,969-12,980, NOVEMBER 10, 1988

LITHOSTRATIGRAPHY OF THE STATE 2-14 BOREHOLE: SALTON SEA SCIENTIFIC DRILLING PROJECT

Charles T. Herzig and James M. Mehegan[1]

Geothermal Resources Program, Institute of Geophysics and Planetary Physics
University of California, Riverside

Charles E. Stelting

Chevron Oil Field Research Company, La Habra, California

Abstract. Sedimentary rocks from the (California) State 2-14 research borehole of the Salton Sea Scientific Drilling Project, located in the Imperial Valley of southern California, were deposited in the continental basin of the Salton Trough. Lacustrine shale and siltstone are the dominant lithologies. Sandstones were deposited in lake margin, meander channel fill, and lacustrine delta environments. Framework modal clast compositions of the sandstones indicate a dominant Colorado River provenance. Rare pebbly mudstones were deposited as storm-induced debris flows. Primary depositional structures in the sediments are commonly disrupted by seismic disturbances. Nonmarine gastropods and ostrocods are relatively uncommon, and occurrences of stratabound sulfides suggest periods of brackish water conditions. Bedded anhydrite and centimeter-scale mudcracks record intervals of dessication. The State 2-14 sedimentary rocks are interpreted as the basinward facies of the Borrego and Brawley formations which range from Pliocene to Pleistocene in age.

Introduction

The Salton Trough, located at the northern end of the Gulf of California, is a continental basin forming by rifting and transform fault motion as the East Pacific Rise/Gulf of California spreading ridge intersects the North American continent (Figure 1) [Atwater, 1970; Crowell, 1974a,b; Elders et al., 1972; Lachenbruch et al., 1985]. The spreading ridge within the Gulf of California is broken by a number of en echelon transform faults [Atwater, 1970; Larson et al., 1968]. During extension along the offset segments of the spreading ridge, large (pull-apart) basins may develop, for example, the Carmen and Guaymas basins in the Gulf of California, and the Salton Trough. These basins are the depocenters for the accumulation of sedimentary sequences.

The (California) State 2-14 research borehole of the Salton Sea Scientific Drilling Project (SSSDP) penetrated 3.22 km of sedimentary rocks in the Salton Sea geothermal system, a small pull-apart basin in the Salton Trough [Elders and Sass, this issue]. This paper presents the results of the study of the lithostratigraphy of the sedimentary rocks penetrated by the State 2-14 research borehole. A detailed evaluation of the subsurface geology in this area of the Salton Trough is possible because an integrated set of cores, cuttings, and wire line logs were acquired during the drilling of the State 2-14 well.

Geologic Setting

The Salton Trough is a sedimentary basin containing 4-6 km of unmetamorphosed sediments of Cenozoic age in its center [Elders and Sass, this issue; Fuis and Kohler, 1984]. On three sides it is bounded by mountains composed of igneous and metamorphic rocks of pre-Tertiary age and opens southward toward the Gulf of California [Dibblee, 1954; Elders et al., 1972]. The San Andreas transform fault cuts the east side of the basin, and an anastomosing system of strike-slip faults cuts the west side of the basin (Figure 1). Strike-slip and normal faults offset rocks in the center of the trough [Elders et al., 1972; Fuis et al., 1984].

Lacustrine, fluvial-deltaic, alluvial, and eolian sediments [van de Kamp, 1973] of Holocene age occupy the central part of the basin. These sediments are stratigraphically underlain by the nonmarine, lacustrine, and fluvial-deltaic sedimentary rocks of the Borrego, Brawley, and Palm Spring formations which range from Pliocene to Pleistocene in age [Babcock, 1969, 1974; Dibblee, 1954, 1984; Downs and White, 1983; Johnson et al., 1983; Winker, 1987]. Marine rocks of the Pliocene Imperial Formation [Dibblee, 1954, 1984; Winker, 1987] in turn underlie the Borrego, Brawley, and Palm Spring formations.

The nonmarine sediments in the Salton Trough were deposited mainly by the Colorado River, whose prograding delta has isolated the northern Salton Trough from the Gulf of California since the Pliocene [Merriam and Bandy, 1965; Muffler and Doe, 1968; van de Kamp, 1973; Winker, 1987]. The lacustrine and fluvial-deltaic sedimentary rocks sampled in the State 2-14 well represent the Colorado River-dominated, depositional

[1]Now at Department of Geology, California State University, San Bernardino.

Paper number 88JB03244.
0148-0227/88/88JB-03244$05.00

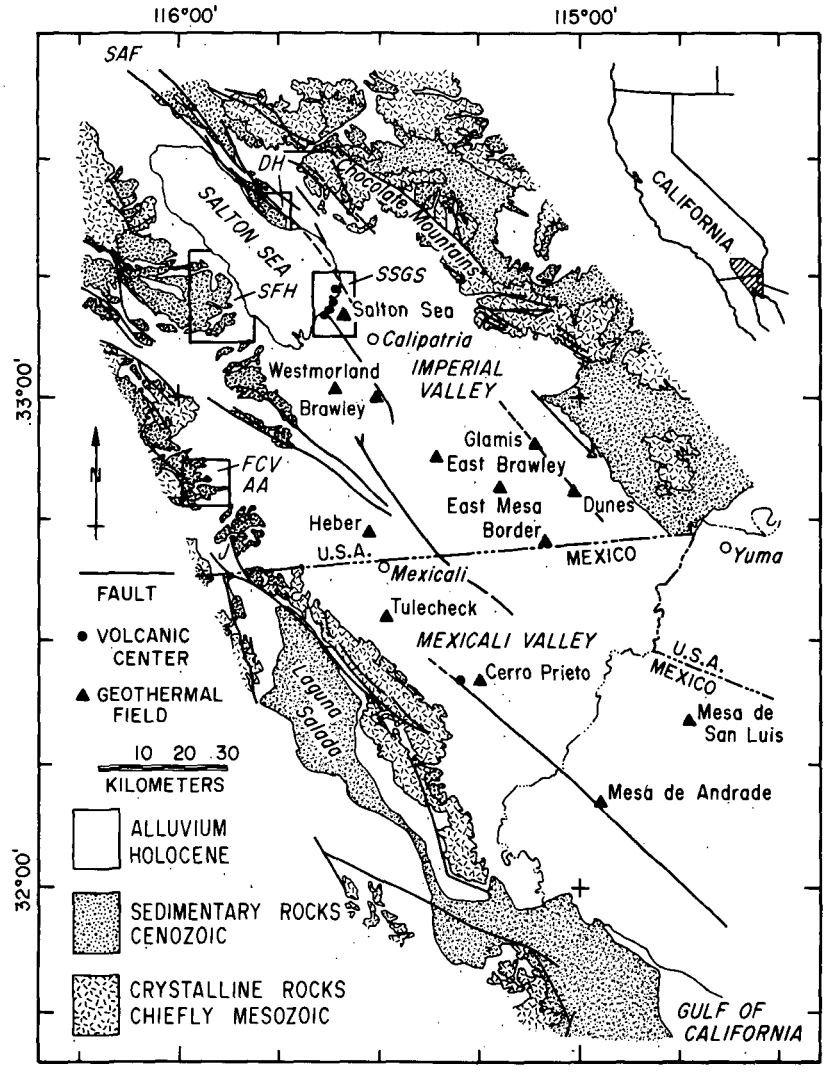

Fig. 1. Generalized map of the Salton Trough. AA, Alverson andesite; DH, Durmid Hills; FCV, Fish Creek-Vallecito; J, Jacumba; SAF, San Andreas Fault; SFH, San Felipe Hills; SSGS, Salton Sea geothermal system. Location of State 2-14 borehole shown by solid triangle within the SSGS.

environment of the northern Salton Trough. The Holocene history of this sedimentary basin has been described by Sykes [1937], Arnal [1961], and Waters [1983]. There have been alternating periods of deposition of sediments and dessication as the Colorado River flowed alternately into the basin or directly into the Gulf of California.

Sampling Program and Documentation

This lithostratigraphic evaluation of the State 2-14 borehole is a part of the Salton Sea Scientific Drilling Project (SSSDP). Two major goals of the SSSDP were the acquisition of core and cuttings and a comprehensive set of wire line logs [Elders and Sass, this issue]. The sampling program during drilling operations consisted of collecting 1 kg of cuttings at 6- to 9-m intervals and retrieving 0.3- to 18-m-long spot cores at approximately 60-m intervals; a total of 222 m of spot cores were obtained. The drill cores were cleaned, oriented, photographed, and videotaped [Herzig and Mehegan, 1986a, b; Lilje and Mehegan, 1986; Mehegan et al., 1986].

Lithologies of the State 2-14 Borehole

Stratigraphy and Structure

The lithostratigraphic column of the State 2-14 borehole is characterized by interbedded shales, siltstones, sandstones, and pebbly mudstones of variable thicknesses (Figure 2). Shale and siltstone are the most abundant rock types; some intervals of shale and siltstone are up to 125 m thick. Less common sandstone intervals range from 9 to 15 m thick, and 1- to 2-m-thick intervals of pebbly mudstones are dispersed throughout the well. Other rock types include a silicic volcanic tuff at a depth of 1704 m. Basaltic sills were encountered at depths of 2880 and 2896 m.

Below about 900 m, the rocks in the State 2-14 well are undergoing greenschist facies metamorphism [Cho et al., this issue; Elders and

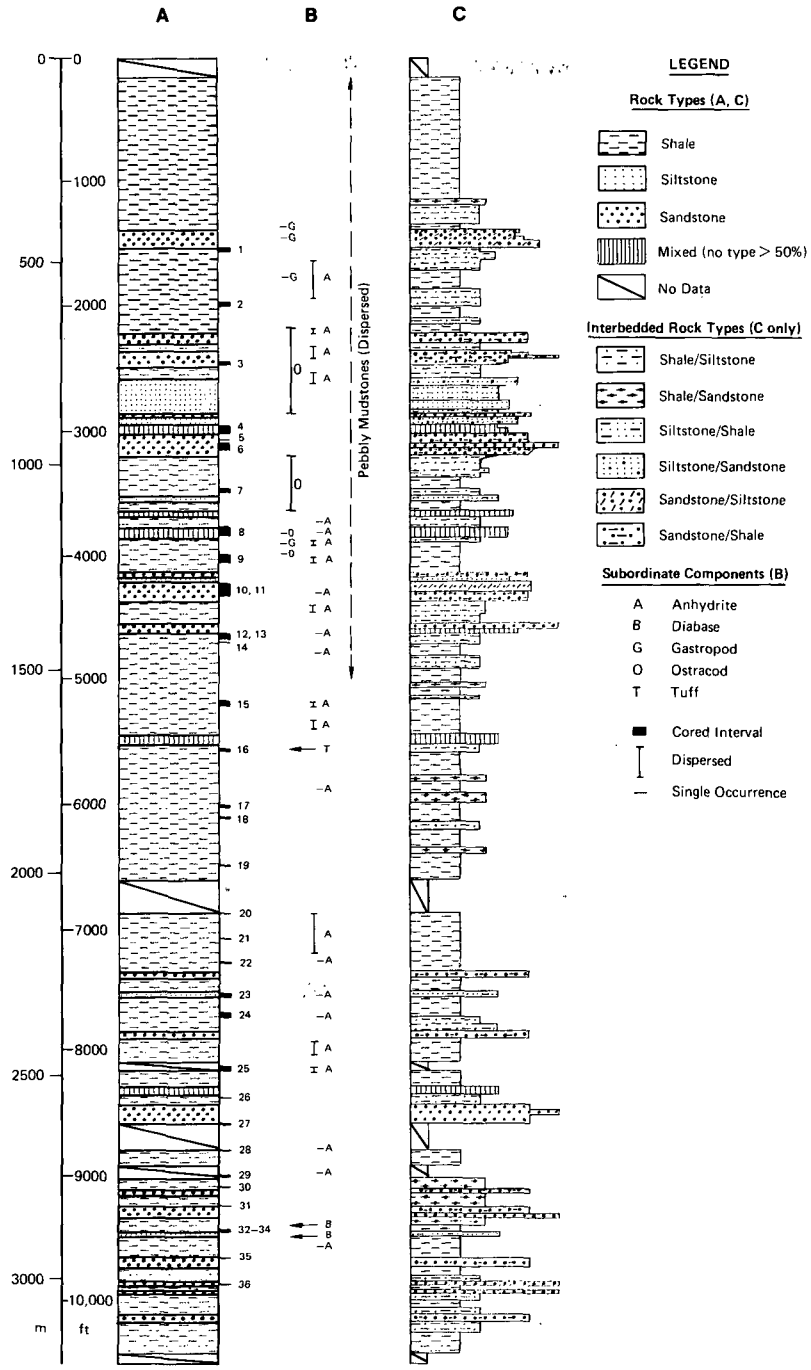

Fig. 2. Lithostratigraphic summary for the sedimentary rocks in the State 2-14 borehole; based on cored intervals, cuttings, and spontaneous potential and gamma ray logs (380-1830 m). Below a depth of 1830 m, the column is based only on the cored intervals and cuttings. (a) Generalized column showing the dominant rock types. (b) Cored intervals and subordinate components. (c) Blocky weathering profile emphasizing contrasts in sedimentary rock lithologies.

Sass, this issue; Shearer et al., this issue], and hornfels textures are being developed. In spite of this secondary alteration, original depositional textures are usually well preserved in the rocks, and sedimentary terminology is used in this paper to describe them.

Bedding in the cored intervals is commonly offset by centimeter-scale normal faults. Some of the normal faults are soft sediment loading structures; however, most are interpreted as resulting from seismic disturbances. These normal faults may contain secondary minerals such as calcite, pyrite, sphalerite, galena, chalcopyrite, and anhydrite [McKibben et al., 1988].

The apparent dip of bedding ranges from horizontal to 70°; the average dip is 20°-25°. Maximum deviation of the drill string was 7°, so the apparent dips are not artifacts of drilling

[Elders and Sass, this issue]. Bedding attitudes between 5° and 20° are most likely depositional [van de Kamp, 1973], whereas the steeply dipping bedding may have resulted from rotation of meter-scale blocks along normal faults.

Shale and Siltstone

The shales and siltstones from the cored intervals in the State 2-14 well exhibit millimeter- to centimeter-scale, planar-bedding and laminae (Figure 3). Ripple lamination is rare, and the shales are rarely bioturbated. Bedding may be disrupted by liquefaction features, sandstone dikes, and soft sediment deformation (Figures 3b and 3d). The apparent liquefaction feature shown in Figure 3b may possibly be a large mudcrack, similar to meter-scale mudcracks of the Borrego Formation in the San Felipe Hills (C. D. Winker, personal communication, 1988). While features of this scale are not readily apparent in cored sections, smaller, centimeter-scale mudcracks are observed locally, lending credence to Winker's suggestion.

Plant fragments occur in shales from the shallow part of the borehole. Gastropod and ostrocod shells are common above a depth of 1500 m. Below this depth, if they were originally present, these shells appear to have been destroyed by reaction with hydrothermal fluids. The presence of stratabound, microcrystalline sulfides suggests brackish water at times and conditions hostile to organisms.

Anhydrite (replacing gypsum) is present in shales and siltstones throughout the sedimentary column (Figure 2). It occurs mainly as nodules above a depth of 1220 m. Masses and bladed crystals of anhydrite along bedding planes are increasingly common below 1220 m (Figure 3c). The nodular anhydrite is similar to textures reported by Babcock [1969] for gypsum occurring in shales from the Borrego Formation in the Durmid Hills (Figure 1), suggesting that the anhydrite in the State 2-14 well probably replaces gypsum with a similar nodular texture.

Sandstone

Planar bedding, consisting of small-scale, interbedded sand and mud, or pure sand, is the most common bed form in the cored intervals of sandstone. Thick intervals (9 m) of sandstone with planar bedding may contain shale intraclasts along scoured, basal contacts with underlying shales (Figure 4b). Cross-bedded intervals (5- to 15-mm ripple height) are present, although rare, in the cored, sandstone intervals. Disrupted and convoluted bedding within sandstone and interbedded sandstone-shale intervals is common (Figure 4).

The most abundant type of sandstone from the State 2-14 borehole is composed dominantly of quartz, with less abundant feldspar and lithic fragments in approximately equal amounts, and are cemented by carbonate. The sandstones are poorly to moderately well sorted, and the grains are dominantly subangular to subrounded. Well-rounded grains are volumetrically rare.

Monocrystalline quartz contains vacuoles, microlites, and rare rutile inclusions. Plagioclase (An_{30-39}, andesine) is the most common feldspar in the carbonate-cemented sandstones. These reported feldspar compositions are from the shallow part of the State 2-14 borehole and are believed to reflect primary compositions little affected by secondary alteration. It is likely that the feldspars from the deeper part of the State 2-14 borehole have been altered to albite and sericite [Cho et al., this issue]. Oligoclase, microcline, orthoclase, and myrmekite are also present. Lithic clasts are composed of mudstone, volcanic fragments, chert, granite, metamorphic rocks, and carbonate rocks. Biotite and muscovite flakes are uncommon.

The carbonate cements are fine-grained, sparry, and sometimes poikilotopic above a depth of 600 m. Carbonate cement below a depth of 600 m is partially replaced by authigenic quartz and feldspar overgrowths which suture the detrital framework grains and destroy the primary sedimentary fabric. Below 2000 m, the carbonate cement appears to have been dissolved by hydrothermal fluids, and the sandstones texturally resemble quartzites.

The composition of a sandstone from the 1603- to 1609-m stratigraphic level is very different from that of the carbonate-cemented sandstones. This sandstone is composed of volcanic lithic fragments, in addition to plagioclase and quartz grains of volcanic origin. The grains are supported by a mud matrix. The volcanic grains are probably derived from the margins of the Salton Trough, whereas the detritus in the carbonate-cemented sandstones was deposited by the Colorado River (see following discussion).

Sandstone Provenance

Modal framework clast compositions of sandstones from the State 2-14 borehole and of sandstones in the Salton Trough described in previous studies are compared on the $Q_mF_tL_t$ diagram in Figure 5. The deepest sandstone point-counted from the State 2-14 borehole is from a depth of 1860 m. Sandstones from the deeper levels of the well could not be compared with outcrop samples because hydrothermal fluids have selectively destroyed feldspar and lithic grains causing the volumetric abundance of quartz to appear greater. Three hundred points were counted for each sandstone.

Many of the State 2-14 sandstones plot within the compositional field of sandstones from the Borrego and Brawley formations of Pliocene and Pleistocene age in the San Felipe Hills [Wagoner, 1977], suggesting that the sandstones share a similar provenance. The framework clast compositions of sandstones in the Borrego Formation at the Durmid Hills [Babcock 1969] are not shown on Figure 5 because the compositional data are unavailable. Babcock [1969], however, reports that sandstones from the Durmid Hills contain 80-95% subangular and well-rounded quartz grains. Other detrital components include biotite, feldspar, and garnet. The State 2-14 sandstones which contain greater than 80% monocrystalline quartz (Figure 5) are therefore believed to represent a primary, depositional grain population similar to that of the Pliocene and Pleistocene Borrego Formation at the Durmid Hills. This correlation once again implies that

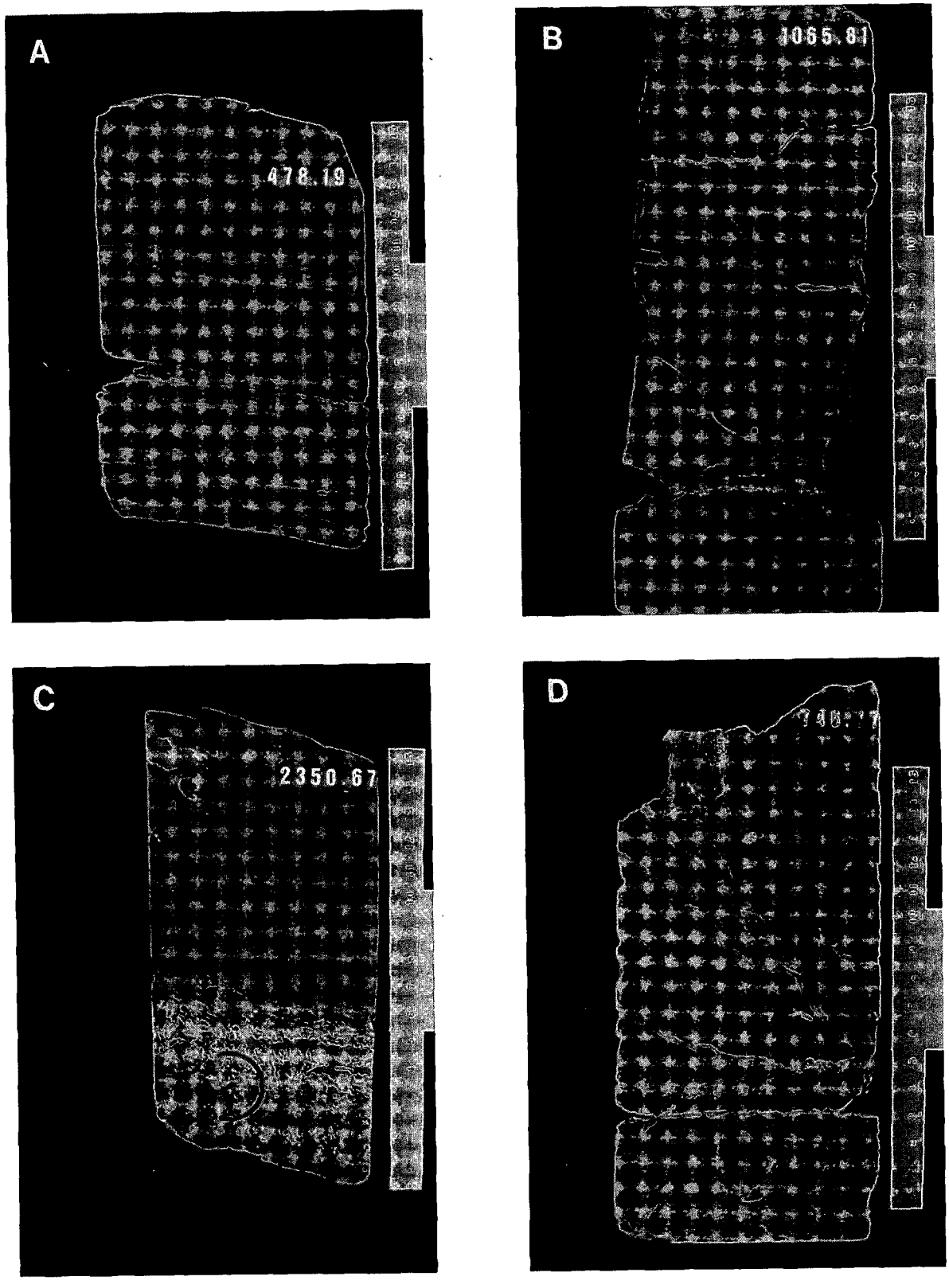

Fig. 3. (a) Subhorizontally laminated shale; possible feeding traces at 478.3 m. (b) Horizontally laminated shale disrupted by liquefaction feature, or possibly a large mudcrack. Normal fault offsets liquefaction feature. (c) Crystals of bladed anhydrite (replacing gypsum) along bedding surface. Nodular anhydrite at 2350.7 m. (d) Soft-sediment disruption and brecciation of shales and siltstones probably due to a seismic disturbance.

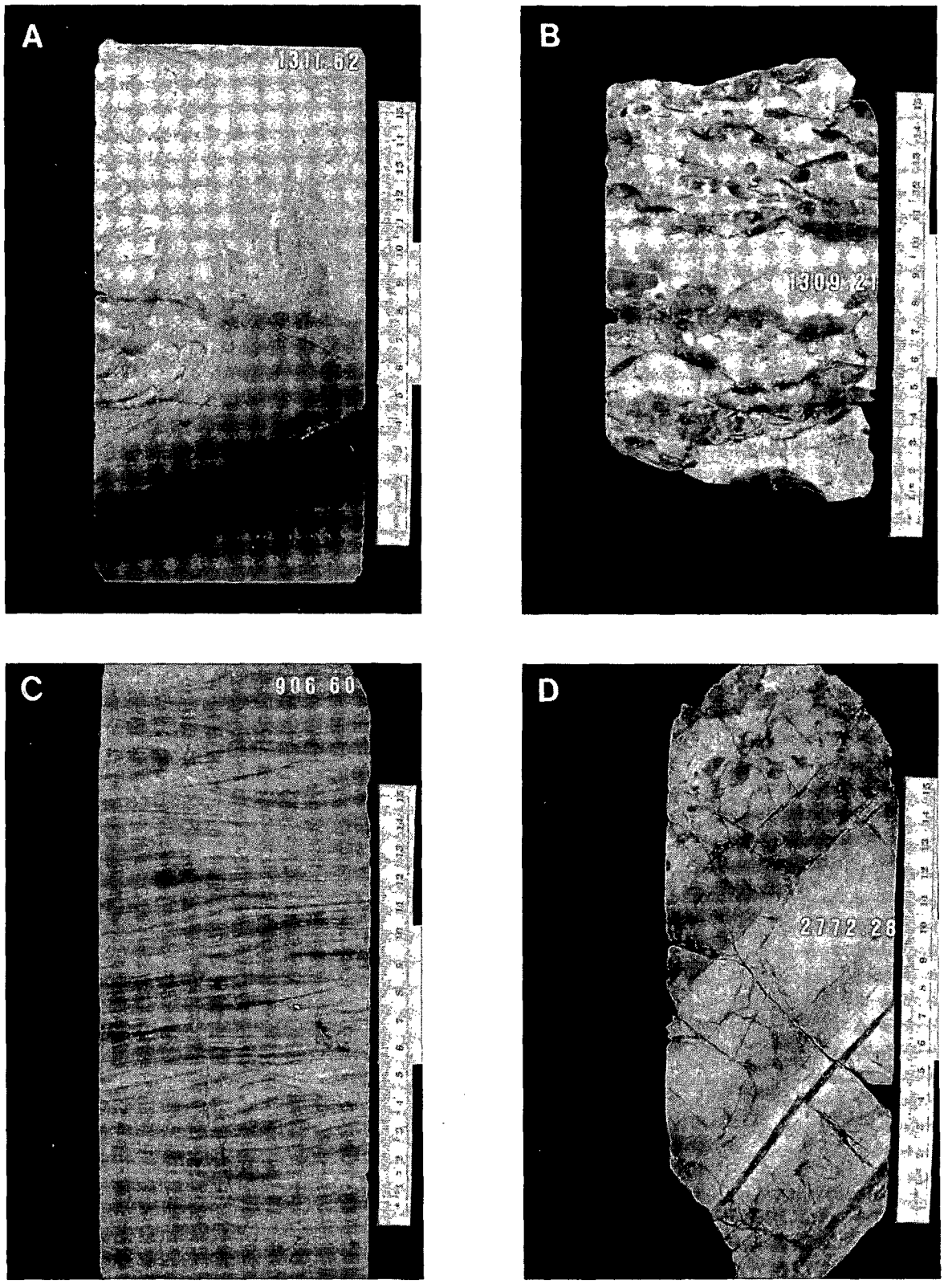

Fig. 4. (a) Disrupted and convoluted sandstones. (b) Meander channel fill sandstone with basal, channel lag, shale clasts. (c) Climbing ripples in lacustrine-delta sandstones. (d) Interbedded sandstone and siltstone showing an apparent dip of 70°. Epidote occurs as porphyroblasts and along bedding surfaces.

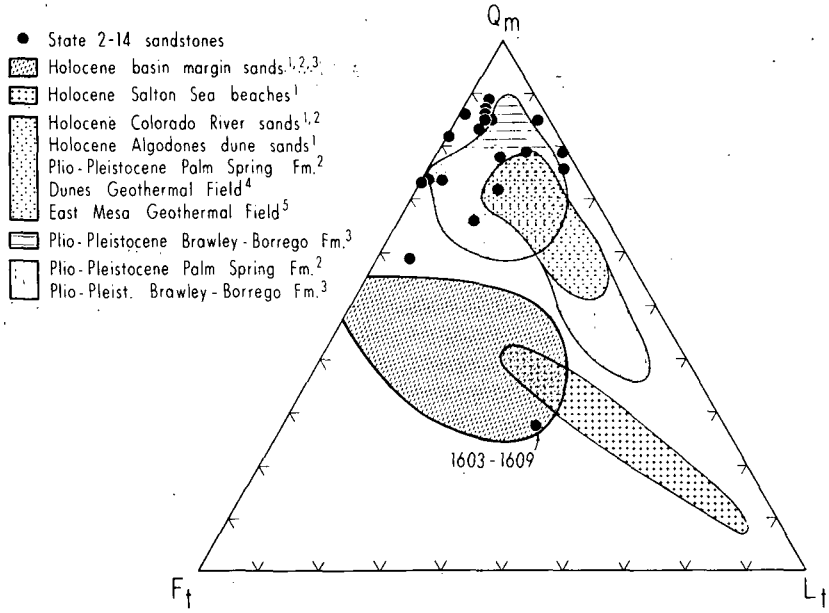

Fig. 5. $Q_mF_tL_t$ diagram showing framework modal clast compositions of sandstones from the State 2-14 well and other sandstones from the Salton Trough. Q_m, monocrystalline quartz; F_t, total feldspar; L_t, total lithic fragments including polycrystalline quartz. Data sources are (1) van de Kamp [1973], (2) Merriam and Bandy [1965], (3) Wagoner [1977], (4) Bird [1975], (5) Hoagland [1976].

the sandstones from the State 2-14 well share a similar provenance with sandstones from the Borrego and Brawley formations.

Some of the State 2-14 sandstone modal framework clast compositions also plot in the field defined for the Colorado River sands [Merriam and Bandy, 1965; van de Kamp, 1973], indicating an eastern Colorado River source for the carbonate-cemented sandstones. A Colorado River source is further evidenced by the occasional presence of carbonate foraminiferal tests presumably derived from the upper Cretaceous Mancos shale of the Colorado plateau [Merriam and Bandy, 1965].

The sandstone from the 1603- to 1609-m level of the State 2-14 borehole, consisting dominantly of volcanic debris, has a modal clast composition similar to that reported for the Holocene basin margin source sands of the Salton Trough [van de Kamp, 1973]. This sandstone thus probably records the deposition of detritus derived from the margin of the Salton basin. The volcanic debris may be derived from Miocene volcanic rocks occurring along the margins of the Salton Trough. A high biotite content in sandstones from the Salton Trough also implies a basin margin provenance [Babcock, 1969; Dronyk, 1977; van de Kamp, 1973; Wagoner, 1977]. Though biotite is rare in the State 2-14 sandstones, some very fine grained sandstones and siltstones are rich in biotite and muscovite, suggesting source regions north and west of the Salton Trough [van de Kamp, 1973].

Pebbly Mudstones

Pebbly mudstones are dispersed in the rocks sampled above 1523 m in the State 2-14 well. Though pebbly mudstones are not observed below this depth, it is likely that they occur at lower stratigraphic levels. Unfortunately, it is difficult to distinguish them in cuttings because with increasing depth a hornfels fabric is developed in the rocks. Furthermore, the pebbly mudstones could not be identified using wire line logs.

The pebbly mudstones are composed of millimeter- to centimeter-sized, subrounded to rounded clasts of shale-siltstone, carbonate-cemented sandstone, silicic volcanic rocks, carbonate fragments, granite, metamorphic rocks, and anhydrite-bearing shales in a mud-supported matrix. Very fine to fine-grained, subangular to subrounded grains of quartz and plagioclase, white mica, and biotite occur in the mud matrix.

Depositional Environments of the State 2-14 Rocks

The interpretation of the depositional environments for the State 2-14 sedimentary rocks presented here is based on the lithostratigraphic sequences and the sedimentary structures observed in the cored intervals (together with the cuttings and wire line data). The absence of a three-dimensional framework prohibits a comprehensive facies analysis; therefore the depositional environments of these rocks are inferred by analogy with older exposed rocks along the margins of the Salton Trough [Babcock, 1969, 1974; Dibblee, 1954; Wagoner, 1977; Winker, 1987] and with the Holocene sediments [van de Kamp, 1973].

The thick shale intervals represent quiet deposition in lake centers. The 125-m-thick, sandstone-free shale interval between the depths of 2100 and 2225 m indicates a long-term, stable lacustrine environment. Bedded anhydrite throughout this and other thinner lacustrine

intervals indicates periodic subaerial exposure and dessication of the lake beds. The anhydrite was most likely precipitated in the sediments, sabhka-style, by displacive growth from capillary brines. If the features shown in Figure 3b are indeed meter-scale mudcracks (C. D. Winker, personal communication, 1988), their large size indicates that such intervals of subaerial exposure and dessication may have been extensive. Fluctuating lake levels, with periodic flooding and drying of different areas within the central basin of the Salton Trough, can account for these intervals of dessication [van de Kamp, 1973].

The lithostratigraphy of a cored interval of a typical lacustrine sequence is illustrated in Figure 6. It is composed dominantly of shales and siltstones with interbedded, very fine grained sandstones. The shales exhibit small-scale planar laminations, with apparent dips of 20°. The rapid change in apparent dip from 20° to horizontal near the bottom of the section (611.7 m) may be due to large-scale slumping and rotation of rocks during seismic disturbances common in the Salton Trough. Organic-rich laminae with some plant fragments are present, though bioturbated intervals are absent. Carbonate-cemented, very fine grained subarkoses occur as centimeter-scale interbeds. These interbedded sandstones in the lacustrine shales are most likely marginal beach sands and/or small, offshore sand bars. The sandstones may also be small subaerial deposits which prograded over the lake muds during periods of low water levels [van de Kamp, 1973].

A pebbly mudstone unconformably overlies the shales at the top of the cored interval. Rapid deposition of the pebbly mudstone is suggested by a discordant contact with the underlying shales. The predominance of shale clasts within the pebbly mudstone may have resulted from the entrainment of underlying lacustrine muds as a muddy debris slurry flowed across the lake bed surface. This pebbly mudstone is therefore interpreted to represent a debris flow probably activated by storm runoff from alluvial fans located along the margins of the Salton Trough. This interpretation is supported by the presence of arkosic sandstone cobbles in the pebbly mudstone, which are similar to sedimentary rocks of pre-Holocene age exposed along the margins of the Salton Trough. Alternatively, the pebbly mudstones may be intraformational collapse breccias generated during seismic disturbances. The presence of extraformational sandstone clasts, however, supports the suggestion that the pebbly mudstones are debris flows.

The lithostratigraphy of an inferred lacustrine-delta sequence within the Salton Trough is illustrated in Figure 7. It is composed of laminated shales and siltstones with interbedded sandstones and pebbly mudstones. The shales are dominantly planar bedded. Disrupted bedding (1161.5-1162.1 m) consists of shale intraclasts in a mud matrix. Sandstone dikes (1166 m) disrupting the shales are suggestive of rapid deposition and/or a seismic disturbance.

Planar-bedded, very fine to fine-grained sandstones are common in this cored interval. Cross-bedded intervals are rare, occurring only in a single 15-cm-thick zone at 1158.9 m. Bedding within the sandstones may also be highly disrupted; load casts, flame structures, and sand balls are common within these zones (1158.2 and 1163.3 m). The disrupted intervals may be either soft sediment deformation due to seismic disturbances or storm-induced debris flows. Sandstone beds with dips of 20°-30° may be either foreset beds on the delta front or large blocks rotated during seismic disturbances. The pebbly mudstones are lithologically similar to those shown in Figure 6, with additional anhydrite-bearing shale clasts.

Another lacustrine delta sequence at a depth of 905-925 m consists dominantly of planar-bedded, fine grained sandstone with uncommon interbeds of siltstone and shale. Planar bedding, trough cross bedding, and climbing ripples (Figure 4c) occur. Delta, mud flat environments

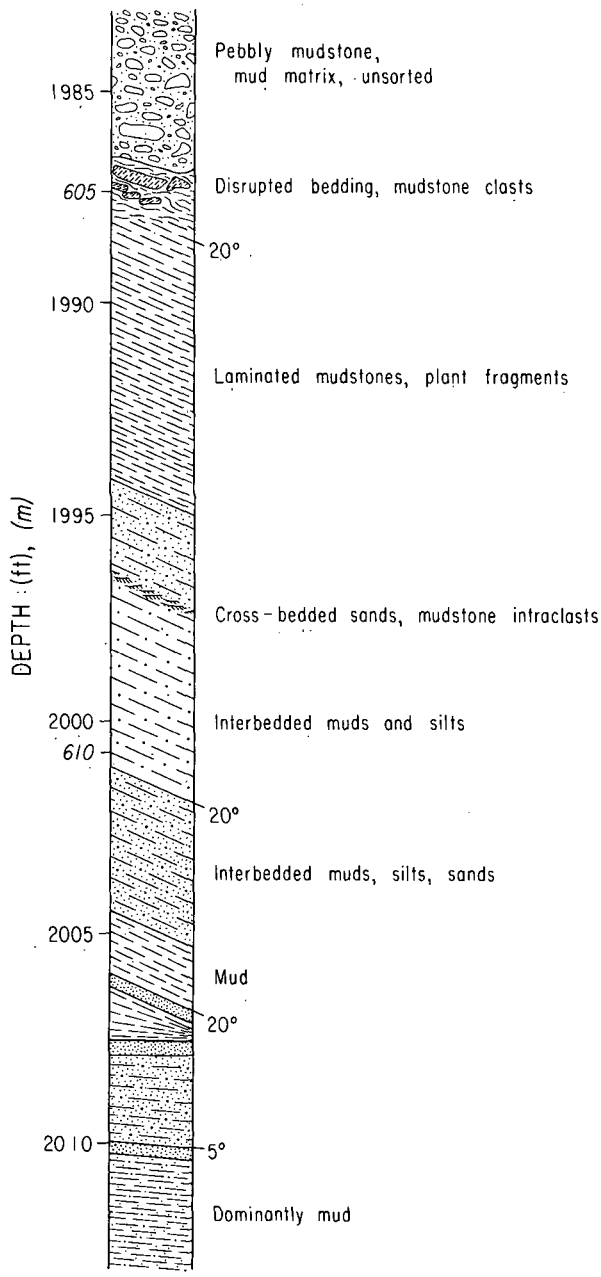

Fig. 6. Graphic representation of the lithostratigraphy of a lacustrine sequence (depth interval of 604.4-613.3 m).

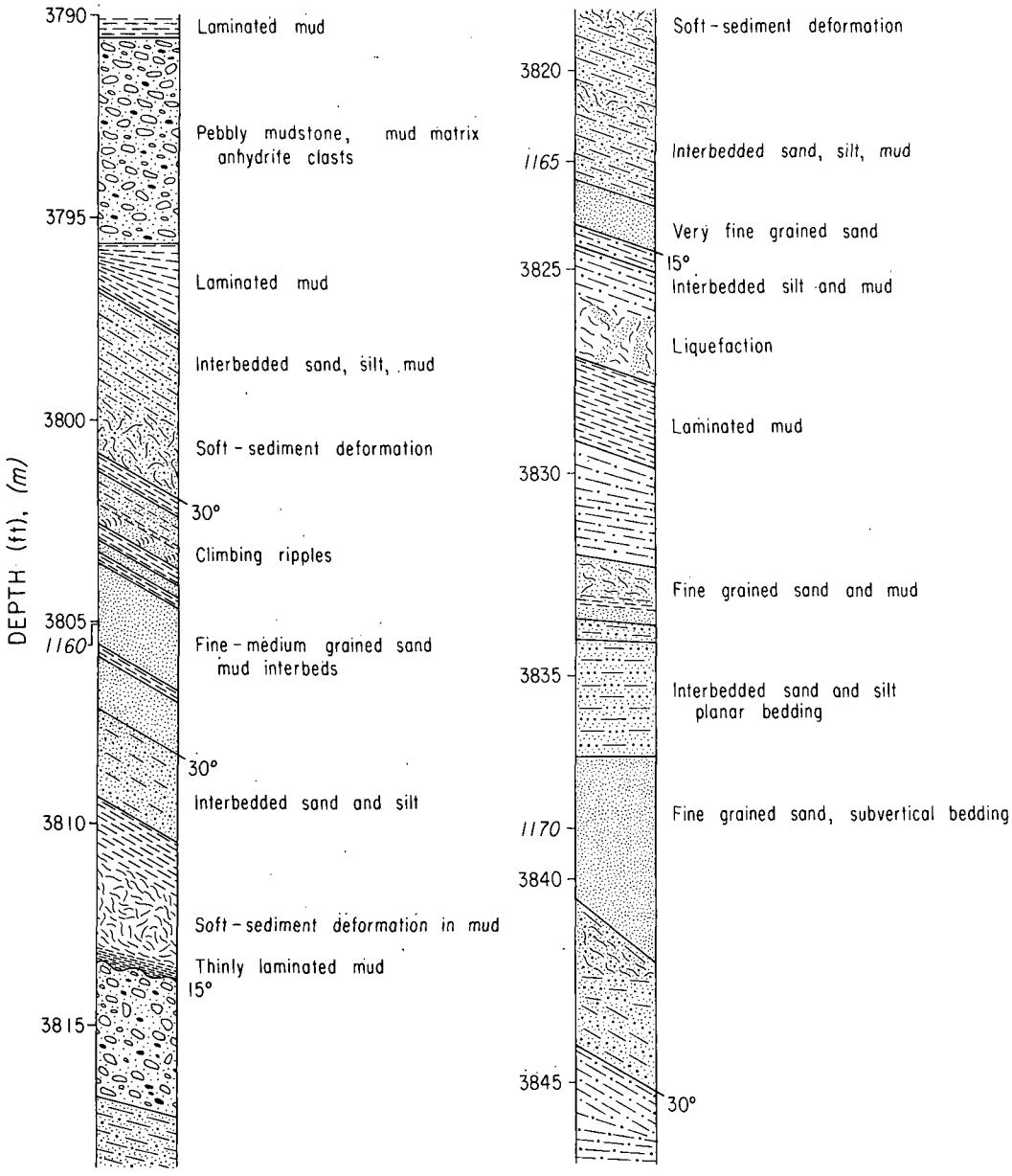

Fig. 7. Graphic representation of the lithostratigraphy of a lacustrine-delta sequence (depth interval of 1155.1-1172.4 m).

are represented by thinly laminated shales containing evaporites and centimeter-scale mudcracks, indicating periods of subaerial exposure and dessication.

Comparison of the lacustrine-delta sequences in the State 2-14 well with the delta of the New River, which originates from the delta of the Colorado River and flows into the Salton Sea, suggests that the State 2-14 rocks represent distributary channel (Figure 4b), mud flat, and delta front environments. Their three-dimensional geometry is probably similar to the Holocene lacustrine deltas in the Salton Trough [Stephen and Gorsline, 1975; van de Kamp, 1973].

Summary and Conclusions

Lacustrine sequences dominate the lithostratigraphy of the State 2-14 research borehole. Distributary channels crosscut the lacustrine deposits. The deltas of distributary rivers are interbedded with the lacustrine sequences. Coarse, basin margin alluvium was not observed in the sedimentary rocks of the State 2-14 borehole. Only the pebbly mudstones, interpreted as storm-induced debris flows originating from the front of alluvial fans, brought coarse-grained basin margin detritus to the area of the Salton Trough sampled by the State 2-14 well.

Both central, lake mud facies and coastal, beach/nearshore bar sand facies [van de Kamp, 1973] are identified in the lacustrine rocks from the State 2-14 well. Evaporites are common in the shales, recording periods of subaerial exposure and dessication in a sabhka-like setting. The interbedding of the lacustrine muds, coastal sand deposits, and evaporite-bearing muds were probably controlled by fluctuations in

paleolake levels and periodic flooding of this region of the Salton Trough by the Colorado River. Although, the 125-m-thick interval of lacustrine muds between 2100 and 2225 m, which completely lack sandstones, records a long-term stable depositional setting.

Thick (9 m) intervals of sandstone, sometimes with basal, lag, clay clasts (Figure 4b), suggest distributary channel facies. The distributary rivers, most likely originating from the delta of the Colorado River, delivered sediment to the northern region of the Salton Trough. Associated deltaic facies may have been deposited along the margins of ancient Colorado River deltas or are small deltas of the distributory rivers, similar to the modern deltas of the Alamo and New rivers [Stephen and Gorsline, 1975; van de Kamp, 1973].

Van de Kamp [1973] reports that sands from the modern Alamo and New rivers are very different in texture and mineralogy. The Alamo River sands are characteristic of a Colorado River source. Sandstones of this composition are the most abundant in the State 2-14 stratigraphic section, implying a dominant Colorado River provenance for the sandstones of the State 2-14 well. In contrast, the New River sands contain more plagioclase and less carbonate and quartz than the Alamo River sands. The framework modal clast composition of the sandstone from the 1603- to 1609-m interval is more like the modern New River sands, composed of detritus derived from the margins of the Salton Trough [van de Kamp, 1973]. The 1603- to 1609-m sandstone is therefore interpreted as a deposit of fine-grained, basin margin detritus.

The paleodepositional environments of the sedimentary rocks in the State 2-14 research borehole are similar to those occurring in the modern sedimentary regime. This similarity implies a steady state depositional system for this region of the Salton Trough during the time interval recorded by the rocks recovered in the State 2-14 well through the present. The sedimentary facies recorded by the rocks in the State 2-14 research borehole and at the present surface north of the international border in the Salton Trough document continental sedimentation in lacustrine, distributary channel, braided stream, alluvial fan, and eolian environments [van de Kamp, 1973]. Marine deposition can be ruled out in this region of the Salton Trough because the delta of the Colorado River now acts as barrier for marine transgressions and has done so since the Pliocene and Pleistocene [van de Kamp, 1973]. This observation is supported by the absence of marine rocks in the State 2-14 well.

The large amount of lacustrine shale, the similar sandstone framework modal clast compositions, the presence of evaporites, the similar lithostratigraphic positions, and a volcanic tuff in both the Durmid Hills and the State 2-14 (1704 m) research borehole with a similar geochemical composition [Mehegan et al., 1987; Herzig and Elders, this issue], all indicate that the rocks recovered in the State 2-14 well are lithologically correlative with the Borrego and Brawley formations which range in age from Pliocene to the Pleistocene. The State 2-14 borehole may have penetrated sedimentary rocks of the upper part of the Pliocene and Pleistocene Palm Spring Formation, based on reported formation thicknesses [Dibblee, 1954], though no major change in lithostratigraphy was noticed.

Sedimentary rocks of the Borrego and Brawley formations, outcropping in the San Felipe and Durmid Hills, contain detritus derived from the mountains along the margins of the Salton Trough [Babcock, 1969, 1974; Dronyk, 1977; Wagoner, 1977] and represent a facies deposited near the basin margins. In contrast, the State 2-14 sedimentary rocks, consisting dominantly of lacustrine muds, were deposited closer to the center of the Salton Trough. Only the pebbly mudstones contain coarse-grained detritus derived from the margins of the Salton Trough. The sandstone from a depth of 1603- to 1609-m is composed of fine-grained detritus derived from the basin margins. The State 2-14 rocks are thus interpreted as the basinward facies of the Borrego and Brawley formations [Babcock, 1969, 1974; Dibblee, 1954; Dronyk, 1977; Tarbet and Holman, 1944; Wagoner, 1977].

Mehegan et al. [1987] and Herzig and Elders [this issue] suggest that the silicic tuff at 1704 m in the State 2-14 research borehole is correlative with a tuff in the Pliocene and Pleistocene Borrego Formation in the Durmid Hills [Babcock, 1969] and is not derived from volcanic activity at Salton Buttes. The tuff in the Durmid Hills may be a deposit of the Bishop Tuff, erupted from the Long Valley caldera of central California at 0.7 Ma [Merriam and Bischoff, 1975; Sarna-Wojcicki et al., 1984]. Such a correlation implies that the tuff at 1704 m deep in the State 2-14 well is from 0.7 Ma and the rate of sedimentation and subsidence in this part of the Salton Trough may have averaged approximately 2.4 mm/yr for 0.7 m.y. Extrapolating this rate to the rest of the stratigraphic column in the Salton Sea geothermal system would imply that the Pliocene-Pleistocene boundary may occur at the depth of 3.8 km, i.e., 600 m deeper than the depth reached by the State 2-14 borehole. The rate of sedimentation and subsidence calculated using the tuff at 1704 m is about twice as fast as rates calculated from radiocarbon ages of shells and plant fragments from the Holocene sediments (1.03-1.66 mm/yr) [van de Kamp, 1973]. Future work will seek to understand how sedimentation and subsidence rates may have been changing with time in this region of the Salton Trough.

Acknowledgments. This work was performed under the direction of W.A. Elders and L.H. Cohen as part of the curation (National Science Foundation grant EAR-8303557) of the State 2-14 cores, cuttings and electric logs (SSSDP). Exlog Smith provided onsite cutting retrieval and mud logging. Jose Abreu washed the cuttings and assisted with the core curation. The following members of the Geothermal Resources Program at UCR assisted with the curation of the samples: J. Andes, C. Carlton, L. Cohen, P. Collier, J. Jackson, D. Jones, A. Lilje, M. McKibben, C. Oakes, R. Sullivan, and A. Williams. K. Miller and J. Brown from Media Resources, UCR videotaped the core. W. Schweller (Chevron Oil Field Research Company) assisted with interpretation of sedimentary structures and depositional environments. Will Osborn helped interpret the sulfate

structures. Linda Jankov drafted the figures for this paper. Finally, the comments by the reviewers of this manuscript are greatly appreciated. This paper is UCR/IGPP report 87/36.

References

Arnal, R., Limnology, sedimentation, and microorganisms of the Salton Sea, California, Geol. Soc. Am. Bull., 72, 427-478, 1961.

Atwater, T., Implications of plate tectonics for the Cenozoic tectonic evolution of western North America, Geol. Soc. Am. Bull., 81, 3513-3536, 1970.

Babcock, E.A., Structural geology and geophysics of the Durmid area, Imperial Valley, California, Ph.D. thesis, Univ. of Calif., Riverside, 1969.

Babcock, E.A., Geology of the northeast margin of the Salton Trough, Salton Sea, California, Geol. Soc. Am. Bull., 85, 321-332, 1974.

Bird, D.K., Geology and geochemistry of the Dunes hydrothermal system, Imperial Valley of California, M.S. thesis, Univ. of Calif., Riverside, 1975.

Cho, M., J.G. Liou and D.K. Bird, Prograde phase relations in the State 2-14 well metasandstones, Salton Sea geothermal field, California, J. Geophys. Res., this issue.

Crowell, J.C., Sedimentation along the San Andreas fault, California, Modern and Ancient Geosynclinal Sedimentation, edited by R.H. Dott and R.H. Shaver, Spec. Publ. Soc. Econ. Paleontol. Mineral., 19, 292-303, 1974a.

Crowell, J.C., Origin of late Cenozoic basins in southern California, Tectonics and Sedimentation, edited by W.R. Dickinson, Spec. Publ. Soc. Econ. Paleontol. Mineral., 22, 190-204, 1974b.

Dibblee, T.W., Geology of the Imperial Valley region, California, in Jahns, R.H., ed., Geology of California, Chapter 2: Geology of the natural provinces, Calif. Div. Mines Bull., 170, 21-28, 1954.

Dibblee, T.W., Stratigraphy and tectonics of the San Felipe Hills, Borrego Badlands, Superstition Hills, and vicinity, in The Imperial Basin - Tectonics, Sedimentation and Thermal Aspects, Publ. 40, edited by C.A. Rigsby, pp. 31-44, Pacific Section, Society of Economic Paleontologists and Mineralogists, Bakersfield, Calif., 1984.

Downs, T., and J.A. White, A vertebrate faunal succession in superposed sediments from late Pliocene to middle Pleistocene in California, Tertiary/Quaternary boundary, Proc. Int. Geol. Congr., 23(10), 41-47, 1968.

Dronyk, M.P., Stratigraphy, structure and a seismic refraction survey of a portion of the San Felipe Hills, Imperial Valley, California, M.S. thesis, Univ. of Calif., Riverside, 1977.

Elders, W.A., and J. Sass, The Salton Sea Scientific Drilling Project, J. Geophys. Res., this issue.

Elders, W.A., R.W. Rex, T. Meidev, P.T. Robinson, and S. Biehler, Crustal spreading in southern California, Science, 178, 15-24, 1972.

Fuis, G.S., and W.M. Kohler, Crustal structure and tectonics of the Imperial Valley region, California, in The Imperial Basin - Tectonics, Sedimentation, and Thermal Aspects, Publ. 40, edited by C.A. Rigsby, pp. 1-13, Pacific Section Society of Economic Paleontologists and Mineralogists, Bakersfield, Calif., 1984.

Fuis, G.S., W.D. Mooney, J.H. Healy, G.A. McMechan, and W.J. Lutter, A seismic refraction survey of the Imperial Valley, California, J. Geophys. Res., 89, 1165-1189, 1984.

Herzig, C.T., and W.A. Elders, The nature and significance of igneous rocks cored in the State 2-14 research borehole, Salton Sea Scientific Drilling Project, California, J. Geophys. Res., this issue.

Herzig, C.T., and J.M. Mehegan (Eds.), Salton Sea Scientific Drilling Project visual core descriptions, vol. 2, Rep. IGPP/UCR-86/2, pp. 222-314, Inst. of Geophys. and Planet. Phys., Univ. of Calif., Riverside, 1986a.

Herzig, C.T., and J.M. Mehegan (Eds.), Salton Sea Scientific Drilling Project core summaries, vol. 2, Rep. IGPP/UCR-86/1, pp. 34-45, Inst. of Geophys. and Planet. Phys., Univ. of Calif., Riverside, 1986b.

Hoagland, J.R., Petrology and geochemistry of hydrothermal alteration in Borehole Mesa 6-2, East Mesa geothermal area, Imperial Valley, California, M.S. thesis, Univ. of Calif., Riverside, 1976.

Johnson, N.M., C.B. Officer, N.D. Opdyke, G.D. Woodard, P.K. Zeitler, P.K., and E.H. Lindsay, Rates of late Cenozoic tectonism in the Vallecito-Fish Creek Basin, western Imperial Valley, California, Geology, 11, 664-667, 1983.

Lachenbruch, A.H., J.H. Sass, and S.P. Galanis, Heat flow in southernmost California and the origin of the Salton Trough, J. Geophys. Res., 90, 6709-6736, 1985.

Larson, R.L., H.W. Menard, and S.M. Smith, Gulf of California: A result of ocean floor spreading and transform faulting, Science, 161, 781-784, 1968.

Lilje, A., and J.M. Mehegan (Eds.), Salton Sea Scientific Drilling Project core summaries, vol. 1, Rep. IGPP/UCR-86/1, pp. 1-33, Inst. of Geophys. and Planet. Phys., Univ. of Calif., Riverside, 1986.

McKibben, M.A, J.P. Andes, Jr., and A.E. Williams, Active ore formation at a brine interface in metamorphosed deltaic-lacustrine sediments: The Salton Sea geothermal system, California, Econ. Geol., 83, 511-523, 1988.

Mehegan, J.M., C.T. Herzig, and R.M. Sullivan (Eds.), Salton Sea Drilling Project visual core descriptions, vol. 1, Rep. UCR/IGPP-86/1, pp. 1-221, Inst. of Geophys. and Planet. Phys., Univ. of Calif., Riverside, 1986.

Mehegan, J.M., C.T. Herzig, W.A. Elders, L.H. Cohen, and A.L. Quintanilla-Montoya, REE geochemistry of continental rift lavas of the Salton Trough, California and Mexico, Geol. Soc. Am. Abstr. Programs, 19, 769, 1987.

Merriam, R., and O.L. Bandy, Source of upper Cenozoic sediments in Colorado delta region, J. Sediment. Petrol., 35, 911-916, 1965.

Merriam, R., and J.L. Bischoff, Bishop ash: A widespread volcanic ash extended to southern California, J. Sediment. Petrol., 45, 207-211, 1975.

Muffler, L.J.P., and B.R. Doe, Composition and mean age of detritus of the Colorado River delta in the Salton Trough, southeastern California, J. Sediment. Petrol., 38, 384-399, 1968.

Sarna-Wojcicki, A.M., H.R. Bowman, C.E. Meyer, P.C. Russell, M.J. Woodward, G. McCoy, J.J. Rowe, Jr., P.A. Baedecker, F. Asaro, and H. Michael, Chemical analyses, correlations, and ages of upper Pliocene and Pleistocene ash layers of east-central and southern California, U.S. Geol. Surv., Prof. Pap., 1293, 1984.

Shearer, C.K., J.J Papike, S.B. Simon, B.L. Davis, F.J. Rich, and J.C. Laul, Mineral reactions in altered sediments from the California State 2-14 well: Variations in the modal mineralogy, mineral chemistry, and bulk chemistry of the Salton Sea Scientific Drilling Project core, J. of Geophys. Res., this issue.

Stephen, M.F., and D.S. Gorsline, Sedimentary aspects of the New River delta, Salton Sea, Imperial Valley, California, in Deltas: Models for Exploration, edited by M.L. Broussard, pp. 267-282, Houston Geological Society, Houston, Tex., 1975.

Sykes, G., The Colorado Delta, Spec. Publ. Am. Geogr. Soc., 19, 193 pp., 1937.

Tarbet, L.A., and W.H. Holman, Stratigraphy and micropaleontology of the west side of the Imperial Valley, Am. Assoc. Pet. Geol. Bull., 28, 1781-1782, 1944.

van de Kamp, P.C., Holocene continental sedimentation in the Salton Basin, California: A reconnaissance, Geol. Soc. Am. Bull., 84, 827-848, 1973.

Wagoner, J.L., Stratigraphy and sedimentation of the Pleistocene Brawley and Borrego formations in the San Felipe Hills area, Imperial Valley, California, U.S.A., M.S. thesis, Univ. of Calif., Riverside, 1977.

Waters, M.R., Late Holocene lacustrine chronology and archaeology of ancient Lake Cahuilla, California, Quat. Res., 19, 373-387, 1983.

Winker, C.D., Neogene stratigraphy of the Fish Creek-Vallecito section, southern California: Implications for early history of the northern Gulf of California and Colorado delta, Ph.D. thesis, Univ. of Ariz., Tucson, 1987.

C.T. Herzig, Geothermal Resources Program, Institute of Geophysics and Planetary Physics, University of California, Riverside, CA 92521.

J.M. Mehegan, Department of Geology, California State University, San Bernardino, CA 92407.

C.E. Stelting, Chevron Oil Field Research Co., P.O. Box 446, La Habra, CA 90633.

(Received September 14, 1987;
revised April 18, 1988;
accepted July 12, 1988.)

JOURNAL OF GEOPHYSICAL RESEARCH, VOL. 93, NO. B11, PAGES 12,981–12,994, NOVEMBER 10, 1988

Analysis of Geophysical Well Logs Obtained in the State 2-14 Borehole, Salton Sea Geothermal Area, California

FREDERICK L. PAILLET AND ROGER H. MORIN

U.S. Geological Survey, Denver, Colorado

A complete suite of conventional geophysical well logs was obtained in the upper part of a 3220-m-deep borehole drilled into geothermally altered alluvial sediments on the southeastern edge of the Salton Sea. In situ temperatures greater than 300°C and an inability to cool parts of the borehole by circulation limited the suite of logs run below 2000 m in depth to deep induction, spontaneous potential, uncalibrated neutron, natural gamma, and temperature. Bottom-hole temperature trends given by repeat temperature logs were extrapolated to undisturbed temperatures approaching 355°C at a depth of 3220 m. Geophysical logs obtained in the State 2-14 borehole indicate that neutron porosity, gamma-gamma, and deep-induction logs provide useful information on lithologic trends with depth. The natural gamma log contains almost continuous, high-frequency fluctuations that obscure lithologic trends and that may be related to recent radioisotope redistribution and departure from radiometric equilibrium. Acoustic transit time logs give unrealistically low in situ compressional velocities ranging from 1.8 to 3.0 km/s, whereas acoustic waveform logs indicate that sediment compressional velocities range from less than 3.0 km/s shallower than 1000 m in depth to almost 5.0 km/s at depths greater than 2000 m. Analyses indicate that most log values lie between two lithologic end points: an electrically conductive claystone with moderate neutron porosity, but no effective porosity, and an electrically nonconductive, fully cemented siltstone that has small but finite porosity. A limited number of clean sandstones depart from this trend; geophysical logs from these sandstones indicate an effective porosity ranging from 5 to 14%, and saturation with brines having equivalent NaCl concentrations greater than 100,000 mg/L. Depth-averaged trends in neutron porosity and deep-induction logs, along with trends in acoustic velocity determined from acoustic waveform logs, demonstrate that major changes in the properties of alluvial sediments occur within the depth range from 1200 to 1800 m. Although caliper logs were not obtained deeper than 2000 m, resistivity values less than 10 ohm m at those depths probably correspond to borehole enlargements in production zones rather than local increases in effective porosity. The transition in sediment properties indicated by the geophysical logs in the depth interval from 1200 to 2000 m apparently represents a detailed vertical profile of the transition from relatively unaltered clay minerals in alluvial sediments to electrically nonconductive alteration products such as epidote and feldspar.

INTRODUCTION

The 3220-m-deep State 2-14 provided a unique opportunity to investigate the physical properties of sediments deposited in a tectonically active basin located at the junction between major geologic provinces in an area marked by anomalously steep geothermal gradients. The Salton Trough (Figure 1) occurs at a point where extensional rifting of the Gulf of California to the south changes into the predominantly transform faulting of southern California to the north [*Elders and Biehler*, 1975; *Lachenbruch et al.*, 1985]. The sediments that fill the valley are interbedded alluvial and lacustrian sediments derived from the adjacent Colorado River delta [*Muffler and Doe*, 1965]. The Salton Trough probably originated as a pull-apart basin within a transform fault system [*Lachenbruch et al.*, 1985]. Anomalously high geothermal gradients occur throughout the trough, and geothermally productive well fields have been established at several locations within the area [*Helgeson*, 1968]. Geophysical and geologic data derived from the Salton Sea Scientific Drilling Project, therefore, will have important applications in research related to geothermal energy production, hydrothermal geochemistry, ore body development, and the relationship between geothermal gradients and seismicity.

Geophysical well log analysis has been an important part of research on the characteristics of geothermal systems [*Society of Professional Well Log Analysts*, 1982]. *Keys* [1979, 1982], *Keys and Sullivan* [1979], and *Browne* [1978] reviewed the application of geophysical logs to many geothermal reservoir types. *Ershaghi and Abdassah* [1984], *Ershaghi et al.* [1979], and *Muramoto and Elders* [1984] described the analysis of geophysical logs obtained from other boreholes and geothermal production wells drilled in the Salton Sea area. Core samples were either not obtained, or a limited number were retrieved from relatively shallow depths during these previous investigations. The combination of geophysical data and extensive core samples from the State 2-14 borehole can be used to characterize the properties of geothermally altered sediments deposited in the Salton Trough. Well log analysis contributes to this investigation by (1) providing an indication of continuous trends in sediment properties with depth on a single vertical scale, and (2) providing in situ values of geophysical properties of sediments for calibration of surface geophysical surveys and for reservoir analyses. The indication of continuous trends is especially important when time-consuming and expensive analyses are done on a necessarily limited set of core samples. The continuous trend of sediment properties on the log indicates how the discrete measurements made on core samples relate to the entire sediment column. The combination of geophysical log data and core sample analyses provides insight into sediment properites and trends in alteration as a function of depth that would not be given by either analysis separately.

Primary emphasis in this investigation is on the characterization of the depth profile of geothermal alteration. This profile cannot be directly read from the geophysical logs

Paper number 7B7108.

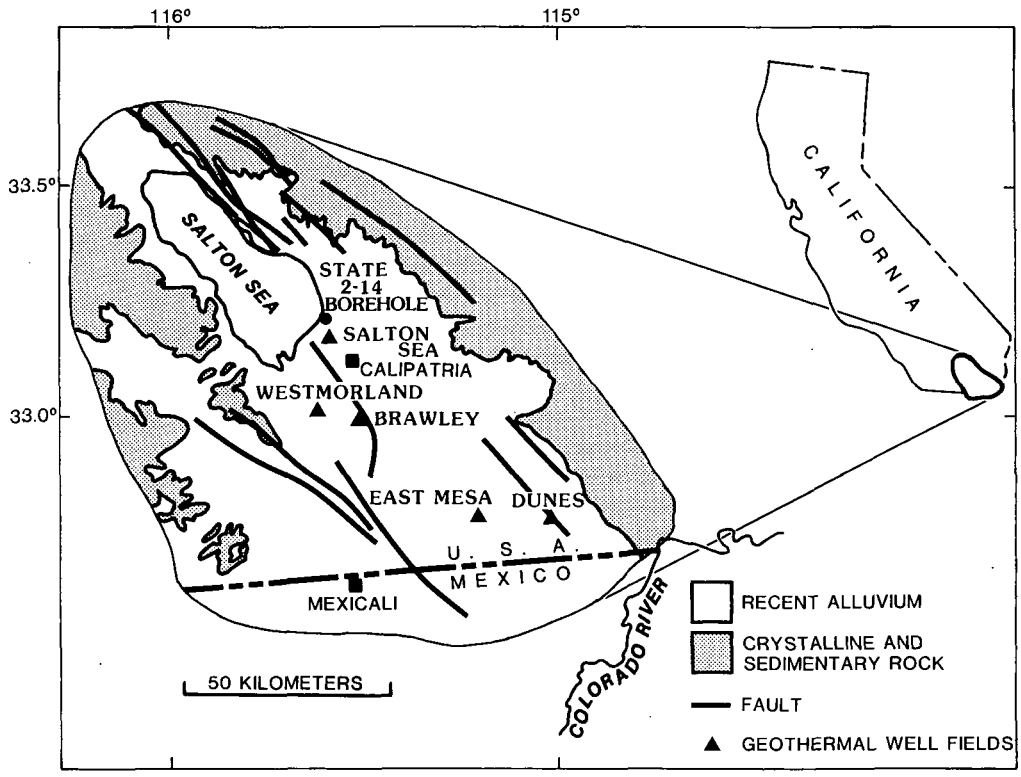

Fig. 1. Location of the State 2-14 borehole and adjacent geothermal fields in the Imperial Valley, southeastern California.

for a number of reasons. First of all, the geophysical logs are composed of measurements, such as epithermal neutron backscatter, acoustic attenuation, and electrical resistivity, that are only indirectly related to the sediment properties being studied. Many standard techniques for establishing the relations required to estimate sediment porosity and permeability and to define major lithologic components exist, but few of them produce unique results. Another significant difficulty is the superposition of other trends on the pattern of geothermal alteration. In the State 2-14 borehole the profiles of physical properties obtained by the logs indicate several different effects: (1) change of apparent physical properties with depth caused by changing environment (increasing temperature, pore fluid pressure, and overburden stress), (2) increasing degree of geothermal alteration with depth, (3) changes in borehole conditions with depth (hole diameter, casing type, drilling mud, etc.), (4) decrease in number and types of logs and degradation of quality with increasingly hostile environment, and (5) possible systematic change in sediment properties related to systematic changes in source area or mechanism of deposition.

Only the last item on this list seems relatively unimportant for the State 2-14 borehole. The apparently rapid subsidence of the Salton Trough and the constant source area for the alluvial sediments indicate that systematic trends in sediment character may not be significant. However, fluctuations in climate and salinity of ephemeral lakes may have resulted in minor variations in the abundance of clay types and degree of flocculation during deposition [*Muramoto and Elders*, 1984]. In situ confining pressure and temperature can have substantial effects on geophysical properties, and many of these are well documented in the literature. For example, *Toksoz et al.* [1976] describe the significant effects of in situ confining pressure on the compressional and shear velocities of sandstones. Changes in borehole conditions with depth of drilling and the limited log suite available from depths greater than 2000 m complicate the analysis of geophysical logs from the State 2-14 borehole.

Hydrothermal Alteration and Geophysical Log Response

Muffler and White [1969] and *Bird and Elders* [1976] describe the primary mechanisms for geothermal alteration of sedimentary rocks in the Salton Sea Trough as (1) alteration of detrital clay minerals such as montmorillonite and illite to chlorite and other minerals of the low-grade greenschist mineral assemblage, and (2) reduction of primary porosity in sandstones by means of calcite and quartz precipitation from geothermal fluids. Hydrothermal alteration increases the bulk density of aquifer rocks from 2.2 to 2.6 g/cm^3, with temperature being the primary control over these transitions; natural lithostatic compaction appears to be a secondary factor. *Browne* [1978], *Muffler and White* [1969], and *Bird and Elders* [1979] indicate that major alteration occurs over the temperature range from 180° to 260°C.

The changes in sediment properties associated with geothermal alteration appear to be measurable by means of conventional geophysical logs, using the criteria on the performance of various logging equipment given by *Hearst and Nelson* [1985]. The systematic increase in density and decrease in porosity described by *Muffler and White* [1969] appear to be directly measurable using neutron porosity and gamma-gamma (density) logs. At the same time, conventional acoustic transit time logs should reflect these trends directly through decreases in apparent porosity derived from the logs and in-

directly through increasing matrix velocities corresponding to increasing matrix density. The response of electrical logs such as long normal and deep induction to decreasing porosity, increasing density, and clay mineral alteration is somewhat more complicated and should depend upon properties of natural formation waters. However, the combined effects of alteration and compaction probably produce increasing resistivity even when superimposed on increasing fluid salinity with depth [*Chen and Fang*, 1981].

Previous geophysical well log studies in the Salton Sea Trough [*Ershaghi and Abdassah*, 1984; *Ershaghi et al.*, 1979; *Muramoto and Elders*, 1984] show that changes in mineral properties apparently associated with hydrothermal alteration can be identified in the well logs. *Ershaghi et al.* [1979] reported that established conventions for estimation of shale fraction [*Doveton*, 1986] could be used as indicators of the degree of geothermal alteration of sediments. The reduction of calculated shale fraction with depth in the Cerro Prieto wells, located south of the Salton Sea province, apparently reflected the degree of alteration of clay minerals in the sediments. *Ershaghi et al.* [1979] also indicated that spontaneous potential (SP) logs correlated with lithology but that several factors could make SP log interpretation difficult. Circulation of drilling mud apparently cooled the borehole fluid enough so that local temperatures measured in the borehole during logging probably were very different from true formation temperatures. At the same time, it was suspected that unidentified contributions to naturally occurring potential differences may have complicated the SP log interpretation procedure. *Ershaghi et al.* [1979] recommended that temperature build-up curves be used to estimate true formation temperatures and that multiple methods be used to bracket estimated values of formation water resistivity.

Muramoto and Elders [1984] conclude that geophysical log responses can be used to identify four mineralogic zones in the Salton Sea sediments: (1) unaltered montmorillonite zone, $<100°$–$190°$C, (2) illite zone, $<190°$–$250°$C, (3) chlorite zone, $240°$–$300°$C, and (4) feldspar zone, $>300°$C. They indicate that the primary factor determining geophysical log response in these zones is the transition in clay mineral properties. The unaltered montmorillonite zone is characterized by the naturally low resistivity of conductive clay minerals and the low density of unaltered sediments. The top of the illite zone is associated with a rapid rise in the resistivity of shales, accompanied by a decrease in sandstone resistivity. Although not explicitly stated, it is assumed that this relative decrease in sandstone resistivity is caused by increasing salinities (decreasing R_w). Both sandstone and shale resistivities continue to increase through the chlorite zone. Resistivities then level off to relatively large values in the feldspar zone. The primary mechanism for the increases in resistivity is assumed to be loss of ion exchange capacity and increase in proportion of relatively non-conductive silicate minerals with alteration. In addition, *Muramoto and Elders* [1984] found that the ratio of sandstone to shale resistivities was a good indicator of the various zone transitions and that electric log analysis gave a good qualitative indication of trends in solute content. SP log analyses appeared to consistently underestimate equivalent NaCl concentrations.

GEOPHYSICAL LOGGING ACTIVITY

The State 2-14 borehole is located on the southeastern shore of the Salton Sea on the northeast flank of surface heat flow and aeromagnetic anomalies associated with the Salton Sea geothermal field [*Newmark et al.*, 1986] (Figure 1). Surface altitude at the site is approximately 100 m below mean sea level. Drilling started on October 23, 1985, and was completed at a total depth of 3220 m on March 17, 1986. Logs were run in stages prior to installation of casing at depths of about 1200 m (borehole diameter $\approx$ 50 cm) and 1800 m (borehole diameter $\approx$ 30 cm). The lowermost interval (1800–3220 m in depth) of the borehole was about 22 cm in diameter except for extensive intervals of borehole enlargement. Additional background information regarding the State 2-14 borehole is reported by *Paillet et al.* [1986].

The geophysical logs referred to in this investigation were obtained by a commercial well logging company, Schlumberger Well Services, using conventional oil field equipment, and by the U.S. Geological Survey using similar equipment which had several modifications designed to improve performance under hostile geothermal conditions. A summary of the logs run during this study is listed in Table 1. Most logs for depth intervals above 1800 m were obtained by the commercial contractor. Borehole temperatures at these depths were generally less than 150°C for at least a few days after circulation of drilling fluids, and logging activity was not hampered. However, most conventional logging equipment was not capable of operating in the hostile environments encountered below 1800 m. Most sophisticated components within geophysical logging sondes are not designed to function at temperatures greater than 150°C. The corrosive properties of geothermal fluids produced in the State 2-14 borehole can damage most metallic or rubber-sheathed surfaces. In addition, the insulating properties of standard commercial logging cables deteriorate at temperatures above 150°C, further interfering with the performance of logging equipment. Commercial logging at depths below 1800 m was limited to a single run using a deep-induction and spontaneous potential logging-tool-combination to a depth of about 2700 m.

The U.S. Geological Survey logging equipment was used to obtain uncalibrated neutron, natural gamma, and temperature logs to almost total depth. In addition, some acoustic televiewer and acoustic full-waveform logs were obtained from selected intervals at depths greater than 1800 m. However, borehole conditions had severely deteriorated during attempts to control lost circulation in the period prior to logging. Inspection of televiewer logs indicated extensive borehole wall caving throughout intervals where producing fractures seemed to intersect the borehole. Because of rig time limitations, televiewer logging was discontinued. Acoustic full-waveform logs also were attempted across a 1050-m interval below 2000 m. Lowering the acoustic probe through extensively caved zones was difficult, and damage to tool centralizers was suspected. Inspection of the logging tool at the end of the run verified that the centralizers had been destroyed. Subsequent analysis of waveform data indicated that the only waveforms in which first arrivals clearly could be recognized were limited to those obtained in the interval from 1100 to 1500 m.

Performance of the U.S. Geological Survey geothermal logging equipment is summarized in Table 2. Design requirements and strategies for protecting geophysical logging tools from the hostile geothermal environment are reviewed by *Veneruso and Coquat* [1979]. All equipment used in this investigation functioned properly at temperatures as high as 250°C or had difficulties unrelated to the geothermal environment. The logging cable used in the State 2-14 borehole was pur-

TABLE 1. Summary of Geophysical Logs, Dates, and Depth Intervals Over Which Logs Were Run in the State 2-14 Borehole

Commercial Log Type	Date Logged	Depth Range, m
Deep induction, spontaneous potential, natural gamma, nuclear porosity, compensated gamma-gamma (density)	Nov. 4, 1985	315–916
Caliper, acoustic transit time	Nov. 5, 1985	315–917
Deep induction, spontaneous potential, natural gamma, acoustic transit time	Nov. 13, 1985	884–1073
Nuclear porosity, compensated gamma-gamma (density)	Nov. 13, 1985	884–1065
Caliper	Nov. 13, 1985	315–1074
Deep induction, spontaneous potential, natural gamma, nuclear porosity, and compensated gamma-gamma (density)	Dec. 9, 1985	1073–1825
Caliper and acoustic transit time	Dec. 9, 1986	1073–1823
Deep induction, spontaneous potential	March 10, 1986	1835–2684
Temperature, natural gamma	Nov. 5, 1985	315–914
Temperature (2), caliper (2), acoustic televiewer, acoustic-transit time (2)	Nov. 6, 1985	315–914
Full waveform acoustic, temperature (2), natural gamma, gamma spectral	Nov. 7, 1985	315–914
Temperature	Dec. 4, 1985	315–914
Temperature	Dec. 9, 1985	1071–1829
Temperature, caliper, acoustic televiewer, natural gamma	Dec. 10, 1985	1071–1829
Gamma spectral, single-point resistance, acoustic transit time, full waveform acoustic (2), caliper, temperature	Dec. 11, 1985	1071–1829
Caliper, neutron	Dec. 12, 1985	1071–1829
Temperature	Dec. 23, 1985	1071–1829
Temperature	Dec. 29, 1985	1071–1829
Temperature	Feb. 15, 1986	1829–3048
Temperature	March 12, 1986	1829–3048
Acoustic televiewer	March 12, 1986	1827–2012
Full-waveform acoustic	March 13, 1986	1829–2134
Natural gamma, neutron	March 29, 1986	1829–3048
Temperature	March 8, 1986	315–3049
Temperature	March 27, 1986	315–3049
Temperature	March 31, 1986	315–3049
Temperature	April 7, 1986	315–3049

chased especially for this project. During initial planning stages there was some uncertainty as to (1) selection of a nickel alloy and teflon-insulated cable made according to available technology and capable of functioning at temperatures as high as 300°C, or (2) design of a new cable using magnesium oxide insulation capable of functioning at temperatures exceeding 450°C [*Miyairi and Itoh*, 1985]. Cable specifications eventually were based on the established teflon insulation technology because cable manufacturers were uncertain whether a seven-conductor cable of sufficient tensile strength could be manufactured with the magnesium oxide insulation.

The MP35N-alloy cable with teflon insulation functioned well throughout the logging operations in the State 2-14 borehole. Only minor cable head current leakage occurred, and this was corrected by relatively simple modifications on site. The geothermal logging cable was repeatedly used to run temperature logs in intervals where temperatures as high as 300°C were recorded, with no functional problems. The damage to the centralizers on the acoustic logging probe resulted from borehole conditions unrelated to temperature and pressure.

The one major failure, that of the caliper motor, occurred when the caliper tool was inadvertently exposed to temperatures greater than 300°C (Table 2). The caliper tool had been lowered to the bottom of the hole after a period of circulation. Apparently, however, borehole conditions prevented proper circulation and cooling in the lowermost part of the borehole, and the caliper arms subsequently failed to open when exposed to temperatures greater than 200°C. In retrospect, these conditions could have been anticipated by obtaining caliper logs in stages across shallower intervals, working downward from the bottom of the casing, rather than attempting to log the entire open hole below 1800 m in one continuous run. The caliper log would have been very useful in the analysis and interpretation of induction and uncalibrated neutron logs obtained in the lower portion of the borehole. Additional discussion of geophysical logging procedures, equipment performance, data storage techniques, depth correlation between various logging runs, and initial data processing are given by *Paillet et al.* [1986].

GEOPHYSICAL LOG ANALYSIS

Numerous temperature logs were obtained intermittently during the drilling operation at the State 2-14 borehole, and additional logs have been recorded since drilling concluded. A composite of several temperature logs is presented in Figure 2. These temperature profiles are the subject of a separate analysis presented by *Sass et al.* [this issue], where the logs are used to characterize reservoir temperature distributions and to identify zones of fluid loss. There were instances where qualitative correlations could be made between the temperature and lithology logs, since the local temperature regime is affected by the thermal conductivity of the surrounding formation. For example, relatively high-porosity sandstones (low thermal conductivity) manifested themselves in the temperature log shown in Figure 2 as zones having greater geothermal gradients. It is anticipated that more frequent and clearer correlations would be possible with an undisturbed log ob-

TABLE 2. Summary of Geothermal Logging Equipment Performance

Probe	Estimated Maximum Temperature, °C	Comments
Epithermal neutron	250	no problems
Acoustic (full waveform and transit time)	220	no problems related to temperature
Natural gamma	250	no problems
Caliper	250	motor failure at 310°C; no deep logs
Temperature	320	no problems, even with extended measurements
Acoustic televiewer	210	possible cablehead leakage; no other problems related to temperature

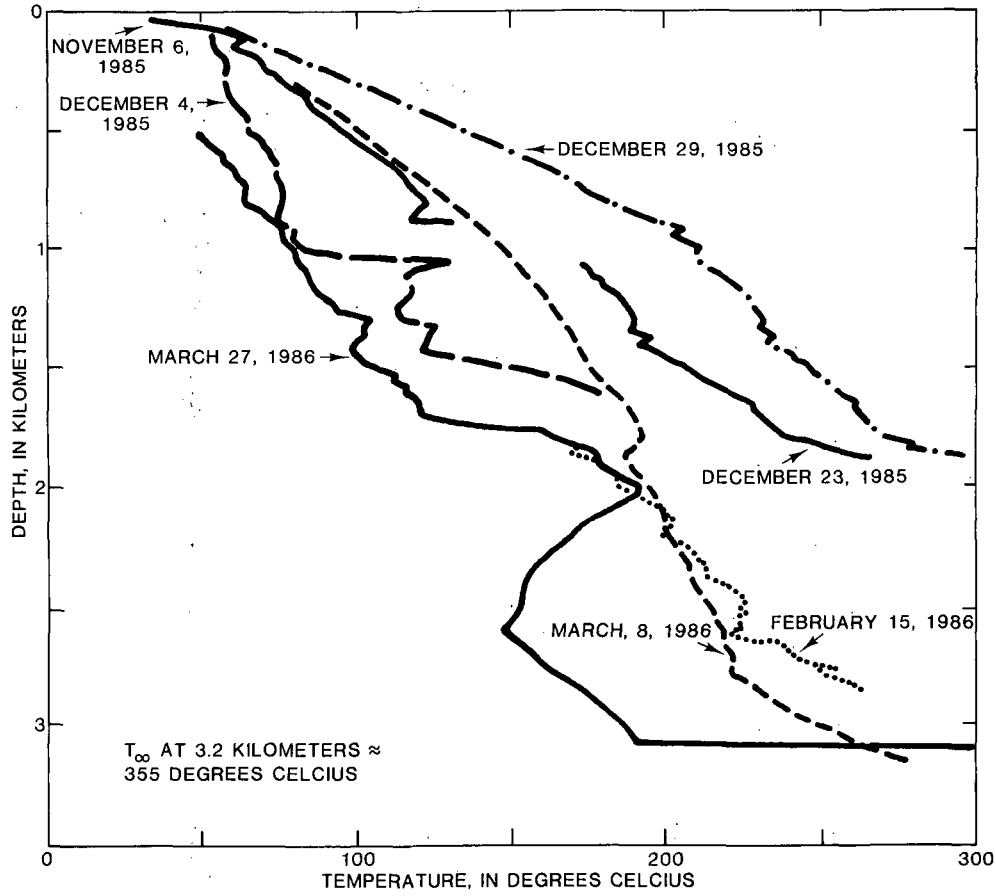

Fig. 2. Composite temperature log of the State 2-14 borehole indicating the temperature profile at various times during drilling.

tained at thermal equilibrium conditions depicting true formation temperatures.

The geophysical logs listed in Table 1 indicate that a full suite of logs was obtained in the portion of the State 2-14 borehole at depths less than 1800 m, while a relatively limited suite was obtained below 1800 m. General lithology logs constructed from recovered cuttings and core [*Mehegan et al.*, 1986] appeared consistent with geophysical logs, even though the State 2-14 borehole encountered more fine-grained, clay-rich sediments than the boreholes described by *Ershaghi et al.* [1984] and *Muramoto and Elders* [1984]. The very low frequency of sandstones in the State 2-14 borehole significantly complicates geophysical log interpretation using the sandstone/shale resistivity criteria given by *Muramoto and Elders* [1984] and hampers the effectiveness of the conventional analysis of "clean" sandstones used to estimate the properties of natural formation waters.

Inspection of the geophysical logs obtained in the State 2-14 borehole indicates significant correlation between geophysical logs presented by *Paillet et al.* [1986] and lithology logs given by *Mehegan et al.* [1986]. Examples of geophysical logs for representative intervals of the borehole are given in Figures 3 and 4. The geophysical log intervals shown in Figure 3 illustrate the correlation between induction, neutron porosity, and self-potential logs, and changes in lithology identified from core and cuttings. In general, large resistivities and low porosities and acoustic transit times correspond to large sandstone fractions on the lithology log, whereas small resistivities and larger porosities and acoustic transit times correspond to large claystone fractions. This correlation is apparent in the interval from 1200 to 1450 m in depth illustrated in Figure 3. Departures from this correlation represent the dependence of geophysical measurements to rock properties other than clay mineral content and on the details of particle size distribution that are not reflected by the lithology log. At depths below 1500 m the alteration of clay minerals apparently accounts for the poor correlation between geophysical and lithology logs. When sediments have been altered, the formation of nonconductive minerals such as epidote and feldspar destroys the electrical conductivity of matrix rocks and eliminates the large difference between the geophysical properties of claystone and sandstone detected by nuclear and acoustic logs. Deflections in deep-induction resistivity and SP logs from uniform background values at depths greater than 1500 m probably represent local changes in borehole diameter rather than changes in lithology.

Changes in transit time on the acoustic log seem to correlate with changes in lithology, but the actual recorded values appear too low for indurated shales and sandstones. For example, the log shows that transit times vary from 280 μs/m (sandstone) to more than 450 μs/m (claystone), corresponding to seismic compressional velocities from 1.8 to 3.0 km/s. However surface seismic surveys [*Daley et al.*, this issue] and core measurements [*Tarif et al.*, this issue] indicate that Salton Sea sediments have velocities in the range of 3.0–5.0 km/s. Inspection of acoustic full-waveform logs obtained over the depth

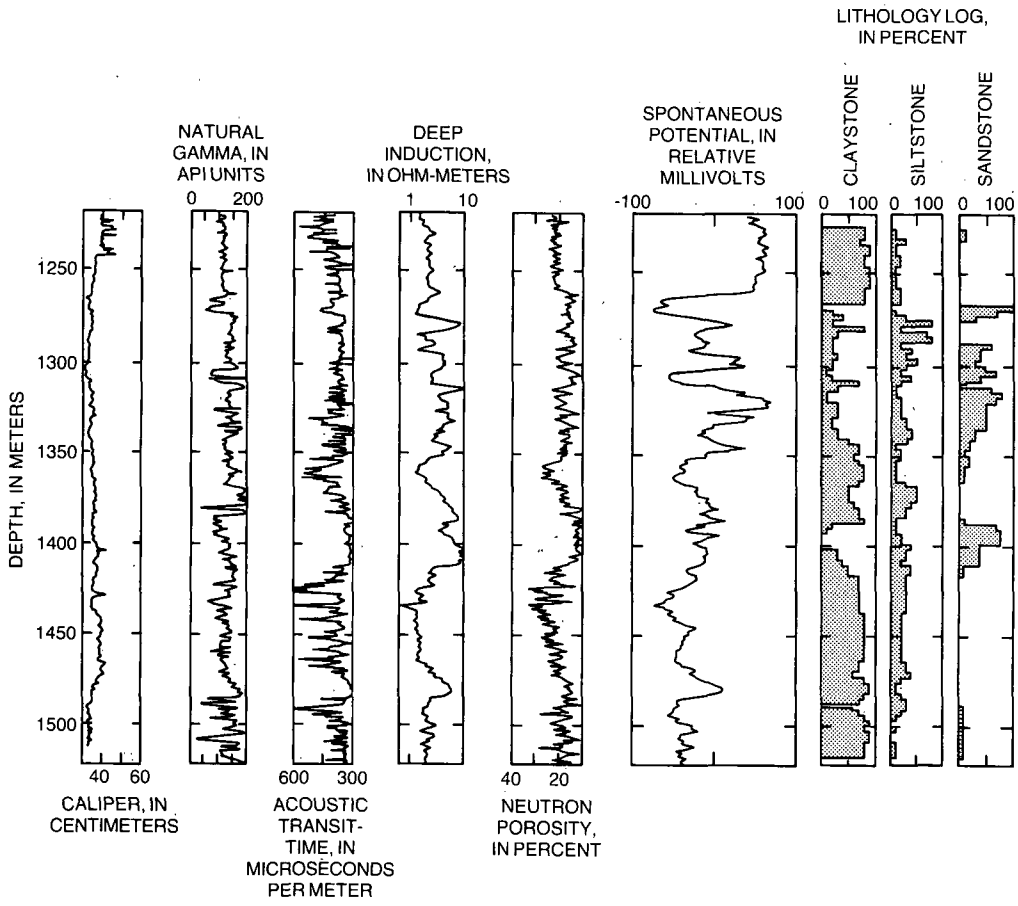

Fig. 3. Caliper, natural gamma, acoustic transit time, deep-induction, neutron porosity, spontaneous potential, and lithology logs for the depth interval from 1200 to 1500 m in the State 2-14 borehole.

interval from 1100 to 1500 m suggests that geophysical logging equipment used by both the U.S. Geological Survey and the commercial logging contractor was incorrectly picking first arrivals. Because large borehole diameters filled with viscous drilling mud significantly attenuated the acoustic signal generated by the tools, the logs were apparently based on one of the first few cycles of the pseudo-Rayleigh mode [*Cheng and Toksoz*, 1981; *Paillet and White*, 1982]. This mode travels at characteristic speeds slightly less than the shear velocity, so that the correlation between transit times and lithology illustrated in Figure 3 is apparently based on an approximate relationship between lithology and shear velocity. The dependence of pseudo-Rayleigh mode amplitude on Poisson's ratio and the inability to separate the effects of lithology from cycle skips within the pseudo-Rayleigh arrivals make the conventional acoustic transit time logs unreliable for quantitative interpretation in the State 2-14 borehole and inferior to most other logs for qualitative interpretation.

Full-waveform logs were made in addition to conventional acoustic transit time logs by recording the full pressure signal arriving at the acoustic receivers as described by *Paillet and White* [1982]. Most full-waveform logs were run in order to record the character of the entire pressure signal. However, borehole conditions such as large diameter and viscous drilling mud inhibited acoustic propagation, resulting in very weak first arrivals which could not be recognized in these records. This difficulty was identified in the field, and an additional waveform logging run was made at the highest possible gain setting to amplify first arrivals. The waveforms obtained with this higher gain are compared to waveforms obtained at conventional settings in Figure 5. First arrivals can be detected in these records, and the high-gain waveforms were used to construct a velocity log for the interval from 1200 to 1600 m (Figure 6). The trend in compressional velocity shown in Figure 6 agrees with the trend in laboratory measurements of compressional velocity made at approximately in situ conditions. The curve given by averaging the individual velocity values obtained from the waveform logs also correlates with the induction log, indicating that the induction log and additional compressional velocity data from laboratory tests on core samples can probably be used to extrapolate the waveform velocity curve in Figure 6 to greater depths (see Figure 10).

The natural gamma log, usually considered to be a good indicator of lithology [*Doveton*, 1986], does not appear to correlate well with lithology in either Figure 3 or Figure 4. Only a few of the sandstones identified by the lithology log in Figure 3 are associated with local minima in natural gamma counts in the log. This contrasts with the results of *Ershaghi et al.* [1979] and *Muramoto and Elders* [1984], when natural gamma logs were found to be good lithology indicators in at least the upper portion of the boreholes. The poor correlation of natural gamma logs evidenced here may be related to the lack of good lithology contrasts in the upper portion of the State 2-14 borehole, where there are few clean sandstones. At greater depths, hydrothermal alteration may have acted to

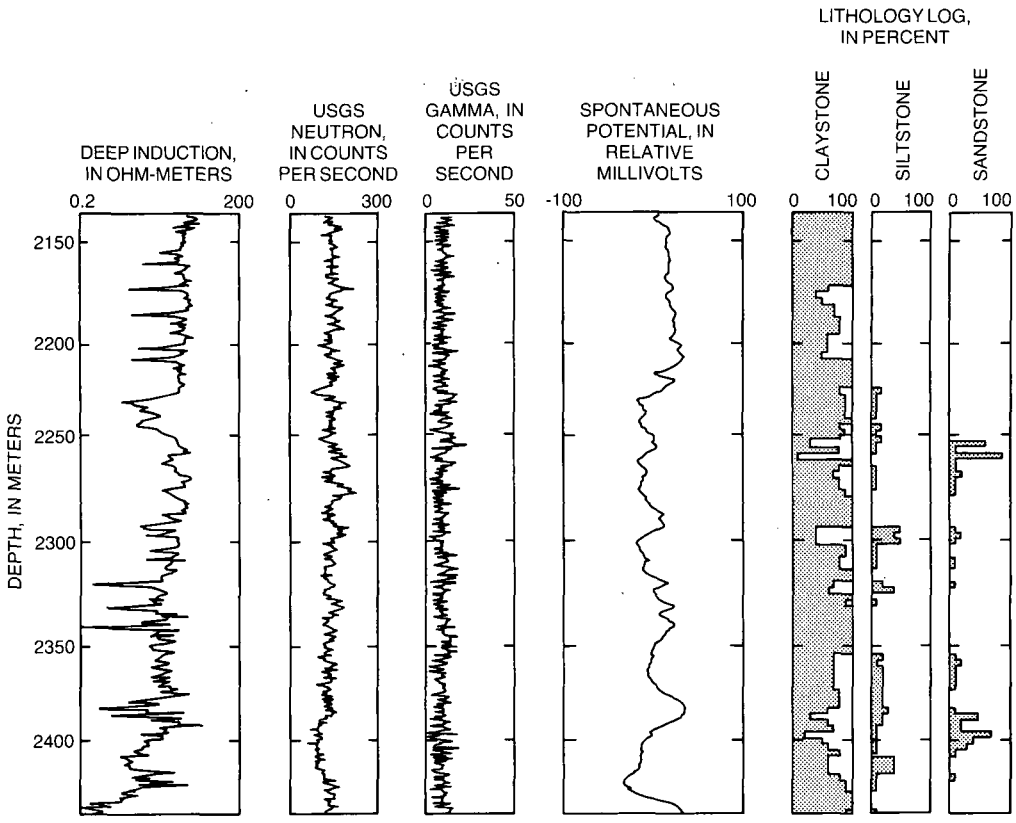

Fig. 4. Deep-induction, uncalibrated neutron, natural gamma, spontaneous potential, and lithology logs for the depth interval from 2100 to 2400 m in the State 2-14 borehole.

redistribute natural radioisotopes, obscuring the initial correlation between sediment type and natural radioactivity. Such a process would be anticipated if reduction in cation exchange capacity was closely associated with hydrothermal alteration of shales.

The SP log depicted in Figure 3 appears to provide a good indication of lithology, whereas the SP log shown in Figure 4 shows poor correlation. Inspection of the SP log for the full length of the State 2-14 borehole indicates that good correlation of SP log with lithology only occurs over an intermediate depth range. For example, the lithology log indicates little sandstone at depths above 1200 m so that little variation in SP would be expected, and there is no way in which the full potential difference between pure sandstone and shale can be determined. However, significant negative SP values occur opposite the sandstones in the upper part of Figure 3 so that quantitative interpretation of SP logs is possible over that depth interval. At depths greater than 1400 m the amplitude of measured negative SP declines and fails to correlate with the lithology log. The interval of relatively large resistivity, small acoustic transit time, and low porosity near 1480 m in depth in Figure 3 corresponds to positive SP and large claystone fraction. The correspondence of low porosity and electrical conductivity with high claystone fraction could indicate significant alteration of clay minerals, accounting for the poor correlation of SP with the lithology log below 1500 m in depth. The poor SP response at depths above 1000 m is probably related to a smaller water quality contrast between formation waters and drilling mud at these shallow depths in addition to the lack of clean sandstones necessary for good lithologic contrast [*Hearst and Nelson*, 1985]. At intermediate depths, natural salinity apparently increases, and the lithology log indicates cleaner sandstones. At still greater depths the hydrothermal alteration of shale reduces and then eliminates the membrane effect which accounts for the production of a natural SP [*Hearst and Nelson*, 1985].

Geophysical Log Interpretation

Analysis of the geophysical logs for the State 2-14 borehole indicates that the primary log response lies between two lithologic endpoints: (1) electrically conductive claystone with moderate to large apparent neutron porosity and no effective porosity, and (2) electrically resistive siltstone and/or sandstone with low neutron porosity and low but finite effective porosity. The large but variable clay mineral fraction and the differences in cation exchange capacity between different naturally occurring clay mineral types account for a poor correlation between electrical resistivity and neutron porosity for the upper portion of the borehole (depths less than 1000 m). The hydrogen content (naturally bound water) in many clay minerals results in measured neutron porosities greater than 30%. Electrical resistivity given by the deep induction log is cross-plotted against neutron porosity for the upper portion of the State 2-14 borehole in Figure 7. The cross plot shows the expected lack of correlation between resistivity and neutron porosity.

At depths greater than 1000 m, hydrothermal alteration of clays such as montmorillonite, with the highest cation exchange capacity, apparently results in a more uniform correlation between neutron porosity and resistivity. Another cross plot between resistivity given by the commercial deep-induction log and neutron porosity given by the commercial

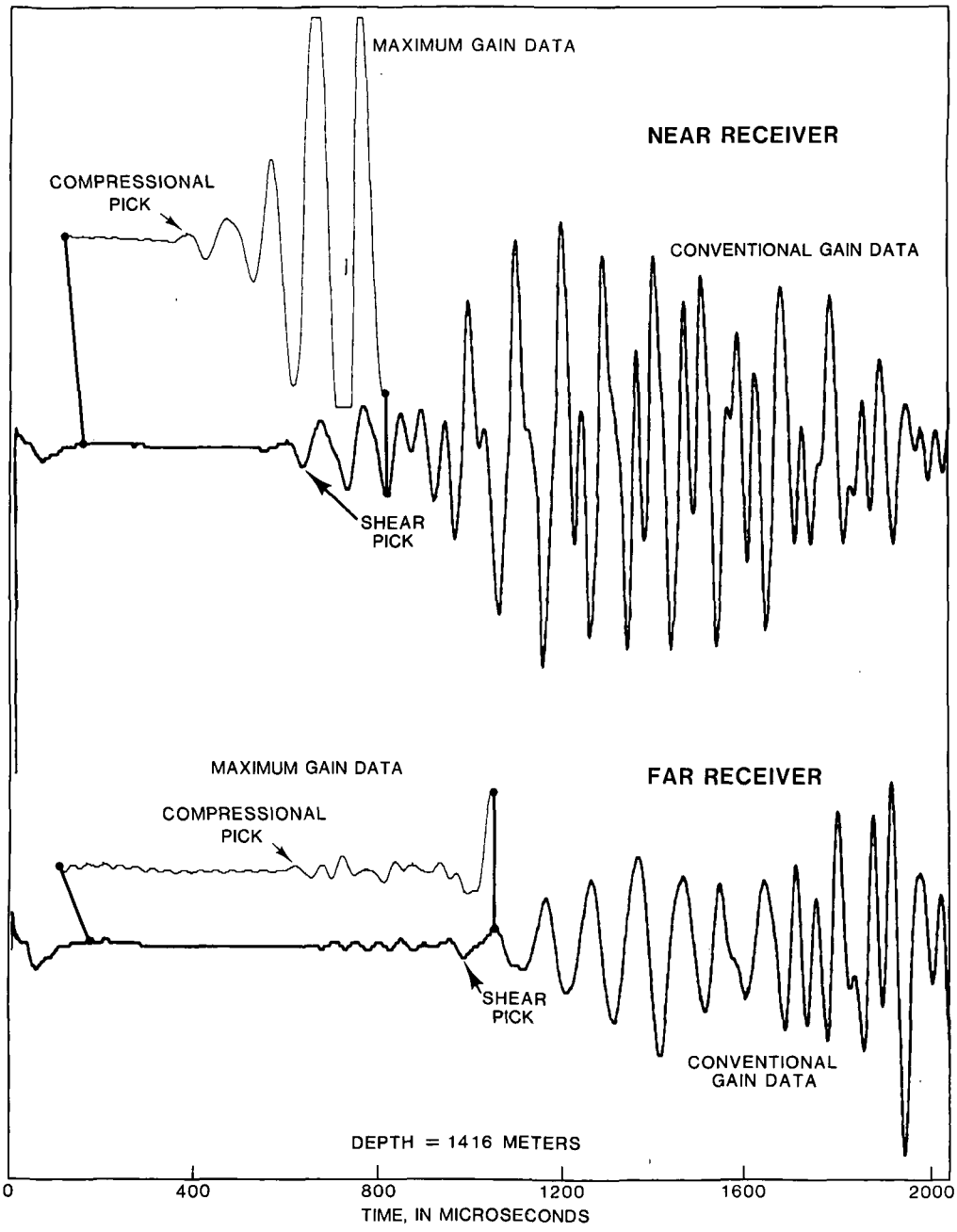

Fig. 5. Acoustic full waveforms digitized using conventional gain settings compared to waveforms at maximum gain, showing picks for compressional and shear arrivals.

neutron log illustrates a significant correlation between resistivity and porosity (Figure 8). This correlation associates higher resistivities with lower porosities, but its physical basis is probably not the same as that represented by *Archie*'s [1942] law. The lowest resistivities and highest neutron porosities in Figure 3 are clearly associated with claystone, whereas lower porosities and higher resistivities are associated with sandstones. For example, at a depth near 1375 m, both deep-induction resistivity and neutron porosity logs shift toward higher resistivities and lower porosities at the contact between claystone above and sandstone below. Archie's law assumes that electrical conduction occurs exclusively by means of ionic conduction in pore spaces, but the geophysical logs in Figure 3 indicate that electrical conduction is more closely correlated with the conductivity of clay minerals.

The one major departure from the relationship between lithology and geophysical log response described above is associated with the few relatively clean sandstones present across the depth interval from 1200 to 1500 m. The term "clean" refers to sandstones and other granular rocks containing negligible quantities of clay minerals. In log analysis the term is applied to cases where the effects of primary, fluid-filled pore spaces dominate clay mineral effects in determining geophysical properties of the composite rock. In this paper, clean sandstones are those sandstones in which clay mineral content is so small that Archie's law may be applied with no more than a small correction for rock matrix conductivity. The induction and porosity logs generally parallel each other in response to the presence of clay minerals, but the induction log shows a local reversal within some of the sandstone inter-

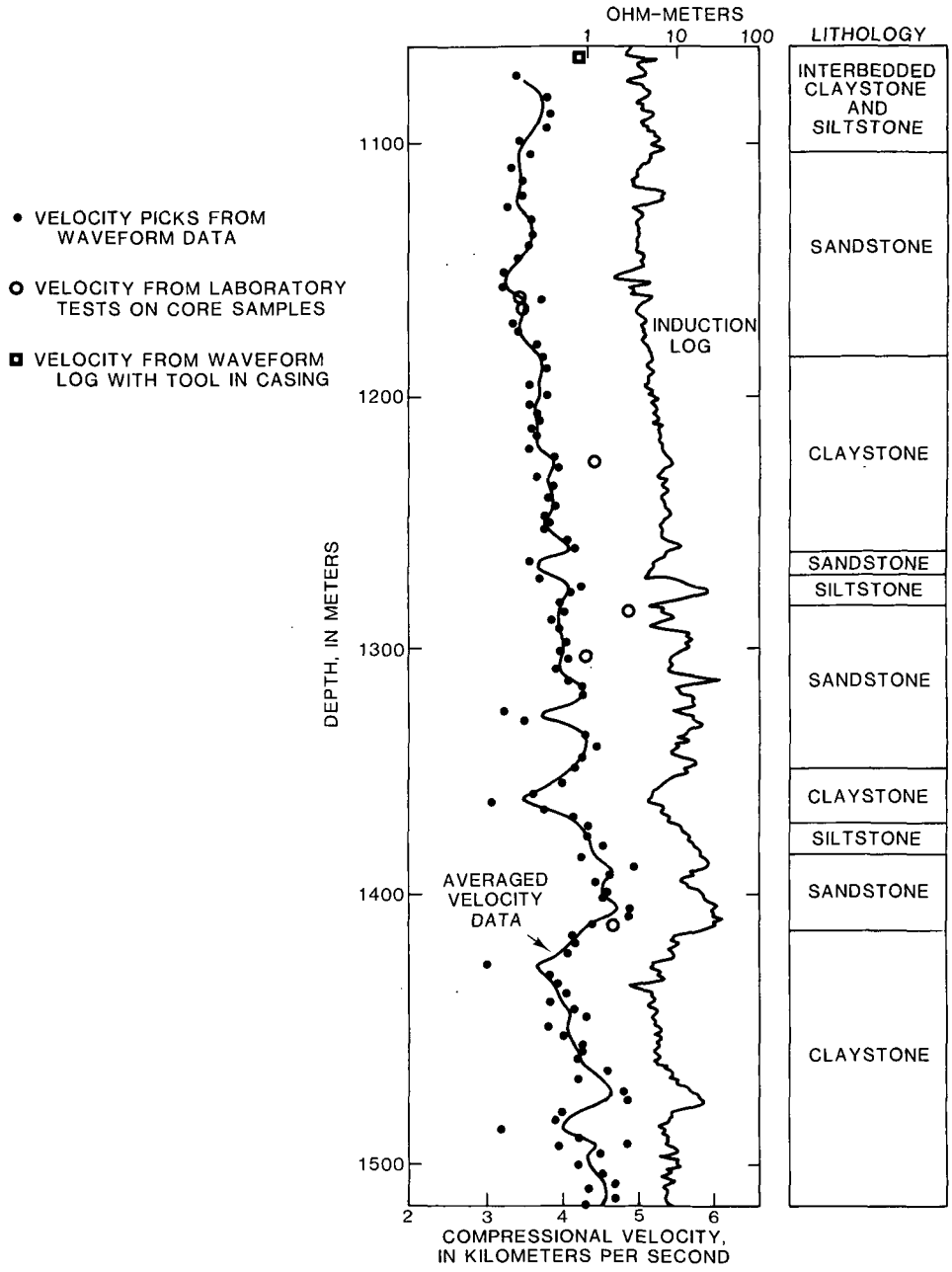

Fig. 6. Compressional velocities determined from full-waveform logs for the depth interval from 1200 to 1600 m in the State 2-14 borehole compared to compressional velocity measurements determined from core samples and the deep induction log.

vals indicated on the lithology log (Figure 9). This reversal is interpreted as the result of residual interconnected porosity in some sands. The porosity of these sandstones can be estimated from several of the geophysical logs. In general, gamma-gamma logs cannot be calibrated in units of porosity because grain densities remain unknown. However, grain densities in clean sandstones may be assumed near that of pure quartz (2.65 g/cm^3). Correspondingly, calibrated porosities for the sandstones with induction log reversals in Figure 9 range from less than 3 to nearly 10% (Table 3). Although the acoustic transit time log shown in Figure 3 cannot be used for porosity calculations, porosity can be estimated from compressional velocities given by the acoustic waveform logs. In this case, sandstone porosities vary from 5 to 14%. If shale corrections are also applied to porosity estimates made from acoustic waveform logs, porosity values (Table 3) nearly coincide with those derived from the gamma-gamma log.

Although relatively few clean sandstones were encountered in the State 2-14 borehole in comparison to the formations described by *Ershaghi et al.* [1979] and *Muramoto and Elders* [1984], estimates of water quality can still be attempted in a few of these intervals. Salinity in equivalent NaCl concentration can be approximated by estimating formation water resistivity using resistivity values obtained from the induction log and also from maximum SP log deflections (known as static self-potential or SSP). These calculations have been made for a few selected sandstones and the results are presented in Table 4. Inspection of the SP and induction logs depicted in Figure 9 indicates that only two sandstones in the depth interval shown are clean enough for Archie's law to

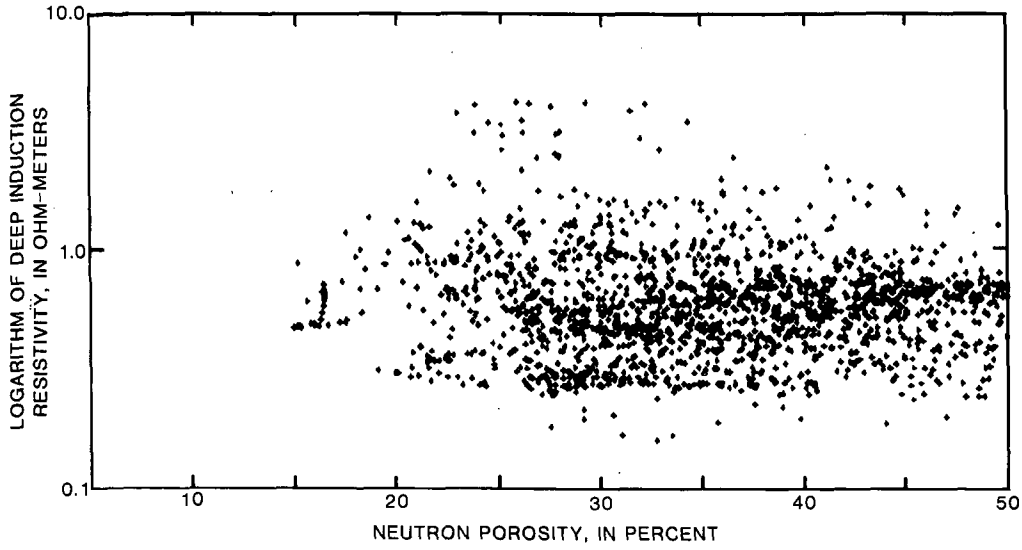

Fig. 7. Cross plot of deep-induction resistivity versus neutron porosity for the depth interval from 500 to 1200 m in the State 2-14 borehole.

be applied and full SSP deflections to be estimated. Two additional relatively clean sandstones have been identified on the logs at depths above 1000 m. However, SP log response appears so poor at these depths that no SSP can be adequately estimated. The results for the two sandstones shown in Figure 9 indicate equivalent NaCl salinities greater than 100,000 ppm using Archie's law (Humble equation) and less than 50,000 ppm using the measured SSP. Clay mineral effects cause Archie's law to overestimate salinities; conversely, they reduce apparent SSP values and cause the estimate of Rw using the SP log to underestimate salinities. These results appear consistent with those of *Muramoto and Elders* [1984] for other Salton Sea boreholes, where fluid salinities derived from SP log analysis were consistently underestimated.

Changes in sediment properties indicated by the geophysical logs obtained in the State 2-14 borehole are shown in Figure 10. Figure 10 shows porosity from neutron and gamma-gamma logs, resistivity from the deep-induction log, and compressional velocity from the full-waveform log. The four curves have been smoothed with a depth-averaging filter to emphasize depth trends unrelated to sedimentary fabric. The neutron porosity log indicates consistently higher porosities because the compensated neutron log is sensitive to both hydrated minerals and the neutron absorption cross section of chlorine. Figure 10 shows the decreases in porosity and increases in compressional velocity expected with increasing lithostatic stress. The compressional velocity trend has been extended beyond the depth limits of the waveform data using the correlation between deep induction and compressional velocity shown in Figure 6 and using the results of laboratory measurements on core samples (given as discrete points in Figure 10). However, the shapes of the deep-induction and acoustic velocity curves in Figure 10 indicate that the significant changes in sediment properties beyond the expected changes associated with increasing stress occur within the depth interval from 1200 to 1800 m. Laboratory tests and

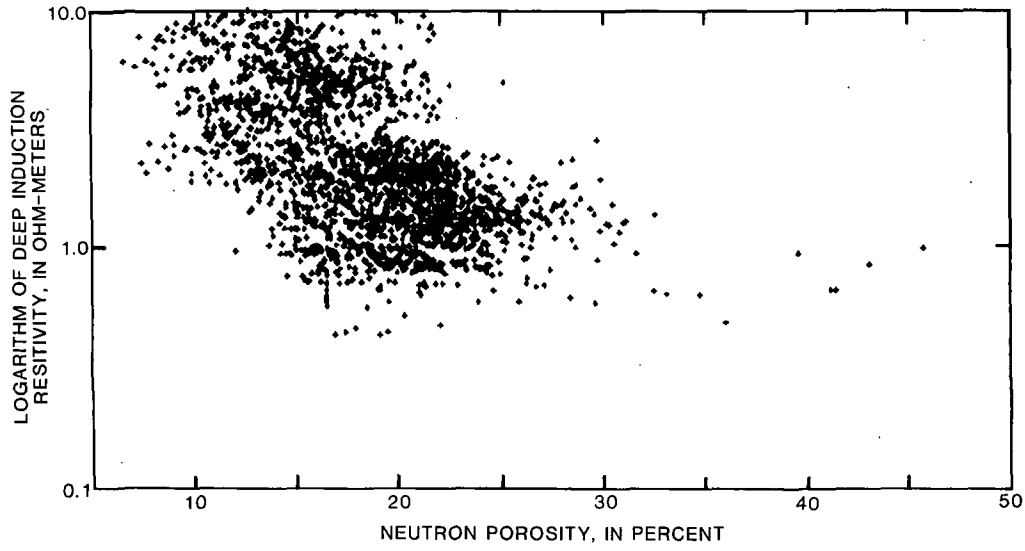

Fig. 8. Cross plot of deep-induction resistivity versus neutron porosity for the depth interval from 1200 to 1800 m in the State 2-14 borehole.

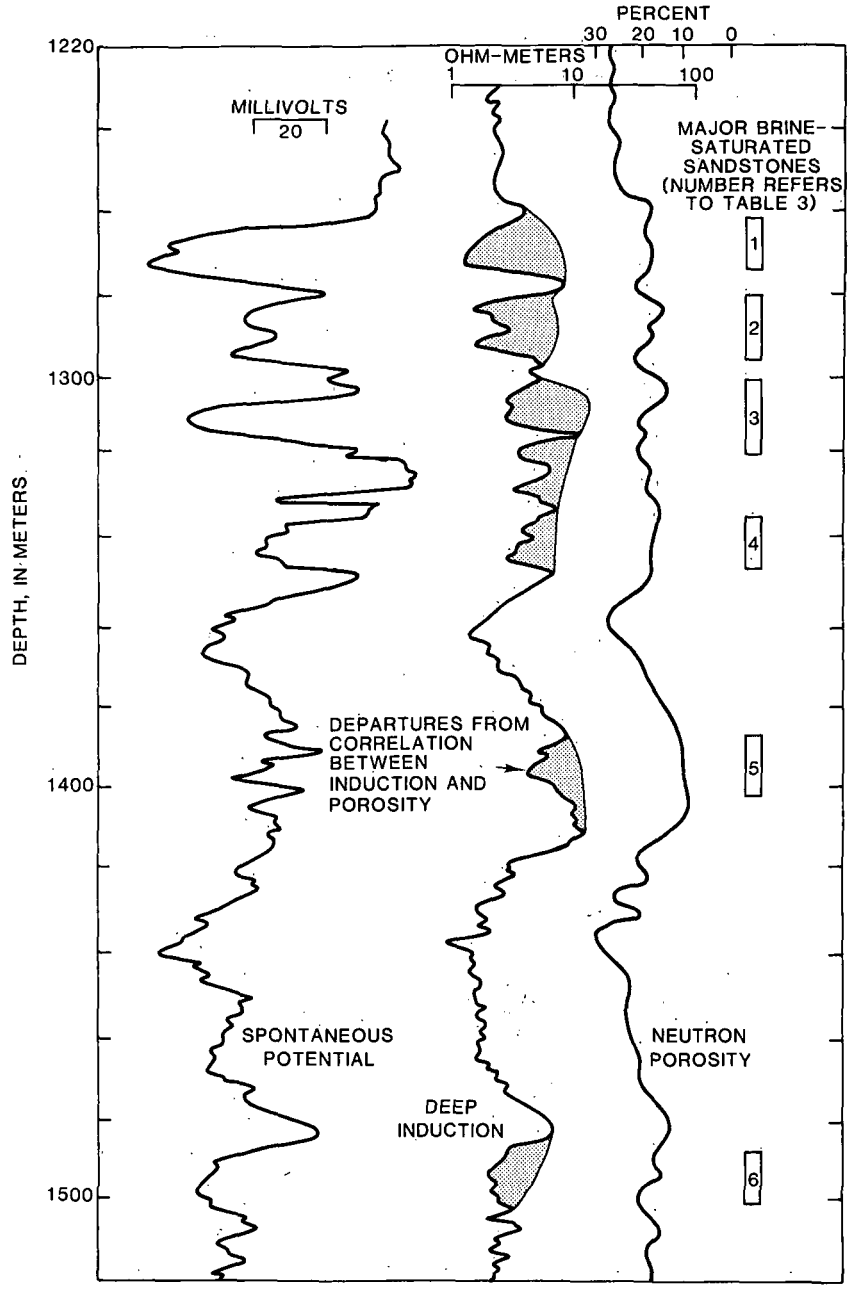

Fig. 9. Comparison of spontaneous potential, deep-induction, and neutron porosity logs for the depth interval from 1200 to 1500 m in the State 2-14 borehole, indicating local resistivity reversals attributed to brine-saturated sandstones.

electron microscope examination of core samples from this interval [*Tarif et al.*, this issue] demonstrate the way in which mineral alteration contributes to the geophysical properties of sediments.

As discussed by *Ershaghi et al.* [1979] and *Muramoto and Elders* [1984], the depth trends in geophysical log values in the Imperial Valley are affected by changes in clay mineral properties resulting from hydrothermal alteration of sediments, as well as by compaction and increasing confining pressure. In contrast, relatively small quantities of minerals, such as calcite, epidote, and biotite, are predominant in the mineral deposits identified by investigators studying fracture infillings. Although these deposits are important when characterizing geothermal alteration, geophysical logs indicate only those changes in sediment properties that affect a substantial volumetric fraction of the entire rock surrounding the borehole. Using the clay mineral alteration zones defined by *Muramoto and Elders* [1984] and *Muffler and White* [1969], the major interval of such alteration (illite and upper chlorite zones) apparently corresponds to the temperature range from 180° to 260°C. The temperature log interpretation given by *Sass et al.* [this issue] indicates that this range corresponds approximately to the depth interval extending from 1000 to 1800 m.

The lithology log for the State 1-14 borehole indicates insufficient sandstone to test the resistivity ratio criteria used by *Muramoto and Elders* [1984] for the identification of clay mineral subzones within the alteration profile. The data listed in Table 4, along with the unresponsive SP log at depths less than 1000 m, may indicate that the salinity of natural forma-

TABLE 3. Estimates of Interval-Averaged Porosity for Sandstones in the Depth Interval From 1200 to 1500 m

Sandstone	Depth Interval, m	Acoustic Porosity, %	Shale Fraction, %	Corrected Acoustic Porosity, %	Density Porosity, %
1	1265–1272	14	10	12	11
2	1283–1298	14	30	8	9
3	1302–1320	10	20	6	6
4	1335–1347	16	35	9	8
5	1387–1402	10	30	4	6
6	1487–1503	16	20	12	9

Shale fraction estimated from self-potential log, and porosity calculated from density log using grain density = 2.65 g/cm^3 and mud density = 1.14 g/cm^3. Major sandstones are located in Figure 9.

tion waters increases with depth. This salinity increase may offset the increase in clay mineral resistivity and the decrease in neutron porosity caused by the alteration of montmorillonite to illite in the shallower part of the borehole. If this offset does occur, then the depth interval corresponding to hydrothermal alteration may extend somewhat above 1200 m in depth.

The depth trend of compressional velocity indicated in Figure 10 appears consistent with compressional velocity information obtained from laboratory tests of core samples reported by *Tarif et al.* [this issue]. The discrete compressional velocity values obtained from laboratory measurements are shown in Figure 10. Values corresponding to depth intervals where valid waveform logs were obtained agree with, or appear somewhat larger than, those velocity values determined from the waveform logs. The slightly larger values probably result from core measurements being run on slightly more competent samples. Acoustic full-waveform logs yield lower velocities than those determined from some of the core samples because the waveform velocities are derived from a much larger sample volume. Laboratory test procedures also contain substantial bias toward stronger samples, hence higher velocities, because some of the weaker samples are destroyed in processing prior to laboratory testing. Nevertheless, the acoustic waveform logs, laboratory velocity measurements, and vertical seismic profile data identify the 1200- to 1800-m-depth interval as a zone of increasing compressional velocity.

CONCLUSIONS

The suite of geophysical well logs obtained in the State 2-14 borehole located in the Salton Sea geothermal field provides a continuous profile of sediment properties that indicates increasing hydrothermal alteration with depth. The lithology log developed from cuttings recovered during drilling correlates with most geophysical logs [*Mehegan et al.*, 1986; *Paillet et al.*, 1986]. Deep-induction, neutron porosity, and gamma-gamma logs are related quantitatively to such sediment properties as clay mineral fraction and porosity. Acoustic transit time logs are related qualitatively to lithology, although values probably approximate shear, rather than compressional, transit times. Compressional velocity data are available from acoustic waveform logs obtained from 1200- to 1600-m-depth interval. These data can be extrapolated to greater depths by correlation of compressional velocity values with the deep-induction log and by using values of compressional velocity obtained from core samples in the laboratory. The spontaneous potential log demonstrates significant lithologic response in the depth interval from 1000 to 1500 m. Water quality contrasts apparently are too small, and sandstones contain too much clay mineral to provide useful SP logs at depths above 1000 m. In addition, clay mineral alteration at depths greater than 1500 m apparently interferes with the shale membrane effect needed to produce potential differences. The natural gamma log does not provide useful indication of lithologic contacts, probably because few clean sandstones occur above 1000 m in depth and radioisotope redistribution apparently has accompanied hydrothermal alteration at greater depths.

The trends in alluvial sediment properties as a function of increasing depth in the State 2-14 borehole seem to be caused by clay mineral alteration superimposed on the effects of increasing in situ stress and temperature and, to a lesser extent, of increasing salinity of natural formation water. The increase in resistivity with depth is apparently associated with a decrease of cation exchange capacity produced by hydrothermal alteration of clay minerals and indirectly indicated by systematic changes in geophysical logs with depth. Local reversals in the trend toward increasing resistivity with depth are related to the presence of relatively clean sandstones with residual porosities ranging from 3 to 14%, which are saturated with

TABLE 4. Equivalent NaCl Salinity Calculated for Selected Sandstones in the State 2-14 Borehole

Sandstone Depth, m	Formation Temperature, °C	Porosity, %	Humble Equation			SP Interpretation			
			Rt	Rw	TDS	SSP	Rmf	Rw	TDS
460	100	28.	1.10	0.082	25,000				
732	125	15.	0.55	0.0124	150,000				
1265–1272	160	11.	1.00	0.0121	150,000	−55	0.916	0.344	20,000
1302–1320	160	08.	1.25	0.008	200,000	−55	0.916	0.344	20,000

Rt, formation resistivity in ohm meters; Rw, formation water resistivity in ohm meters; Rmf, mud resistivity corrected to formation temperature in ohm meters; SSP, static self-potential in negative millivolts; TDS, total dissolved solids in parts per million equivalent NaCl solution; Porosity, calculated using gamma-gamma density log with assumed matrix density = 2.65 g/cm^3.

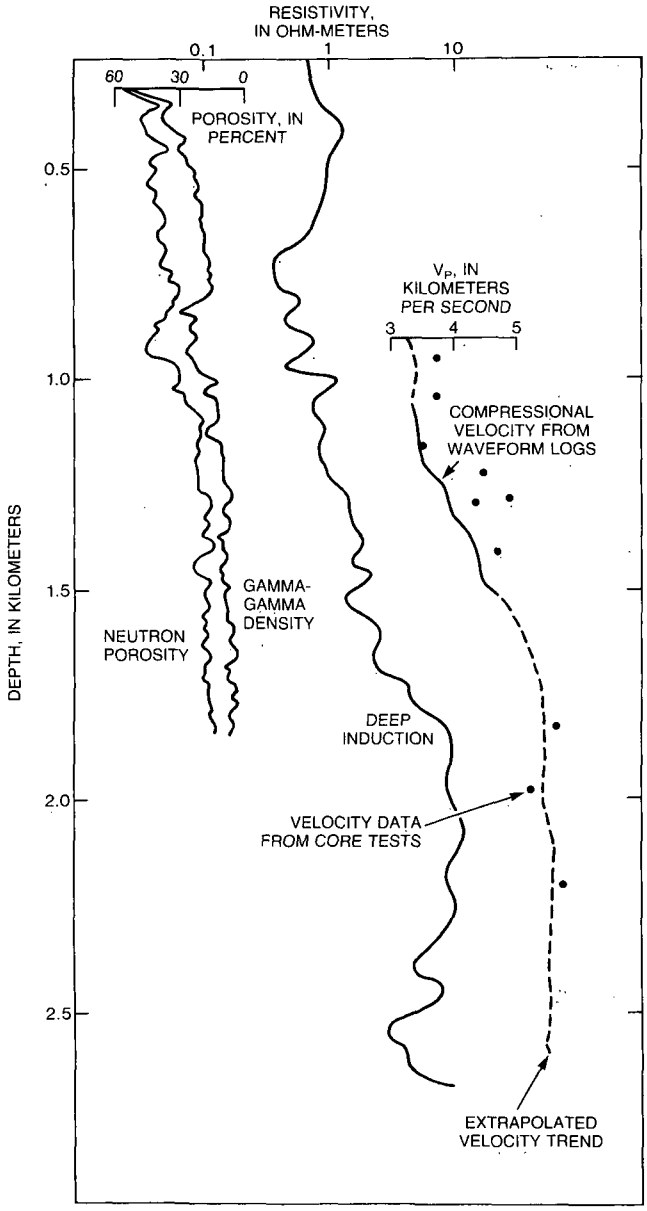

Fig. 10. Depth trends in averaged neutron porosity, deep-induction resistivity, and compressional velocity indicated by geophysical logs in the State 2-14 borehole.

brines of equivalent NaCl salinity greater than 100,000 ppm. The deep-induction and neutron porosity logs, as well as the compressional velocity data calculated from first arrivals in acoustic full-waveform logs, indicate that much of the hydrothermal transformation of clay minerals occurs in the depth interval extending from 1200 to 1800 m. Previous studies of geophysical well log characterization of hydrothermal alteration indicate that these changes are associated with temperatures ranging from 180° to 260°C. These temperatures and depths are consistent with those estimated from temperature logs run at various times during drilling of the State 2-14 borehole [*Sass et al.*, this issue].

Analysis of the geophysical logs indicates that the increasing hydrothermal alteration of sediments with depth is portrayed best by the depth-averaged trends in acoustic velocity, electrical resistivity, and nuclear porosity given in Figure 10. Although the geophysical logs provide a continuous profile of sediment properties, the most significant problem in recognizing the trend in alteration is its separation from other trends imposed by increasing in situ stress and temperature, changing borehole conditions, and eliminating some logs by increasingly hostile borehole environment. At least some of the decreases in nuclear porosity and increases in resistivity and compressional velocity apparent in Figure 10 are the direct result of increasing temperature and pressure and do not represent a permanent alteration of minerals in alluvial sediments deposited in the Salton Trough. The alteration of electrically conductive clay minerals to nonconductive minerals such as feldspar and epidote apparently accounts for most of the increasing electrical resistivity with depth in the State 2-14 borehole. Therefore the deep-induction resistivity log is more directly indicative of hydrothermal alteration than any of the other geophysical logs in Figure 10. Variations in electrical conductivity related to variations in effective porosity and increasing solute content of brines with depth are superimposed on the alteration profile given by the resistivity log, somewhat complicating the interpretation of geothermal alteration from the deep-induction log alone. Effects of increasing temperature and pressure with depth are also superimposed on the profile of compressional velocity in Figure 10, but laboratory measurements of compressional velocity of core samples [*Tarif et al.*, this issue] provide a means for distinguishing among changes in velocity caused by in situ conditions, differences in lithology, and alteration. The two nuclear porosity trends in Figure 10 are given only for the upper portion of the borehole. However, independent information on the variation in porosity with depth is very useful in separating the effects of clay mineral alteration from variations in pore solute conductivity in the interpretation of the deep-induction resistivity log. For all of these reasons, the composite of the four geophysical logs illustrated in Figure 10 provides a useful indication of the depth profile of alteration which would not be given by any one of the logs alone. The combination of nuclear porosity, acoustic waveform, and deep-induction resistivity logs confirms that the transition from abundant, electrically conductive clay mineral fraction at shallow depths to abundant nonconductive feldspar, epidote, and other alteration products at greater depths occurs in the interval extending from 1200 to 1800 m in depth in the State 2-14 borehole.

Acknowledgments. We wish to thank R. Wallace and J. Sass for helpful discussions and reviews of this manuscript, and W. Elders for coordination of field operations and access to core descriptions and samples. The use of the firm name in this report is for identification purposes only and does not constitute endorsement by the U.S. Geological Survey.

REFERENCES

Archie, G. E., The electrical resistivity log as an aid in determining some reservoir characteristics, *Trans. Soc. Min. Eng., AIME, 146*, 54-62, 1942.

Bird, D. K., and W. A. Elders, Geology and geochemistry of the Dunes hydrothermal system, Imperial Valley, California, paper presented at 2nd U.N. Symposium on the Development and Use of Geothermal Resources, San Francisco, Calif., 1976.

Browne, P. R. L., Hydrothermal alteration in active geothermal fields, *Annu. Rev. Earth Planet. Sci., 6*, 229–250, 1978.

Chen, H. C., and J. H. Fang, Sensitivity analysis of the parameters in Archie's water saturation equation, *Log Anal., 22*, 39-44, 1981.

Cheng, C. H., and M. N. Toksoz, Elastic wave propagation in a fluid-filled borehole and synthetic acoustic logs, *Geophysics, 46*, 1042–1053, 1981.

Daley, T. M., T. V. McEvilly, and E. L. Majer, Analysis of *P* and *S* wave vertical seismic profile data from Salton Sea Scientific Drilling Project, *J. Geophys. Res.*, this issue.

Doveton, J. H., *Log Analysis of Subsurface Geology: Concepts and Computer Methods*, 273 pp., John Wiley, New York, 1986.

Elders, W. A., and S. Biehler, Gulf of California rift system and implications of its tectonics for western North America, *Geology*, *3*, 85–87, 1975.

Ershaghi, I., and D. Abdassah, Well log interpretation of certain geothermal fields in the Imperial Valley, California, *Los Alamos Natl. Lab., Rep. LA-10067-MS*, 23 pp., 1984.

Ershaghi, I., L. B. Phillips, E. L. Dougherty, L. L. Handy, and M. Mathews, Applications of oilfield well log interpretation to the Cerro Prieto geothermal field, *Trans. SPWLA Annu. Logging Symp.*, *20*, PP1-PP11, 1979.

Hearst, J. R., and P. H. Nelson, *Well Logging for Physical Properties*, 571 pp., McGraw-Hill, New York, 1985.

Helgeson, H. C., Geologic and thermodynamic characteristics of the Salton Sea geothermal system, *Am. J. Sci.*, *266*, 129–166, 1968.

Keys, W. S., Borehole geophysics in igneous and metamorphic rocks, *Trans. SPWLA Annu. Logging Symp.*, *20*, OO1–OO26, 1979.

Keys, W. S., Borehole geophysics in geothermal exploration, in *Developments in Geophysical Exploration Methods*, vol. 3, edited by A. A. Fitch, pp. 239–268, Applied Science, London, 1982.

Keys, W. S., and J. K. Sullivan, Role of borehole geophysics in defining the physical characteristics of the Raft River geothermal field, Idaho, *Geophysics*, *44*, 1116–1141, 1979.

Lachenbruch, A. H., J. H. Sass, and S. P. Galanis, Jr., Heat flow in southernmost California and the origin of the Salton Trough, *J. Geophys. Res.*, *90*, 6709–6736, 1985.

Mehegan, J. M., C. T., Herzig, and R. M. Sullivan, SSSDP, California state 2-14 well, visual core descriptions, vol. 1, *Publ. UCR/IGPP-86/1*, 221 pp., Univ. of Calif., Riverside, 1986.

Miyairi, M., and T. Itoh, Super high temperature geothermal logging system, *Trans. SPWLA Annu. Logging Symp.*, *26*, Y1–Y16, 1985.

Muffler, L. J. P., and B. R. Doe, Composition and mean age of detritus of the Colorado River delta in the Salton Trough, southeastern California, *J. Sediment Petrol.*, *38*, 384–399, 1965.

Muffler, L. J. P., and D. E. White, Active metamorphism of upper Cenozoic sediments in the Salton Sea geothermal field and the Salton Trough, southeastern California, *Geol. Soc. Am. Bull.*, *80*, 157–181, 1969.

Muramoto, F. S., and W. A. Elders, Correlation of wireline log characteristics with hydrothermal alteration and other reservoir properties of the Salton Sea and Westmorland geothermal fields, Imperial Valley, California, *Los Alamos Natl. Lab. Rep. LA-10128-MS*, 100 pp., 1984.

Newmark, R. L., P. W. Kassemeyer, L. W. Younker, and P. C. Lysne, Research drilling at the Salton Sea geothermal field, California: The shallow thermal gradient project, *Eos Trans. AGU*, *67*, 98–107, 1986.

Paillet, F. L., and J. E. White, Acoustic modes of propagation in the borehole and their relationship to rock properties, *Geophysics*, *47*, 1215–1228, 1982.

Paillet, F. L., et al., Preliminary report on the geophysical well-logging activity on the Salton Sea Scientific Drilling Project, Imperial Valley, California, *U.S. Geol. Sur. Open File Rep.*, *86-544*, 99 pp., 1986.

Sass, J. H., J. D. Hendricks, S. S. Priest, and L. C. Robison, Temperatures and heat flow in the state 2-14 well, Salton Sea Scientific Drilling Program (abstract), *Eos Trans. AGU*, *68*, 16, 1987.

Sass, J. H., S. S. Priest, L. E. Duda, C. C. Carson, J. D. Hendricks, and L. C. Robison, Thermal regime of the state 2-14 well, Salton Sea Scientific Drilling Project, *J. Geophys. Res.*, this issue.

Society of Professional Well Log Analysts, *Geothermal Log Interpretation Handbook*, SPWLA Reprint Volume, Houston, Tex., 1982.

Tarif, P. A., R. H. Wilkens, C. H. Cheng, and F. L. Paillet, Laboratory studies of the acoustic properties of samples from the Salton Sea Scientific Drilling Project and their relation to microstructure and field measurements, *J. Geophys. Res.*, this issue.

Toksoz, M. N., C. H. Cheng, and Aytekin Timur, Velocities of seismic waves in porous rocks, *Geophysics*, *41*, 21–45, 1976.

Veneruso, A. F., and J. A. Coquat, Technology development for high temperature logging tools, *Trans. SPWLA Annu. Logging Symp.*, *20*, PP54–PP59, 1979.

Younker, L. W., P. W. Kassemeyer, and J. Tewhey, Geological, geophysical, and thermal characteristics of the Salton Sea geothermal field, California, *Vulcanol. Geotherm. Res.*, *12*, 221–227, 1982.

R. H. Morin and F. L. Paillet, U.S. Geological Survey, MS 403, Box 25046, Denver Federal Center, Denver, CO 80225.

(Received August 3, 1987;
revised April 13, 1988;
accepted May 10, 1988.)

JOURNAL OF GEOPHYSICAL RESEARCH, VOL. 93, NO. B11, PAGES 12,995–13,004, NOVEMBER 10, 1988

Thermal Regime of the State 2-14 Well, Salton Sea Scientific Drilling Project

J. H. SASS AND S. S. PRIEST

U.S. Geological Survey, Flagstaff, Arizona

L. E. DUDA AND C. C. CARSON

Sandia National Laboratory, Albuquerque, New Mexico

J. D. HENDRICKS AND L. C. ROBISON[1]

U.S. Geological Survey, Flagstaff, Arizona

Temperature logs were made repeatedly during breaks in drilling and both during and after flow tests in the Salton Sea Scientific Drilling Project well (State 2-14). The purpose of these logs was to assist in identifying zones of fluid loss or grain and to characterize reservoir temperatures. At the conclusion of the active phase of the project, a series of logs was begun in an attempt to establish the equilibrium temperature profile. Initially, we were able to log to depths below 3 km, but beginning in late May of 1986, it was impossible to log below about 1.8 km owing to casing failure. Our best estimates of formation temperature below 1.8 km are 305° ± 5°C at 1890 m and 355° ± 10°C at 3170 m. For the upper 1.8 km the latest temperature log (October 24, 1986), using a digital "slickline" (heat-shielded downhole recording) device, was within a few degrees Celsius of equilibrium, as confirmed by a more recent log (July 31, 1987) to a depth of ~1 km. As in most other wells in the Salton Sea geothermal field, there is an impermeable, thermally conductive "cap" on the hydrothermal system; this cap extends to a depth of more than 900 m at the State 2-14 well. Thermal conductivities of 19 samples of drill cuttings from this interval were measured at room temperature. The conductivity values were corrected for in situ porosity as determined from geophysical logs and for the effects of elevated temperature. Thermal gradients decrease from about 250 mK m^{-1} (same as degrees Celsius per kilometer) in the upper few hundred meters to just below 200 mK m^{-1} near the base of the conductive cap. Using one interpretation, thermal conductivities increase with depth (mainly because of decreasing porosity), resulting in component heat flows that agree reasonably well with the mean of about 450 mW m^{-2}. This value agrees well with heat flow data from shallow wells within the Salton Sea geothermal field. A second interpretation, in which measured temperature coefficients of quartz- and carbonate-rich rocks are used to correct thermal conductivity, results in lower mean conductivities that are roughly constant with depth and, consequently, systematically decreasing heat flux averaging about 350 mW m^{-2} below 300 m. This interpretation is consistent with the inference (from fluid inclusion studies) that the rocks in this part of the field were once several tens of degrees Celsius hotter than they are now. The age of this possible disturbance is estimated at a few thousand years.

INTRODUCTION

A major goal of the Salton Sea Scientific Drilling Project was the acquisition of a complete set of wire line geophysical logs. To this end, a standard set of commercial logs was obtained (limited by the temperature capabilities of the tools) and both complementary and redundant logs were obtained by the Water Resources Division of the U.S. Geological Survey (USGS) using tools that were designed to operate at higher temperatures than conventional, commercial tools [*Paillet*, 1986]. A description and analysis of both sets of logs are the subject of a companion paper [*Paillet and Morin*, this issue]. The characterization of formation and reservoir temperatures at the site and of the thermal regime of the surrounding region was of particular importance. Regional heat flow and its tectonic implications were discussed by *Lachenbruch et al.* [1985], and models for the Salton Sea hydrothermal system have been developed by *Younker et al.* [1982] and by *Kasameyer et al.* [1984, 1985]. The thermal regime of the unconsolidated sediments of the Imperial Valley as a whole (Figure 1) was presented by *Sass et al.* [1984]. Recently, *Newmark et al.* [1986, this issue] have conducted a thorough study of the shallow (~100 m) heat flow from the Salton Sea geothermal field (Figure 1).

Temperature logs were obtained during the active drilling and testing phase to identify fluid loss zones, to predict equilibrium formation temperatures, and (during flow tests) to provide information required for characterization of the thermodynamics of the flow zone. These temperatures were measured with a platinum resistance thermometer (RTD) attached to four conductors of a logging cable, or with modified oil field downhole recording devices ("Kuster" gauges) which employ mechanical transducers (bimetallic strips). The latter devices are less accurate and have a much longer time constant (minutes as opposed to seconds) than the RTD, but with the recorder section in a dewar, are capable of withstanding much higher temperatures (400°C as opposed to 250°–300°C) than the RTD with surface readout. A selection of temperature logs obtained during the drilling phase of the project is shown as Figure 2 of *Paillet and Morin* [this issue].

The dewared mechanical temperature tools were available as backup and as an independent check for temperature measurements postdrilling; however, all of the temperature

[1]Now at Sergent, Hauskins, and Beckwith, Salt Lake City, Utah.

Paper number 7B7141.
0148-0227/88/007B-7141$05.00

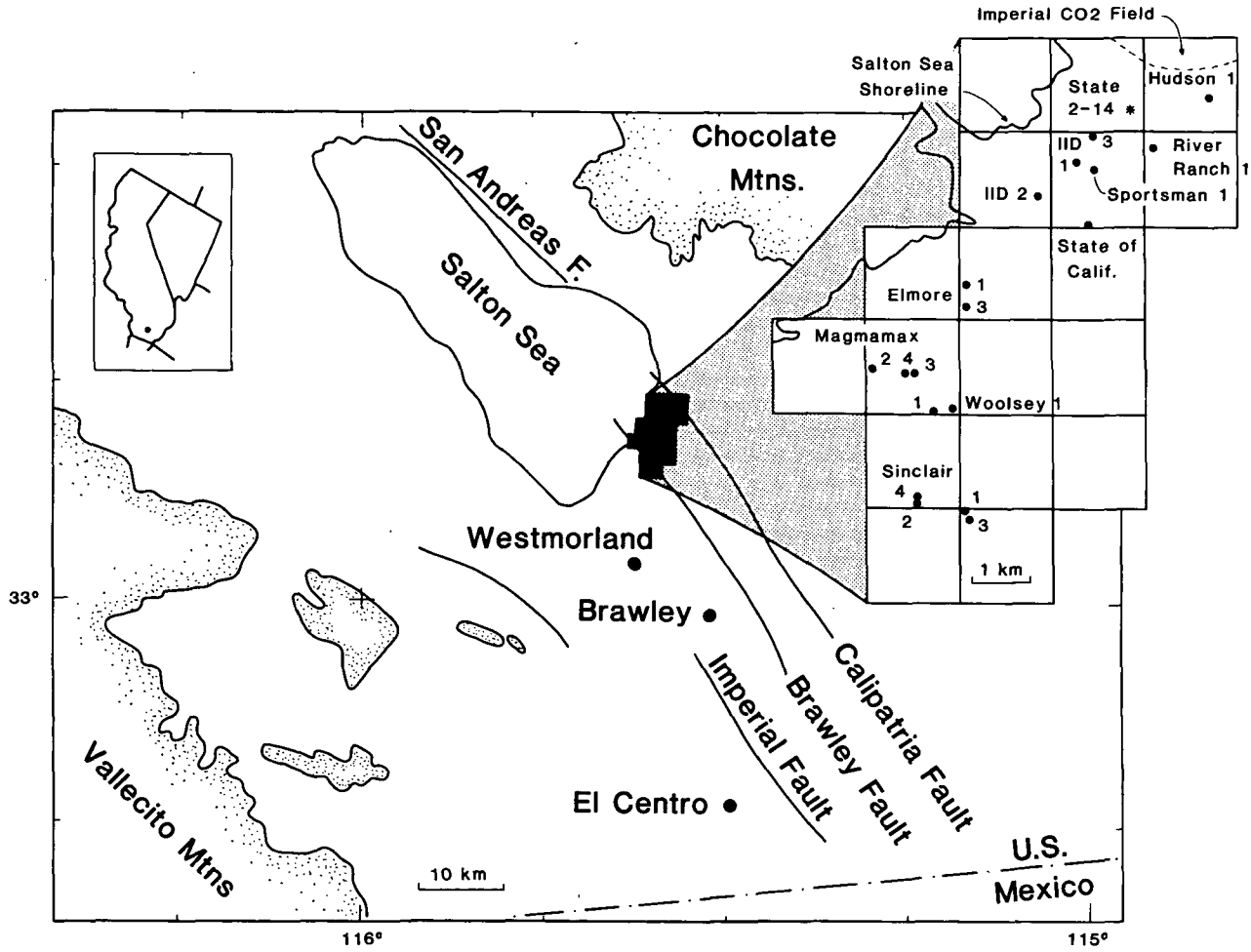

Fig. 1. Map of the Imperial Valley, adjoining ranges, and major faults [after *Younker et al.*, 1982]. Inset shows location of State 2-14 and other wells in the Salton Sea geothermal field.

data presented here were obtained with platinum RTDs deployed either in a conventional mode (surface readout via four electrical conductors) or in a downhole recording digital "memory tool" either of which allows a much higher density of data than do the conventional tools with mechanical transducers. The memory tool is described briefly in the following section. A time series of temperature logs is then presented together with an analysis of equilibrium temperatures, some measurements of thermal conductivity from the upper 1 km of the well, and some estimates of conductive heat flux.

Digital Temperature-Pressure Tool

The downhole memory tool, which measures both the temperature and pressure of the well bore fluid, was developed to provide a smaller and more accurate alternative to the electromechanical tools. This tool is a self-contained instrument operating on a "slickline"; that is, there is no direct communication of the tool with the surface. The temperature and pressure measurements are recorded in internal digital memory. The electronic circuitry is protected from the hot well bore fluid temperatures by a vacuum heat shield or "dewar." The tool was built to Sandia National Laboratories' specifications by Service Systems Engineering of Mansfield, Texas (now Madden Systems, Inc., of Odessa, Texas). Tool specifications are summarized in Table 1 and a sketch of the tool is presented as Figure 2.

The temperature is measured with a platinum resistance temperature detector (RTD) mounted inside a tube that extends into the well bore fluid. The resistance of the RTD is converted to frequency by a voltage-controlled oscillator. Pressure is measured by a quartz crystal transducer mounted inside the dewar and uses a stainless steel capillary tube to transmit the pressure from the well bore fluid. The output of the transducer is a frequency. Both frequency components are then stored in the internal memory. The heat shield is an integral pressure housing and vacuum dewar built by PDA Engineering of Santa Ana, California. The pressure housing was built from corrosion resistant Inconel 718. This heat

TABLE 1. Summary of Specifications for the Downhole Memory Tool

	Value
Diameter	89 mm
Mass	45 kg
Length	1.5 m
Temperature range	0°–600°C
Accuracy	2°C
Sensitivity	0.02°C
Pressure range	0–15,000 psi (0–100 MPa)
Accuracy	3 psi (20 kPa)

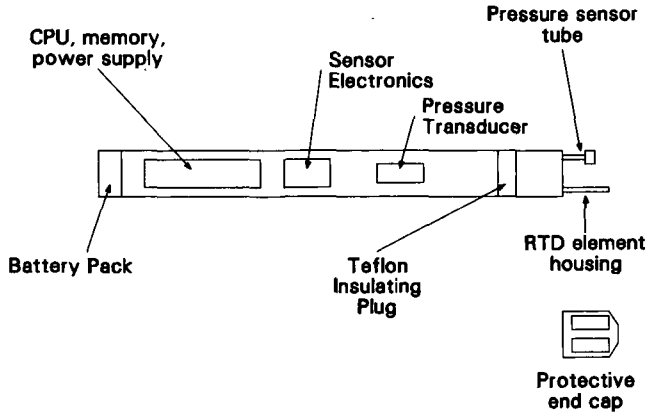

Fig. 2. Diagram of the downhole memory tool showing the arrangement of the sensor head, electronic circuitry, and battery power. The Inconel pressure vessel is not shown.

shield will allow the tool to operate for 10 hours at an ambient temperature of 400°C.

The data acquisition in the tool is controlled by an RCA 1802 microprocessor. Prior to a logging run, the microprocessor is programmed at the surface, using a personal computer, for up to 20 fixed-time interval readings. For example, the first reading may be delayed 20 min for tool and wireline makeup. Then 800 readings at 15-s intervals may be obtained as the tool is lowered in the well bore. The on-board memory consists of 8 kbyte of RAM which allows for the storage of up to 1000 temperature and pressure readings. When the tool is returned to the surface, the data are transferred to a personal computer via an RS-232 interface for further processing.

The design specifications outlined in Table 1 were essentially those used in soliciting bids from potential suppliers. As such, they constituted minimum standards by which to judge contractor performance. From internal consistency of repeated calibrations and repeated log segments, we are confident that the accuracy of the temperature portion of the tool is significantly better than the 2°C design specifications, more of the order of a few tenths of a degree Celsius.

TEMPERATURE DATA

The memory tool was used on four occasions between April 8 and October 24, 1986, to obtain temperature profiles in State 2-14. A fifth attempt on July 31 to August 1, 1987, was unsuccessful owing to failure of the metal-to-metal seal between dewar and instrument housing. These logs are shown in Figure 3, together with an earlier log obtained using the USGS logging unit and a profile labeled "Equil. Temps." A profile obtained with the USGS logging unit on July 31, 1987, is discussed later.

The log of April 1, 1986, was begun immediately upon cessation of the injection of nearly 10^4 m^3 of cooled brine (which had earlier been produced during a flow test) and irrigation water. There are several striking features in this profile (see also log of March 27, 1986, from *Paillet and Morin* [this issue]). There is a pronounced temperature reversal just below

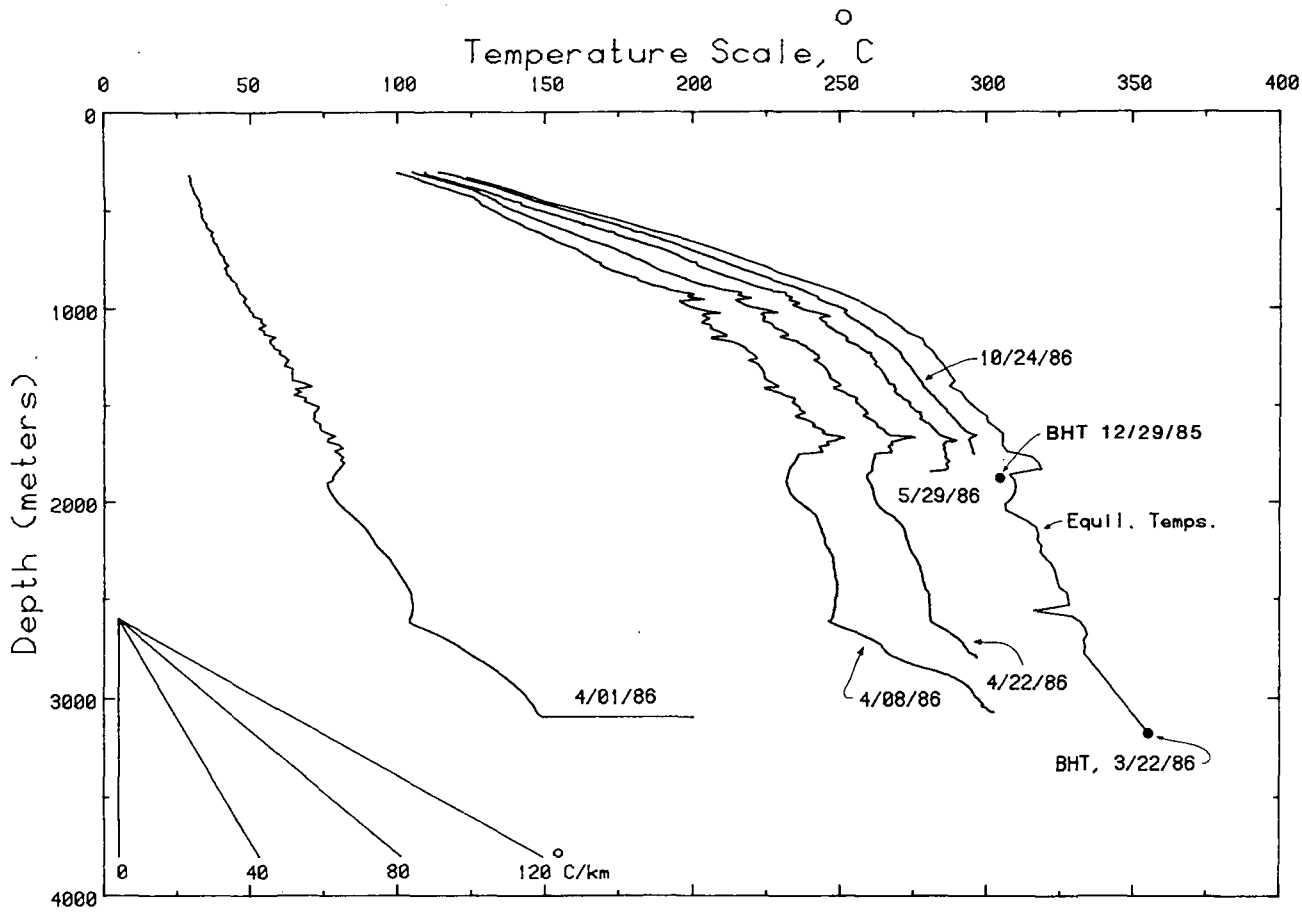

Fig. 3. Temperature profiles obtained at various times in State 2-14. The profile labeled "Equil. Temps." was obtained by extrapolation of the previous four logs (see text and Figure 4). Dots labeled "BHT" are bottom-hole temperatures obtained on the dates shown.

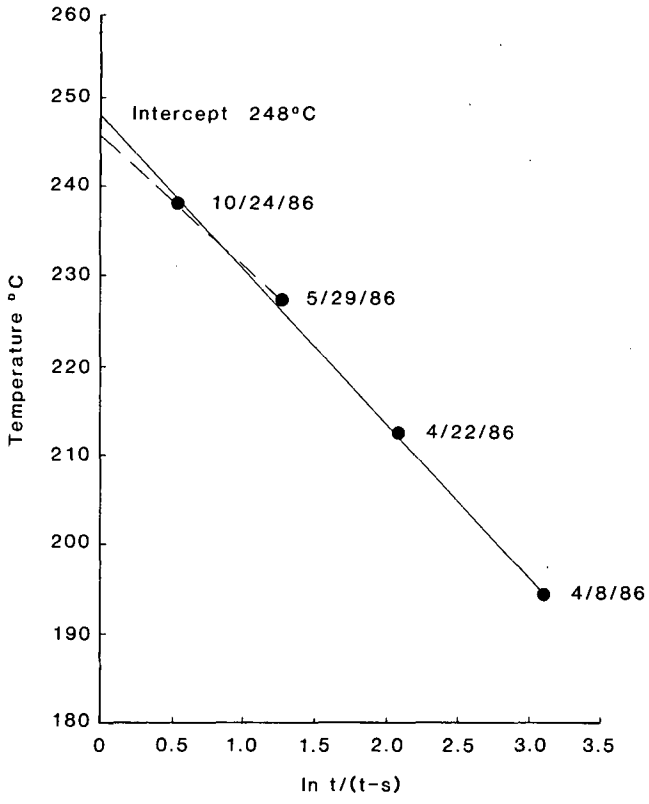

Fig. 4. Extrapolation to infinite time of temperatures measured on the dates shown at a depth of 914 m in State 2-14.

the $9\frac{5}{8}$-inch (244 mm) outside-diameter casing at a depth of ~1830 m. This was the depth of the first production zone tested in December 1985, and it evidently accepted a large amount of injected fluid. There was recurrent loss of fluid while drilling between this depth and ~2800 m. The strong reversal at about 2620 m (Figure 3) indicates a very permeable zone there also. The casing configuration after drilling to total depth included a 7-inch (178 mm) o.d. liner hung (but not grouted) from a depth of 1725 m to a total depth of 3093 m [see *Sass and Elders*, 1986, Figure 3]. At this depth there is a sharp increase in temperature in the April 1 log, indicating that (1) very little, if any, fluid was injected below the liner, and (2) most, if not all, of the fluid injected flowed around the bottom of the liner, up the annulus and entered the formation at various depths, mostly around 1850 and 2620 m. Profiles on subsequent dates retain the memory of the massive injection below 1830 m and show a conductively decaying spike at about 1670 m, most likely the result of injection of a large quantity of cement behind the $9\frac{5}{8}$-inch casing at that depth. This spike and another one at about 1 km depth, are misaligned by about 15 m in the October 24 profile, indicating some slippage of our depth counter at shallower depths on that date. The temperature data support the hypothesis that most of the fluid produced in the March 1986 flow test was coming from behind the liner, not from the expected flow zone between 3093 and 3220 m.

Disturbances to the thermal regime caused by circulation of drilling fluids persist for several drilling periods [*Bullard*, 1947; *Lachenbruch and Brewer*, 1959; *Jaeger*, 1956, 1961]; however, when the drilling history is relatively simple and no loss of drilling fluid occurs, it is a relatively straightforward matter to predict equilibrium temperatures. Also, equilibrium thermal gradients are approached within a few percent much more rapidly than are equilibrium temperatures [*Lachenbruch and Brewer*, 1959; *Jaeger* 1961]. In the case of State 2-14, the drilling-testing history is very complex. During the 160-day active phase of site operations [see *Sass and Elders*, 1986, Figure 2; *Elders and Sass*, this issue, Figure 5] there were two flow tests; we experienced recurring episodes of lost circulation, during which times both mud and cement were introduced at various levels (mostly below 1800 m); and we twice deliberately disposed of about 10^4 m^3 of cold fluid during the periods December 28–29, 1985, and March 26-31, 1986. The task of measuring or predicting equilibrium temperatures was further complicated by failure of the liner which limited access to a depth of ~1.8 km from May 1986 onward.

Notwithstanding the difficulties mentioned above, we were able to estimate equilibrium temperatures in the upper 1.8 km with some confidence, using the four logs that reached that depth. Following *Lachenbruch and Brewer* [1959], we plotted measured temperature versus the quantity $\ln t/(t-s)$, where t is the time, in days, since the drill bit first reached a given depth and s is the duration of the drilling process at that depth. An example from a depth of 914 m is given in Figure 4. In oil field parlance this is a "Horner" plot. Extrapolation to $\ln t/(t-s) = 0$ (infinite time) yields the equilibrium temperature. The example shown in Figure 4 is typical of this data set in that while the four points define an excellent straight line ($R^2 = 0.998$), extrapolation of the two most recent logs (dashed line, Figure 4) results in an estimate some 2° or 3°C lower than the least squares line for all four points. In Figure 5 a profile obtained on July 31, 1987, to 980 m using the USGS Water Resources Division's logging unit is juxtaposed against the October 24, 1986, log and the extrapolated "equilibrium" temperatures. There is reasonable agreement between 300 and 500 m, but the most recent log diverges from the "equilibrium" temperatures below that depth. It is likely that the divergence is due, at least in part, to the tendency of the slope of the temperature-log time line to decrease as the abscissa approaches zero. This tendency can, in turn, be attributed to the departures from theoretical assumptions of the source term for the temperature disturbances. We thus conclude that our extrapolated equilibrium temperatures are most likely overestimated but are probably reasonable upper limits to a depth of about 1800 m (Figure 3) where there is a proboscislike computational artifact. Below that depth, the extrapolations are controlled by only the two early logs and also reflect the large amounts of fluid lost to the formation. Even so, they are in reasonable accord with the two bottom-hole temperatures obtained during the flow tests in December 1985 and March 1986 using a platinum resistance transducer (RTD) and the heat-shielded Kuster tool, respectively (Figure 3).

From the logs of the upper portion of State 2-14 (Figure 5) we may make some additional observations. From the October 24, 1986, logs a measure of the thermal inertia of the "bullnose" (protective metal housing) and other metal immediately adjacent to the temperature transducer can be obtained. The RTD tracks temperature to within ~0.1°C while moving, but when the tool is stopped (to check synchronization with the surface depth-time log), a complex interaction between RTD and sorrounding metal takes place. For all logs the logging speed was 0.15 m s^{-1}, and the duration of each stop was 5 min. When the tool began moving again, there was an inertial lag of a few tenths of a degree Celsius which took

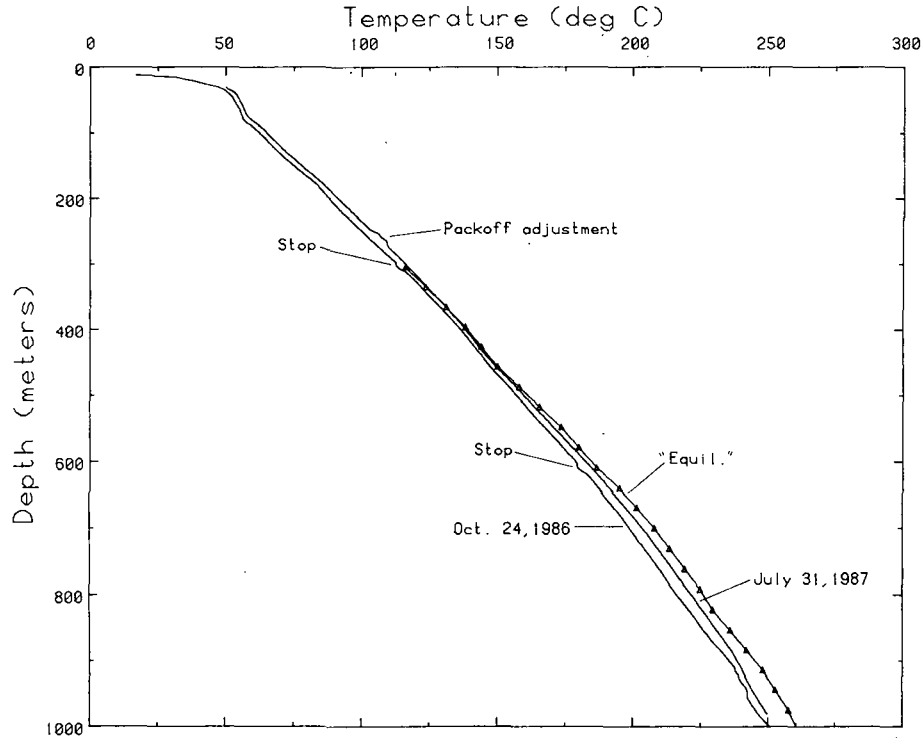

Fig. 5. Temperature profiles from the upper kilometer of State 2-14. Curve labeled "Equil." was calculated from the four logs between April 4 and October 24 (see text).

about a minute (~10 m) to stabilize, hence the slight dip in the temperature profile. A redesign of the bullnose in which its diameter and weight is reduced would alleviate this problem. The profile of July 31, 1987, exhibits some irregularities at about 250 m. The well was under pressure of 300 psi (~2 MPa). During the early part of the log we were adjusting the hydraulic pack-off to allow free movement of the logging line with a minimum of leakage. At about 250 m the cable stopped moving owing to excess pressure on the pack-off. While the slack in the line was being taken up, the tool dropped suddenly and several liters of fluid leaked past the pack-off causing the disturbance observed. Apart from this "glitch" we consider the profile of July 31, 1987, to be the best estimate of formation temperatures in the upper 1 km of the well, and that data set is used in our estimates of conductive heat flux.

Representative temperature profiles from the Salton Sea geothermal field (Figure 1) are shown for comparison with the "equilibrium" temperatures from State 2-14 in Figure 6. Indi-

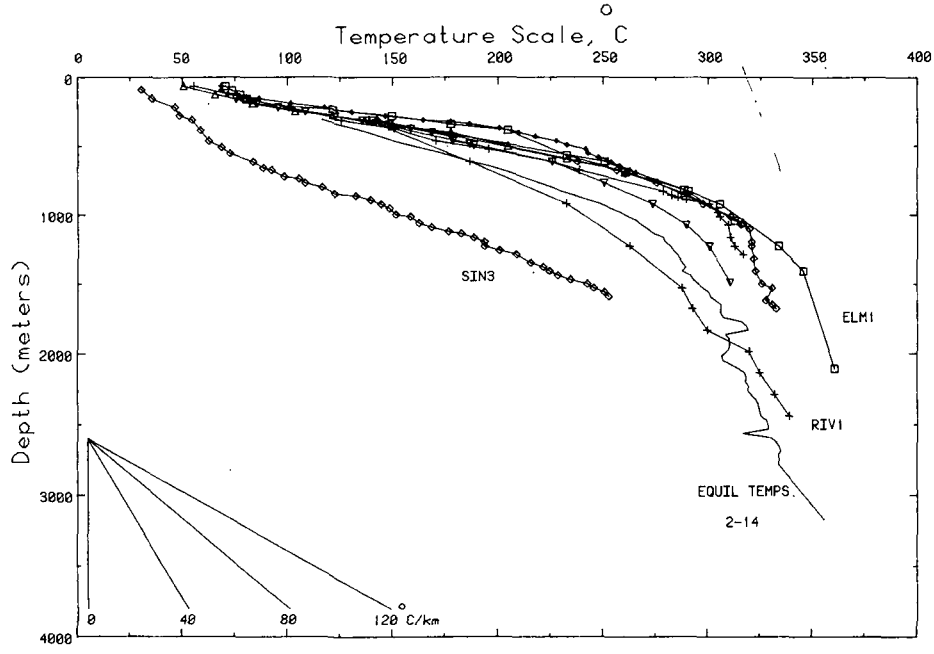

Fig. 6. Representative temperature profiles from the Salton Sea geothermal field (Figure 1) and calculated equilibrium temperatures for State 2-14.

TABLE 2. Thermal Conductivity of Drill Cuttings From State 2-14

Depth, m	Lithology	Thermal Conductivity, W m^{-1} K^{-1}			
		λ_s*	ϕ,†%	λ_{corr}‡ a	λ_{corr}‡ b
306	claystone	2.62	40	1.53	1.45
373	siltstone	3.80	45	1.77	1.56
401	claystone	3.51	28	2.22	1.88
437	sandstone	4.31	35	2.27	1.93
474	claystone	2.29	30	1.60	1.33
510	sandstone	3.90	20	2.75	2.21
529	claystone	3.74	23	2.53	2.04
556	claystone	3.45	21	2.45	1.95
584	sandstone	3.26	20	2.38	1.87
625	claystone	2.99	19	2.25	1.74
643	claystone	3.36	17	2.56	1.98
674	claystone	2.77	17	2.18	2.65
710	siltstone	3.11	15	2.47	1.84
735	sandstone	3.38	15	2.65	1.96
765	claystone	3.40	13	2.75	2.01
796	sandstone	2.97	22	2.13	1.59
828	siltstone	3.07	30	1.93	1.48
895	sandstone	3.24	17	2.46	1.77
917	sandstone	3.16	15	2.48	1.75

*Thermal conductivity of the solid component of drill cuttings at ~25°C.

†Percentage porosity, based on borehole-compensated density log, assuming a grain density of 2.65 g cm^{-3} (see Figure 7).

‡Corrected thermal conductivity: a, corrected for porosity only; b, corrected porosity and temperature. The temperature coefficient used is that for carbonate- or quartz-rich rocks [*Birch and Clark*, 1940].

vidual profiles were presented by *Palmer* [1975] and were analyzed in some detail by *Younker et al.* [1982]. With the exception of Sinclair 3 (SIN3) which is near the southern edge of the field, temperature profiles have a characteristic shape, with a linear or gently curved high-gradient upper portion a few hundred meters to 1 km thick, below which the temperature gradient drops off sharply, indicating nonconductive heat transfer. Elmore 1 (ELM1) is the hottest well in the field for which data are available, and there are some many others hotter than State 2-14 at comparable depths. The profile from State 2-14 most resembles that from River Ranch 1 (RIV1) which is located about a kilometer to the southeast (Figure 1). A comparison of the widely spaced measurements (obtained using conventional mechanical transducers) of Figure 6 with the profiles of Figure 3 emphasizes the advantage of being able to resolve details of the thermal profile using the dewared, downhole-recording electronic tool.

THERMAL CONDUCTIVITY

In common with many other wells in the Salton Sea geothermal field (Figure 6) the temperature profile from State 2-14 appears to reflect mainly conductive heat transfer to a depth of about 900 m (see also Figures 3 and 5); below that depth, there is a sharp drop in temperature-gradient, suggesting that convection dominates the heat transfer process. As a check on the validity of the inference of conductive heat flux and in an attempt to estimate a heat flow value, we sampled drill cuttings at ~30-m intervals between 300 and 900 m (no cutting samples were available above 300 m). Grain thermal conductivities were determined at a temperature of about 25°C using the "chip" method of *Sass et al.* [1971].

The grain conductivities do not vary systematically with depth (Table 2, column 3), despite a ~20% decrease in gradient over the same interval (Figure 7). To a depth of nearly 800 m, the decrease in gradient is matched by a decrease in porosity (Table 2, column 4, and Figure 7). Assuming little or no variation of the solid component of thermal conductivity with temperature (assumption a, Table 2), in situ conductivities increase by about the same percentages as the gradient decreases to about 800 m (Figure 8).

Unfortunately, it was not possible to evaluate the temperature variation of thermal conductivity experimentally. Over the range 0°–250°C, the most authoritative source of data remains *Birch and Clark* [1940]. Their careful and systematic experiments established that the thermal conductivity of rock-forming materials can increase (glasses) by ~10% per 100°C, have practically no variation (feldspars and mafic minerals) or decrease with temperature (quartz, carbonates) over this temperature range. Clay minerals and their metamorphic derivatives are the most difficult to evaluate because of the myriad chemical reactions and physical changes of state that occur over the temperature range 0°–250°C. Such data as do exist indicate that the decrease with temperature, if any, is modest relative to quartz and carbonates [*Birch and Clark*, 1940; *Clark*, 1966]. In Table 2 we show the porosity-corrected thermal conductivity with no temperature adjustment, assumption a, and with a correction, assumption b, equivalent to that established by *Birch and Clark* [1940] for quartz- and carbonate-rich rocks. The effect of making the extreme correction of assumption b is to lower the overall conductivity and to make it constant over the interval 300–900 m.

HEAT FLOW

Conductive heat flow was calculated over the interval 91–152 m (Table 3) by combining the least squares temperature gradient from the July 31, 1987, log with the average of 93 "in situ" conductivity determinations made at various locations in the Imperial Valley over the same depth range [*Mase et al.*, 1981; *Sass et al.*, 1984]. Between 305 and 884 m, component heat flows were calculated using the least squares gradients and thermal conductivity values from Table 2 calculated according to two different assumptions: assumption a, that thermal conductivity does not vary with temperature; and assumption b, that the temperature coefficient of thermal conductivity obtained by *Birch and Clark* [1940] for carbonate- and quartz-rich rocks apply. There is considerable scatter, but the component heat flows calculated according to assumption a generally agree to within their combined standard errors and with the independent determination between 91 and 152 m.

For either assumption there is a suggestion of a systematic decrease in heat flow below 457 m, but particularly for assumption a the scatter is such that we can just as well assume constant heat flow with depth. For assumption b on the other hand, there is a definite systematic difference between the shallow heat flow of 462 mW m^{-2} and the mean of 351 ± 24 for the lowermost ~600 m.

The implication of heat flows calculated by assumption a is that the system is in equilibrium on a time scale of 10 kyr (the thermal time constant of a ~1-km-thick layer; see Figure 9 of *Lachenbruch and Sass* [1977]). On the other hand, if the thermal conductivity structure of assumption b is appropriate, we must conclude that the hydrothermal system is cooling on this time scale. Alternatively, all or part of the observed curvature could reflect a thermal boundary layer separating the vigor-

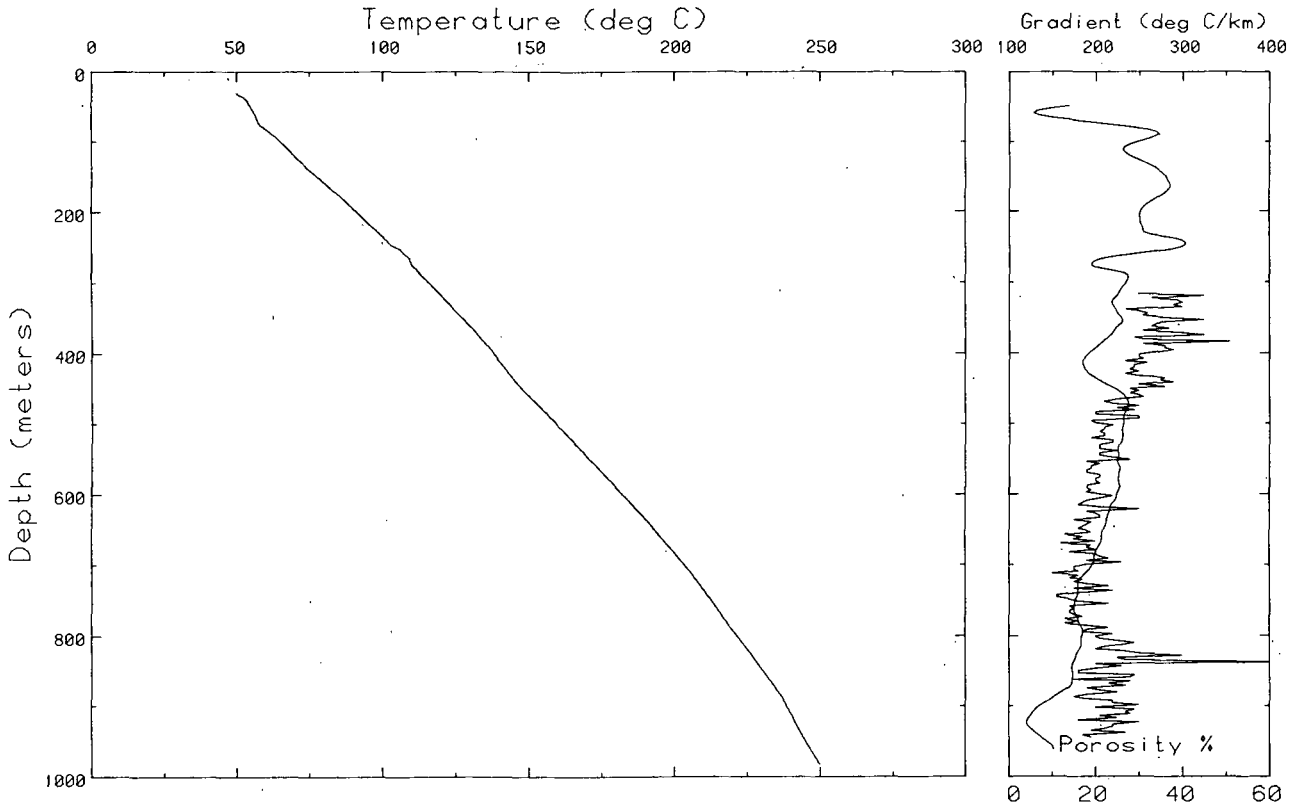

Fig. 7. Temperature, gradient, and porosity profiles for the uppermost kilometer of State 2-14. The porosity profile begins at a depth of 310 m.

ously convecting zone deeper than 1 km from the impermeable cap in the upper few hundred meters. There is, however, no evidence for the distribution of vertical permeability that would be required to sustain such a layer.

Under assumption b, conductivities are approximately constant with depth (Table 2). If we further assume a conductive thermal regime above ~900 m, then the departure from the extrapolated shallow temperatures (dashed line, Figure 8) will

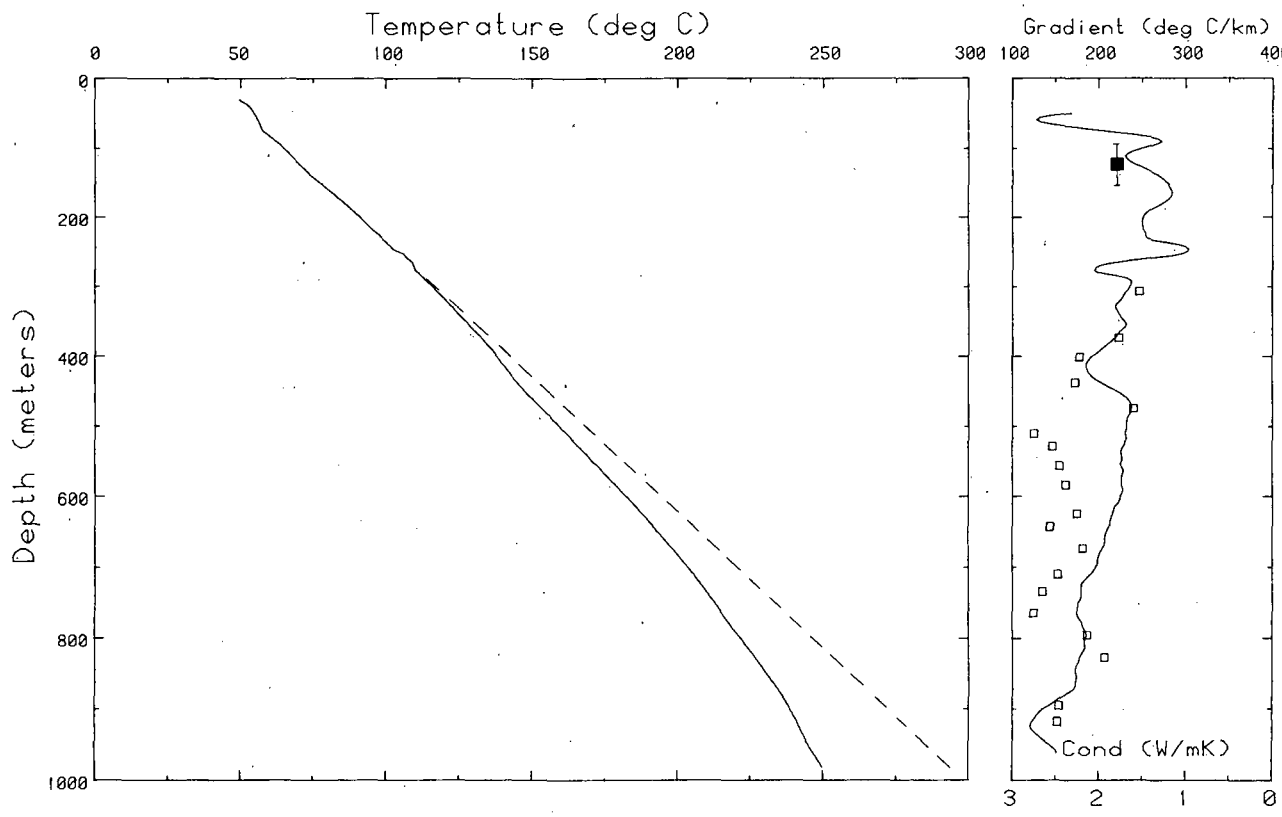

Fig. 8. Temperature, gradient, and thermal conductivity (discrete squares) profiles for the uppermost kilometer of State 2-14. Dashed line extrapolated from near-surface gradients (see discussion of heat flow).

TABLE 3. Heat Flow Over Discrete Depth Intervals in State 2-14

Depth Interval, m	Temperature Gradient, °C/km^{-1}	Number of Conductivities	Harmonic Mean Conductivity† W m^{-1} °C^{-1}		Heat Flow mW m^{-2}	
			a	b	a	b
91–152	246 ± 2	93*	1.88 ± 0.04		462 ± 14	
305–457	209.8 ± 1.1	4	1.90 ± 0.18	1.68 ± 0.12	399 ± 40	352 ± 27
457–610	229.4 ± 0.3	5	2.26 ± 0.23	1.82 ± 0.18	518 ± 53	418 ± 42
610–762	198.3 ± 1.0	5	2.41 ± 0.09	1.82 ± 0.06	478 ± 20	361 ± 14
762–884	178.9 ± 0.4	5	2.31 ± 0.15	1.70 ± 0.09	413 ± 28	304 ± 17
Average					454 ± 22	351 ± 24

*In situ determinations over this depth range in other parts of the valley.
†Assumption a, corrected for porosity only; assumption b, corrected for porosity and temperature (see Table 2).

be a measure of departure from equilibrium. As pointed out by *Lachenbruch et al.* [1976] (see also *Lachenbruch and Sass* [1977]), the effective age of the resulting disturbance depends, among other things, on whether the disturbance is a sudden temperature change or a change in source strength. A step change in temperature will be felt at a distance much more quickly than the gradual waning of the hydrothermal system due to cooling of its heat source, even though the ultimate effect might be the same. In any event, if conductivity assumption b is correct, we have a heat sink whose effect is propagating upward from the base of the conductive cap, whose age is the order of a few thousand years, that has caused a lowering of temperature of about 30°–40°C at the base of the conductive cap. This degree of cooling is consistent with estimates of homogenization temperatures from fluid inclusion studies [*Roedder and Howard*, 1987, this issue; *Andes and McKibben*, 1987; *McKibben et al.*, 1987]. These paleotemperatures are higher on average by several tens of degrees Celsius between 600 and 1700 m than the inferred equilibrium temperatures (Figure 3).

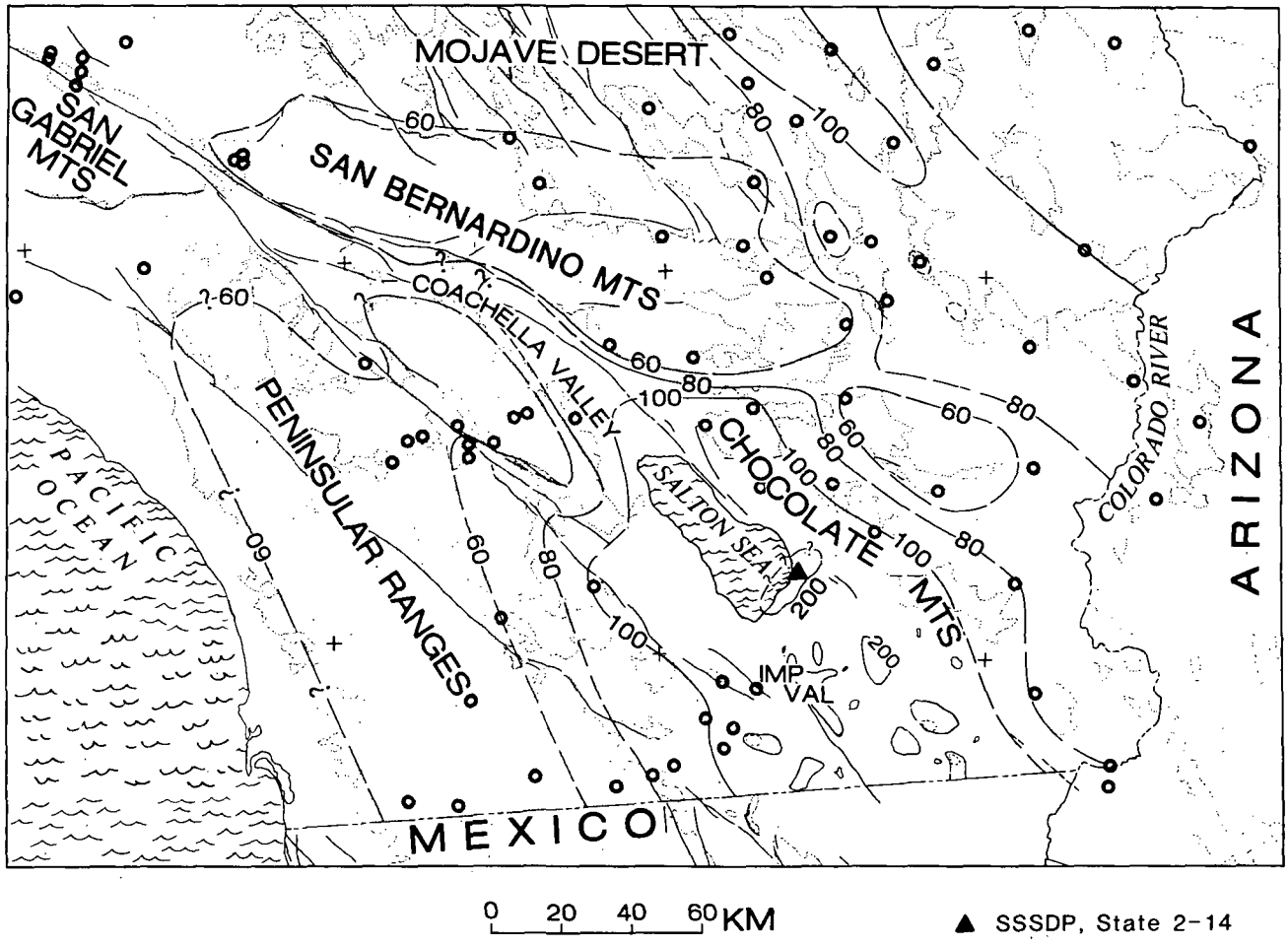

Fig. 9. Regional thermal setting of the Salton Sea system [after *Lachenbruch et al.*, 1985]. Contours are milliwatts per square meter. Control is shown as open circles.

From the internal consistency of component heat flows and the expected correlation between porosity and thermal gradient over a substantial depth interval (Figure 7), taken with fragmentary evidence for a very low temperature coefficient of thermal conductivity for clays and alteration products, we favor the interpretation of assumption a (Tables 2 and 3) and abopt a rounded mean conductive heat flux of 450 mW m^{-2} at this site. This is within the range of shallow heat flow estimates for this area [*Sass et al.*, 1984; *Newmark et al.*, this issue]. We should emphasize, however, that conductivity assumption b, while less plausible, is also possible; in which case, heat flow is presently decreasing with depth and reflects either a thermal transient introduced by recent cooling of this part of the field or a thermal boundary layer. At present, we have no high-temperature thermal conductivity data or data on vertical permeability, which would better allow us to discriminate among the three interpretations.

SUMMARY AND CONCLUSIONS

The regional thermal setting of the Salton Sea geothermal system [*Lachenbruch et al.*, 1985] is illustrated in Figure 9. The entire Imperial Valley and surrounding ranges are enclosed by the 100 mW m^{-2} contour, and there are several large areas of heat flow greater than 200 mW m^{-2} within the region. Of these, the zone at the southeast margin of the Salton Sea (Figure 9) is by far the hottest, with some conductive heat flows greater than 1 W m^{-2}.

Detailed temperature logs to depths of 3 km or greater and to temperatures of 350°C or greater are extremely rare. Mechanical transducers can provide individual, widely spaced points to these depths and temperatures (Figure 6). Temperature-sensitive electrical resistors with surface readout are limited to between 250° and 300°C in the case of Teflon-insulated cables or to depths of a few hundred meters (because of strength limitations and high conductor resistance) in the case of oxide-insulated conductor cables. We have shown that a downhole-recording electronic tool with sensitive components housed in a dewar container, is capable of repeated logs with high data density, rapid response, and good reproducibility. This configuration provides the best combination of characteristics for obtaining reliable, detailed temperature data in the hostile environment of a geothermal field.

The State 2-14 well was sited off the main axis of volcanic centers and its temperature-depth profile lies significantly below those of many wells in the field. Temperatures in State 2-14 were also lower than those predicted before the well was spudded, based on extrapolation of contoured isotherms from other wells. On the most plausible interpretation, heat flow within the upper ~900 m does not vary significantly with depth, suggesting a relatively stable thermal regime over the past 10,000 years or so. There remains the possibility, however, based on ambiguities in the interpretation of thermal conductivities measured at room temperature, that the hydrothermal system deeper than 900 m has cooled from a maximum temperature several tens of degrees Celsius higher than the present profile, a possibility also suggested by fluid-inclusion studies.

Acknowledgments. We thank Jack Kennelly and Walt Wendt for their help in obtaining the data. David Blackwell, Jim Combs, Wilfred Elders, Art Lachenbruch, and Paul Morgan provided constructive criticism of earlier versions of the manuscript.

REFERENCES

Andes, J. P., Jr., and M. A. McKibben, Thermal and chemical history of mineralized fractures in cores from the Salton Sea Scientific Drilling Project, *Eos Trans. AGU, 68*, 439, 1987.

Birch, F., and H. Clark, The thermal conductivity of rocks and its dependence upon temperature and composition, *Am. J. Sci., 238*, 529–558, 613–635, 1940.

Bullard, E. C., The time necessary for a borehole to attain temperature equilibrium, *Mon. Not. R. Astron. Soc., Geophys. Suppl., 5*, 127–130, 1947.

Clark, S. P., Jr., Thermal conductivity, *Mem. Geol. Soc. Am., 97*, 459–482, 1966.

Elders, W. A., and J. H. Sass, The Salton Sea Scientific Drilling Project, *J. Geophys. Res.*, this issue.

Jaeger, J. C., Numerical values for the temperatures in radial heat flow, *J. Math. Phys., 34*, 316–321, 1956.

Jaeger, J. C., The effect of the drilling fluid on temperatures measured in bore holes, *J. Geophys. Res., 66*, 563–569, 1961.

Kasameyer, P. W., L. W. Younker, and J. M. Hanson, Development and application of a hydrothermal model for the Salton Sea Geothermal Field, California, *Geol. Soc. Am. Bull., 95*, 1242–1252, 1984.

Kasameyer, P. W., L. W. Younker, and J. M. Hanson, Inversion approach for thermal data from a convecting hydrothermal system, *J. Geodyn., 4*, 165–181, 1985.

Lachenbruch, A. H., and M. C. Brewer, Dissipation of the temperature effect of drilling a well in Arctic Alaska, *U.S. Geol. Surv. Bull.*, 1083C, 73–109, 1959.

Lachenbruch, A. H., and J. H. Sass, Heat flow in the United States and the thermal regime of the crust, in *The Earth's Crust, Geophys. Monogr. Ser.*, vol. 20, edited by J. G. Heacock, pp. 626–675, AGU, Washington, D. C., 1977.

Lachenbruch, A. H., J. H. Sass, R. J. Munroe, and T. H. Moses, Jr., Geothermal setting and simple heat conduction models for the Long Valley caldera, *J. Geophys. Res., 81*, 769–784, 1976.

Lachenbruch, A. H., J. H. Sass, and S. P. Galanis, Jr., Heat flow in southernmost California and the origin of the Salton Trough, *J. Geophys. Res., 90*, 6709–6736, 1985.

Mase, C. W., J. H. Sass, C. A. Brook, and R. J. Munroe, Shallow hydrothermal regime of the East Brawley and Glamis KGRA's, Salton Trough, California, *U.S. Geol. Surv. Open File Rep., 81-834*, 1981.

McKibben, M. A., A. E. Williams, W. A. Elders, and C. S. Eldridge, Saline brines and metalogenesis in a modern sediment filled rift: The Salton Sea Geothermal Systems, California, USA, *Appl. Geochem., 2*, 563–578, 1987.

Newmark, R. L., P. W. Kasameyer, L. W. Younker, and P. C. Lysne, Research drilling at the Salton Sea Geothermal Field, California: The shallow thermal gradient project, *Eos Trans. AGU, 67*, 698–707, 1986.

Newmark, R. L., P. W. Kasameyer, and L. W. Younker, Shallow drilling in the Salton Sea Region: The thermal anomaly, *J. Geophys. Res.*, this issue.

Paillet, F. L. (Ed.), Preliminary report on geophysical well-logging activity on the Salton Sea Scientific Drilling Project, Imperial Valley, California, *U.S. Geol. Surv. Open File Rep., 86-544*, 1986.

Paillet, F. L., and R. H. Morin, Analysis of geophysical well logs obtained in the state 2-14 borehole, Salton Sea geothermal area, California, *J. Geophys. Res.*, this issue.

Palmer, T. D., Characteristics of geothermal wells located in the Salton Sea Geothermal Field, Imperial County, California, *Rep. UCRL-51976*, Lawrence Livermore Natl. Lab., Livermore, Calif., 1975.

Roedder, E., and K. W. Howard, Fluid inclusions in SSSDP core: Preliminary results, *Eos Trans. AGU, 68*, 439, 1987.

Roedder, E., and K. W. Howard, Fluid inclusions in Salton Sea Scientific Drilling Project core: Preliminary results, *J. Geophys. Res.*, this issue.

Sass, J. H., and W. A. Elders, Salton Sea Scientific Drilling Project: Scientific Program, *Geotherm. Resour. Counc. Bull., 15*, 21–26, 1986.

Sass, J. H., A. H. Lachenbruch, R. J. Munroe, G. W. Greene, and T. H. Moses, Jr., Heat flow in the western United States, *J. Geophys. Res., 76*, 6376–6413, 1971.

Sass, J. H., S. P. Galanis, Jr., A. H. Lachenbruch, B. V. Marshall, and R. J. Munroe, Temperature, thermal conductivity, heat flow, and radiogenic heat production from unconsolidated sediments of the

Imperial Valley, California, *U.S. Geol. Surv. Open File Rep., 84-490*, 1984.

Younker, L. W., P. W. Kasameyer, and J. D. Tewhey, Geological, geophysical and thermal characteristics of the Salton Geothermal Field, California, *J. Volcanol. Geotherm. Res., 12*, 221–258, 1982.

C. C. Carson and L. E. Duda, Sandia National Laboratories, Albuquerque, NM 87185.

J. D. Hendricks, S. S. Priest, and J. H. Sass, U.S. Geological Survey, 2255 North Gemini Drive, Flagstaff, AZ 86001.

L. C. Robison, Sergent, Hauskins, and Beckwith, 4030 5500W, Suite 900, Salt Lake City, UT 84123.

(Received October 1, 1987;
revised April 22, 1987
accepted April 25, 1988.)

JOURNAL OF GEOPHYSICAL RESEARCH, VOL. 93, NO. B11, PAGES 13,005–13,023, NOVEMBER 10, 1988

Shallow Drilling in the Salton Sea Region: The Thermal Anomaly

ROBIN L. NEWMARK, PAUL W. KASAMEYER, AND LELAND W. YOUNKER

Earth Sciences Department, Lawrence Livermore National Laboratory
University of California, Livermore

During two shallow thermal drilling programs, thermal measurements were obtained in 56 shallow (76.2 m) and one intermediate (457.3 m) depth holes located both onshore and offshore along the southern margin of the Salton Sea in the Imperial Valley, California. These data complete the surficial coverage of the thermal anomaly, revealing the shape and lateral extent of the hydrothermal system. The thermal data show the region of high thermal gradients to extend only a short distance offshore to the north of the Quaternary volcanic domes which are exposed along the southern shore of the Salton Sea. The central thermal anomaly has an arcuate shape, about 4 km wide and 12 km long. Across the center of the anomaly, the transition zone between locations exhibiting high thermal gradients and those exhibiting regional thermal gradients is quite narrow. Thermal gradients rise from near regional (0.09°C/m) to extreme (0.83°C/m) in only 2.4 km. The heat flow in the central part of the anomaly is greater than 600 mW/m^2 and in the two local anomalies exceeds 1200 mW/m^2. The shape of the thermal anomaly is asymmetric with respect to the line of volcanoes previously thought to represent the center of the field, with its center line offset south of the volcanic buttes. There is no broad thermal anomaly associated with the magnetic high that extends offshore to the northeast from the volcanic domes. The Salton Sea thermal anomaly can be described as three nested thermal features superimposed on the regional Salton Trough heat flux: a broad region of elevated conductive heat flow with constant temperature gradients of about 0.1°C/m, a central anomaly of high (0.4°C/m) near-surface gradients observed through a conductive thermal cap underlain by a nearly isothermal zone of hydrothermal circulation, and two local anomalies with shallow temperature gradients as high as 0.8°C/m superimposed on the central geothermal system. These observations of the thermal anomaly provide important constraints for models of the circulation of the hydrothermal system. Thermal budgets based on a simple model for this hydrothermal system indicate that the heat influx rate for local "hot spots" in the region may be large enough to account for the rate of heat flux from the entire Salton Trough.

INTRODUCTION

The Salton Trough is a sediment-filled rift zone resulting from the oblique motion of the North American and Pacific tectonic plates over the last 4–5 m.y. It represents the transition between oceanic spreading in the Gulf of California to the south and the San Andreas continental transform fault system to the north [*Elders et al.*, 1972] (Figure 1). The thermal and structural processes that formed the Salton Trough were initiated when the East Pacific Rise intersected the North American plate margin, about 30 m.y. ago [*Blake et al.*, 1978]. Since that time, the northward migration of the Mendocino triple junction and the southward migration of the Rivera triple junction marked the termination of subduction and the initiation of transform shear over a broad region [*Atwater*, 1970]. This shear eventually produced the system of offset strike slip faults observed in the trough. At present, the relative plate motion takes place primarily along transform faults such as the Imperial and San Andreas faults, with local zones of extension occurring whenever the faults are offset in a right-lateral sense, allowing magmatic intrusions to "leak" into the crust. These intrusions provide heat sources to drive hydrothermal activity. Several small Quaternary volcanic domes (Figure 2) on the southeastern shore of the Salton Sea are direct evidence of the location of one of these "leaks".

The Salton Trough is a region of high heat flow. Heat flow values in the U.S. portion of the trough are above 100 mW/m^2 [*Lachenbruch et al.*, 1985], more than twice the worldwide average. In addition, a number of small areas have especially high heat flow, >200 mW/m^2. These areas of hydrothermal circulation represent some of the largest and most accessible geothermal areas in North America, one of which is the Salton Sea geothermal field (SSGF).

The Salton Sea geothermal field has been extensively studied through regional geophysical surveys as well as shallow and deep drilling in the region southeast of the volcanic domes [e.g., *Helgeson*, 1968; *Younker et al.*, 1982; *Elders and Cohen*, 1983]. A wedge-shaped zone of seismicity (the Brawley seismic zone) coincides closely with the northern segment of the Imperial fault and extends northward through Obsidian Butte at the southeastern end of the Salton Sea toward the southern tip of the Banning-Mission Creek branch of the San Andreas fault, in a diffuse pattern nearly coincident with the inferred location of the Brawley fault [*Hill et al.*, 1975; *Fuis et al.*, 1982, 1984]. This is generally considered to be a spreading center in the form of a pull-apart basin. A local gravity maximum is centered over part of the geothermal field [*Biehler*, 1971] (Figure 3). This anomaly has been attributed to either an increase in density of the sediments resulting from hydrothermal alteration, the intrusion of dikes and sills into the sedimentary section, or a combination of these factors [*Elders et al.*, 1972]. A pronounced magnetic anomaly appears in *Kelley and Soske*'s [1936] and *Griscom and Muffler*'s [1971] magnetic surveys. The magnetic anomaly is centered over the volcanic domes and extends offshore into the Salton Sea along the zone in which seismicity has been detected, at a slight angle to the extension of the gravity anomaly. Two elliptical northeast trending anomalies are superimposed on the main trend, one over the volcanic domes and the other about 8 km offshore. The main magnetic anomaly has been interpreted to be due to the presence of intrusive rocks at depths greater than 2 km and the two smaller, elliptical anomalies (with intensity >1850 gammas) to be a result of dikes and sills at

Paper number 88JB03258.
0148-0227/88/88JB-03258$05.00

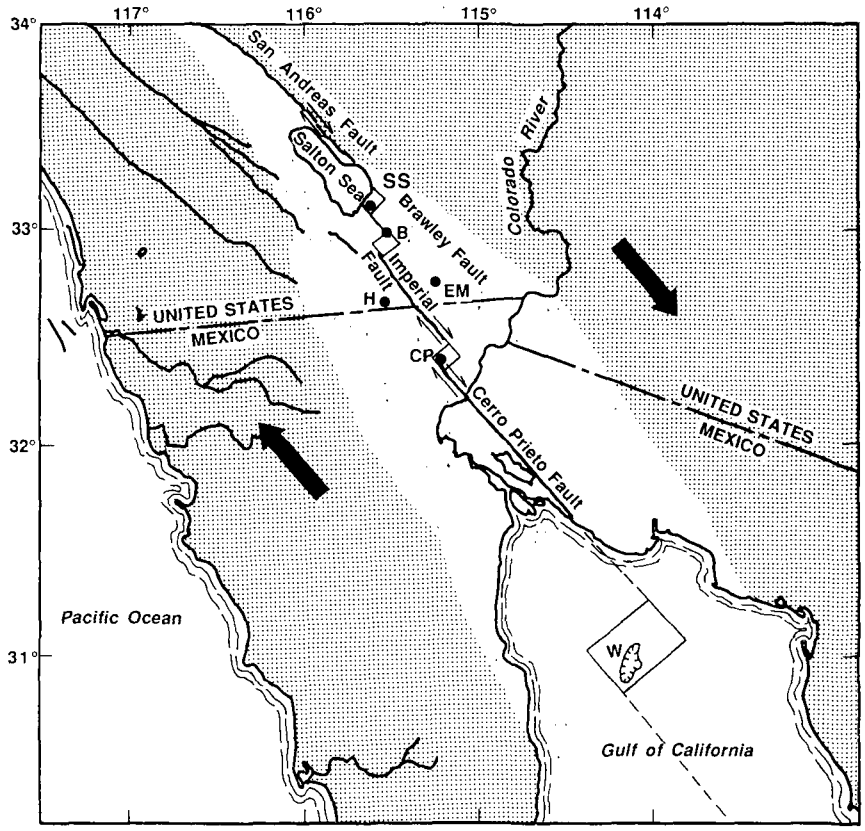

Fig. 1. Schematic structural relations in the Salton Trough adapted from *Lachenbruch et al.* [1985]. Stippled area represents extent of crystalline basement from *Goddard* [1965]. Dots represent major geothermal areas. Abbreviations are SS, Salton Sea; B, Brawley; EM, East Mesa; H, Heber; CP, Cerro Prieto; W, Wagner Basin. Squares indicate inferred zones of pull-apart spreading. Heavy arrows indicate relative plate motion.

depths of about 1 km [*Griscom and Muffler*, 1971]. A shallow heat flow survey utilizing a 2-m lance conducted in 1977 indicated extremely high thermal gradients in the vicinity of the offshore elliptical magnetic high (P. A. Wilde, personal communication, 1977).

Two features of the temperature field in the southeastern part of the SSGF put strong constraints on models of the hydrothermal system [*Younker et al.*, 1982] (Figure 2). First, uniform steady state heat flow is observed in a 500-m-thick thermal cap over a circular area about 30–40 km^2. Second, at the margin of the field a narrow transition region, with a low near-surface gradient and an increasing gradient at greater depths, separates the high-temperature resource from areas of normal gradient. A simple conceptual model of flow in the sampled portions of the field has been developed using these constraints [*Kasameyer et al.*, 1984]. There were many unknowns about the field when this model was developed. The major uncertainty results because thermal gradients were measured only in part of the anomaly, and its extent beneath the sea was unknown (Figure 2).

Regional geophysics including the seismicity, gravity, and magnetic studies mentioned above suggest that the "pull-apart" zone extends under the Salton Sea. Very shallow temperature probes [*Lee and Cohen*, 1979] suggest that the hydrothermal system similarly extends under the sea. Assuming symmetric flow patterns around the domes, we anticipated that an area of high (4–5 times normal) and uniform heat flow would be found offshore, and it could be detected and delineated by relatively shallow heat flow measurements in the conductive thermal cap. This paper describes the results of two shallow thermal surveys that complete coverage around the edges of the SSGF and into the previously unexplored area beneath the Salton Sea.

In the spring and summer of 1982, Kennecott-Bear Creek Mining Company (K-BCM) conducted a shallow drilling program to investigate the extent of the thermal anomaly along the southern shore of the Salton Sea. The temperature data and cuttings descriptions were released by K-BCM as part of their participation in the U.S. Department of Energy's Salton Sea Scientific Drilling Project (SSSDP). These data indicated that the thermal anomaly could be traced offshore and that the transition zone from areas exhibiting thermal gradients similar to those throughout the trough to those exhibiting high thermal gradients is relatively narrow.

During the fall of 1985 the Lawrence Livermore National Laboratory and Sandia National Laboratories (LLNL-SNL) cooperated in drilling a series of shallow (80 m) holes for thermal studies in the southern Salton Sea [*Newmark et al.*, 1986, 1988]. The intent was to complete the surficial coverage of the thermal anomaly offshore in the region north of the line of exposed Quaternary volcanoes thought to represent the center of the thermal anomaly. These surveys have produced data that significantly change our view of the hydrothermal system at the Salton Sea.

METHODS AND INSTRUMENTATION

Drilling

During the months of May–August 1982, Kennecott-Bear Creek Mining Company (K-BCM) drilled 41 holes both on-

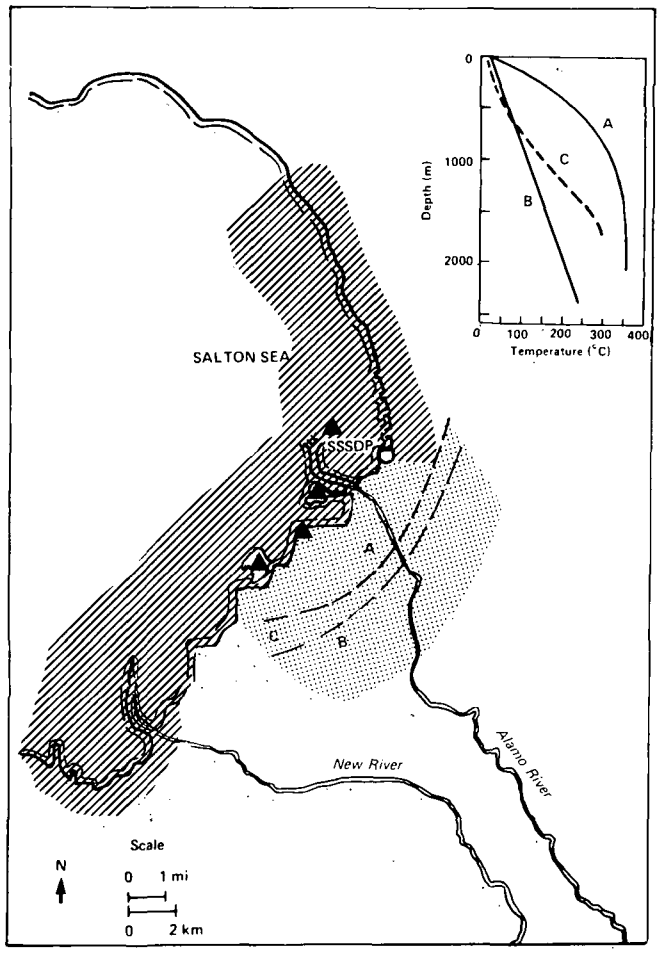

Fig. 2. The Salton Sea geothermal area. The dotted pattern shows the region in which previous studies have provided data used in modeling the system [*Kasameyer et al.*, 1984]. Triangles mark the locations of the Quaternary volcanoes. Temperature profiles from the central part of the geothermal field (A) show that this part of the field (A) is characterized by a broad region of moderately high uniform heat flow in the upper few hundred meters and a nearly isothermal zone at depth. The outer region (B) is characterized by relatively low heat flow and uniform thermal gradients. The narrow transition region between A and B is characterized by thermal profiles showing a relatively low heat flow near the surface, but the gradient increases with depth (C) [after *Newmark et al.*, 1986]. Diagonal lines mark the area investigated by the two shallow drilling programs presented in this paper. The SSSDP is indicated by an open circle.

shore and offshore along the southeastern and southwestern margins of the Salton Sea. Details of the drilling plan and temperature logging systems for both the K-BCM and LLNL-SNL programs are given by *Newmark et al.* [1988]. Hole locations are known to be within 15 m. Forty holes were drilled to 80 m with hole diameters ranging from 12.07 to 12.70 cm. An additional hole (P6-4) was drilled to 457 m onshore in the southwestern part of the Salton Sea geothermal field. Table 1 lists the hole locations, the date drilled, and the date on which the last temperature log was run in each hole for all but two of these holes. One (P1-3) was lost during early data collection, and another (P2-11) was redrilled (P2-11A). All holes were abandoned by the end of 1982.

In November and December 1985, LLNL-SNL drilled 19 additional holes 80 m below lake level offshore in the region north and west of the volcanic domes that lie along the southern shore of the Salton Sea. Some holes were lost before the logging phase of the project was completed, due to a combination of adverse weather, the weight of rapid barnacle growth, and vandalism. One of the holes, RDO6D, was lost before any temperature logs were acquired in it. Table 2 lists the hole locations, the date drilled, and the date on which the last temperature log was run in each hole. The LLNL-SNL holes were sealed and abandoned by the fall of 1986.

Lithology

During both drilling programs, cuttings samples were collected every 3 m when possible. The holes penetrate alluvial sediments composed predominently of clays, silts, and sands. Quartz is the major silt and sand component. Volcanic glass occurs commonly in trace amounts and is occasionally the primary component. Plant and rock fragments, gypsum, biotite, chlorite, muscovite, and calcareous materials, including shell fragments, gastropods, and ostracods, are common minor or trace components.

Temperature Logging

Temperatures were logged periodically in each hole in order to establish the thermal rebound history of the holes and to obtain equilibrium thermal profiles. All temperature profiles were logged going downhole. In the KBCM program, two different systems were used for temperature logging: a Doric temperature probe that utilizes a 100-Ω platinum resistance temperature device (RTD) and an Environ Lab temperature

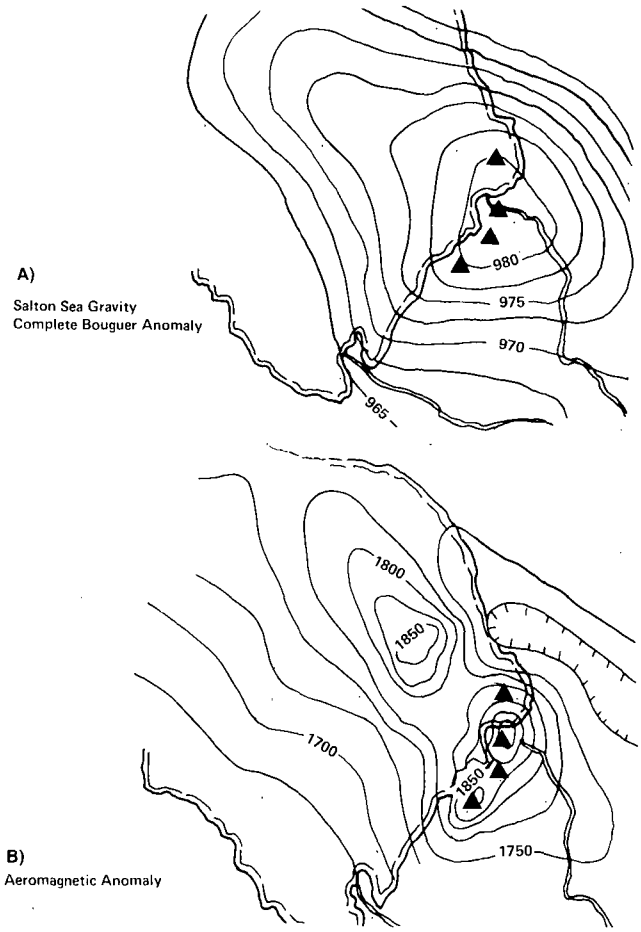

Fig. 3. Geophysical anomalies in the southern Salton Sea region [after *Younker et al.*, 1982]. Triangles mark the locations of the volcanic domes. (*a*) Complete Bouguer gravity anomaly [after *Biehler*, 1971]. Contour interval is 2.5 mGal. (*b*) Aeromagnetic anomaly [after *Griscom and Muffler*, 1971]. Contour interval is 25 gammas.

TABLE 1. Kennecott-Bear Creek Mining Program

Hole	Location		Date Drilled	Last Temperature Log	Thermal Gradient, °C/m	Thermal Gradient 95% Confidence,* °C/m	Heat Flow, mW/m²
	Latitude °N	Longitude °W					
P1-1	33.184	115.675	Aug. 23, 1982	Oct. 20, 1982	0.114	0.0034	177
P1-2	33.169	115.692	Aug. 31, 1982	Sept. 10, 1982	0.139	0.0021	252
P1-4	33.155	115.708	Aug. 28, 1982	Oct. 20, 1982	0.110	0.0021	209
P1-5	33.148	115.692	Aug. 29, 1982	Oct. 20, 1982	0.179	0.0031	322
P1-6	33.155	115.675	Aug. 30, 1982	Oct. 20, 1982	0.500	0.0111	996
P1-7	33.141	115.726	Aug. 26, 1982	Oct. 20, 1982	0.084	0.0037	137
P1-8	33.133	115.708	Aug. 27, 1982	Oct. 20, 1982	0.084	0.0019	151
P1-9	33.133	115.683	Aug. 30, 1982	Oct. 20, 1982	0.117	0.0035	212
P1-11	33.118	115.726	Aug. 25, 1982	Oct. 15, 1982	0.070	0.0030	108
P1-14	33.125	115.667	July 21, 1982	Oct. 11, 1982	0.182	0.0038	204
P1-17	33.104	115.708	Aug. 24, 1982	Oct. 15, 1982	0.071	0.0031	129
P1-19	33.104	115.683	May 18, 1982	July 14, 1982	0.073	0.0018	94
P1-20	33.104	115.672	May 17, 1982	July 2, 1982	0.058	0.0017	92
P2-1	33.321	115.623	July 16, 1982	Oct. 11, 1982	0.086	0.0019	111
P2-2	33.307	115.614	July 10, 1982	Oct. 11, 1982	0.102	0.0016	100
P2-4	33.293	115.606	July 8, 1982	Oct. 11, 1982	0.102	0.0022	100
P2-6	33.278	115.597	July 7, 1982	Oct. 11, 1982	(NL)†	...	...
P2-9	33.264	115.588	July 19, 1982	Oct. 11, 1982	(NL)†	...	...
P2-10	33.250	115.588	July 5, 1982	Oct. 11, 1982	0.162	0.0042	298
P2-11A	33.250	115.579	July 3, 1982	Oct. 11, 1982	0.178	0.0123	338
P2-13	33.235	115.579	May 13, 1982	May 20, 1982	(NL)†	...	...
P2-14	33.227	115.579	May 11, 1982	July 2, 1982	0.189	0.0086	299
P2-15	33.220	115.570	July 2, 1982	Oct. 11, 1982	0.200	0.0068	255
P3-2	33.307	115.649	Aug. 10, 1982	Sept. 24, 1982	0.073	0.0045	105
P3-3	33.307	115.632	Aug. 8, 1982	Oct. 17, 1982	0.087	0.0029	94
P3-7	33.293	115.632	Aug. 13, 1982	Oct. 17, 1982	0.085	0.0041	125
P3-9	33.286	115.623	Aug. 14, 1982	Oct. 17, 1982	0.089	0.0025	109
P3-10	33.278	115.632	Aug. 15, 1982	Sept. 24, 1982	0.103	0.0039	175
P3-12	33.271	115.623	Aug. 16, 1982	Oct. 17, 1982	0.097	0.0043	136
P3-15	33.264	115.606	Aug. 17, 1982	Oct. 17, 1982	0.106	0.0038	219
P3-17	33.250	115.606	Aug. 18, 1982	Oct. 17, 1982	0.222	0.0128	380
P3-20	33.235	115.587	Aug. 22, 1982	Oct. 17, 1982	0.446	0.0155	793
P4-9	33.141	115.667	July 20, 1982	Aug. 20, 1982	0.743	0.0169	1421
P4-13	33.118	115.692	July 30, 1982	Oct. 12, 1982	0.107	0.0025	217
P4-14	33.090	115.731	July 30, 1982	Oct. 12, 1982	0.056	0.0015	97
P4-16	33.090	115.692	July 23, 1982	Oct. 12, 1982	0.067	0.0026	77
P4-17	33.082	115.717	July 28, 1982	Oct. 12, 1982	0.080	0.0023	80
P4-18	33.082	115.701	July 26, 1982	Oct. 12, 1982	0.074	0.0038	101
P6-4	33.082	115.701	Sept. 9–12, 1982	Oct. 16, 1982	0.080	0.0018	83

*Using the relationship described by *Freund* [1962].

†(NL) is a nonlinear temperature profile where changes in thermal gradient are apparently not related to changes in dominant lithology.

probe that also utilizes an RTD sensor. The probes were calibrated using ice baths and boiling water frequently during the logging periods. The response time for these instruments is of the order of 1 min.

In the LLNL-SNL program a temperature logging system developed by Sandia National Laboratories was used (R. Meyer, personal communication, 1987). The temperature sensor is a platinum resistance bulb (Weed model 101-1A, 1000 Ω) having a published response time of 1 s [*Newmark et al.*, 1988]).

Figure 4 shows the complete suite of temperature logs run in holes P1-14 and RDO7S, representing both drilling programs. Thermal rebound histories from the two programs differ in direction because of the differences in drilling fluid temperatures and manner of cement emplacement, whose heat of hydration also affects the thermal rebound. Theory predicts that the temperature disturbance in these holes due to drilling alone (neglecting such factors as zones of lost circulation and heat of hydration of the cement) should decrease almost completely within a few days [e.g., *Jaeger*, 1965]. However, temperatures recorded in the shallow programs took longer to equilibrate, reaching near-equilibrium within the first few weeks after drilling.

Hole P1-14 was drilled onshore during the K-BCM survey. The early temperature profiles are hot because the water used as drilling fluid was heated by the Sun while being delivered to the drill site and the cement emplaced through the drill pipe provided a source of heat over the entire hole. The greater portion of the temperature disturbance subsided within the first few weeks after drilling. Locally high temperatures indicate zones of invasion of drilling fluid into zones of relatively high permeability, for example, near 10 and 20 m. Such zones

TABLE 2. Shallow Salton Thermal Gradient Project (LLNL-SNL)

Hole	Location		Date Drilled	Last Temperature Log	Thermal Gradient, °C/m	Thermal Gradient 95% Confidence,* °C/m	Heat Flow, mW/m²
	Latitude °N	Longitude °W					
RDO6D†	33.249	115.658	Nov. 24, 1985	...	...	...	...
RDO6E	33.264	115.640	Dec. 10, 1985	Jan. 8, 1986	0.154	0.0006	284
RDO6K	33.169	115.649	Dec. 1, 1985	April 4, 1986	0.313	0.0010	503
RDO6N	33.242	115.606	Dec. 8, 1985	April 5, 1986	0.507	0.0024	866
RKO6T	33.235	115.632	Nov. 23, 1985	April 5, 1986	0.269	0.0012	516
RKO6U	33.227	115.614	Dec. 9, 1985	April 3, 1986	0.712	0.0133	1212
RKO6Y	33.220	115.623	Nov. 19, 1985	Jan. 10, 1986	0.214	0.0072	383
RKO6Z	33.206	115.623	Nov. 25, 1985	April 5, 1986	0.915	0.0007	353
RDO7A	33.220	115.606	Nov. 17, 1985	April 3, 1986	(NL)‡	...	...
RDO7B	33.213	115.597	Nov. 16, 1985	April 3, 1986	0.797	0.0015	1317
RDO7E	33.198	115.649	Nov. 30, 1985	Feb. 5, 1986	0.088	0.0007	161
RDO7F	33.184	115.640	Nov. 27, 1985	Feb. 5, 1986	0.110	0.0007	204
RDO7I	33.191	115.623	Nov. 26, 1985	April 4, 1986	0.269	0.0008	498
RDO7M	33.162	115.683	Dec. 6, 1985	Feb. 5, 1986	0.213	0.0007	383
RDO7P	33.169	115.667	Dec. 7, 1985	Feb. 5, 1986	0.090	0.0006	175
RDO7S	33.148	115.667	Dec. 5, 1985	Feb. 5, 1986	0.833	0.0021	1488
RDO7U	33.133	115.667	Dec. 4, 1985	April 4, 1986	0.311	0.0011	644
RDO7Y	33.162	115.658	Dec. 2, 1985	April 4, 1986	0.139	0.0009	265
RDO7Z	33.155	115.662	Dec. 3, 1985	April 4, 1986	0.354	0.0009	556

*Using the relationship described in *Freund* [1962].
†Hole RDO6D was lost before any temperature logs were obtained.
‡(NL) is a nonlinear temperature profile where changes in thermal gradient are apparently not related to changes in dominant lithology.

may have required a larger volume of cement, resulting in additional heat production.

Hole RDO7S was drilled in 1985 as part of the LLNL-SNL survey. This program was drilled in the winter, and the drilling fluid taken from the Salton Sea was much cooler than the downhole temperatures. As the cement was emplaced no deeper than 45.7 m from a stinger pipe alongside the casing, the lowermost 30 m of these holes were unaffected by the heat of hydration of the cement. In fact, the lack of difference in temperature recovery above and below the cement level indicates that the additional heat of hydration due to the cement was not significant at this hole. The thermal profiles from the LLNL-SNL program rebound more rapidly to thermal equilibrium than the holes drilled during the K-BCM survey. The final temperature logs for each hole are shown in Figures 5–8. In all cases, the zero depth for the temperature profiles lies within about 1.0 m above lake level for those holes drilled offshore, or from the well top (within 1.0 m of ground level) for those drilled onshore. The zero depth for all profiles is between 70 and 72 m below sea level. The very gradual relief found nearshore (the vertical gradient is 1 in 1000) makes the assumption of no elevation change between holes a reasonable one.

Most of the holes exhibit fairly linear thermal profiles, indicative of conductive heat transfer. Changes in the thermal gradient with depth in most cases can be related to changes in the primary lithology, indicating conductive cooling. For example, hole RDO6N (Figure 9) first penetrated about 45 m of predominently clay, then encountered a mixture of silt, sand, and volcanic glass. The thermal gradient in the upper part of the hole is fairly constant and significantly higher than that below about 45 m, where it changes from about 0.68°C/m to about 0.44°C/m. This is a direct response to the change in primary lithology. Hole P3-17 (Figure 6) penetrated 39.6 m of clay, underlain by sand. There is a distinct change in the thermal gradient at about 40 m, with a higher gradient in the upper portion. Applying reasonable values of thermal conductivity for each dominant lithology results in a constant heat flux through the formation.

Holes P2-6, P2-9, P2-13, and RDO7A (Figure 8) all exhibit slightly concave upward thermal profiles (not apparently related to changes in primary lithology). The nonlinear thermal profiles are indicative of nonconductive or non–steady state heat transfer and do not have a "thermal gradient" entry in Table 2.

The lower section of hole RDO6U (Figure 7) below about 46 m shows a decrease in equilibrium temperature with depth. Below 46 m, the hole penetrated volcanic glass before circulation was lost over the lowermost 18 m. Although the lowermost part of the hole indicates some circulation, probably lateral flow in the zone of highly permeable volcanic glass and sand, the upper section of the final thermal profile has a constant thermal gradient. Therefore the thermal gradient at this location is included in Table 2.

Thermal Conductivity

Thermal conductivity measurements were made on four cores, representing the bottom 1 m of holes RDO6T, RDO6Z, RDO7A, and RDO7B using a needle probe system [*Von Herzen and Maxwell*, 1959] provided by T.-C. Lee of University of California, Riverside (UCR) (Table 3). The values range from 0.89 W/mK for what is probably a sandy clay to 3.23 W/mK for a silty sand (Table 3). Five measurements made at 7.6-cm intervals along the core from RDO6T show a 40% variation in thermal conductivity over only 30.5 cm. The wide range in thermal conductivities probably is a result of the changing lithology downhole. These measurements have two

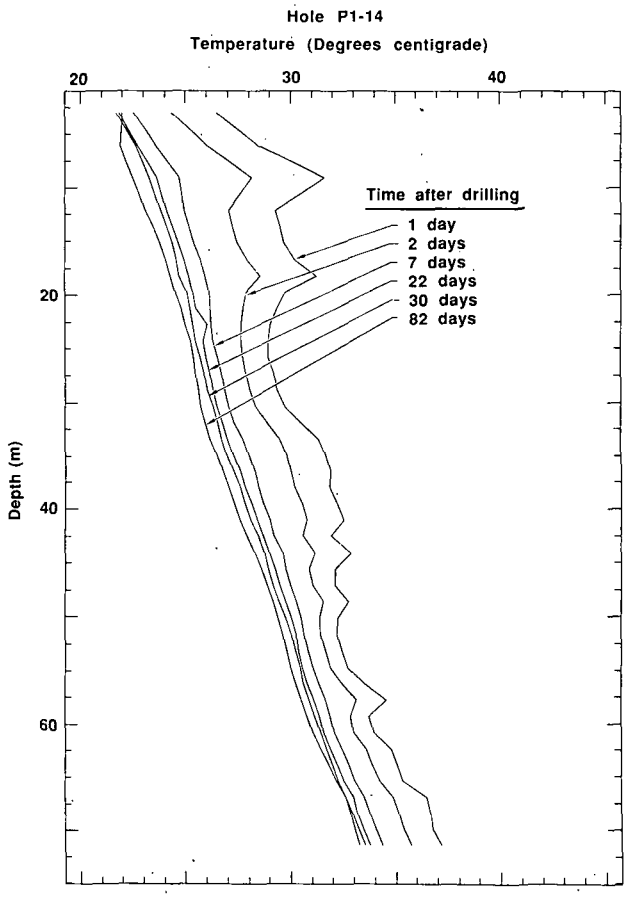

Fig. 4*a*. Temperature profiles obtained in hole P1-14 ranging from 1 day to 82 days after drilling. Depth shown is depth below lake bottom. The holes were drilled with a small truck-mounted rotary rig. Water was used as the drilling fluid: fresh for the onshore holes, seawater in a closed system for the offshore holes. Small amounts (a few kilograms) of drilling gel were added as needed. Drilling was relatively rapid, generally taking from 1 to 4 hours for the shallow holes. For those holes drilled offshore the rig was set on a floating barge. Hydraulically activated legs were driven into the lake bed in order to stabilize the drilling platform. The holes were cased with 2.54-cm-diameter polyvinyl chloride (PVC) pipe (cement reaching to total depth), filled with fresh water (to reduce corrosion of the temperature logging equipment), and sealed at the bottom against infiltration of formation or surface fluids. The PVC pipe was left standing about 0.61 m above the surrounding area level (land or sea) for temperature logging.

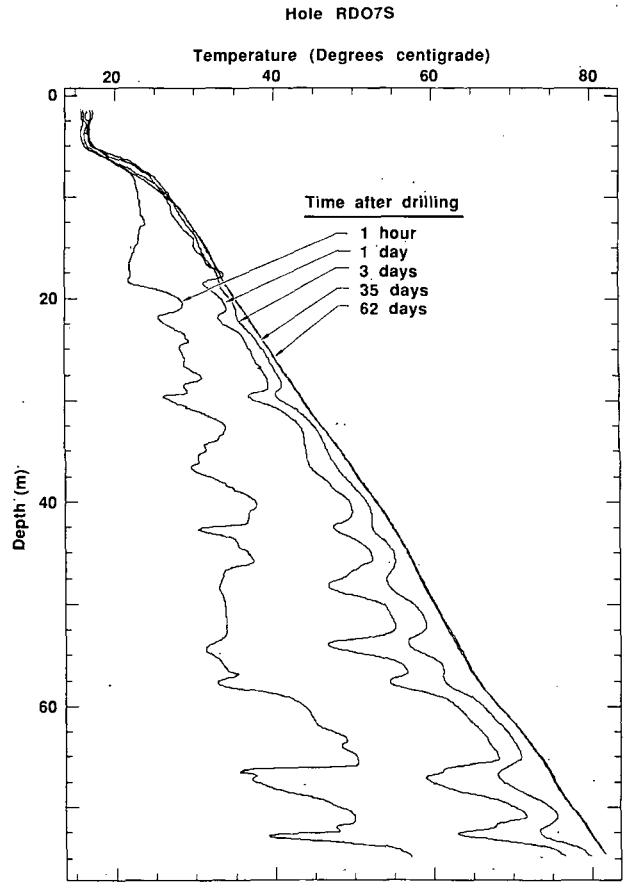

Fig. 4*b*. Temperature profiles obtained in hole RDO7S ranging from 1 hour to 62 days after drilling. Depth shown is depth below lake surface. Drilling took an average of 2 hours. Lost circulation was not unusual, and it resulted in some holes, such as RDO7Y, RDO6U, and RDO6Y being shorter than planned. The holes were then cased with 2.54-cm-diameter PVC pipe, filled with seawater and sealed at the bottom against infiltration of formation or surface fluids. Unlike the K-BCM program, cement was emplaced no deeper than 45.7 m, and high-temperature PVC (CPVC schedule 40) was used for casing the lower 30.5 m for most holes to prevent closing and buckling of the PVC due to exposure to high temperatures over the following months. See text for discussion.

Fig. 4. Temperature histories of selected holes.

limitations. The coring process most certainly changes the water content of the cores, an effect for which we are unable to provide a correction. In addition, the measurements were made on both extruded and unextruded cores, which would also be expected to result in a difference in water content. The importance of these measurements is in documenting the wide range of values in these sediments, rather than in defining a detailed conductivity profile for these few sites.

Preliminary results of laboratory measurements of thermal conductivity of drill cuttings by T.-C. Lee and others at UCR [*Lee et al.*, 1986, also personal communication, 1986] indicate a bimodal distribution of values, with the higher mode (1.9 W/mK) corresponding to silty sand and the lower mode (1.0 W/mK) to silty clay. Comparison of the early temperature profiles and the preliminary thermal conductivity values reveals a trend toward higher thermal conductivity in zones of early temperature disturbance. This supports the theory that early disturbance in the temperature profiles is indicative of relatively high-permeability sandy material. The early temperature profile of hole RDO6N shows a few small zones of relatively low temperature (Figure 9). Through the upper 20 m, the thermal gradient appears relatively stable, and the conductivity values average about 1.0 W/mK, indicative of the dominant clay content. At about 26 m a local low in the temperature profile indicates thermal disturbance in a zone comprising about 90% silt. This is accompanied by an increase in the thermal conductivity to almost 1.7 W/mK. Between about 35 and 50 m, the stable thermal gradient is reestablished, and the one thermal conductivity measurement is low. Thermal disturbances from 53 to 61 m and about 75 m

are similarly accompanied by increased thermal conductivities. Cuttings from these zones show an increase in silt content. Unfortunately, the sample frequency is not sufficient to apply these values of thermal conductivity directly to the thermal gradients measured downhole for the calculation of heat flow.

RESULTS

Thermal Gradients

Although most of the LLNL-SNL program holes were logged up to 5 months after drilling, during which time a stable thermal gradient was established, many of them had not reached thermal equilibrium. For each of these holes we employed the method of *Barelli and Palama* [1981], which uses the temperature rebound history in the holes after a finite drilling disturbance to estimate the formation equilibrium temperature at each depth. Thermal gradients were calculated over the lower section of the predicted equilibrium temperature profiles (below 30 m depth) using a least squares fit. This method does not account for the heat of hydration of the cement. For the LLNL-SNL holes the cement only extended to 46 m depth, and the presence of the cement does not significantly affect our thermal gradients calculated below 30 m. Ninety percent of the thermal gradients calculated over the lower 46 m of the last temperature log for each hole were within 5% of those obtained from the predicted equilibrium temperatures, showing that a stable thermal gradient had been established even though equilibrium temperatures had not yet been reached. The results are presented in Table 2 and Figure 10*a*. The thermal gradient values are accurate to within $\pm 3.5\%$ (95% confidence limits).

We were unable to apply the Barelli and Palama technique to the K-BCM program holes for a number of reasons: (1) cementing the entire length of the hole resulted in an early time source of heat, which affected the thermal rebound history for each hole in a manner for which the Barelli and Palama method cannot correct, (2) temperatures were obtained in a coarser spacing, making it difficult to clearly define the temperature rebound in zones of early temperature disturbance, and (3) most of the holes were not logged frequently enough to establish the rebound history. Vertical thermal gradients for the K-BCM program holes are calculated over the lower 46 m using a least squares fit, with accuracies within $\pm 7\%$ (95% confidence limits). The results are presented in Table 1 and Figure 10*a*.

The two new data sets were combined with previously published data from shallow and deep holes and new temperatures measured in State 2-14 [*Sass et al.*, this issue]. The deep well data came from two sources. *Younker et al.* [1982] estimated average thermal gradients in the cap for 11 deep holes in the SSGF, using temperatures from a number of sources. We estimated gradients from temperature data reported by *Muramoto and Elders* [1984] for four deep wells with nearly uniform gradients in the Westmorland and Niland areas. Shallow gradient values from *Sass et al.* [1984], were retrieved from their heat flow map by dividing out their assumed thermal conductivity, 1.88 W/mK. All measurements in these data sets are based on observations below 30 m in boreholes and therefore require no corrections for annual temperature cycles.

These data allow us to complete the surficial coverage of shallow thermal gradients in the area surrounding the SSGF. The dominant features of the contour map (Figure 10*a*) are two extremely high thermal gradient zones, or bullseyes, which we call the Mullet Island anomaly, located at the northeast corner of the established onshore geothermal field, and the Kornbloom Road anomaly, located to the southwest. High temperatures were expected at Mullet Island because of the high mud return temperatures observed in well Pioneer Development Corporation 1, drilled on the island in 1927. Mud was heated to 65°C when the hole depth was 45 m, indicating a high thermal gradient, perhaps above 1.0°C/m (R. Corbaley, California State Division of Oil and Gas, personal communication, 1986). The Kornbloom Road anomaly was not reported before this survey. The central portion of the thermal anomaly is arcuate, about 4 km wide and about 12 km long. It extends only a short distance offshore, primarily in the northern and southern edges of the geothermal field. The central anomaly is not centered on the chain of volcanic buttes. Its northwestern boundary follows an arc roughly coincident with the pattern of the buttes. The high-temperature region in the south extends beyond the magnetic anomaly, in contrast to the northeastern region where the thermal and magnetic anomalies appear to be closely correlated. There is no evidence of a broad local thermal anomaly associated with the offshore magnetic high, but because of our loss of hole RDO6D before temperatures could be measured, coverage of that anomaly is poor.

Heat Flow

In previous studies [e.g., *Sass et al.*, 1984] an average value of thermal conductivity for the region (e.g., 1.88 W/mK) was applied to the thermal gradient for each hole. Preliminary results indicate that the thermal conductivities may vary by a factor of 2 between observed lithologies (T.-C. Lee, unpublished data, 1986), which could result in a maximum factor of 2 difference in the calculated heat flow. In this study the cuttings descriptions allow us to refine the estimate of thermal conductivity according to the dominant lithology over an interval.

Heat flow values from the shallow holes are calculated using the average thermal conductivity measured for the primary lithology in the interval over which the thermal gradient is measured. These values of thermal conductivity are averages of the preliminary thermal conductivities measured on the cuttings samples from the LLNL-SNL holes by Lee and others (T. C. Lee, personal communication, 1986) and are as follows: clay = 1.0 W/mK, clay with some silt = 1.3 W/mK, silty clay = 1.4 W/mK, clayey silt = 1.7 W/mK, silt = 1.8 W/mK, and sand or sandy silt = 1.9 W/mK. These values are accurate to within about 17%. Whenever possible, heat flow was calculated over intervals where the primary lithology is clay, whose measured thermal conductivity is less sensitive to the proper reconstitution of the water content. In holes in which there is more than one interval with a dominant lithology, the heat flow calculations using these average values agree closely. The results are listed in Tables 1 and 2 and are plotted in Figure 10*b*. The heat flow values for the K-BCM program are accurate to within $\pm 20\%$, and those calculated for the LLNL-SNL program are accurate to within $\pm 13\%$ (95% confidence limits in thermal gradients and ± 0.20 W/mk in thermal conductivity).

There is some evidence that the assumption of steady state conductive cooling in the upper cap is not valid throughout the field. The four holes exhibiting nonlinear temperature profiles uncorrelated with changes in lithology lie along the northeastern edge of the field, in the vicinity of the Imperial

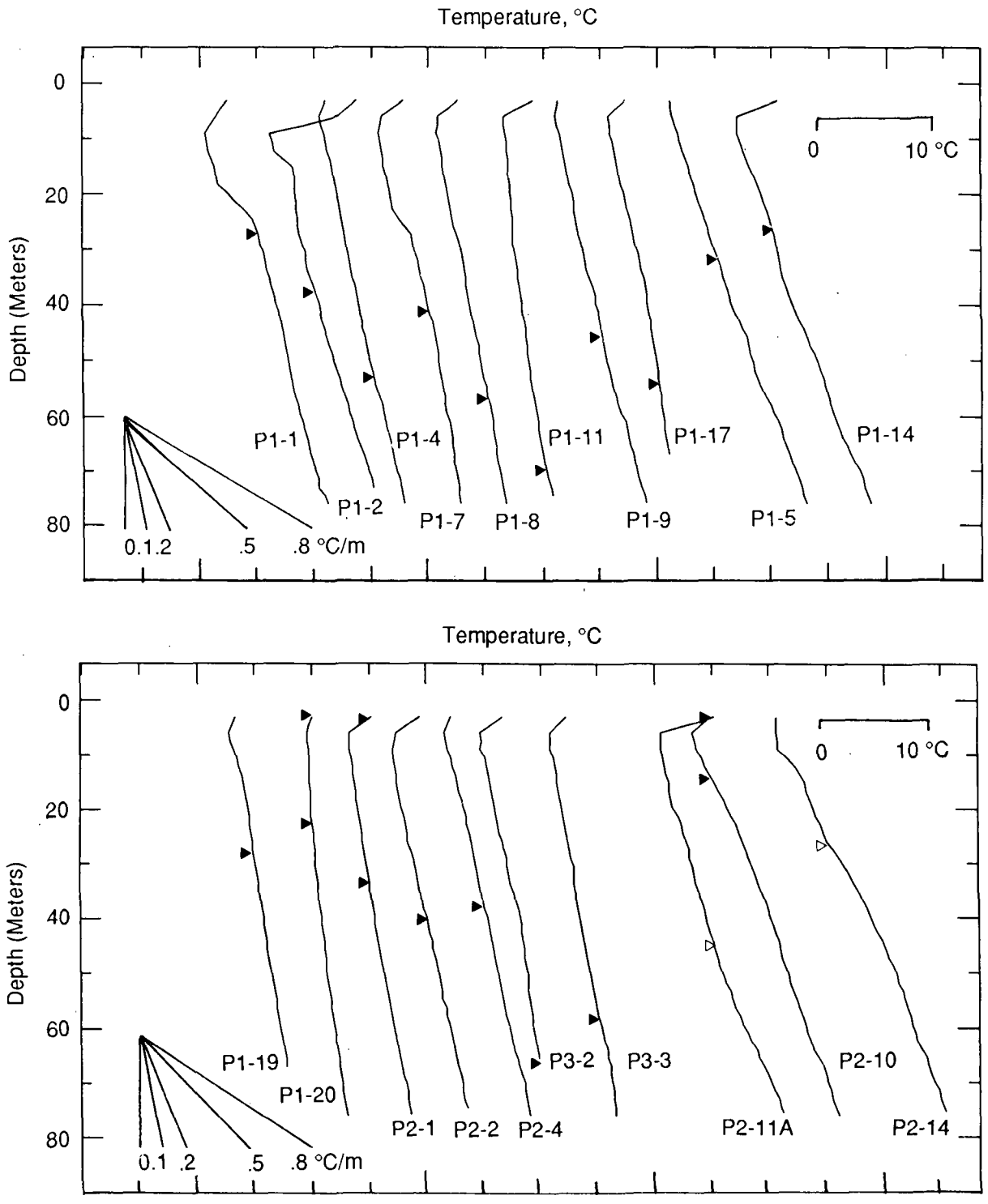

Fig. 5. Final temperature profiles for holes exhibiting generally low thermal gradients <0.20°C/m. For ease of presentation, the starting temperatures of consecutive profiles are offset by 5°C. Each profile has a symbol marking a reference temperature. Solid arrows mark 25°C; open arrows mark 30°C on profiles of higher temperature. Depth shown is depth below lake surface (offshore) or ground level (onshore). All logs project to a surface temperature of about 20°C. Temperatures were recorded every 3.05 m through the upper 18.3 m and every 1.52 m in the K-BCM program except for P6-4 which was logged every 6.1 m. Holes drilled as part the K-BCM program include interpolated values at 4.6, 7.6, 10.7, 13.7, and 16.7 m. Temperatures were logged every 3 cm in the LLNL-SNL program.

CO_2 Field, itself suggestive of shallow circulation. Hole RDO7A lies within a few tens of meters of a number of offshore boiling mud pots. Other evidence of shallow circulation in the area are the nonconductive temperature profile in the upper few tens of meters in the Salton Sea Scientific Drilling Project (SSSDP) hole, State 2-14 [*Sass et al.*, this issue], and the presence of several mud volcanoes which occur a few hundred meters southwest of hole RDO7A, within sight of State 2-14. These features, which lie along a northwesterly linear trend running through the Mullet Island anomaly, are evidence of circulation, probably associated with faulting, which may mean that the Mullet Island anomaly results are

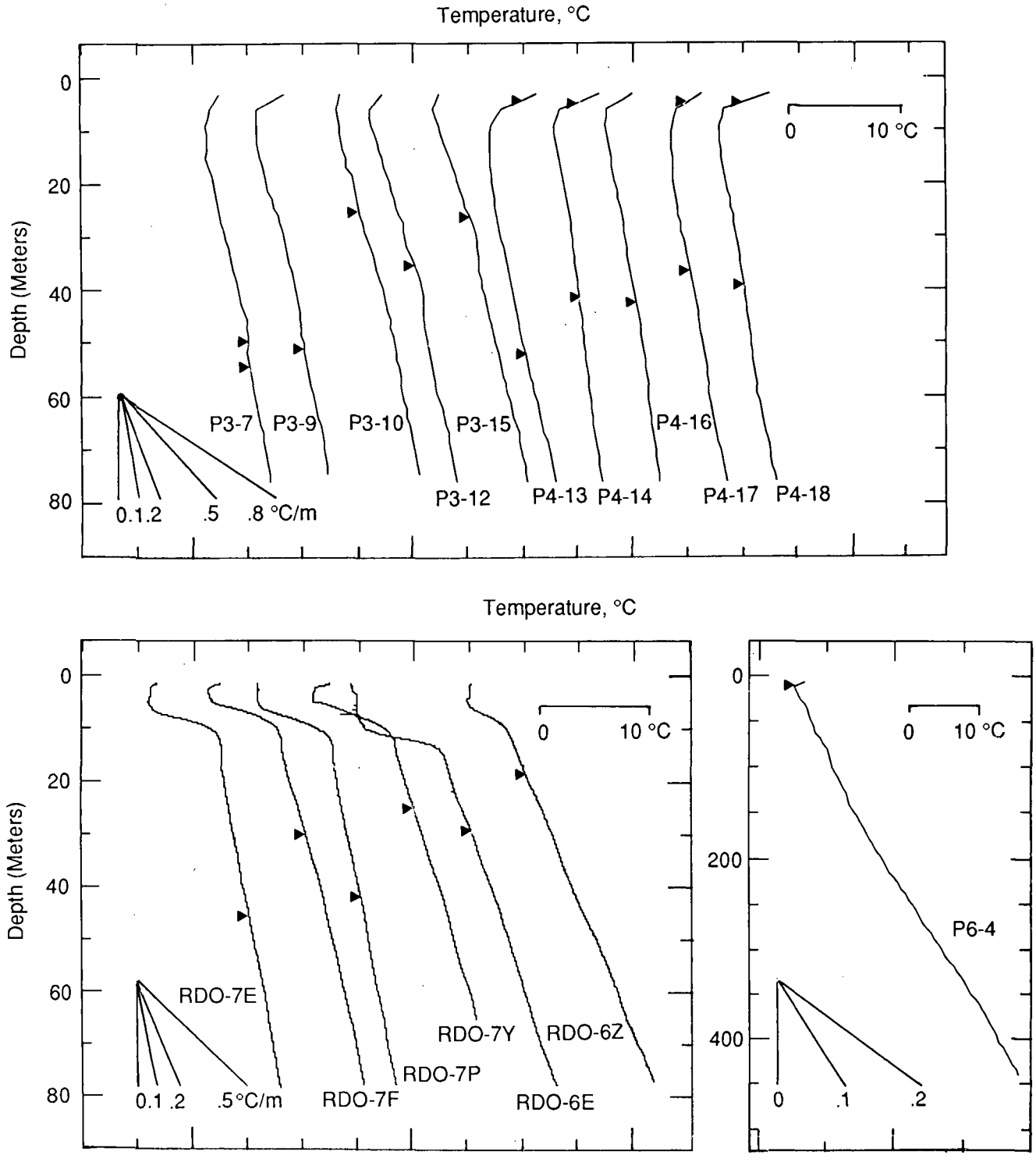

Fig. 5. (continued)

mainly from leakage. There is no surficial evidence of shallow circulation or leakage in the vicinity of the Kornbloom Road anomaly.

The heat flow contours follow roughly the same pattern as the gradient map. *Lachenbruch et al.* [1985] showed that most of the Salton Trough has a background heat flux between 100 and 200 mW/m^2. Mean global heat flow is 80 mW/m^2, leaving a reduced heat flow for the Imperial Valley of about 125 mW/m^2. The heat flow in the central part of the Salton Sea anomaly is generally in excess of 500 mW/m^2 and in the Mullet Island and Kornbloom Road anomolies exceeds 1200 mW/m^2. The center of the zone of highest heat flow follows an arc with about 8-km radius of curvature, centered SE of the domes.

Factors Affecting Thermal Gradients

Do our measured thermal gradients accurately represent the undisturbed gradients in the conductive zones of the Salton

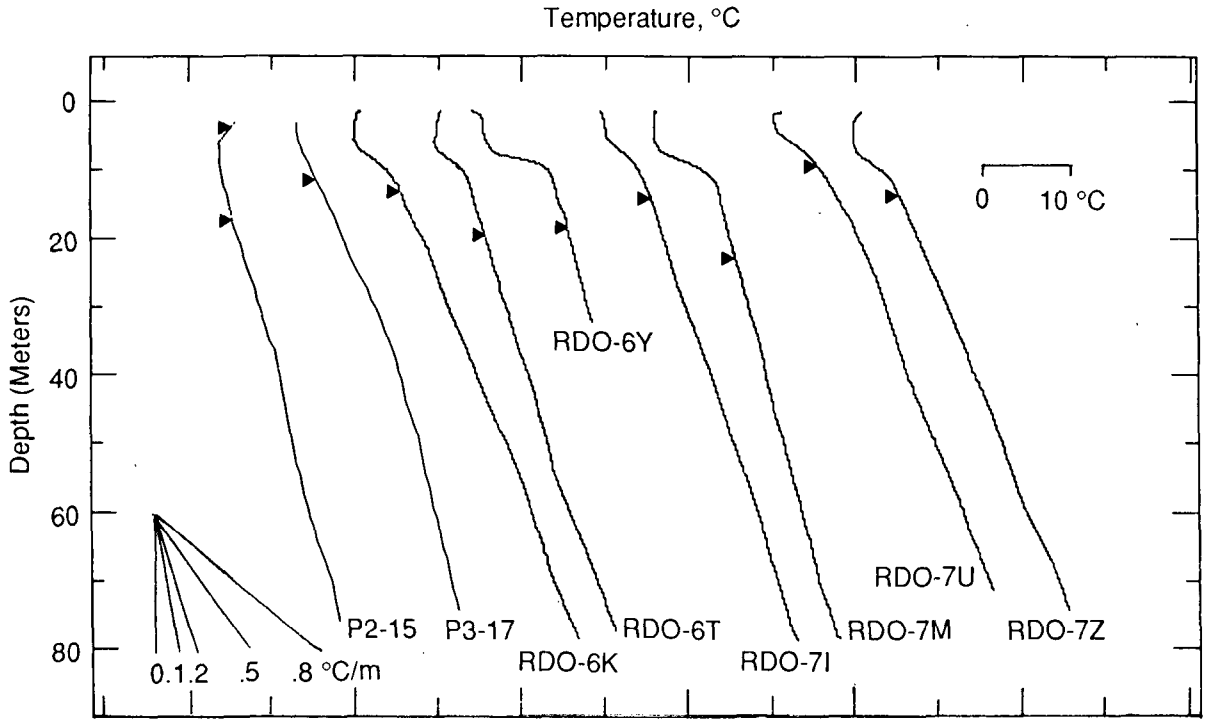

Fig. 6. Final temperature profiles for holes exhibiting intermediate thermal gradients, 0.20°–0.40°C/m. Starting temperatures are offset by 10°C for all logs. Temperature profiles project to a surface temperature of about 20°C. Depth and symbols as for Figure 5.

Sea geothermal system? Topography, changes in climate, occasional formation of lakes, and incursions of the ocean into the Salton Trough all may disturb the shallow gradient. In this area, topographic effects are certainly small, and climate changes can be ignored, but the lakes, particularly occasional ones, can have effects on both onshore and offshore heat flow measurements in shallow holes. The general concordance of shallow surveys and temperatures from deep wells here and throughout the Imperial Valley suggests that these fluctuations in surface conditions have produced only insignificant perturbations in the gradients measured in shallow holes. However, we do observe a substantial change in the thermal

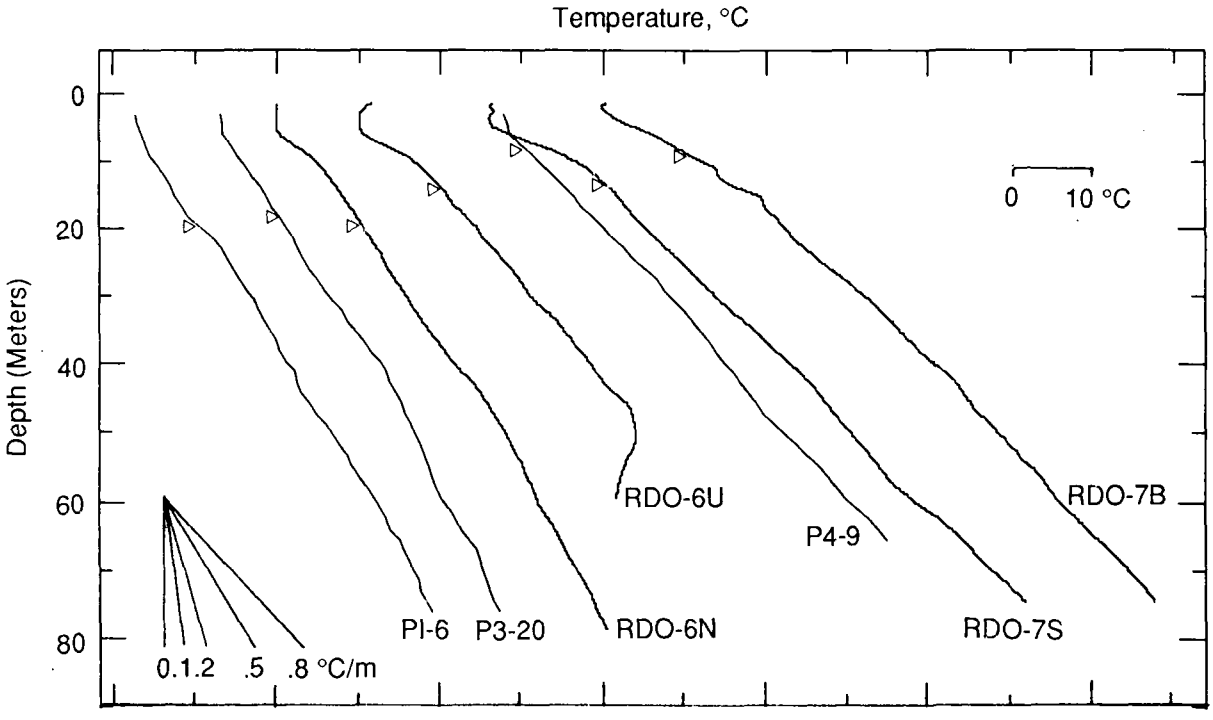

Fig. 7. Final temperature profiles for holes exhibiting high thermal gradients, >0.40°C/m. Starting temperatures are offset by 10°C, for consecutive profiles and project to a surface temperature of about 20°C. Depth and symbols as for Figure 5.

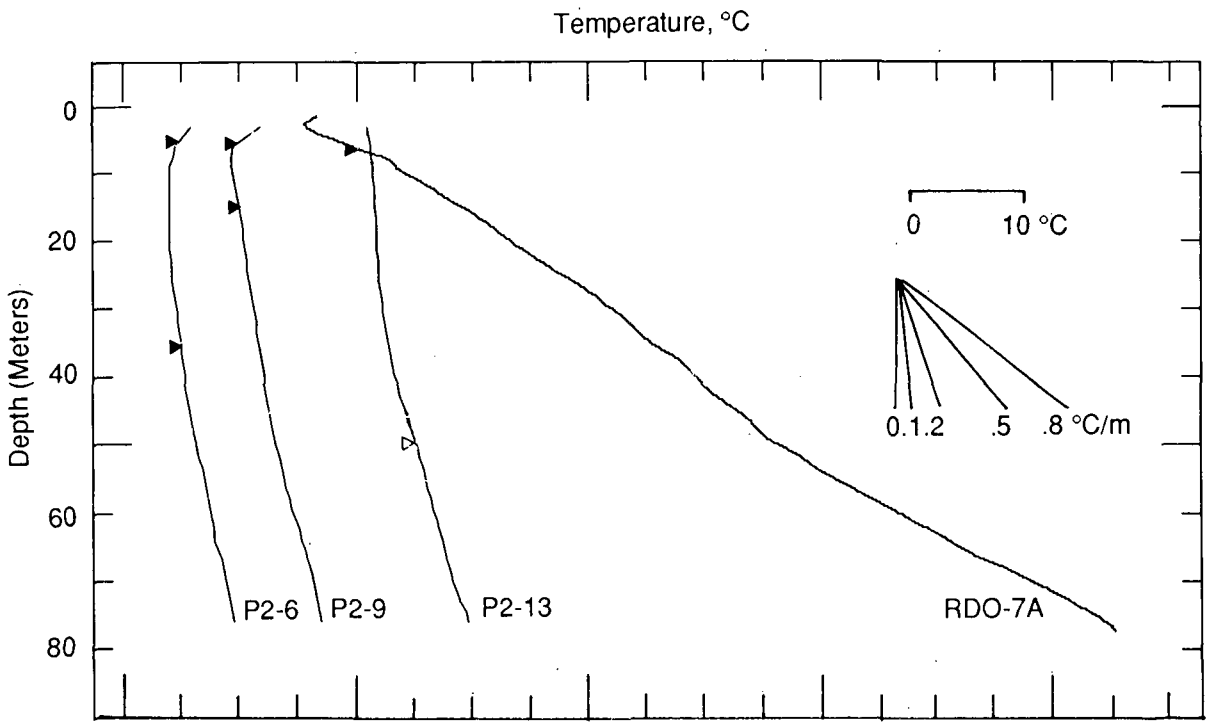

Fig. 8. Final temperature profiles for holes exhibiting substantially nonlinear thermal gradients which are not related to changes in lithology (and thus thermal conductivity). Starting temperatures are offset by 5°C for consecutive profiles and project to a surface temperature of about 20°C. Depth and symbols as for Figure 5.

gradient at the edge of the central anomaly that is nearly coincident with the present shore of the lake. In order to evaluate if this rapid change is merely an artifact of the present size of the lake, we estimate conductive effects of the lake and examine the possibility that downward infiltration of fluids has reduced the gradient. Our conclusion is that these effects are negligible and the abrupt change in gradient is real.

The creation of a lake can impose an average surface tem-

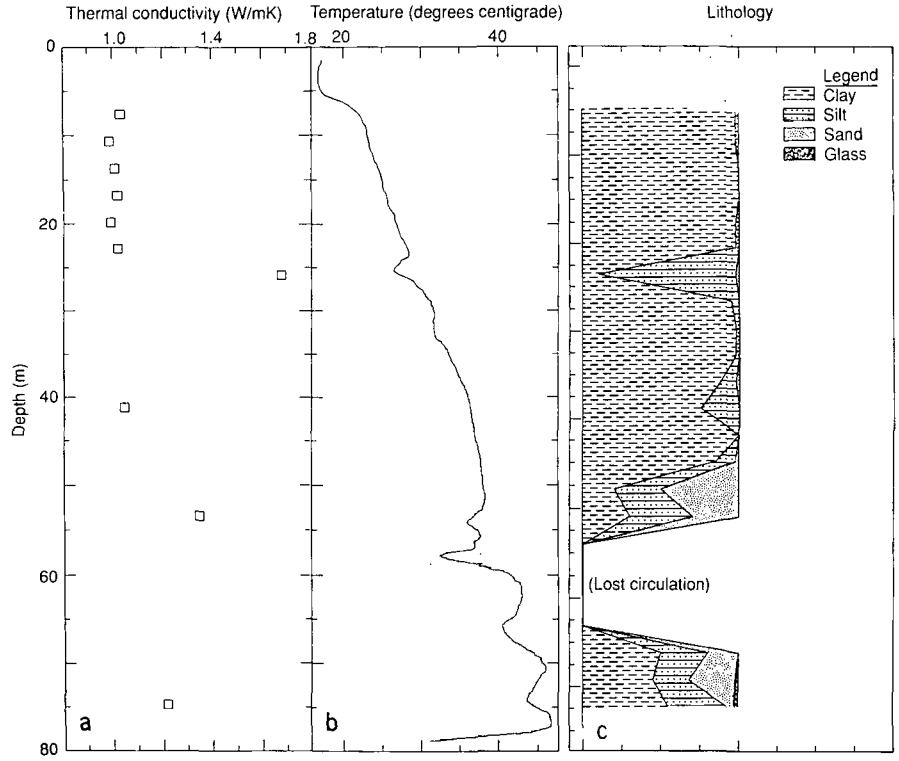

Fig. 9. (*a*) Thermal conductivity measured on drill cuttings from hole RDO6N by *Lee et al.* [1986, also unpublished data, 1986]. (*b*) Temperature log run in hole RDO6N within a few hours of drilling. (*c*) Lithology log from cuttings descriptions. Low-temperature zones in the early temperature log, indicative of greater invasion of (cool) drilling fluid is accompanied by increases in thermal conductivity, indicative of greater silt content.

TABLE 3. Thermal Conductivity Measurements in Bottom Cores

Sample	Description	Thermal Conductivity, W/mK
	Hole RDO6T†	
C1	core top; sandy	1.17
C2	core bottom; clay layer	1.37
C3	30.5 cm from bottom*	1.49
C4	15.2 cm from bottom*	0.91
C5	22.9 cm from bottom*	0.89
C6	28.1 cm from bottom*	1.14
C7	45.7 cm from bottom*	1.06
	Hole RDO6Z	
C1	core top; sandy	1.54
C2	50 cm from top; sandy	2.17
C3	25 cm from bottom; sandy clay	1.47
C4	near bottom of core; sandy clay	1.57
C5	5 cm from bottom; clay	1.32
	Hole RDO7A	
C1	core top; clay	1.18
C2	core bottom; clay to silty clay	1.43
C3	middle of core; sandy	3.23
	Hole RD07B	
C2	core bottom; dry sandy silt	1.08
C3	core bottom; dry sandy silt (after shaking)	2.12
C4	core top; reddish silt	1.58

†Extruded except when noted.
*Measured through holes drilled in core.

perature different from the mean annual temperature, disturbing the gradient at depth. *Lee and Cohen* [1979] estimated that the mean annual temperature at the bottom of the Salton Sea is 5.5°C below the mean air temperature. We have used two approaches to evaluate the effect of this instantaneous temperature change on our measurements.

The disturbance in the surface gradient due to a step change in surface temperature of ΔT at $t = 0$ is given by $\Delta T/(\pi\alpha t)^{1/2}$ [*Jaeger*, 1965]. Using a diffusivity $\alpha = 3.78 \times 10^{-7}$ m^2/s (*Lee and Cohen*'s [1979] mean value) and 80 years for the age of the Salton Sea, we estimate that the offshore gradients could be artificially raised by 0.10°C/m at the surface and by 0.01°C/m at a depth of 30 m; below which the thermal gradients were calculated. Most of the southern part of the lake is less than 6 m deep, so the difference between the mean annual temperature of the lake and the ground surface is probably smaller; thus this value is probably an upper limit for the surface disturbance. *Lachenbruch* [1957] used a two-dimensional solution to include the perturbation on the shore of the body of water. This effect, which is no larger than the one-dimensional value under the lake, can possibly be seen in the upper 20 m of some of our data near the shoreline. We conclude that this disturbance, about 3 times greater than the normal upper crustal gradient at the surface, would produce only a 1.0% increase in our gradients measured below 30 m depth.

Sedimentation can reduce the thermal gradient locally, and the magnitude of the effect on the surface heat flux depends on the rate and duration of sedimentation, as well as the thermal properties of the sediments. The thermal blanketing effect of instantaneous sedimentation of a layer of thickness d reduces the steady surface gradient by erfc $[d/2(\alpha)^{1/2}]$ [*Von Herzen and Uyeda*, 1963]. For sediment thickness of d of 1, 2, 4, and 8 m, the reduction is 1, 2, 4, and 7% of the steady gradient, respectively. Alternatively, if a 3-m layer of sediments were deposited at a constant rate over the past 80 years (a rate of 3.75 cm/yr, or twice that observed just south of the lake (J. D. Simms and M. J. Ryner, personal communication, 1986), the reduction in surface thermal gradient would be about 11% [*Jaeger*, 1965]. This reduction decreases to 0.02°C/m at a depth of 30 m, below which the thermal gradients were calculated. Thus the effect of sedimentation might reduce the observed gradient by no more than about 2%.

Infiltration can drastically decrease the thermal gradients beneath bodies of water. *Bredehoeft and Papadopulos* [1965] found a solution for steady state, one-dimensional infiltration to depth L:

$$T(z) = T_0 + g_0 L \frac{\exp(\beta z/L) - 1}{\exp(\beta) - 1}$$

where $\beta = VL/\alpha$, V is the Darcy velocity of the infiltrating water (positive downward), and g_0 is the undisturbed gradient. We can use our observation that over the 80-m depth of our wells, represented by ΔZ, the observed gradient is constant to within about 10% (i.e., $\Delta g/g$ is less than 0.10) to put an upper bound on the infiltration velocity. Differentiating twice, we find that

$$0.1 > \frac{\Delta g}{g} = \frac{\partial T^2/\partial z^2}{\partial T/\partial z} \Delta z \geq \beta \frac{\Delta z}{L}$$

or $v < 0.015$ m/yr using the definition of β above. Any higher velocity would produce detectable curvature on our profiles. Even such a low infiltration velocity could reduce the observed gradients significantly, depending on the depth of infiltration. However, in the 80 years since the Salton Sea formed in 1905–1907, infiltration at this rate could not penetrate far into the sediments, less than 12 m if the porosity is 10%, or only 2.4 m if the porosity is 50% (for the same Darcy velocity). We conclude that recent infiltration has not reduced the gradients measured below 30 m. Without detailed knowledge of previous lake shorelines and lifetimes, it is not possible to determine the cumulative effect of infiltration. However, to cause the observed localized change in gradient, we would require that short-lived lakes had their shorelines in the same place for thousands of years, an unlikely possibility in this area with no topographic relief.

At the depth interval over which the thermal gradients were calculated, all of these effects are relatively small. The reduction in thermal gradient due to sedimentation is potentially the largest effect that may influence the thermal gradients obtained in the shallow holes. This is partly offset by the potential increase in thermal gradient due to the creation of the Salton Sea. At most, the offshore thermal gradients are as much as about 0.01°C/m higher than measured. The close agreement between the thermal gradients and heat flow determined in holes located directly offshore and those determined for nearby holes located directly onshore on the northeast and southwest edges of the thermal anomaly supports the conclusion that the thermal gradients are not substantially affected by the presence of the lake.

DISCUSSION

Several factors control the size, shape, and characteristics of thermal anomalies in the Earth's crust. These factors include

the location and characteristics of the heat source, heat transfer mechanisms (including preferential flow pathways), preexisting thermal structure, and time since the inception of the system. Previous studies have provided constraints on these factors. A conceptual model was developed involving a localized heat source near the volcanic buttes and the transport of heat primarily by horizontal fluid flow to the southeast [*Younker et al.*, 1982]. Alternative flow pathways to the northwest have been proposed [*Riney et al.*, 1977], but they are inconsistent with the data from the field [*Kasameyer et al.*, 1984].

The shallow temperature surveys have provided the basis for refining this conceptual view of the system. We now have a good idea of the plan view of the region of elevated heat flow, both its area and shape. Because of the existence of the conductive thermal cap, we can also make inferences about the deeper thermal structure.

Nature of the Salton Sea Thermal Anomaly

Three nested thermal features are superimposed on the regional Salton Trough heat flux, as is shown schematically in Figure 11. The Broad anomaly is a region of elevated conductive heat flow, covering more than 300 km^2, characterized by constant temperature gradients of the order of 0.1°C/m persisting to depths of over 2500 m and producing 250°C bottom-hole temperatures. The Central anomaly occupies an area of 30–40 km^2 asymmetrically distributed about the volcanic buttes. Very high (0.4°C/m) near-surface gradients are observed through a thermal conductive cap to depths of approximately 500 m. A nearly isothermal zone underlies this conductive zone to depths greater than 2500 m. Bottom-hole temperatures of the order of 350°C have been observed in this area. The boundary between the Central anomaly and the Broad conductive anomaly is characterized by temperature gradients that increase with depth near the base of the thermal cap. Two local anomalies (the Mullet Island anomaly and the Kornbloom Road anomaly) with shallow temperature gradients as high as 0.8°C/m are superimposed on the main hydrothermal system. The vertical extent of these very high gradients is unknown, but plausible temperature arguments limit these features to be less than a few hundred meters thick.

The nature of the Central anomaly is illustrated in the anomalous temperature cross sections shown in Figure 11. Assuming that the Central anomaly is superimposed on the Broad anomaly, a constant gradient (0.10°C/m) profile has been subtracted from all temperatures, leaving only the excess due to the Central anomaly. Section A-A′ shows a broad uniform temperature zone across the anomaly and an abrupt drop-off at its edges, particularly to the SE, where the contours are constrained by deep wells. Section B-B′ crosses the same anomaly nearly perpendicular to its easternmost edge. Here the anomalous temperatures drop off more gradually. The anomaly lies mainly to the southeast of the volcanoes. The anomalous temperature contours close to the SE, but the absence of deep data under the Salton Sea leaves uncertainty about whether the NW boundary is similar to the SE.

A comparison of the shape of the thermal anomaly with the pattern of the geophysical anomalies and the location of the volcanic buttes adds constraints to conceptual models of the system. A broad area of high electrical conductance extends southeast away from the volcanic buttes [*Younker et al.*, 1982]. This resistivity anomaly probably reflects the boundary of the saline brine and lends support to a model in which hot fluid is channeled to the southeast in a permeable aquifer beneath the thermal cap. The gravity anomaly is also offset slightly to the SE from the buttes (Figure 3), reflecting the region of sediments which have been altered by interaction with the hot brine. The coincidence of the pattern of volcanic buttes and the shape of the elliptical magnetic anomaly (Figure 3) indicates that the buttes likely overlie a deeper magmatic heat source in the form of distributed dikes and sills. The similarity of the arcuate NW boundary of the thermal anomaly to the spatial pattern of the volcanic buttes suggests that this region may also mark the location of the upwelling of the hot fluids (Figure 10). The abrupt termination of the Central anomaly to the SE along A-A′ (Figure 11) provides further support for heat transport by lateral flow, and the more gradual transition along B-B′ suggests that flow may be less important on the eastern edge of the system. The position of flow upwelling is not well constrained, and it could be located somewhat to the SE of the volcanic buttes.

There is no evidence for flow of hot fluids past the position of the volcanics to the northwest. The flow of hot fluids to the southeast is possibly controlled by one or a combination of the following: primary depositional permeability in the sedimentary section, existence of flow barriers related to the emplacement of dikes, or regional fluid flow directions. The sedimentary beds of the lithologic cap dip to the northwest. This configuration may provide preferential flow paths updip through the more permeable beds to the south but prevents shallow circulation to the north. If this is the dominant effect, vigorous circulation may occur at greater depth in the region north of the volcanic chain. Alternatively, *Rex* [1983] has proposed a model based on chemical arguments in which regional flow is directed southeast along the Salton Trough through the field.

Thermal Regime of the Salton Sea Scientific Drilling Project Site, State 2-14

The above discussion provides a context within which to view the thermal regime of State 2-14, which is located on the edge of two of the nested thermal features in the field. First, it is on the boundary of the Mullet Island anomaly, and second, it is near the edge of the Central anomaly representing the main hydrothermal system. *Sass et al.* [this issue] report that State 2-14 has an unusually high near-surface gradient perhaps associated with the shallow thermal plume near Mullet Island. Below 150 m the well has temperatures intermediate between wells in the central axial zone and wells in the broad conductive zone. There is, however, no evidence in section B-B′ to suggest lateral flow of hot fluids away from the center of the field, such as is observed in the region between the Central anomaly and the conductive zone along the axis of the trough to the south. This difference may reflect the effects of a fault barrier or lateral changes in the permeability of the sedimentary section.

One of the intriguing results of the SSSDP has been documentation of a retrograde thermal regime [*Andes and McKibben*, 1987; *Sturtevant and Williams*, 1987]. Fluid inclusion and pore fluid studies suggest that the upper 1 km of the well may have cooled by 40°–100°C. If, as is suggested by *Kasameyer and Hearst* [this issue], the portion of the broad thermal anomaly to the northeast of State 2-14 represents a cooling, earlier pulse of hydrothermal activity, then thermal profiles at State 2-14 may reflect transient cooling from this earlier activity. The proximity of the Mullet Island thermal plume to

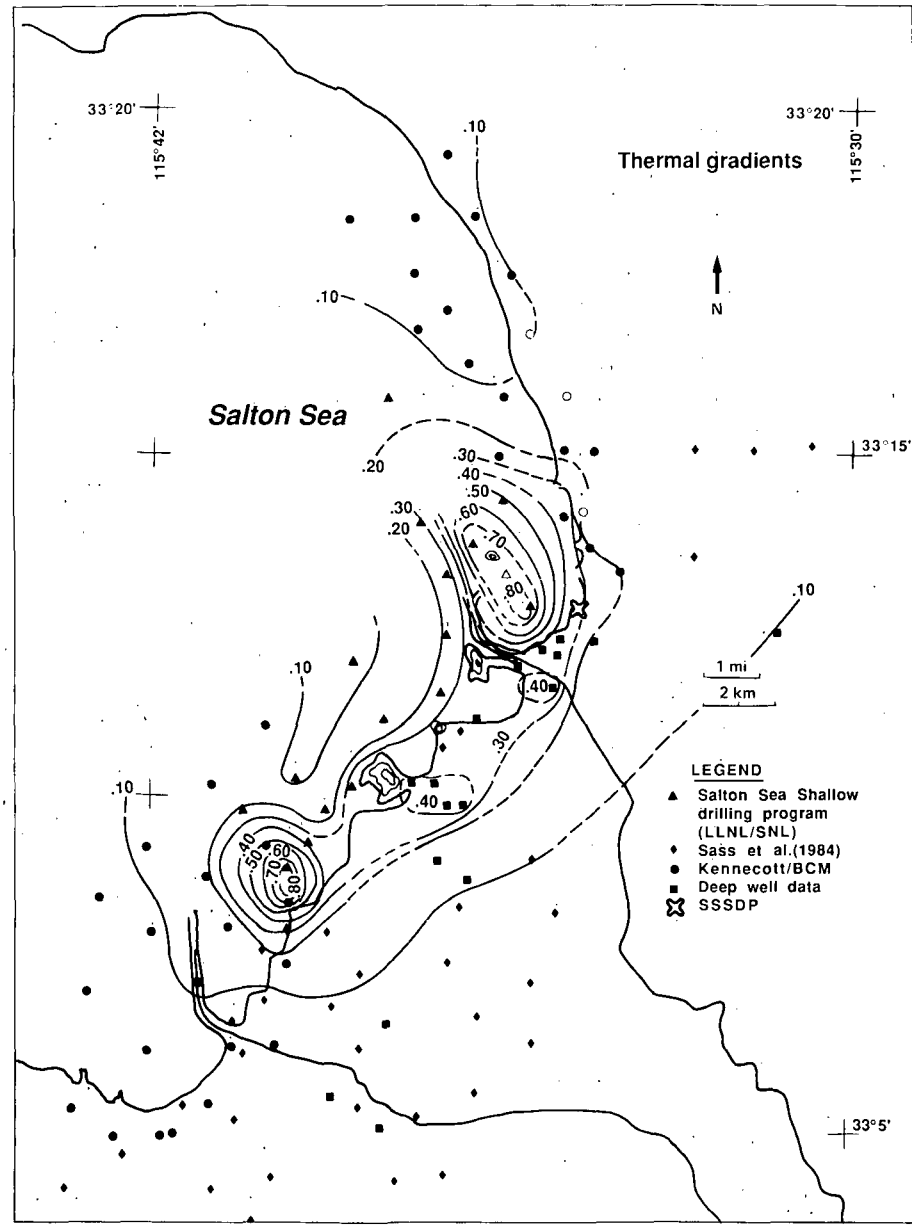

Fig. 10*a*. Thermal gradients in the southern Salton Sea region. Contour interval is 0.10°C/m.

the State 2-14 site can provide an alternative explanation for the observed retrograde thermal regime. Anomalously high heat flow is currently being pumped from the area due northwest of the SSSDP, drawing relatively cooler fluids in from the surrounding area. In this process, heat to drive the plume may, in part, be coming from deeper, higher-temperature regions surrounding the plumes. This presumably transient process superimposed on the main hydrothermal activity would be expected to produce localized regions of retrograde thermal activity.

Salton Sea Geothermal System and Crustal Rifting in the Salton Trough

The processes of crustal extension and rifting in the Salton Trough may be viewed on many different scales (Figure 12). On the smallest scale the thermal zones, each less than about 10 km wide, are believed to be the current locus of spreading [*Elders et al.*, 1972]. A pattern of modern intense seismicity suggests to others that a zone perhaps 30 km wide is actively deforming in response to the crustal rifting process [*Fuis et al.*, 1982, 1984]. On an even larger scale, regional heat flow considerations indicate that extension and basalt intrusion must occur throughout a diffuse zone of deformation 150 km wide in order to be consistent with the observed crustal structure and appropriate strain rates [*Lachenbruch et al.*, 1985]. Any model for crustal rifting in the trough must reconcile observations on these diverse scales.

On the smallest scale there appears to be a strong connection between the thermal features and rifting associated with the pull-apart region between the San Andreas and Brawley fault zones. *Crowell* [1974] has described and qualitatively analyzed features associated with the development of pull-apart basins of this type. *Rodgers* [1980] and *Segall and Pollard* [1980] developed mathematical models to describe the patterns of basin formation and faulting related to the evolution of pull-apart basins. *Segall and Pollard* [1980] concluded

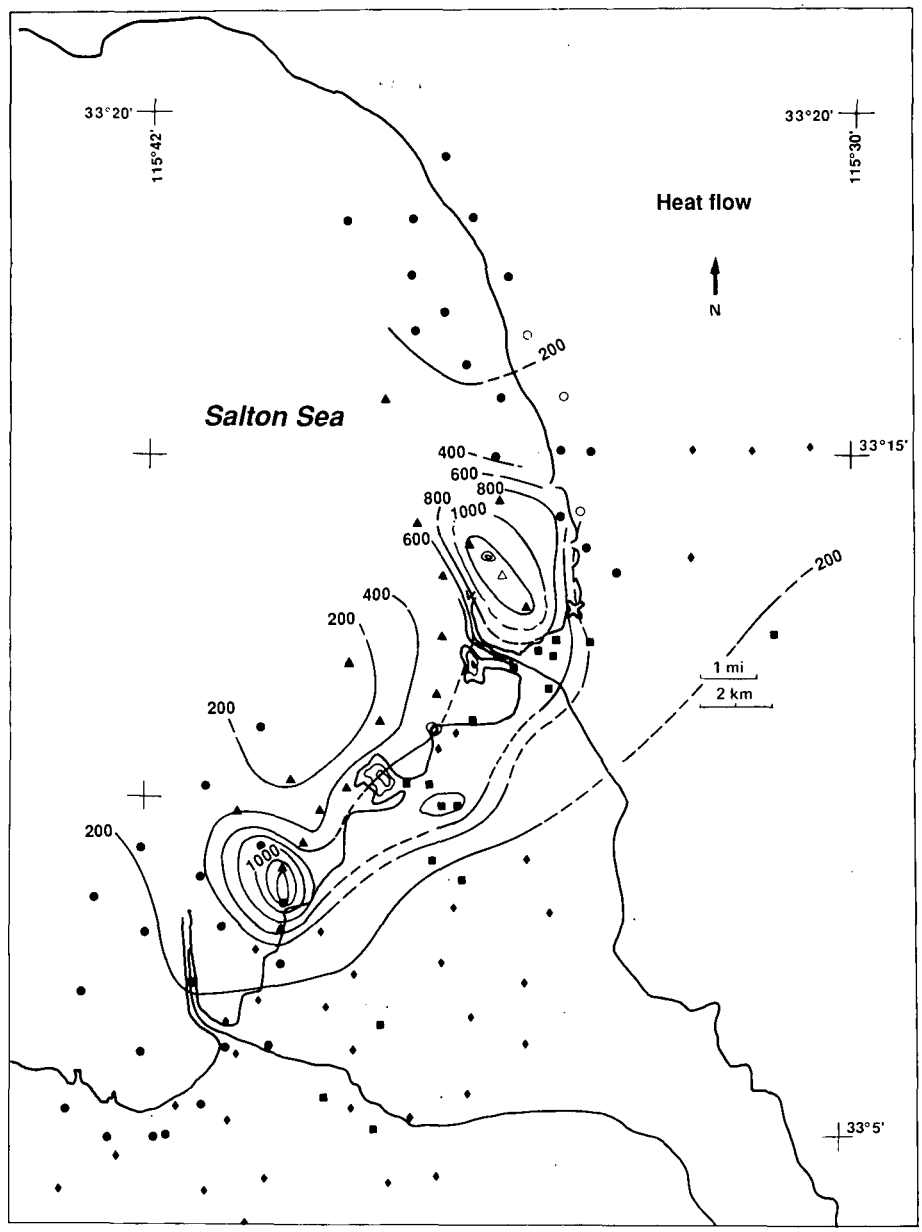

Fig. 10b. Heat flux in the southern Salton Sea region. Contour interval is 200 mW/m^2. See text for discussion.

that dike intrusion would be favored in the region of reduced mean stress between offset right-lateral faults.

The stress regime due to major faults in the Salton Sea region has been calculated by *Full* [1980]. The San Andreas and Brawley fault zones are modeled as elastic dislocation surfaces within a semi-infinite homogeneous elastic medium [*Full*, 1980]. The calculations use the basic theory and equations derived and discussed by *Chinnery* [1961, 1963]. Figure 13 shows Full's calculation of normal stress in the plane of the ground surface for two faults with geometry and characteristics broadly representative of the Banning-Mission Creek branch of the San Andreas fault and the Brawley fault. The results indicate the presence of a relative tensile region concentrated at the northwest end of the smaller and shallower Brawley fault and a smaller one at the southwest tip of the Banning-Mission Creek fault. The zone of maximum relative tension runs between the two faults, describing an arc coincident with the arcuate pattern of the volcanic chain and mirroring the northwest boundary of the thermal anomaly. Enhanced vertical permeability due to fracturing would be expected to facilitate localized upwelling of fluids in these regions. These areas would also mark the most likely locations for shallow intrusion of basaltic and rhyolitic dikes. The subsurface igneous activity in the region is evidenced by the discovery of altered basaltic and silicic dikes and sills in several of the geothermal wells in the field [*Robinson et al.*, 1976; *Herzig and Mehegan*, 1986; *Lilje and Mehegan*, 1986].

On a larger scale we have not resolved the relationship of the individual geothermal anomalies to the overall process of crustal rifting in the trough. One view is that these systems represent localized, relatively unimportant near-surface perturbations of the regional rifting process. An alternative view is that these geothermal systems actually are the current locus of spreading in the trough, reflecting regions of elevated mantle heat flux into the trough.

An analysis of thermal budgets provides one means for link-

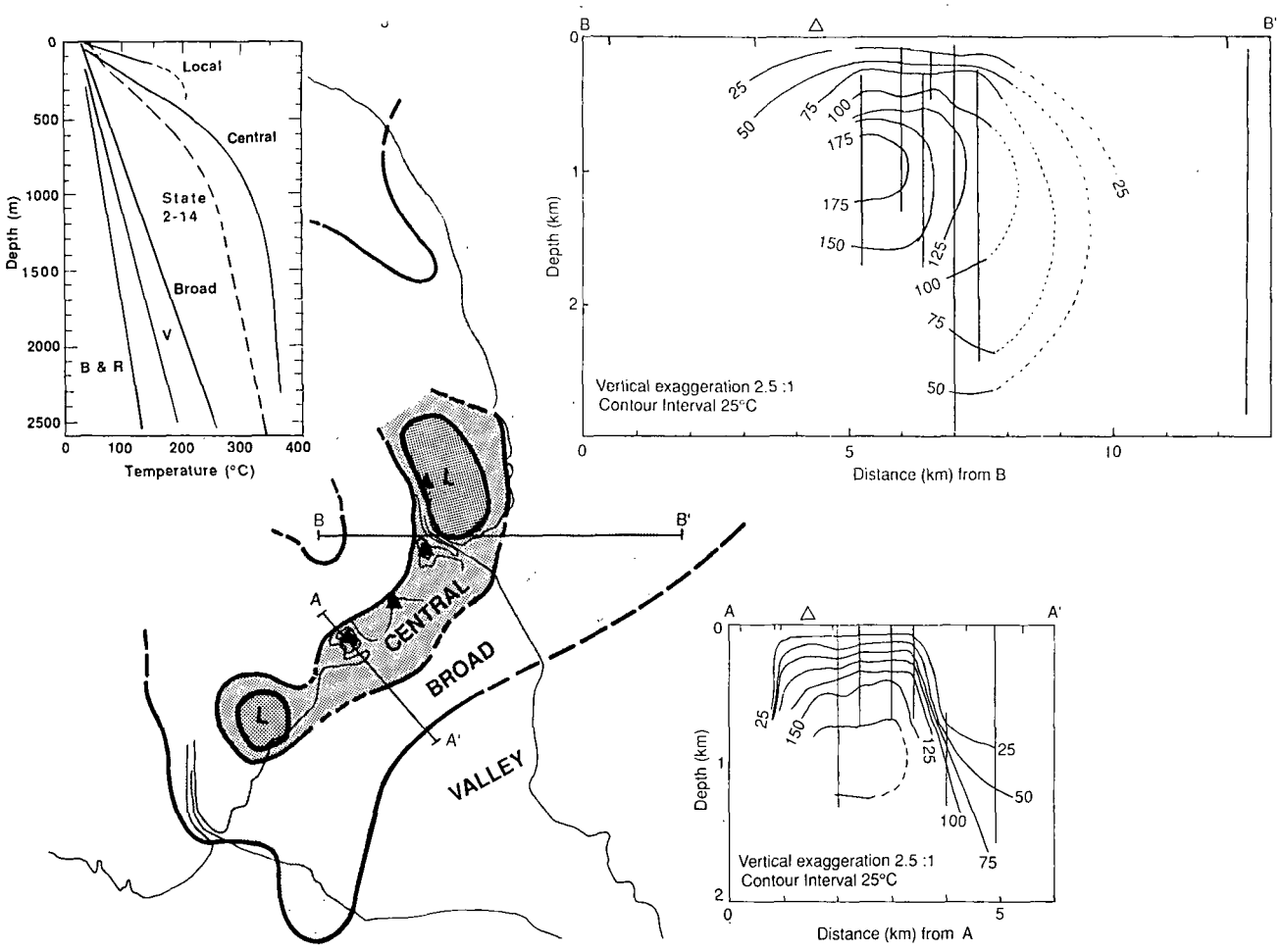

Fig. 11. Schematic representation of three scales of thermal anomalies at the Salton Sea geothermal field. The letter "L" identifies two local features bounded by the 0.5°C/m contour, the Mullet Island anomaly to the northeast and the Kornbloom Road anomaly to the southwest, which were discovered during this survey. The Central anomaly, modeled by *Kasameyer et al.* [1984], is defined to lie within the 0.3°C/m contour. The approximate boundary of the Broad anomaly is given by the 0.09°C/m contour, which extends outside the area of thermal measurements. The Local and Central anomalies have relatively sharp and well-defined boundaries, but the edge of the Broad anomaly is not well defined. Schematic temperature profiles are shown in the inset for the Local, Central, and Broad anomalies, as well as average profiles for the Imperial Valley (V) and the Basin and Range (B&R) average heat flow in sediments. Profiles A-A′ and B-B′ show anomalous temperatures in the axial anomaly. The anomalous temperatures were calculated from the actual temperatures by subtracting the idealized temperature profile for the broad anomalous zone, $T(z) = 23°C + 0.10\ z(m)$. Data from wells within ± 2 km of the line were projected onto a vertical plane. The vertical black lines indicate portions of wells where temperatures were available. The short vertical lines indicate locations of shallow gradient wells in Tables 1 and 2, or from *Sass et al.* [1984]. The temperature profiles from these wells were extrapolated to a depth of 500 m by assuming conductive heat flow. The deep well data are from *Younker et al.* [1982]. The triangle represents the location of the volcanic arc. Section B-B′ is similar to A-A′ except the data were taken from wells within ± 1 km from the line. Data from State 2-14 [*Sass et al.*, this issue] have been added.

ing the local systems with the regional rifting process. An important question to address is how large a contribution to the total heat flow comes from the local areas of high heat flow? *Sass et al.*'s [1984] area heat flow survey of the Imperial Valley indicates that the zones of anomalously high heat flow (the geothermal fields), representing 10% of the area, contribute only 25% of the total heat flow out of the valley. The local systems providing a relatively small portion of the heat flow out of the valley might, therefore, be relatively insignificant features in the context of the trough-wide rifting process.

What is the rate of heat flow into these areas? If they are young and growing rapidly enough, their heat input could satisfy the entire thermal budget of the trough. The heat flux into a geothermal system cannot be measured directly with near-surface observations. The conceptual model for the Salton Sea field [*Kasameyer et al.*, 1985] does, however, provide a basis for estimating the heat flux into that system.

Field observations, mostly notably the width of the transition zone between the central hydrothermal system and the conductive anomaly, were used to estimate the rate of influx into the system. To fit the observations from the Salton Sea geothermal area, the ratio of heat flux into the system by advection to the rate of heat flow from the top of the system by conduction is somewhere between 2.8 and 10 [*Kasameyer et al.*, 1984]. If the predictions of this model are valid and if other local hot spots are growing as rapidly as the Salton Sea geothermal field, then these small geothermal fields, which presently account for only 25% of the observed heat output of the Salton Trough, may, over time, be equivalent to the entire heat input to the region.

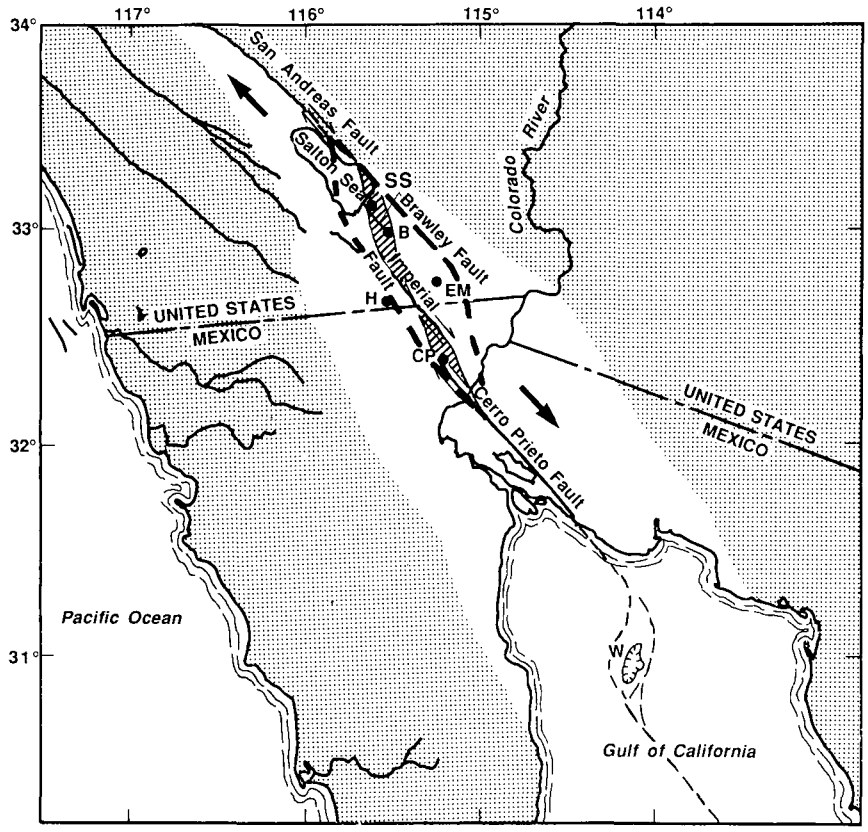

Fig. 12. Three scales of deformation in the Salton Trough [from *Lachenbruch et al.*, 1985]. Dots mark the locations of geothermal fields. Cross-hatched areas mark the location of intense modern seismicity [after *Fuis et al.*, 1982]. Dashed curves enclose region of basin-wide extension predicted by regional modeling [*Lachenbruch et al.*, 1985]. Other features as in Figure 1.

Lachenbruch et al. [1985] showed that if these local hot spots were long-lived (analogous to mid-ocean spreading centers), a large part of the crust would melt, which is not the case. Thus these areas of intense thermal activity must be relatively short-lived.

The Salton Trough could represent a broad region that has undergone spatially variable pull-apart basin development and growth. Shallow hydrothermal systems in the pull-apart region between active strike-slip faults are the near-surface expression of the rifting process. Transfer of motion between adjacent fault zones and extension of fault traces in response to the southward passage of the Rivera triple junction would change the position of these zones of active spreading with time. Heat input to the trough is localized in the regions of active pull-apart development. As the complex system of subparallel faults evolved, new pull-apart structures and zones of spreading developed, as *Crowell* [1974] has discussed. Total heat flow out of the trough is a result of the transient cooling of the previously active spreading centers coupled with the heat flow from the current centers. Thus relatively small, spatially variable, ephemeral zones of intrusion can create a broad zone of high heat flow consistent with the model of *Lachenbruch et al.* [1985].

SUMMARY AND CONCLUSIONS

Two shallow thermal gradient surveys have bounded the spatial extent of the Salton Sea high-temperature hydrothermal system and documented the presence of two superimposed shallow high-temperature plumes. The Salton Sea field can now be characterized as a system of four nested thermal zones with each zone representing the dominance of different mechanisms of thermal transport. The largest zone covering most of the Imperial Valley has an anomalous high thermal gradient of about 0.07°C/m [*Sass et al.*, 1984]. At an intermediate scale a broad zone with nearly conductive temperature profiles of 0.1°C/m surrounds the highest temperature hydrothermal system on at least three sides. The central part of the geothermal field is identified as a region of uniformly high near-surface gradient (0.4°C/m) and decreasing gradients at depth implying convective transport. Within this region, two localized intense shallow zones with gradients as high as 0.8°C/m have been identified.

The characteristics of the thermal anomaly, coupled with the geophysical data from the area, provide the basis for developing a conceptual model for the Salton Sea system. Localized upwelling of hot fluids near the volcanic buttes is followed by horizontal flow to the southeast in a permeable aquifer beneath a thermal cap. The location of the region of upwelling is controlled by the complex stress regime in the pull-apart region between the San Andreas and Brawley fault zones. The preferential flow pathways to the southeast likely reflect either primary permeability variations or interactions with the regional flow system.

A simple quantification of this conceptual model allows us to make inferences about the thermal budget of the Salton Sea field. Estimates of the total area of the field, the heat flux out of the field, the thickness of the circulating zone, and the abruptness of the transition to the regional gradient are used

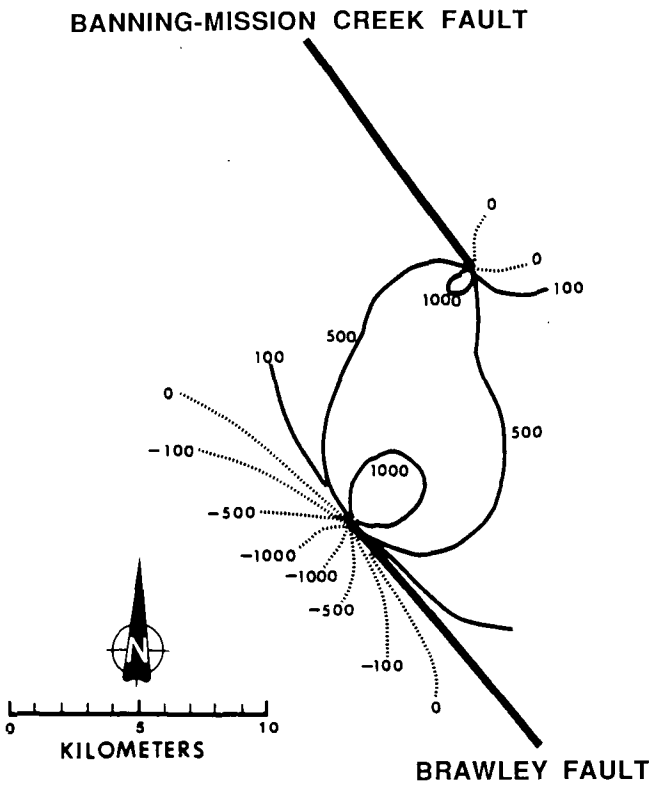

Fig. 13. Normal stress in the plane of the ground surface for two faults with geometry and characteristics similar to the Banning-Mission Creek-Brawley fault system [from *Full*, 1980]. Contour interval is $\times 10^5$ dyn/cm^2. See text for discussion.

to calculate the rate of heat flux into the field. The results suggest that the Salton Sea field is young and growing. These observations provide support for a model in which small, spatially variable, ephemeral geothermal zones may account for the total heat flow from the Salton Trough.

Acknowledgments. This work was supported by the Office of Energy Research, Division of Engineering and Geosciences, U.S. Department of Energy, as part of the Continental Scientific Drilling Program. We thank George Kolstad, Jim Coleman, Dan Weill, and Ed Schreiber for their support for this project and the overall Department of Energy Continental Scientific Drilling Program. The Geoscience Research Drilling Office of Sandia National Laboratories, under the direction of Jim Dunn and Peter Lysne, had complete responsibility for operations and logistical support for the project. We especially thank Peter Lysne for his enormous efforts and technical contributions. Bob Meyer and Ron Jacobson of Sandia designed the temperature logging system and fielded it under conditions that were often quite difficult. They are responsible for the high quality of the data. This project would not have been possible without the support of the geothermal industrial community. Kennecott Geothermal, UNOCAL Geothermal, Trans-Pacific Geothermal, Inc., and I. Sheinbaum Company, Inc. all provided access to their lease holdings. We would like to thank Larry Grogan (Kennecott Corporation, Salt Lake City, Utah) and Pam Irvine (formerly of UNOCAL) for their enthusiastic support of the project, along with Ian Padden and his drilling and marine support crew for their hard work and efforts through what were often difficult and windy working conditions. T. C. Lee, John Sass, Norm Burkhard, and an anonymous reviewer greatly improved the content of this paper. This work was performed under the auspices of the U.S. Department of Energy by Lawrence Livermore National Laboratory under contract W-7405-Eng-48. This document was prepared as an account of work sponsored by an agency of the U.S. Government. Neither the U.S. Government nor the University of California nor any of their employees makes any warranty, express or implied, or assumes any legal liability or responsibility for the accuracy, completeness, or usefulness of any information, apparatus, product, or process disclosed or represents that its use would not infringe privately owned rights. Reference herein to any specific commerical products, process, or service by trade name, trademark, manufacturer, or otherwise does not necessarily constitute or imply its endorsement, recommendation, or favoring by the U.S. Government or the University of California. The views and opinions of authors expressed herein do not necessarily state or reflect those of the U.S. Government or the University of California and shall not be used for advertising or product endorsement purposes.

REFERENCES

Andes, J. P., Jr., and M. A. McKibben, Thermal and chemical history of mineralized fractures in cores from the Salton Sea Scientific Drilling Project (abstract), *Eos Trans. AGU, 68*, 439, 1987.

Atwater, T., Implications of plate tectonics for the Cenozoic tectonic evolution of western North America, *Geol. Soc. Am. Bull., 81*, 3513–3536, 1970.

Barelli, A., and A. Palama, A new method for evaluating formation equilibrium temperature in holes during drilling, *Geothermics, 10*, 95–102, 1981.

Biehler, S., Gravity studies in the Imperial Valley, in *Cooperative Geological-Geophysical Investigations of Geothermal Resources in the Imperial Valley Area of California*, pp. 29–41, University of California, Riverside, 1971.

Blake, M. C., Jr., R. H. Campbell, T. W. Dibblee, Jr., D. G. Howell, T. H. Nilsen, W. R. Normark, J. C. Vedder, and E. A. Silver, Neogene basin formation in relation to plate-tectonic evolution of the San Andreas fault system, California, *Am. Assoc. Pet. Geol. Bull., 62*, 344–372, 1978.

Bredehoeft, J. D., and I. S. Papadopulos, Rates of vertical groundwater movement estimated from the Earth's thermal profile, *Water Resour. Res., 1*, 325–328, 1965.

Chinnery, M. A., The deformation of the ground around surface faults, *Bull. Seismol. Soc. Am., 51*, 355–372, 1961.

Chinnery, M. A., The stress changes that accompany strike-slip faulting, *Bull. Seismol. Soc. Am., 53*, 921–932, 1963.

Crowell, J. C., Origin of late Cenozoic basins in southern California, in *Tectonics and Sedimentation, Spec. Pap. 22*, edited by W. R. Dickinson, pp. 190–204, Society of Economic Paleontologists and Mineralogists, Tulsa, Okla., 1974.

Elders, W. A., and L. H. Cohen, The Salton Sea geothermal field, California, as a near-field material analog of a radioactive waste repository in salt, *Publ. BMI/ONWI-513*, 138 pp., Battelle Mem. Inst., Columbus, Ohio, 1983.

Elders, W. A., R. W. Rex, T. Meidav, P. T. Robinson, and S. Biehler, Crustal spreading in southern California, *Science, 178*, 15–24, 1972.

Freund, J. E., *Mathematical Statistics*, 389 pp., Prentice-Hall, Englewood Cliffs, N. J., 1962.

Fuis, G. S., W. D. Mooney, J. H. Healy, G. A. McMechan, and W. J. Lutter, Crustal structure of the Imperial Valley region, The Imperial Valley, California, Earthquake of October 15, 1979, *U.S. Geol. Surv. Prof. Pap., 1254*, 25–49, 1982.

Fuis, G. S., W. D. Mooney, J. H. Healy, G. A. McMechan, and W. J. Lutter, A seismic refraction survey of the Imperial Valley region, California, *J. Geophys. Res., 89*, 1165–1189, 1984.

Full, W. E., Processes of lithosphere thinning and crustal rifting in the Salton Trough, southern California, Master's thesis, Univ. of Ill., Urbana, 1980.

Goddard, E. N. (Chairman), Geologic map of North America, North American Geologic Map Committee, U.S. Geological Survey, Reston, Va., 1965.

Griscom, A., and L. J. P. Muffler, Aeromagnetic map and interpretation of the Salton Sea geothermal area, California, *U.S. Geol. Surv., Geol. Invest. Map, GP754*, 1971.

Helgeson, H. C., Geologic and thermodynamic characteristics of the Salton Sea geothermal system, *Am. J. Sci., 266*, 129–166, 1968.

Herzig, C. T., and J. M. Mehegen (Eds.), Salton Sea scientific drilling project, California State 2-14 well visual core descriptions, *Rep. UCR/IGPP-86/1*, Inst. of Geophys. and Planet Phys., Univ. of Calif., Riverside, 1986.

Hill, D. P., P. Mowinckel, and Z. G. Peake, Earthquakes, active faults and geothermal areas in the Imperial Valley, California, *Science, 188*, 1306–1308, 1975.

Jaeger, J. C., Application of the theory of heat conduction to geothermal measurements, in *Terrestrial Heat Flow*, Geophys. Monogr.

Ser., vol. 8, edited by W. H. K. Lee, pp. 7–23, AGU, Washington, D. C., 1965.

Kasameyer, P. W., and J. R. Hearst, Borehole gravity measurements in the Salton Sea Scientific Drilling Program well State 2-14, *J. Geophys. Res.*, this issue.

Kasameyer, P. W., L. W. Younker, and J. M. Hansen, Development and application of hydrothermal model for the Salton Sea geothermal field, California, *Geol. Soc. Am. Bull.*, *95*, 1242–1252, 1984.

Kelley, V. C., and J. L. Soske, Origin of the Salton volcanic domes, Salton Sea, California, *J. Geol.*, *44*, 496–509, 1936.

Lachenbruch, A. H., Thermal effects of the ocean on permafrost, *Geol. Soc. Am. Bull.*, *68*, 1515–1530, 1957.

Lachenbruch, A. H., J. H. Sass, and S. P. Galanis, Jr., Heat flow in southernmost California and the origin of the Salton Trough, *J. Geophys. Res.*, *90*, 6709–6736, 1985.

Lee, T.-C., and L. Cohen, Onshore and offshore measurements of temperature gradients in the Salton Sea geothermal area, California, *Geophysics*, *44*, 206–215, 1979.

Lee, T.-C., T. L. Henyey, and B. N. Damiata, A simple method for the absolute measurement of thermal conductivity of drill cuttings, *Geophysics*, *51*, 1580–1584, 1986.

Lilje, A., and J. M. Mehegan (Eds.), Salton Sea scientific drilling project, California State 2-14 well core summaries, *Rep. UCR/IGPP-86/2*, Inst. of Geophys. and Planet. Phys., Univ. of Calif., Riverside, 1986.

Muramoto, F. S., and W. A. Elders, Correlation of wireline log characteristics with hydrothermal alteration and other reservoir properties of the Salton Sea and Westmorland Geothermal Fields, Imperial Valley, California, USA, *Los Alamos Natl. Lab. Rep., LA-10128-MS*, 1984.

Newmark, R. L., P. W. Kasameyer, L. W. Younker, and P. C. Lysne, Research drilling at the Salton Sea g–othermal field, California: The shallow thermal gradient project, *Eos Trans. AGU*, *67*, 698–707, 1986.

Newmark, R. L., P. W. Kasameyer, and L. W. Younker, Preliminary report on shallow drilling in the Salton Sea Region, *UCID 21484*, Lawrence Livermore Natl. Lab., Univ. of Calif., 1988.

Rex, R. W., The origin of brines of the Imperial Valley, California, *Trans. Geotherm. Resour. Counc.*, *7*, 321, 1983.

Riney, T. D., J. W. Pritchett, and S. K. Garg, Salton Sea geothermal reservoir simulation, paper presented at the Third Workshop on Reservoir Engineering, Stanford Univ., Stanford, Calif., 1977.

Robinson, P. T., W. A. Elders, and L. J. P. Muffler, Quaternary volcanism in the Salton Sea geothermal field, Imperial Valley, California, *Geol. Soc. Am. Bull.*, *87*, 347–360, 1976.

Rodgers, D. A., Analysis of basin development produced by en echelon strike slip faults, in *Sedimentation in Oblique-Slip Mobile Zones*, edited by P. F. Ballance and H. C. Reading, pp. 27–41, International Association of Sedimentologists, Oxford, England, 1980.

Sass, J. H., S. P. Galanis, Jr., A. H. Lachenbruch, B. V. Marshall, and R. J. Munroe, Temperature, thermal conductivity, heat flow, and radiogenic heat production from unconsolidated sediments of the Imperial Valley, California, *U.S. Geol. Surv. Open File Rep., 84-490*, 37 pp., 1984.

Sass, J. H., S. S. Priest, L. E. Duda, C. C. Carson, J. D. Hendricks, and L. C. Robinson, Thermal regime of the State 2-14 well, Salton Sea Scientific Drilling Project, *J. Geophys. Res.*, this issue.

Segall, P., and D. D. Pollard, Mechanics of discontinuous faults, *J. Geophys. Res.*, *85*, 4337–4350, 1980.

Sturtevant, R. G., and A. E. Williams, Oxygen isotopic profiles for the State 2-14 Geothermal Well: Evidence for a complex thermal history (abstract), *Eos Trans. AGU*, *68*, 445, 1987.

Von Herzen, R. P., and A. E. Maxwell, The measurement of thermal conductivity of deep sea sediments by a needle probe method, *J. Geophys. Res.*, *64*, 1557–1563, 1959.

Von Herzen, R. P., and S. Uyeda, Heat flow through the eastern Pacific ocean floor, *J. Geophys. Res.*, *68*, 4219–4250, 1963.

Younker, L. W., P. W. Kasameyer, and J. Tewhey, Geological, geophysical and thermal characteristics of the Salton Sea geothermal field, California, *J. Volcanol. Geotherm. Res.*, *12*, 221, 1982.

P. W. Kasameyer, R. L. Newmark, and L. W. Younker, Earth Sciences Department, Lawrence Livermore National Laboratory, University of California, Livermore, CA 94550.

(Received September 25, 1987;
revised March 22, 1988;
accepted May 9, 1988.)

JOURNAL OF GEOPHYSICAL RESEARCH, VOL. 93, NO. B11, PAGES 13,025–13,036, NOVEMBER 10, 1988

Analysis of *P* and *S* Wave Vertical Seismic Profile Data From the Salton Sea Scientific Drilling Project

THOMAS M. DALEY, THOMAS V. MCEVILLY, AND ERNEST L. MAJER

Center for Computational Seismology, Lawrence Berkeley Laboratory, University of California, Berkeley

As part of the Salton Sea Scientific Drilling Project at California State well 2-14, vertical seismic profile (VSP) data were collected from *P* and *S* wave sources at two distances from the well. Use of a three-component geophone, along with rotation of the recorded data traces into a wave front-based coordinate system, allows analysis of many aspects of seismic wave propagation properties around the well. Standard VSP analysis techniques were used to measure interval *P* and *S* wave velocities and to identify reflecting horizons both within and below the survey interval (from 455 to 1735 m). A reflection from below the survey interval, seen with both *P* and *S* sources, seems to be associated with a fractured reservoir near 2100 m. Indications of fracturing were observed, including vertical scattering of *P* waves from a zone near 915 m. Orthogonally polarized shear waves were generated at each offset to study anisotropy by travel time measurement and particle motion analysis of the shear wave arrivals. Three-component particle motion analysis of shear wave arrivals was found to be effective for characterizing the subtleties in the *S* wave splitting throughout the various zones in the well. The SH_1 source (horizontal and transverse to the well) produced complicated, elliptical particle motion while the SV source (in-line with the well) produced linear particle motion. The difference in linearity of particle motion from orthogonally polarized shear wave sources was unexpected and may be related to regional tectonics. Anomalous zones may be related to transition depths in the Salton Sea geothermal field. Travel time difference between *SV* and *SH* waves, while clearly observable, indicates only about 1% average anisotropy.

INTRODUCTION

In March 1986 the Salton Sea Scientific Drilling Project (SSSDP) completed drilling California State well 2-14, near the Salton Sea geothermal field in southern California, to a depth of 3200 m. The well was drilled by the Department of Energy (DOE) as part of the Geothermal Technology Development program with scientific studies in the well funded by the Basic Energy Sciences Office of DOE, the National Science Foundation, and the U.S. Geological Survey (USGS). As part of the SSSDP, a *P* and *S* wave vertical seismic profile (VSP) was conducted by the Earth Sciences Division, University of California, Lawrence Berkeley Laboratory. The objectives of this VSP were to obtain information on the seismic velocity near the well; to identify reflective horizons within, and possibly beneath, the well interval; to detect evidence of fracture zones surrounding the well, including indications of geothermal reservoirs; and to incorporate a shear wave source to investigate seismic shear wave velocity distribution and anisotropy, which can be influenced by fracturing.

The VSP method has been proven a useful tool for the delineation of seismic wave propagation properties near a well [*Hardage*, 1985]. It is assumed that the reader is somewhat familiar with VSP data, including the extraction of upgoing and downgoing waves, the presence of tube waves, and the identification of reflector depth. Several good review articles are available, such as *Oristaglio* [1985] and *Kennett et al.* [1980]. The use of VSP to study fracture-induced anisotropy is a growing field of study [*Majer et al.*, 1988; *Becker and Perelberg*, 1987; *Corrigan et al.*, 1987]. The SSSDP VSP provides fairly complete data from an area of complex geology, where structure and fracture properties are not well understood but may be expected to affect wave propagation. Previous geophysical surveys in the area and the general stratigraphy of the Salton Sea geothermal field (SSGF) are summarized by *Younker et al.* [1982].

The Salton Sea VSP data analysis is divided into basic interpretation (velocity and reflectivity analysis) and the anisotropy study. A combined interpretation of the results, with proposed geologic causes for observed events, is presented within the anisotropy section. Interpretation of the various observations from VSP data must incorporate good geologic control, especially in the use of the more experimental techniques such as particle motion analysis. Currently, only preliminary findings about the SSSDP section are available. Available lithologic information (Figure 1) gives the fractional content of sandstone, siltstone, and claystone with the amount of alteration from sulfides, anhydrite, chlorite, and epidote. Gaps such as the one from 2040 to 2100 m are due to lost circulation which prevented mud logging and core samples. Among the factors which may affect the VSP data are the local stratigraphy, fractures with or without fluid, and regional tectonic stress.

SURVEY DESIGN AND DATA ACQUISITION

Data were collected from two source locations, a near offset of 91 m from the well and a far offset of 701 m (note that English units, still in predominant use in the drilling industry for depths and diameters, were used for the VSP design and acquisition and have been rounded off to the nearest meter). The number of source locations, along with other design parameters, was constrained by a time limit, known beforehand, of about 40 hours of data acquisition. The survey was designed to obtain maximum scientific information within this time constraint. High temperatures and unstable open hole conditions restricted the geophone receiver to the cased section of the well above 1750 m. To obtain multicomponent

Paper number 88JB03073.
0148-0227/88/88JB-03073$05.00

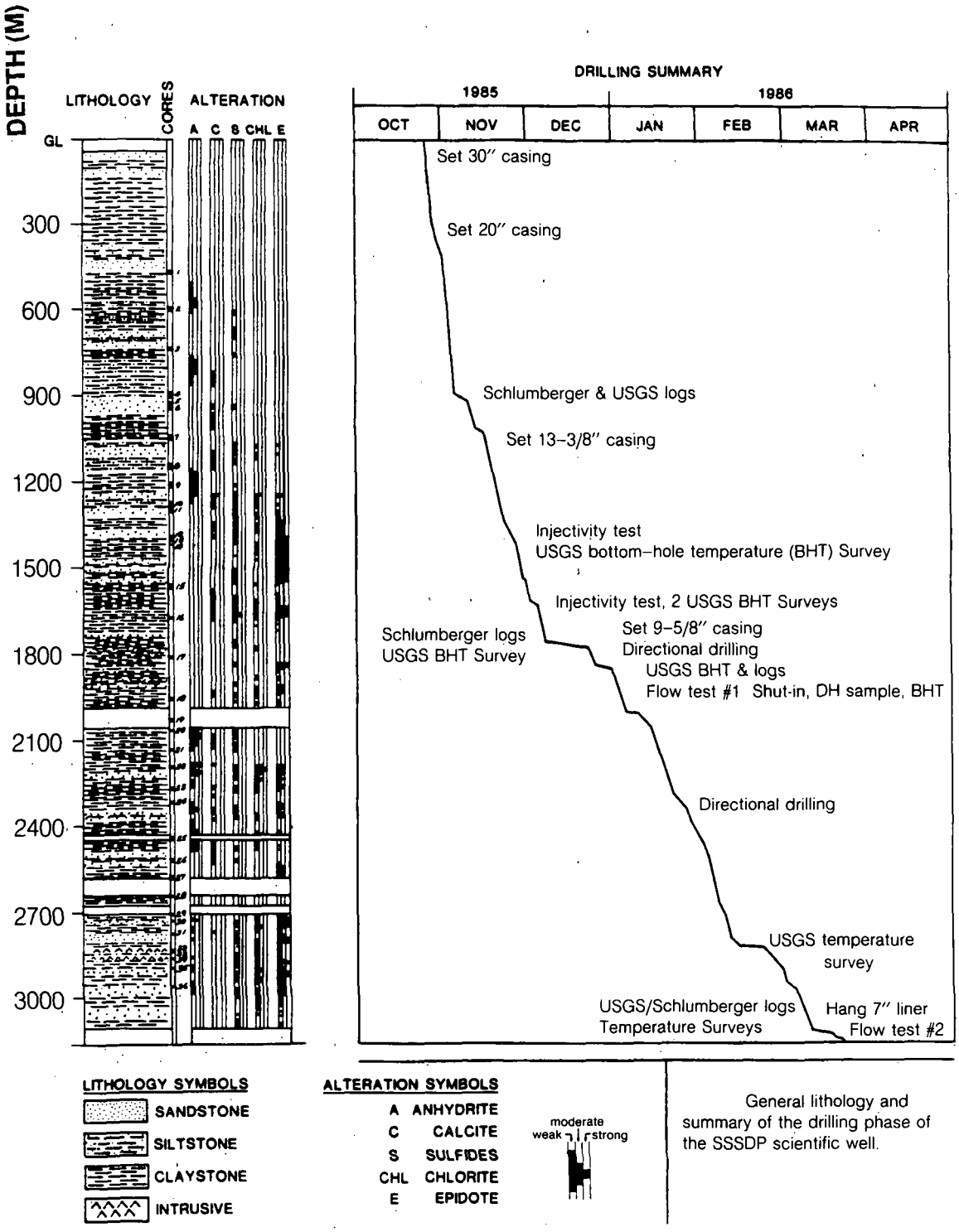

Fig. 1. General lithology of SSSDP well and summary of drilling activities [from *Elders*, 1986].

seismic information, *P* wave and shear wave Vibroseis (a trademark of CONOCO Inc.) sources were used.

The vibrator source sweep was a 16-s, 8- to 55-Hz upsweep. A Failing Y600 BD *P* wave vibrator and a Mertz model 13 shear wave vibrator were used. The vibrators were provided by Lawrence Berkeley Laboratory and the wireline service was provided by the USGS. The planned investigation of the three-dimensional nature of the seismic wave field necessitated a three-component borehole geophone, which was provided by Seismograph Service Corporation. Data were recorded on a Texas Instruments DFS-IV 24-channel seismic data acquisition system, uncorrelated, at 2-ms sample rate, with a 20-s record length including the 16-s sweep.

Two orthogonal polarizations of the shear wave vibrator were used for investigation of anisotropy. The labeling convention used here for the shear sources is based on the geometry of the transverse particle motion expected for the *S* wave in an isotropic media (see Figure 2). For the sources labeled SH_r and SV the vibrator pad moves radially toward the well. The term SH_r is used at the near offset where all *S* wave

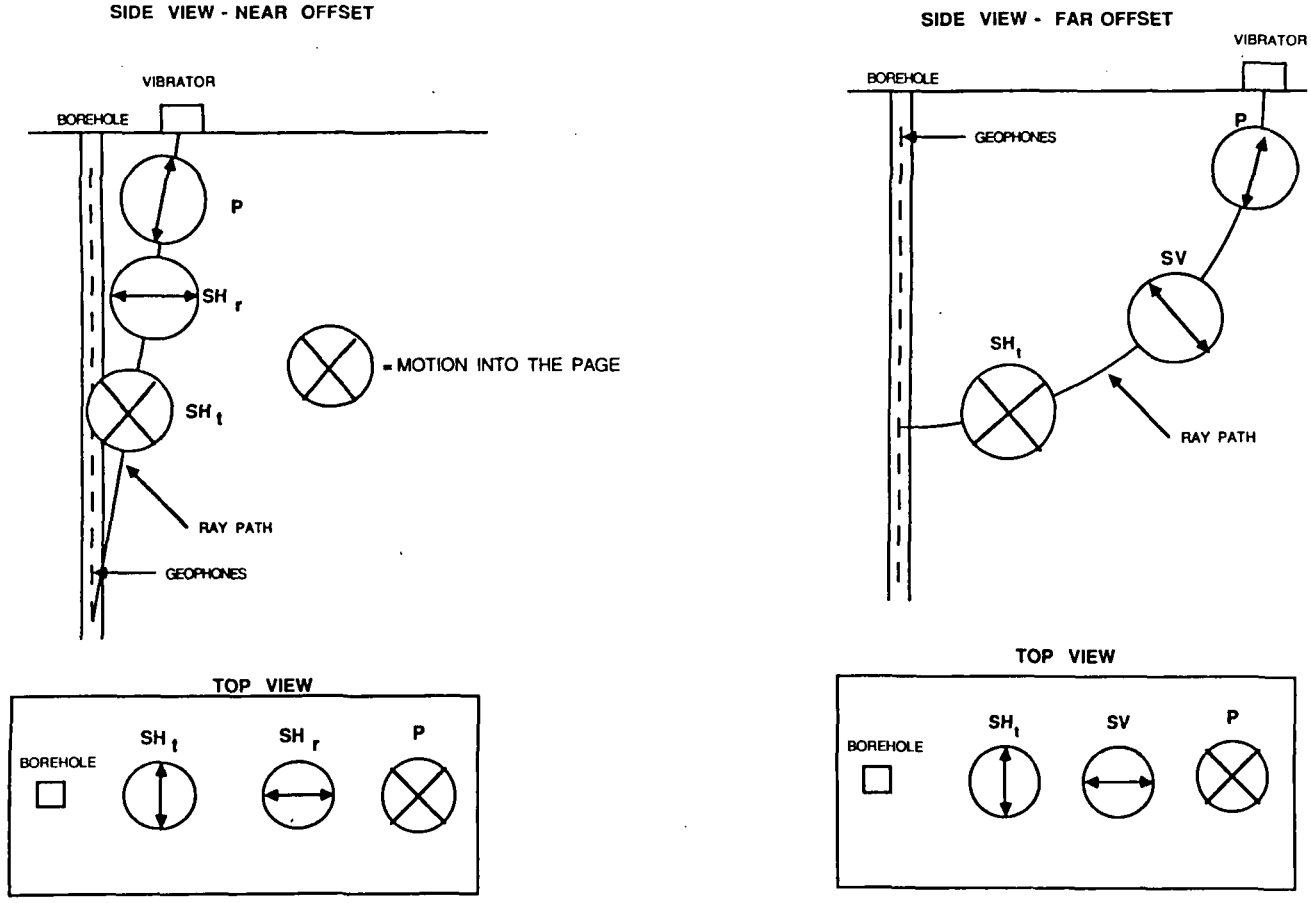

Fig. 2. Diagram of expected particle motion for the three sources used at each offset. Side views shows motion with respect to ray path for isotropic material. Top view shows polarization of sources. Arrows indicate direction of isotropic particle motion.

polarizations will produce essentially horizontal particle motion at the receiver positions, and the conventional term SV is used at the far offset. For both offsets the term SH_t is used for the shear source with vibrator pad moving transverse to a line from the well, generating, in an idealized medium, the conventional *SH* wave (Figure 2).

The labeling of shear wave arrivals is complicated since the VSP data show the surrounding material to be anisotropic, implying that a simple model of separate *SV* and *SH* propagation does not hold. The shear wave first arrivals have a complex three-dimensional particle motion, presumably due to interference of the split *S* wave phases which are only slightly separated in time. The terms *SH* and *SV* will be taken generally to mean the component of shear wave particle motion in the horizontal plane or in the vertical plane, respectively. Source names are not italicized (i.e., SH_t, SH_r, SV) in order to differentiate them from seismic wave arrivals and from geophone components.

The near-offset data, taken at 15.24-m depth intervals, provided velocity information for vertical wave propagation. The 22.86-m depth intervals were used in the far offset, sacrificing spatial sampling for time constraints. The azimuth of both offsets was S45E, corresponding to the strike of the Salton Trough. This azimuth orients the two shear wave polarizations parallel and perpendicular to the axis of the trough.

Severe noise problems hampered the near-offset survey. Noise was worst in the depth range between 760 and 1220 m, affecting the horizontal components more than the vertical. High temperatures in the well stopped an effort to extend the survey to 2165 m depth at the far offset when the tool failed after two levels (2165 and 2135 m) were recorded with the *P* source.

ROTATION OF BOREHOLE GEOPHONE COMPONENTS

Three orthogonal components of ground motion were recorded at each level in the well, with the *Z* component aligned on the axis of the tool which should be vertical since the VSP was performed in a nearly vertical section of the well ($<10°$ deviation). The orientation of the horizontal components, *X* and *Y*, is unknown because a borehole geophone rotates around its axis on the wireline cable that supports it, causing the horizontal geophones to be oriented differently at each level.

Assuming that the first arrival is a *P* wave with linear particle motion, the orientation of the three geophone components can be determined with respect to the *P* wave particle motion.

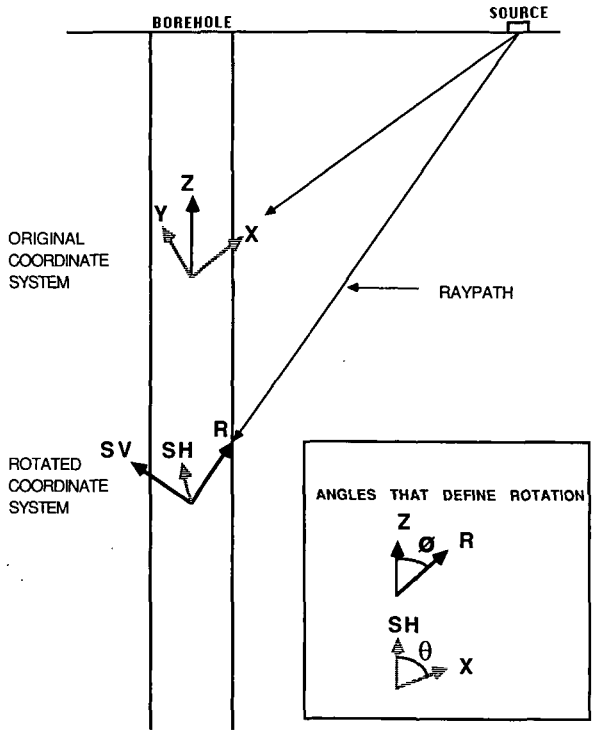

Fig. 3. Diagram of coordinate rotation for three-component borehole geophone. Original, randomly oriented horizontal coordinate system (top) is rotated into the "wave front" coordinate system (bottom) for data analysis. The rotation requires two angles ϕ and θ. Shaded arrows are in the horizontal plane.

New data decompositions can then be generated by projecting the geophone motion onto any orthogonal coordinate system. This projection or "rotation" of coordinates is defined by the angles ϕ and θ (Figure 3). The wave front-based coordinate system used here has coordinates oriented in directions in which the P wave, SH wave, and SV wave arrivals would be polarized for an isotropic material (labeled radial (R), SH, and SV, respectively). The coordinates will have a different orientation at each depth, depending on the P wave ray path. Only if the axial geophone component is vertical and the ray paths lie in a vertical plane will the wave front rotation give an absolute orientation with respect to the surface.

The method used to rotate the VSP data is the eigenvector analysis of the covariance matrix [*Kanasewich*, 1981] which gives the two rotation angles ϕ and θ from the direct P wave arrival. New data traces in the wave front coordinate system, R, SV, and SH, are computed from the recorded components (X, Y, and Z) by the following matrix operation:

$$\begin{bmatrix} R \\ SV \\ SH \end{bmatrix} = \begin{bmatrix} \cos\phi & \cos\theta\sin\phi & \sin\phi\sin\theta \\ -\sin\phi & \cos\theta\cos\phi & \sin\theta\cos\phi \\ 0 & -\sin\theta & \cos\theta \end{bmatrix} \begin{bmatrix} Z \\ X \\ Y \end{bmatrix} \quad (1)$$

The quality of the data-derived rotation angles depend on the degree of linearity in the recorded P wave arrival particle motion. The consistency of the resulting angles suggest that the orientation of the wave front is estimated with uncertainties no greater than 5° or 10°. For data with noisy or dead traces, θ was determined by interpolation of values at nearby levels.

For the near-offset the P wave rotation was applied to the P, SH, and SV source data, which assumes the shear waves have essentially the same near-vertical ray path as the P waves. For the far-offset with nonvertical rays, the first arrival times show that the ray paths were different for P and S waves (Figures 4 and 5). The shear waves have a turning point at about 850 m (Figure 5) with upward propagation in the shallow section, whereas the P wave direction of propagation is downward through the entire depth range (Figure 4), demonstrating different vertical velocity gradients.

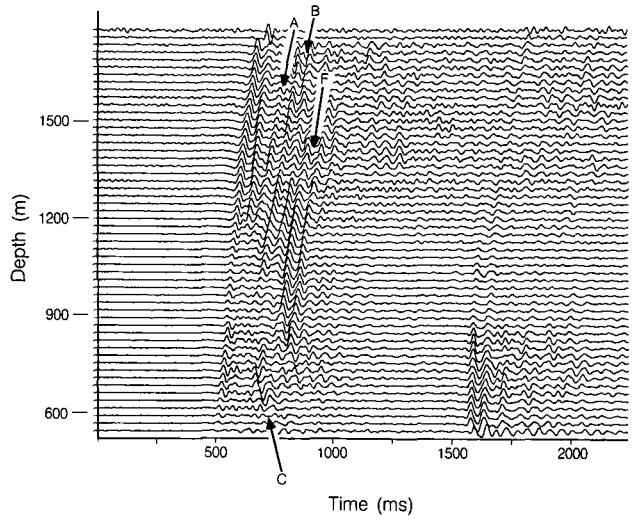

Fig. 4. Far-offset P source, vertical component data. Events A, B, C, and F are interpreted as vertically traveling, scattered P wave energy. The event at 1.6 s is a shear wave arrival.

A method of correcting the rotation to the shear wave ray path is available from analysis of the SV source data. After the P wave rotation angles were applied, linear particle motion for the S wave arrival from the SV source is seen to be rotated from the P wave based SV component. The angle between the SV-generated motion and the P wave based SV component

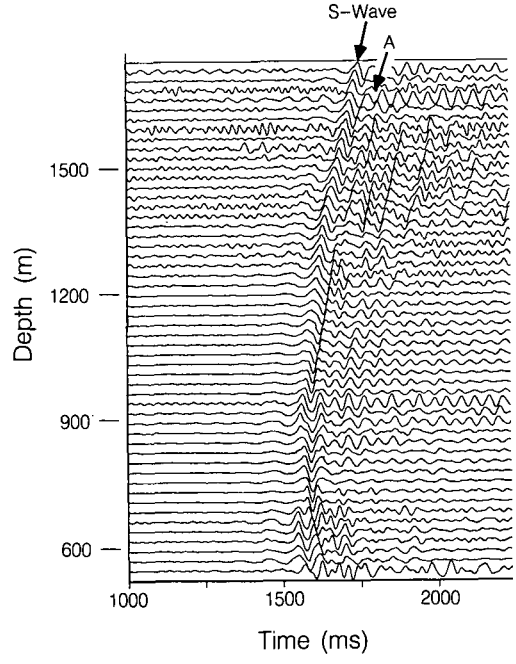

Fig. 5. Far-offset SH_t and SH component data. Event A is interpreted as a vertically scattered P wave event. Note the turning point for the S wave at about 850 m.

varies with depth in a consistent manner, and it is interpreted to be the angular difference δ between the P wave incidence and the S wave incidence. The angular difference δ can be found with a two dimensional application of the covariance matrix algorithm [*Kanasewich*, 1981] and then added to ϕ from the P wave rotation, providing a further rotation of the SV-generated data. The SH component is not changed since the ray path error is assumed to be in the R-SV plane.

S wave arrivals from SH_t and SV sources exhibit different angles of incidence, but the difference angle for the SH_t source cannot be recovered because the SH_t source data do not have linear arrivals. The SH_t source data were therefore rotated with the same angles used for data for the SV source. The difference between SH_t and SV ray paths, fortunately, should be much less than the difference between P and SV ray paths since the error comes from differences in the respective velocity gradients.

DATA ANALYSIS

Velocity and Poisson's Ratio Measurement

Near-offset VSP data provide a direct measurement of vertical travel times to each receiver depth, allowing interval velocities to be computed between receivers. First arrival times were picked on the first peak of the P wave wavelet and the first trough of the shear wave wavelet. The shear wave arrival was picked differently because its trough had consistently better signal-to-noise ratio than its peak. The static time shift between picks of P and S arrivals needs no correction for interval velocity calculation. The P wave travel time was picked from the rotated R component, the SH_t travel time was picked from the rotated SH component, and the SH_r and SV travel times were picked from the rotated SV component. The quality of near-offset data ranges from excellent for the P wave source to very poor quality for both shear sources between 760 and 1220 m. Many of the near-offset shear wave arrivals were too noisy to pick.

Interval velocities were calculated between those depth levels with usable first arrivals and averaged over intervals where signals were to noisy to pick. Estimated uncertainty of the picks is ± 2 ms for P waves, and ± 5 ms for S waves.

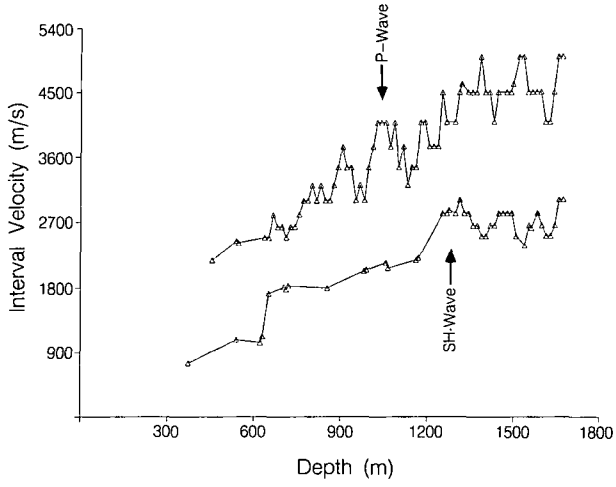

Fig. 6. Measured interval velocities (in meters per second) for near-offset P source and SH_t source. The points plotted area at the center of the computed interval which was 30.5 m unless poor arrivals required a larger interval to be used.

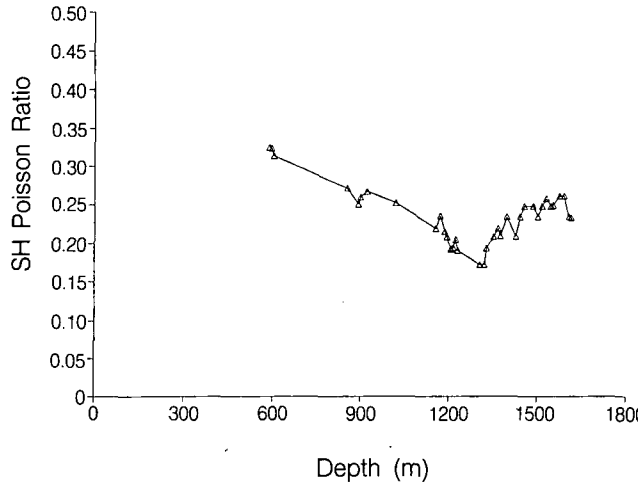

Fig. 7. Poisson's ratio calculated from measured interval velocities. The points plotted are at the center of the computed interval which was 152.4 m unless poor arrivals required a larger interval be used.

When calculating velocities, a straight ray path assumption is used to correct the borehole depth for the extra propagation distance due to the 91-m source offset. Figure 6 shows the computed velocities across intervals of 30.5 m. Poisson's ratio σ was computed from the P and SH_t wave velocities and results are given in Figure 7 for 150-m averaging intervals. The σ appears to decrease fairly smoothly from typical values for sedimentary rocks at 610 m to values, below 1220 m, that are generally characteristic of dry or crystalline rock. Below 1220 m there is a large increase in sulfite, chlorite, and epidote alteration (Figure 1), and the seismic signals exhibit much greater signal-to-noise ratios than shallower. A possible cause of this transition is the beginning of large-scale hydrothermal activity which is indicated by the increased alteration.

Reflectivity Analysis

The VSP data sets provide measurement of seismic reflection properties of the material surrounding the SSSDP well for both P and S waves. Surface reflection surveys in geothermal areas have generally poor data quality [*Severson*, 1987], but VSP has the advantage of receivers at depth [*Hardage*, 1985]. The events identified in data from this VSP survey include primary reflections, multiples, tube waves, and scattered waves. The near-offset P wave survey and all the far-offset surveys show strong reflections. The near-offset shear source surveys were too noisy to be used for reflection identification.

Identification of Events Within VSP Survey Depths

The reflectors within the depth range covered by the VSP survey are relatively weak, and none are seen to be generated by all of the sources. The vertical component near-offset P source data contain numerous events (Figure 8), but data recorded from the far-offset P source are probably the most interesting and unusual in the survey. The SV component (Figure 9) is quite anomalous, with a number of unexpected downgoing events dominating the first second of data. The downgoing events do not have the same apparent velocity as the downgoing first arrivals. Rather, the downgoing events labeled A and B, and the upgoing event C, have the same moveout as the near-offset P wave arrivals, implying that

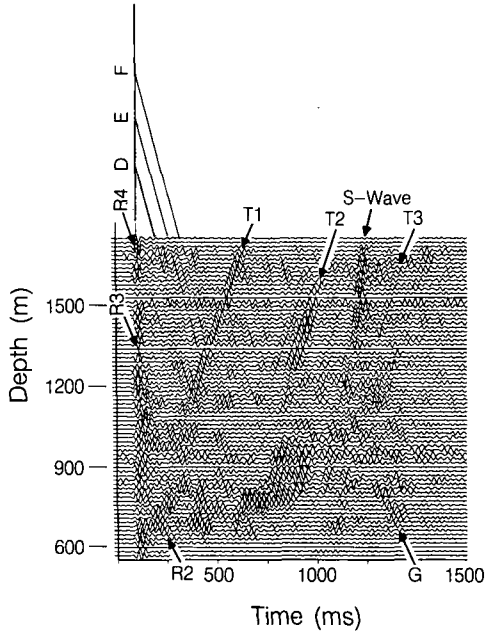

Fig. 8. Near-offset *P* source, vertical component data. Section is dip filtered to attenuate downgoing *P* wave energy, high-pass filtered at 25 Hz, and time shifted to align first *P* wave arrivals at 100 ms. Events T1, T2, and T3 are tube waves with average velocity, measured from moveout of event T1, of 1465 m/s. Events D, E, and F are reflections from below the survey interval at approximately 2025, 2135, and 2310 m, respectively. Note that event D appears on only a few traces, but it does have the moveout of a reflection. Events R2, R3, and R4 are reflections from within the data interval at approximately 885, 1340, and 1660 m, respectively. Even G is a *P* wave converted reflection generated by the shear wave at about 1250 m. This reflection appears to be a mode-converted *P* wave, based on its estimated velocity of 3200 m/s compared to the *P* wave velocity of 2955 m/s in the same zone. T3 also appears to be generated by the shear wave at about 915 m.

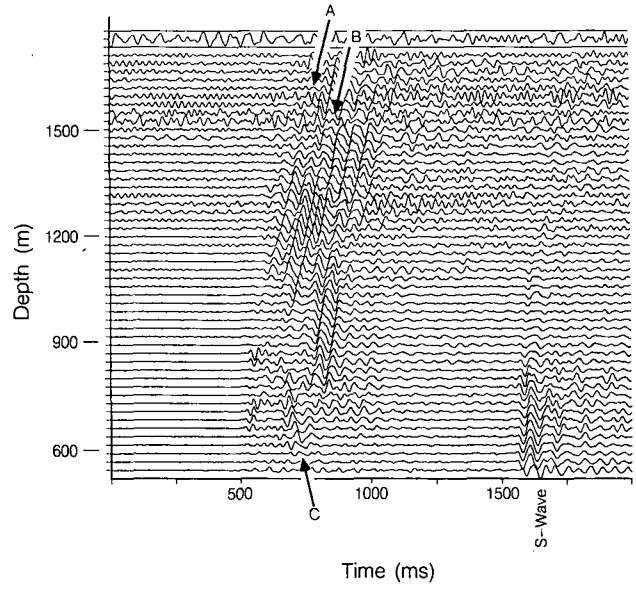

Fig. 9. Far-offset *P* source, *SV* component data. Events A, B, and C have anomalous moveouts, equivalent to near-offset *P* waves. They appear to be vertically scattered *P* wave energy generated near 915 m.

these events are vertically traveling *P* waves. Vertically traveling *P* waves would be seen on the *SV* component because the rotation angle ϕ, for the far-offset *P* source, is between 50° and 85°. This renders the *SV* component largely vertical, thus sensitive to vertically traveling *P* waves, whether upgoing or downgoing. To best see a vertically polarized wave, the original unrotated vertical geophone component (Figure 4) should be used. Events A, B, and C are strong and coherent, even though the direct *P* ray has oblique incidence and the first arrival is weak. The event labeled F is more coherent here than on the *SV* component (Figure 9). The best interpretation of events A, B, C, and F is that they are *P* wave energy that has been scattered near the well. The depth of generation can be estimated by looking at events B and C which may be upgoing and downgoing waves from the same source. They have opposite polarity and can be traced back to a common point at the 915 m depth. They appear some 100 ms after the first arrival, implying they were generated at some finite but small offset from the well, causing the delay. Figure 10 shows a schematic of the proposed scattering phenomenon.

A likely cause of *P* wave scattering, given the known geologic environment, is a localized zone of fracturing or, perhaps, a boundary zone between open fractured rock and impermeable sealed rock. This explanation is suggested by studies of cores taken between 918 and 920.5 m, which were found to have fractures which are "presently open and permeable" in a matrix of "chloritized and epidotized crossbedded sandstone and shales" [*McKibben and Andes*, 1986]. This depth is also the only zone above 1830 m which had fluid loss during drilling and was considered a possible flow zone. In fact, it was thought that a reservoir might be found near this depth because of projections made from wells in the SSGF, but the low rate of fluid loss and low permeability led to a decision to not test this zone (J. H. Sass, personal communication, 1987). Near this zone, the far-offset *P* source vertical component data (Figure 11) indicate a reflection from approximately 855 m (labeled event D), which is probably from the same horizon as event R2 in Figure 8. The different moveout between events D and C illustrates the different apparent velocity of energy scattered near the well and reflected energy.

In the *SH* component data for the far-offset SH_1 source (Figure 5) there is a turning point at 855 m where the *S* wave ray path is horizontal at the well (exhibiting very high apparent vertical velocity). The first arrival wavelet changes at 945 m with a downgoing event (event A) emerging and exhibiting different moveout than the direct shear arrival. This event has the same apparent vertical velocity as the near-offset, vertically propagating *P* waves. Apparently, the zone near 915 m is

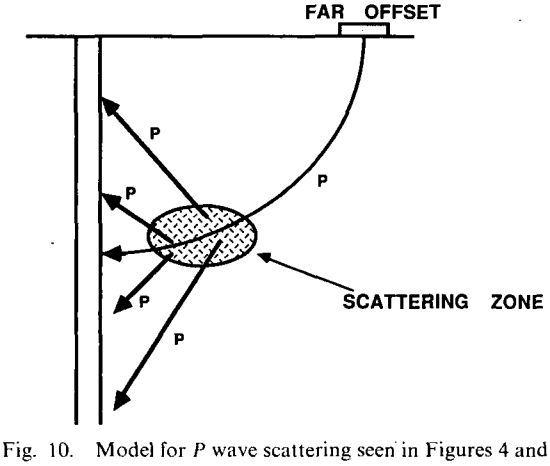

Fig. 10. Model for *P* wave scattering seen in Figures 4 and 9.

scattering P waves near the well from the more horizontally incident shear waves, with the scattered waves propagating vertically downward with a slower apparent vertical velocity than the incident shear waves.

The far-offset SV source data (Figure 12) show the first arrival having nearly constant travel time between 610 and 760 m, in contrast to the upturned ray path seen for SH_t (Figure 5), indicating a less steep shallow velocity gradient for SV. The radial component of the SV source (Figure 13) shows some energy in the main shear arrival, and two separate events before the shear arrival, labeled K and L. These events are probably forward scattered P waves, generated away from the well, which have moved out in front of the shear waves. An estimate can be made of the distance from the well at which these scattered P waves were generated by using the measured velocities with the relation

$$X = \frac{\Delta T V_P V_S}{V_P - V_S} \tag{2}$$

where

X distance of scatterer from well;
ΔV Travel time difference between scattered P wave and first S wave;
V_P P wave average velocity;
V_S S wave average velocity.

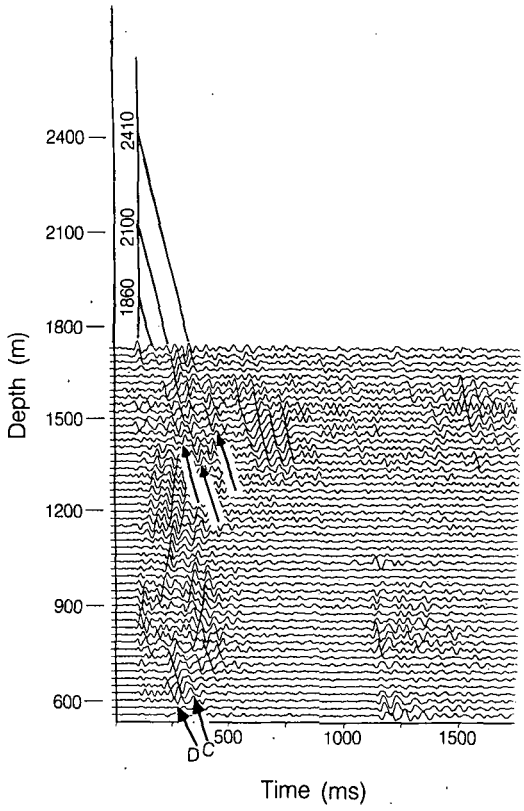

Fig. 11. Reflector depth estimation for far-offset P source, vertical component. Section is time shifted to align first arrivals and dip filtered to attenuate downgoing energy. Three deep events are identified with generation depths estimated at 1860, 2100, and 2410 m. Event D is a P wave reflection from 855 m. Event C is a vertically scattered P wave event. The different moveout of events D and C indicate different modes of generation.

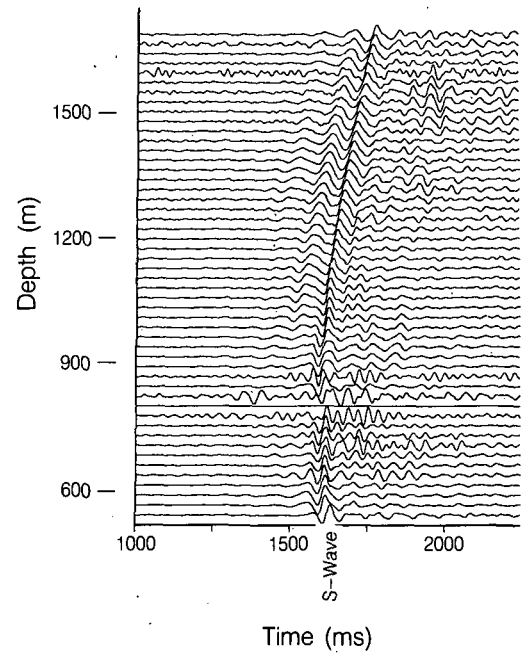

Fig. 12. Far-offset SV source, SV component data. Compare the ray turning to SH_t data in Figure 5.

The distance from the well to the scattering source is estimated to be 490 m for event K, which would be roughly half the distance from the source to the receiver at the 610 m depth. Given the near-horizontal incidence of the ray paths at this depth, it seems reasonable to assume the scatterer is offset horizontally. A second scattered event (labeled "L") is seen later on the radial component, apparently from a scatterer 455 m from the receiver at the 915 m depth. It is likely, though not necessary, that events K and L are scattered from the same type of heterogeneity as the vertically scattered P waves generated by the P and SH_t sources.

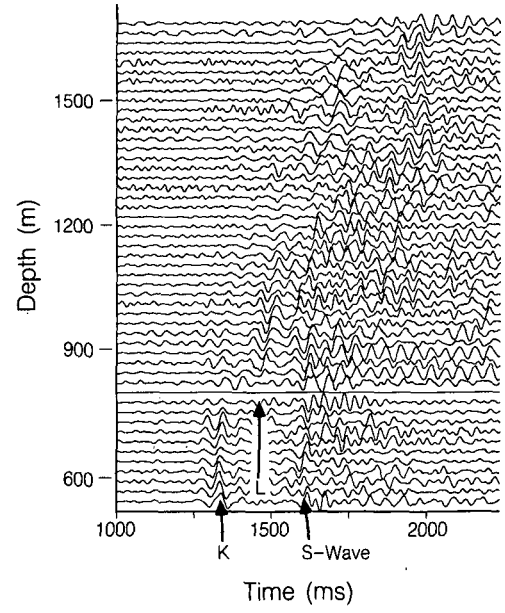

Fig. 13. Far-offset SV source, radial component data. Events K and L are interpreted as P wave events which are forward scattered by the shear wave and have separated in time. A strong reflection from below the survey interval is seen at 1.9 s.

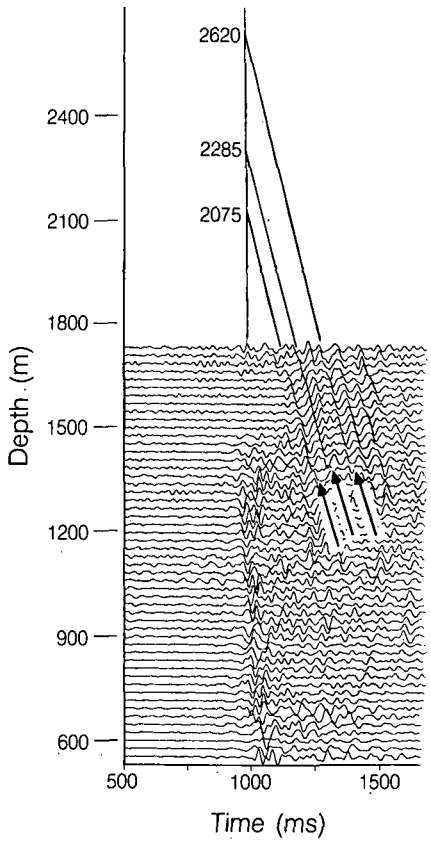

Fig. 14. Estimated reflector depth for far-offset SH_t source, vertical component data. Section is dip filtered to attenuate downgoing energy and time shifted to align first arrivals. Three reflections are identified with estimated generation depths of 2075, 2285, and 2620 m. The 2620-m event could be an interval reflection between the 2075- and 2285-m reflectors, but its strength suggests that it is a primary event.

Identification of Reflections From Below Survey Depths

Although the VSP survey was limited to receivers above 1720 m, there is sufficient energy reflected from below this depth to allow estimation of the depth of sources for this energy, providing information relating to deeper structures. In the near offset *P* source data (Figure 8), event E is the strongest reflection, and it is difficult to say if later events, such as event F, are upgoing multiples of E, or primary reflections. The depth at which a reflection is generated may be estimated by projecting the event down the section until it intersects the first arrival [*Hardage*, 1985]. The depth of intersection is the depth of generation, assuming a constant average velocity over the projection. Reflections from the far-offset *P* source were found when the vertical component section was dip filtered [*Hale and Claerbout*, 1983] to attenuate downgoing energy. Figure 11 shows reflections with estimated depths of 1860, 2100, and 2410 m. Later upgoing events (after 0.6 s) appear to be primary reflections of the vertically scattered *P* wave energy in addition to multiples of the primary reflections. Figure 14 shows an aligned dip filtered section of the SH_t source vertical component data. The traces were aligned for optimization of dip filtering and to allow easier identification of reflection depths. Reflector depths were estimated at 2075, 2285, and 2620 m; 2075–2135 m is a zone of lost circulation, suggesting that the reflection generated in this zone, and seen on all sections, is associated with a fractured reservoir. Identification of fractured zones in geothermal fields by *P* and *S* wave surface reflection profiles has not been generally successful [*Severson*, 1987], but here the reflections are quite clear.

Anisotropy Analysis

Travel time measurements. With two polarizations of near-offset *SH* waves, SH_r, and SH_t, it is possible to look for anisotropy in the horizontal plane, information rarely measured in situ. Travel time difference between orthogonal polarizations is evidence of anisotropy. The data available from 1295 to 1720 m show that SH_r is faster than SH_t, with an apparent trend of increasing separation between SH_t and SH_r [*Daley*, 1987]. The average travel time difference in this depth range is 9 ms, or approximately 0.5% velocity anisotropy. While this is not a large amount of anisotropy, it is consistent enough over this depth interval of 1400 feet to show the presence of an azimuthal polarization dependence of vertical shear wave velocity in this area.

The far-offset data allow comparison of conventional *SH* and *SV*. The SH_t source arrivals were picked on the *SH* component and the SV source arrivals were picked on the *SV* component. Figure 15 shows the travel time difference at each depth where both arrivals could be picked. The dominant feature is a trend of *SV* motion becoming increasingly faster than *SH* motion with increasing depth. The travel time data also show a crossover in velocity structure, with *SH* propagation faster shallow and *SV* propagation faster at depth. This crossover occurs at the *S* wave turning point depth (Figure 5), so it may represent the influence of shallow ray path geometry. The local high in *SH* propagation velocity from 915 to 1065 m may also be related to the near-horizontal ray paths around 915 m. From 445 to 640 m the SH_t velocity is higher, but at 695 m the travel times become equal. This abrupt change corresponds to changes in wavelet character and travel time for the SH_t propagation. Below 1080 m the SV arrival becomes increasingly faster than SH_t. The total travel time difference of 16 ms at 1675 m represents about 1% velocity anisotropy. As with the 0.5% horizontal plane anisotropy seen

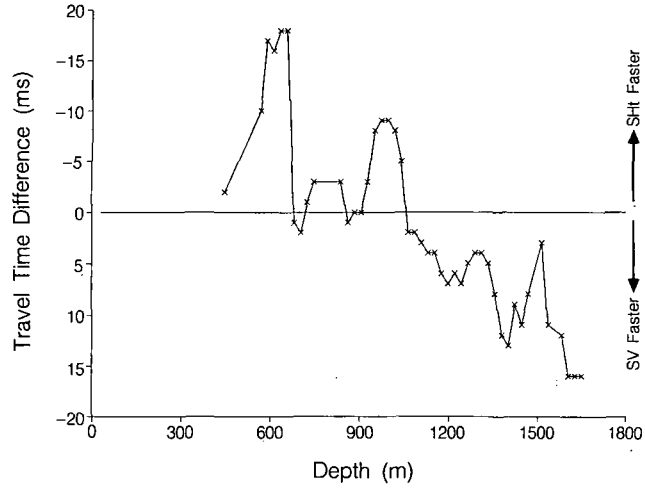

Fig. 15. Measured travel time difference between far-offset shear sources. Data points are *SV* time minus SH_t time. Points are to the right of the zero line when SH_t is faster and to the left when *SV* is faster. The error of any one point is estimated to be ±5 ms. Difference of 16 ms at bottom of survey represents about 1% anisotropy. Note the crossover from faster SH_t to faster *SV*.

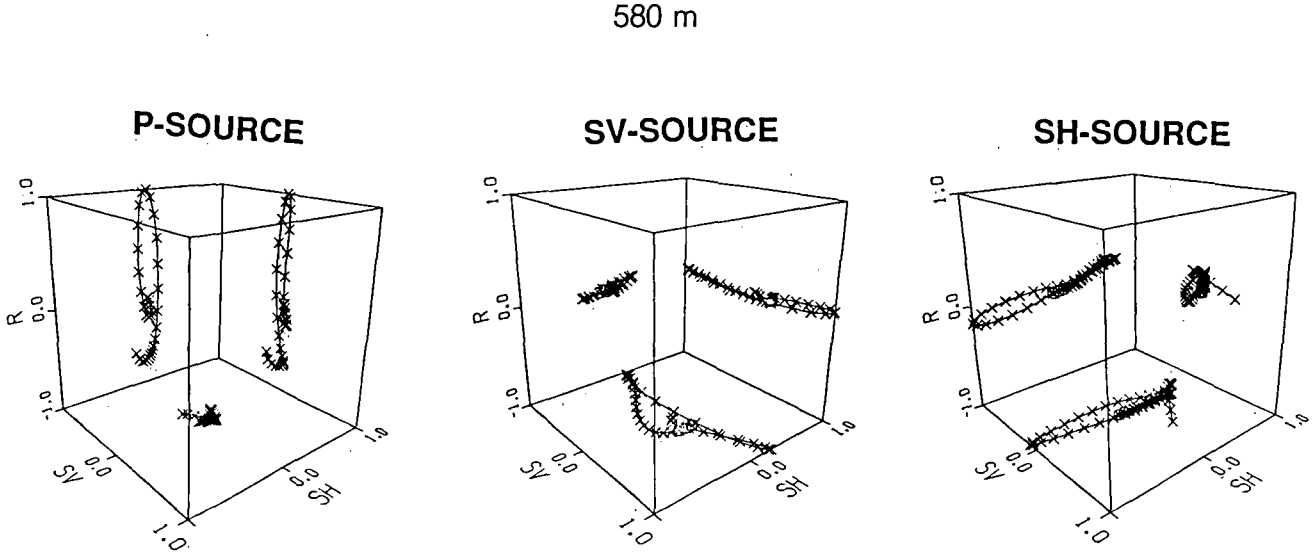

Fig. 16. Three-component particle motion hodographs for all three far-offset sources at 580 m recording depth. Plotted points are 2 ms apart. Each axis of the cube displays one component of motion, giving three two-dimensional projections. The vertical axis is the radial direction, while the horizontal axes show *SH* and *SV* components. Pure transverse motion, *SH* versus *SV*, is shown on the bottom of the cube. Purely isotropic *S* wave propagation would produce linear trajectories in the *SV-SH* plane shown on the cube's bottom. While the *SH* versus *SV* plot is often the only one displayed, the radial component can provide much information about the three-dimensional nature of particle motion.

at the near-offset, this is a small but measurable level of anisotropy.

Particle motion interpretation. The analysis of particle motion provides a second method of investigating anisotropy [*Crampin*, 1985; *Majer et al.*, 1988]. A three-component geophone provides the ability to look at the particle motion within any two-dimensional plane or in three dimensions. Figure 16 shows particle motion within the first-arrival windows for each of the three far-offset sources recorded at the 580 m depth. A 70-ms time window was used to produce these hodographs. The plots show three orthogonal two-dimensional slices which describe the complete particle motion, plotted on the faces of a cube whose axes are the three ideal *P*, *SH*, *SV* components. It would be possible to plot the particle motion as a single three-dimensional path, but in practice, such a plot is difficult to interpret since its appearance is dependent on the viewing angle. Figure 16 is representative of the particle motion one would expect from largely isotropic propagation. The *P* source first arrival has predominantly radial motion, the *SH* source arrival is *SH* motion, and the *SV* source arrival is largely *SV* motion. Inspection of hodographs from every depth showed the arrivals from the *P* wave source are stable, linear motion [*Daley*, 1987]. The shear wave particle motion contains information about anisotropic propagation along the ray path, and given the observations of velocity anisotropy detailed above, we would expect to see shear wave splitting on plots of the *S* wave particle motion [*Crampin*, 1985].

The near-offset shear wave data constitute a horizontal plane anisotropy experiment because ray paths from both near-offset shear source polarizations are nearly vertical. The results are summarized in Figure 17. There are limitations with the near-offset particle motion analysis. The data are incomplete, lacking shallow SH_r data. Also, the determination of the horizontal rotation angle θ is difficult for vertically incident waves, so the actual orientation of the rotated *SH* and *SV* components may vary with depth. However, the rotated data do have good phase consistency, implying accurate rotation. Furthermore, since the rotated components are orthogonal, the observed nonlinear particle motion implies shear wave splitting. Such anisotropy at shallow depths may be due to a depositional history of the dominantly northwestward transport of sediments from the Colorado River to the Salton Sea and its predecessors; another possible cause is the horizontal component of the tectonic stress field within the Salton Trough.

The far-offset data constitute a traditional *SH* versus *SV* anisotropy experiment, and they are a more complete data set. Figure 18 summarizes the far-offset travel time and particle motion data. Several distinct zones are seen. The shallow zone above above 455 m appears to be fairly isotropic with equal *SH* and *SV* travel times to 455 m and linear particle motion

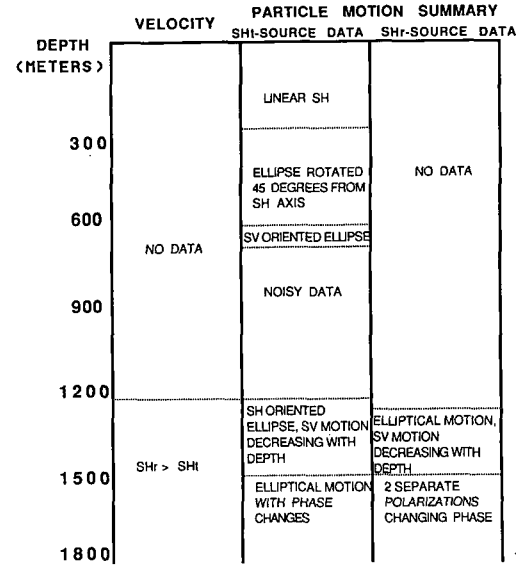

Fig. 17. Summary of near-offset horizontal plane anisotropy data.

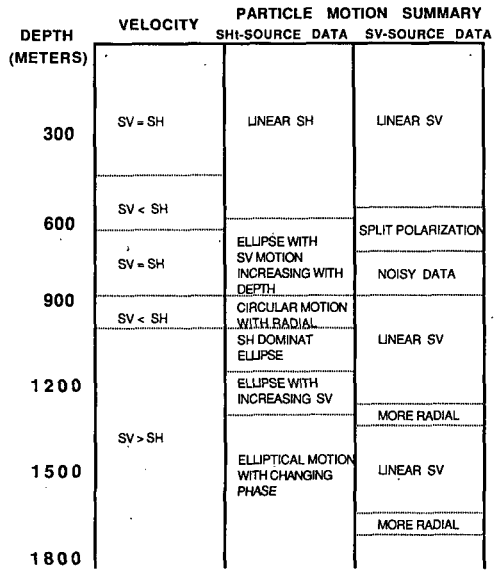

Fig. 18. Summary of far-offset anisotropy data.

from both shear sources at that depth. From 580 to 670 m depths, the SH_t-generated waves are increasingly faster than those from the SV source. Near 670 m the travel times and particle motions both indicate a change in properties. Velocity increases are seen for both *P* and *S* waves near 670 m with the *S* wave velocity showing a large increase. There are indications of reflections near this depth, but accurate identification is not possible because of the lack of shallow data. There appears to be a general transition in material properties near 670 m. From 520 to 640 m there is the first anhydrite alteration, possibly marking the "cap rock" seen in the SSGF. The seismic effects may be related to the transition from anhydrite alteration in a mostly claystone layer to an alteration free sandstone layer at 670 m.

The zone from 885 to 975 m has a number of anomalous properties. At 915 m a local high in the *SH/SV* velocity ratio develops with a peak *SH/SV* ratio at 990 m. The SH_t-generated first arrival gives nearly circular polarization in this zone, and both shear sources give a large amount of radial motion. Figure 19 shows the hodographs for the SH_t source first arrivals from 875 to 970 m. The 875-m hodograph shows a narrow ellipse in the *SH-SV* plane with dominant *SH* motion, but the amount of radial and *SV* motion increases in the hodographs at 900 and 920 m before decreasing at 970 m, leaving the motion similar to the 875-m depth. A possible interpretation of the increased radial energy is *P* wave scattering within that interval, caused by an inhomogeneity near the well. A more distant inhomogeneity would allow the scattered *P* wave energy to separate from the shear wave arrival, as with events K and L (Figure 13). Vertically scattered *P* waves produced by the far-offset *P* source (Figure 11) appear to originate from about 885 m, and indications of scattering from 915 m are seen on the SH_t source data (Figure 5). The near-offset *P* source data show a reflection at 885 m, and the *P* velocity increases sharply at 915 m. All these effects suggest a heterogeneity, such as a fracture zone, around 900 m.

From 1240 to 1290 m a radial component of motion is seen in the SH_t-generated shear arrival [*Daley*, 1987]. Again, this radial motion has associated *SV*, motion and it may represent *P* wave scattering from *SV* motion incident on a near-well inhomogeneity. This depth zone also has an *S*-to-*P* reflection generated near 1250 m (event G in Figure 8). The zone from 1190 to 1280 m contains anhydrite and some epidote alteration (Figure 1), suggesting hydrothermal activity and associated fracture permeability. Either the alteration zone or the fracturing could cause the seismic wave mode conversions. Poisson's ratio reachs a minimum value in this depth zone (Figure 7), which is another indication of a transition in material properties (such as the beginning of large scale hydrothermal activity).

In general, the SH_t-generated waves show a complicated mix of *SH*, *SV*, and radial motion, whose relative amplitudes varied with depth (Figures 19 and 20). The SH_t-generated particle motion indicates anisotropic propagation which can be explained by the amount of travel time difference between arrivals from SH_t and SV sources (up to 1%). SV-generated particle motion (Figure 20) appears to indicate a stable propagation mode which only shows anisotropic particle motion in the 640- to 760-m range (the 760- to 855-m traces are too noisy to use). Deeper than 855 m and shallower than 640 m, the SV source data have consistently linear *SV* motion in the *SH-SV* plane with some radial motion seen at various depths. Given the complexity in the SH_t data, the lack of splitting in the SV-generated first arrival is unexpected. Velocity differences cannot be causing an *SH* component of motion generated by the SV source to move out of the *S* wave arrival because the maximum travel time difference is 15 ms, while the wavelets were analyzed with windows at least 50 ms long. In some zones, shear arrivals from the SV source did show significant radial motion, which seems to be scattering of *P* wave

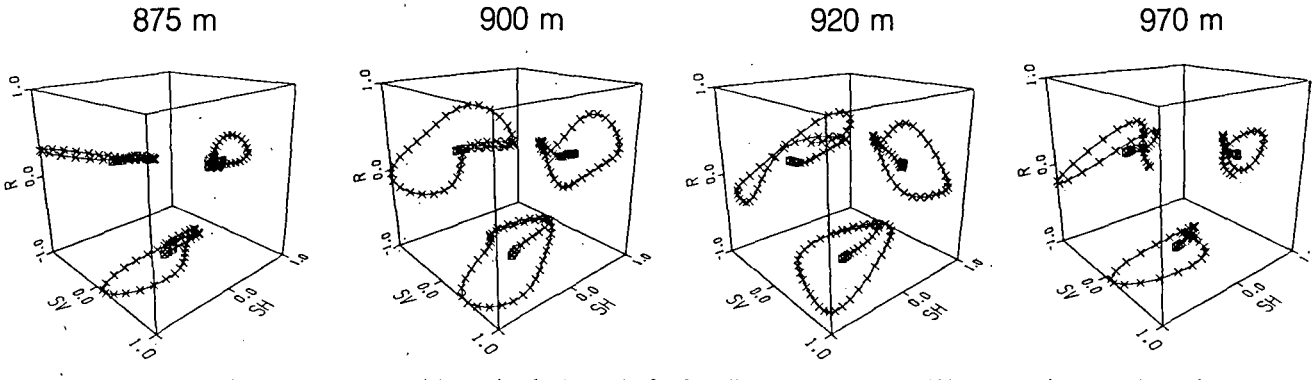

Fig. 19. Three-component particle motion hodographs for far-offset SH_t source near 900-m scattering zone. Note the increase in radial (*R*) motion and broadening of the *SH-SV* ellipse at 890 and 920 m which suggests fracture-induced anisotropy. Data points are 2 ms apart. The first three points in time are circled to provide identification of initial motion.

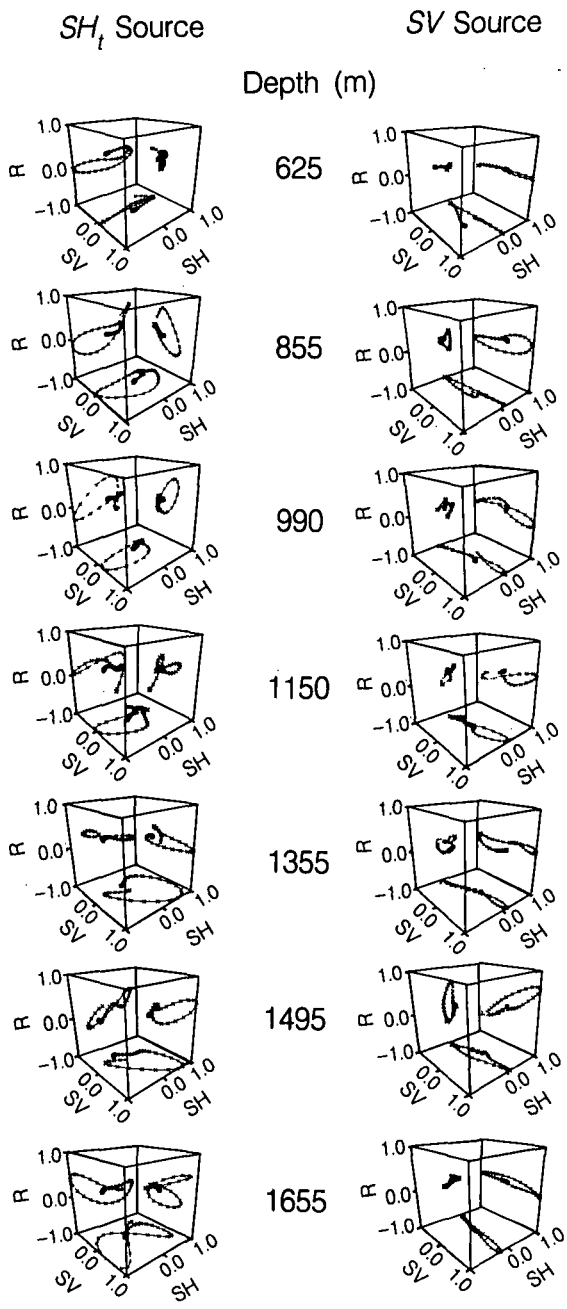

Fig. 20. Three-component particle motion hodographs for far-offset shear sources. Motion shown is within a window centered on the first shear arrival. The linear motion generated by the SV source and observed in the *SH-SV* plane (bottom of cube) is very unexpected given the observed velocity anisotropy and the nonlinear motion generated by the SH_t source. This difference between SV-generated waves and SH_t-generated waves shows that the anisotropy cannot be transverse isotropy and that the direction of SV source motion produced shear waves which do not split.

energy within the shear wavelet. Figure 20 illustrates the consistent pattern of linearly polarized *SV*-generated arrivals from the SV source.

The nearly isotropic propagation of SV-polarized waves may be a regional effect because this polarization direction is oriented along the axis of spreading in the Salton trough, while the SH_t orientation is perpendicular to the axis. Another possible explanation is that all the anisotropy is in relatively thin horizontal beds to which the *SV* motion, with its long vertical wavelength, is not sensitive. More tests would be necessary to confirm either hypothesis. One such test would be another far-offset VSP, 90° in azimuth away from the existing VSP, giving the SV and SH_t sources opposite polarization from this survey, and then looking for linear *SH* or *SV* motion. If the *SH* motion in such a survey were linear, it would indicate a regional cause, and if the *SV* motion remained linear, it would indicate a local bedding effect.

CONCLUSIONS

All the dip filtered sections show a reflection from the known fractured reservoir between 2042 and 2105 m. A surface seismic survey could probably track this strong event and possibly delineate the reservoir. The relative strength of the shear wave reflections on the vertical component indicates the advantage of three-component recording. It is unfortunate that good quality VSP data are not available through this zone to provide better information on its physical properties and effects on seismic wave propagation.

Two possible zones of transition in properties were identified within the survey. Near 670 m there are changes in *P* and *S* wave velocity and *S* wave anisotropy which, combined with the appearance of anhydrite alteration, may indicate the "cap rock" zone of the SSGF [*Younker et al.*, 1982]. The 1190- to 1280-m zone yields changes in Poisson's ratio and *S* wave particle motion which, together with epidote alteration, indicate a possible transition to large-scale hydrothermal activity seen in the altered reservoir rock identified in the SSGF by *Younker et al.* [1982].

A heterogeneity near 915 m is indicated by vertically scattered *P* waves from the far-offset *P* source and SH_t source. This zone also gives a reflection on the near-offset *P* source survey and produces radial particle motion within the SH_t-generated shear arrival. A local maximum of the shear wave velocity anisotropy at this depth suggests localized fracturing. The core from 918 to 920 m had an "open and permeable fracture zone" with indications that "this fracture zone presently contains a brine" [*McKibben and Andes*, 1986]. There is anhydrite alteration above 885 m, possibly indicating an impermeable cap. The nuclear porosity log showed an increase in porosity between 885 and 945 m [*Paillet*, 1986]. The lithology is mostly sandstone from 915 to 975 m with some shale, siltstone, and claystone. The various seismic effects seem most likely to be caused by a fluid-filled fracture zone near the well.

The splitting and travel time differences measured from the near-offset sources indicate that horizontal plane anisotropy is not negligible in this section. Although the absolute orientation of the near-offset shear wave particle motion is poorly determined, splitting of the waveform is clearly seen. Since the SV-generated *S* wave particle motion has a component of motion with the polarization of the SH_r source, strong anisotropy in the horizontal plane could be misinterpreted as *SV* versus *SH* anisotropy. This is especially true for surface reflection data using *SH* and *SV* sources because they have no horizontal plane information. In this survey the horizontal plane anisotropy is about half that of the *SH-SV* anisotropy (0.5% versus 1.0%).

The scattered *P* wave events on the radial component of the SV source data (events K and L on Figure 13) are probably generated by fracture zones, and it may be possible to map these fractures through a suitable inversion calculation. The appearance of radial motion within the shear wave first arrival

may also be an indication of P wave scattering from fractures. Assuming that the rotation is reasonably accurate, it would take severe anisotropy to cause any significant shear motion along the propagation direction. The forward scattering of P energy off heterogeneities by the propagating S wave seems a most likely explanation of the large amount of radial motion seen within the shear arrival at some depths.

Linear particle motion of the SV-generated shear wave is intriguing. The SH_t-generated shear wave shows the type of anisotropic particle motion suggested by the observed travel time differences and scattered waves. The apparently isotropic nature of the SV-generated arrivals, with their stable linear particle motion, is unexpected. Linear SV waves appearing with split SH waves is inconsistent with transverse isotropy with a vertical axis. The area surrounding the SSSDP thus appears to have a more complicated geometry of anisotropy, one which has an axis of symmetry aligned with our SV source motion, preventing splitting of the waveform. It may be possible to resolve the role of regional and local effects in the anisotropy with the addition of data from other source azimuths.

Acknowledgments. This work was supported through U.S. Department of Energy contract DE-AC03-76SF00098 by the Assistant Secretary for Energy Research, Office of Basic Energy Sciences, Division of Engineering and Geosciences; and the Assistant Secretary for Conservation and Renewable Energy, Office of Renewable Technology, Division of Geothermal and Hydropower Technologies. Computations were carried out at the Center for Computational Seismology at the Lawrence Berkeley Laboratory.

REFERENCES

Becker, D. F., and A. I. Perelberg, Seismic detection of subsurface fractures (abstract), *Geophysics*, *52*, 708, 1987.

Corrigan, D., M. G. Justice, and E. B. Neitzel, Estimate of shear-wave anisotropy using multicomponent seismic data (abstract), *Geophysics*, *52*, 710, 1987.

Crampin, S., Evaluation of anisotropy by shear-wave splitting, *Geophysics*, *50*, 142–152, 1985.

Daley, T. M., Analysis of *P*- and *S*-wave VSP data from the Salton Sea geothermal field, M.S. thesis, Univ. of Calif., Berkeley, 1987.

Elders, W. A., *Salton Sea Scientific Drilling Program Monitor*, issue 5, Feb 11–Apr 1, 1986, U.S. Dep. of Energy, Geotherm. Technol. Div., Washington, D. C., 1986.

Hale, D., and J. F. Claerbout, Butterworth dip filters, *Geophysics*, *48*, 1033–1038, 1983.

Hardage, B. A., *Vertical Seismic Profiling—Part A: Principles*, Geophysical Press, London, 1985.

Kanasewich, E. R., *Time Sequence Analysis in Geophysics*, p. 334, University of Alberta Press, Edmonton, 1981.

Kennett, P., R. L. Ireson, and P. J. Conn, Vertical seismic profiles: Their applications in exploration geophysics, *Geophys. Prospect.*, *28*, 676, 1980.

Majer, E.L., T. V. McEvilly, F. Eastwood, and L. Myer, Fracture detection using *P*- and *S*-wave VSPs at The Geysers geothermal field, *Geophysics*, *53*, 76–84, 1988.

McKibben, M. A., and J. P. Andes, Ore mineralization and related fluid inclusion properties in the SSSDP cores, Report to the SSSDP Principal Investigators' Session, Geotherm Resources Council Meeting, Palm Springs, Calif., Sept. 1986.

Oristaglio, M. L., A guide to the current uses of vertical seismic profiles, *Geophysics*, *50*, 2473, 1985.

Paillet, F. L. (Ed.), Preliminary report on geophysical well-logging activity on the Salton Sea Scientific Drilling Project, Imperial Valley, California, *U.S. Geol. Surv. Open File Rep.*, *86-544*, 1986.

Severson, L. K., Interpretation of shallow crustal structure of the Imperial Valley, California, from seismic reflection profiles, M.S. thesis, 68 pp., Univ. of Calif., Berkeley, 1987.

Younker, L. W., P. W. Kasameyer, and J. D. Tewhey, Geological, geophysical and thermal characteristics of the Salton Sea geothermal field, California, *J. Volcanol Geotherm. Res.*, *12*, 221–258, 1982.

T. M. Daley, E. L. Majer, and T. V. McEvilly, Center for Computational Seismology, Lawrence Berkeley Laboratory, University of California, Berkeley, CA 94720.

(Received September 16, 1987;
revised February 22, 1988;
accepted May 26, 1988.)

JOURNAL OF GEOPHYSICAL RESEARCH, VOL. 93, NO. B11, PAGES 13,037–13,045, NOVEMBER 10, 1988

Borehole Gravity Measurements in the Salton Sea Scientific Drilling Project Well State 2-14

PAUL W. KASAMEYER AND JOSEPH R HEARST

Lawrence Livermore National Laboratory, Livermore, California

Borehole gravity measurements over a depth range from 1737 to 1027 m and the vertical gradient of gravity above ground were measured at the Salton Sea Scientific Drilling Project well State 2-14. Uncorrected borehole gravimetric densities match values from gamma-gamma logs, indicating that the high densities seen in State 2-14 in the depth range 0.5–3 km extend for a few kilometers from the well. The aboveground gradient was found to be 4.1 μGal/m higher than expected; correcting for this value increases the gravimetric density in the borehole. Combining the borehole gravity and estimated vertical gravity gradients on the surface, we find that this densified zone coincides with much of a broad thermal anomaly that has been found to the northeast of the Salton Sea geothermal field.

INTRODUCTION

The Salton Sea Scientific Drilling Project (SSSDP) drilled borehole State 2-14 into the hydrothermal system at the Salton Sea geothermal field (SSGF). *Elders et al.* [1972] described how the Salton Trough was formed over the last 4 m.y. by oblique relative motion between the Pacific and North American plates and identified a number of pull-apart zones where the spreading currently appears to be concentrated. The northernmost pull-apart zone lies under the SSGF, the largest, hottest geothermal system in the Salton Trough. Here, heat and material from the mantle are modifying young sediments and ultimately augmenting the continental crust. The SSSDP provides the opportunity to study the system's thermal and chemical evolution and, ultimately, to learn more about the nature of this process of crustal development.

Density is important for understanding geothermal systems in the Salton Trough [*Muramoto and Elders*, 1984]. The trough is filled with young deltaic sediments, whose density would normally be expected to increase with depth along well-known compaction curves. In the geothermal systems the sediments have undergone substantial alteration and metamorphism; consequently, they are much denser than predicted from compaction curves. Muramoto and Elders used the increase in bulk density with depth for both sand and shales, as well as resistivity logs, to identify zones of increasing thermal alteration with depth in the wells from the SSGF and to infer the maximum temperature seen by the sediments. State 2-14 provides the opportunity to extend these studies with an large set of cores, cuttings, and well logs.

Because density in the Salton Trough is diagnostic of the degree of alteration, it is correlated with temperature. As a result, routine surface gravity surveys [*Biehler et al.*, 1964] have been used to identify potential geothermal fields. This approach is so successful that *Combs* [1971] reports a one-to-one correspondence between gravity anomalies and thermal anomalies in the Imperial Valley. A +20 mGal residual gravity anomaly, inferred to be caused by a combination of altered sediments and possible deeper intrusions [*Biehler et al.*, 1964], is centered on the SSGF. Because of the ambiguity inherent in gravity interpretation, surface measurements cannot distinguish between laterally extensive, near-surface altered sediments and deeper, denser intrusions. Interpretation of the logs and detailed sampling of State 2-14 will provide additional constraints on the density distribution with depth.

State 2-14 lies near the edge of a zone of high heat flow inferred to mark the active convecting portion of the hydrothermal system and therefore might be near the edge of the zone of high-density sediments. A borehole gravity survey was planned to place constraints on the distance to this edge and on the depth distribution of anomalously dense sediments. In this paper we describe the results of that survey and their implications for the thermal history of the SSGF.

THERMAL STRUCTURE OF THE SALTON SEA GEOTHERMAL FIELD

The temperature distribution in the SSGF is discussed by *Newmark et al.* [this issue] and *Sass et al.* [this issue]. Newmark et al. report on shallow thermal gradient measurements in and surrounding the SSGF and identify areas with four distinct temperature-depth profiles representing the dominance of different mechanisms of thermal transport. The areas are shown in Figure 1. Figure 2*a* shows typical thermal profiles for each area. The largest area (V) covers most of the Imperial Valley, which *Lachenbruch et al.* [1985] recognized has an anomalously high thermal gradient of about 0.07°C/m. Surrounding the SSGF on at least three sides is the Broad (B) anomaly with nearly conductive temperature profiles and a typical gradient of 0.1°C/m. Deep holes have been drilled in two locations identified in Figure 1 as the South Broad (SB) and North Broad (NB) areas. The Central (C) area of the geothermal field is a 4-km-wide swath with a uniformly high surface gradient of about 0.4°C/m. Decreasing gradients at depth imply convective transport in this area. Finally, within the Central area are two localized, intense convective areas (called the Mullet Island anomaly (M) and the Kornbloom Road anomaly (K)), with gradients as high as 0.8°C/m.

State 2-14 lies near the outer boundaries of both the M and C high-gradient areas. *Sass et al.* [this issue] report on thermal measurements in State 2-14, which has an unusually high near-surface gradient, perhaps associated with the M anomaly. Below 150 m, State 2-14 has temperatures intermediate between wells within the C and B areas.

Paper number 88JB03106.
0148-0227/88/88JB-03106$05.00

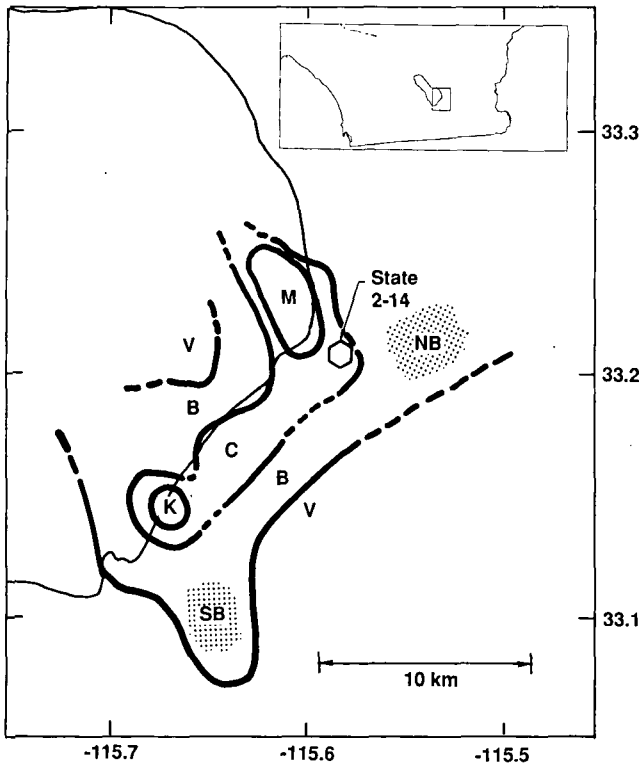

Fig. 1. Thermal zones at the Salton Sea geothermal field. The inset map shows the location of the figure near the Salton Sea and the southern end of the San Andreas fault zone in southern California. The heavy lines indicate the approximate boundaries of thermal regimes defined by *Newmark et al.* [this issue]: V, Valley-Wide; B, Broad; C, Central; and M and K represent two local anomalies, the Mullet Island and Kornbloom Road features. Geothermal data have been published for two portions of the B area indicated by shading: the Westmorland Field, called South Broad (SB) in this paper, and the Niland Field, called North Broad (NB). The smoothed 1959 boundary of the Salton Sea [after *Army Map Service*, 1959] and the approximate location of State 2-14 are also indicated.

Density Logs From the SSGF Wells

Muramoto and Elders [1984] examined the changes in resistivity logs and gamma-gamma density logs with depth in the SSGF to study the mechanisms and distribution of alteration. They developed empirical relationships to infer the degree of hydrothermal alteration from examination of the logs. They concluded that within the C and SB areas, different ranges of shale density are associated with each zone of alteration and therefore each temperature interval. Their conclusions, summarized in Table 1, can be used to estimate temperatures. A shale density of 2.15 is diagnostic of temperatures near 190°C, 2.25 is diagnostic of 240°C, and a rise in shale density to 2.6 is diagnostic of temperature near 295°C. At any depth, densities in the SB anomaly are lower, consistent with the observed lower temperatures.

Figure 2*b* shows idealized shale density profiles based on Muramoto and Elders' data from the northeastern part of the C anomaly and from the SB anomaly. Idealized temperature profiles for these same areas, from *Newmark et al.* [this issue] are shown in Figure 2*a*. Temperature data [*Sass et al.*, this issue] and density data from State 2-14 are also included in Figure 2. The State 2-14 temperatures are lower than those seen in the C anomaly, but the density-depth data are similar.

Using the density-temperature relationship described above, we have calculated the temperatures implied by the density log from State 2-14. Shown as circles in Figure 2*a*, the implied temperatures are higher than the temperatures observed in the well and above 1 km are much closer to the temperature-depth profile for the C area. This observation is consistent with conclusions of *Andes and McKibben* [1987], who inferred that paleotemperatures were 40°–100°C higher than present temperatures based on fluid inclusions from veins in State 2-14, and with *Sturtevant and Williams* [1987], who found that the calcium isotopic profile was similar to that observed in the higher gradient wells in the center of the SSGF.

A similar density-depth relationship is suggested for the NB area. *Muramoto and Elders* [1984] reported Britz 3 density logs, between 200- and 1000-m depth. These logs showed anomalously higher densities than could be predicted from the observed temperature-depth curves, which are similar to those from the SB area. Idealized shale density from the Britz 3 well in the NB area is also shown in Figure 2*b*.

The temperature and density logs show that although State 2-14 is situated off the edge of the central thermal anomaly, its densities are as high as any measured in the SSGF. These high densities suggest that in the past it was as hot as the Central area is now. Since borehole gravity measurements are sensitive to density out to several hundred meters from the borehole, we can estimate how far from State 2-14 the densified area extends by comparing borehole gravity and density logs.

Measurements in State 2-14

The gamma-gamma density data measured in State 2-14 from 1027 to 1750 m are shown in Figure 3. The gamma-gamma density data were obtained with a standard Schlumberger compensated density log (FDC); the collection and processing of these data are described by *Paillet* [1986]. The tool has two detectors designed to compensate the measured density for gaps between the sonde and borehole wall, as discussed by *Hearst and Nelson* [1985]. The gravimetric density was obtained from a gravimeter survey conducted by EDCON, Inc. in March 1986. The field procedures and analysis are described by *EDCON Inc.* [1986]. Measurements started at a depth of 1737 m, near the bottom of the production casing, and were stopped at 1027 m because of difficulties with the equipment. Forty-six readings were taken with the instrument clamped at 36 different depth stations selected to encompass zones of uniform density as determined from the density log; the results are displayed in Table 2. The gravity data were corrected for drift and tide by standard methods [*EDCON, Inc.*, 1986]; no terrain correction was required at this site. Drift corrections were made by reoccupying stations approximately every half hour and by requiring the gravity readings to agree. Uncertainty of the density, based on the variability of drift-corrected gravity readings, is estimated to vary between 0.001 and 0.007 g/cm^3.

The gravimetric density (calculated from equation (4) discussed below) is overlaid on the gamma-gamma density data in Figure 3. The gravimetric density anomaly (the gravimetric density minus the gamma-gamma density data averaged over the interval between gravity measurements) is shown on the left side of Figure 3. Dashed intervals indicate depth intervals where the gamma-gamma data are suspect because the gap and mudcake compensation is greater than 0.07 g/cm^3, the maximum value that we consider acceptable.

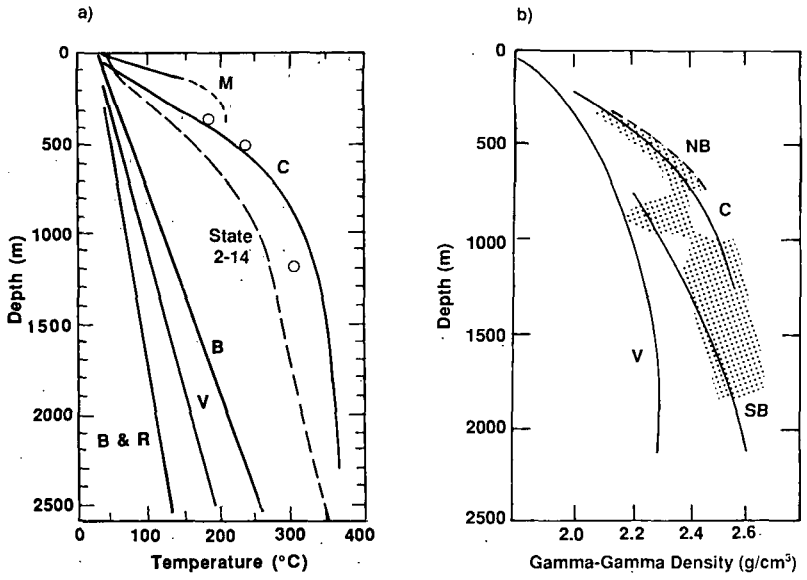

Fig. 2. Idealized (*a*) temperature-depth and (*b*) density-depth profiles for areas defined in Figure 1 and for State 2-14. A typical profile from the Basin and Range (B&R) has been added in Figure 2*a* to show that all the areas described have elevated heat flow. The State 2-14 temperature profile is from *Sass et al.* [this issue], and all others are from *Newmark et al.* [this issue]. The three circles represent temperatures inferred from the density data in State 2-14, as is described in the text. The shaded area in Figure 2*b* represents all density log points with compensation less than 0.07 g/cm^3 in State 2-14 [*Paillet*, 1986]; all other profiles are from *Muramoto and Elders* [1984]. The lines represent average shale densities for the SB, NB, and C anomalies and an estimate of the unaltered compaction curves for the V area.

Several details of the log density are matched by the gravimetric density, (e.g., step changes at 1570, 1271, and 1173 m), indicating that the depths of the two measurements were well aligned. The similarity of the offsets on the gravimetric and gamma-gamma density logs can be used to estimate the lateral extent of the small density fluctuations seen in State 2-14. Some of these small zones must extend horizontally a large distance from the borehole. For example, the density log shows an average density increase of about 0.1 g/cm^3 between 1569 and 1661 m. On the basis of the mud logs from *Paillet* [1986], this higher-density zone contains less sandstone and siltstone than the material above and below it. Figure 3 shows that the gravimetric density response to this zone is about 90% of the gamma-gamma response. We assume that the high-density zone is a cylinder centered in the borehole and embedded in a material with the density of the zones above it. Using the formula for the density effect of a cylinder [*Hearst et al.*, 1980], we find that to produce a 90% response, the cylinder radius must be greater than 5 times the thickness, or several hundred meters in this case. Some zones may be much smaller in extent. For the sandy zone between 1359 and 1377 m the gravimetric density response is less than 30% of the density log response, indicating that the zone radius could be as small as half the thickness, or less than 10 m.

Throughout the borehole, the gravimetric and log densities match well. Except in the lateral from 1289 to 1338 m, the gravimetric density is slightly higher than the log density, a somewhat surprising result given the high densities seen by the log. The mean gravimetric density anomaly (not including the suspect intervals) is 0.02 g/cm^3. This value is near the limit of the density log's systematic uncertainty caused by changes in water content and the presence of unusual temperatures, indicating that the true anomaly could be zero. Consequently, when taken at face value, the borehole gravity data suggest that there is no significant anomaly, that on a large scale, density depends on depth only with no lateral variation and that State 2-14 is far from the density boundary of the SSGF. To evaluate this result and to estimate how close the density boundary might be, we look at the analysis of the borehole gravity in detail.

TABLE 1. Characteristic Densities for Different Metamorphic Zones

Metamorphic Zone	Transition Temperature, °C	Shale Density, g/cm^3	Sand Density, g/cm^3
Montmorillonite		<2.05	2.00–2.15
	100–190		
Illite		2.15–2.25	2.05–2.20
	230–250		
Chlorite		2.25–2.6	2.20–2.40
	290–300		
Feldspar		2.25–2.65	2.25–2.35

Use of Borehole Gravity to Infer Lateral Changes in Density

A gamma-gamma density log and a borehole gravimeter are often used together to infer lateral changes in density that do not intersect the borehole [*Hearst and Nelson*, 1985]. The interpretation approach is based on the gravity response for an infinite slab of density ρ. Above and below the infinite slab the gravity is constant, and the difference in gravity (Δg) measured at the top and bottom of the slab is given by

$$\Delta g/\Delta z = -4\pi K\rho \qquad (1)$$

where Δz is the depth difference for the measurements, z in-

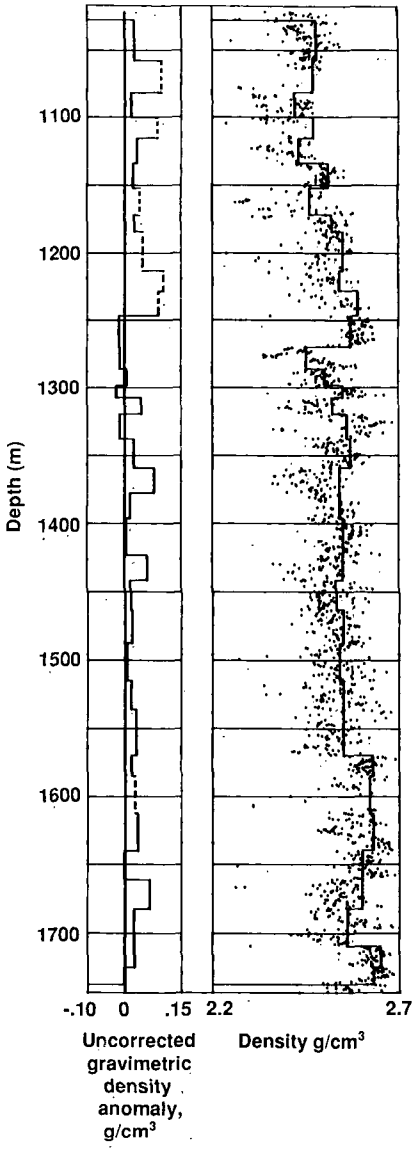

Fig. 3. Gravimetric and gamma-gamma log densities for State 2-14 from 1027 to 1750 m depth. The solid line in the right-hand column is the gravimetric density calculated from equation (4). The density log was sampled every foot, and those points for which the compensation was less than 0.07 g/cm³ are plotted. The uncorrected gravimetric density anomaly, plotted on the left at the same scale, is calculated by subtracting the average of the acceptable density values in an interval from the gravimetric density, as in equation (5). The dashed intervals indicate sections of the density log where the majority of compensation values were greater than 0.07.

creases downward, and K is the gravitational constant. We divide the actual density distribution within the Earth into four components:

$$\rho(x, y, z) = \rho_W(x, y, z) + \rho_L(z) + \rho_A(x, y, z) + \rho_R(x, y, z) \quad (2)$$

where the subscripts have the following meanings:

W rotating oblate spheroid Earth which produces the free-air anomaly $F_W(z)$ given by the formula of *Heiskanen and Vening Meinesz* [1958] with constants given by *Robbins* [1978];

L set of infinite, flat-lying layers passing through the well bore;

A difference between ρ_L and the local anomalous masses that we intend to model, i.e., the "density contrast" of the anomalies;

R regional masses outside the zone that we intend to model.

Following the approach of *Mueller* [1960] (as cited by *Beyer* [1971]) we define regional masses to be those distant enough that their effect on the gradient is constant over the depth of the hole, and we recognize that we must include any closer ones in our local model.

In the following equations, all measurement locations refer to depth within or directly above the borehole, so the x and y parameters are omitted. The measured gravity difference, identified by the superscript m, between z and $z + \Delta z$ in the borehole is the sum of the contributions of the four density components:

$$\Delta g^m(z)/\Delta z = F_W - 4\pi K\rho_L + \Delta g_R/\Delta z + \Delta g_A(z)/\Delta z \quad (3)$$

where the contribution from the term representing the layer density has been converted by using equation (1).

If there were no regional and local anomalies, the last two terms on the right-hand side of equation (3) would be zero, and the density-depth distribution could be estimated from the gravity measurements using the standard formula for

TABLE 2. Borehole Gravity Data From State 2-14

Depth Range, m	Delta g, mGal	Gravimetric Density, g/cm³
1027–1057	3.086	2.48
1057–1082*	2.485	2.47
1082–1100	1.942	2.42
1100–1115*	1.554	2.47
1115–1133	1.913	2.43
1133–1152	1.796	2.51
1152–1171*	2.032	2.46
1171–1184	1.194	2.52
1184–1213*	2.758	2.55
1213–1228*	1.458	2.54
1228–1246*	1.676	2.59
1246–1269	2.144	2.57
1269–1286	1.736	2.45
1286–1298	1.214	2.50
1298–1307	0.871	2.55
1307–1319	1.194	2.52
1319–1338	1.729	2.56
1338–1359	2.001	2.57
1359–1377	1.756	2.54
1377–1395	1.761	2.54
1395–1423	2.598	2.55
1423–1441	1.737	2.55
1441–1463	2.071	2.53
1463–1487	2.317	2.55
1487–1514	2.639	2.54
1514–1536	2.032	2.55
1536–1569	3.184	2.55
1569–1584	1.349	2.63
1584–1612*	2.454	2.62
1612–1639	2.415	2.63
1639–1661	1.944	2.60
1661–1682	1.946	2.60
1682–1709	2.577	2.56
1709–1725	1.327	2.65
1725–1737	1.001	2.63

*Questionable log.

gravimetric density:

$$\rho^m(z) = \frac{1}{4\pi K}\left[F_W(z) - \Delta g^m(z)/\Delta z\right] \quad (4)$$

The density log, ρ_{LOG}, measures the density of the hypothetical layers plus the density contrast of any anomalous masses that intersect the borehole. The uncorrected gravimetric density anomaly can be derived from equations (3) and (4):

$$\rho^m(z) - \rho_{LOG} = \rho_A{}^g(z) - \rho_A{}^t(z) + \rho_R{}^g \quad (5)$$

We have divided the gravity gradient terms on the right-hand side of equation (3) by $-4\pi K$ to express them in terms of their density effect $\rho^g(z)$ at depth z. The superscript "g" is used to distinguish the contribution of a mass to the gravimetric density measured at $x = 0$, $y = 0$ from its true density (indicated by superscript "t"). For the infinite layers, $\rho_L{}^t(z) = \rho_L{}^g(z)$, so they do not contribute to the anomaly. We see that the anomalous mass can be detected if its effect on gravimetric density at any depth differs from its density contrast in the borehole at that depth.

In State 2-14 the uncorrected gravimetric density anomaly is small; from equation (5) we see that two cases are possible. In the first case, either there is no anomalous mass that influences the gradient over the depth range studied, or the anomalous mass extends so far from the borehole that it is in effect a layer. In the second case, the anomalous mass produces a uniform gravity gradient that is cancelled by a regional anomaly of opposite sign. As in most gravity problems, if regional effects are not adequately removed, they contaminate the data to be modeled; in this case, the regional masses add a constant to the uncorrected gravimetric density anomaly. One way to remove the effects of regional masses is to subtract the estimated density calculated from the gradient observed above the ground surface, where the density of air can be neglected, from the gravimetric density at depth to get the corrected gravimetric density,

$$d\rho^m(z) = \rho^m(z) - \rho^m(0) \quad (6)$$

and the corrected gravimetric anomaly is again found by subtracting the log density, and using the assumption stated above that the regional vertical gradient is constant,

$$d\rho^m(z) - \rho_{LOG}(z) = \rho_A{}^g(z) - \rho_A{}^t(z) - \rho_A{}^g(0) \quad (7)$$

Equation (7) describes the relationship between measurements and the density distribution:

1. On the right-hand side is the actual anomalous mass, as reflected in its density effect at the surface and at depth and its true density along the borehole.

2. On the left-hand side are the observations, reflected in the density effects of the measured gradients at the surface and at depth, and the well log.

VERTICAL GRADIENT OF GRAVITY NEAR STATE 2-14

To estimate the corrected gravimetric density anomaly at State 2-14, we found the vertical gradient above the surface by two independent means: by measuring it on the drill rig and by estimating it from gravity measurements on the Earth's surface within 100 km of State 2-14. The gradients obtained by these independent methods agree and produce a slightly positive corrected gravitational anomaly throughout the borehole.

M. R. Millett and D. J. Felske of Lawrence Livermore National Laboratory measured the free-air gradient at this site by occupying gravity stations on the drill rig at heights 8.1 and 32.5 m above ground surface. Their measurements are reported in Table 3. The measured free-air gradient was 312.9 μGal/m, 4.1 μGal/m more than F_W (which is 308.8 μGal/m).

Measured gradients can be disturbed by very local features, such as the mass of the drill rig, mud pits, and subtle local topography [*Beyer*, 1971]. To determine if our measured gradient is disrupted by local features, we used a method described by Beyer to calculate the anomalous free-air gradient from surface gravity measurements surrounding State 2-14. We selected all 7423 values of the simple Bouguer anomaly (corrected with density 2.67 g/cm^3) within a 100-km radius of State 2-14 from a data set compiled by the National Oceanographic and Atmospheric Administration (unpublished data, 1982). The vertical gradient was estimated at each of 495 observation points in the rectangle covered by Figure 1. For each point the Bouguer anomaly data were averaged over 20° azimuthal zones within each of 15 distance rings with outer radii covering a geometric series from 1 to 100 km. The average of the filled zones in each ring was used to estimate the average gravity value as a function of distance, and the gradient at the surface due to anomalous and regional masses was calculated using Beyer's equation 14. To ensure adequate azimuthal coverage, we interpolated gravity values over the southeastern end of the Salton Sea.

The simple Bouguer anomaly data around State 2-14 are contoured in Figure 4, and the calculated gradient anomalies are shown in Figure 5. The estimated anomalous vertical gradient at State 2-14 is 4.3 μGal/m, within 10% of the measured value, raising our confidence in its applicability.

When we use this measured free-air gradient in equations (4) and (7), the corrected gravimetric density is larger than the uncorrected value by almost 0.05 g/cm^3, giving an average anomaly of 0.07 g/cm^3, a significant value. Equation (7) shows that this nearly uniform density anomaly could be produced either by a model with a density effect at depth such that $\rho^g(z) > \rho^t(z)$, or one with a negative density effect at the surface.

MODELING

Models That Produce a Positive Density Anomaly at State 2-14

The observed corrected gravimetric density anamaly of 0.07 g/cm^3 is surprising in view of the high densities and high shale content observed in State 2-14 and the expectation that cooler regions surrounding it would have lower density. This anomaly could, in principle, be explained by either of two simple models with $\rho^g(z) > \rho^t(z)$. The first model has infinite horizontal layers with density 0.07 g/cm^3 larger than the gamma-gamma density. The observed log values would then be produced by an anomalous mass of -0.07 g/cm^3 surrounding the borehole. The second model requires the presence of a large amount of high-density material near but not intersecting the borehole. There is no independent geological evidence for higher-density material near the borehole. Possible sources of excess mass include dense intrusions, intense alteration at the M thermal anomaly, and lithologic changes such as a drastic increase in shale content near the borehole.

For a model to be useful, however, it should have some

TABLE 3. Gravity Measurements Above State 2-14 on April 8, 1986

	Tide Correction, mGal	Corrected Gravity, mGal	
		8.11 m	32.47 m
Time LT			
0700	−0.056	3357.646	
0722	−0.040		3350.040
0733	−0.032	3357.660	
0743	−0.024		3350.035
0754	−0.014	3357.658	
0805	−0.005		3350.036
0815	−0.004	3357.663	
0823	0.011		3350.046
0832	0.019	3357.669	
Average		3357.659	3350.039

Gradient is 7.620 mGal/24.36 m = 312.9 μGal/m.

corroboration from independent observations. We use the surface gravity field for corroboration. Since the surface gravity anomaly contours (Figure 4) are somewhat circular, we restrict our models to cylinders of radius r_c with a vertical axis at the center of the surface gravity anomaly, as shown in Figure 6. We simplify the problem by considering the measured value of the corrected gravimetric density anomaly, the left side of equation (7), to be 0.07 g/cm^3 over the depth range 1027–1737 m. Values of the anomaly are calculated along the borehole axis ($r = r_0$), as functions of the cylinder radius r_c, using the formulation of *Singh* [1977].

First, we consider the possibility that State 2-14 lies outside of the cylinder ($r_c < r_0$). In Figure 2*b* we see that the density from State 2-14 is very similar to values observed in the central portion of the geothermal field. The highest log values detected in C area, from Magmamax 2 (but incorrectly labeled by *Muramoto and Elders* [1984, Figure 43] as Magmamax 3), are no more than 0.1 g/cm^3 greater than the shale densities at State 2-14. To see if higher densities in the C area could cause the borehole gravimetric anomaly, we model this possible high-density anomaly as a cylinder with $r_c < r_0$, top depth $z_1 = 500$ m, bottom depth $z_2 = 3000$ m, and density contrast $\Delta\rho = 0.1$. The curve marked model 1 in Figure 7 shows the depth-averaged corrected gravimetric anomaly that would be seen in State 2-14, as a function of the radius r_c assumed for the cylinder. (Making z_2, the depth to the bottom of the cylinder, larger decreases the size of the anomaly.) It appears that excess density in the center of the field can cause a positive anomaly, but not as large as the one observed.

Next, we evaluate the alternative that State 2-14, which has a large proportion of high-density shale, lies within the anomalous mass ($r_c > r_0$). Of course, the outer boundary of this mass would cause a negative gravimetric anomaly, the opposite of that which was detected. But that subsurface mass anomaly also affects the measured free-air gradient, in some cases producing a negative density effect at the surface. If the negative density effect at the surface is larger than the negative effect at depth, a positive corrected gravimetric anomaly will be produced. Lacking constraints from borehole gravity data

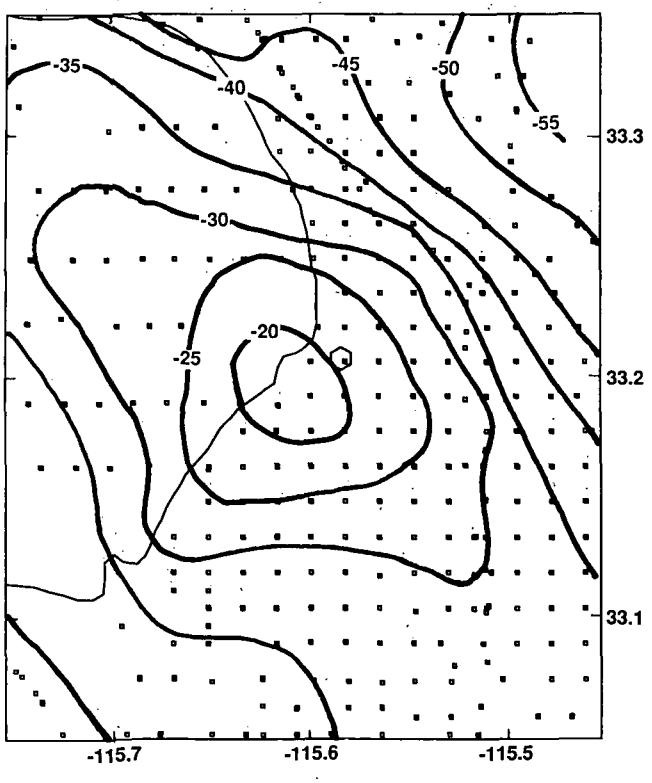

Fig. 4. Gravity data in the area covered by Figure 1. Contours derived from Bouguer corrected observations (using a density of 2.67 g/cm^3) near State 2-14, whose location is indicated by a hexagon. The squares represent gravity station locations in the mapped area. The data were obtained from NOAA and are very consistent with the gravity map of *Biehler et al.* [1964]. The contour interval is 5 mGal.

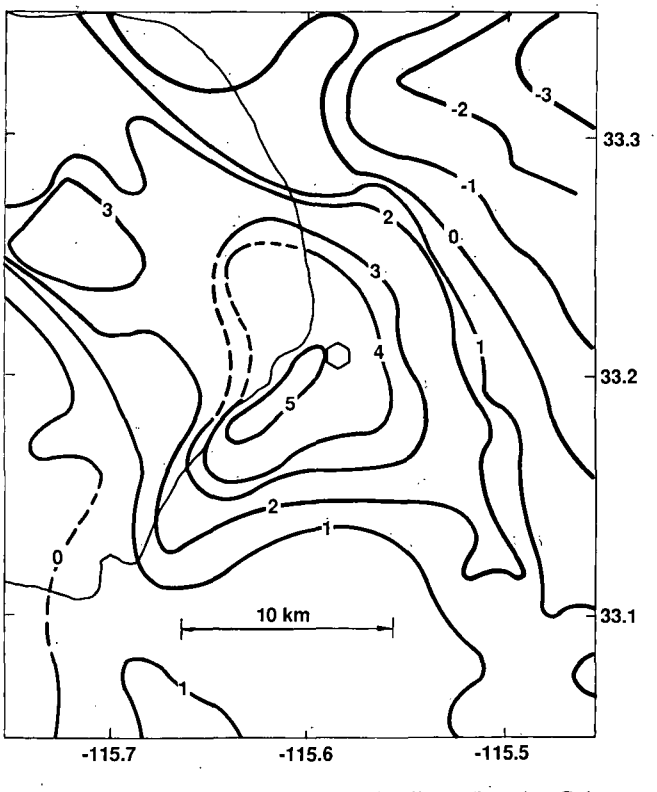

Fig. 5. Anomalous vertical gravity gradients (in microGals per meter) estimated from surface gravity measurements within 100 km of State 2-14, whose location is indicated by a hexagon. Data from a much larger area than is shown in Figure 4 were used to calculate the vertical gradients in Figure 5. The method of calculation is discussed in the text.

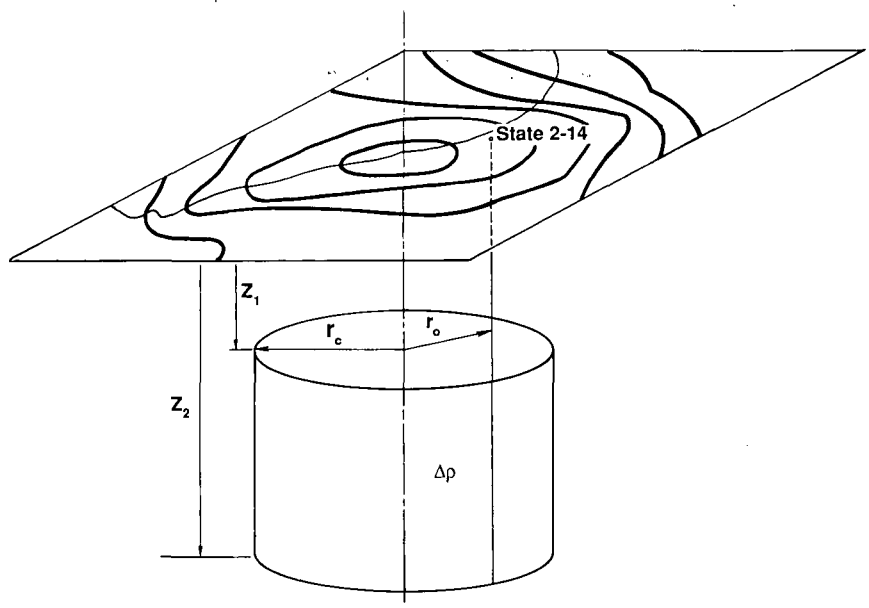

Fig. 6. The gravity model discussed in this paper. A cylinder with a vertical axis is assumed to lie beneath the center of the gravity anomaly. Different values of the parameters z_1, z_2, r_c, and $\Delta\rho$ are discussed in the text. State 2-14 lies at a distance $r_0 = 3962$ m from the center of the axis.

near the surface, we can make only simple models that indicate what is required to fit the data.

Shallow dense cylinders can produce the corrected gravimetric anomaly that was detected. A cylinder with r_c slightly greater than r_0 produces an anomalous gradient at the surface. For model 2 we arbitrarily set $\Delta\rho = 0.45$, the largest difference in density between the C and V curves in Figure 2, $z_1 = 50$ m and $z_2 = 500$ m. (If z_2 were much larger, this model would

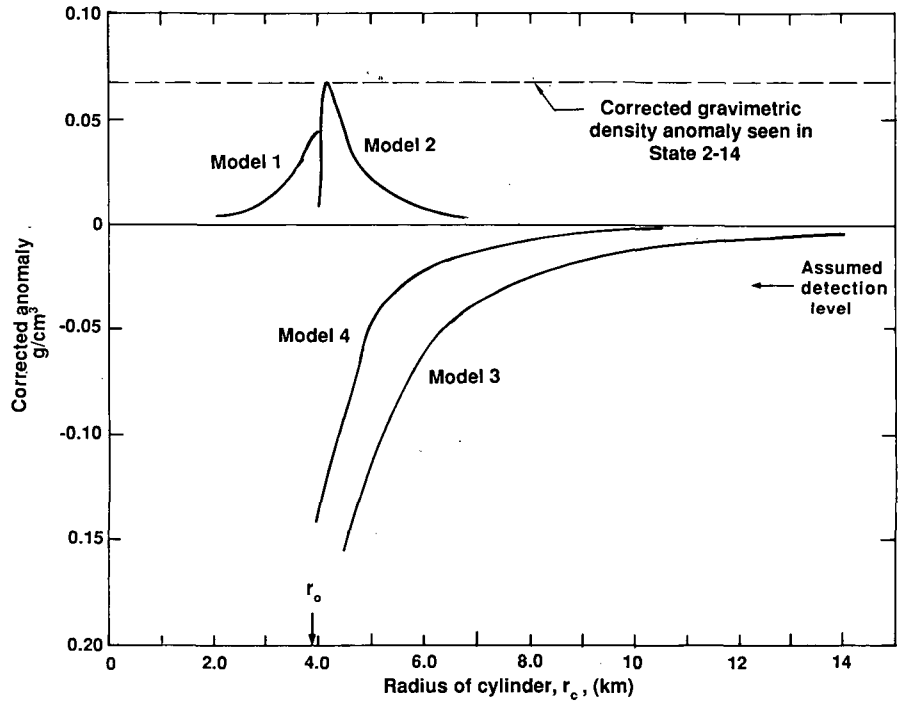

Fig. 7. Calculated corrected gravity anomaly at State 2-14 due to cylindrical models, as a function of the model cylinder radius r_c. The arrow at the bottom shows r_0, the radius from the center of the cylinder to State 2-14. The corrected anomaly is given by the right-hand side of equation (7), and the model parameters are described in Figure 6. Model 1 has a density contrast of 0.1, corresponding to the largest difference in density between the C area and the density observed at State 2-14, $z_1 = 500$ m and $z_2 = 3000$ m. Model 2, the "shallow" model, has a contrast of 0.45, corresponding to the difference in density between the C area and the average density in the Imperial Valley, $z_1 = 50$ m, and $z_2 = 500$ m. Model 3 has the same density contrast as model 2, but $z_1 = 500$ m, $z_2 = 5000$ m. Model 4 has a contrast of 0.25, corresponding to the difference in density between the C area and the SB area, with $z_1 = 500$ m and $z_2 = 3000$ m. Only the shallow model 2 produces the observed positive anomaly of 0.07 g/cm^3.

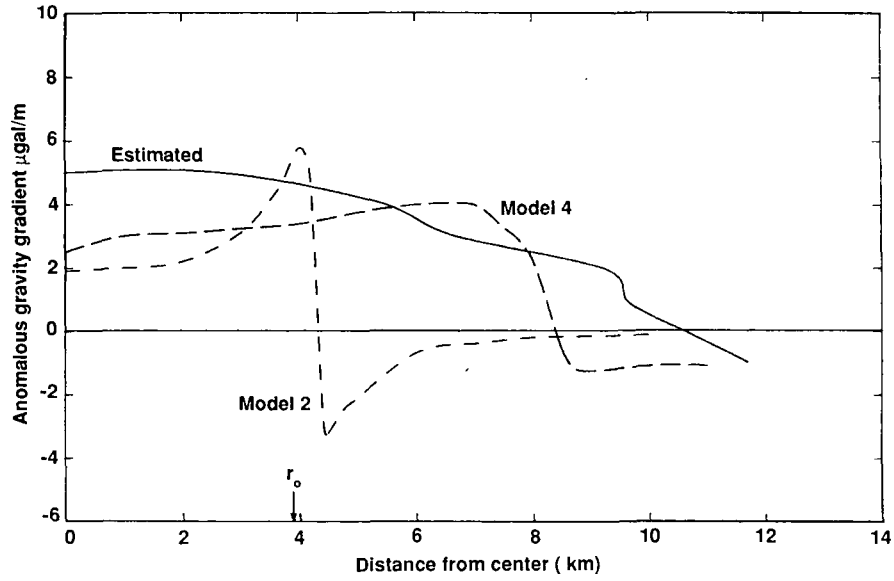

Fig. 8. Estimated vertical gradient anomaly data (from Figure 5) sampled along a northwest trending line from the center of the gravity anomaly, compared to calculated anomalous vertical gradients at the surface, for specific values of the model cylinder radius r_c, for models 2 and 4 from Figure 7. All curves are plotted as a function of distance of the measuring point from the center of the cylinder. The arrow at the bottom shows r_0, the radius to State 2-14. Model 2 is a shallow cylinder with $r_c = 4300$ m and produces the positive corrected gravimetric density anomaly seen in State 2-14 but does not match the surface observations shown here. Model 4, a deeper cylinder with $r_c = 8$ km, matches the estimated vertical gradient profile along the surface but produces almost no anomaly in the borehole.

cause variations in the anomaly over the depth range where we detected it to be constant.) The curve shown as model 2 in Figure 7 shows that a shallow body with r_c a few hundred meters greater than r_0 could produce our observed corrected gravitational anomaly of 0.07 g/cm^3. This was the basis of an earlier published claim that we may have detected a shallow edge of the densified zone just east of State 2-14 [*Kasameyer and Hearst*, 1987]. However, all shallow models that produce a high surface gradient at State 2-14 produce very large changes in vertical gradient as a function of distance, inconsistent with the results shown in Figure 5. This rapid change in gradient is illustrated in Figure 8, which shows the estimated anomalous vertical gradients along a northeast trending line from the center of the gravity anomaly obtained from the measured data shown in Figure 5, compared to surface gradient anomaly as a function of distance from the center of the cylinder calculated from two models. For the curve marked model 2 in Figure 8, we have set r_c to be 338 m greater than r_0. The change in gradient for this model is much more rapid than that seen in the curve estimated from surface data. Therefore we now reject near-surface features as a means to produce the observed positive corrected gravimetric anomaly and conclude that the positive borehole gravity anomaly indicates that the densely altered zone extends far enough from State 2-14 that its edge was not detected.

Models That Indicate Distance From State 2-14 to Edge of Density Anomaly

Models 3 and 4 indicate that the edge of the densely altered zone would produce a large negative anomaly unless it is far from State 2-14. We calculate corrected gravimetric density anomalous for two types of cylinders as a function of r_c. The depths and density contrasts are chosen, based on the log density data in Figure 2, to reflect two different possible views of the density anomaly. In the first view, represented by model 3, we note that the center of the geothermal field (C) has densities about 0.45 g/cm^3 above normal compaction curves (V). This contrast, $\Delta\rho = 0.45$, is applied to a cylinder with $z_1 = 500$ m and $z_2 = 5000$ m, starting shallow enough to produce a uniform disturbance over the depths studied in State 2-14 and extending deep into the sedimentary section. In the second view, model 4, we assume that the central anomaly lies within rock of densities similar to those seen in the SB area. It is modeled by a cylinder with $\Delta\rho = 0.25$, $z_1 = 500$ m, and $z_2 = 3000$ m. As their radii vary, these cylinders cause the anomalies shown as models 3 and 4 in Figure 7. Assuming that a negative anomaly of 0.03 g/cm^3 would have been detected, model 4 exceeds that limit if $r_c < 5.4$ km (1.4 km beyond State 2-14), and model 3 exceeds it if $r_c < 8$ km (4 km beyond State 2-14). Consequently, we conclude that the inner boundary of the B area is no closer than 1.4 km to State 2-14 and a boundary where densities return to "normal" is no closer than about 4 km to State 2-14.

The borehole gravity data require that material as dense or denser than that found in State 2-14 exists out to a distance of at least a few kilometers at depths from 1 to 2 km. There is a strong suggestion from the vertical gradient anomaly map (Figure 5) that this distance is of the order of 2–6 km, where there is a zone of very rapid decrease in vertical gradient anomaly from about 2.5 μGal/m to about −1 μGal/m. To illustrate this, the surface gradient calculated from model 4 with a fixed cylinder radius $r_c = 8$ km is compared in Figure 8 to the anomalous surface gradient estimated from surface gravity. It is clear that cylindrical models of this type, which have almost no effect on borehole gravity in State 2-14, can produce many features of the estimated vertical gradient. Both have a broad central area with a constant positive anomalous

gradient and fall rapidly through zero. The model falls off more rapidly, suggesting that the actual boundary is less abrupt or deeper. A comparison of Figures 1 and 5 indicates that the most abrupt decrease in the gradient lies to the east of the NB zone, roughly along an extension of the San Andreas fault zone. Thus the high-density zone probably continues to the NB area, where densities are similar to State 2-14.

CONCLUSIONS AND DISCUSSION

Our borehole gravity measurements indicate that the dense rocks that penetrated between 1- and 2-km depth in State 2-14 must extend several kilometers from the well. We see a slightly positive corrected gravimetric anomaly whose cause is not known. There is no evidence from the borehole gravity data collected to date that the SSSDP well is near the edge of the high-density zone that it penetrates. This conclusion is reinforced by the vertical gravity-gradient anomaly map (Figure 5), which shows a zone of uniform gradient surrounding the SSSDP. The zone of rapid decrease in gradient NE of State 2-14 and the high densities observed in a well from the NB area suggest that the boundary lies about 6 km from the well in that direction, roughly along a line extending south-southeast from the end of the San Andreas fault zone.

Hydrothermal alteration is the accepted cause of the high densities seen in sedimentary rocks in the SSGF. The occurrence of a large area of high densities to the NE of State 2-14 implies that the upper 2 km of the NB thermal area has been as at least as hot in the past as the C zone of the SSGF is today. Our results suggest that the thermal history of this zone is quite different from the history of the SB area, even though the present-day temperatures are similar [*Newmark et al.*, this issue]. From the location of the NB area between the plate boundary, as defined by the San Andreas fault zone, and the locus of present spreading, as defined by the SSGF, we speculate that this shallow dense area represents an earlier locus of spreading similar to the SSGF today. The nearly constant temperature gradient observed in the NB area (Figure 2) suggests that heating at shallow depths ceased long enough ago for the area to return to steady state conduction. The present elevated temperatures could represent the residual heat from that event, or something independent of it. Assuming that the cooling occurred by conduction and using a diffusivity α for compacted sedimentary rocks of the order of 40 m^2/yr and a half thickness L of 1500 m for the thermal zone, we estimate its characteristic thermal time L^2/α to be of the order of 60,000 years. More than twice that time would be required to reach steady state conduction. Thus the minimum age of this paleothermal zone is about an order of magnitude greater than ages of 6000 to 20,000 years estimated for the C anomaly of the Salton Sea geothermal field [*Kasameyer et al.*, 1984].

Acknowledgments. We appreciate the help and support of Tom Ashcraft, Doug Joiner, Don Wolcott, and Don Farchone of EDCON, Inc., who collected the data; On-site Science Manager John Sass of the U.S. Geological Survey, who ran the show at State 2-14; Al Duba of Lawrence Livermore National Laboratory (LLNL), who stayed up all night with the experiments; and Mel Millett and Don Felske of LLNL-Nevada, who collected the above ground gravity measurements. Support from George Kolstad of the Department of Energy, Office of Basic Energy Sciences, Geosciences Program, made this project possible. Work performed under the auspices of the U.S. Department of Energy by the Lawrence Livermore National Laboratory under contract W-7405-ENG-48. Two reviewers provided comments that led to significant improvements in the paper. Fred Paillet suggested restructuring the paper to make it easier to understand. Shawn Biehler detected a serious mistake in the scales on our original figures and assisted in the clarification of many of our ideas. We appreciate their efforts.

REFERENCES

Andes, J. P., Jr., and M. A. McKibben, Thermal and chemical history of mineralized fractures in cores from the Salton Sea Scientific Drilling Project (abstract), *Eos Trans. AGU*, *68*, 439, 1987.

Army Map Service, Western United States 1:250,000 series, *Map NI 11-9*, U.S. Geol. Surv., Reston, Va., 1959.

Beyer, L. A., The vertical gradient of gravity in vertical and near-vertical boreholes, Ph.D. thesis, Stanford Univ., Stanford, Calif., 1971.

Biehler, S., R. L. Kovach, and C. R. Allen, Geophysical framework of the northern end of Gulf of California structural province, Marine Geology of the Gulf of California, edited by T. H. van Andel and G. G. Shor, Jr., *Mem. Am. Assoc. Pet. Geol.*, *3*, 126–143, 1964.

Combs, J., Heat flow and geothermal resource estimates for the Imperial Valley, in *Cooperative Geological-Geophysical-Geochemical Investigations of Geothermal Resources in the Imperial Valley Area of California*, edited by R. W. Rex, pp. 5–27, University of California, Riverside, 1971.

EDCON, Inc., State well 2-14 Niland, California, *Rep. UCRL-15945*, Lawrence Livermore Nat. Lab., Livermore, Calif., 1986.

Elders, W. A., R. Rex, T. Meidav, P. T. Robinson, and S. Biehler, Crustal spreading in southern California, *Science*, *178*, 15–24, 1972.

Hearst, J. R, and P. H. Nelson, *Well Logging for Physical Properties*, McGraw-Hill, New York, 1985.

Hearst, J. R, J. W. Schmoker, and R. C. Carlson, Effects of terrain on borehole gravity data, *Geophysics*, *45*, 234–243, 1980.

Heiskanen, W. A., and F. A. Vening Meinesz, *The Earth and Its Gravity Field*, McGraw-Hill, New York, 1958.

Kasameyer, P. W., and J. R. Hearst, Borehole gravity measurements in the SSSDP (abstract), *Eos Trans. AGU*, *68*, 445, 1987.

Kasameyer, P. W., L. W. Younker, and J. M. Hanson, Development and application of a hydrothermal model for the Salton Sea geothermal field, California, *Geol. Soc. Am. Bull.*, *95*, 1242–1252, 1984.

Lachenbruch, A. H., J. H. Sass, and S. P. Galanis, Jr., Heat flow in southernmost California and the origin of the Salton Trough, *J. Geophys. Res.*, *90*, 6709–6736, 1985.

Mueller, I. I., The gradients of gravity and their applications in geodesy, Ph.D. thesis, Ohio State Univ., Columbus, 1960.

Muramoto, F. S., and W. A. Elders, Correlation of wireline log characteristics with hydrothermal alteration and other reservoir properties of the Salton Sea and Westmorland geothermal fields, Imperial Valley, California, USA, *Los Alamos Natl. Lab. Rep.*, *LA-10128-MS*, 1984.

Newmark, R. L., P. W. Kasameyer, and L. W. Younker, Shallow Drilling in the Salton Sea region:, The thermal anomaly *J. Geophys. Res.*, this issue.

Paillet, F. L., (Ed.), Preliminary report on geophysical well-logging activity on the Salton Sea Scientific Drilling Project, Imperial Valley, California, *U.S. Geol. Surv. Open File Rep.*, *86-544*, 1986.

Robbins, S. L., Re-examination of the values used as constants in calculating rock density from borehole gravity data, *Geophysics*, *46*, 208–210, 1978.

Sass, J. H., S. S. Priest, L. E. Duda, C. C. Carson, J. D. Hendricks, and L. C. Robinson, Thermal regime of the State 2-14 well, Salton Sea Scientific Drilling Project, *J. Geophys. Res.*, this issue.

Singh, S. K., Gravitational attraction of a vertical right circular cylinder, *Geophys. J. R. Astron. Soc.*, *50*, 243–246, 1977.

Sturtevant, R. G., and A. E. Williams, Oxygen isotopic profiles for the State 2-14 geothermal well: Evidence for a complex thermal history, (abstract), *Eos Trans. AGU*, *68*, 445, 1987.

J. R Hearst and P. W. Kasameyer, Mail Stop L-209, Energy Program, Lawrence Livermore National Laboratory, P. O. Box 808, Livermore, CA 94550.

(Received September 30, 1987;
revised April 12, 1988;
accepted May 25, 1988.)

JOURNAL OF GEOPHYSICAL RESEARCH, VOL. 93, NO. B11, PAGES 13,047–13,056, NOVEMBER 10, 1988

Laboratory-Determined Transport Properties of Core From the Salton Sea Scientific Drilling Project

WUNAN LIN AND WILLIAM DAILY

Lawrence Livermore National Laboratory, Livermore, California

Two cores from the Salton Sea Scientific Drilling Project have been studied in the laboratory to determine electrical resistivity, ultrasonic velocity, and brine permeability at pressures and temperatures close to estimated borehole conditions. Both samples were siltstones; the first sample was from 1158-m depth, and the other was from 919-m depth. A synthetic brine with 13.6 weight percent NaCl, 7.5 weight percent $CaCl_2$, and 3.2 weight percent KCl was used as a pore fluid. The dry bulk density of the first sample was 2.44 Mg m^{-3} with an effective porosity of 8.7%. The second sample had a dry bulk density of 2.06 Mg m^{-3} with an effective porosity of 22.2%. At the midplane of the first sample, electrical impedance tomography was used to map the spatial variation of resistivity during the experiment. Also, at the midplane of both samples, ultrasonic tomography was used to map the spatial variation of *P* wave velocity. In addition, resistivity was measured with six pairs of electrodes along the sample axis. Both samples showed a strong anisotropy in resistivity and ultrasonic velocity measured perpendicular and parallel to the sample axis. The brine permeability of the first sample decreased from 5 μD to about 1.6 μD during the experiment. The second sample permeability had the same trend, but the permeability values were about 3 orders of magnitude larger. The second sample was subjected to temperatures and pressures exceeding those experienced in situ. Permeability, resistivity, and ultrasonic velocity of this sample showed a discontinuous change just beyond these in situ conditions. This discontinuity implies a structural change in the rock under conditions which would be found below its origin depth in the borehole. A model is proposed to explain the observed velocity anisotropy and variations in velocity, electrical resistivity anisotropy, and permeability with effective depth. When in situ stress is released, microcracking may occur along grain boundaries preferentially oriented parallel to bedding. This microcracking controls velocity and resistivity anisotropy at room conditions. When pressure and temperature are restored, competing effects of compaction and thermal softening of the minerals cause a reversal in the anisotropy. At temperatures and pressures above those at in situ conditions, thermal fracturing or geochemical alteration along grain boundaries causes a discontinuous change in sample physical properties.

INTRODUCTION

The Salton Trough is a region where two plate tectonic features interact: the oceanic rift on the East Pacific rise system to the south and the strike-slip transform motion of the San Andreas fault system to the north [*Elders*, 1979]. This is one of the few areas in the world where an extensional plate boundary encroaches upon continental crust [*Elders et al.*, 1972]. These facts combined with the large geothermal energy resource and high geothermal gradient in the Salton Trough make the area scientifically interesting and economically attractive.

Objectives of the Salton Sea Scientific Drilling Project (SSSDP) are the investigation of spreading ridges on land, geothermal energy close to the heat source, formation of ore deposits by hydrothermal alteration, and fracture opening and sealing. To meet these objectives, a hole (State 2-14) was drilled to a depth of 3.2 km into the Salton Trough. Now, information on the formations of the Imperial Valley is directly accessible from borehole logs and study of the physical and chemical properties of borehole core. The purpose of this paper is to report the results of a laboratory study of brine permeability, electrical resistivity, and *P* and *S* wave ultrasonic velocities measured on two core samples from the SSSDP borehole under pressure, temperature, and pore fluid chemistry designed to simulate in situ conditions. Results from this work may be useful in interpreting the well log and regional geophysical data.

Paper number 7B7128.
0148-0227/88/007B-7128$05.00

SAMPLE DESCRIPTION AND EXPERIMENTAL PROCEDURE

The samples were machined to right circular cylinders about 10.16 cm long and 8.89 cm in diameter; the edges of both ends were beveled about 2 mm deep to facilitate a good match to the Hastalloy end cap of our system (see Figure 1). Both samples come from the chlorite-calcite alteration zone in the State 2-14 well [*Cho et al.*, 1987]. In the first sample, from 1158-m depth, bedding was essentially perpendicular to the sample axis. The second sample, from 919-m depth, was machined with its axis about 70° from the bedding so that a partially healed fracture would extend longitudinally through its length. Both samples are siltstones although the second sample is more sandy than the first sample [*Mehegan et al.*, 1986]. Sample descriptions are summarized in Table 1. Effective porosity was measured by weighing each sample dry (after several days in vacuum at 35°C) and water saturated (after several days in water at 0.7 MPa). The effective porosity was 8.7% and 22.2% for the first and second samples, respectively. The dry bulk density of the first sample was 2.44 Mg m^{-3}, and grain density (as measured on a crushed sample in a helium autopycnometer) was 2.7 Mg m^{-3}. The total porosity of this sample is therefore 10.2%. The principal minerals of this sample were quartz, calcite, albite, and chlorite, with trace amounts of muscovite or illite and k-feldspar. The dry bulk density of the second sample was 2.06 Mg m^{-3}, and the grain density was 2.7 Mg m^{-3}. The total porosity of this sample is therefore 24.6%. Mineralogical composition of the second sample was similar to that of the first except the muscovite and illite were replaced by kaolinite. The first sample contained a fracture which extended from one end to about its midplane; the other end was intact.

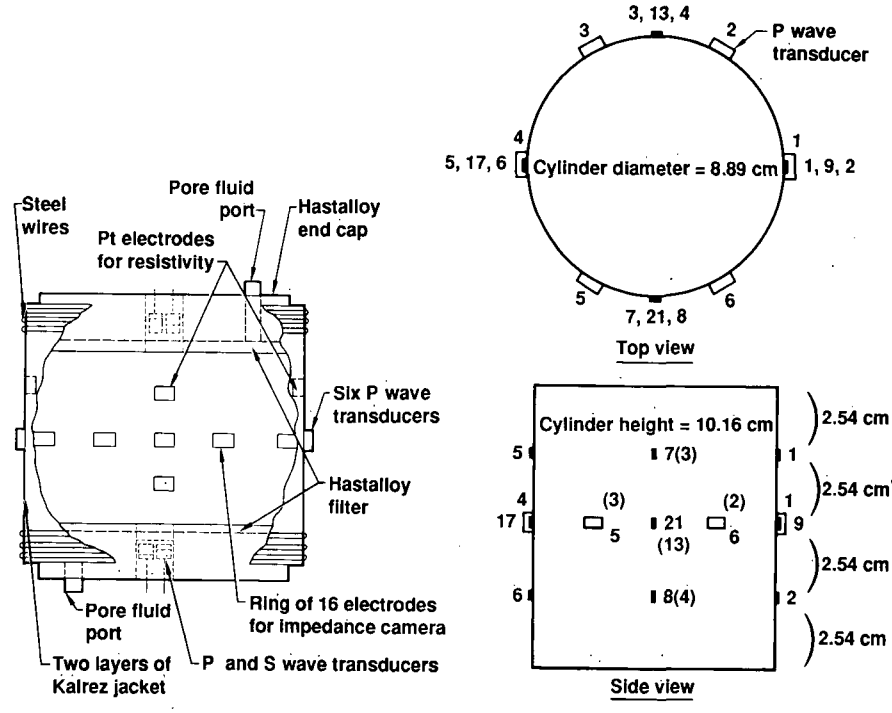

Fig. 1. Sample assembly schematic for both samples. (Left) Assembly of the sample, the Kalrez jacket, Hastalloy end caps, and the transducers used for resistivity and ultrasonic velocity. (Right) Detailed positions of resistivity electrodes and *P* waves transducers used for ultrasonic tomography.

Instrumentation on both samples was identical. Platinum electrodes were used as shown in Figure 1 for the electrical resistance measurements. The ring of 16 electrodes at the sample midplane was used for electrical impedance tomography (EIT) [see *Daily et al.*, 1987]. Ultrasonic piezoelectric transducers of both compressional (*P*) and shear (*S*) wave modes were mounted in the Hastalloy end caps. From these transducers the ultrasonic velocities were measured along the sample axis. Six *P* wave piezoelectric transducers were mounted in a ring around the midplane of the sample (outside the jacket but directly over the EIT ring). From this ring of ultrasonic transducers, *P* wave velocity tomographs were made at the sample midplane. A Kalrez jacket was used to isolate the sample from the silicone-based confining pressure medium. Essentials of the sample assembly are shown in Figure 1.

The experimental apparatus is described by *Daily and Lin* [1985]. It consists of three subsystems: the confining pressure system, the pore pressure system, and the electronics and computer system for data acquisition and experiment control. A commercial automatic conductance bridge measured the sample resistance between pairs of Pt electrodes. A Pt-Pt 10% Rh thermocouple located inside the pressure vessel near the sample measured the sample temperature.

The piezoelectric transducers, with a natural frequency of 1 MHz, were driven by a 90-V pulse. The output of the piezoelectric detector was preamplified, and a time delay oscilloscope was used to measure the pulse travel time. Brine permeability was calculated using Darcy's law from measured volumetric flow rate with a constant pore pressure difference across the sample. The temperature dependence of brine viscosity [*Piwinskii et al.*, 1977] was accounted for in the permeability calculation.

Hastalloy was used in the pore fluid plumbing instead of stainless steel to avoid the formation of iron colloids which could affect the permeability measurements [*Potter et al.*, 1981]. EIT was performed periodically on the first sample to detect any inhomogeneity in electrical conductivity. Because some leads were broken inside the pressure vessel during the experiment, EIT was not performed on the second sample. Tomographs were also made of ultrasonic velocity at the midplane of both samples. After each sample was jacketed but prior to its installation in the pressure vessel for test, X ray tomographs were made of several planes perpendicular to the axis.

Experimental pressures and temperatures representing a given depth were determined using the data in Figure 2. Each sample was tested at conditions prevailing at several depths, up to the depth from which the sample was obtained. Sample 2 was exposed to higher pressure and temperature. These pressure and temperature conditions, referred to as "effective depth," represent an attempt to determine the effect of various in situ conditions on physical properties of typical SSSDP core. An effective depth was chosen and the confining pressure, pore pressure, and sample temperature were determined. The borehold temperature estimated by *Nicholson* [1986] was used to determine sample temperature at an effective depth. For the first sample the hydrostatic confining pressure was chosen to equal the lithostatic overburden pressure (for an overburden density of 2.5 Mg m^{-3}) at the given depth. For the second sample we attempted to estimate a more realistic pressure profile by integrating the borehole density log. The pore fluid pressure was chosen to be the hydrostatic pressure

TABLE 1. Sample Descriptions

	Sample 1	Sample 2
Lithology	siltstone	siltstone
Depth of origin, m	1158	919
Dry bulk density, Mg m^{-3}	2.44	2.06
Grain density, Mg m^{-3}	2.7	2.7
Effective porosity, %	8.7	22.2
Total porosity, %	10.2	24.6

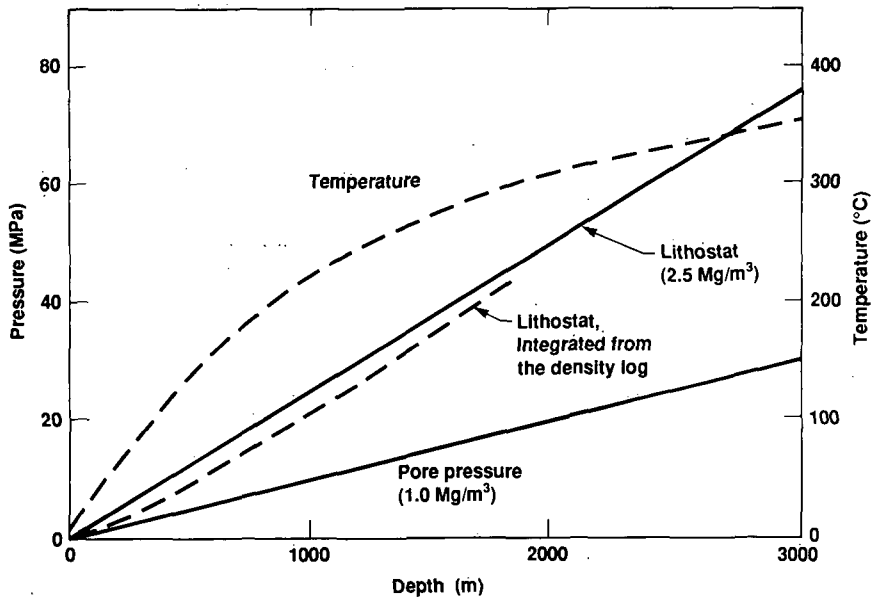

Fig. 2. Curves used to determine experimental confining pressure, pore pressure, and temperature as a function of effective depth. The thermal profile as a function of depth is the equilibrium borehole temperature from *Nicholson* [1986]. For the first sample the confining pressure as a function of depth was calculated assuming a lithostatic pressure due to an overburden density of 2.5 Mg m^{-3}. For the second sample the confining pressure was calculated by integrating the density log. The pore pressure was calculated assuming a hydrostatic pressure from a fluid of 1.0 Mg m^{-3} density.

of a 1 Mg m^{-3} fluid at the simulated depth. (The increase in brine density due to dissolved solids is approximately offset by a decrease in density due to increased temperature.) Conditions imposed on the two samples are summarized in Figures 3*a* and 3*b*. Both experiments were terminated by a failure in the sample jacket from the extreme temperatures and pressures. Jacket failure on the first sample prevented running the experiment beyond the sample origin. To observe any effects of extreme borehole conditions on the rock, the second sample was taken to conditions existing approximately 780 m below the sample origin.

A pore fluid was synthesized to contain the principal constituents of the preflash borehole fluid as determined by *Michels* [1986]. The composition was 13.4 wt % NaCl, 7.5 wt % $CaCl_2$, and 3.2 wt % KCl. This synthetic brine was constituted to simulate the chemistry of the in situ pore fluid. We were unable to measure directly the electrical conductivity of the synthetic brine. By mixing it with 5 parts by volume distilled

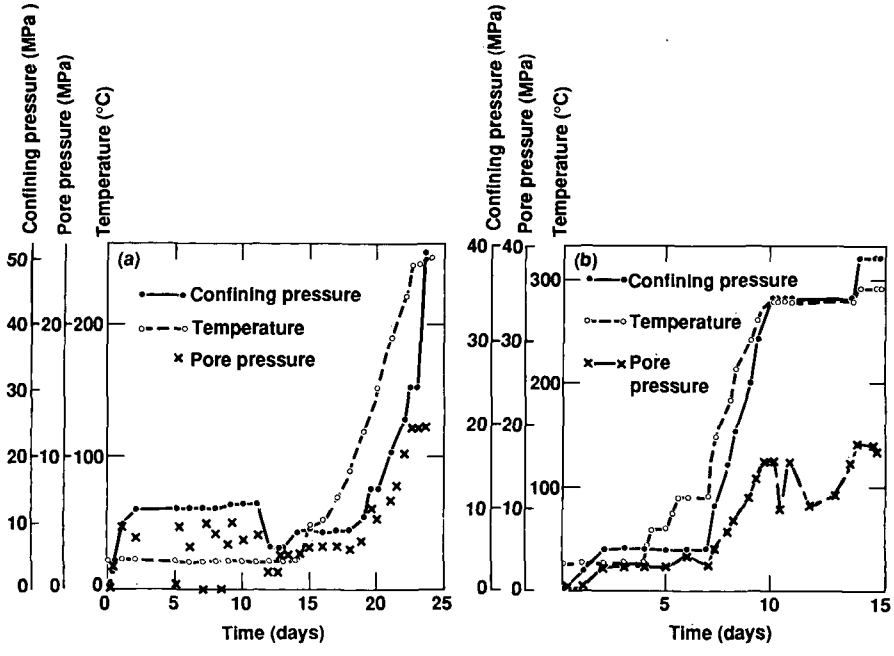

Fig. 3. Experimental confining pressure, pore pressure, and temperature histories. (*a*) First sample. (*b*) Second sample.

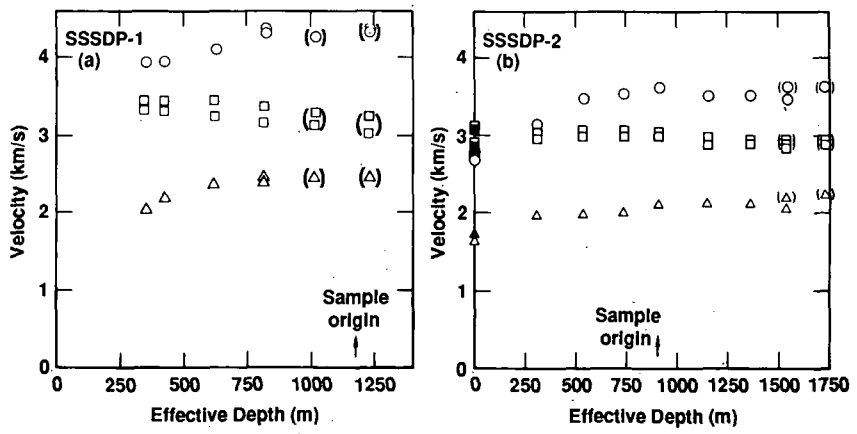

Fig. 4. Laboratory-determined ultrasonic *P* wave velocity as a function of effective depth. Open circles, longitudinal *P* wave velocity. Solid circles, postexperimental longitudinal *P* wave velocity. Open triangles, longitudinal *S* wave velocity. Solid triangles, postexperimental longitudinal *S* wave velocity. Open squares, diametrical *P* wave velocity. Solid squares, postexperiment diametrical *P* wave velocity. Data points in parentheses may have been affected by a leak in the sample jacket. (*a*) First sample. (*b*) Second sample.

water (0.001 S m^{-1}) we measured a conductivity of 8.6 S m^{-1} and used a volumetric mixing rule to estimate the conductivity of the brine to be about 50 S m^{-1} (an equivalent resistivity of 0.02 ohm m). Electrical conductivity of the in situ brine is not known. The same pore fluid was used in both experiments.

Results and Discussion

Tomographs

Three types of tomographic imaging were used to characterize the samples before and during the experiment: X ray, electrical impedance, and ultrasonic. X ray tomographs were made of several planes in both samples before the experiment. Electrical impedance and ultrasonic tomographs were made of the first sample during various stages of the experiment. Ultrasonic tomographs of the second sample were made during the experiment. Broken electrical leads on this sample made impedance tomography impractical.

Plate 1 shows tomographs from the first sample. The ultrasonic and impedance tomographs were filtered by an image taken at 4.3-MPa confining pressure, 1.3-MPa pore pressure, and 20°C (just before application of the simulated in situ pressures and temperatures to the sample). The filtering was accomplished by subtracting, pixel by pixel, the two images so that these tomographs show the change of sample *P* wave velocity and resistivity resulting from changes in the experimental conditions. No change in the resistivity and velocity is indicated by red and blue, respectively. The dark edge and lighter core of the X ray image is probably an artifact from the high-density contrast at the air-rock boundary. The ultrasonic tomograph was spatially filtered as described by *Ramirez and Daily* [1987].

Note that there is evidence for both healed fractures (high-density lineaments) and open fractures (low-density lineaments) in the X ray image. Some of these fractures are visible in the sample surface on close inspection. Because these fractures do not appear to extend the full length of the sample, we have considered this sample intact. The triangular anomaly in the X ray image is an enhanced density feature which runs through the core midplane. Only six transducers were used for the travel time image so that the spatial resolution is very poor, especially near the image edge. However, the triangular high-density anomaly in the X ray tomograph may be related to the region of small velocity change (blue color) in the ultrasonic tomograph. This tomograph also indicates that most of the image area outside the anomaly shows increasing travel time with increasing effective depth, just as shown in the diametrical velocity plotted in Figure 4*a*. The region of resistivity increase imaged by EIT (green and blue colors) also corresponds to this triangular density feature. At the surface this feature seems to be an area of coarser grain size.

Ultrasonic Wave Velocities

As mentioned previously, compressional and shear wave velocities were measured along the sample axis (parallel to the well bore axis) and orthogonal to the sample axis near the sample midplane, in three directions separated by about 60°. These measurements were made at various confining pressures, pore fluid pressures, and temperatures. Figure 2 was used to convert these conditions into effective depth. Maximum effective depth for the first sample was 1218 m (corresponding to a temperature of 245°C) and for the second sample was 1719 m (290°C). Figure 4 shows the ultrasonic velocities versus effective depth for both samples. The measured travel times were corrected for the system delay time through the Hastalloy end caps (for propagation along the sample axis) and the Kalrez jacket (for diametrical propagation) at room temperature. Data points in parentheses may have been affected by a leak in the sample jacket. Measurement precision of first arrival time of the pulse results in a random error of about 2% in the calculated *P* wave velocities and about 5% in the calculated *S* wave velocities.

Compressional and shear wave velocities, longitudinal to the axes in both samples, increase with increasing depth to the sample origin. In contrast, the diametrical compressional wave velocity is nearly depth independent at effective depths less than 610 m but decreases slowly at deeper effective depths. Both samples show a strong *P* wave anisotropy. Ultrasonic *P* wave velocity measured along the sample axes is as much as 40% larger than that measured diametrically (see Figure 4).

Longitudinal and diametrical *P* wave velocities of the second sample show a discontinuous drop at the effective depth corresponding to the sample origin (between 910- and 1100-m effective depth). Below this depth the longitudinal velocity is virtually independent of effective depth and the diametrical velocity decreases slightly.

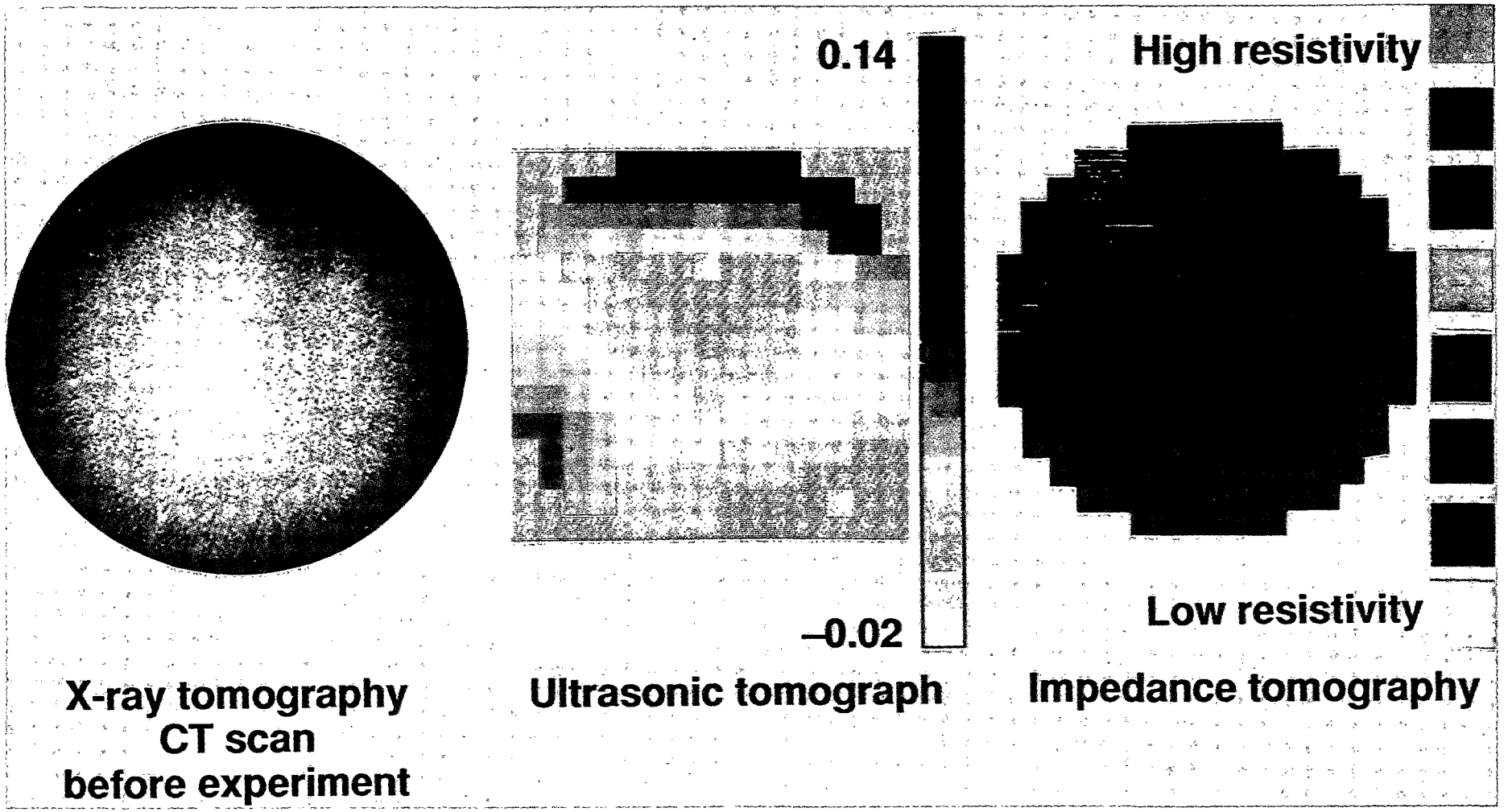

Plate 1. Tomographic imaging of the first sample. (Left) X ray tomograph near the midplane before the experiment. Darker shades represent higher density. The azimuthally symmetric pattern is probably an artifact of the high-density contrast between the sample and air. (Middle) Ultrasonic *P* wave velocity tomograph. The tomograph is an alterant image of changes in inverse velocity between when the sample was at near-surface conditions and at about 300-m depth. Blue represents no change in travel time. (Right) Electrical impedance tomograph. This is an alterant tomograph, as in the middle graph, of electrical resistivity at 1 kHz. Red represents no change in resistivity.

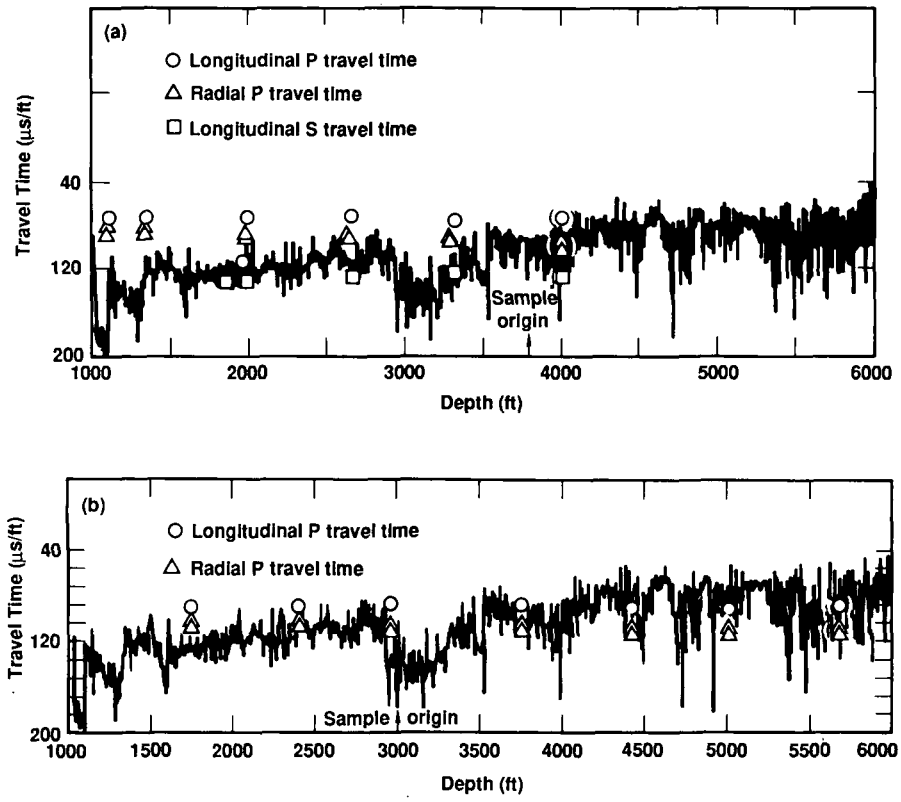

Fig. 5. Ultrasonic *P* wave travel time as a function of depth measured in the laboratory (points) and in situ from the borehole sonic log (line). Data points in parentheses may have been affected by a leak in the same jacket. (*a*) First sample. (*b*) Second sample.

An important conclusion from these data is that the compressional wave velocity is strongly anisotropic between the longitudinal and diametrical directions. At room conditions and shallower than 300-m effective depth the samples are not transversely isotropic (i.e., there is significant anisotropy in the diametrical plane (Figure 4*b*)). The axis of the second sample was about 20° from perpendicular to bedding and this may explain the initial diametrical anisotropy in that sample. Deeper than about 300 m the compressional velocity for both samples becomes nearly tranversely isotropic. The velocity difference in the diametrical plane may be due to inclination of that plane to bedding. At room conditions the compressional wave velocity seems controlled by microcracks oriented parallel to bedding so that the longitudinal velocity is smaller than the diametrical velocity (Figure 4*b*). However, when pressures and temperatures were increased (i.e., at effective depths greater than 300 m), the longitudinal compressional wave velocity became greater than the diametrical velocity (Figure 4*a* and 4*b*).

Thin section studies on a sample from 1157 m showed micaceous minerals oriented along the bedding (L. A. Noblet, personal communication, 1987). Therefore it is probably appropriate to assume that the clay minerals in our sample are aligned with the bedding. If the samples contain minerals preferably oriented transverse to the sample axis (such as these clay minerals), upon removal from the in situ environment, microcracks may form along the preferred orientation of the minerals so that the measured ultrasonic velocity data may be explained as follows. At room conditions the measured compressional wave velocity is presumed to be dominated by these microcracks and is therefore quite low. As pressures were increased, these microcracks closed. Because of the preferred orientation of the defects, these closures affected the longitudinal velocity much more than the diametrical velocity. Increased temperature tends to decrease the rock moduli and thereby the compressional velocity. The net effect of increasing pressure and temperature was to increase the longitudinal and decrease the diametrical velocities, especially with such a large geothermal gradient. This explains why the longitudinal *P* wave velocity increased and the diametrical velocity decreased at effective depths shallower than the sample origin. Below the sample origin, the decrease in all *P* wave velocities was probably due to the dominating temperature effect since most of the stress relief microcracks would have been closed at the sample origin pressure. Subvertical to vertical cracks (from micro to macro in size) have been reported in situ (L. J. Caruso, personal communication, 1987). The velocity anisotropy at the in situ conditions may also be caused by these fractures. Of course the measured velocities were not corrected for the variations of sample dimensions at pressures and temperature. This correction will likely decrease the difference between the velocity parallel to the sample axis and the velocity orthogonal to the sample axis. However, this correction would probably be less than a few percent while we observe up to 40% anisotropy. For a transversely isotropic material, as most sedimentary rocks are likely to be, ultrasonic wave velocity parallel to bedding is greater than that perpendicular to bedding [*Lin*, 1985]. The reverse anisotropy (velocity perpendicular is up to 40% greater than that parallel to bedding) in these SSSDP samples may have important implications on interpretation of seismic and seismic refraction data in the Salton Trough. *Hill* [1977] predicted that seismic velocity in the Imperial Valley would be anisotropic. However, *Fuis et al.* [1984] did not report seismic velocity anisotropy in their seis-

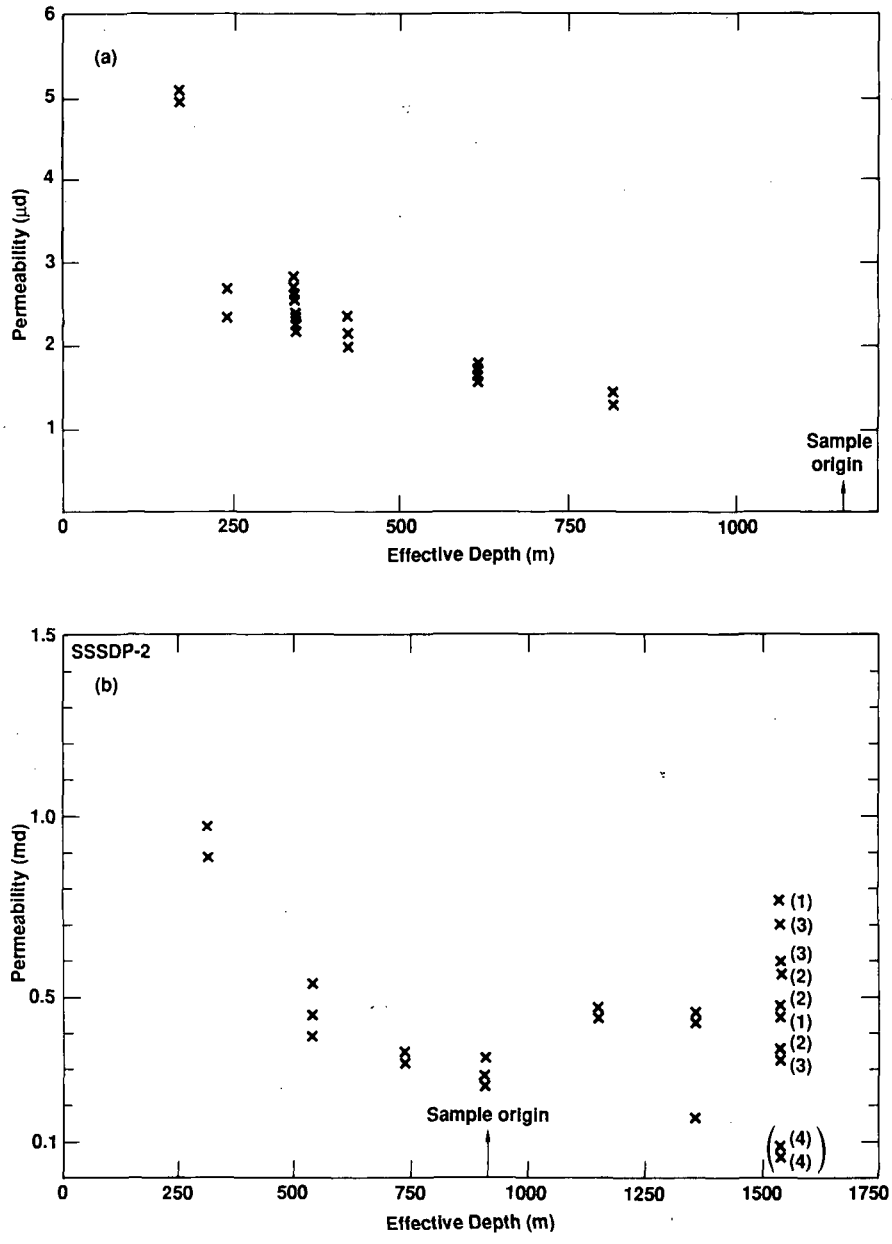

Fig. 6. Brine permeability as a function of effective depth. Data points in parentheses may have been affected by a leak in the sample jacket. Numbers in parentheses indicate sequence of data collection. (*a*) First sample. (*b*) Second sample.

mic refraction survey of the region. Additional seismic sounding in the Salton Trough should be done to look for this anisotropy and account for it in the data interpretation.

The laboratory *P* wave velocity data are also compared with the borehole sonic log in Figure 5. Only the *P* wave travel time is available in the borehole log. At effective depths shallower than the sample origin (1158 m for Figure 5*a* and 919 m for Figure 5*b*), the sonic log travel time is greater than the laboratory ultrasonic travel time. This is to be expected, since the rocks at shallower depths are either of different lithology or at a different state (integrity, compaction, cementation, etc.) from our sample. At the depth of origin for each sample, the ultrasonic travel time is within 10% of the borehole sonic log travel time. The low borehole sonic velocity from 884 m to 1067 m results from a major fracture zone [*Daley et al.*, 1987].

From laboratory studies on samples of different rock type and alteration it may be possible to generate a data base from which to interpret well log data and field seismic sounding results. Then it may be possible to identify rock type and/or alteration from well log data when no core is recovered. Extension of the data base to conditions deeper than the total depth of a borehole may allow inferences of rock type and/or alteration from deep seismic sounding.

Brine Permeability

Brine permeability of the samples was measured by flow along the sample axes. Calculated values have an uncertainty between 12 and 15%, owing to uncertainties in measurement of pore fluid volume, pore pressure gradient, and elapsed time [*Daily and Lin*, 1985]. Results are plotted as a function of effective depth in Figure 6. For both samples, permeability decreases with depth at effective depths less than the sample origin. This implies compaction of the rock toward the original in situ state. At conditions at effective depths deeper than the sample origin, permeability increased. This result supports

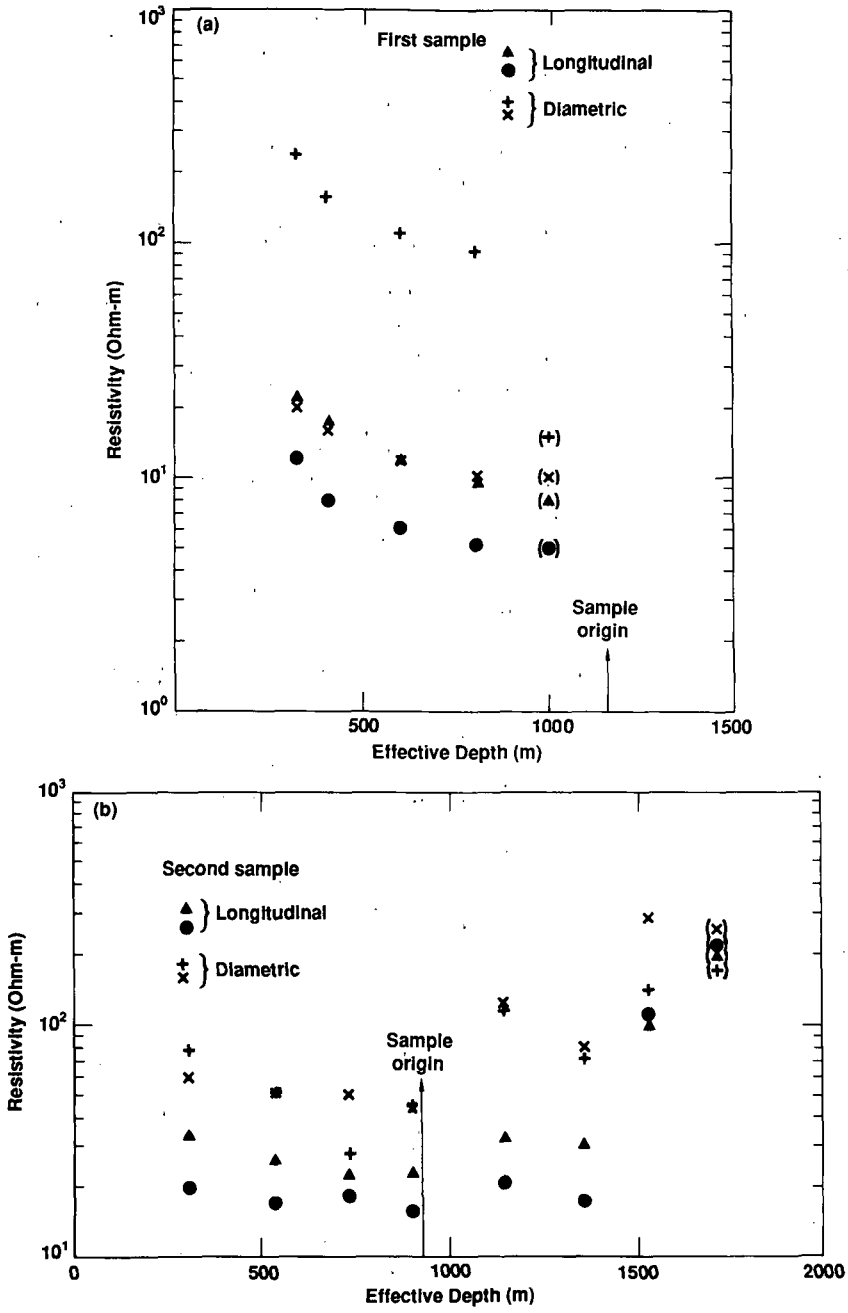

Fig. 7. Electrical resistivity at 1 kHz as a function of effective depth. Data points in parentheses may have been affected by a leak in the sample jacket. (*a*) First sample. (*b*) Second sample.

our model of thermal cracking invoked to explain the ultrasonic velocity and resistivity discontinuity (see below) at sample origin depth. X ray diffraction studies on the first sample showed no measurable change in mineralogy after the experiment. However, changes in sample mineralogy as small as a few percent, which would be undetected in the X ray analysis, may account for significant changes in physical properties such as permeability. To investigate this possibility, thin section and scanning electron microscope studies are now in progress.

There are no field data available for comparison with these measured permeabilities. However, the laboratory results are consistent with those of *Brace* [1980] for intact shale and siltstone. The first sample contains a visible hairline crack extending from one end to about the middle. The X ray tomograph shows that this fracture is intersected by another internal to the sample and that there are two other apparently healed fractures along the sample axis. The effective porosity is only 8.7%, which is small for a siltstone or shale. This low effective porosity and the absence of throughgoing fractures are probably the causes of the low permeability. The second sample has a prominent fracture extending its length. The X ray tomograph shows this as a low-density feature. Therefore it is either open or partially filled with secondary mineralization of lower density than the bulk composition. Measured permeability of this sample is nearly 3 orders of magnitude larger than the first sample, implying that any healing of that fracture may be only partial. Of course, the larger permeability of the second sample may also be due to its large (22%) effective porosity.

Electrical Resistivity

Electrical resistivity of the samples was measured from 14 electrode pair combinations of 12 electrodes (Figure 1, right). The resistivity to current flow predominately in the diametric direction was measured by pairs 1-5, 9-17, 2-6, 3-7, 13-21, and 4-8. In the longitudinal direction, along the sample side, the resistivity was measured by pairs 1-9, 9-2, 3-13, 13-4, 5-17, 17-6, 7-21, and 21-8. Uncertainty in the electrical resistance measurements was less than 5%. There are large differences in the measured values representing different parts of the samples, especially in the diametrical measurements. Inhomogeneity of the sample is largest in the diametrical direction: about 1 order of magnitude. The maximum difference among the resistivity measured along the sample side is about 100%. Also, for both samples the resistivity measured along the sample axis near the surface is smaller than that measured diametrically across the sample. For example, the ratio of the smallest values of diametrical and longitudinal resistivity on both samples ranged between 1.7 and 3.0

Selected resistivity measurements are shown for both samples in Figure 7. Similar to the ultrasonic velocity, the resistivity measured at some locations in the samples approaches the in situ value obtained by the borehole log when the effective depth approaches the sample origin. However, this agreement is only coincidental, and for this reason the laboratory and log data are not compared explicitly. Rock resistivity is strongly influenced by the brine electrical resistivity, and the synthetic brine used in the laboratory was not constituted to match formation water resistivity.

At effective depths shallower than the sample origin, measurements from the two samples are similar in magnitude and trend. Several competing factors may account for the resisitivity trend at these depths. First, gradual compaction at increasing pressures closes pores and microcracks to increase resistivity with increasing effective depth [*Daily and Lin*, 1985]. Second, brine resistivity decreases at increasing temperature to decrease resistivity with increasing effective depth [*Daily and Lin*, 1985]. Third, a small amount of alteration along grain boundaries (not detectable by X ray diffraction) may result in a decrease in resistivity with time. Apparently, the second and third factors dominate because the net effect is a decrease in measured resistivity with effective depth.

Only the second sample was taken to temperatures and pressures greater than its origin. However, just as for the ultrasonic velocity and permeability, there is a resistivity discontinuity near that depth (see Figure 7) with a continuation of the earlier trend deeper than 1372 m. (The data at effective depths greater than 1524 m are probably contaminated by a leak in the sample jacket which occurred sometime near the end of the experiment.) This resistivity increase may be caused by the generation of thermally induced microcracks or pressure-induced pore failure due to extreme conditions not previously experienced by the sample. Either effect would open some of the isolated porosity. If this newly induced porosity does not contain pore fluid, sample resistivity will increase until this porosity becomes saturated. If the newly induced porosity contains fluid less saline than the synthetic brine with which it is mixed, resistivity of the pore fluid mixture will increase, also resulting in a net resistivity increase for the sample.

SUMMARY AND CONCLUSIONS

Laboratory-measured *P* wave velocity in two SSSDP cores from the chlorite-calcite alteration zone indicates that *P* wave velocity is strongly anisotropic in the Salton Trough. Experimental conditions of confining pressure, pore fluid pressure, and temperature were used to simulate in situ borehole conditions. These conditions were designed to return the core to its original in situ state; one sample was then exposed to temperatures and pressures greater than those to which it had ever been exposed. When at their original in situ conditions, *P* wave velocity was within 10% of that obtained by the sonic log. At greater pressures and temperatures the measured ultrasonic velocities had a discontinuous decrease with effective depth.

Laboratory results revealed a strong *P* wave velocity anisotropy in the sample which may be present in situ. A model which is compatible with the experimental results, rock petrography, and known fracturing explains the room condition anisotropy by the presence of microcracks resulting from stress relief when the rock is removed from the formation. As pressure and temperature are applied to the samples, this anisotropy is changed by several factors, making the anisotropy a function of the geothermal and pressure gradient. The model used to explain the experimental data beyond the sample origin calls for structural damage to the sample, either due to thermal cracking or collapsing of isolated pores, at higher pressures and temperatures.

Tomographic images of the sample before and during the experiment contributed to our understanding of the internal structure of the sample. Such images may be important to studies of alteration, especially in a fractured sample where alteration or deposition may be concentrated along the fracture. Mineralogical alteration was not observable by X ray diffraction analysis on the first sample. However, alteration may occur over longer times and at higher temperatures.

Acknowledgments. The authors are grateful for the laboratory technical support of J. Carbino. D. Guenther and J. Beatty provided computer hardware and software support. Many helpful discussions on experimental procedure and data interpretation were provided by P. Kasameyer, R. Newmark, and H. Heard. Valuable comments that greatly improved the manuscript were received from J. Berryman, A. Duba, and R. Newmark. The manuscript has also been carefully reviewed by H. Olsen, J. Sass, and R. Wilkens. This work was supported by the Office of Basic Energy Sciences, G. Kolstad, director, and administered at Lawrence Livermore National Laboratory by L. Younker. Work performed under the auspices of the U.S. Department of Energy by the Lawrence Livermore National Laboratory under contract W-7405-ENG-48.

REFERENCES

Brace, W. F., Permeability of crystalline and argillaceous rocks, *Int. J. Rock Mech. Min. Sci. Geomech. Abstr.*, *17*, 241–251, 1980.

Cho, M., J. G. Liou, and D. K. Bird, Prograde phase relations in the California State 2-14 well meta-sandstones, Salton Sea Geothermal Field, *Eos Trans. AGU*, *68*, 445, 1987.

Daily, W., and W. Lin, Laboratory-determined transport properties of Berea sandstone, *Geophysics*, *50*, 775–784, 1985.

Daily, W., W. Lin, and T. Buscheck, Hydrological properties of Topopah Spring tuff: Laboratory measurements, *J. Geophys. Res.*, *92*, 7854–7864, 1987.

Daley, T. M., T. V. McEvilly, and E. L. Major, Analysis of VSP data at the Salton Sea Scientific Drilling Project, *Eos Trans. AGU*, *68*, 445, 1987.

Elders, W. A., The geological background of the geothermal fields of the Salton Trough, in *Geology and Geothermics of the Salton Trough, Campus Museum Contrib. 5*, edited by W. A. Elders, University of California, Riverside, Calif., 1979.

Elders, W. A., R. Rex, T. Meidav, P. T. Robinson, and S. Biehler, Crustal spreading in southern California, *Science*, *178*, 15–24, 1972.

Fuis, G. S., W. D. Mooney, J. H. Healy, G. A. McMecham, and W. J. Lutter, A seismic refraction survey of the Imperial Valley region, California, *J. Geophys. Res.*, *89*, 1165–1189, 1984.

Hill, D. P., A model for earthquake swarms, *J. Geophys. Res.*, *82*, 1347–1352, 1977.

Lin, W., Ultrasonic velocities and dynamic elastic moduli of Mesaverde rocks, *UCID-20273-Rev. 1*, Lawrence Livermore Nat. Lab., Livermore, Calif., 1985.

Mehegan, J. M., C. T. Herzig, and R. M. Sullivan, *Salton Sea Scientific Drilling Project California State 2-14 Well Visual Core Descriptions, UCR/IGPP-86/1*, vol. 1, University of California, Riverside, Calif., 1986.

Michels, D. E., SSSDP fluid composition at the first flow test of State 2-14, *Geotherm. Resour. Counc. Trans.*, *10*, 461–465, 1986.

Nicholson, R. W., Extensive coring in the deep hot geothermal wells, *Geotherm. Resour. Counc. Trans.*, *10*, 467–471, 1986.

Piwinskii, A. J., R. Netherton, and M. Chan, Viscosity of brines from the Salton Sea geothermal field, Imperial Valley, California, *UCRL-52344*, Lawrence Livermore Nat. Lab., Livermore, Calif., 1977.

Potter, J. M., W. E. Dibble, Jr., and A. Nur, Effects of temperature and solution composition on permeability of St. Peter sandstone—Role of iron (III), *J. Pet. Technol.*, *33*, 905–907, 1981.

Ramirez, A., and W. D. Daily, Underground research laboratory grout trials—Geotomography results, *UCID-21139*, Lawrence Livermore Nat. Lab., Livermore, Calif., 1987.

W. Daily and W. Lin, Earth Sciences Department, Lawrence Livermore National Laboratory, Livermore, CA 94550.

(Received September 14, 1987;
revised November 23, 1987;
accepted November 25, 1987.)

JOURNAL OF GEOPHYSICAL RESEARCH, VOL. 93, NO. B11, PAGES 13,057–13,067, NOVEMBER 10, 1988

Laboratory Studies of the Acoustic Properties of Samples From Salton Sea Scientific Drilling Project and Their Relation to Microstructure and Field Measurements

P.A. TARIF, R.H. WILKENS,[1] AND C.H. CHENG

Earth Resources Laboratory, Department of Earth, Atmospheric and Planetary Sciences Massachusetts Institute of Technology, Cambridge

F.L. PAILLET

U.S. Geological Survey, Denver, Colorado

Compressional and shear wave velocities were measured at confining pressures up to 200 MPa for 12 core samples from the depth interval of 600–2600 m in the California State 2-14 borehole. Samples were selected to represent the various lithologies, including clean, heavily cemented sandstones, altered, impermeable claystones, and several intermediate siltstones. Velocities measured at ultrasonic frequencies in the laboratory correspond closely with velocities determined from acoustic waveform logs and vertical seismic profiles. The samples exhibit P wave velocities around 3.5 km/s at depths above 1250 m but increase to nearly 5.0 km/s at 1300 m in depth. Further increases with depth result in compressional wave velocity increasing to nearly 6.0 km/s. These increases in velocities are related to systematic variations in lithology, microstructure, and hydrothermal alteration of originally clay-rich sediments. Scanning electron microscope observations of core samples confirm that local core velocities are determined by the combined effects of pore size distributions and the proportion of clays and alteration minerals such as epidote present in the form of pore fillings and veins.

INTRODUCTION

The Salton Sea Trough is an active tectonic depression that has been collecting sediments from the adjacent Colorado River Delta for thousands of years. It is located at the junction of the active extensional rift of the Gulf of California and the transform faults of southern California. The geothermal gradient throughout the area is anomalously high. Thus the Salton Sea Trough provides a perfect setting for studying how the sediments in the basin are altered by the high temperatures and hydrothermal circulation. The primary objective of the laboratory study of cores from the State 2-14 borehole at the edge of the Salton Sea was the development of an understanding of the relationship between such core properties as local mineralization and pore size spectra and compressional and shear wave velocities. An in-depth understanding of the velocity–lithology relationship is especially important in analysis of data from the 3250 m deep State 2-14 borehole of the Salton Sea Scientific Drilling Project because both vertical seismic profiles and acoustic logs are available. Although ultrasonic laboratory measurements provide comparison velocities for a limited number of samples, examination of such velocity data and the microscopic structure of core lithologies yields important insight into the relationship between lithology and velocity throughout the borehole. These results are subsequently used in the evaluation of velocity distributions given by acoustic waveform logs and vertical seismic profiles. The data suggest how the extent of hydrothermal alteration and core mineralization over the total depth of the borehole are reflected in velocity variations measured at several scales.

The State 2-14 borehole was drilled as part of a major scientific study of the Salton Sea Geothermal reservoir. Seismic data at various scales of investigation were intended to provide indications of geothermal reservoir properties (pressure, porosity, and permeability) and indications of geothermal activity (alteration and mineralization). The increase in seismic velocity associated with increasing confining and effective pressure in laboratory studies is well known [*Toksöz et al.*, 1976; *Todd and Simmons*, 1972; *Nur and Simmons*, 1969]. Various theories can be used to relate such increases in velocity with pressure to the spectrum of pore shapes and microfractures within the rock fabric [*Cheng and Toksöz*, 1979; *O'Connell and Budiansky*, 1974]. The experimental results obtained when subjecting individual rock samples to increasing pressures may be seen as a partial analog to increases of velocity with depth, as it is expected that fewer thin cracks remain open as pressure increases. In practice, closing of cracks with depth is often accomplished through chemical alteration rather than mechanical pressure and might more reasonably be termed crack filling. At the State 2-14 borehole the extreme temperature gradient also complicates the analogy since temperature increases generally decrease velocities in opposition to the pressure effect.

The one important effect of in situ conditions on acoustic wave propagation that is not indicated by the ultrasonic velocities determined from core samples is the effect large-scale fractures have on measured seismic velocities. Open or partially open fractures reduce the mechanical strength of rocks, reducing seismic velocities and increasing attenuation. Intact cores are often not recovered from fractured zones, and experimental methods require relatively sound samples to withstand the processing required to produce specimens of the proper dimension for testing. The com-

[1] Now at Hawaii Institute of Geophysics, Honolulu

Paper number 7B7113.
0148-0227/88/007B-7113$0.500

TABLE 1. Description and Mineralogy of the Samples as Given in the Visual Core Description

Depth, m	Depth, ft	Unit	Description	Mineralogy
606.2	1988.7	13.1	very fine-grained, light gray mudstone	microcrystalline clay
911.0	2988.7	37b.4	fine-grained green sandstone with interbedded siltstone	quartz, clay, feldspar
954.5	3131.5	69.1	light green-gray sandstone	quartz, feldspar
1060.2	3478.5	86.1	light green calcareous thinly laminated siltstone	muscovite, clay, quartz
1170.2	3839.2	114.1	light gray-green medium-grained sandstone	quartz, black lithics, muscovite
1228.4	4030.1	128.1	medium dark gray laminated shale	clay, quartz
1294.4	4245.9	144.1	medium gray laminated siltstone	clay,quartz
1305.7	4283.8	159.1	green fine-grained sandstone, interbedded gray siltstone	quartz, feldspar, clay
1320.1	4331.0	175.1	medium gray laminated shaley siltstone	clay
1415.9	4645.5	182.1	gray green laminated siltstone	clay
1837.1	6026.8	220.1	medium to dark gray shale	clay, silicified appearance.
1984.6	6511.0	228.1	green, fine-grained sandstone, interbedded coarse siltstone	clays, quartz, recrystallization signs, epidote throughout
2226.6	7305.0	245.1	gray-green siltstone	clay, quartz
2618.4	8590.5	289.1	light green fine-grained massive sandstone	quartz

From *Mehegan et al.*, [1986].

parison between predicted velocities for intact samples of representative lithologies in the State 2-14 borehole given as a function of in situ confining pressure provides an important means for separating velocity anomalies associated with varying lithologies from those produced by the presence of fractures in the geothermal reservoir.

SELECTION AND PREPARATION OF THE SAMPLES

Because ultrasonic core velocity measurements were used to relate the microscopic structure of a limited number of discrete samples to the macroscopic velocity structure given by well logs and vertical seismic profiles, sample selection was a critical factor in the completion of this study. Fourteen samples, evenly distributed over the depth intervals of core available, were selected to represent the full spectrum of lithologies. Sample selection was made on the basis of visual core description given by *Mehegan et al.* [1986] and checked against geophysical log data given by *Paillet* [1986]. The depths and visual descriptions of the 14 samples are given in Table 1. Among these 14 samples, seven can be considered as lithologic endpoints based on quartz content:

TABLE 2. Properties of the Core Samples

Depth, m	Depth, ft	Wet Density, g/cm^3	Porosity, %	Grain Density, g/cm^3	A	B	C	D	E	F	G	H	I	J
606.2	1988.7	2.32	24.1	2.74					2.40	3.90			0	0
911.0	2988.7	2.38	17.8	2.68	3.30	4.05	1.75	2.30	2.60	3.90	1.80	1.76	1	1
954.5	3131.5	2.28	21.1	2.62	3.70	4.11	1.83	2.35	3.40	4.12	1.94	1.75	0	1
1060.2	3478.5	2.53	13.4	2.76	3.75	4.20	2.16	2.43	3.60	4.30	1.67	1.73	1	0
1170.2	3839.2	2.38	17.0	2.66	3.45	4.00	1.94	2.41	3.15	4.00	1.73	1.66	1	1
1228.4	4030.1	2.61	5.1	2.70	4.45	4.90	2.31	2.46	4.12	4.70	1.88	1.99	1	0
1294.4	4245.9	2.67	6.3	2.79	4.90	5.30	2.65	2.99	4.62	5.30	1.80	1.77	0	0
1305.7	4283.8	2.49	10.4	2.66	4.35	4.95	2.60	3.00	3.60	4.95	1.60	1.65	1	1
1320.1	4331.0				4.70	5.00			4.02	5.00			1	0
1415.9	4645.5	2.59	10.7	2.78	4.70	5.00	2.68	2.92	4.58	5.15	1.71	1.71	1	0
1837.0	6026.8	2.66	2.8	2.71	5.62	5.80	2.64	2.88	5.51	5.75	2.11	2.01	0	0
1984.6	6511.0	2.72	11.5	2.94	5.02	5.30	2.87	3.09	4.90	5.30	1.71	1.72	0	1
2226.6	7305.0	2.69	3.1	2.74	5.75	5.87	3.11	3.19	6.00	6.05	1.84	1.84	0	0
2618.4	8590.5	2.53	6.5	2.64	5.45	5.60	3.14	3.39	5.20	5.60	1.70	1.65	0	1

A, V_P at in situ effective pressure measured on sample fully saturated with water. B, V_P at 200 MPa effective pressure measured on sample fully saturated with water. C, V_S at in situ effective pressure measured on sample fully saturated with water. D, V_S at 200 MPa effective pressure measured on sample fully saturated with water. E, V_P at in situ effective pressure measured on dry sample. F, V_P at 200 MPa effective pressure measured on dry sample. G, V_P/V_S at in situ effective pressure measured on sample fully saturated with water. H, V_P/V_S at 200 MPa effective pressure measured on sample fully saturated with water. I, Orientation of the plug. 1 means plug axis is parallel to hole axis. 0 means plug cut normal to borehole axis. J, 1 means that the rock is classified as a sandstone. 0 means siltstone or shale.

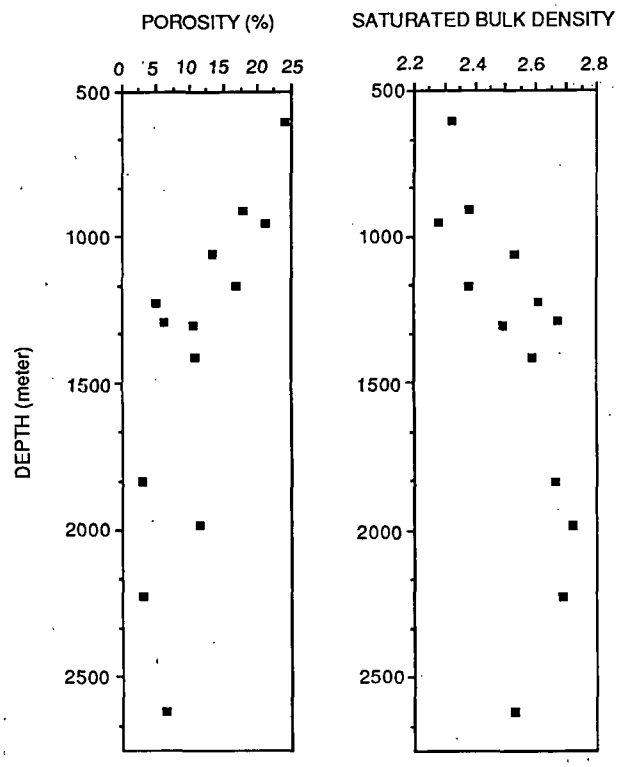

Fig. 1. Wet bulk density and measured porosity for all the core samples as a function of their in situ depths.

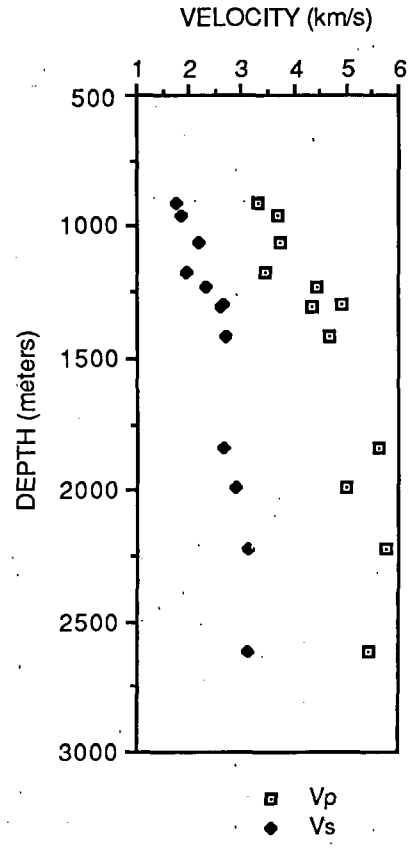

Fig. 3. V_P and V_S for all the core samples fully saturated with water at the in situ effective pressure as a function of their in situ depth.

samples from depths of 1060, 1837, and 2226 m for the claystone and shale group and 954, 1170, 1305, and 2618 m for the sandstone group (the names of the samples in further discussion will correspond to their in situ depths).

Individual samples for ultrasonic testing were prepared by cutting 2.5-cm-diameter cylinders from sections of the core. Measurements of seismic velocities of stratified Salton Sea sediments may show differences between measurements parallel and transverse to bedding planes, even after hydrothermal alteration. For this reason, cores were processed to allow velocity measurement transverse to bedding for comparison with velocities of vertically polarized shear waves measured in vertical seismic profiles and seismic velocities

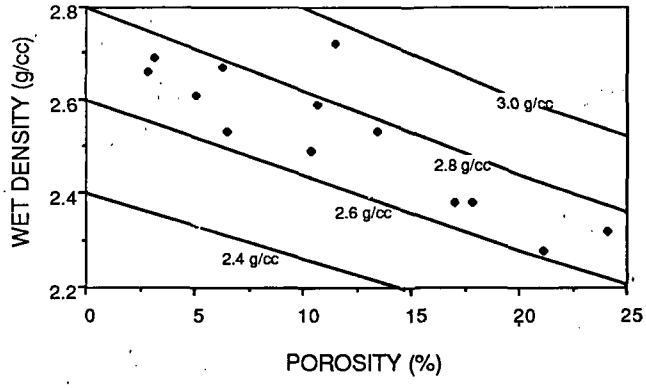

Fig. 2. Wet bulk density for all the core samples versus their measured porosity. The straight lines have been calculated for porous media of grain densities between 2.4 and 3.

determined from acoustic waveform logs. For seven of the selected depths, sample cylinders were cored with their axes parallel to the axis of the well. Otherwise, they were cored with axes perpendicular to the axis of the well. The ends of the cores were cut using a precision wafering saw which produced flat surfaces suitable for the velocity tests. Lengths of the samples ranged between 12 and 50 mm, depending primarily on the friability of the rock. Due to the abundance of cracks in certain well cores, it was impossible to prepare any sample longer than 12 mm.

The effective porosity and bulk density of the cores were calculated from the weights of each core after oven drying, saturation with water, and immersion in water. Dry measurements were made after the samples had been baking in a vacuum oven at 60°C for 2 days. Saturated measurements were made after immersion of the dry samples in degassed water under vacuum for 24 hours and then under atmospheric pressure for 24 hours. The shaley samples were reweighed after testing in order to insure that their grain densities and porosities had not changed due to saturation with freshwater pore fluid. Sample volumes were obtained by weighing fully saturated in water.

The measured properties of the samples are summarized in Table 2. The data clearly show an increase in the saturated bulk density with increasing depth, reflecting mainly a decrease in porosity (Figure 1). Effective porosities range between 3.1% and 24.1%. Porosity versus bulk density is presented in Figure 2. Theoretical straight lines have been calculated for media of varying porosities and grain densi-

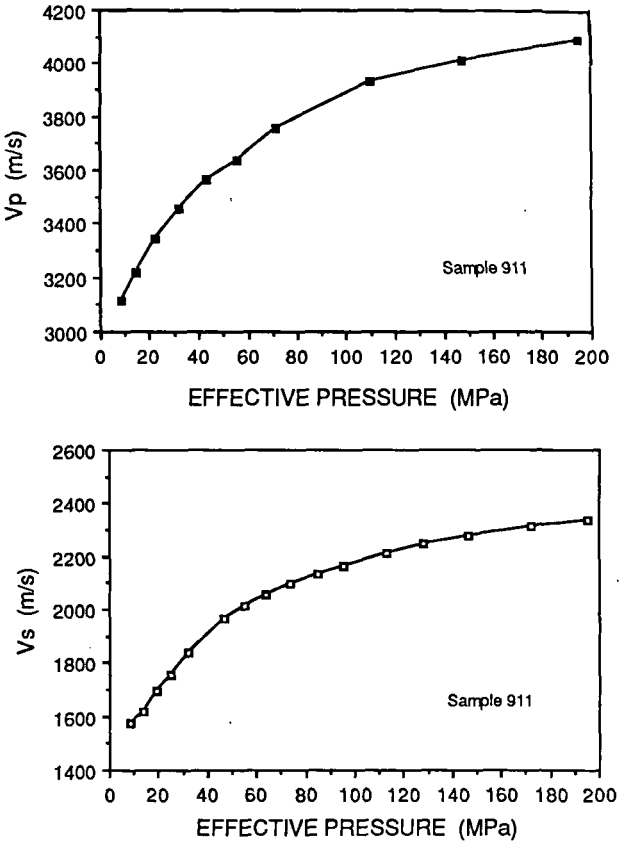

Fig. 4. V_P and V_S of siltstone sample 911 fully saturated with water as a function of effective pressure.

ties. The position of each sample provides the reader with an indication of its average grain density. Although a small residual amount of porosity may not be measured by immersion techniques, previous studies have shown that this error is small in sandstones and shaley clastics [*Caruso et al.*, 1985]. The average grain density gives a first rough idea of the mineralogical composition of the samples; for instance, a clean quartz sandstone would lie on the theoretical line of grain density of 2.65 g/cm^3. The averaged grain densities of the samples have been listed in Table 2; all but sample 1984 lie in the range 2.62–2.79 g/cm^3.

VELOCITY MEASUREMENTS

Compressional and shear wave velocities were measured under varying hydrostatic confining pressure on dry and saturated samples. As widely recognized in the literature [e.g., *Wyllie et al.*, 1958; *Todd and Simmons*, 1972], the effects of in situ state of stress on the physical properties of a given rock can be described by taking into account only the effective pressure, which is defined as the difference between the confining pressure and the pore fluid pressure. In the measurements described here, effective stress was controlled by draining the samples without desiccating clay minerals, setting the pore pressure at atmospheric pressure and recording measurements as a function of confining pressure.

Two 500-kHz piezoelectric crystals were used to record transmitted ultrasonic signals through the samples. Each of them is protected from the confining pressure in a steel case, and a steel buffer 37.5 mm thick separates each transducer from the sample. A neoprene jacket isolates the pore space from the pressurized kerosene.

Table 2 summarizes the data collected for the 14 samples. Measurements were made on the same samples during repeated pressure cycles. Compressional and shear wave velocities are reported for two pressures: 200 MPa and the calculated in situ pressure. The first value is an estimate of the effective pressure experienced by the sample in situ, calculated assuming an average rock density of 2.45 g/cm^3 for the sedimentary column and 1.00 g/cm^3 for the pore fluid. The second value is the velocity at the maximum confining pressure attainable with our experimental setup. The relation between ultrasonic velocities at in situ pressure and depth for all the samples is shown in Figure 3. Temperature was not taken into account, although increased downhole temperatures lower velocity values of the order 0.10–0.20 km/s [*Stewart and Peselnick*, 1977]. This is equivalent to the size of the symbols in most of our plots. The expected trend of increasing velocities with increasing depth is clearly indicated.

Apart from its mineralogy (both grains and cement), the mechanical properties of a sedimentary rock are mainly governed by the volume and the distribution of its pore spaces. A plot of the velocities as a function of the effective pressure yields information about the distribution of this porous volume into various pore shape factors [*Cheng and Toksöz*, 1979]. Different relations between the P or S wave velocities and the effective pressure are illustrated in Figures 4–7. Samples containing relatively larger volumes of low aspect ratio pores (cracks) exhibit larger increases in measured velocity as confining pressure is increased. Sample 911, a very

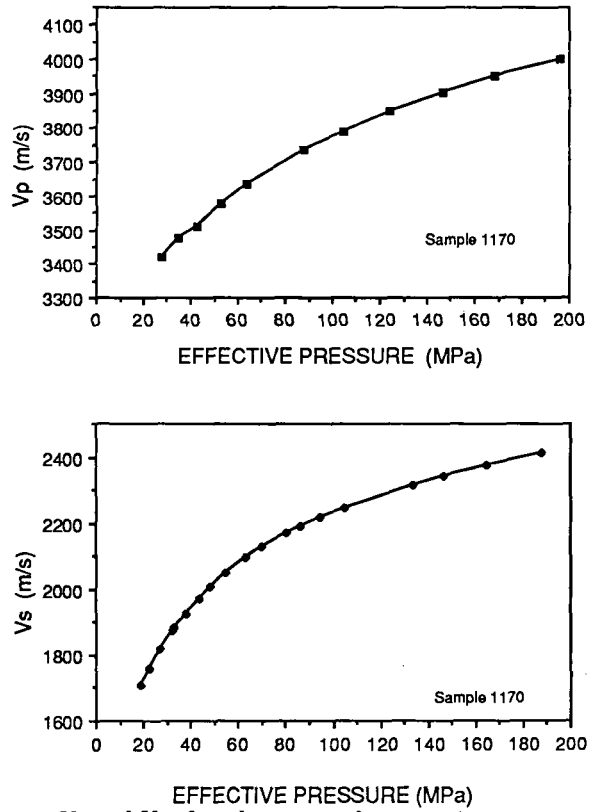

Fig. 5. V_P and V_S of sandstone sample 1170 fully saturated with water as a function of effective pressure.

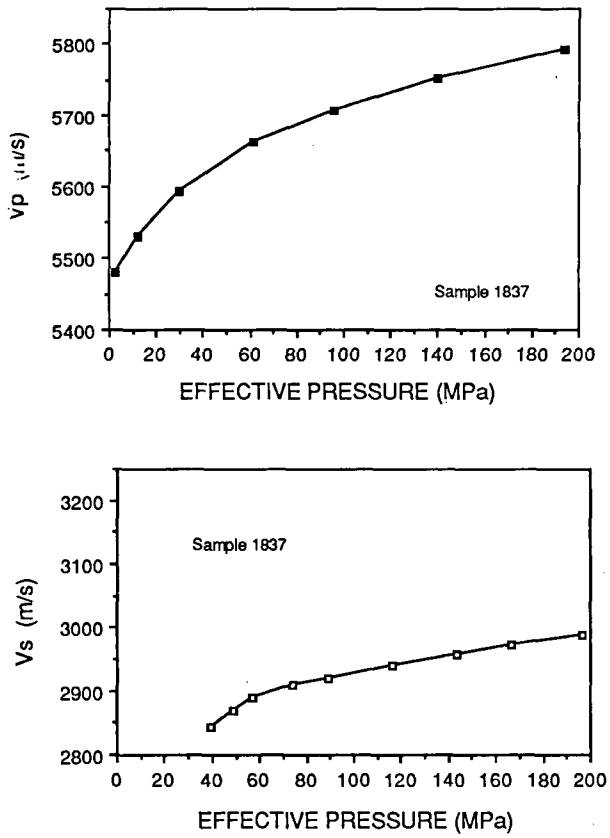

Fig. 6. V_P and V_S of shale sample 1837 fully saturated with water as a function of effective pressure.

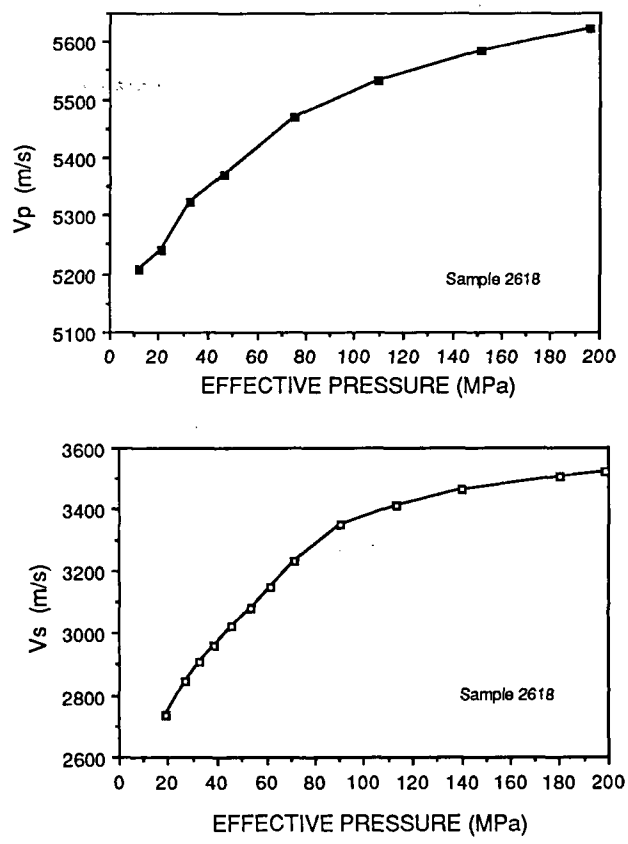

Fig. 7. V_P and V_S of sandstone sample 2618 fully saturated with water as a function of effective pressure.

porous, poorly cemented and highly fractured shallow siltstone exhibits this type of behavior, increasing 0.8 km/s in P wave velocity between pressures of 20 and 200 MPa (Figure 4). A highly cemented, low-porosity shale (sample 1837, Figure 6) has a very small pressure dependence, exhibiting a velocity increase of only 0.25 km/s over the same interval of confining pressure. The same kind of comparative statement could be made between the shallow sandstone (sample 1170, Figure 5) and a sandstone recovered from deeper in the hole (sample 2618, Figure 7).

Due to the pressure dependence of the velocities, the influence of the mineralogical composition is best studied using the data collected at high confining pressure where most of the flat cracks are closed. The value of V_p at 200 MPa confining pressure has been plotted versus the measured porosity of each core in Figure 8. Velocity-porosity curves plotted in Figure 8 were calculated using Wyllie et al.'s [1958] time average relationship for a monomineralic rock. The minerals considered here are quartz (V_P =6.05 km/s) and epidote (V_P =6.96 km/s). The equation states that if V_G is the velocity of compressional waves in the mineral grains and V_W the velocity of compressional waves in the pore-filling fluid, then the velocity of compressional waves V_P in this rock will be written as

$$\frac{1}{V_P} = \frac{\phi}{V_W} + \frac{1-\phi}{V_G}$$

where ϕ is the porosity. The time average equation has been derived from experimental observations made on sandstones; it is not supported by any rigorous theoretical basis. Nevertheless, eight out of the 12 samples for which there are complete set of measurements fall between the two modeled time average curves.

DISCUSSION

It has been established that both the lithology and the distribution and shapes of pores and cracks determine the variations in the ratio V_P/V_S [e.g., *Tatham*, 1982]. High ratios suggest a relatively greater abundance of flat cracks in rocks of the same composition. We have plotted the values of V_P/V_S at 200 MPa effective pressure versus V_P/V_S at the in situ effective pressure for each fully water-saturated sample

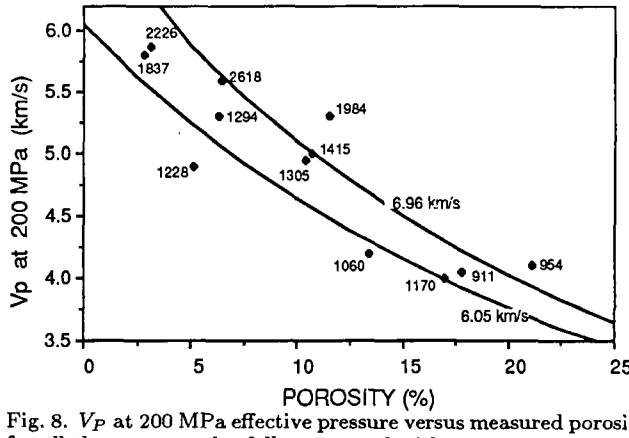

Fig. 8. V_P at 200 MPa effective pressure versus measured porosity for all the core samples fully saturated with water.

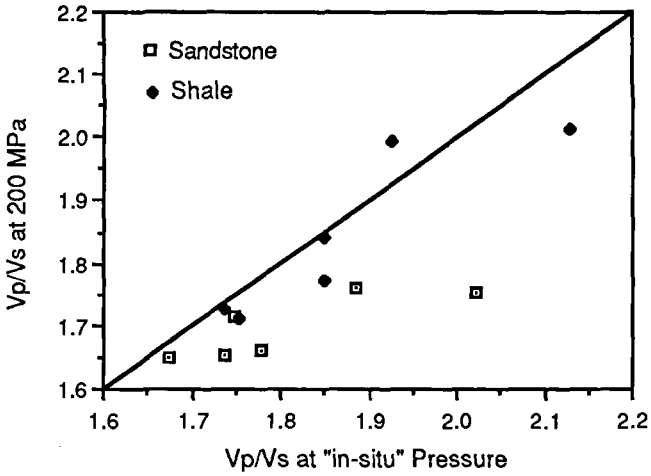

Fig. 9. V_P/V_S ratio at 200 MPa effective pressure versus V_P/V_S ratio at the in situ effective pressure.

in Figure 9. The samples are separated into two classes according to their quartz content (see Table 2). Six of the samples are composed primarily of sand-sized quartz grains and thus have been termed sandstones. The other eight samples are either fine grained siltstones and claystones or shales.

There are two interesting aspects of the data displayed in Figure 9. At confining pressures of 200 MPa the range of values for the ratio V_P/V_S is appreciably lower for the sandstones than for the other samples. This is related to the low value of the V_P/V_S ratio of quartz (1.45) compared to most other minerals (1.8–2.0) [*Pickett*, 1963; *Wilkens et al.*, 1984]. This effect is not evident at the in situ pressures, where open cracks seem to dominate the velocity values. In addition, all but one of the high-pressure ratios is smaller than the in situ ratios of the same sample. This can be explained by the greater sensitivity of S waves to the presence of low aspect ratio pore volume, i.e., to the presence of cracks which close as the differential pressure applied to the rock increases. Figure 9 illustrates ways in which both porosity and mineralogical composition have important influence on the mechanical properties of a given rock sample.

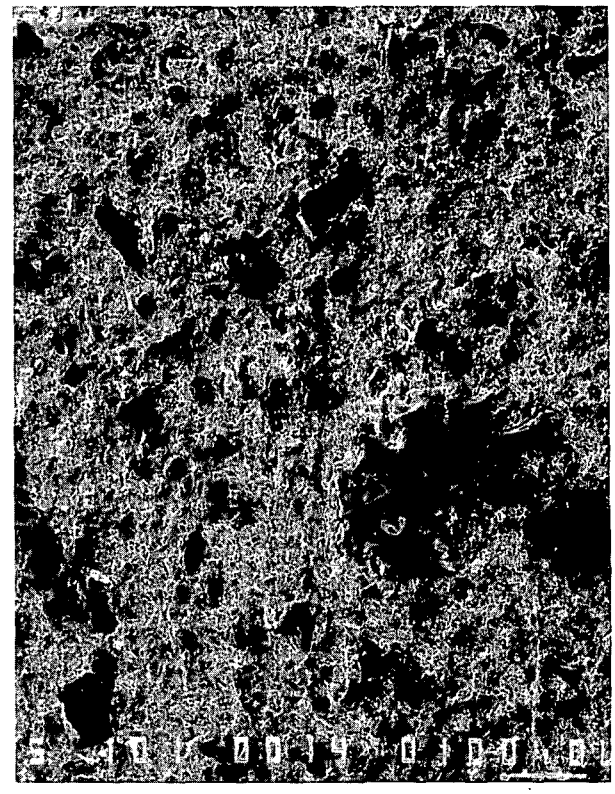

Fig. 11. Sample 1060. Depth, 1060.2 m. Mag 100. Scale bar = 100 μm. Scanning electron microscope photomicrograph of backscattered electron image. Black, holes left by plucked grains (most certainly quartz). Dark gray, quartz grains. The bulk of the rock is mainly made of clays.

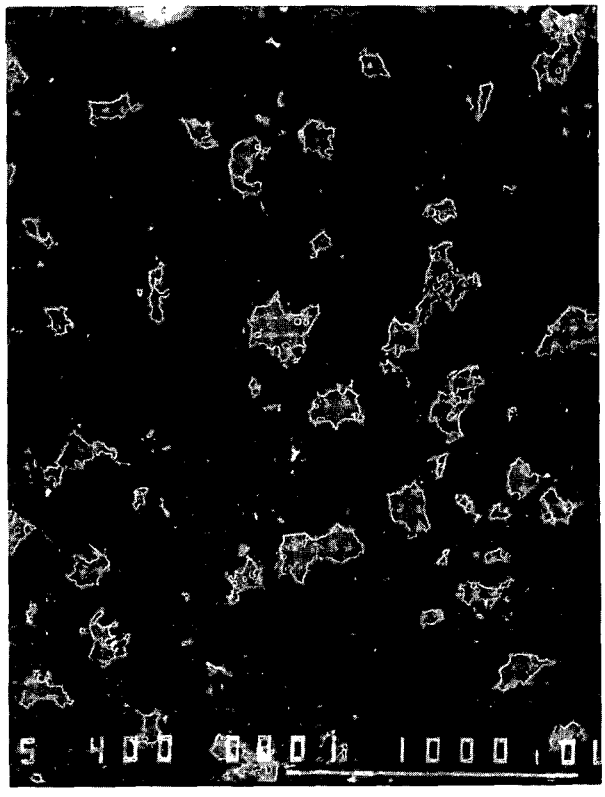

Fig. 10. Sample 954. Depth, 954.5 m. Mag 40. Scale bar = 1 mm. Scanning electron microscope photomicrograph of backscattered electron image. Black, empty pores filled with epoxy. Dark gray, quartz grains. Light gray, potassic feldspar, clay.

Discussion of the SEM Results

The end cuts from 25-mm-diameter cores obtained during the preparation of the samples for the ultrasonic measurements were used to prepare samples for scanning electron microscope (SEM) investigations. A first inspection was performed on polished sections of dry samples. Such images show the three-dimensional geometry of pores in great detail. However, it is difficult to get any quantitative analysis of such images. Hence a second observation was performed on samples fully saturated with epoxy in order to examine reliably the pore geometries and the main mineral phases on a two-dimensional image. The images shown in Figures 10–17 have been obtained with a backscattered electron detector and are presented at the same magnification in each

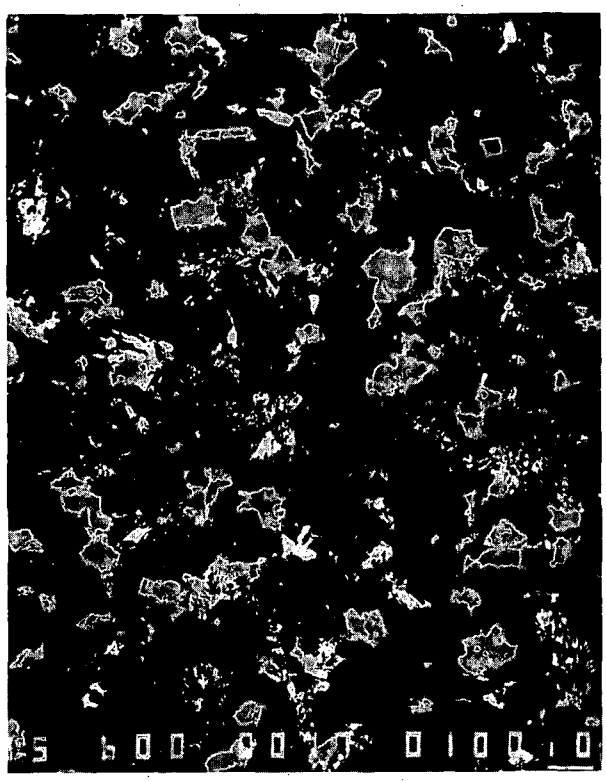

Fig. 12. Sample 1170. Depth, 1170.2 m. Mag 60. Scale bar = 100 μm. Scanning electron microscope photomicrograph of backscattered electron image. Black, empty pores. Dark gray, quartz grains. Light gray, plagioclase feldspar, clay. White, heavy minerals such as pyrite, epidote, calcite.

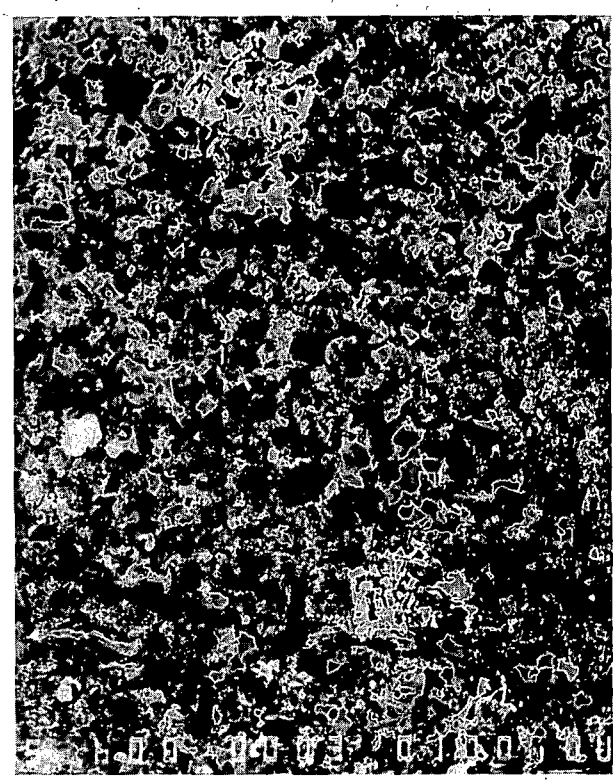

Fig. 14. Sample 1294. Depth, 1294.2 m. Mag 60. Scale bar = 100 μm. Scanning electron microscope photomicrograph of backscattered electron image. Dark gray, quartz grains. White, pyrite (massive crystal center left), halite crystals covering the walls of the pores. An important fraction of the rock is clay.

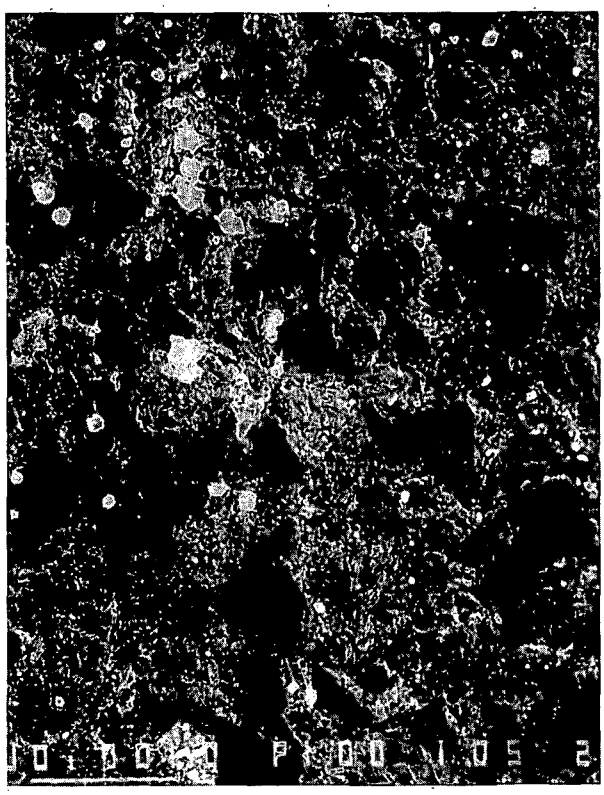

Fig. 13. Sample 1228. Depth, 1228.4 m. Mag 200. Scale bar = 100 μm. Scanning electron microscope photomicrograph of backscattered electron image. Dark gray, quartz grains. White, pyrite. The bulk of the rock is mainly clays.

plate. The response of this detector is proportional to the atomic number of the material which is under the beam. For instance, epoxy will appear black in the pictures, while relatively light silica will appear dark gray and dense minerals like pyrite will appear bright white. The microscope is also equipped with an energy dispersive system which yields quick, low-cost qualitative analyses of all the elements encountered by the beam whose atomic number exceeds 11. Table 3 summarizes the results of our observations. Estimations of frequencies with which certain given phases occur in the pictures are given when possible. These estimations result from point counts made on several frames of the sample under scan. Those samples for which no estimation has been given are mainly those which were difficult to fully saturate with epoxy. These were the low-permeability claystones.

The SEM photomicrographs in Figures 10–17 provide considerable insight into the effects of pore size distributions and mineral composition on seismic velocities of rock samples. These effects may be considered by comparing the SEM photographs for three groups of samples, along with the results displayed in Figures 2 and 8. Groups A and B were chosen to represent samples that exhibited very different velocities while sharing similar porosities. Group C has a different sense; samples of nearly the same velocity that have a wide range of porosities.

Group A: 2618, 1294, 1228. SEM photomicrographs of an epidotized sandstone (2618), a siltstone (1294), and a shale (1228) are shown in Figures 17, 14, and 13, respectively. The average grain density of 2618 stands close to

Fig. 15. Sample 1415. Depth, 1415.9 m. Mag 60. Scale bar = 100 μm. Scanning electron microscope photomicrograph of backscattered electron image. Black, empty spaces (mainly in the veins not totally healed). Dark gray, quartz grains. Light gray, patches of bulky mineral, the composition of which is the composition of potassic feldspar (probably clay). White, epidote, filling the cracks (and then crystallizing in large euhedral shapes) or filling the pore spaces throughout the sample. Crossing the field of the image, from the top left to the lower right, a crack totally free of any trace of healing suggests a non in situ origin.

the grain density of quartz (see Table 2 and Figure 2) while the grain density of the two shales is larger, reflecting the presence of clays, whose grain density is highly variable (for instance, illite: 2.6–2.9 g/cm^3 [*Berry et al.*, 1983]). These three samples have in common a low porosity (from 5.1% to 6.3%), but their P wave velocities at 200 MPa differ substantially (0.75 km/s). The SEM photomicrographs reveal very different textures for the three samples, ranging from the relatively large grain size and open pore spaces in the sandstone (2618) to the fine grain size and small micropores of the shale (1228). Theoretical models [e.g., *Kuster and Toksöz*, 1974; *Cheng and Toksöz*, 1979] show that the effect of pores on the ultrasonic properties of rocks is a function of the aspect ratio distribution of the porosity. The result is that in samples of equal porosity, the flatter the pores, the lower the P and S wave velocities.

Group B: 1984, 1415, 1060. An epidotized sandstone (1984), an epidotized shale (1415), and a relatively unaltered shale (1060) are presented in Figures 16,15, and 11, respectively. As in the case of group A, these samples have similar porosities (10.4–11.5 %) but different velocities at 200 MPa (5.30–4.20 km/s, Figure 8), and the sample with the lowest velocity (1060) also has small, flat pores. Cementation of grains is another important factor in the velocities of these three samples. Sample 1984 has been cemented with epidote. Epidote is a heavy mineral, the density of the more common mineral phases ranging between 3.3 and 3.6 g/cm^3, which explains the high average grain density of sample 1984. The presence of epidote, filling the cracks and hardening the rock, is responsible for the greater ultrasonic velocities of sample 1984 (the most epidotized) over sample 1415 (some epidote) and 1060 (no epidote or any other pore-filling material).

Group C: 954, 1170, 1060. Figures 10, 12, and 11 are SEM photomicrographs of a clean sandstone (954), a shaley sandstone (1170) and a shale (1060), respectively. The average grain density of the latter (see Table 2 and Figure 2) agrees well with the typical values of clay grain density, while the two other samples are close to the grain density of quartz (2.65 g/cm^3). These three samples, despite their range of porosities (from 13.4% to 21.1%), have very similar ultrasonic P wave velocities at 200 MPa (4.00–4.20 km/s, Figure 8). The difference between 1060 (shale) and the two sandstones is another illustration of the greater effect that flat pores have on the decrease of the P wave velocity. The low-porosity shale has more flat pores which result in a velocity similar to the higher-porosity sandstone.

The case of the two sandstones is somewhat different. Theoretical models have been developed [*Cheng and Toksöz*, 1979] and successfully applied to explain the ultrasonic P wave velocities of sandstones [*Wilkens et al.*, 1986]. They found that concentrations of clays in sandstone pores have little effect on the moduli of the rock and thus the velocity

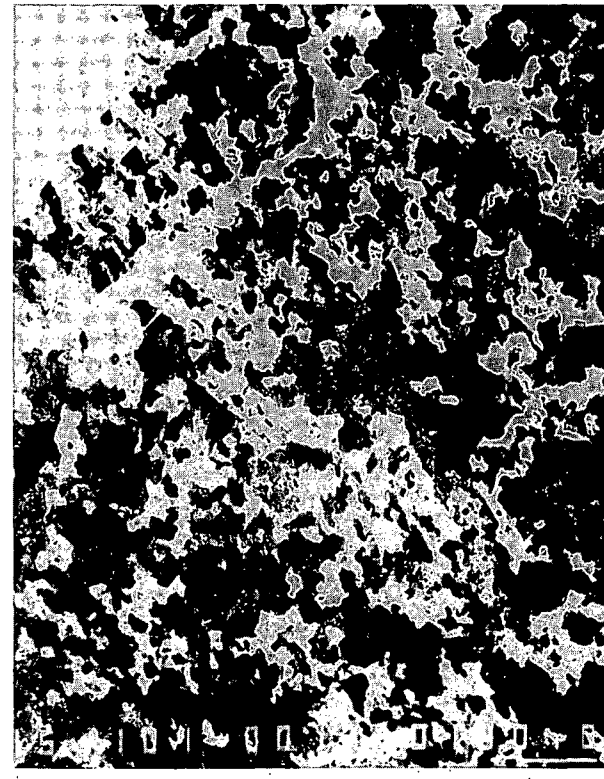

Fig. 16. Sample 1984. Depth, 1984.6 m. Mag 100. Scale bar = 100 μm. Scanning electron microscope photomicrograph of backscattered electron image. Dark gray, quartz grains. Light grays, clays and empty pores. White, epidote, filling the cracks (upper left), or the pore space throughout the sample. For this sample the full saturation with epoxy has been difficult to reach, hence the bad visualization of the pore space.

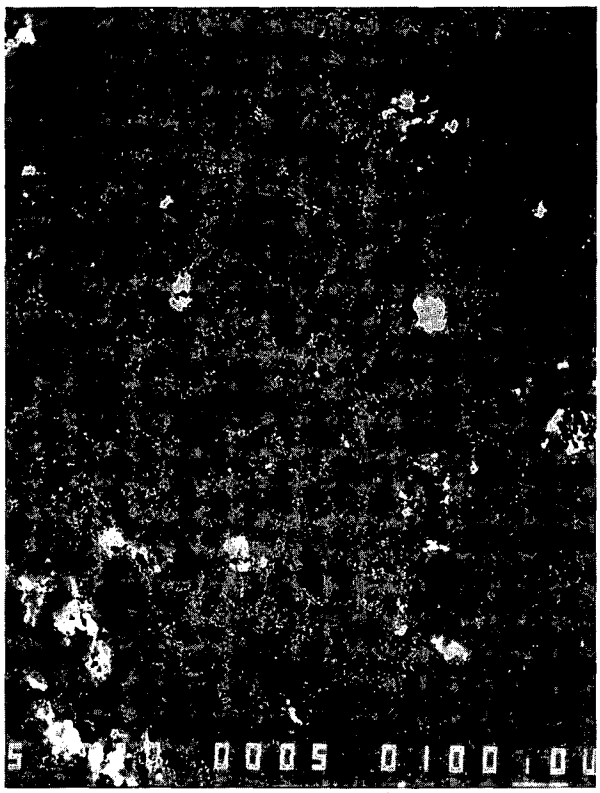

Fig. 17. Sample 2618. Depth, 2618.4 m. Mag 72. Scale bar = 100 μm. Scanning electron microscope photomicrograph of backscattered electron image. Black, empty pores (here filled with epoxy). White, mainly epidote, some crystals of rutile. Gray, quartz. We can distinguish between grains having a plain aspect and those having a mottled texture, suggesting different origins.

of that sandstone. The clays do, however, reduce the void volume (porosity) of a sandstone. Thus, samples 954 and 1170 appear to have roughly the same volume of quartz, the mineral that composes their framework and dictates velocity, while 1170 contains clay in the pores, lowering porosity without effect on velocity.

The use of SEM images provided us with qualitative information suitable for explaining the behavior of our samples. Differences can be attributed to mineralogy, microstructure, and alteration. Mineralogy of the framework may influence overall velocities and the presence of quartz is particularly noticeable in V_p/V_s ratios at higher pressures. The role of the microstructure changes with pressure. Some cracks (low aspect ratio pores) appear to remain open at in situ pressures based on a comparison of in situ and 200 MPa velocities and velocity ratios. At higher pressures, with most of the finer cracks closed, microstructural effects are more likely to include those of alteration. Clays filling pores, while not substantially changing the velocity of a sample, tend to mask the true volume of the framework of the rock, changing porosity values for samples of similar framework volume. Alteration is also important in the formation of the cement which binds grains together. Small volumes of alteration minerals such as epidote acting as cement may increase velocities in a sample out of proportion to its abundance due to its effect of strengthening the framework of the rock.

Comparison With Other Seismic Velocity Data

The great difference in size between the cores cut for the ultrasonic measurements and the much larger volumes of rock sampled by the conventional acoustic logs and vertical seismic profiles complicate the comparison of different veloc-

TABLE 3. SEM Observations

Depth, m	Depth, ft	Observations
606.2	1988.7	Mostly clays. Bedding visible, underlined with detrital quartz grains and anhydrite. Presence of rutile.
911.0	2988.7	Quartz grains and clays are predominant. A lot of pores are plugged with halide.
954.5	3131.5	Mostly quartz grains. Abundant clays. Presence of pyrite. Quartz grains: 65%. Pores + clays: 22%. K-feldspar: 12%.
1060.2	3478.5	Mostly clays. Bedding underlined with small (10 μm) quartz grains.
1170.2	3839.2	Mostly quartz grains: 78 %. Abundant calcite as pore-filling material.
1228.4	4030.1	Mostly clays. Detrital quartz grains throughout.
1294.4	4245.9	Mostly clays. Quartz grains: 12%. Quartz grains interspersed within surrounding bulky denser mineral of composition identical to composition of K-feldspar: 13%, halide: $\cong$1%.
1305.7	4283.8	Detrital quartz: 60%. Detrital grains of K-feldspar or clays: 16%. Pores: 22%.
1320.1	4331.0	Mostly shale. Abundant small quartz grains (20 μm) throughout.
1415.9	4645.5	Small quartz grains surrounded by bulky mineral of composition identical to the composition of K-feldspar: 40%. Pores are abundantly filled with clays: 20%. Epidote fills the cracks and partly the pores: 40%.
1837.0	6026.8	Mostly silty clays (crystals a few microns wide). Abundant porosity: 20–30%
1984.6	6511.0	Quartz grains: 30%. Epidote filling the cracks and the pores: 30%. Quartz grains are interspersed in the surrounding epidote or clays.
2226.6	7305.0	Mostly silty clays. Detrital quartz throughout.
2618.4	8590.5	Mostly quartz: 91%. Epidote: 3%. pores: 5.5%.

It has not always been possible to give the mineralogical composition of the rock from the indications given by the energy dispersive system of the scanning electron microscope.

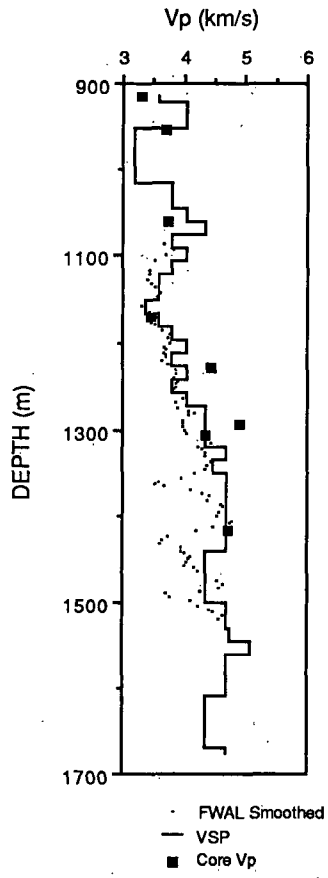

Fig. 18. Compressional velocities determined from maximum gain FWAL (small dot), VSP (line, from *Daley et al.* [1987]) and ultrasonic core measurement (solid diamond).

ity data sets. These scale differences can be illustrated by considering the differences in effective seismic wavelengths under the assumption of a typical compressional velocity of 4.0 km/s. The appropriate frequencies of 500, 15, and 0.2 kHz for the ultrasonic, acoustic log, and vertical seismic profile measurements yield wavelength scales of 0.008, 0.27, and 20 m, respectively. In addition to this great difference in scale, the velocity dispersion introduced by intrinsic attenuation [*Sachse and Pao*, 1978] makes a close agreement between these various measurements even less likely. The combined effects of velocity dispersion and the elimination of the more friable samples during the sample preparation process are expected to cause the ultrasonic velocity values to average slightly greater than velocities determined in situ.

A comparison of compressional wave velocities determined from the high gain full waveform acoustic log (FWAL [*Paillet and Morin*, this issue]), vertical seismic profile (VSP [*Daley et al.*, 1987]), and our measured core velocities is presented in Figure 18. All three velocities agree well with each other. There are two depths (1228 and 1294 m) where the core velocities are significantly higher than the VSP and FWAL velocities. These two points correspond to places where the cores are highly fractured (especially along bedding planes), and it was difficult to obtain an intact sample. Thus the laboratory samples are more competent than the surrounding rocks in these two areas and consequently, they have higher velocities. The two samples with velocities less than the VSP (910 and 1060) are probably due to local variations; they probably represent slower layers in the stratified column. The VSP velocities are averaged over a 60 m interval [*Daley et al.*, 1987] and thus failed to pick up the three thin, low-velocity zones at around 1350, 1450, and 1500 m in depth. The VSP does show a decrease in velocity between 1410 and 1470 m but, as expected, does not have the depth resolution of the FWAL. Over an area where the velocity changes are more gradual (1150–1320 m) the VSP and FWAL velocities are in excellent agreement.

Figure 19 compares the core measured shear wave velocities with *SH* (Figure 19*a*) and *SV* (Figure 19*b*) velocities determined from VSP [*Daley et al.*, 1987]. Except for one core (1294) in this interval, all the velocities are measured in line with the axis of the borehole. Given the relatively shallow dip of bedding through most of this interval, vibration directions for the shear waves were in the bedding planes. In the case of 1294 velocities were measured normal to the axis of the borehole but with vibration again in the plane of the bedding. The core-measured velocities are in general agreement with the VSP velocities, better with the *SH* than the *SV* due to the coincidence of vibration in the two determinations.

The three velocity profiles superimposed in Figure 17 follow a general trend. Velocities are relatively low above 1200 m and gradually increase over a depth interval from 1150 m to approximately 1320 m. Below this level, while the

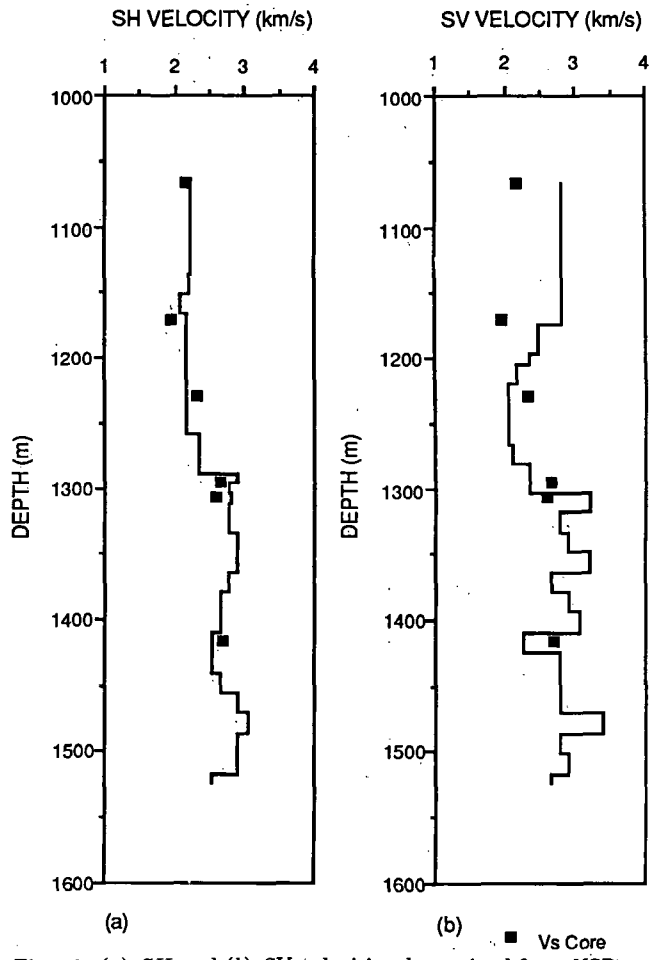

Fig. 19. (*a*) *SH* and (*b*) *SV* velocities determined from VSP [*Daley et al.*, 1987]. Ultrasonic core shear velocities are plotted (solid square) on both.

acoustic log suggests several excursions to lower velocities, VSP velocities remain constant. These rapid increases in V_P and V_S between 1200 and 1300 m can be related to the major interval of clay mineral transformation discussed in *Paillet and Morin* [this issue]. They correspond to the depth of appearance on the SEM photomicrographs of denser zones. These zones have a K-feldspar composition (see Table 3) and constitute bulky homogeneous areas around certain quartz grains. Figure 14 is a good illustration of this phenomenon (see upper left side).

The consistency of the three velocity data sets also indicates the apparent lack of macroscopic fractures above a depth of 2000 m in the State 2-14 well. No indications of major permeable fractures have been found in the geophysical logs for this upper portion of the borehole, and flow tests confirmed the low production of geothermal fluids [*Paillet*, 1986]. Major permeable fractures were encountered at greater depths where borehole conditions precluded acquisition of vertical seismic profiles and waveform log data. Ultrasonic velocities determined from intact core samples below 2000 m in depth would not be expected to indicate the presence of fractures.

CONCLUSIONS

The good agreement between the seismic velocities determined from the ultrasonic core tests described here and the velocities given at much larger scales of investigation by the acoustic waveform logs and vertical seismic profiles data help in the interpretation of the in situ velocity distribution. The two individual core samples which yielded velocities slightly greater than those given by the log data can be attributed to the selection for intact specimens in the sample preparation process. All seismic velocity data indicate a transition zone in the interval from 1200 to 1800 m in depth where velocity increases are significantly greater than expected from the normal increase in confining pressure with depth. These increases appear to be associated with the hydrothermal alteration of clay minerals in alluvial sediments and are consistent with temperature logs given for the State 2-14 borehole by *Paillet* [1986] and the mineralogic zonation for wells in the Salton Sea Geothermal field given by *Muramoto and Elders* [1984]. Scanning electron photomicrographs of core samples confirm that the measured ultrasonic velocities represent the combined effects of mineralogy, pore size distributions, and alteration minerals. The consistency between all three independently obtained velocity data sets indicates that surface seismic data and acoustic waveform logs can be used to relate observed velocities and the extent of hydrothermal alteration.

Acknowledgements. We would like to thank Tom Daley of the University of California, Berkeley, for providing us with the VSP data. This work was supported by U.S. Geological Survey grant 14-08-001-A-0328. P.A.T. was also supported by an Elf-Aquitaine postdoctoral fellowship.

REFERENCES

Berry, L.G., B. Mason, and R.V. Dietrich, *Mineralogy–Concepts, Descriptions, Determinations*, 2nd ed., W.H. Freeman, New York, 1983.

Caruso, L., G. Simmons, and R. H. Wilkens, The physical properties of a set of sandstones, I, The samples, *Int. J. Rock Mech. Min. Sci. Geomech. Abstr., 22,* 381–392,1985.

Cheng, C.H., and M.N. Toksöz, Inversion of seismic velocities for the pore aspect ratio spectrum of a rock, *J. Geophys. Res., 84,* 7533–7543, 1979.

Daley, T.M., T.V. McEvilly, and E.L. Majer, Analysis of VSP data at the Salton Sea Scientific Drilling Project (abstract), *Eos Trans. AGU, 68,* 445, 1987.

Kuster, G.T., and M.N. Toksöz, Velocity and attenuation of seismic waves in two-phase media; part I, Theoretical formulations, *Geophysics, 39,* 587–606, 1974.

Mehegan, J.M., C.T. Herzig, and R.M. Sullivan, Salton Sea Scientific Drilling Project–California State 2-14 well–Visual core descriptions, vols. 1 and 2, Univ. of Calif., Riverside, 1986.

Muramoto, F.S., and W.A. Elders, Correlation of wireline log characteristics with hydrothermal alteration and other reservoir properties of the Salton Sea and Westmorland geothermal fields, Imperial Valley, California, *Los Alamos Natl. Lab. Rep. LA-10128-MS,* 100 pp., 1984.

Nur, A., and G. Simmons, The effect of saturation on velocity in low porosity rocks, *Earth Planet. Sci. Lett., 7,* 99–108, 1969.

O'Connell, R.J., and B. Budiansky, Seismic velocities in dry and cracked saturated solids, *J. Geophys. Res., 79,* 5412–5426, 1974.

Paillet, F.L., Preliminary report on geophysical well-logging activity on the Salton Sea Scientific Drilling Project, Imperial Valley, California, *U.S. Geol. Surv., Open File Rep., 86-544,* 1986.

Paillet, F.L., and R.H. Morin, Analysis of geophysical well logs obtained in the state 2-14 borehole, Salton Sea Geothermal Area, California, *J. Geophys. Res.,* this issue.

Pickett, G.R., Acoustic character logs and their application in formation evaluation, *J. Pet. Technol., 15,* 659–667, 1963.

Sachse, W., and Y.H. Pao, On the determination of phase and group velocities of dispersive waves in solids, *J. Appl. Phy., 49,* 4320–4327, 1978.

Stewart, R.M. and L. Peselnick, Velocity of compressional waves in dry Franciscan rocks to 8 kbar and 300°C, *J. Geophys. Res., 82,* 2027–2039, 1977.

Tathman, R.H., V_P/V_S and lithology, *Geophysics, 47,* 336-344, 1982.

Todd, T., and G. Simmons, Effect of pore pressure on the velocity of compressional waves in low-porosity rocks, *J. Geophys. Res., 77,* 3731–3743, 1972.

Toksöz, M.N., C.H. Cheng, and A. Timur, Velocities of seismic waves in porous rocks, *Geophysics, 41,* 621–645, 1976.

Wilkens, R.H., G. Simmons, and L. Caruso, The ratio V_P/V_S as a discriminant of composition for siliceous limestones, *Geophysics, 49,* 1850–1860, 1984.

Wilkens, R.H., G. Simmons, T.M. Wissler, and L. Caruso, The physical properties of a set of sandstones – Part III. The effects of fine-grained pore-filling material on compressional wave velocity, *Int. J. Rock Mech. Min. Sci. Geomech. Abstr., 23,* 313–326, 1986.

Wyllie, M.R.J., A.R. Gregory, and G.H.F. Gardner, An experimental investigation of factors affecting elastic wave velocities in porous media, *Geophysics, 23,* 459–493, 1958.

C.H. Cheng and P.A. Tarif, Earth Resources Laboratory, Department of Earth, Atmospheric and Planetary Sciences, Massachusetts Institute of Technology, Cambridge, MA 02139.

F.L. Paillet, U.S. Geological Survey, MA 403, Box 25046, Denver Federal Center, Denver, CO 80225.

R.H. Wilkens, Hawaii Institute of Geophysics, 2525 Correa Road, Honolulu, HI 96822.

(received August 6, 1987;
revised January 5, 1988;
accepted February 16, 1988.)

JOURNAL OF GEOPHYSICAL RESEARCH, VOL. 93, NO. B11, PAGES 13,069-13,080, NOVEMBER 10, 1988

NATURE AND SIGNIFICANCE OF IGNEOUS ROCKS CORED IN THE STATE 2-14 RESEARCH BOREHOLE: SALTON SEA SCIENTIFIC DRILLING PROJECT, CALIFORNIA

Charles T. Herzig and Wilfred A. Elders

Institute of Geophysics and Planetary Physics University of California, Riverside

Abstract. The State 2-14 research borehole of the Salton Sea Scientific Drilling Project penetrated 3.22 km of Pleistocene to Recent sedimentary rocks in the Salton Sea geothermal system, located in the Salton Trough of southern California and northern Baja California, Mexico. In addition, three intervals of igneous rocks were recovered; a silicic tuff and two sills of altered diabase. The chemical composition of the silicic tuff at 1704 m depth suggests that it is correlative with the Durmid Hill tuff, cropping out 25 km NW of the geothermal system. In turn, both of these tuffs may be deposits of the Bishop Tuff, erupted from the Long Valley caldera of central California at 0.7 Ma. The diabases are similar to basaltic xenoliths found in the nearby Salton Buttes rhyolite domes. These diabase are interpreted as hypabyssal intrusions resulting from magmatism due to rifting of the Salton Trough as part of the East Pacific Rise/Gulf of California transtensional system. The sills apparently intruded an already developed geothermal system and were in turn altered by it.

Introduction

The geothermal systems of the Salton Trough, located in southern California and northern Baja California, Mexico, originate in a rift zone transitional between the transform San Andreas fault system to the north and the divergent Gulf of California/East Pacific Rise system to the south (Figure 1; see also Figure 2 and related discussion of Elders and Sass [this issue]). In this context, the study of igneous rocks recovered from deep boreholes within these geothermal areas provide insights into the heat sources for the geothermal systems. The 3.22-km-deep research borehole (California) State 2-14, of the Salton Sea Scientific Drilling Project (SSSDP) was drilled into the active Salton Sea geothermal system (SSGS) [Elders and Sass, this issue]. The borehole penetrated hydrothermally altered sedimentary rocks of the Colorado River delta, and a silicic tuff, and two sills of diabase. The purpose of this paper is to describe the petrology, geochemistry, and secondary mineralization of the igneous rocks recovered during the SSSDP and to discuss their possible relationships with other igneous rocks in and around the Salton Trough.

Geologic Setting

The SSGS is one of a number of active geothermal systems in the Salton Trough, the landward extension of the Gulf of California rift system. However, the trough has been isolated from the marine environment of the Gulf by the progradation of the delta of the Colorado River across the rift since the Pliocene [Merriam and Bandy, 1965; Muffler and Doe, 1968; van de Kamp, 1973]. Together with the Afar and Red Sea rift system, this region is one of two locations today where an oceanic spreading center is acting on a continent. Within the gulf, long en echelon transform faults have small spreading segments between them, forming "pull-apart" basins, such as the Guaymas Basin (Figure 1) [Atwater, 1970; Atwater and Molnar, 1973]. This tectonic style persists into the Salton Trough where the "pull-apart" basins, filled with thick sequences of continental sediments deposited by the Colorado River, are the loci of intense geothermal activity, such as the Cerro Prieto geothermal system (CPGS) and the SSGS [Elders et al., 1972].

The deeper basement beneath the central part of the Salton Trough is interpreted as oceanic in character based on seismic and gravity data [Fuis et al., 1982, 1984]. High regional heat flow and temperature gradients [Lachenbruch et al., 1985] suggest that greenschist facies metamorphism should be widespread below a depth of 5 km in the center of the trough. High temperatures at these depths suggest the presence of an elevated lithosphere-asthenosphere boundary, characteristic of rift systems worldwide. Greenschist facies metamorphism locally occurs at even shallower depths within the geothermal fields [Muffler and White, 1969]. For example, authigenic epidote is first observed at approximately 900 m deep in the (SSGS) and lower amphibolite facies assemblages occur at 3 km depth [Cho et al., this issue].

Igneous Rocks in the Salton Trough

In contrast to the Afar and Red Sea region, few volcanic rocks of Tertiary or Quaternary age are exposed within the Salton Trough or along its margins. Miocene volcanics are found in the mountains surrounding the Salton Trough [Hawkins, 1970; Crowe, 1978; Gjerde, 1982]. The origin of these Miocene extrusives may have been related to the formation of a proto-Gulf of California, a rift system associated with subduction zones which formerly constituted the boundaries between the Farallon, Pacific, and North American plates [Karig and Jensky, 1972; Dickinson and Snyder, 1979; Moore and Curray, 1982]. Because the Miocene volcanics formed in a tectonic environment different from the modern oceanic spreading regime, they will not be considered further in this paper.

Volcanoes of Quaternary age are associated with the Cerro Prieto and Salton Sea geothermal systems. The 275-m-high Cerro Prieto volcano

Paper number 88JB03245.
0148-0227/88/88JB-03245$05.00

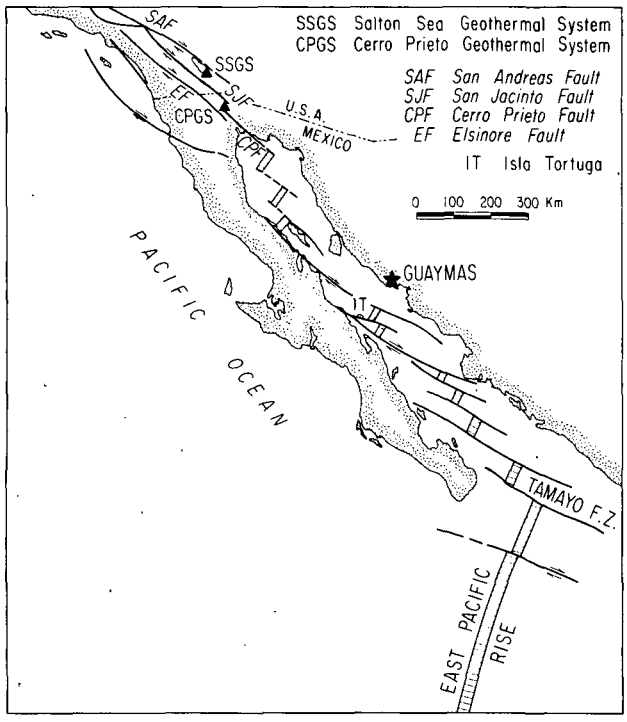

Fig. 1. Generalized map showing the location of the Salton Sea and Cerro Prieto geothermal fields within the Salton Trough and Gulf of California tectonic system.

west of the CPGS is composed of lithoidal, calc-alkaline dacite [de Boer, 1980; Reed, 1984]. On the basis of chemistry and limited Sr isotope data, Reed [1984] concluded that the dacite resulted from melting and remobilization of granitic basement of the Mesozoic Penisnsular Ranges Batholith (PRB) due to the heat generated by a gabbroic magma within the Cerro Prieto pull-apart basin.

Five small rhyolite domes occur along a NE-SW trend within the SSGS and are collectively known as the Salton Buttes. The volcanoes consist primarily of lithoidal, rhyolite of alkalic composition and obsidian with minor amounts of pyroclastics and hyaloclastic breccias [Robinson et al., 1976]. A single K-Ar determination of the westernmost dome, Obsidian Butte, yielded an age of 16,000 ± 16,000 years [Muffler and White, 1969]. Friedman and Obradovich [1981] reported ages of 2500 to 8400 years old for obsidian samples from Obsidian Butte and Red Island domes based on thicknesses of hydration rinds.

The Salton Buttes volcanoes contain xenoliths of basalt and gabbro of tholeiitic composition. In addition, xenoliths of sedimentary and granitic rocks occur. Robinson et al., [1976] interpreted the granite xenoliths as fragments of the PRB, based primarily on their highly remelted character and on the limited amount of Sr isotope data available.

Igneous rocks have been encountered in cuttings from geothermal drill holes in the Salton Trough. All of these rocks exhibit varying degrees of hydrothermal alteration. They include basalts and dacites from the CPGF [Elders et al., 1978, 1981; Mehegan et al., 1987]; basalts and microgabbros from the Heber geothermal field [Browne and Elders, 1976; Browne, 1977]; basalts and andesites from the East Brawley geothermal field [Keskinen and Sternfeld, 1982]; and diabases and rhyolites from the SSGS [Robinson et al., 1976]. Robinson et al. [1976] noted the similarity of the subsurface basalts and silicic rocks from the SSGS with those from the Salton Buttes, except that the mineralogy and chemistry of the subsurface rocks have been altered by hydrothermal fluids. The study of basalts and microgabbros from the Heber geothermal field [Browne and Elders, 1976; Browne, 1977] focused on the secondary mineralization of the mafic rocks. Keskinen and Sternfeld [1982] reported apparent K-Ar ages of 8.1-10.5 Ma for altered, subsurface basalts from the East Brawley geothermal field. These ages are considerably older than the apparent Plio-Pleistocene age of the sediments which they intruded and are therefore suspect.

Silicic tuffs crop out along the basin margins. These include a tuff in the Plio-Pleistocene Borrego Formation in the Durmid Hills [Babcock, 1969, 1974] and a tuff in the Plio-Pleistocene Palm Springs Formation [Johnson et al., 1983; Winker, 1987]. Merriam and Bischoff [1975] and Sarna-Wojcicki et al. [1984] correlated the tuff in the Durmid Hills with the Bishop Tuff, erupted 0.7 m.y. ago from the Long Valley caldera of central California.

Igneous Rocks in the State 2-14 Borehole

The samples recovered from the State 2-14 borehole are primarily sedimentary and metasedimentary rocks, progressively altered to greenschist facies mineral assemblages at temperatures up to 355°C [Elders and Sass, this issue]. They consist dominantly of lacustrine shales up to 125-m-thick, with interbedded fluvial-deltaic sandstones and pebbly mudstones ranging in thickness from a few centimeters to 10 meters (Figure 2; see Herzig et al. [this issue] for a detailed description). The framework modal clast compositions of the sandstones indicate that they were deposited by the Colorado River; basin margin detritus is rare. On the basis of their lithologies and stratigraphic occurrence, these (meta)sedimentary rocks in the State 2-14 borehole are correlated with the Borrego and Brawley formations of Pliocene to Pleistocene age [Babcock, 1969, 1974; Dibblee, 1954]. Only three intervals of igneous rocks were recovered in the borehole. These include a silicic tuff from 1704 m, and two altered sills of diabase at 2880 and 2896 m.

Silicic Tuff

A light gray to buff-colored, altered, silicic tuff was cored at 1704 m. A thickness of 0.25 m, together with its lower contact with the metasedimentary rocks, was recovered. Its true thickness is unknown, as it lacks a well-defined signature on wire line logs. This tuff lacks sedimentary bedding structures, a feature differentiating it from the metasedimentary rocks. The tuff is composed of feldspar and quartz grains, 0.07-0.15 mm in size, within a microcrystalline groundmass too fine to identify optically. Quartz consists of dominantly clear, fractured bipyramids of obvious volcanic origin.

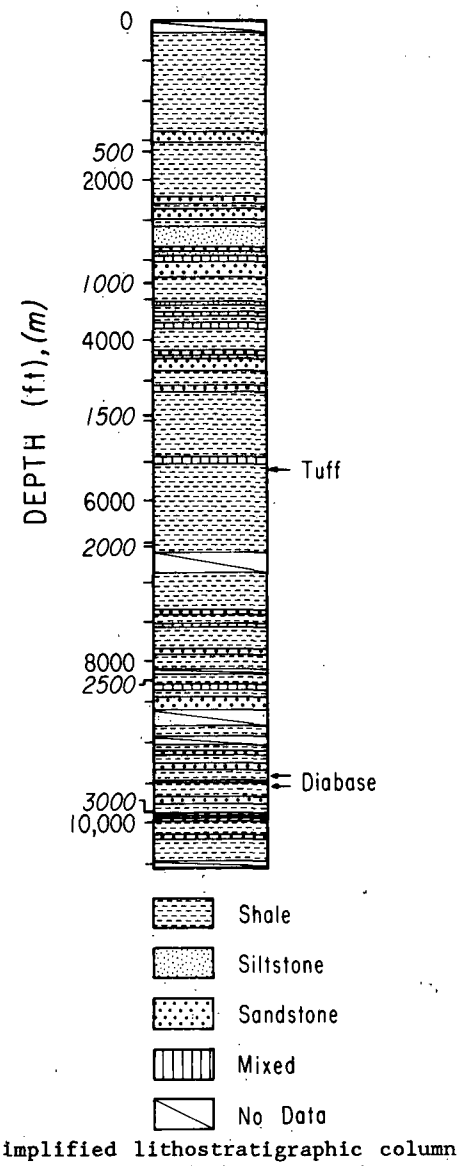

Fig. 2. Simplified lithostratigraphic column of the State 2-14 research borehole showing the stratigraphic positions of the silicic tuff and the diabase sills.

However, some quartz grains appear to be reworked from the underlying sediments. Fairly abundant crystals of chlorite replace primary biotite. Opaque minerals are scarce. The microcrystalline groundmass appears to be altered glass; however, volcanic glass has not been observed either optically or by X ray diffraction.

Hydrothermal alteration of the tuff is apparent. In addition to the chlorite pseudomorphs after biotite, some plagioclase crystals are partly to completely altered to adularia. The core of tuff is cut by millimeter-wide fractures containing epidote and adularia, and minor amounts of authigenic epidote and sphene occur in the groundmass.

Diabase

A diabase, believed to be a sill, was cored from 2881 to 2883 m and is 3.1 m thick, based on drill cuttings. A second diabase sill is only known from drill cuttings from the 2896- to 2905-m depth interval and its thickness may be up to 9 m. These two sills are petrographically identical. The primary minerals of labradorite feldspar and clinopyroxene exhibit an intergranular to subophitic texture. Plagioclase laths range from 0.65 to 1.4 mm in length and normally lack zoning. Accessory minerals include anhedral opaques and euhedral apatite. Orthopyroxene has not been observed; if present originally, it has now been entirely altered.

Although the chilled margin of the lower contact of the cored sill at 2883 m is subparallel to the bedding in the metasedimentary rocks, on a finer scale it is very irregular and brecciated (Figure 3). Apophyses of diabase

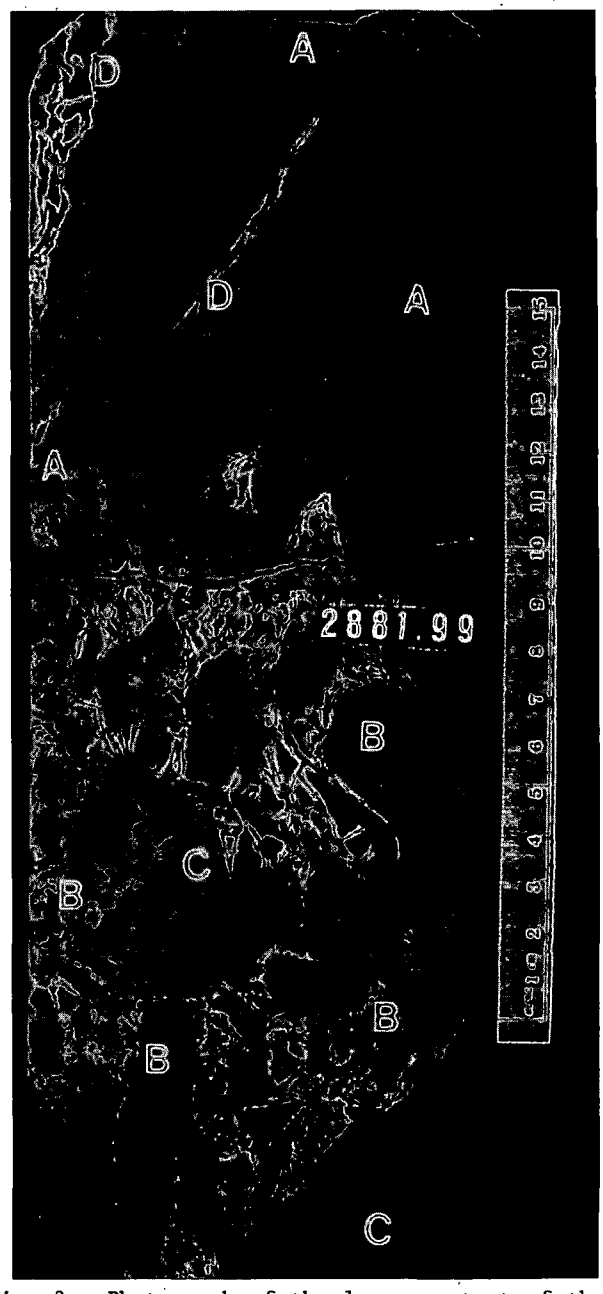

Fig. 3. Photograph of the lower contact of the diabase sill and the metasedimentary rocks from the State 2-14 borehole. A, diabase; B, diabase apophyses, note chilled contacts. Bleached margins composed of adularia and albite; C, bedded metasedimentary rocks; D, subvertical fractures filled with epidote and chlorite. Bleached margins composed of adularia and albite.

TABLE 1. Compositions of Oxidized Chlorites From a Diabase Sill in the State 2-14 Research Borehole

	Sample										
	9455						9455.5A		9455.5C		
	11[a]	12[a]	13[a]	14[a]	17[a]	18[a]	00[a]	19[a]	1[a]	2[a]	6[a]
	Weight Percent										
SiO_2	28.5	28.2	28.2	28.4	28.2	27.7	28.5	28.3	28.2	28.2	28.3
Al_2O_3	18.9	19.0	19.5	18.9	19.2	18.0	18.7	19.5	18.7	19.3	19.5
FeO	19.3	19.0	17.7	18.9	19.7	18.7	20.2	18.3	17.6	19.2	17.5
MnO	0.2	0.2	0.2	0.1	0.2	0.4	0.2	0.2		0.2	
MgO	22.7	22.7	23.2	23.1	22.6	22.2	22.2	23.5	17.6	22.6	23.7
CaO			0.1								
Total	89.6	89.1	88.9	89.4	89.9	87.0	89.8	89.8	82.1	89.5	89.0
	Cations										
Si	5.673	5.646	5.621	5.654	5.618	5.694	5.689	5.595	5.651	5.619	5.628
Al	2.327	2.354	2.379	2.346	2.382	2.306	2.311	2.405	2.349	2.381	2.372
Total	8.000	8.000	8.000	8.000	8.000	8.000	8.000	8.000	8.000	8.000	8.000
Al	2.115	2.126	2.199	2.093	2.116	2.046	2.087	2.144	2.058	2.150	2.186
Fe^{2+}	3.214	3.174	2.946	3.150	3.273	3.213	3.367	3.021	2.948	3.198	2.899
Mn	0.025	0.038	0.037	0.017	0.035	0.069	0.039	0.032		0.040	
Mg	6.738	6.777	6.883	6.866	6.708	6.802	6.618	6.933	7.141	6.728	7.009
Ca			0.010								
Total	12.092	12.115	12.065	12.126	12.132	12.130	12.111	12.130	12.147	12.116	12.094

	Sample										
	9455.5C			9455.5C				9453.4			
	10[a]	13[a]	14[a]	4[b]	9[b]	16[b]	24[b]	1[b]	2[b]	3[b]	7[b]
	Weight Percent										
SiO_2	27.4	27.8	28.6	29.0	28.6	28.6	28.5	29.4	29.8	28.9	29.8
Al_2O_3	19.8	19.6	18.2	18.9	18.9	18.8	18.8	19.0	19.0	18.6	19.6
FeO	19.5	19.5	18.3	17.7	17.6	17.6	18.8	18.6	17.9	17.4	18.0
MnO	0.3	0.2	0.2	0.2			0.2	0.4	0.2		0.2
MgO	22.4	22.4	23.3	23.2	23.2	23.2	22.7	23.2	22.5	22.0	23.4
CaO				0.1	0.1		0.1	0.3	0.3	0.2	0.3
K_2O				0.4	0.3	0.6		0.1	0.1	0.1	
Total	89.4	89.5	88.6	89.5	88.7	88.8	89.1	91.0	89.8	87.2	91.3
	Cations										
Si	5.493	5.552	5.741	5.747	5.711	5.720	5.693	5.757	5.869	5.846	5.764
Al	2.507	2.448	2.259	2.253	2.289	2.280	2.307	2.243	2.131	2.154	2.236
Total	8.000	8.000	8.000	8.000	8.000	8.000	8.000	8.000	8.000	8.000	8.000
Al	2.163	2.160	2.029	2.165	2.168	2.136	2.121	2.126	2.267	2.285	2.240
Fe^{2+}	3.272	3.250	3.059	2.938	2.941	2.947	3.152	3.047	2.948	2.947	2.917
Mn	0.043	0.039	0.031	0.030			0.041	0.063	0.037		0.029
Mg	6.694	6.683	6.952	6.850	6.889	6.899	6.753	6.766	6.598	6.643	6.755
Ca				0.014	0.026	0.009	0.024	0.049	0.065	0.045	0.057
K				0.097	0.074	0.163	0.005	0.017	0.031	0.030	
Total	12.172	12.132	12.071	12.094	12.098	12.154	12.096	12.068	11.946	11.950	11.998

Formula has been calculated on the basis of 28 oxygen equivalents. All analyses performed using the electron microprobe.

[a] Green vein chlorite.

[b] Purple vein chlorite.

[c] Groundmass chlorite.

crosscut the metasedimentary bedding, suggesting small downward intrusions of magma. Near this contact, the sill is cut by centimeter-wide veins containing hydrothermal minerals, and the chilled margins of the apophyses of diabase intruding the metasedimentary rocks are bleached by hydrothermal alteration.

Veins within the diabase are most abundant near the contact with the metasedimentary rocks and are filled with epidote and chlorite, formed in multiple stages from circulating hydrothermal fluids. Bleached zones in the diabase form selvages to the veins and consist of mixtures of fine-grained albite and adularia. Within the largely sealed fractures, straw-colored epidote is the most abundant mineral. As determined by electron microprobe, its composition ranges between $Ca_2(Fe_{0.64},Al_{2.36})Si_3O_{12}(OH)_2$ and $Ca_2(Fe_{0.97},Al_{2.03})Si_3O_{12}(OH)_2$.

Chlorite within the veins occurs as microspherules enclosed within epidote. It varies in color from pale to olive green; has low birefringence and occasionally shows anomalous purple interference colors. Electron microprobe analyses of chlorites occurring in the veins of solution origin, and of chlorites occurring in the diabase groundmass of replacement origin, are shown in Table 1 and Figure 4. The compositions

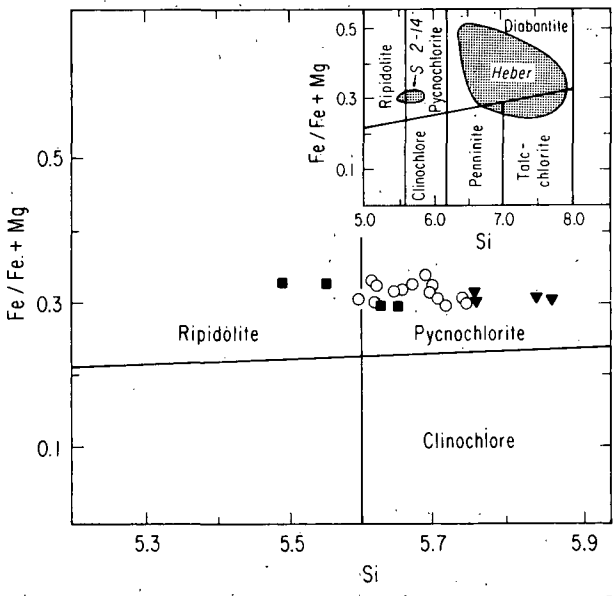

Fig. 4. Variation diagram showing compositions of oxidized chlorites from a diabase sill in the State 2-14 well. Fe/Fe + Mg are total iron and magnesium; Si is number of silicon cations per 28 oxygen atoms. Open circles and solid squares are analyses from a vein within the diabase; inverted solid triangles are from within the groundmass of the diabase. Insert diagram compares State 2-14 and Heber (Holtz 1) [Browne, 1977] chlorites from the diabases.

of all the chlorites straddle the boundary of the ripidolite-pycnochlorite fields. The total Fe/total Fe + Mg ratios range between 0.29 and 0.34 whereas the number of silicon cations per 28 oxygen atoms is between 5.3 and 5.8.

Vein chlorites with anomalous, purple interference colors have compositions falling within the Fe-Mg-Si fields of the coexisting vein chlorites with normal birefringence (Figure 4). However, some of the former are slightly enriched in potassium (0.4-0.6 wt % compared with about 0.1% for the others), suggesting that perhaps those chlorites with anomalous interference colors have occasional interlayers of illite.

Alteration of this sill diminishes away from the contact with the metasedimentary rocks and secondary veins. In the center of the sill, plagioclase grains are partially replaced by different proportions of chlorite, adularia, sphene, and, more rarely, epidote. Toward the contact, plagioclase is completely replaced by adularia and, less commonly, albite. Chlorite, sphene, rutile, and ferroactinolite replace, or partially replace, clinopyroxene. Iron and titanium oxides have been replaced by pyrite. In the contact zone pyrite is abundant, replacing silicate minerals.

Geochemistry of the State 2-14 Igneous Rocks

Major Elements

The chemical composition of the silicic tuff from the State 2-14 borehole is compared to unaltered tuffs in Table 2. The analyses of fresh tuffs include a sample from the nearest known outcrop of tuff to the State 2-14 well, the Durmid Hill tuff [Babcock, 1969, 1974], occurring 25 km to the northwest, and with the Bishop Tuff, Green Mountain ash, and Pearlette-like ash. The latter three silicic ash samples are representative deposits of the three major rhyolitic volcanic centers active during the Pleistocene in the western United States [Izett et al., 1970; Borchardt et al., 1972; Hildreth, 1979]. We compare the State 2-14 and Durmid Hill silicic tuffs with the other three because they are the most likely sources for Pleistocene tuffs in the Salton Trough. The materials erupted from these volcanic centers have clearly distinguishable petrographic and chemical properties, and they differ to such a degree that the eruptive source of the State 2-14 and Durmid Hill tuffs may be "fingerprinted."

The abundances of oxides such as SiO_2 and Al_2O_3 are similar amongst these tuffs; however, the State 2-14 tuff is enriched in TiO_2, MgO, K_2O, and iron in comparison to the Durmid Hill and other tuffs. The enrichment of these oxides in the State 2-14 tuff reflects the formation of secondary, hydrothermal minerals, such as sphene, chlorite, adularia, and pyrite, respectively.

In Table 3 the compositions of the major element oxides of the State 2-14 diabase are compared to a basalt xenolith from the Salton Buttes [Robinson et al., 1976], and with basalts from the Guaymas Basin [Saunders, 1983] and Isla Tortuga [Batiza et al., 1979] in the Gulf of California, and with basalts from the East Pacific Rise [Saunders, 1983] and the CPGS. These rocks were chosen for comparison to test if the State 2-14 diabase is the product of the oceanic spreading regime similar to that of the Gulf of California and East Pacific Rise.

The hydrothermal alteration of the State 2-14 diabase is reflected in the abundances of the major element oxides. Compared with the basaltic xenolith from the Salton Buttes and with the basalts from the Gulf of California and East Pacific Rise, the State 2-14 diabase is strongly enriched in TiO_2, reflecting the formation of hydrothermal sphene, and K_2O, due to the presence of hydrothermal adularia. In addition, the State 2-14 diabase is depleted in CaO, MnO, and MgO in comparison to the other basalts, once again, a result of hydrothermal alteration of the diabase.

Trace Elements

The abundances of the trace elements Sr and Ba are strongly enriched in the State 2-14 tuff in comparison to the Durmid Hill tuff and other tuffs (Table 2) and are interpreted as a result of hydrothermal alteration of the subsurface rock. Other trace elements, such as Zr, Sc, Cr, and Ni appear to be somewhat enriched, and Rb appears to be slightly depleted in the State 2-14 tuff in comparison to the unaltered tuffs. Though some of the variation in abundances of these elements between the State 2-14 tuff and the other tuffs is certainly primary, it may also reflect hydrothermal alteration of the State 2-14 tuff.

Borchardt et al. [1972] used discrimant function analysis to determine that Mn and Sm were the most useful elements for distinguishing chemically between the Bishop, Green Mountain Reservoir, and Pearlette-like ashes. A plot of Mn versus Sm for the State 2-14 and Durmid Hill

TABLE 2. Whole Rock Analyses of the State 2-14 and Durmid Hill Tuffs Compared With the Bishop Tuff, Green Mountain Reservoir Ash, a Pearlette-like Ash, and the S.B. Rhyolite

	Sample									
	State 2-14	DH	Bishop T.[a] (E)	Bishop Ashes[b,c] 3	7	10	G. M. R.[b,c] 12	13	Pear. A.[b,c] 14	S.B. Rhyolite[d] I70-21P
SiO_2	74.60	73.81	77.4	72.8	73.2	73.1	71.5	71.5	72.1	74.5
TiO_2	0.14	0.07	0.07	0.07	0.07	0.08	0.03	0.07	0.12	0.24
Al_2O_3	12.18	12.53	12.3	12.4	11.5	12.1	13.2	13.3	11.7	13.52
Fe_2O_3	0.62	0.88								0.12
FeO	0.98	0.38	0.7[e]	0.7[e]	0.6[e]	0.7[e]	0.4[e]	0.4[e]	1.2[e]	2.83
MgO	1.39	0.09	0.01	0.04	0.04	0.08	0.07	0.08	0.02	0.12
CaO	0.38	0.43	0.45	0.41	0.42	0.46	0.69	0.67	0.49	0.92
Na_2O	3.16	4.14	3.9	3.30	3.28	2.73	3.48	3.50	2.44	4.62
K_2O	5.67	3.55	4.8	5.05	4.86	4.59	4.45	4.13	6.11	4.16
P_2O_5	0.03	0.01	0.01	NA	NA	NA	NA	NA	NA	0.04
LOI	1.03	2.72		3.98	4.31	4.08	4.68	4.61	3.89	
Total	100.18	98.61	99.64	98.75	98.28	97.92	98.50	98.26	98.07	101.10
La	20	21	19	17	18	27	11	12	81	51
Ce	45	51	45	34	31	47	23	23	139	137
Nd	18	14	17	20	8	15	21	20	65	53
Sm	4.21	4.13	3.6	4.0	3.9	3.6	7.1	6.7	12.5	12.5
Eu	0.29	0.23	0.05	0.03	0.03	0.10	0.20	0.17	0.46	1.80
Tb	0.51	0.56	0.57	0.44	0.37	0.40	1.66	0.97	1.73	2.91
Dy	3.14	4.03	3.7	4.1	3.7	3.1	9.2	9.4	12.3	14.4
Yb	1.91	2.68	2.6	1.4	1.5	1.3	4.7	4.7	8.0	14.1
Lu	0.31	0.38	0.37	0.49	0.45	0.39	1.27	1.18	1.28	1.98
Rb	124	169	190	169	153	145	286	267	213	136
Sr	179	10	10	8	12	18	18	20	8	290
Zr	94	86	85	76	88	75	63	88	177	301
Ba	1055	84	10	51	68	106	119	204	179	390
Mn	233	265	270	249	244	213	834	831	232	369
Th	19.0	20.9	20.5	19.0	17.9	16.3	14.0	13.7	30.3	20.2
U	5.58	7.29	6.5	7.1	6.9	5.8	15.9	14.2	6.7	6.3
Hf	4.2	3.8	4.2	3.6	3.3	3.2	4.6	4.5	7.6	12.7
Ta	2.6	2.7	2.1	2.1	2.0	1.7	5.4	5.2	3.6	2.5
Sc	3.4	2.9	3.0	2.6	2.4	2.2	9.09	8.69	1.40	2.75
Cr	4	2	3.0	1.1	2.1	1.9	3.8	2.9	3.0	4.5
Ni	6	5	3	NA	NA	NA	NA	NA	NA	NA
Zn	36	29	38	NA	NA	NA	NA	NA	NA	77

DH, Durmid Hill. Bishop T., (E), early unit of the Bishop Tuff[a]. G.M.R., Green Mountain Reservoir. Pear. A., Pearlette-like ash. Bishop ash bed localities[b,c], 3, Pleistocene lake beds, Lake Tecopa, Inyo County, California; 7, Harpole Mesa Formation, Grand County, Utah; 10, ash bed in alluvium, Nuckolls County, Nebraska; 12, Pleistocene deposits, Montrose County, Colorado; 13, Pleistocene deposits, Summit County, Colorado; 14, type locality of Sappa Formation, Harlan County, Nebraska. S.B. rhyolite, Salton Buttes rhyolite. Major element analyses of State 2-14 and DH samples by ICP; precision stated by Kroneman et al. [1984]. Trace element and REE analyses of State 2-14, DH, and S.B. rhyolite samples during this study by INAA [Minor et al., 1981; Garcia et al., 1982]. NA, not analyzed. LOI, loss on ignition. Major oxides in weight percent. Trace elements in ppm.

[a] Hildreth [1979].
[b] Izett et al. [1970].
[c] Borchardt et al. [1972].
[d] Robinson et al. [1976].
[e] Total iron as FeO.

tuffs and the Bishop, Green Mountain Reservoir and Pearlette-like ashes is shown in Figure 5. In Figure 5, the Mn and Sm abundances of the State 2-14 and Durmid Hill tuffs would classify them with the Bishop ash units. However, the manganese concentration in the hydrothermal brines of the SSGS is around 1000 ppm, presumably derived by leaching from the host rocks by hydrothermal alteration. Thus the exchange of Mn between the State 2-14 tuff and the brine could have occurred. However, the tight clustering of the State 2-14 tuff data with that of the Bishop Tuff units suggests that the change in Mn composition has been slight. As will be discussed below, the rare earth elements also support this assertion.

The abundances of the trace elements Rb, Zr, and Ba are strongly enriched in the State 2-14 diabase (Table 3) in comparison with the basalts from the Salton Buttes, the Gulf of California, and the East Pacific Rise. The enrichment of these elements in the State 2-14 diabase undoubt-

TABLE 3. Whole Rock Analyses of the State 2-14 Diabase and Basalts From the Salton Buttes, Gulf of California, East Pacific Rise, and the CPGS

	Sample									
	State	SBV[a]	GOC-Guaymas Basin[b]			Is. T.[c]	East Pacific Rise[b]			CPGS
	2-14	Xen.	477A2	4784	481110	2-20	474A2a	474A7	474A8	3354
SiO_2	49.60	51.15	49.0	48.8	50.1	47.0	44.5	48.3	48.7	50.59
TiO_2	3.02	1.59	1.76	1.44	1.97	1.42	1.28	1.59	2.27	2.29
Al_2O_3	14.39	15.08	17.4	16.1	15.2	16.4	15.2	16.4	15.2	13.97
Fe_2O_3	3.33	2.45	9.66[d]	9.59[d]	10.89[d]	1.30	10.77[d]	10.61[d]	11.66[d]	4.61
FeO	5.31	7.35				7.80				6.38
MnO	0.10	0.17	0.15	0.15	0.17	0.15	0.17	0.17	0.16	0.20
MgO	6.89	7.70	7.23	8.80	7.05	8.50	14.87	7.50	7.25	5.48
CaO	8.15	11.31	11.81	10.35	10.38	11.79	9.59	12.31	10.84	8.98
Na_2O	3.00	3.32	3.10	3.09	3.20	3.50	2.47	2.42	2.80	2.68
K_2O	3.21	0.26	0.25	0.29	0.37	0.07	0.00	0.11	0.23	0.69
P_2O_5	0.46	0.34	0.23	0.20	0.25	0.16	0.09	0.10	0.26	0.27
LOI	1.88				0.46	0.3	1.22		0.50	2.39
Total	99.34	100.72	100.58	98.77	100.04	98.39	100.07	99.45	99.91	98.54
La	12.0	NA	5.6	4.5	6.1	NA	1.1	4.9	6.6	10.8
Ce	36.7	NA	16.1	13.9	18.0	13.6	6.9	13.2	20.8	29.1
Nd	27	NA	12.9	11.0	15.8	10.9	9.2	11.4	11.2	28
Sm	7.5	NA	4.2	3.5		3.4	3.5	4.1	5.5	5.1
Eu	2.18	NA	1.56	1.3	1.65	3.5	1.40	1.4	2.1	2.1
Tb	1.53	NA	0.86	0.75	1.07	NA	0.73	0.86	1.34	1.04
Dy	8.36	NA	NA	NA	NA	5.1	NA	NA	NA	4.97
Yb	5.06	NA	2.99	2.67	3.48	3.7	2.68	3.37	4.93	4.52
Lu	0.80	NA	0.47	0.43	0.56	0.48	0.43	0.53	0.80	0.69
Rb	148	10	1	3	4	1	1	1	1	15
Sr	225	205	241	198	203	245	106	147	158	213
Zr	195	100	123	106	123	NA	70	101	147	176
Ba	409	30	22	81	71	17	22	24	36	560
Ni	62	70	66	81	80	91	522	110	87	46
Cr	221	300	191	228	180	229	797	277	200	103
Th	1.56	0.49[e]	0.33	0.47	0.61	NA	0.10	0.32	0.58	1.25
Hf	6.29	3.07[e]	3.01	2.55	3.40	NA	2.49	2.84	3.80	4.93
Ta	0.82	0.48[e]	0.33	0.27	0.41	NA	0.01	0.25	0.47	0.63
Th/Hf	0.24	0.16	0.11	0.18	0.18		0.04	0.11	0.15	0.25
Th/Ta	1.90	1.02	1.00	1.74	1.49			1.28	1.23	1.98

SBV, Salton Buttes volcanics; GOC, Gulf of California; Is. T., Isla Tortuga. CPGS, Cerro Prieto geothermal system. Major element analyses of State 2-14 diabase and CPGS sample by ICP, precision stated by Kroneman et al. [1984]. Trace element and REE analyses of State 2-14 diabase and CPGS sample by INAA [Minor et al. 1981; Garcia et al. 1982]. Major oxides in weight percent. Trace elements in ppm. NA, not analyzed. LOI, loss on ignition.

[a] Robinson et al. [1976].
[b] Saunders [1983].
[c] Batiza et al. [1979].
[d] Total iron as Fe_2O_3.
[e] Analyzed during this study by INAA.

edly reflects its hydrothermal alteration. The amount of Sr in the State 2-14 diabase is comparable to that in the basalts from the Salton Buttes and the Gulf of California. However, the mobility of Sr in rocks subjected to hydrothermal alteration is documented by Saunders [1983]; thus it may be simply fortuitous that the Sr abundance of the State 2-14 diabase is similar to that of the unaltered basalts.

Rare Earth Elements

The abundances of the rare earth elements (REE) are believed to be less affected by secondary alteration and are therefore useful for fingerprinting different igneous rocks. Figure 6a shows the chondrite-normalized patterns for the rare earth elements of the silicic tuffs (Table 2). The negative Eu anomaly exhibited by all of the tuffs is typical of that seen in many silicic rocks. The light rare earth elements (LREE) are slightly enriched relative to the flat profile of the heavy rare earth elements (HREE) for all the tuffs except for those of the Green Mountain Reservoir. The REE pattern of the State 2-14 tuff closely resembles that of the Durmid Hill tuff. In turn, with the exception of differing degrees of Eu depletion, the State 2-14 and Durmid Hill tuffs both more nearly resemble the patterns of the Bishop ash flow tuff units. Dif-

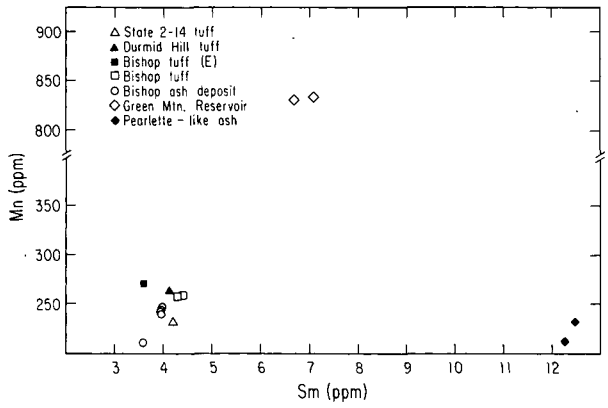

Fig. 5. Cross plot of Mn versus Sm for silicic ash flow tuffs. Diagram after Borchardt et al. [1972]. Additional data not shown in Table 2 from Borchardt et al. [1972]. State 2-14 and Durmid Hill data from this study.

ferences in the size of the Eu anomaly and the shapes of the patterns may in part be explained by small amounts of local detrital materials being incorporated into the ash deposits. In addition, zoning in the pre-eruption magma chamber [Hildreth, 1979] or tephra of different compositions being erupted may account for the differences in REE compositions.

In Figure 6b, the REE patterns of the State 2-14 diabase are compared with those of basalts from the Gulf of California and East Pacific Rise. The State 2-14 diabase exhibits a relatively flat pattern, with concentrations 25-45 times those in chondrites [Nakamura, 1974]. The concentration of the REEs in the State 2-14 diabase is higher than those of the Gulf of California and East Pacific Rise basalts, and the LREEs are slightly enriched relative to the HREEs in the State 2-14 sample.

Discussion

Silicic Tuff

The State 2-14 tuff is the first pyroclastic rock reported from the subsurface in the Salton Trough. Altered tuffs have probably been overlooked in drill cuttings from other geothermal wells due to their superficial textural similarity with arenitic siltstones. The correlation of the State 2-14 tuff with a volcanic source would yield an important time-stratigraphic marker for the subsurface in this region of the Salton Trough.

The tuff of Durmid Hill, interbedded with the lacustrine deposits of the Borrego and Brawley formations of Pliocene and Pleistocene age in the Durmid Hills [Babcock, 1969; 1974] was identified by Merriam and Bischoff [1975] and Sarna-Wojcicki et al. [1984] as a deposit of the Bishop Tuff. This correlation was based upon the presence of biotite phenocrysts in the Durmid Hill tuff, considered to be a diagnostic phenocryst of the Bishop ash [Izett et al., 1970], and upon their similar trace element abundances. The trace element compositions of the Durmid Hill sample analyzed during this study, specifically the abundances of Mn Sm, and the REE compositions, strongly support the correlation with the Bishop ash, as suggested by previous workers.

Hydrothermal alteration has obliterated the groundmass of the State 2-14 tuff, so petrographic correlation with its source is not very easy. However, the presence of chlorite crystals, interpreted as replacing biotite phenocrysts is consistent with it being the Bishop Tuff. Due to hydrothermal alteration, the abundances of the major elements, Sr, and Ba in the State 2-14 tuff are useless for correlating the deposit. However, we believe that the Mn, Sm, and other REE abundances more closely represent the primary composition of the State 2-14 tuff and therefore permit correlation with its eruptive source.

A comparison of the chemistry of the State 2-14 silicic tuff with the rhyolite of the Salton Buttes (Table 2) [Robinson et al., 1976] indicates that the State 2-14 tuff cannot be a deposit derived from these volcanoes [Sarna-Wojcicki et al., 1984]. Furthermore, given its depth of occurrence, the State 2-14 tuff must be much older than the volcanoes.

In spite of hydrothermal alteration the Mn and Sm abundances of the State 2-14 tuff are very similar to those of the Durmid and Bishop tuffs. The REE pattern of the State 2-14 tuff is nearly identical to that of the Durmid Hill tuff, which, in turn, are very similar to the REE patterns of the Bishop ash flow tuffs, with only minor differences in Eu content. The differences of the

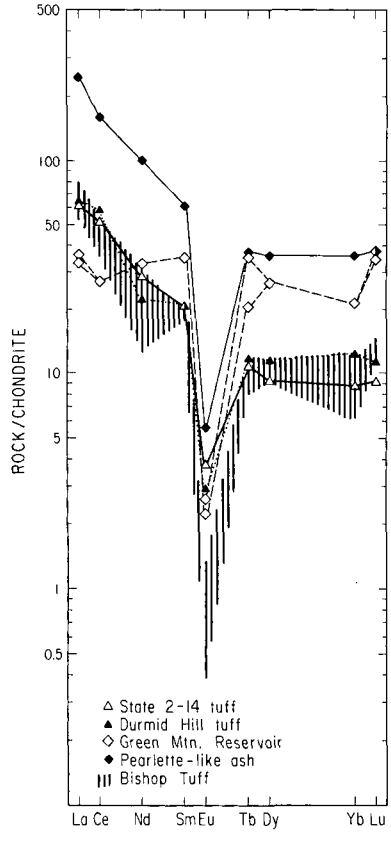

Fig. 6a. Chondrite-normalized, rare earth element (REE) diagram for sililcic ash flow tuffs (normalizing factors from Nakamura [1974]).

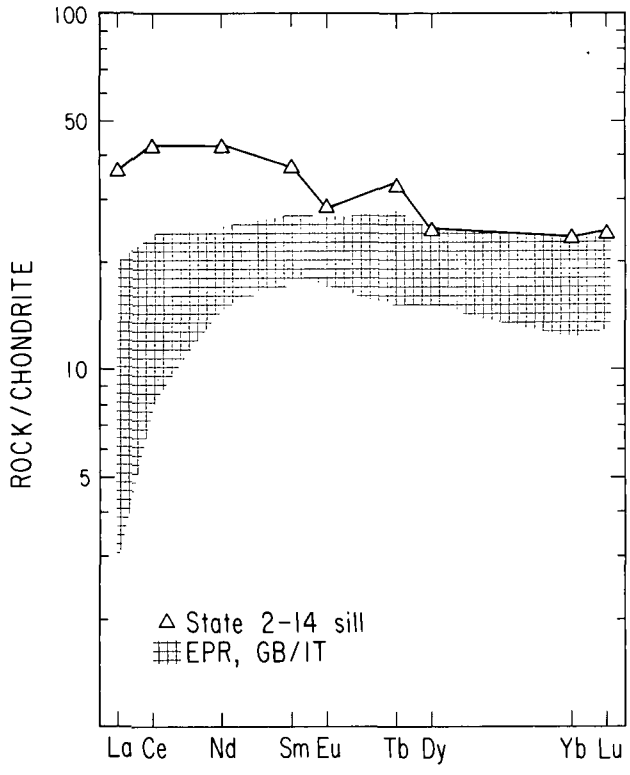

Fig. 6b. Chondrite-normalized, REE diagram comparing the State 2-14 diabase sill with basalts from the East Pacific Rise and Gulf of California [Batiza et al., 1979; Saunders, 1983]. EPR, East Pacific Rise; GB/IT, Guaymas Basin/Isla Tortuga.

REE patterns of the State 2-14 and Bishop Tuffs from those of the Green Mountain and Pearlette-like ashes also supports the correlation of the State 2-14 tuff with the Bishop Tuff. Thus, on the basis of the petrographic and trace element data currently available, the State 2-14 tuff is correlated with the Durmid Hill tuff, and both are believed to be deposits of the Bishop Tuff.

Diabase

Although partly altered to greenschist facies mineral assemblages, the State 2-14 diabase is similar texturally and mineralogically to the basalt xenoliths of the Salton Buttes. However, it is difficult to link the State 2-14 diabase to basaltic xenoliths based upon their chemical composition alone. Robinson et al. [1976] suggested that the basaltic xenoliths are chemically similar to typical oceanic tholeiite erupted along the East Pacific Rise. The major, trace element, and REE compositions of the State 2-14 diabase do not permit such a direct correlation because the diabase has been altered by hypersaline hydrothermal fluids. However, the diabase sills have intruded sediments of late Plio-Pleistocene age [Herzig et al., this issue]. The current rift regime in the Salton Trough is Pliocene or younger [Elders et al., 1972; Moore and Curray, 1982]. Thus it is reasonable to suggest that the sills are shallow intrusions of upper mantle materials similar to those within the Gulf of California and along the East Pacific Rise as rifting occurs within the Salton Trough.

The State 2-14 diabase is enriched in LREE relative to basalts from the Gulf of California and the East Pacific Rise [Batiza et al., 1979; Saunders, 1983]. Various explanations could satisfy the observations, for example, (1) the LREE enrichment is the product of hydrothermal alteration; for example, vein epidotes in the SSGS have been reported to be enriched in Y, Ce, and La [Younker et al., 1982], (2) the mantle sources are heterogeneous, (3) the melting processes are different, or (4) the magmas beneath the Salton Trough may have acquired a small continental component during intrusion.

The information currently available does not allow discrimination between these differing hypotheses as yet. However, the authors favor the last alternative because a fresh unaltered, subsurface basalt from the CPGS exhibits a small LREE enrichment, nearly identical to that of the altered State 2-14 diabase (Table 3). If this enrichment is not due to alteration, we prefer the hypothesis that it probably reflects an addition of a small continental component to the magmas.

At first sight, the hydrothermal alteration of the State 2-14 sills, postdating their emplacement, would suggest that the sills are older than the onset of the geothermal system in this region of the Salton Trough. However, hydrothermal alteration of the metasedimentary rocks in the State 2-14 borehole is widespread and progressively increases with depth in the borehole as temperature increases [Cho et al., this issue], The alteration is thus not directly related to proximity of the two sills. Specific contact metamorphic effects are not seen in the metasedimentary rocks adjacent to the cored diabase. It appears to us, therefore, that these sills intruded into an already hot, geothermal environment. However, the hydrothermal activity clearly continued after intrusion of the sills as evidenced by the partial to complete replacement of their primary constituents and the presence of hydrothermal veins cutting the diabase.

The alteration of the State 2-14 diabase is comparable to that previously described from a sill in a geothermal well in the Heber geothermal field [Browne and Elders, 1976; Browne, 1977]. There the 1570-m-deep Holtz 1 borehole penetrated a basalt between 1335 and 1366 m, where the ambient temperature today approaches 200°C. In this rock, chlorite is the most abundant secondary mineral replacing olivine, plagioclase, and early hydrothermal minerals [Browne, 1977]. The composition of the chlorites from the Holtz 1 sill are shown in Figure 4 for comparison with the State 2-14 basalt. The Heber chlorites cover a much broader compositional range, mostly in the diabantite field. In comparison, the compositional range of chlorite in the State 2-14 diabase is slight irrespective of whether crystals formed by replacement or deposited directly from solution. Though not studied in detail at this time, the difference in compositions between the chlorites in the SSGS and Heber geothermal system probably reflects different temperatures of formation (200°C at Heber, 355°C at SSGS) and different chemistry of the hydrothermal fluids. A more detailed treatment of chlorite and other hydrothermal mineral chemistry is found by Cho et al. [this issue].

Summary and Conclusions

The first cores of hypabyssal diabase intrusions from the Salton Sea geothermal system (SSGS), recovered during the SSSDP, support previous models for the tectonic setting of the Salton Trough. Whereas geophysical evidence has inferred the existence of a deep basement beneath the trough with seismic velocities and densities comparable to basaltic oceanic crust [Fuis et al., 1982, 1984], the mafic intrusives encountered in drilling and as xenoliths in the Salton Buttes provide direct evidence for basaltic magma in this rift system. Although the State 2-14 diabase sills cannot be directly linked to a magma type because of their secondary alteration, the young age of these rocks (late Plio-Pleistocene) implies that they are probably derived from upper mantle magmas, most likely similar to those of the Gulf of California/East Pacific Rise oceanic spreading system, generated during crustal rifting of the Salton Trough.

These diabase sills are probably outliers of larger intrusions in the Salton Trough which are the heat sources driving the hydrothermal systems within the geothermal fields [McKibben et al., 1987]. For example, a positive aeromagnetic anomaly of 1000 nT is associated with the SSGS, which suggests the presence of a large basaltic intrusion at the depth of a few kilometers [Griscom and Muffler, 1971]. Multiple sills which are intruded before and after the hydrothermal system is established suggest that the magma chambers are long-lived or are resupplied. Hydrothermal alteration of the surrounding metasedimentary rocks is unrelated directly to intrusion of these small sills and operates on a much broader scale in the SSGS.

The silicic tuff in the State 2-14 borehole is chemically distinct from the rhyolites of the Salton Buttes and Cerro Prieto volcanoes [Robinson et al., 1976; Reed, 1984] and also cannot be a deposit derived from the volcanoes because of stratigraphic constraints. The geochemical data presented here permit correlation between the State 2-14 and Durmid Hill tuffs, both of which may be deposits erupted from the Long Valley caldera of central California at 0.7 Ma. Such a correlation implies that the tuff at 1704 m depth in the State 2-14 research borehole is 0.7 Ma. Thus the rate of sedimentation and subsidence in this part of the SSGS would have averaged approximately 2.4 mm/yr for 0.7 Ma. Extrapolating this rate to the rest of the stratigraphic column in the SSGS would imply that the Plio-Pleistocene boundary should occur at a depth of approximately 3.8 km, i.e., 600 m deeper than the depth reached by the State 2-14 borehole. In comparison, on the basis of paleontological data, Ingle [1982] tentatively assigned the Plio-Pleistocene boundary to a depth of 2000 m in a borehole in the CPGS, close to the axis of the Colorado River delta.

Acknowledgments. This investigation was supported by National Science Foundation grant EAR-8502402 as part of the Salton Sea Scientific Drilling Project. Linda Jankov drafted the figures and P. Collier prepared the thin sections for this study. Our understanding of igneous rocks in the Salton Trough has benefited from discussions with J.M. Mehegan and L.H. Cohen. P.R.L. Browne helped with our interpretation of the hydrothermal alteration. This paper is UCR/IGPP report 88/6.

References

Atwater, T., Implications of plate tectonics for the Cenozoic tectonic evolution of western North America, Geol. Soc. Am. Bull., 81, 3513-3536, 1970.

Atwater, T., and P. Molnar, Relative motion of the Pacific and North American plates deduced from sea-floor spreading in the Atlantic, Indian, and South Pacific oceans, Conference Proceedings, Tectonic Problems of the San Andreas Fault System, edited by R.L. Kovach and A. Nur, Stanford Univ. Publ. Geol. Sci., 13, 136-148, 1973.

Babcock, E.A., Structural geology and geophysics of the Durmid area, Imperial Valley, California, Ph.D. dissertation, 145 pp., Univ. of Calif., 1969.

Babcock, E.A., Geology of the northeast margin of the Salton Trough, Salton Sea, California, Geol. Soc. Am. Bull., 85, 321-332, 1974.

Batiza, R., K. Futa, and C.E. Hedge, Trace element and strontium isotope characteristics of volcanic rocks from Isla Tortuga: A young seamount in the Gulf of California, Earth Planet. Sci. Lett., 43, 269-278, 1979.

Borchardt, G.A., P.J. Aruscavage, and H.T. Millar, Jr., Correlation of the Bishop ash, a Pleistocene marker bed, using instrumental neutron activation analysis, J. Sediment. Petrol., 42, 301-306, 1972.

Browne, P.R.L., Occurrence and hydrothermal alteration of diabase, Heber geothermal field, Imperial Valley, Calif., IGPP Publ. 77/9, 70 pp., Inst. of Geophys. and Planet. Phys., Univ. of Calif., Riverside, 1977.

Browne, P.R.L. and W.A. Elders, Hydrothermal alteration of diabase, Heber geothermal field, Imperial Valley, California, Geol. Soc. Am. Abstr. Programs, 8, 793, 1976.

Cho, M., J.G. Liou, and D.K. Bird, Prograde phase relations in the State 2-14 well metasandstones, Salton Sea geothermal field, California, J. Geophys. Res., this issue.

Crowe, B.M., Cenozoic volcanic geology and probable age of inception of basin-range faulting in the southeasternmost Chocolate Mountains, California, Geol. Soc. Am. Bull., 89, 251-264, 1978.

de Boer, J., Paleomagnetism of the Quaternary Cerro Prieto, Crater Elegante, and Salton Buttes volcanic domes in the northern part of the Gulf of California rhombochasm, in Proceedings 2nd Symposium on the Cerro Prieto Geothermal Field, Baja California, Mexico, pp. 91-102, Comision Federal de Electricidad, Mexicali, 1980.

Dibblee, T.W., Geology of the Imperial Valley region, California, Geology of California, chapter 2: Geology of the Natural Provinces, edited by R.H. Jahns, Calif. Div. of Mines Bull., 170, 21-28, 1954.

Dickinson, W.R., and W.S. Snyder, Geometry of subducted slabs related to San Andreas transform, J. Geol., 87, 609-627, 1979.

Elders, W.A., and J. Sass, The Salton Sea Scientific Drilling Project, J. Geophys. Res., this issue.

Elders,W.A., R. Rex, T. Meidev, P.T. Robinson, and S. Biehler, Crustal spreading in southern California, Science, 178, 15-24, 1972.

Elders, W.A., J.R. Hoagland, E.R. Olson, S.D. McDowell, and P. Collier, A comprehensive study of samples from geothermal reservoirs: Petrology and light stable isotope geochemistry of twenty-three wells in the Cerro Prieto geothermal field, Baja California, Mexico, IGPP Rep. 78/26, 128 pp., Inst. of Geophys. and Planet. Phys., Riverside, 1978.

Elders, W.A., A.E. Williams, and J.R. Hoagland, An integrated model for the natural flow regime in the Cerro Prieto hydrothermal system, B.C., Mexico, based upon petrological and isotope geochemical criteria, Proceedings of the 3rd Symposium on the Cerro Prieto Geothermal Field, Mar. 24-26, San Francisco, Calif., Rep. LBL-11967, Lawrence Berkeley Lab., Berkeley, Calif., 1981.

Friedman, I., and J. Obradovich, Obsidian hydration dating of volcanic events, Quat. Res., 16, 37-47, 1981.

Fuis, G.S., W.D. Mooney, J.H. Healy, G.A. McMechan, and W.J. Lutter, Crustal structure of the Imperial Valley, The Imperial Valley, California Earthquake of October 15, 1979, U.S. Geol. Surv. Prof. Pap., 1254, 25-49, 1982.

Fuis, G.S., W.D. Mooney, J.H. Healy, G.A. McMechan, and W.J. Lutter, A seismic refraction survey of the Imperial Valley, California, J. Geophys. Res., 89, 1165-1189, 1984.

Garcia, S.R., W.K. Hensley, M.M. Denton, and M.A. Fuka, An automated multidetector system for instrumental neutron activation analysis of geological and environmental materials, in Atomic and Nuclear Methods in Fossil Energy Research, edited by R.H. Filby, B.S. Carpenter, and R.C. Ragiani, pp. 133-140, Plenum Publ. Corp., New York, 1982.

Gjerde, M.W., Petrography and geochemistry of the Alverson Formation, Imperial County, California, M.S. thesis, 85 pp., San Diego State Univ., Calif., 1982.

Griscom, A., and L.P.J. Muffler, Aeromagnetic map and interpretation of the Salton Sea geothermal area, California, U.S. Geol. Surv., Geophys. Invest. Map, GP 754, 1971.

Hawkins, J.W., Petrology and possible tectonic significance of late Cenozoic volcanic rocks, southern California and Baja California, Geol. Soc. Am. Bull., 81, 3323-3338, 1970.

Herzig, C.T., J. Mehegan, and C. Stelting, Lithostratigraphy of the State 2-14 borehole: Salton Sea Scientific Drilling Project, J. Geophys. Res., this issue.

Hildreth, W., The Bishop Tuff: Evidence for the origin of compositional zonation in silicic magma chambers, Spec. Pap. 180, Geol. Soc. Am., 43-75, 1979.

Ingle, J., Microfaunal evidence of age and depositional environments of the Cerro Prieto section (Plio-Pleistocene), Baja California, Mexico, Rep. LBL-13897, Lawrence Berkeley Lab., Berkeley, Calif., 1982.

Izett, G.A., R.E. Wilcox, H.A. Powers, and G.A. Desborough, The Bishop ash bed, a Pleistocene marker bed in the western United States, Quat. Res., 1, 121-132, 1970.

Johnson, N.M., C.B. Officer, N.D. Opdyke, G.D. Woodard, P.K. Zeitler, and E.H. Lindsay, Rates of late Cenozoic tectonism in the Vallecito Fish Creek Basin, western Imperial Valley, California, Geology, 11, 664-667, 1983.

Karig, D.E., and W. Jensky, The proto-Gulf of California, Earth Planet. Sci. Lett., 17, 169-174, 1972.

Keskinen, M., and J. Sternfeld, Hydrothermal alteration and tectonic setting of intrusive rocks from East Brawley, Imperial Valley: An application of petrology to geothermal reservoir analysis, paper presented at 8th Geothermal Reservoir Workshop, Stanford Univ., Stanford, Calif., Dec. 1982.

Kroneman, R.L., K.R. Yorgason, and J.N. Moore, Preferred methods of analysis for chemical tracers in moderate- and high-temperature geothermal environments, Rep. UURI (DOE/ID/12079-128; ESL-84001-TR), Earth Sci. Lab., Salt Lake City, Utah, 1984.

Lachenbruch, A.H., J.H. Sass, and S.P. Galanis, Jr., Heat flow in southernmost California and the origin of the Salton Trough, J. Geophys. Res., 90, 6709-6736, 1985.

Mehegan, J.M., C.T. Herzig, W.A. Elders, L.H. Cohen, and A.L. Quintanilla-Montoya, REE geochemistry of continental rift lavas of the Salton Trough, California and Mexico, Geol. Soc. Am. Abstr. Programs, 19, 769, 1987.

Merriam, R., and O.L. Bandy, Source of upper Cenozoic sediments in Colorado delta region, J. Sediment. Petrol., 35, 911-916, 1965.

Merriam, R., and J.L. Bischoff, Bishop ash: A widespread volcanic ash extended to southern California, J. of Sediment. Petrol., 45, 207-211, 1975.

McKibben, M.A., A.E. Williams, W.A. Elders, and C.S. Eldridge, Saline brines and metallogenesis in a modern sediment-filled rift: The Salton Sea geothermal system, California, U.S.A., Appl. Geochem., 2, 563-578, 1987.

Minor, M.M., W.K. Hensley, M.M. Denton, and S.R. Garcia, An automated activation analysis system, Radioanal. Chem., 70, 459, 1981.

Moore, D.G., and J.R. Curray, Geologic and tectonic history of the Gulf of California, Initial Reps. Deep Sea Drill. Proj., 64, 1279-1294, 1982.

Muffler, L.J.P., and B.R. Doe, Composition and mean age of detritus of the Colorado River delta in the Salton Trough, southeastern California, J. Sediment. Petrol., 38, 384-399, 1968.

Muffler, L.J.P., and D.E. White, Active metamorphism of upper Cenozoic sediments in the Salton Sea Geothermal Field and the Salton Trough, southeastern California, Geol. Soc. Am. Bull., 80, 157-182, 1969.

Nakamura, N., Determination of REE, Ba, Fe, Mg, Na and K in carbonaceous and ordinary chondrites, Geochim. Cosmochim. Acta, 38, 757-775, 1974.

Reed, M.J., Relationship between volcanism and hydrothermal activity at Cerro Prieto, Mexico, Trans. Geotherm. Resour. Counc., 8, 217-221, 1984.

Robinson, P.T., W.A. Elders, L.J.P. Muffler, Quaternary volcanism in the Salton Sea geothermal field, Imperial Valley, California, Geol. Soc. Am. Bull., 87, 347-360, 1976.

Sarna-Wojcicki, A.M., H.R. Bowman, C.E. Meyer, P.C. Russell, M.J. Woodward, G. McCoy, J.J. Rowe, Jr., P.A. Baedecker, F. Asaro, and H.

Michael, Chemical analyses, correlations and ages of upper Pliocene and Pleistocene ash layers of east-central and southern California, U.S. Geol. Surv. Prof. Pap., 1293, 1984.

Saunders, A.D., Geochemistry of basalts recovered from the Gulf of California during leg 65 of the Deep Sea Drilling Project, Initial Rep. Deep Sea Drill. Proj., 65, 591-621, 1983.

van de Kamp, P.C., Holocene continental sedimentation in the Salton Basin, California: A reconnaissance, Geol. Soc. Am. Bull., 84, 827-848, 1973.

Winker, C.D., Neogene stratigraphy of the Fish Creek-Vallecito section, southern California: implications for early history of the northern Gulf of California and Colorado delta, Ph.D. dissertation, 494 pp., Univ. of Ariz., Tucson, 1987.

Younker, L.W., P.W. Kasameyer, and J.D. Tewhey, Geological, geophysical, and thermal characteristics of the Salton Sea geothermal field, California, J. Volcanol. and Geotherm. Res., 12, 221-258, 1982.

W.A. Elders and C.T. Herzig, Institute of Geophysics and Planetary Physics, University of California, Riverside, CA, 92521.

(Received February 10, 1988;
revised June 27, 1988;
accepted June 29, 1988.)

JOURNAL OF GEOPHYSICAL RESEARCH, VOL. 93, NO. B11, PAGES 13,081–13,103, NOVEMBER 10, 1988

Prograde Phase Relations in the State 2-14 Well Metasandstones, Salton Sea Geothermal Field, California

MOONSUP CHO[1], J. G. LIOU, AND DENNIS K. BIRD

Department of Geology, Stanford University, Stanford, California

Seventy-five core samples of medium- to fine-grained metasandstones from the State 2-14 borehole were studied petrologically and mineralogically to evaluate compositional variations of geothermal minerals and prograde metamorphic reactions. Three distinct metamorphic zones are defined based on the appearance of index minerals. With increasing grade, they are (1) chlorite-calcite (Chl-Cc) zone at depths between 610 and 2480 m; (2) biotite (Bt) zone between 2480 and 3000 m; and (3) clinopyroxene (Cpx) zone between 3000 and 3180 m. All of the studied metasandstones at depths greater than 906 m contain epidote (Ep) and quartz (Qtz) with or without albite (Ab). Characteristic assemblages (+ Ep + Qtz ± Ab) are (1) Chl + Cc ± K-feldspar (Ksp) ± phengitic muscovite for the Chl-Cc zone; (2) Bt + Chl ± Ksp ± anhydrite (Anh) and Bt + Act ± Chl for the Bt zone; and (3) diopside-salite + Act ± Bt ± oligoclase ± actinolitic hornblende for the Cpx zone. Epidote exhibits a compositional variation ranging from 0.11 to 0.42 X_{Fe} (= Fe/(Fe+Al)). Many amphibole grains of the clinopyroxene zone show patchy or lamellar intergrowths of both actinolite and actinolitic hornblende on a scale less than a few tens of micrometers. These amphiboles show distinct compositional discontinuities such as in Al_2O_3 contents (2.7 - 4.8 wt %) and Fe/(Fe+Mg) ratios (0.41 - 0.55). The Cpx zone samples thus mark the transition from the greenschist to amphibolite facies. Other important secondary phases include rutile or anatase (depths<1427 m; 2745 - 3020 m), aluminous titanite (>940 m), peristerite (1235 m), and Mn-salite (2484 m). The observed assemblages and compositions of minerals are chemographically interpreted utilizing an epidote projection in the simple system, Al_2O_3 - K_2O - MgO - CaO - SiO_2 - H_2O - CO_2. Reactions for the appearance of index minerals are elucidated in a qualitative T - X_{CO2} diagram. The results indicate that (1) the compositions of Chl and Bt are highly variable depending on the bulk composition; however, Chl in the Chl-Cc zone becomes enriched in Mg with increasing depth; (2) Bt forms by a discontinuous reaction, Ksp + Chl + Cc = Bt + Ep + Qtz + H_2O + CO_2; hence the first appearance of Bt is greatly affected by the fluid composition; (3) the hydrothermal fluid in equilibrium with the analyzed assemblages is very low in X_{CO2} (<0.03); and (4) the absence of wairakite and prehnite is attributed to the high f_{O2} values of the Salton Sea geothermal system.

INTRODUCTION

Mineralogic and petrologic characteristics of the Salton Sea geothermal system have been studied by many investigators [e.g., *Muffler and White*, 1969; *McDowell and Elders*, 1980, 1983; *Bird and Norton*, 1981; *McKibben and Elders*, 1985]. Their studies, however, were done primarily using drilling chip samples mostly less than ~1 cm in maximum dimension. Thus it was often difficult to elucidate in detail the prograde nature of metamorphic reactions. The Salton Sea Scientific Drilling Project successfully drilled to a depth of 3220 m and temperatures exceeding ~350°C, recovering more than 224 m of cores in the State 2-14 well [*Elders and Sass*, 1987; *Herzig and Mehegan*, 1987]. The cores provide a unique opportunity for investigation of progressive metamorphism accompanying hydrothermal metasomatism in an active geothermal system within the Salton Trough of southern California. We collected samples from the recovered cores, along with samples at depths between 3000 and 3180 m from drilling chips. Systematic and integrated studies on the mineralogical, petrological, and geochemical aspects of the drill core samples were completed. This study describes chemical characteristics of authigenic minerals, prograde phase relations of medium- to fine-grained recrystallized sandstones, and metamorphic reactions responsible for the appearance of index minerals; the details for secondary mineralization in veins are described by *Caruso et al.* [this issue] and for geothermal epidotes by *Bird et al.* [this issue].

The State 2-14 well is located at the northeastern flank of the Salton Sea geothermal field (Figure 1). It shows mineralogic characteristics similar to those observed in the previously investigated wells [e.g., *McDowell and Elders*, 1980]. Most of the analyzed metasandstone cores preserve clastic textures; however, some exhibit well-developed hornfelsic intergrowth of metamorphic minerals and contain abundant epidote and quartz. Based on the appearance of

[1]Now at Department of Earth and Space Sciences, University of California, Los Angeles.

Paper number 7B7105.
0148-0227/88/007B-7105$05.00

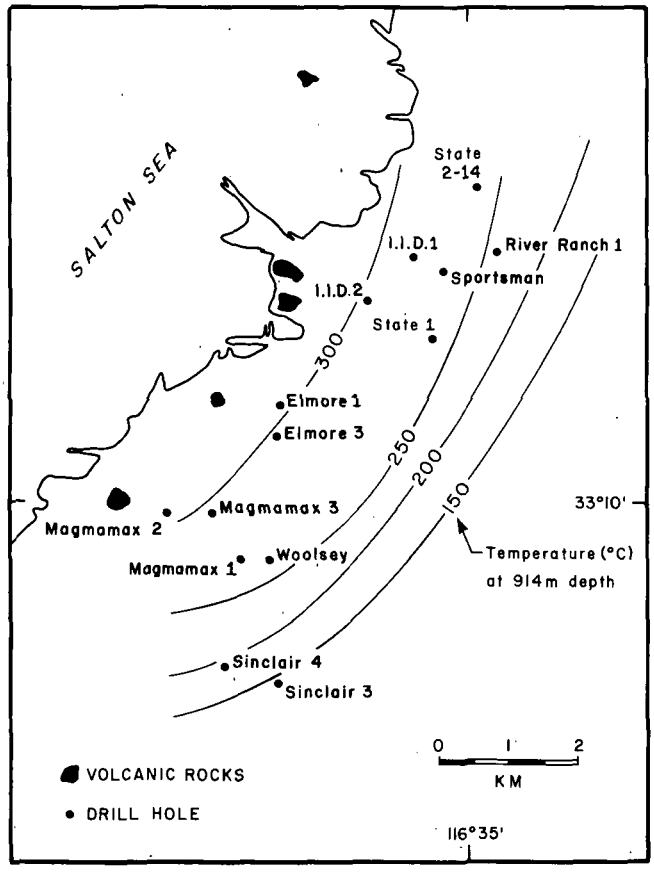

Fig. 1. Location map of the State 2-14 well together with previous wells of the Salton Sea geothermal field. Isothermal lines at 150°, 200°, 250° and 300° C at 914 m depth are after *McDowell and Elders* [1983]. Solid symbols with irregular shapes represent rhyolite extrusives in the Salton Sea geothermal field.

index minerals, three distinct metamorphic zones are established with increasing depth: chlorite-calcite, biotite, and clinopyroxene zones. The clinopyroxene zone is newly defined in this study by the occurrence of clinopyroxene ± actinolite ± actinolitic hornblende ± albite ± oligoclase. This assemblage suggests that the transition between greenschist and amphibolite facies occurs near the bottom of the State 2-14 well.

The purposes of this study are threefold: (1) to delineate metamorphic zones in response to the active hydrothermal metamorphism at elevated temperatures; (2) to determine compositions of metamorphic minerals with increasing depth and to analyze their phase relations employing a model system, Al_2O_3 - K_2O - MgO - CaO - SiO_2 - H_2O - CO_2; and (3) to define chemical reactions responsible for the observed mineral parageneses and to understand their T - X_{CO2} relations. The effect of f_{O2} on the occurrence of wairakite and prehnite in active geothermal systems is briefly discussed employing the A'CF diagram [*Liou et al.*, 1985; *Cho et al.*, 1986]. These data together with available chemical and isotopic properties of geothermal fluids are essential for understanding water-rock interactions, mineral-solution equilibria, and geochemical mass transport in the Salton Sea geothermal system.

MINERAL ZONATIONS

General structures, textures, and mineral assemblages of drill hole core samples in the State 2-14 well have been catalogued by *Herzig and Mehegan* [1987]. Seventy-five samples of medium- to fine-grained metasandstones at depths between 470 and 3180 m were collected for the present study. Among them, mineral compositions and phase relations for 39 samples, mostly with abundant quartz and epidote, were analyzed in detail. In our petrologic study we have focused on medium- to fine-grained metasandstones in order to reduce the effect of different bulk rock compositions, associated with different sedimentary environments in the Colorado River delta, on phase relations and compositions. Parageneses of secondary minerals along fractures and veins are described elsewhere [*Caruso et al.*, this issue]. Table 1 lists the end-member compositions and abbreviations of the minerals considered in this study. Mineral assemblages of some selected metasandstones are shown with increasing depth in Table 2. Note that sample numbers of this study correspond to the depth of each sample in feet.

Three distinct metamorphic zones were delineated with increasing depth: (1) a chlorite-calcite zone at depths between 610 and 2480 m; (2) a biotite zone between 2480 and 3000 m; and (3) a clinopyroxene zone between 3000 and 3180 m. These metamorphic zones are defined by the first appearance of chlorite, biotite, and Mn-free clinopyroxene, respectively. All of the analyzed metasandstones at depths greater than 906 m contain epidote and quartz with or without albite. Characteristic assemblages (+ Ep + Qtz ± Ab) for each zone are (1) chlorite + calcite ± K-feldspar ± phengitic muscovite for the chlorite-calcite zone; (2) biotite + chlorite ± K-feldspar ± anhydrite, and biotite + actinolite ± chlorite for the biotite zone; and (3) diopside-salite + actinolite ± biotite ± oligoclase ± actinolitic hornblende for the clinopyroxene zone. Samples of the clinopyroxene zone contain many amphibole grains showing patchy or lamellar intergrowths of both actinolite and actinolitic hornblende, together with albite and/or oligoclase. The clinopyroxene zone thus marks the P-T conditions transitional between the greenschist and amphibolite facies [*Maruyama et al.*, 1983].

It should be emphasized that three metamorphic zones as defined above may vary in their depth (temperature) ranges due to a difference in original bulk rock compositions (e.g., pelitic versus psammitic; see below for further discussion). Mineral assemblages and petrographic details of the chlorite-calcite and biotite zones are generally consistent with those described by *McDowell and Elders* [1980]. They have established four prograde metamorphic zones in metasandstones of the Elmore 1 well in the Salton Sea geothermal field: (1) the dolomite-ankerite zone at depths < 439 m (or < ap190°C), characterized by dolomite-ankerite + calcite + mixed layer illite-smectite + hematite ± quartz ± titanite; (2) the chlorite-calcite zone at depths between 439 and 1135 m (190°-325°C), in which chlorite + illite-smectite or phengite + epidote + calcite + albite + K-feldspar + quartz + titanite + pyrite occur; (3) the biotite zone at depths from 1135 to 2120 m 325°-360°C), in which biotite + quartz + epidote + K-feldspar + albite + talc + pyrite +

TABLE 1. Mineral Compositions and Abbreviations Used in This Study

Mineral	End-Member Formula	Abbreviation
Actinolite		Act
Tremolite	$Ca_2Mg_5Si_8O_{22}(OH)_2$	Tr
Ferroactinolite	$Ca_2Fe_5Si_8O_{22}(OH)_2$	Ft
Anhydrite	$CaSO_4$	Anh
Biotite	$KMg_3Si_3AlO_{10}(OH)_2$	Bt
Calcite	$CaCO_3$	Cc
Chlorite	$Mg_5Al_2Si_3O_{10}(OH)_8$	Chl
Clinopyroxene		Cpx
Diopside	$CaMgSi_2O_6$	Di
Hedenbergite	$CaFeSi_2O_6$	Hd
Dolomite	$CaMg(CO)_3$	Dol
Epidote	$Ca_2Al_3Si_3O_{12}(OH)$	Ep
Hematite	Fe_2O_3	Hm
Hornblende	$Ca_2Mg_4AlSi_7AlO_{22}(OH)_2$	Hb
K-feldspar	$KAlSi_3O_8$	Ksp
Plagioclase		Pl
Albite	$NaAlSi_3O_8$	Ab
Anorthite	$CaAl_2Si_2O_8$	An
Prehnite	$Ca_2Al_2Si_3O_{10}(OH)_2$	Pr
Quartz	SiO_2	Qtz
Rutile	TiO_2	Rt
Titanite	$CaTiSiO_5$	Ttn
Wairakite	$CaAl_2Si_4O_{12}\cdot 2H_2O$	Wk

titanite ± actinolite occur with traces of phengite, chlorite, and vermiculite; and (4) the garnet zone at depths greater than 2155 m (>360°C), in which andradite garnet occurs with biotite, quartz, epidote, albite, actinolite, pyrite, and trace titanite. Shallow-depth (<470 m) samples of the State 2-14 well, possibly belonging to the dolomite-ankerite zone, were not investigated in the present study. The garnet zone assemblage was not observed near the base of the State 2-14 borehole.

Epidote first occurs at a depth of 906 m and is present in all of the analyzed samples from depths >906 m except a few calcite-rich ones (e.g., sample 7713.1 of Table 2). Other common phases include quartz, albite, and pyrite. K-feldspar, phyllosilicates (Mus, Chl, and Bt), and chain silicates (Act and Cpx) are usually minor in their occurrences and modal abundances. Calcite is commonly observed at shallow depths whereas anhydrite is locally abundant in both chlorite-calcite and biotite zones. Rutile or anatase is observed in both shallow (550 - 1427 m) and deep (2745 - 3020 m) samples. Aluminous titanite commonly occurs at depths below 940 m. A few samples contain both rutile and titanite (Table 2). Minor amounts of various sulfide and oxide phases are often associated with pyrite in both matrix and fracture [*McKibben and Elders*, 1985; *Andes and McKibben*, 1987; *Caruso et al.*, this issue]. It should be noted that Ca-zeolites (particularly wairakite) and prehnite were not found in the State 2-14 well samples (see below for further discussion).

MINERAL CHEMISTRY

Analytical Methods

Mineral compositions were determined using an automated JEOL 733A microprobe with a beam size of 3 - 10 μm, 15 kV accelerating voltage, and 15-nA beam current. Both natural and synthetic phases were used as standards: albite (for Na, Al, Si); orthoclase (K); diopside (Ca, Mg); kaersutite (Fe, Ti); spessartine (Mn); and chromite (Cr). The *Bence and Albee* [1968] method was employed for matrix corrections. At least several grains of each mineral were analyzed in order to confirm the chemical homogeneity. Moreover, backscattered electron (BSE) microscopy was often used to detect any compositional zoning and fine-grained intergrowth. Representative point analyses of epidote, white mica, chlorite, biotite, clinopyroxene, and amphibole are presented in Tables 3 - 8. The ferric iron contents in amphiboles and clinopyroxenes were calculated using the computer program by *Papike et al.* [1974]. The compositions of amphiboles in Table 8 list the medium values between the possible maximum and minimum Fe^{3+} contents. The Fe^* used in the text refers to total Fe.

Epidote

Prismatic epidotes smaller than 50 μm in length first appear at a depth of 906 m, closely associated with albite, K-feldspar, chlorite, and calcite (+ quartz). With increasing

TABLE 2. Summary of Metamorphic Phases Observed in Representative Samples

Sample No.[a]	Sample Depth, m	Ksp[b]	Mus	Chl	Bt	Act	Cpx	Cc	Anh	Rt	Ttn
					Chlorite-Calcite Zone						
1553.3	473.4	x	x					x		x	
1996.2	608.4	x	x	x				x		x	
2450.7	746.9	x	x	x				x			x
2971.1	905.5	x		x				x		x	
3083	939.7	x	x	x						x	x
4015.5	1223.9		x	x				x			x
4053.5	1235.4	x	x	x				x	x		
6507.4	1983.4	95-96	x	x				x			x
6762.8	2061.2	95-97		x							x
7549.5	2301.0	95-96	x	x				x			
7713.1	2350.8		x	x				x	x		
					Biotite Zone						
8146.6	2483.0				x	x					
8148.5	2483.5	93-95					x				
8153.5	2485.1			x					x		x
9007	2745.2	94-97		x	x				x		
9097A	2772.6			x	x					x	
9696	2955.2			x	x				x	x	
9698B	2955.8			x	x					x	
					Clinopyroxene Zone						
9907	3019.5					x	x			x	
10160	3096.6					x	x				x
10230	3118.0				x	x	x				x

a. All samples are with excess quartz, albite, and epidote, except 1553.3, 1996.2, 2450.7, and 7713.1, which contain no epidote. Oligoclases are also observed in some samples of three metamorphic zones (see Figure 9 for details). Sample numbers correspond to the depths of core samples in feet.

b. The contents of $KAlSi_3O_8$ component in K-feldspar are listed in mole percent.

TABLE 3. Representative Analyses of Epidote

Sample No.	2971.1	6507.4	6762.8	9007	9097A	9698B	9907B	10160	10160	10230
SiO_2	36.72	38.50	37.95	37.04	37.05	38.11	37.66	37.10	37.91	38.09
TiO_2	0.12	0.27	0.07	n.d.[a]	n.d.	0.09	n.d.	0.01	0.06	0.06
Al_2O_3	19.38	23.05	23.75	21.03	17.83	24.86	20.91	20.13	25.40	27.97
Fe_2O_3[b]	17.44	13.61	12.50	16.04	19.97	11.68	16.70	17.29	10.16	7.28
MnO	0.49	0.07	0.21	0.06	0.02	0.03	0.06	0.02	0.62	0.21
MgO	0.03	0.05	0.04	n.d.	0.04	0.06	0.03	n.d.	0.02	0.02
CaO	22.13	23.60	23.22	22.87	22.99	23.04	23.06	22.68	23.03	23.56
Total	96.31	99.15	97.73	97.04	97.91	97.87	98.42	97.23	97.20	97.19
					Cations per 12.5 Oxygens					
Si	3.025	3.027	3.017	3.008	3.029	3.009	3.019	3.018	3.008	2.987
Ti	0.007	0.016	0.004	0.000	0.000	0.005	0.000	0.001	0.003	0.004
Al	1.881	2.137	2.226	2.013	1.718	2.314	1.975	1.930	2.376	2.586
Fe^{3+}	1.081	0.805	0.748	0.981	1.229	0.694	1.008	1.059	0.606	0.429
Mn	0.034	0.005	0.014	0.004	0.002	0.002	0.004	0.001	0.041	0.014
Mg	0.003	0.006	0.004	0.000	0.005	0.007	0.003	0.000	0.003	0.002
Ca	1.953	1.988	1.978	1.990	2.014	1.950	1.980	1.977	1.958	1.979
Sum	7.984	7.984	7.991	7.996	7.997	7.981	7.989	7.986	7.995	7.991
X_{Fe3}	0.365	0.274	0.252	0.325	0.417	0.231	0.338	0.354	0.203	0.143

a. Not detected.

b. Total Fe as Fe_2O_3.

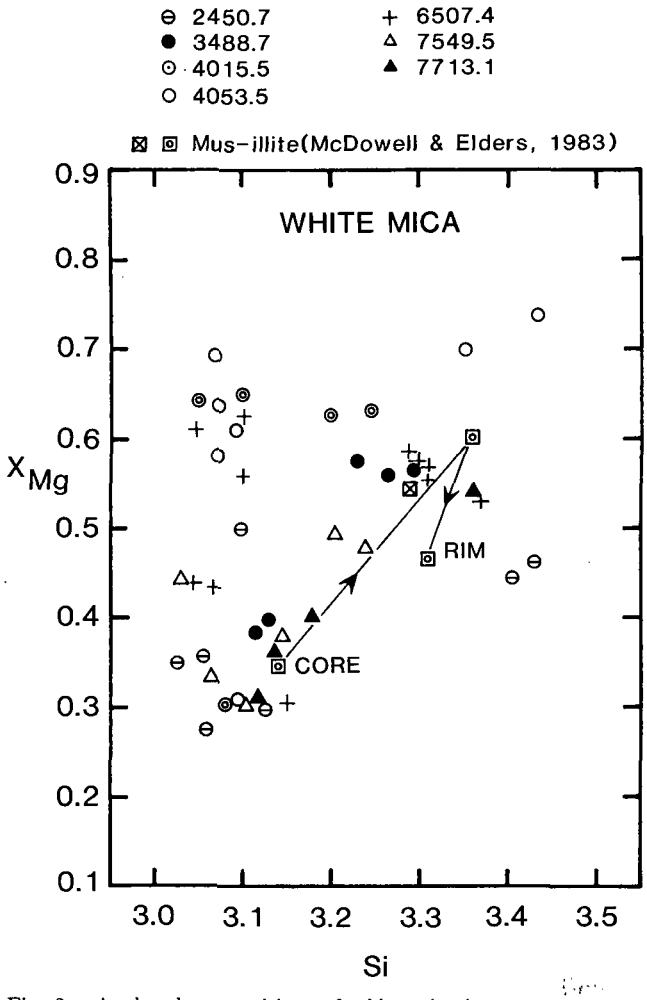

Fig. 2. Analyzed compositions of white mica in terms of moles Si per 11 anhydrous oxygen and the mole fraction of Mg (X_{Mg} = Mg/(Mg + Fe*)). Core, middle, and rim compositions of one relict muscovite grain analyzed by *McDowell and Elders* [1983] are connected by arrows. A typical composition of their authigenic white mica is also shown. White micas with Si > 3.3 are presumably authigenic.

depth, epidote becomes coarser in grain size and more abundant, filling the pores and/or replacing allogenic phases such as calcic plagioclase, and also occurs commonly in veinlets. Epidote exhibits a wide compositional variation with the mole fraction of $Ca_2Fe_3Si_3O_{12}(OH)$ (X_{Fe} = Fe*/(Fe* + Al)) ranging from 0.11 to 0.42 (Table 3). Epidote grains are commonly zoned either with a complex pattern or with Fe-rich rim and Al-rich core or vice versa. The first epidote occurring at 906 m is the most Fe-rich (X_{Fe} = 0.36 - 0.39; Table 3). With increasing depth in the chlorite-calcite zone, the average X_{Fe} value generally decreases to ~0.25, with local minima at 1220 and 2480 m. However, it increases abruptly from ~0.25 to ~0.33 in the lower-grade biotite zone (2480 - 2600 m). The average X_{Fe} value decreases gradually to the bottom of the borehole in both biotite and clinopyroxene zones. Further details on compositional, structural, and isotopic properties of geothermal epidotes from the State 2-14 well are described by *Bird et al.* [this issue] and *Caruso et al.* [this issue].

White Mica

Thin flakes of detrital and authigenic white mica are rarely observed in the chlorite-calcite zone metasandstones but occur as an ubiquitous minor phase in the associated metapelites. The analyzed compositions of white mica from several metasandstones are widely variable as shown in Figure 2 and Table 4. This variation is primarily due to partial preservation of the composition from allogenic muscovite. Thus a chemical distinction between allogenic and authigenic white micas is often difficult, although allogenic mica is usually high in TiO_2 content (Table 4 [*McDowell and Elders*, 1983]). Significant compositional variations of white mica have been commonly described in subgreenschist facies metaclastics; this has been attributed to the preservation of relict muscovites during subsequent recrystallization [e.g., *Frey*, 1987].

The (Mg,Fe)$SiAl_{-2}$ or Tschermakitic substitution is one of the most important exchange variables in muscovite solid solution. The X_{Mg} (= Mg/(Mg+Fe*)) values and the number of Si atoms per 11 anhydrous oxygen formula for analyzed white micas are shown in Figure 2 for each sample. The Si content, which is the preferred measure of the extent of Tschermakitic substitution [*Miyashiro and Shido*, 1985; *Pattison*, 1987], varies from 3.03 to 3.43. Moreover, one detrital muscovite with Si = 3.05 - 3.15 in a very fine-grained metasandstone sample 6507.4, is rimmed by illitic or phengitic white mica with Si contents of 3.3 - 3.4. A similar compositional variation has been documented by *McDowell and Elders* [1983], as illustrated by the arrows in Figure 2. Thus we presume in our subsequent discussion on phase equilibria that phengitic muscovites with Si contents between 3.30 and 3.43 are close to the equilibrium composition in the chlorite-calcite zone assemblages.

Chlorite

Chlorite is one of the most common phyllosilicates in metasandstones and metapelites of both chlorite-calcite and biotite zones. It occurs typically as a pore-filling phase and less commonly as a Ti-rich allogenic phase (Table 5). Most of the chlorites contain minor amounts of MnO ranging up to about 1.5 wt % (Table 5). Analyzed compositions of chlorites from metasandstones in the State 2-14 and Elmore 1 (*McDowell and Elders*, 1980) drill holes from the Salton Sea geothermal system are shown in Figure 3. Two analytical electron microscope (AEM) analyses of chlorite from metapelites of the Elmore 1 well [*Yau*, 1986] are also shown. These chlorites, distinctively high in Si content, plot within the diabantite compositional field. Chlorite compositions of the chlorite-calcite zone in the State 2-14 well show a wide variation in Fe content, compared to those described in the previous work. Chlorites of the biotite zone exhibit a bimodal distribution in Fe content (Figure 3). On the other hand, all of the analyzed chlorites show relatively constant Si content, ranging mostly from 2.8 to 3.1 on the basis of 14 anhydrous oxygens, and most are of pycnochlorite composition. No systematic variations in Si content, or Tschermakite component, are observed with increasing grade; this relationship is probably due to the high-variance nature of the

TABLE 4. Representative Analyses of White Mica

Sample No.	1996.2	2450.7	2450.7	2450.7	4053.5	4053.5	4053.5	6507.4
Type [a]	D	D	A	A (?)	D	A	I	A
SiO_2	44.86	46.03	49.67	45.11	45.69	49.38	45.93	48.96
TiO_2	0.97	1.23	0.05	0.03	0.91	0.27	n.d. [b]	0.21
Al_2O_3	29.38	34.15	27.32	35.32	34.28	28.14	35.60	26.76
FeO [c]	5.07	1.38	3.95	2.07	0.96	2.19	1.49	4.11
MnO	0.09	0.03	0.02	n.d.	n.d.	n.d.	n.d.	n.d.
MgO	1.43	0.77	1.78	0.64	0.84	2.87	0.37	2.61
CaO	0.03	0.14	0.03	0.04	0.04	0.02	0.19	0.06
Na_2O	0.26	0.39	0.10	0.80	0.49	0.34	1.68	0.09
K_2O	10.94	9.94	10.36	9.65	10.36	10.46	7.59	10.87
Total	93.02	94.05	93.28	93.68	93.59	93.66	92.85	93.66
				Cations per 11 Oxygens				
Si	3.146	3.097	3.405	3.056	3.092	3.352	3.095	3.367
Ti	0.051	0.062	0.003	0.002	0.046	0.014	0.000	0.011
Al	2.429	2.708	2.207	2.820	2.734	2.252	2.827	2.169
Fe^{2+}	0.297	0.077	0.227	0.117	0.055	0.124	0.084	0.236
Mn	0.005	0.002	0.001	0.000	0.000	0.000	0.000	0.000
Mg	0.150	0.077	0.182	0.065	0.085	0.290	0.037	0.267
Ca	0.002	0.010	0.002	0.003	0.003	0.001	0.014	0.004
Na	0.036	0.051	0.014	0.105	0.065	0.045	0.219	0.012
K	0.979	0.853	0.906	0.834	0.894	0.906	0.653	0.954
Sum	7.095	6.937	6.947	7.002	6.974	6.984	6.929	7.020
X_{Fe^*}	0.665	0.501	0.555	0.645	0.391	0.300	0.692	0.469

a. D, detrital muscovite; A, authigenic white mica; I, illitic white mica formed as aggregates of thin flakes.

b. Not detected.

c. Total Fe as FeO.

chlorite-bearing mineral assemblages. Thus no correlation between tetrahedral Al and metamorphic grade is apparent. This conclusion is in contrast to the linear increase of Al^{IV} content with increasing temperature suggested by *Cathelineau and Nieva* [1985] for chlorites occurring at 130°-300°C in altered andesites of the Los Azufres geothermal system, Mexico.

The mole fraction of total iron ($X_{Fe} = Fe^*/(Fe^*+Mg)$) for analyzed phyllosilicates is plotted in Figure 4 as a function of depth. Chlorites have X_{Fe} values greater than those of the coexisting phengitic white micas. Chlorites at shallow depths of 608 and 747 m show significant variations in both X_{Fe} values (0.39-0.59) and Si contents (2.86-3.01), but their variations in each sample become restricted at depth. With increasing grade in the chlorite-calcite zone the X_{Fe} values of chlorites generally decrease from about 0.53 to 0.31. The Mg-enrichment trend with increasing temperature is consistent with the result of *McDowell and Elders* [1980]. Biotite zone chlorites have very restricted X_{Fe} values for each sample and show bimodal compositions with no distinct trend. Thus they may reflect the difference in bulk rock or fluid composition rather than in temperature.

Biotite

Authigenic biotites, pleochroic from pale green to colorless, first appear in the matrix of sample 8146.6 where they are closely associated with actinolite (+ Ep + Ab + Qtz). With increasing depth, tabular biotites or aggregates of fine-grained biotites are more commonly observed in both sandstone matrices and veins together with chlorite, anhydrite, and/or K-feldspar (+ Ep + Ab + Qtz). Minor amounts of detrital biotite are found throughout the analyzed samples; they are highly pleochroic from dark green to brown, and some are partially altered to authigenic chlorite.

Most of the analyzed authigenic biotites in the biotite zone show compositions with low totals (90-92 wt %) probably due to their intergrowth with minor chlorite and/or white mica. Biotite also showed significant vacancies in the interlayer crystallographic site which generally range between 0.16 and 0.13 (Table 6). This result is in contrast to the systematic decrease in interlayer site vacancy from 0.35 at 330°C to 0.15 at 360°C reported in the Elmore 1 well by *McDowell and Elders* [1980].

Compositions of biotites are plotted on the Al - Fe - Mg diagram of Figure 5. Compositional fields of biotites from the biotite and garnet zone metasandstones as well as detrital biotites analyzed by *McDowell and Elders* [1983] from the Elmore 1 drill hole are shown for comparison. Two AEM analyses of authigenic biotites from the IID 2 well are from *Yau* [1986]. As pointed out by *McDowell and Elders* [1983], detrital biotites from the Salton Sea geothermal sys-

TABLE 5. Representative Analyses of Chlorite

Sample No.	1996.2	1996.2	2971.1	3083	4053.5	4053.5 [a]	6507.4	8153.5	9007	9698B
SiO_2	26.08	27.12	25.32	25.24	27.13	28.05	28.77	29.10	27.57	27.91
TiO_2	0.04	0.03	0.02	n.d. [b]	0.03	1.65	0.10	0.18	n.d.	0.14
Al_2O_3	19.18	18.56	18.25	16.93	19.22	19.58	19.38	20.03	18.09	18.25
FeO [c]	28.09	22.38	30.24	26.33	23.19	20.08	19.32	16.37	22.18	12.49
MnO	0.52	0.51	0.86	1.29	0.40	0.14	0.50	0.27	0.58	0.17
MgO	11.66	16.98	11.29	13.10	16.80	16.78	18.26	20.51	17.76	22.40
CaO	0.08	0.06	0.08	0.06	0.11	0.37	0.15	0.08	0.09	0.13
Na_2O	0.06	n.d.	n.d.	0.22	n.d.	0.05	n.d.	n.d.	0.05	n.d.
K_2O	0.03	0.03	n.d.	n.d.	n.d.	0.10	0.28	0.16	n.d.	0.04
Total	85.74	85.67	86.05	83.17	86.89	86.79	86.76	86.71	86.32	81.53
					Cations per 14 Oxygens					
Si	2.861	2.884	2.816	2.865	2.852	2.895	2.959	2.940	2.906	2.950
Ti	0.003	0.003	0.001	0.000	0.002	0.128	0.008	0.014	0.000	0.011
Al	2.480	2.326	2.393	2.265	2.381	2.382	2.350	2.386	2.248	2.274
Fe^{2+}	2.577	1.991	2.813	2.500	2.038	1.733	1.662	1.383	1.956	1.104
Mn	0.048	0.046	0.081	0.124	0.036	0.013	0.043	0.023	0.052	0.015
Mg	1.907	2.691	1.871	2.216	2.633	2.582	2.800	3.088	2.791	3.530
Ca	0.010	0.007	0.009	0.007	0.013	0.041	0.016	0.009	0.010	0.014
Na	0.013	0.000	0.000	0.048	0.000	0.010	0.000	0.000	0.010	0.000
K	0.004	0.004	0.000	0.000	0.000	0.013	0.037	0.021	0.000	0.005
Sum	9.903	9.952	9.984	10.025	9.955	9.797	9.875	9.864	9.973	9.903
X_{Fe^*}	0.575	0.425	0.601	0.530	0.436	0.402	0.373	0.309	0.412	0.250

a. Detrital chlorite.

b. Not detected.

c. Total Fe as FeO.

tem are characterized by high Al and Ti contents (Table 6). Authigenic biotites analyzed in the present study, however, are more aluminous than those described in *McDowell and Elders*. Furthermore, the Mg contents of biotite do not show any systematic trend with metamorphic grade (Figure 4). Such a relationship is in contrast to the Fe enrichment of biotite with increasing grade reported by *McDowell and Elders* [1983] (Figure 5). The effect of bulk composition, as stated in the previous sections, must be an important factor in determining equilibrium compositions of phyllosilicates. A similar conclusion has been reached from studies of low-grade metapelites (see a review by *Guidotti* [1984]).

Amphibole and Clinopyroxene

Euhedral to subhedral calcic amphiboles and/or salite-diopside (± epidote and quartz) are commonly observed filling the pores in the biotite and clinopyroxene zones. Clinopyroxenes also occur as fine-crystalline masses or aggregates. Mn-bearing clinopyroxene in the lower biotite zone (sample 8148.5) contains up to 2.6 wt % MnO, in contrast to clinopyroxene zone salites with less than 0.45 wt % MnO (Table 7). It is thus inferred that Mn substitution in clinopyroxene enlarges its stability field toward lower temperatures.

The analyzed compositions of calcic amphiboles and clinopyroxene are plotted in the Ca - Mg - Fe diagram of Figure 6. The Ca contents of the analyzed chain silicates are more or less constant, except for those in one sample 9907, which show a variation from that of actinolite to Mg-salite. Such intermediate compositions may represent either mixed analyses of actinolite and clinopyroxene or Ca-pyriboles with variable proportions of single and multiple chains. Back-scattered electron photomicrographs did not reveal any compositional heterogeneity, and further transmission electron microscopy (TEM) study is necessary to solve such a problem. In fact, *Yau et al.* [1986] have recently identified through a TEM study some wide-chain Ca-pyriboles from the IID 2 well of the Salton Sea geothermal field. These phases consist primarily of irregularly alternating (010) slabs of double or triple chains, with rare quadruple and quintuple chains. Average compositions of these Ca-pyriboles from four separate samples near the transition boundary between the chlorite-calcite and biotite zones from *Yau et al.* [1986] are shown in Figure 6.

The Mg/Fe ratios of chain silicates vary widely, and no distinct compositional trend with metamorphic grade is observed. It is, however, apparent that calcic amphiboles extend to more Fe-rich compositions than clinopyroxenes (Figure 6). Most of the calcic amphiboles are actinolite (Table 8) and do not show a significant chemical heterogeneity under the BSE microscope. However, amphiboles near the bottom of the well in the clinopyroxene zone exhibit complicated zonal patterns such as patchy or lamellar intergrowths (Figures 7*a* and *b*). In sample 10230, amphiboles range from

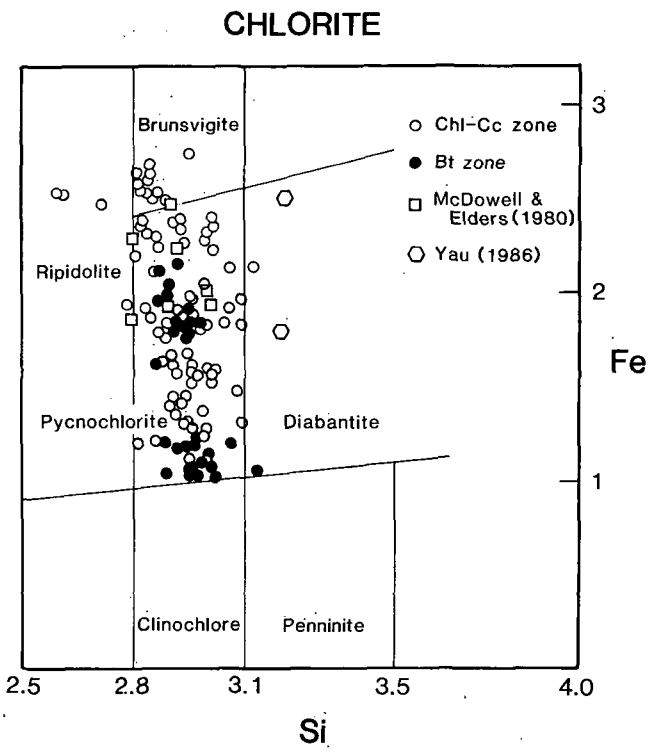

Fig. 3. Compositions of chlorites from both chlorite-calcite and biotite zones of the State 2-14 drill hole, together with those reported by *McDowell and Elders* [1983] and *Yau* [1986] from the Salton Sea geothermal system, are shown in the diagram of *Hey* [1954]. Lower-grade chlorites tend to vary significantly in composition, whereas those of the biotite zone cluster into two distinct compositional fields. Most of the analyzed chlorites of both metamorphic zones, however, belong to the pycnochlorite composition.

actinolite, through ferroactinolite and ferro-actinolitic hornblende, to ferro-hornblende (Table 8), following the nomenclature of *Leake* [1978]. These compositional zonings were optically indistinguishable but can be observed by BSE technique. Two types of calcic amphiboles, actinolite, and ferro-actinolitic hornblende, commonly coexist on a scale less than 10 μm. The boundaries between these intergrown amphiboles are sharp, indicating a compositional discontinuity or gap such as in Al contents (see Table 8 for compositions of the coexisting amphiboles).

The X_{Fe} values and Al_2O_3 wt % of calcic amphiboles for each sample are plotted in Figure 8. The Al_2O_3 content is less than 3 wt % in the biotite zone and increases up to 6 wt % in the clinopyroxene zone. Moreover, two types of amphiboles, as shown in Figures 7*a* and *b*, occur in the deep core samples of the clinopyroxene zone. Their compositions are connected by tie lines (Figure 8). Note that mixed analyses of two amphiboles may fill the apparent compositional gap. In general, it is evident that Fe content increases with increasing Al in calcic amphibole, as previously known in both metamorphic and hydrothermal environments [e.g., *Tagiri*, 1977; *Robinson et al.*, 1982; *Kimball et al.*, 1985; *Bird et al.*, 1986]. Similarly, submicron-scale intergrowth of actinolite and hornblende has been recently described in the Nesjavellir hydrothermal system of Iceland [*Hreggvidsdottir and Bird*, 1987].

Coexistence of actinolite and hornblende has been documented in many metabasites transitional between the greenschist and amphibolite facies [e.g., *Maruyama et al.*, 1983]. *Graham and Navrotsky* [1986] have recently attributed the association of actinolite and hornblende to metastable equilibrium, whereas *Oba and Yagi* [1987] experimentally reversed the compositional gap between actinolite and pargasite. Apparently, further studies are still needed to understand fully the compositional gap for calcic amphibole. In particular, a systematic study employing the BSE technique may provide important textural and compositional information on a submicron-size scale, which cannot be obtained by conventional microprobe technique.

Plagioclase

Albitic plagioclase is one of the most common minerals in the analyzed metasandstones. It replaces detrital calcic plagioclase and fills the pore space together with other

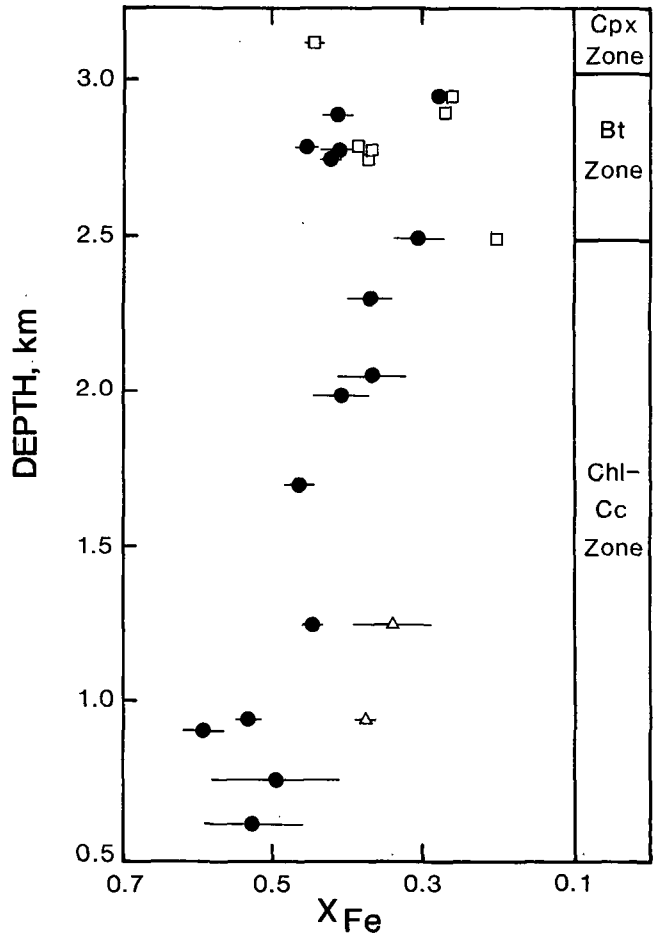

Fig. 4. The X_{Fe} (= $Fe^*/(Fe^* + Mg)$) values of phengitic white mica (triangles), chlorite (circles), and biotite (squares) plotted against depth. Error bars indicate one sigma of each analysis. The range of 1σ in most biotites is smaller than that represented by the size of the symbol. It is apparent that chlorite becomes enriched in Mg with increasing depth in the chlorite-calcite zone.

TABLE 6. Representative Analyses of Biotite

Sample No.	8146.6	9007	9097A	9698B	10230	10230 [a]
SiO_2	42.06	39.15	38.15	39.61	40.06	38.40
TiO_2	0.77	0.23	0.29	0.40	0.75	0.75
Al_2O_3	11.18	12.34	11.78	12.47	13.05	18.59
FeO [b]	8.78	16.18	15.65	11.97	19.44	11.13
MnO	0.11	0.09	0.14	0.08	0.11	0.23
MgO	19.22	15.05	15.24	18.32	13.33	16.32
CaO	0.63 [c]	0.06	0.09	0.07	0.07	0.08
Na_2O	0.11	0.11	0.07	0.03	0.05	0.33
K_2O	8.17	8.69	8.60	8.62	8.94	9.52
Total	91.02	91.91	90.01	91.57	95.81	95.35
			Cations per 11 Oxygens			
Si	3.145	3.028	3.016	3.007	3.010	2.795
Ti	0.043	0.013	0.017	0.023	0.042	0.041
Al	0.985	1.125	1.097	1.116	1.156	1.595
Fe^{2+}	0.549	1.046	1.035	0.760	1.222	0.677
Mn	0.007	0.006	0.009	0.005	0.007	0.014
Mg	2.142	1.735	1.796	2.074	1.493	1.771
Ca	0.050	0.005	0.008	0.005	0.005	0.007
Na	0.016	0.017	0.010	0.005	0.007	0.047
K	0.779	0.857	0.868	0.835	0.857	0.884
Sum	7.716	7.832	7.856	7.830	7.799	7.831
X_{Fe*}	0.204	0.376	0.366	0.262	0.450	0.277

a. Detrital biotite.

b. Total Fe as FeO.

c. High calcium content probably due to the actinolite component in the Bt+Act mixture.

metamorphic phases. It is fine- to medium-grained in size, anhedral to subhedral in form, and usually cloudy due to many inclusions.

The values of X_{An} (=Ca/(Ca+Na+K)) in all the analyzed plagioclases are shown in Figure 9 with increasing depth. In the clinopyroxene zone, plagioclase is primarily of oligoclase composition and occurs together with albite showing no apparent compositional discontinuity. Most of the lower-grade plagioclases are albitic with X_{An} value less than 0.04, but several exceptions are noted at various depths as shown in

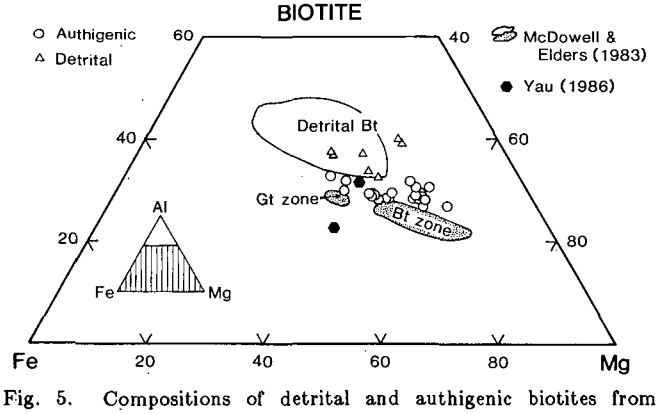

Fig. 5. Compositions of detrital and authigenic biotites from present and previous studies, plotted in an Al-total Fe-Mg diagram (see inset). Open symbols denote analysis from the State 2-14 drill hole. Two AEM analyses of biotite from the IID 2 well [*Yau*, 1986] show a significant variation in Al contents, although the estimated temperatures for the formation of each biotite are 310° and 330° C, respectively. The compositional fields of biotites from biotite (Bt) and garnet (Gt) zones (stippled) together with those of detrital biotites are from *McDowell and Elders* [1983].

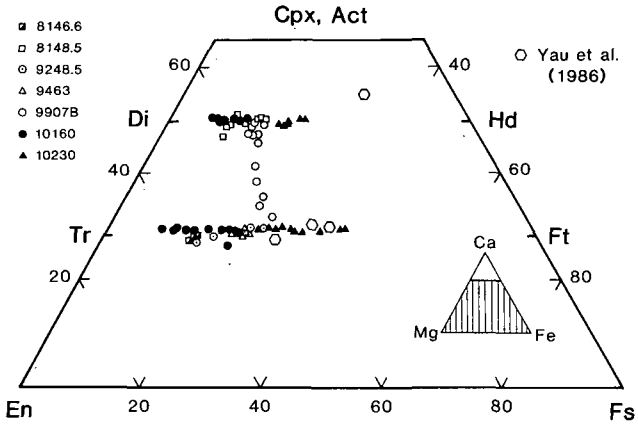

Fig. 6. Ca-Mg-Fe plot of the analyzed compositions of calcic amphiboles and clinopyroxenes. The chemical compositions of one clinopyroxene and three amphiboles intergrown with wider-chain pyriboles are analyzed using AEM by *Yau* et al. [1986]. See Table 1 for abbreviations.

TABLE 7. Representative Analyses of Clinopyroxene

Sample No.	8148.5	9907	10160	10160	10230	10230	10230
SiO_2	53.45	53.28	54.36	54.22	53.54	53.08	53.11
TiO_2	0.03	0.03	0.02	0.05	n.d. [a]	0.02	0.05
Al_2O_3	0.71	0.29	0.24	0.28	0.18	0.17	0.25
Fe_2O_3 [b]	n.r. [c]	0.08	0.43	n.r.	n.r.	n.r.	n.r.
FeO [b]	8.73	9.86	4.94	6.11	9.61	13.77	13.62
MnO	1.15	0.25	0.09	0.11	0.17	0.35	0.44
MgO	11.75	12.05	14.69	14.26	12.23	9.62	9.34
CaO	23.30	23.96	24.50	24.53	24.74	24.07	23.98
Na_2O	0.15	0.23	0.33	0.20	0.08	0.10	0.08
Total	99.27	100.03	99.60	99.76	100.55	101.18	100.87
			Cations per 6 Oxygens				
Si	2.016	2.004	2.009	2.009	2.003	2.009	2.014
Al^{VI}	0.032	0.013	0.010	0.012	0.008	0.008	0.011
Ti	0.001	0.001	0.001	0.001	0.000	0.001	0.001
Fe^{3+}	0.000	0.002	0.012	0.000	0.000	0.000	0.000
Fe^{2+}	0.275	0.309	0.153	0.189	0.301	0.436	0.432
Mn	0.037	0.008	0.003	0.003	0.005	0.011	0.014
Mg	0.660	0.675	0.809	0.787	0.682	0.543	0.528
Ca	0.942	0.966	0.970	0.974	0.992	0.976	0.975
Na	0.011	0.017	0.024	0.014	0.006	0.007	0.006
Sum	3.982	3.996	3.967	3.991	3.996	3.990	3.981
X_{Fe*}	0.18	0.31	0.16	0.19	0.31	0.45	0.45

a. Not detected.

b. Fe^{3+}/Fe^{2+} ratio was calculated using the computer program by *Papike et al.* [1974].

c. Ferric iron is not required by the above calculation.

Figure 9. These compositions may represent the peristerite solvus or transitional gap [*Goldsmith*, 1982; *Maruyama et al.*, 1982; *Ishizuka*, 1985]. However, it is often difficult to distinguish between primary and metamorphic Ca-plagioclase due to the persistence of detrital grains.

The most important clue for this problem was obtained from the BSE study of textural and compositional relations of plagioclase grains. Two examples are shown in Figures 7*c* and *d*:

1. Figure 7*c* of sample 9007 from the biotite zone illustrates that detrital calcic plagioclases ($Ab_{60.4}An_{37.0}Or_{2.6}$ or $Ab_{79.9}An_{19.2}Or_{0.9}$) ± K-feldspar ($Ab_{4.2}An_{0.1}Or_{95.7}$) are rimmed by metamorphic albite ($Ab_{97.6}An_{1.8}Or_{0.6}$ or $Ab_{96.7}An_{2.8}Or_{0.5}$). Such zoned plagioclase grains consistently showed the albite-rich rim with calcic core. The latter calcic cores exhibit a wide compositional range and yield various combinations of the coexisting pair compositions (e.g., An_{14} - An_2; An_{20-21} - An_{1-2}; An_{25} - An_{2-3}; An_{39} - An_3). Moreover, no discrete grains of calcic plagioclase without albitic rim were found. Thus these calcic plagioclase cores are interpreted to be remnants of detrital plagioclase even in the biotite zone samples.

2. At a shallow depth of 1235 m, both albite ($Ab_{94.7}An_{4.1}Or_{1.2}$) and oligoclase ($Ab_{82.7}An_{16.3}Or_{1.0}$) occur together with Ksp + Cc + Ttn + Qtz (+ Ep + Anh) (Figure 7*d*). Some calcic plagioclases are fine grained in size, commonly less than 10 μm in maximum dimension. They may yield mixed analyses. Albite either occurs as separate grains or is in a sharp contact with rimming oligoclase. Thus these two phases are stable together and may represent the peristerite compositional gap.

The observations described above suggest that peristerite occurs even in low-grade samples of the chlorite-calcite zone. *Donaghe and Peacor* [1987] also described the coexisting albite and calcic plagioclase (to An_{38}) at a depth of 1582 m in the State 2-14 well. The general T - X_{An} shape of the peristerite gap, defined by either solvus [*Maruyama et al.*, 1982] or transitional loop [*Ishizuka*, 1985], cannot be determined due to analyses of fine-grained mixtures and persistence of primary compositions, as evidenced in Figure 7*c*. However, the consolute temperature of the possible peristerite solvus (Figure 9) is determined to be close to 350°C, which approximates the temperature for the beginning of the clinopyroxene zone (Figure 9). This temperature is significantly lower than those at higher pressures such as ~420°C at 2 kbar and ~500°C at 5 kbar (see later section for discussion). These results are apparently different from those described by *McDowell* [1986], who rarely observed authigenic plagioclase with an oligoclase composition in the Salton Sea geothermal system.

Titanite

Titanites occur commonly as aggregates of fine granules in samples at depths greater than 750 m. Their compositions

TABLE 8. Representative Analyses of Amphibole

Sample No.	8146.6	9248.5	10160	10160	10160	10160	10230	10230	10230	10230	10230
SiO_2	55.40	52.22	55.18	55.19	54.91	53.04	53.72	51.09	49.47	49.82	47.06
TiO_2	0.03	0.15	0.02	0.04	0.08	0.13	0.05	0.07	0.15	0.13	0.14
Al_2O_3	0.74	2.62	1.34	2.30	3.11	3.85	1.22	2.39	4.12	4.75	6.07
Cr_2O_3	n.a. [a]	n.a.	n.a.	n.a.	n.a.	n.a.	n.a.	0.05	0.05	n.a.	0.07
Fe_2O_3 [b]	n.r. [c]	n.r.	n.r.	n.r.	n.r.	n.r.	n.r.	1.29	1.83	1.38	1.15
FeO [b]	8.62	13.82	7.47	11.15	10.40	12.05	16.68	14.52	18.42	19.43	20.53
MnO	0.24	0.34	0.09	0.14	0.22	0.09	0.45	0.20	0.22	0.20	0.20
MgO	16.78	13.61	18.47	15.80	16.10	14.81	12.60	12.89	10.00	9.67	8.03
CaO	12.10	12.62	12.97	12.99	12.96	12.56	12.30	12.22	12.15	12.30	12.09
Na_2O	0.10	0.22	0.11	0.23	0.25	0.40	0.29	0.18	0.37	0.40	0.45
K_2O	0.02	0.07	0.03	0.12	0.13	0.18	0.06	0.07	0.19	0.33	0.63
Total	94.03	95.67	95.58	97.96	98.16	97.11	97.37	94.97	96.97	98.41	96.43
					Cations per 23 Oxygens						
Si	8.082	7.738	7.896	7.849	7.770	7.659	7.906	7.687	7.457	7.421	7.238
Al^{IV}	0.000	0.262	0.104	0.151	0.230	0.341	0.094	0.313	0.543	0.579	0.763
Al^{VI}	0.127	0.196	0.123	0.235	0.289	0.315	0.118	0.111	0.190	0.256	0.338
Ti	0.003	0.017	0.002	0.004	0.009	0.014	0.006	0.008	0.017	0.015	0.016
Cr	0.000	0.000	0.000	0.000	0.000	0.000	0.000	0.006	0.006	0.000	0.009
Fe^{3+}	0.000	0.000	0.000	0.000	0.000	0.000	0.000	0.146	0.208	0.155	0.134
Fe^{2+}	1.052	1.713	0.896	1.326	1.231	1.455	2.053	1.827	2.322	2.420	2.641
Mn	0.030	0.043	0.011	0.017	0.026	0.011	0.056	0.026	0.028	0.025	0.026
Mg	3.648	3.006	3.946	3.349	3.396	3.187	2.764	2.890	2.247	2.147	1.841
Ca	1.892	2.004	1.992	1.980	1.965	1.944	1.940	1.970	1.963	1.963	1.992
Na (M4)	0.028	0.000	0.008	0.020	0.035	0.056	0.060	0.016	0.020	0.020	0.004
Na (A)	0.000	0.063	0.023	0.043	0.034	0.056	0.022	0.037	0.088	0.096	0.130
K	0.004	0.013	0.006	0.022	0.024	0.033	0.011	0.050	0.037	0.063	0.124
X_{Fe*}	0.22	0.36	0.18	0.28	0.27	0.31	0.43	0.41	0.53	0.55	0.60

a. Not analyzed.

b. Fe^{3+}/Fe^{2+} ratio was calculated using the method described by *Papike et al.* [1974]. Midpoint between the maximum and minimum Fe^{3+} values is listed.

c. Ferric iron is not required by the above calculation.

are shown in the Al - Ti - Fe ternary diagram of Figure 10. Titanites contain less than 9 mol % Fe, but exhibit a significant substitution of Al (10 - 33 mol %) for Ti. Similar variation in Al contents was observed in the nearby Cerro Prieto geothermal system (Figure 10*a*, [*Schiffman et al.*, 1985]). Note that the maximum Ti content of titanite, defined by Ti-saturation due to the coexisting rutile, is 82 mol % in a chlorite-calcite zone sample 3083. All of the other titanites from the chlorite-calcite zone contain less Ti than this maximum, but those from the clinopyroxene zone contain significantly higher Ti. Thus it is apparent that titanites become less aluminous with increasing temperature, according to the $Al(OH,F)Ti_{-1}O_{-1}$ substitution [e.g., *Evans and Patrick*, 1987]. This trend is consistent with that deduced from the compositional fields of the zeolite and greenschist facies defined by *Kawachi et al.* [1983] (Figure 10*b*).

Other Phases

Other metamorphic minerals include K-feldspar, calcite, anhydrite, rutile or anatase, quartz, and sulfides. Rutile or anatase was observed at depths (1) shallower than 1427 m, and (2) between 2745 and 3020 m. Some of the very fine-grained Ti phases at shallow depths yielded low totals in microprobe analyses and may contain hydroxyl components in the structure such as in anatase. *Yau* [1986] has identified anatase through TEM analyses at temperatures between 115°C and 260°C in IID 2 well, Salton Sea geothermal system.

K-feldspar. K-feldspar occurs commonly as a minor phase in most of the analyzed metasandstones primarily from the chlorite-calcite zone. Both detrital and authigenic orthoclases have been described in the Salton Sea geothermal system [*McDowell*, 1986]. K-feldspar is restricted in its composition with its X_{Or} (= K/(K+Na+Ca)) value ranging from 0.93 to 0.97. No systematic compositional variation was observed with increasing grade.

Calcite. Most of the analyzed calcites are homogeneous, containing the $CaCO_3$ component greater than 95.4 mol % (Figure 11). This value is consistent with the results of *McDowell and Paces* [1985], who analyzed compositions of the coexisting calcite and dolomite-ankerite in the Salton Sea geothermal system. No other carbonates such as dolomite or ankerite were observed in the metasandstones studied.

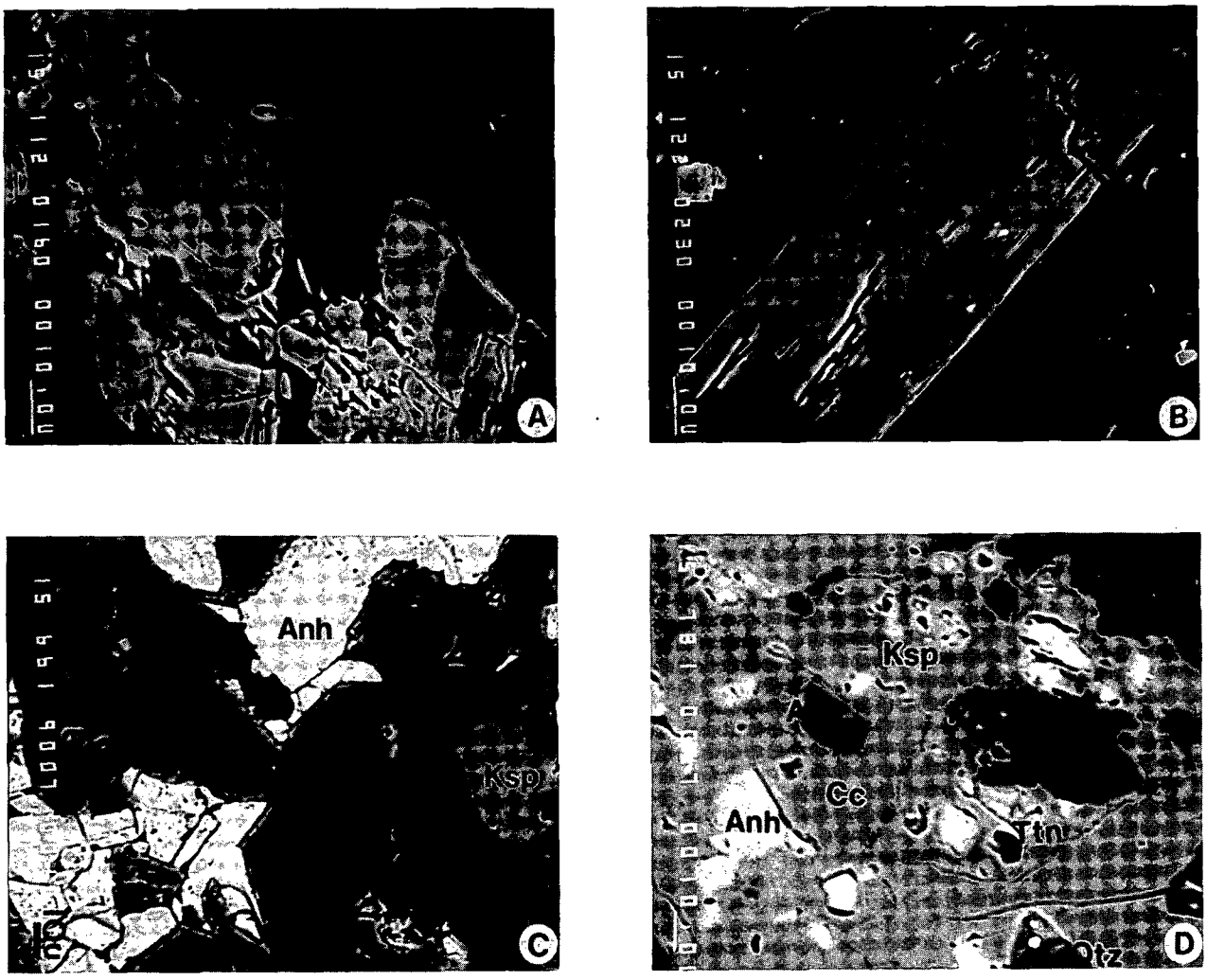

Fig. 7. Backscattered electron (BSE) photomicrographs of calcic amphiboles and plagioclases. Scale bars represent 10 μm. (*a*) Coexisting pairs of Ca-amphiboles in sample 10160. Note the distinct boundaries between low-Al (darker) and high-Al (lighter) actinolites, suggesting an apparent compositional discontinuity in calcic amphibole solid solution. The surrounding phase (dark gray) is albite. (*b*) Complex zonations in a calcic amphibole grain resulting from lamellar intergrowth of actinolite and actinolitic hornblende (sample 10230). (*c*) Remnants of detrital K-feldspar and plagioclase (oligoclase to andesine composition) observed in some cores of the analyzed feldspar grains (sample 9007). Authigenic albites not only armour these detrital grains but also commonly fill pores in the matrix. For abbreviations, see Table 1. (*d*) Plagioclase consisting of the coexisting albite (core) and oligoclase (rim) in sample 4053.5. Associated phases include K-feldspar, titanite, albite, calcite, anhydrite, and quartz. Note that anhydrites (brightest) occur as anhedral fine grains and appear to be replaced by calcite and other authigenic phases.

PHASE EQUILIBRIA

Model System and Graphical Analysis

In order to discuss the prograde phase relations of the three metamorphic zones described in the previous sections, we have adopted a simple model system, Al_2O_3 - K_2O - MgO - CaO - SiO_2 - H_2O - CO_2 (AKFCSH - CO_2). This model system does not take into account minor components such as MnO and further assumes that (1) Na_2O is retained only in albite, and TiO_2 in either rutile or titanite; (2) Al_2O_3 and Fe_2O_3 can be treated as one component; and (3) $MgFe_{-1}$ substitutions do not significantly affect the phase relations in the model system. The latter assumption is advocated because the X_{Mg} values among sheet and chain silicates, in general, vary systematically with each other.

Minerals considered in this study are plotted on an A' (Al_2O_3 + Fe_2O_3 - K_2O - Na_2O) - K (K_2O) - F (FeO + MgO) - C (CaO) tetrahedron of Figure 12*a*, assuming that quartz, albite, and fluid are present in excess. The effect of titanite on the CaO component is ignored because Ti contents in most of the analyzed phases are negligible. The possible ranges of the Tschermakitic substitutions in muscovite, biotite, and chlorite are indicated as heavy lines in Figure 12.

In order to facilitate the visual illustration of phase equilibria, epidote was chosen as a projection point onto the basal

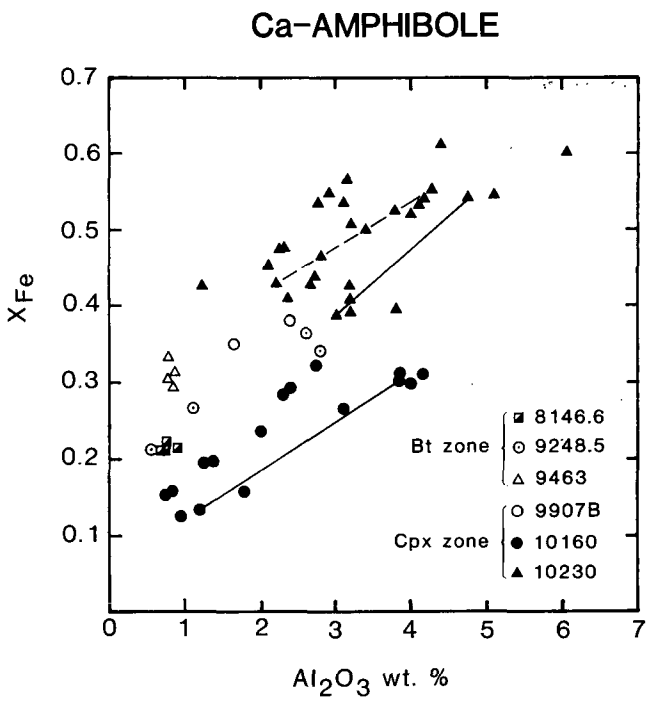

Fig. 8. Compositions of Ca-amphiboles shown in terms of Al_2O_3 wt % and X_{Fe} (= $Fe^*/(Fe^*+Mg)$). Compositions of the coexisting amphiboles in two samples 10160 and 10230 are connected by tie lines. Solid lines are for those amphiboles shown in Figures 7*a* and *b*. Note that amphibole compositions are enriched in total iron with increasing Al_2O_3 content.

plane of A'KF. This epidote projection can be justified because of (1) ubiquitous occurrence and constant A'KF composition of epidote in the analyzed samples and (2) no overlapping compositions of the projected metamorphic minerals on the A'KF plane. Moreover, the A'KF diagram can effectively illustrate the Tschermakitic substitutions in chlorite, biotite, and muscovite of various epidote-bearing assemblages and metamorphic grades.

The result of the epidote projection is shown in Figure 12*b*. The plotting coordinates for the three components in the epidote projection are

$$A' = Al_2O_3 + Fe_2O_3 - 0.75\ CaO - K_2O - Na_2O$$

$$K = K_2O$$

$$F = FeO + MgO$$

Note that calcite and anhydrite are plotted on the infinite point in Figure 12*b*, and that actinolite, clinopyroxene, and dolomite are on the extension of the A' - F join.

Bulk rock compositions of 11 sandstones from the IID 1 well of Salton Sea geothermal field, analyzed by *Muffler and White* [1969], are also shown in Figure 12*b* for reference. It should be pointed out that most of the analyzed samples, including Colorado River delta sediments, contain a significant amount of CaO (6-9 wt %). These high Ca contents together with lower Al contents than those of the average pelitic composition result in either minor or even negative A' component in the epidote projection. The difference in bulk rock composition between metasandstones and metapelites in Figure 12*b* may result in different mineral parageneses (compare *McDowell and Elders* [1980] together with the present data).

In the following discussion of prograde phase relations, anhydrite is considered to be equivalent to calcite because calcite and anhydrite conversion may be described primarily by a change in fluid composition. For example, this transition can be defined by a reaction,

$$CaCO_3 + H_2S + 2\ O_2 = CaSO_4 + H_2O + CO_2$$

Further reactions involving anhydrite and calcite together with various aqueous species and/or reduction-oxidation can be formulated (for examples, see *Anderson and Garven* [1987]). Thus the occurrence of anhydrite does not affect topologic relations based on calcite-bearing assemblages with excess fluid. Further details on the interaction between fluid and minerals and on the occurrence of either calcite or anhydrite are described by *Caruso et al.* [this issue].

Calcite/Anhyrite-Free Assemblages

Calcite/anhydrite-free assemblages are minor in the hydrothermal recrystallization of Colorado deltaic quartzofeldspathic sandstones initially cemented with clay or carbonate. The observed phase relations for these calcite- or

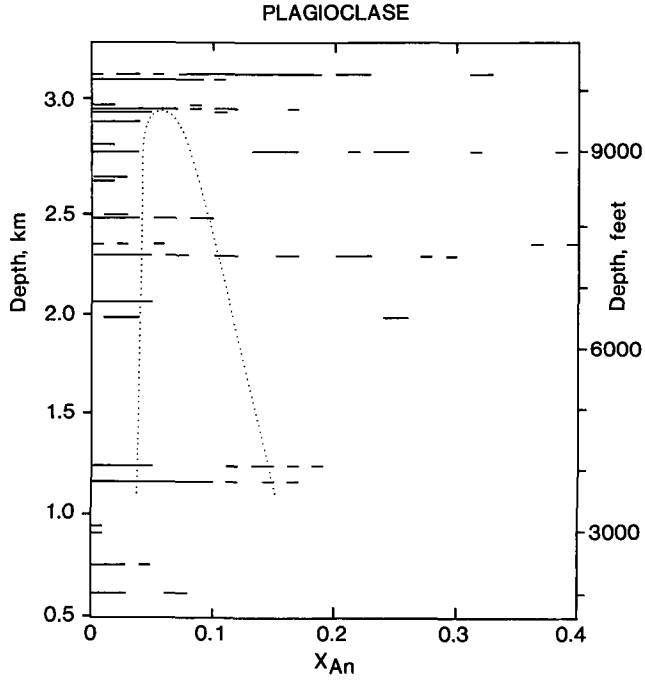

Fig. 9. The observed range of X_{An} values in the analyzed plagioclases with increasing depth. The apparent peristerite gap is schematically shown as a dotted curve, assuming that those compositions of plagioclase filling the gap are due to the mixed analyses. Note that oligoclase and andesine in sample 9007 represent relict compositions (cf. Figure 7*c*).

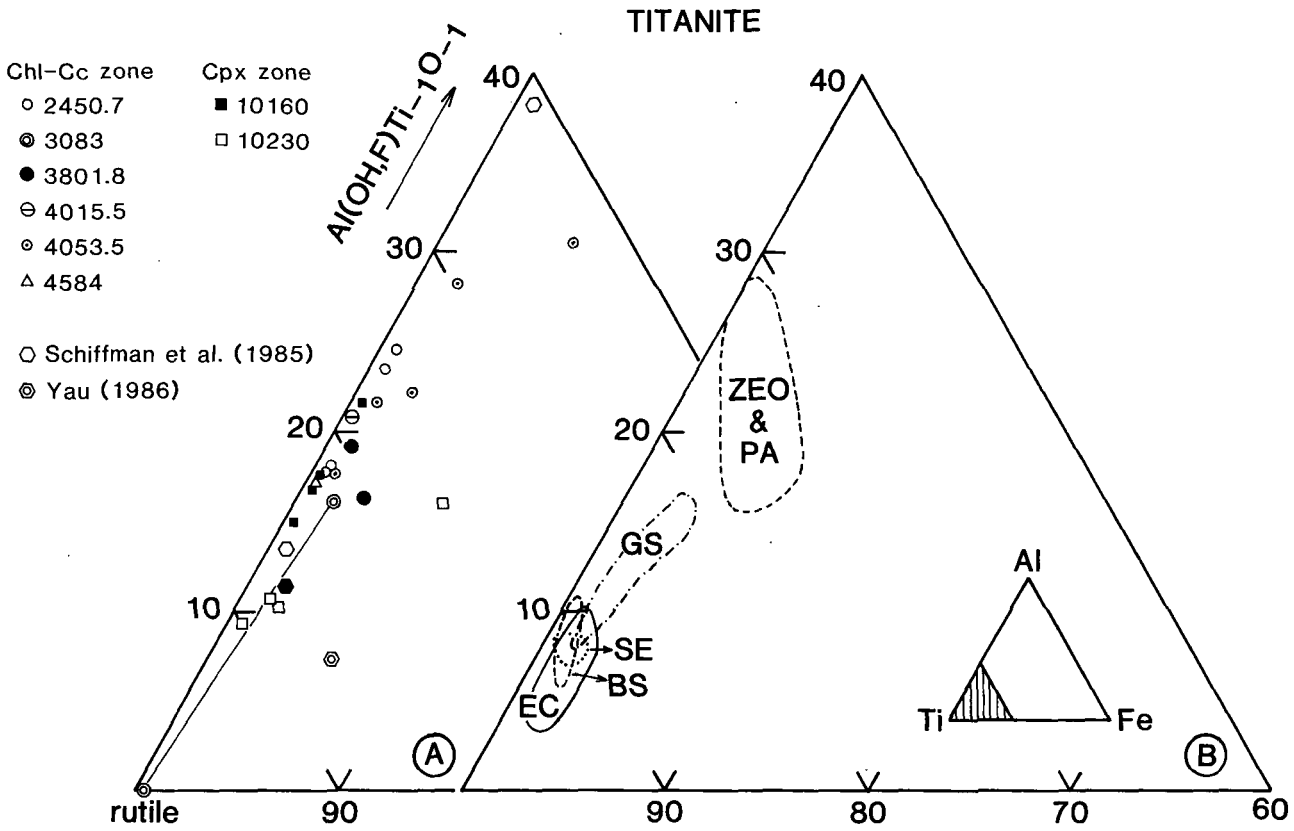

Fig. 10. Al-Ti-Fe plot of analyzed titanites to show (*a*) their compositional variation and (*b*) comparison with those observed in various metamorphic terranes, compiled by *Kawachi et al.* [1983]. For a comparison, two AEM analyses of titanite from the Elmore 2 and IID 1 wells [*Yau*, 1986], and two from the Cerro Prieto geothermal field [*Schiffman et al.*, 1985] are also shown in Figure 10*a*. The tie line in Figure 10*a* connects the compositions of the coexisting titanite and rutile in sample 3083.

anhydrite-free assemblages are depicted in Figure 13. In the chlorite-calcite zone the K-feldspar + chlorite (+ Ep + Qtz) assemblage is characteristic, whereas chlorite + biotite or biotite ± actinolite (+ Ep + Qtz) are observed in the biotite zone. Chlorite disappears in the clinopyroxene zone which is characterized by the assemblage clinopyroxene ± actinolite ± biotite. K-feldspar was not observed in calcite/anhydrite-free assemblages of the biotite and clinopyroxene zones. Biotite and actinolite are intimately intergrown in the biotite zone sample 8146.6, yielding mixed analyses (Figure 13 and Table 6). Moreover, the biotite of this Bt + Act assemblage is less aluminous than that of the Chl + Bt assemblage. This relationship suggests the importance of mineral assemblages or bulk rock compositions in controlling the Al content of biotite, as described previously. The observed calcite- or anhydrite-free assemblages shown in Figure 13 are always high variant. Thus it is difficult to determine which mineral reactions are responsible for the first appearance of biotite, actinolite, and clinopyroxene in calcite/anhydrite-free assemblages.

Calcite/Anhydrite-Bearing Assemblages

Phase relations and compositions of calcite- or anhydrite-bearing assemblages in both chlorite-calcite and biotite zones are illustrated in Figure 14. Apparently, in the deeper clinopyroxene zone, calcite and anhydrite are no longer stable with clinopyroxene and actinolite. This relationship may reflect the limited number of samples from this zone as well as compositional control. It should be noted that the equilibrium tie lines of the chlorite-calcite zone are only ap-

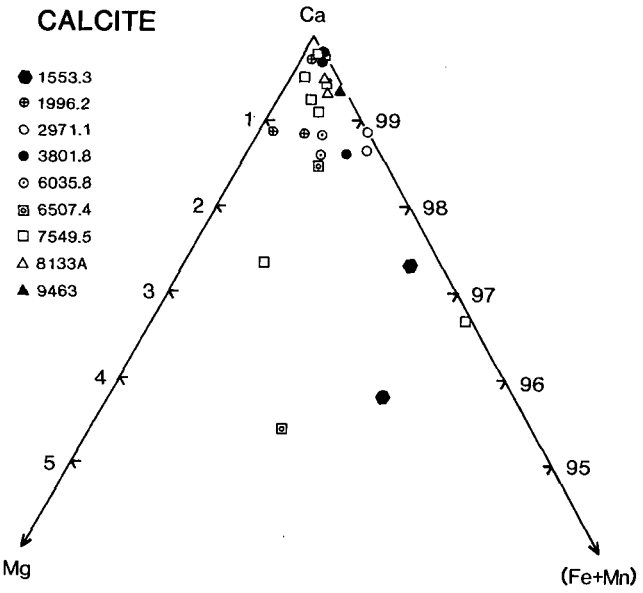

Fig. 11. Compositions of analyzed calcites plotted in the Ca-Mg-(Fe + Mn) diagram.

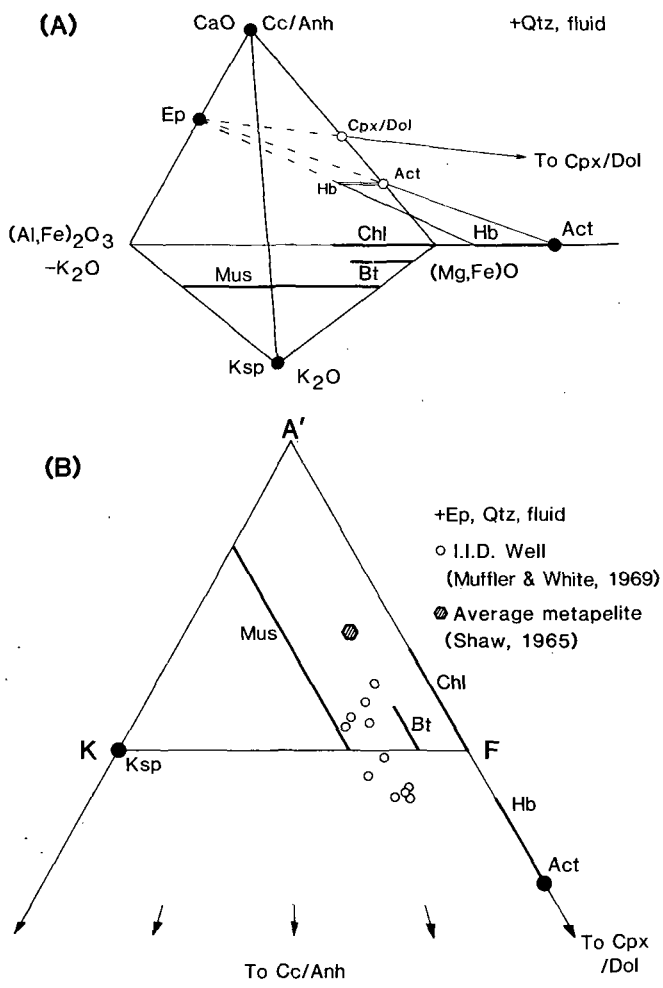

Fig. 12. (*a*) Phases plotted in the $((Al,Fe)_2O_3 - K_2O) - K_2O - (Mg,Fe)O - CaO$ (A'-K-F-C) tetrahedron. Quartz and fluid are assumed to be in excess. Heavy lines indicate the possible compositional ranges of muscovite, biotite, chlorite and Ca-amphibole. (*b*) An A'KF diagram, showing compositions of common authigenic phases projected from epidote onto the A'KF plane. Note that epidote, quartz, and fluid are assumed to be in excess. Compositions of 11 metasandstones from the IID 1 well of the Salton Sea geothermal field [*Muffler and White*, 1969] are also shown. Hatched symbol denotes the average composition of metapelites from *Shaw* [1965].

proximate because the analyzed compositions of muscovite are highly variable. However, we assumed that Si-rich or less aluminous phengitic mica are in equilibrium with calcite and chlorite.

In the chlorite-calcite zone, characteristic low-variance assemblages (+ Ep + Qtz) are Mus + Chl + Cc, Ksp + Mus + Chl + Cc and less commonly Ksp + Chl + Cc (Figure 14). Note that the four-phase assemblage defines a discontinuous reaction,

$$Mus + Cc + Qtz = Ksp + Chl + Ep + H_2O + CO_2 \quad (1)$$

The stoichiometric coefficients of this and other reactions considered in this study are listed in Table 9. They are obtained from mass-balance employing $KAl_2Mg_{0.5}Si_{3.5}O_{10}(OH)_2$ for muscovite, and other end-member mineral compositions shown in Table 1. Reaction (1) is univariant in the model system and may occur at a restricted temperature (depth) interval. However, the reaction (1) assemblage occurs at four different depths between 608 and 2301 m (Figure 14). These deviations from the model system indicate that the other variables such as $MgSiAl_{-2}$ substitutions in both phyllosilicates and chain silicates as well as the change in fluid composition have affected the observed phase relations in metasandstones. Further details on the effect of fluid composition are described below.

Three mineral assemblages characteristic for biotite zone metasandstones are also shown in Figure 14. They are Ksp + Chl + Anh, Ksp + Chl + Anh + Bt, and Bt + Chl + Anh. At a depth of 2445 m (sample 9007), biotite first appears according to a discontinuous reaction,

$$Ksp + Chl + Anh = Bt + Ep + Qtz + H_2O + H_2S + O_2$$

This reaction is equivalent to calcite-bearing reaction (2) listed in Table 9. Both the analyzed biotite and chlorite of the reaction assemblage in sample 9007 have restricted compositions, as can be expected from its low-variance nature. Note also that biotite in the anhydrite-bearing assemblages first appears at a depth of 2745 m, about 260 m deeper than that of calcite- or anhydrite-free samples. It is thus apparent that fluid composition may have played an important role in governing the first appearance of biotite (see discussion below).

DISCUSSION

T - X_{CO_2} Relations

In order to discuss the observed phase relations, an isobaric T - X_{CO_2} section (Figure 15) is schematically drawn for the 12 reactions listed in Table 9 employing the method of Schreinemakers [*Zen*, 1966]. Five univariant reactions radiate from an invariant point in the model AKFCSH - CO_2 system with excess epidote, quartz, and fluid. Three invariant points (I_1, I_2, and I_3) are presumed to be stable from the observed phase relations and, in particular, from reactions (1) and (2) described above. The qualitative T - X_{CO_2} slopes of these dehydration and mixed-volatile reactions are after *Greenwood* [1967]. Reactions containing both H_2O and CO_2 as product phases have very steep and positive slopes in the H_2O-rich portion of T - X_{CO_2} section. In addition, Figure 15 is a pseudobinary section assuming a constant molal NaCl to H_2O ratio. For a highly saline fluid, such as with 10 - 20 wt % NaCl in the Salton Sea geothermal field [*Helgeson*, 1968; *Roedder and Howard*, 1987; *Andes and McKibben*, 1987], an immiscibility between H_2O-rich liquid and CO_2-rich vapor occurs when X_{CO_2} is greater than 0.03 at $P < 500$ bars and $T < 400°C$ [*Bowers and Helgeson*, 1983a]. Because two fluid phases, H_2O- and CO_2-rich, respectively, have not been encountered in the deep core samples of the Salton Sea geothermal system [e.g., *Helgeson*, 1968], it is likely that reactions shown in Figure 15 occur only at very low X_{CO_2} conditions.

Three dolomite-bearing reactions (6), (7), and (8) and one

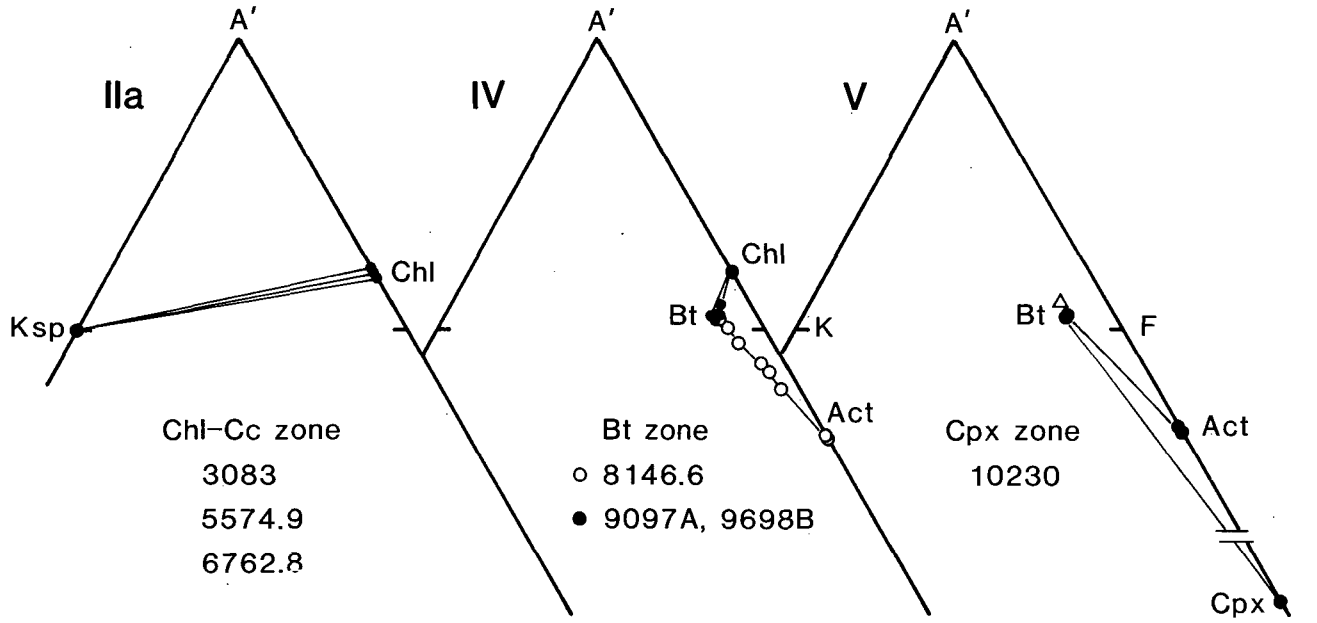

Fig. 13. A'KF diagrams depicting progressive phase relations observed for the calcite- and anhydrite-free assemblages in three metamorphic zones. The analyzed compositions of each silicate are shown as circles. Note mixed analyses of biotite and actinolite in sample 8146.6 of the biotite zone. Relict biotite in the clinopyroxene zone (open triangle; see Table 6 for chemical composition) is more aluminous than the authigenic biotite coexisting with actinolite or clinopyroxene. Roman numerals (IIa, IV, and V) correspond to the T - X_{CO_2} field of each assemblage shown in Figure 15.

invariant point I_2 are included in Figure 15 for low-temperature parageneses. Although dolomite and/or ankerite are not observed in this study, they are commonly reported at shallow depths in the dolomite-ankerite zone of the Salton Sea geothermal system [*McDowell and Elders*, 1980; *McDowell and Paces*, 1985]. Dolomite and ankerite generally disappear in the chlorite-calcite zone, and epidote has not been reported in the dolomite-ankerite zone. Thus epidote is probably not stable with dolomite for most of the Salton Sea metasandstones. In consequence, reactions containing dolomite and epidote may be metastable at low X_{CO_2}. At higher X_{CO_2}, however, reaction (6) may define the low-temperature limit of the Chl + Cc + Ep assemblage occurring at depths greater than 906 m, or the upper limit for the dolomite-ankerite zone.

The first appearance of biotite is defined by three terminal reactions (11), (2), and (5), respectively, as the X_{CO_2} values increase (Figure 15). Thus it is evident that temperatures for biotite-in reactions are highly dependent on the fluid composition. Reactions (9) and (12) governing the first appearance of actinolite and clinopyroxene, respectively [*Yau et al.*, 1986], are also shown in Figure 15.

X_{CO_2} of the Salton Sea Geothermal Fluid

The T - X_{CO_2} stability limits for the observed phase assemblages are illustrated by different patterns of shading in Figure 15. Roman numerals of Figure 15 correspond to those shown in Figures 13 and 14. For the chlorite-calcite zone, Mus + Cc + Chl (I) and Ksp + Chl ± Cc (IIa+IIb) assemblages (+ Ep + Qtz) are related by the reaction (1) assemblage. Note also that the presence or absence of calcite in the latter assemblage depends on the CaO and Al_2O_3 contents of the metasandstones at given T and X_{CO_2} conditions.

The chlorite-calcite zone assemblages of the State 2-14 well are consistent with the "calcite-chlorite" assemblage of calcite + chlorite + epidote + quartz, defined by *Cho and Liou* [1987] in thermally metamorphosed Karmutsen Volcanics. *Cho and Liou* [1987] have concluded that with increasing chemical potential of CO_2 in the fluid, the "calcite-chlorite" assemblage drastically expands its P - T stability field at the expense of prehnite- and pumpellyite-bearing assemblages in the H_2O-rich region. A similar result can be also achieved by increasing the NaCl content at constant X_{CO_2}, as demonstrated by *Bowers and Helgeson* [1983*b*]. Thus the absence of prehnite-pumpellyite or prehnite-actinolite facies assemblages indicates that CO_2 or NaCl contents of the Salton Sea geothermal system were greater than those of the Karmutsen metabasites.

For the biotite zone, Ksp + Chl + Anh (IIb), reaction (2) assemblage or Ksp + Chl + Anh + Bt, and Bt + Chl + Anh (III) are characteristic for carbonate/anhydrite-bearing assemblages. On the other hand, actinolite-bearing assemblages occur at lower X_{CO_2} defined by the T - X_{CO_2} of (IV) in Figure 15. Note also that assemblages for reactions (4) and (5) or invariant point I_1 are not observed. Thus it is probable that the fluid equilibrated with Salton Sea core samples at depths has not evolved into the X_{CO_2} composition higher than that of the invariant point I_1. This conclusion is further supported by the occurrence of Cpx + Act assemblage (V in Figgure 15) not only in the clinopyroxene zone but also in the biotite zone of the IID 2 well [*Yau et al.*, 1986].

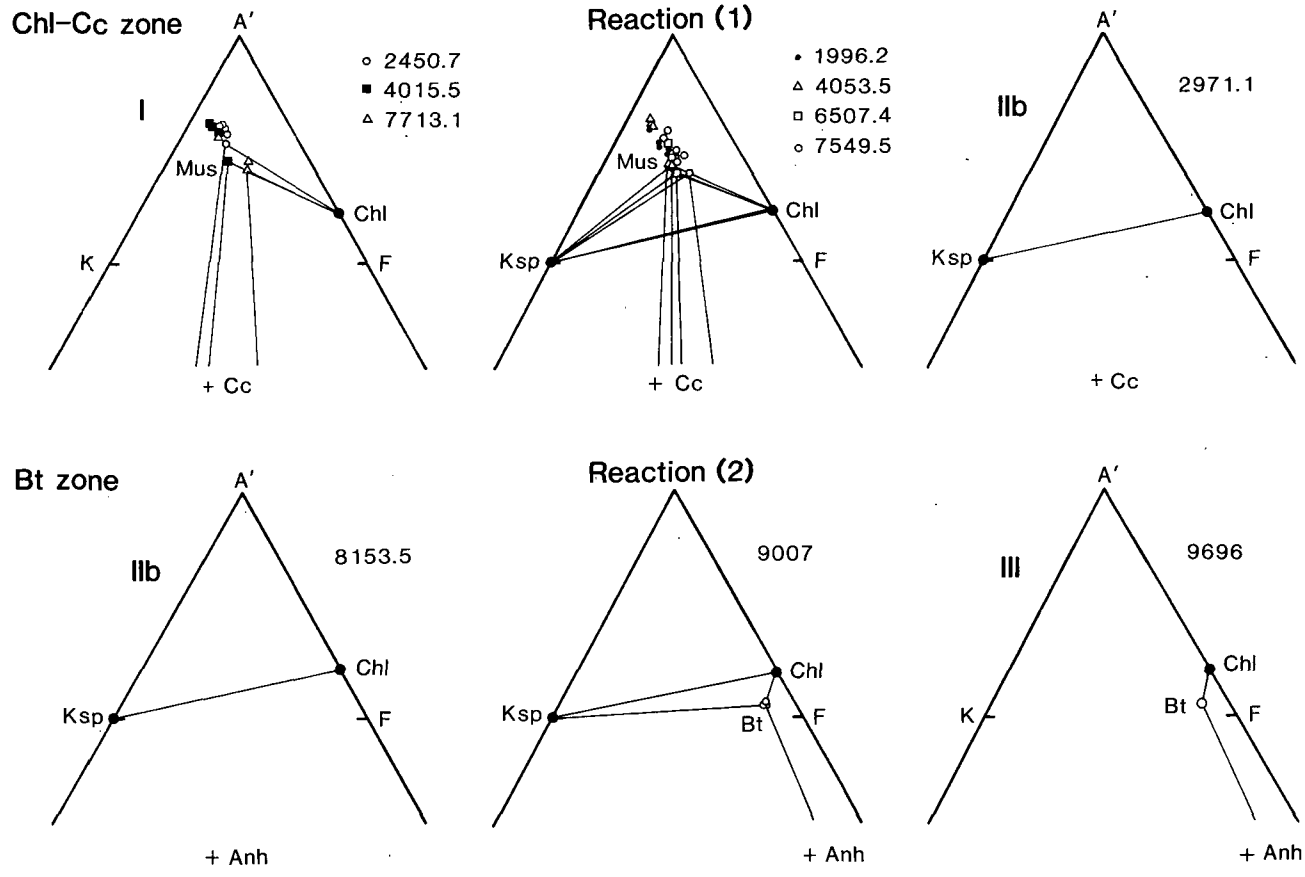

Fig. 14. Progressive phase relations observed for the calcite- and anhydrite-bearing assemblages of the chlorite-calcite and biotite zones are shown in a series of A'KF diagrams. The analyzed compositions of low-variance mineral assemblages are illustrated for each metamorphic zone. Muscovite is highly variable in its Tschermakite contents. Tie lines for muscovite-bearing assemblages are only approximate, assuming that the most Tschermakite-rich muscovite represents the equilibrium composition. Two assemblages defined by reactions (1) and (2), respectively, are most important in delineating phase relations of the metasandstones. Roman numerals (I, IIb, and III) correspond to the T - X_{CO_2} field of each assemblage in Figure 15.

Yau et al. [1986] have calculated the X_{CO_2} value for the coexistence of clinopyroxene and actinolite to be 0.03 - 0.06 at $T = 310°$ - 330°C based on a simple system in equilibrium with H_2O - CO_2 binary fluid. *Schiffman et al.* [1984] have also obtained an X_{CO_2} value of 0.05 at $T = 325°C$ in the Cerro Prieto geothermal system, based on the same assemblage of reaction (12). These predicted values should be greatly reduced to less than 0.03 in the Salton Sea fluid with high NaCl concentration. Our estimate of $X_{CO_2} < 0.03$, based on phase relations shown in Figure 15, is also consistent with the measured value of 0.0008 at the production zone (for further discussion, see *Caruso et al.*, this issue).

Biotite-Isograd

Various reactions of either continuous or discontinuous type have been proposed to account for the first appearance of biotite in low-grade metamorphic rocks (see the recent review by *Guidotti* [1984] and also *Miyashiro and Shido* [1985] and *Wang et al.* [1986]). Among these reactions, several discontinuous-type reactions are described below.

For carbonate-free pelitic assemblages, a dehydration reaction,

$$\text{Ksp} + \text{Chl} = \text{Mus} + \text{Bt} + \text{Qtz} + \text{H}_2\text{O} \quad (3)$$

has been proposed by many workers (*Thompson and Norton* [1968] and *Mather* [1970] among others), and recently further supported by *Miyashiro and Shido* [1985] and *Wang et al.* [1986]. For Fe-rich compositions and carbonate-free assemblages, *Brown* [1971] determined that stilpnomelane and actinolite react to form biotite by a dehydration reaction of the discontinuous type:

$$\text{Mus} + \text{stilpnomelane} + \text{Act} = \text{Bt} (+ \text{Chl} + \text{Ep} + \text{H}_2\text{O})$$

This reaction commonly occurs in higher pressure terranes than reaction (3) [*Brown*, 1975].

For carbonate-bearing assemblages, both *de Bethune* [1976] and *Ferry* [1976] proposed two discontinuous reactions based on both graphical and petrochemical analyses of low-grade calcitic metapelites and metacarbonates:

$$\text{Mus} + 8\ \text{Dol} + 3\ \text{Qtz} + 4\ \text{H}_2\text{O} = \text{Bt} + \text{Chl} + 8\ \text{Cc} + 8\ \text{CO}_2 \quad (13)$$

and

TABLE 9. Mineral Reactions Among K-Feldspar, Muscovite, Chlorite, Biotite, Actinolite, Clinopyroxene, Calcite And Dolomite (+ Ep + Qtz + fluid).

Reaction No.	Reaction
(1)	30 Mus+16 Cc+18 Qtz = 30 Ksp+3 Chl+8 Ep+14 H_2O+16 CO_2
(2)	5 Ksp+3 Chl+4 Cc = 5 Bt+2 Ep+3 Qtz+6 H_2O+4 CO_2
(3)	10 Ksp+3 Chl = 6 Mus+4 Bt+6 Qtz+2 H_2O
(4)	6 Mus+4 Cc+3 Qtz = Bt+5 Ksp+2 Ep+4 H_2O+4 CO_2
(5)	6 Mus+3 Chl+8 Cc = 6 Bt+4 Ep+10 H_2O+8 CO_2
(6)	15 Dol+2 Ep+3 Qtz+11 H_2O = 19 Cc+3 Chl+11 CO_2
(7)	6 Mus+7 Cc+5 Qtz = 6 Ksp+3 Dol+2 Ep + 5H_2O+CO_2
(8)	38 Mus+16 Dol+12 Qtz = 38 Ksp+7 Chl+8 Ep+6 H_2O+32 CO_2
(9)	3 Chl+10 Cc+21 Qtz = 3 Act+2 Ep+8 H_2O+10 CO_2
(10)	5 Bt+6 Cc+24 Qtz = 3 Act+5 Ksp+2 H_2O+6 CO_2
(11)	6 Act+25 Ksp+9 Chl = 25 Bt+6 Ep+57 Qtz+14 H_2O
(12)	Act+3 Cc+2 Qtz = 5 Cpx+H_2O+3 CO_2

For phase abbreviations see Table 1. Compositions of phengite, $KAl_2Mg_{0.5}Si_{3.5}O_{10}(OH)_2$, and clinochlore, $Mg_5Al_2Si_3O_{10}(OH)_8$, are used for mass-balance.

$$5\ \text{Mus} + 3\ \text{Chl} + 8\ \text{Cc} + 7\ \text{Qtz} = 5\ \text{Bi} + 8\ \text{An} + 12\ H_2O + 8\ CO_2 \quad (14)$$

Moreover, similar decarbonation reactions involving siderite and ankerite have been formulated for the biotite-isograd in pelitic schists of south central Maine [*Ferry*, 1984].

Reaction (2), which has not been previously identified, is proposed in this study as the biotite-in isograd reaction for the calcite/anhydrite-bearing assemblages in the Salton Sea geothermal field. As pointed out by *de Bethune* [1976], either epidote or anorthite can be the product phase of the biotite-forming decarbonation reactions. The epidote-bearing reaction (2) occurs only at lower X_{CO2} compared to reaction (14) because epidote will be replaced by Ca-plagioclase + calcite at high X_{CO2} by the reaction:

$$2\ \text{Zoisite (in Ep)} + CO_2 = 3\ \text{An (in Pl)} + \text{Cc} + H_2O \quad (15)$$

Moreover, the biotite-forming reaction (5), Mus + Chl + Cc = Bt + Ep + H_2O + CO_2, intersects with reactions (14) and (15) to form another invariant point which is stable at higher X_{CO2} conditions than those of this study. The reader is referred to Figure 15 of *Ferry* [1976], who constructed a qualitative T - X_{CO2} diagram involving the reactions (14) and (15).

Reaction (11), Act + Ksp + Chl = Bt + Ep + Qtz + H_2O, is another biotite-forming dehydration reaction as shown in Figure 15. This reaction intersects with (2), (9), and (10) at the invariant point I_3 which is suggested to be stable based on the observations that (1) biotite and actinolite are closely associated in sample 8146.6; and (2) biotite appears at lower temperature in carbonate/anhydrite-free assemblages. Moreover, *Yau* [1986] has observed through TEM work that actinolite (+ Ca-pyribole + Cpx) appears even in the chlorite-calcite zone metapelites of the IID 2 well, Salton Sea geothermal field. Although it is difficult to confirm due to the insufficient number of carbonate/anhydrite-free assemblages in the studied samples, reaction (11) is proposed for the discontinuous dehydration reaction that first produces biotite in an extremely CO_2-depleted environment.

The T - X_{CO2} relations of Figure 15 also indicate that the classical reaction (3) for the biotite-isograd in metapelites occurs at temperatures higher than those defined by reactions (2) and (11). Thus it should be emphasized again that the first appearance of biotite is highly dependent on both bulk rock and fluid compositions.

In summary, we propose two reactions, (2) and (11), to be responsible for the first appearance of biotite in the Salton Sea geothermal field. Epidote instead of calcic plagioclase is produced in conjunction with these biotite-forming reactions, accounting for the modal increase of epidote with increasing metamorphic grade. Note also that biotite may form by a decarbonation reaction at the expense of carbonates or by desulfidation of anhydrite even at very low X_{CO2} (<0.03) conditions. Our results further substantiate the suggestion of *Ferry* [1984] that biotite may commonly form by decarbonation reactions in low-grade metasediments.

Greenschist to Amphibolite Transition in the Salton Sea Geothermal System

Phase relations related to the greenschist-amphibolite transitional facies have been extensively studied through experimental work [e.g., *Liou et al.*, 1974; *Apted and Liou*, 1983; *Moody et al.*, 1983] and through observations of natural mineral parageneses [e.g., *Robinson et al.*, 1982; *Maruyama et al.*, 1983]. This transition zone is characterized by the occurrence of two Na-plagioclases and two Ca-amphiboles together with chlorite, epidote, quartz, titanite, and/or carbonate. Oligoclase appears in the transition zone prior to hornblende at low pressures and vice versa at high pressures.

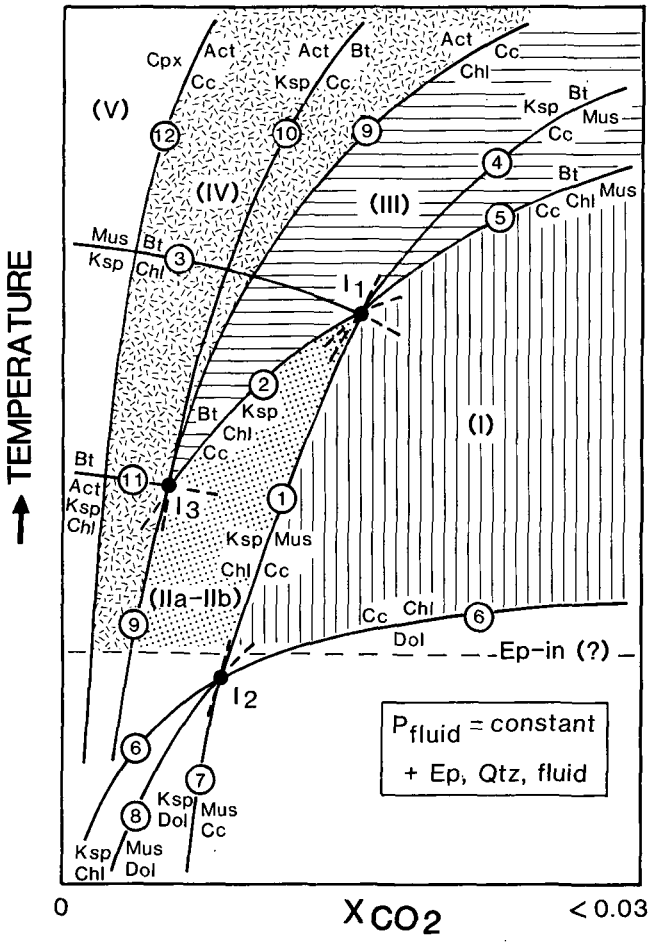

Fig. 15. A schematic isobaric T - X_{CO_2} diagram for the 12 mineral reactions (Table 3) in the model system, AKFCSH - CO_2, assuming excess epidote, quartz, and fluid. The T - X_{CO_2} stability fields for the observed assemblages are also shown in Roman numerals (I-V). These numbers correspond to the phase relations shown in the A'KF diagrams of Figures 13 and 14. Below the epidote-in temperature approximately located in the figure (dashed line), epidote is not stable, and three reactions (6), (7), and (8) together with an invariant point I_2 become metabstable.

At higher temperature the transition assemblage reacts to form amphibolite facies assemblages of hornblende + calcic plagioclase (± Ep, Chl, Qtz, Ttn, and garnet for metabasites).

Transitional facies assemblages occur in the clinopyroxene zone of the State 2-14 well, as described in the previous section. Two sodic plagioclases defined by the peristerite compositional gap are apparently stable at depths ranging from approximately 1200 to 3000 m (Figure 9). Furthermore, in the deepest sample (10230), oligoclase-andesine (An_{11-33}) is far more abundant than albite. It is thus inferred that the closure of the peristerite gap occurs approximately at the onset of the clinopyroxene zone. Temperature of the latter is estimated to be ~350°C from the measured downhole temperature of a flow test (<355°C at 3089 m, *Elders and Saas* [1987]). Pressure at a depth of 3000 m is assumed to be 275 bars because measured borehole pressures in the Salton Sea geothermal system closely match those of the hydrostatic gradient (91.1 bars/km [*Helgeson*, 1968]).

The estimated P-T values of the peristerite gap closure are shown in Figure 16, in conjunction with those from various thermal and regional metamorphic terranes [*Maruyama et al.*, 1982, and references therein; *Grapes and Otsuki*, 1983; *Ashworth and Evirgen*, 1985*a*, *b*]. *Maruyama et al.* [1982] have determined the consolute temperature of 420°-430°C for the peristerite solvus in the Kasugamura thermal aureole, Japan. They further compiled the data available for high-pressure terranes (Vermont and Sanbagawa) and concluded that the peristerite solvus is sensitive to pressure. *Grapes and Otsuki* [1983] have also determined the P-T values (5.5-7 kbar and 510°-520°C) of the peristerite gap closure in the Haast Schist terrane, New Zealand. Two sets of P-T estimates for central Menderes Massif, Turkey [*Ashworth and Evirgen*, 1985*a*, *b*] are deduced from different calibrations for the kyanite-staurolite zone assemblages in which two plagioclases occur. The results of Figure 16 are consistent with the suggestion by *Maruyama et al.* [1982] that the consolute temperatures for the peristerite gap increase with pressure. Moreover, our data provide an important

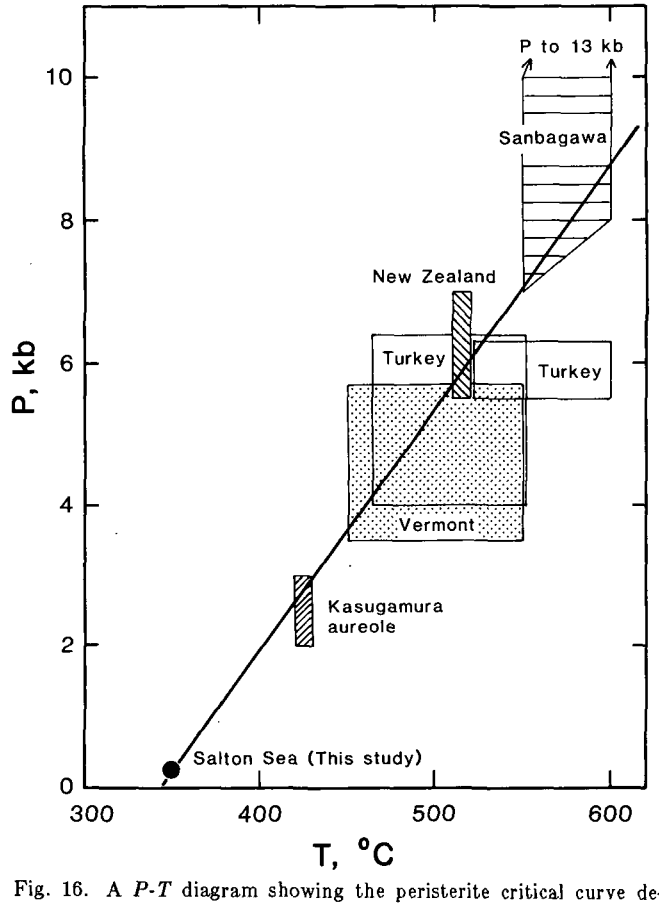

Fig. 16. A P-T diagram showing the peristerite critical curve deduced from the present data and those of high-pressure terranes [*Maruyama et al.*, 1982; *Grapes and Otsuki*, 1983; *Ashworth and Evirgen*, 1985*a*, *b*]. Two sets of P-T estimates based on different geothermobarometry are shown for central Menderes Massif, Turkey.

bracket at very low pressure, uniquely based on the measured pressure and temperature in the active geothermal system.

Figure 16 also shows the approximate P-T curve for the closure of the peristerite gap, which is drawn to be linear assuming a H_2O-conservative reaction involving albite and oligoclase. However, many metamorphic reactions are proposed to account for the disappearance of two Na-plagioclases or the oligoclase isograd (see the review of *Goldsmith* [1982]). The closure temperature, defined by H_2O- and/or CO_2-bearing reactions, may depend upon other variables than pressure (e.g., a_{H2O}, f_{O2}, or bulk rock composition). Thus the P-T locations of the peristerite gap closure may appear as a divariant zone.

Two coexisting amphiboles are first found in the clinopyroxene zone (T >350°C) of the State 2-14 well. A similar observation has been made in Nesjavellir geothermal system, Iceland, at temperatures between 350°C and 380°C [*Hreggvidsdottir and Bird*, 1987]. It should be further noted that two amphiboles appear at higher temperature than the consolute temperature of the peristerite gap closure in the Salton Sea geothermal system. This result is consistent with the first appearance of oligoclase at the low pressure transition zone and in contrast with the concurrent appearance of hornblende and oligoclase at 2 kbar [*Maruyama et al.*, 1982].

Calc-Silicate Mineralization in Geothermal Systems

Calc-silicate mineralization is one of the most important processes in active geothermal systems and has been extensively described and thermodynamically analyzed (for review, see *Bird et al.* [1984]). The most common calc-silicates include heulandite, laumontite, wairakite, prehnite, epidote, garnet, titanite, clinopyroxene, actinolite, and wollastonite. A distinct sequence with progressive dehydration with increasing depth, hence temperature, is generalized: heulandite and laumontite occur at temperatures below 200°C; wairakite, epidote, prehnite, and actinolite at temperatures from 200° to >300°C; and andradite garnet, clinopyroxene, and wollastonite at temperatures greater than 300°C.

Detailed parageneses of calc-silicates together with the measured temperature, pressure, and the chemical characteristics of associated hydrothermal fluids are well established in the Cerro Prieto geothermal system of the Salton Trough by *Schiffman et al.* [1984, 1985] and *Bird et al.* [1984]. Their thermodynamic analyses indicate that P_{CO2} of the epidote + wairakite + calcite assemblage, at temperatures of 230°-300°C and P_{fluid} of about 75 bars, is in excess of 15 bars [*Elders et al.*, 1981], corresponding to an X_{CO2} value greater than 0.20 [*Schiffman et al.*, 1984]. For the first appearance of clinopyroxene near 320°C, *Schiffman et al.* [1984] estimated an X_{CO2} value of 0.05 based on the experimental data on the reaction (12) [*Slaughter et al.*, 1975]. The calculated f_{O2} values at 320°-360°C are of the order of 10^{-33} to 10^{-37} and are about 5 orders of magnitude more reducing than those at the Salton Sea geothermal system, which are close to the hematite-magnetite buffer [see *Bird et al.*, 1984, Figure 23].

A significant difference in calc-silicate mineralization is apparent between the State 2-14 well of the Salton Sea system and the nearby Cerro Prieto geothermal field. Both geothermal fields are located in the same Salton Trough rift zone and are underlain by similar deltaic sediments of the Colorado River, consisting of interbedded sandstones, siltstones, and mudstones. In the chlorite-calcite zone for both geothermal systems, the X_{CO2} of the fluid phase was too high to stabilize laumontite. However, for biotite and clinopyroxene zone metasandstones, differences in mineral assemblage and composition in both systems are apparent: (1) ubiquitous occurrence of minor hematite and abundant epidote; (2) higher pistacite content of epidote; and (3) lack or general absence of both wairakite and prehnite in the Salton Sea geothermal system. Minor magnetite occurs in the Cerro Prieto geothermal system. Such differences have been attributed to contrasting fluid compositon, particularly in f_{O2} [*Bird et al.*, 1984].

The A'CF diagram of *Liou et al.* [1985] and *Cho et al.* [1986] is used to illustrate the difference in observed mineral assemblages and compositions mentioned above. In fact, the assemblages Ep - Act - Cc and Ep - Cc - Pr (+ Chl + Ab + Qtz) in Cerro Prieto are similar to the transitional assemblages between prehnite-pumpellyite and greenschist facies in the Karmutsen metabasites (for details, see *Cho and Liou* [1987]). As shown in Figure 17, at P and T of the biotite zone, mineral assemblages (+ Chl + Ab + Qtz) of Hm - Wr - Ep, Hm - Ep, and Ep - Act - Hm are stable for rocks with high Fe_2O_3 (higher in Fe^{3+}/Al ratio), and various CaO/Al_2O_3 ratios. Although wairakite has been rarely reported in the Salton Sea geothermal system, Ep + Act ± Hm assemblages (+ Bt ± Chl + Ab + Qtz) are characteristic for biotite zone metasandstones of the State 2-14 well. At extremely low X_{CO2} condition and for rocks with higher CaO/Al_2O_3, andradite garnet is stable with Fe-rich epidote ± hematite; this assemblage has also been recorded in the garnet zone of the Salton Sea geothemal system [*McDowell and Elders*, 1980]. Also shown in the diagram is the systematic increase in X_{Fe3+} value for epidote from assemblage Ep + Pr + Wr through Ep + Pr + Cc and Ep + Cc + Act to Ep + Hm + Act.

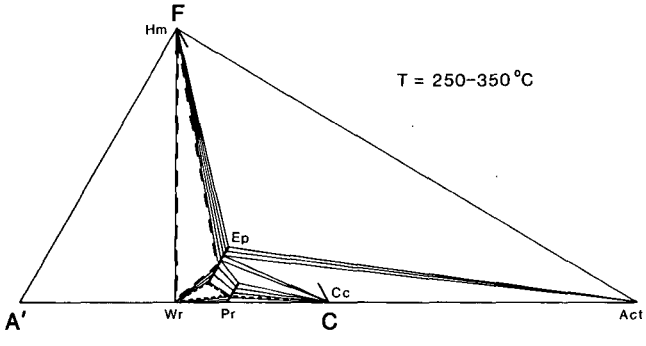

Fig. 17. A schematic A'CF diagram showing a possible phase relation among hematite- and prehnite-bearing assemblages in active geothermal systems at temperatures between about 250° and 350° C (cf. Figure 8*b* of *Cho and Liou* [1987]). The f_{O2} defined by hematite + wairakite + epidote (long-dashed line) is greater than that of prehnite + wairakite + epidote (short-dashed line).

Figure 17 thus offers a unique explanation for the observed difference in mineral assemblage and in epidote composition between the Salton Sea and Cerro Prieto geothermal fields. This explanation is consistent with the large difference in f_{O_2} between the two systems suggested by *Bird et al.* [1984]. At high f_{O_2} values close to those of the hematite-magnetite buffer as in the Salton Sea system, metasandstones would have higher Fe^{3+}/Al ratios; hence hematite may occur in equilibrium with Fe-rich epidote. On the other hand, at the f_{O_2} values lower than those of the quartz-magnetite-fayalite buffer as in the Cerro Prieto system, metasandstones contain lower Fe^{3+}/Al ratios, and wairakite and/or prehnite are stable with Fe-poor epidote ($\pm$ calcite, actinolite, and magnetite).

It should be noted that Figure 17 is constructed at constant T and P but not necessarily at constant f_{O_2} value. The f_{O_2} of a given system is buffered by the mineral assemblages, and two examples of equal f_{O_2} contours are shown in Figure 17. For example, the assemblage Hm + Wr + Ep of Figure 17 defines a unique f_{O_2} value at constant P and T. Bulk compositions within the Hm - Wr - Ep triangle may have very different Fe^{3+}/Al and Fe^{3+}/Fe^{2+} ratios but yield identical mineral assemblage and same f_{O_2} value at given P and T. Thus the f_{O_2} value of the Hm + Ep + Act assemblage in the Salton Sea geothermal system should be different (higher according to the calculation by *Bird et al.* [1984]) from that of the Wr + Ep + Cc assemblage of the Cerro Prieto geothermal system.

Our petrologic analysis of the State 2-14 well metasandstones of the Salton Sea geothermal system permits characterization of chemical reactions responsible for the observed mineral parageneses associated with progressive geothermal metamorphism. Moreover, the results of this study provide an important data set at very low pressures in conjunction with the measured temperatures and fluid compositions. All of these data are essential for understanding fluid-rock interactions, mineral-solution equilibria, and geochemical transport in the Salton Sea geothermal system.

Acknowledgments. This research, part of the Salton Sea Scientific Drilling Project, was supported by National Science Foundation grant, EAR 84-18147. We thank W. A. Elders, J. B. Hulen, M. A. McKibben, and P. S. Schiffman for many helpful comments on the manuscript.

REFERENCES

Anderson, G.M., and G. Garven, Sulfate-sulfide-carbonate associations in Mississippi valley-type lead-zinc deposits, *Econ. Geol., 82*, 482-488, 1987.

Andes, J.P., Jr., and M.A. McKibben, Thermal and chemical history of mineralized fractures in cores from the Salton Sea Scientific Drilling Project (abstract), *Eos Trans. AGU, 68*, 439, 1987.

Apted, M.J., and J.G. Liou, Phase relations among greenschist, epidote amphibolite, and amphibolite in a basaltic system, *Am. J. Sci., 283A*, 328-354, 1983.

Ashworth, J.R., and M.M. Evirgen, Plagioclase relations in pelites, central Menderes massif, Turkey, I, The peristerite gap with coexisting kyanite, *J. Metamorph. Geol., 3*, 207-218, 1985*a*.

Ashworth, J.R., and M.M. Evirgen, Plagioclase relations in pelites, central Menderes massif, Turkey, II, Perturbation of garnet-plagioclase geobarometers, *J. Metamorph. Geol., 3*, 219-229, 1985*b*.

Bence, A.E., and A.L. Albee, Empirical correction factors for the electron microanalysis of silicates and oxides, *J. Geol., 76*, 382-403, 1968.

Bird, D.K, and D.L. Norton, Theoretical prediction of phase relations among aqueous solutions and minerals: Salton Sea geothermal system, *Geochim. Cosmochim. Acta, 45*, 1479-1493, 1981.

Bird, D.K, P. Schiffman, W.A. Elders, A.E. Williams, and S.D. McDowell, Calc-silicate mineralization in active geothermal system, *Econ. Geol., 79*, 671-695, 1984.

Bird, D.K., R.D. Rogers, and C.E. Manning, Mineralized fracture systems of the Skaergaard intrusion, East Greenland, *Medd. Gronl., 16*, 1-68, 1986.

Bird, D.K., M. Cho, C.J. Janik, J.G. Liou, and L.J. Caruso, Compositional, order/disorder, stable isotope characteristics of Al-Fe epidote, State 2-14 drill hole, Salton Sea geothermal system, *J. Geophys. Res.*, this issue.

Bowers, T.S., and Helgeson, H.C., Calculation of the thermodynamic and geochemical consequences of nonideal mixing in the system H_2O - CO_2 - NaCl on phase relations in geologic systems: Equation of state for H_2O - CO_2 - NaCl fluids at high pressures and temperatures, *Geochim. Cosmochim. Acta, 47*, 1247-1275, 1983*a*.

Bowers, T.S., and Helgeson, H.C., Calculation of the thermodynamic and geochemical consequences of nonideal mixing in the system H_2O - CO_2 - NaCl on phase relations in geologic systems: metamorphic equilibria at high pressures and temperatures, *Am. Mineral., 68*, 1059-1075, 1983*b*.

Brown, E.H., Phase relations of biotite and stilpnomelane in the greenschist facies. *Contrib. Mineral. Petrol., 31*, 275-299, 1971.

Brown, E.H., A petrogenetic grid for reactions producing biotite and other Al-Fe-Mg silicates in the greenschist facies, *J. Petrol., 16*, 258-271, 1975.

Caruso, L.J., D.K.Bird, M. Cho, and J.G. Liou, Epidote-bearing veins in State 2-14 drill hole: Implications for hydrothermal fluid composition, *J. Geophys. Res.*, this issue.

Cathelineau, M., and D. Nieva, A chlorite solid solution geothermometer: The Los Azufres (Mexico) geothermal system, *Contrib. Mineral. Petrol., 91*, 235-244, 1985.

Cho, M., and J.G. Liou, Prehnite-pumpellyite to greenschist facies transition in the Karmutsen metabasites, Vancouver Island, B.C. *J. Petrol. 28*, 417-443, 1987.

Cho, M., J.G. Liou, and S. Maruyama, Transition from the zeolite to prehnite-pumpellyite facies in the Karmutsen metabasites, Vancouver Island, British Columbia. *J. Petrol. 27*, 467-494, 1986.

Crawford, M.L., Composition of plagioclase and associated minerals in some schists from Vermont, U.S.A., and South Westland, New Zealand, with inferences about the peristerite solvus, *Contrib. Mineral Petrol., 13*, 269-295, 1966.

de Bethune, S., Formation of metamorphic biotite by decarbonation, *Lithos, 9*, 309-318, 1976.

Donaghe, L.L., and D.R. Peacor, Textural and mineralogic transitions in SSSDP argillaceous sediments (abstract), *Eos Trans. AGU, 68,* 454, 1987.

Elders, W.A., and J.H. Sass, An overview of the SSSDP (abstract), *Eos Trans. AGU, 68,* 438, 1987.

Elders, W.A., J.R. Hoagland, and A.E. Williams, Distribution of hydrothermal mineral zones in the Cerro Prieto geothermal field of Baja California, Mexico, *Geothermics, 10,* 245-253, 1981.

Evans, B.W., and B.E. Patrick, Phengite-3T in high-pressure metamorphosed granitic orthogneisses, Seward Peninsula, Alaska, *Can. Mineral., 25,* 141-158, 1987.

Ferry, J.M., Metamorphism of calcareous sediments in the Waterville-Vassalboro area, south-central Maine: Mineral reactions and graphical analysis, *Am. J. Sci., 276,* 841-882, 1976.

Ferry, J.M., A biotite isograd in south-central Maine, U.S.A.: Mineral reactions, fluid transfer, and heat transfer, *J. Petrol, 25,* 871-893, 1984.

Frey, M., Very low-grade metamorphism of clastic sedimentary rocks, in *Low-Temperature Metamorphism,* edited by M. Frey, pp. 9-58, Blackie, Glasgow, 1987.

Goldsmith, J.R., Review of the behavior of plagioclase under metamorphic conditions, *Am. Mineral., 67,* 643-652, 1982.

Graham, C.M., and A. Navrotsky, Thermochemistry of the tremolite-edenite amphiboles with applications to amphibole-plagioclase-quartz equilibria, *Contrib. Mineral. Petrol., 93,* 18-32, 1986.

Grapes, R., and M. Otsuki, Peristerite compositions in quartzofeldspathic schists, Franz Josef-Fox Glacier Area, New Zealand, *J. Metamorph. Geol., 1,* 47-61, 1983.

Greenwood, H.J., Mineral equilibria in the system MgO - SiO_2 - H_2O - CO_2, in *Researches in Geochemistry, vol. II,,* edited by P.H. Abelson, pp. 542-567, John Wiley, New York, 1967.

Guidotti, C.,V., Micas in metamorphic rocks, in *Micas, Rev. Mineral., vol. 13,* edited by S.W. Bailey, pp. 357-467, Mineralogical Society of America, Washington, D.C., 1984.

Helgeson, H.C., Geologic and thermodynamic characteristics of the Salton Sea geothermal system, *Am. J. Sci., 266,* 129-166, 1968.

Herzig, C.T., and J.M. Mehegan, The lithostratigraphy of the Colorado River Delta in the active SSGF pull-apart basin, California (abstract), *Eos Trans. AGU, 68,* 444-445, 1987.

Hey, M.H., A new review of the chlorites, *Mineral. Mag. 30,* 277-292, 1954.

Hreggvidsdottir, H., and D. K. Bird, Actively forming amphibolite facies metamorphic minerals in the Nesjavellir hydrothermal system, southwest rift zone of Iceland (abstract), *Eos Trans. AGU, 68,* 469, 1987.

Ishizuka, H., Prograde metamorphism of the Horokanai ophiolite in the Kamuikotan zone, Hokkaido, Japan, *J. Petrol., 26,* 391-417, 1985.

Kawachi, Y., R.H. Grapes, D.S. Coombs, and M. Dowse, Mineralogy and petrology of a piemontite-bearing schist, western Otago, New Zealand, *J. Metamorph. Geol., 1,* 353-372, 1983.

Kimball, K.L., F.S. Spear, and H.J.B. Dick, High temperature alteration of abyssal ultramafics from the Islas Orcadas Fracture Zone, South Atlantic, *Contrib. Mineral. Petrol., 91,* 307-320, 1985.

Leake, B.E., Nomenclature of amphiboles, *Can. Mineral., 16,* 501-520, 1978.

Liou, J.G., S. Kuniyoshi, and K. Ito, Experimental studies of the phase relations between greenschist and amphibolite in a basaltic system, *Am. J. Sci., 274,* 613-632, 1974.

Liou, J.G., S. Maruyama, and M. Cho, Phase equilibria and mineral parageneses of metabasites in low-grade metamorphism. *Min. Mag., 49.,* 321-333, 1985.

Maruyama, S., J.G. Liou, and K. Suzuki, The peristerite gap in low-grade metamorphic rocks, *Contrib. Mineral. Petrol., 81,* 268-276, 1982.

Maruyama, S., K. Suzuki, and J.G. Liou, Greenschist-amphibolite transition equilibria at low pressures, *J. Petrol., 24,* 583-604, 1983.

Mather, J.D., The biotite isograd and the lower greenschist facies in the Dalradian rocks of Scotland. *J. Petrol., 11,* 253-275, 1970.

McDowell, S.D., Composition and structural state of coexisting feldspars, Salton Sea geothermal field, *Mineral. Mag., 50,* 75-84, 1986.

McDowell, S.D., and W.A. Elders, Authigenic layer silicate minerals in borehole Elmore 1, Salton Sea Geothermal Field, California, USA. *Contrib. Mineral. Petrol., 74,* 293-310, 1980.

McDowell, S.D., and W.A. Elders, Allogenic layer silicate minerals in borehole Elmore #1, Salton Sea Geothermal Field, California, *Am. Mineral., 68,* 1146-1159, 1983.

McDowell, S.D., and J.B. Paces, Carbonate alteration minerals in the Salton Sea geothermal system, California, USA, *Mineral. Mag., 49,* 469-479, 1985.

McKibben, M.A., and W.A. Elders, Fe-Zn-Cu-Pb mineralization in the Salton Sea geothermal system, Imperial Valley, California, *Econ. Geol., 80,* 539-559, 1985.

Miyashiro, A., and F. Shido, Tschermak substitution in low- and middle-grade pelitic schists, *J. Petrol., 26,* 449-487, 1985.

Moody, J.B., D. Meyer, and J.E. Jenkins, Experimental characterization of the greenschist/amphibolite boundary in mafic systems, *Am. J. Sci., 283,* 48-92, 1983.

Muffler, L.P.J., and D.E. White, Active metamorphism of Upper Cenozoic sediments in the Salton Sea geothermal field and the Salton Trough, southeastern California. *Geol. Soc. Am. Bull., 80,* 157-182, 1969.

Oba, T., and K. Yagi, Phase relations on the actinolite-pargasite join, *J. Petrol., 28,* 23-36, 1987.

Papike, J.J., K.L. Cameron, K.L., and K. Baldwin, Amphiboles and clinopyroxenes: Characterization of 'other' than quadrilateral components and estimates of ferric iron from microprobe data (abstract), *Geol. Soc. Am. Abstr. Programs, 6,* 1053-1054, 1974.

Pattison, D.R.M., Variations in Mg/(Mg+Fe), F, and (Fe,Mg)Si = 2Al in pelitic minerals in the Ballachulish thermal aureole, Scotland, *Am. Mineral., 72,* 255-272, 1987.

Robinson, P., F.S. Spear, J.C. Schumacher, J. Laird, C. Klein, B.W. Evans, and B.L. Doolan, Phase relations of metamorphic amphiboles: Natural occurrence and theory, in *Amphiboles: Petrology and Experimental Phase Relations, Rev. Mineral.* vol. 9B , edited by D.R. Veblen and P.H. Ribbe,R, pp.1-227, Mineralogical society of American, Washington, D.C. 1982.

Roedder, E., and K.W. Howard, Fluid inclusions in SSSDP core: Preliminary results (abstract), *Eos Trans. AGU, 68,* 439, 1987.

Schiffman, P.S., W.A. Elders, A.E. Williams, S.D. McDowell, and D.K. Bird, Active metasomatism in the Cerro Prieto geothermal system, Baja California, Mexico: A telescoped low-pressure, low-temperature metamorphic facies series, *Geology, 12,* 12-15, 1984.

Schiffman, P.S., D.K. Bird, and W.A. Elders, Hydrothermal mineralogy of calcareous sandstones from the Colorado River delta in the Cerro Prieto geothermal system, Baja California, Mexico, *Min. Mag., 49,* 435-449, 1985.

Shaw, D.M., Geochemistry of pelitic rocks, III, Major elements and general geochemistry, *Geol. Soc. Am. Bull., 67,* 919-934, 1965.

Slaughter, J.D., D.M., Kerrick, and V.J. Wall, Experimental and thermodynamic study of equilibria in the system CaO - MgO - SiO_2 - H_2O - CO_2, *Am. J. Sci., 275,* 143-162, 1975.

Tagiri, M., Fe-Mg partition and miscibility gap between coexisting calcic amphiboles from the Southern Abukuma Plateau, Japan, *Contrib. Mineral. Petrol., 62,* 271-281, 1977.

Thompson, J.B., Jr., and S.A. Norton, Paleozoic regional metamorphism in New England and adjacent areas, in *Studies of Appalachian Geology, Northern and Maritime,* edited by E-an Zen, pp. 319-327, Wiley-Interscience, New York, 1968.

Wang, G.F., S. Banno, and K. Takeuchi, Reactions to define the biotite isograd in the Ryoke metamorphic belt, Kii Peninsula, Japan. *Contrib. Mineral. Petrol., 93,* 9-17, 1986.

Yau, Y.C., Microscopic studies of hydrothermally metamorphosed shales from the Salton Sea geothermal field, California, USA, *Ph.D. thesis, Univ. Mich., Ann Arbor,* 159pp., 1986.

Yau, Y.C., D.R., Peacor, and E.J. Essene, Occurrence of wide-chain Ca-pyriboles as primary crystals in the Salton Sea geothermal field, California, USA, *Contrib. Mineral. Petrol., 94,* 127-134, 1986.

Zen, E., Construction of pressure-temperature diagrams for multicomponent systems after the method of Schreinemakers - A geometric approach, *U.S. Geol. Surv. Bull., 1225,* 56 pp, 1966.

J. G. Liou and D. K. Bird, Department of Geology, stanford University, Stanford, CA 9435.

M. Cho, Department of Earth and Space Sciences, University of California, Los Angeles, CA 90024.

(Received August 3, 1987;
accepted February 17, 1988.)

JOURNAL OF GEOPHYSICAL RESEARCH, VOL. 93, NO. B11, PAGES 13,104-13,122, NOVEMBER 10, 1988

MINERAL REACTIONS IN ALTERED SEDIMENTS FROM THE CALIFORNIA STATE 2-14 WELL: VARIATIONS IN THE MODAL MINERALOGY, MINERAL CHEMISTRY AND BULK COMPOSITION OF THE SALTON SEA SCIENTIFIC DRILLING PROJECT CORE

C.K. Shearer, J.J. Papike, S.B. Simon, and B.L. Davis

South Dakota School of Mines and Technology, Rapid City

J.C. Laul

Battelle, Pacific Northwest Laboratories, Richland, Washington

Abstract. X ray diffraction-reference intensity method (XRD-RIM) modes, whole rock chemistry, and mineral chemistry were determined on 36 samples from the Salton Sea Scientific Drilling Project (SSSDP) core. These samples display a wide variation in grain size (shale to sandstone), bulk composition (SiO_2 = 36.2-81.2 wt %; Al_2O_3 = 5.1-17.1 wt %; CaO = 1.2-21.1 wt % and (total Fe as Fe_2O_3) $Fe_2O_3/(Fe_2O_3 + MgO)$ wt ratio = 0.48-0.98) and mineral assemblage. Seven mineral assemblages have been identified in this sample suite: (1) chlorite + calcite + quartz + plagioclase ± K-feldspar ± illite (476-2559 m), (2) chlorite + quartz + plagioclase + K-feldspar (918.7-1984.3 m), (3) chlorite + epidote + quartz ± plagioclase ± calcite ± K-feldspar ± illite ± magnetite (905.6-2954.8 m), (4) chlorite + biotite ± calcite + quartz + plagioclase + K-feldspar (2700.0-2819.2 m), (5) epidote + quartz ± plagioclase (1424.2-2954.8 m), (6) epidote + actinolite + quartz ± biotite ± chlorite ± plagioclase ± K-feldspar ± anhydrite (2880.2-3021.2 m), and (7) epidote + clinopyroxene + actinolite + quartz (2484.7 m). These assemblages define three metamorphic zones in the SSSDP well: calcite-chlorite zone, biotite zone, and actinolite zone. Accompanying these transitions in mineral assemblages are changes in the Si-Al ordering in K-feldspar and an increase in the anorthite component in plagioclase. Fe/(Fe+Al) in epidote shows very little systematic variation downhole (in the sediments) but can be highly zoned and shows considerable systematic variation between vein systems and sedimentary pore space. Quantitative modal mineralogy and whole rock chemistry can be utilized in determining mineral reactions and their importance and in evaluating the evolution of mineral assemblages. For example, epidote-forming reactions precede actinolite-epidote- and biotite-epidote-forming reactions in numerous bulk compositions and result in the formation of high modal abundances of epidote. The production of fluids with high X_{CO2} from epidote-, actinolite-, biotite-, and diopside-forming reactions in rocks in equilibrium with fluids with $X_{CO2} < 0.1$ indicates extensive interaction between fluid and the shales. This is also indicated by the leaching of Cu, Zn, and Mn and the enrichment of Sr. Numerous elements, however, do not show evidence of exchange between sediments and fluid.

Paper number 88JB03074.
0148-0227/88/88JB-03074$05.00

Introduction

Changes in the mineralogy of metamorphic rocks have long been used as monitors of the grade of metamorphism. With the addition of mineral chemistries and experimental studies in natural and synthetic metamorphic systems, petrologists have attempted, with varying degrees of success, to predict conditions of metamorphism (pressure, temperature, fluid composition (e.g., X_{CO2}), and closure characteristics of a system) and to evaluate phase equilibria in natural metamorphic environments. Geothermal areas provide a unique geologic situation in which the transition from diagenesis to active metamorphism occurs at relatively accessible depths. In addition, in situ measurement of T and P and estimates of fluid composition and system closure characteristics can be made [Janik et al., 1987; Valette-Silver et al., 1987, Campbell et al., 1987, Williams, 1987; Sass et al., 1987; Noblet and McDowell, 1987; McDowell and Elders, 1980; Muffler and White, 1969; Helgeson, 1968].

Within the Salton Sea geothermal area in southern California, petrologic and geothermal studies [e.g., McDowell and Elders, 1980; Helgeson, 1967; Muffler and White, 1969] have identified a sequence of metamorphic zones within the Salton Sea Trough sediments, and approximate temperature and fluid conditions are known. McDowell and Elders [1980] recognized (1) a dolomite/anhydrite zone at temperatures less than 190°C, (2) calcite-chlorite zone at temperatures between 190° and 325°C, (3) a biotite zone at temperatures between 325° and 365°C, and (4) a garnet zone at temperatures in excess of 360°C. In addition to changes in mineral assemblage, McDowell [1987] also observed extensive geochemical alteration of sediments in the Magmamax and Elmore wells. The location of the Salton Sea Scientific Drilling Project (SSSDP) drill site is given by Elders and Sass [this issue].

The SSSDP provides a unique opportunity for a comprehensive and multidisciplinary study of an active geothermal system. Previous studies of the prograde phase relations in the Salton Sea geothermal area have focused extensively on the observations in metasandstones [McDowell and McCurry, 1977; Keith et al., 1968; McDowell and Elders, 1980, 1983; Bird and Norton, 1981; Kramer and McDowell, 1987; Cho et al. 1987] and mineralized fractures [Caruso et al., 1987; Andes

and McKibben, 1987]. The shales which make up approximately 70% of the sediments in the Salton Sea geothermal system [Kendall, 1976] have received somewhat less attention due to their much smaller grain size. The difference in permeability between the shales and sandstones will impact the degree of mineralogic and isotopic equilibrium [Kendall, 1976]. Due to the difficulty of using standard optical microscopy for the interpretation of modal abundances and mineral textures in sediments with grain sizes of less than 2 μm, reactions in the shales have been estimated utilizing qualitative X ray diffraction techniques to determine the presence or absence of mineral phases [Muffler and White, 1969]. Recently, scanning transmission electron microscope (STEM) and scanning electron microscope (SEM) techniques have been used to define reactions in shales based on textural observations or interpretations at grain surfaces [Yau et al., 1986; McDowell, 1986; Donaghe and Peacor, 1987]. To complement these previous and ongoing SEM studies of grain surface textural interpretations, our study focuses upon bulk rock mineralogical and chemical evaluation of reactions in the shale using quantitative mineral modes determined by X ray diffraction-reference intensity method (XRD-RIM) and whole rock chemistry determined by a variety of analytical techniques. In addition, these data can be then used to determine downhole mineral reactions and their effect on selected bulk compositions and to evaluate fluid-sediment interaction and its effect on bulk rock chemistry.

Analytical Techniques

Thirty-six samples were selected from the Salton Sea core for petrographic, mineralogical and chemical analysis. Sample depth ranged from 476.0 to 3021 m. Sample distribution is summarized in Table 1. To present a relevant and coherent data set, great care was taken to ensure that the petrographic observations, XRD-RIM modes, whole rock chemistry, microprobe analyses, and reflectivity data were obtained on homogeneous sample splits. All samples were photodocumented at the South Dakota School of Mines and Technology (SDSM&T). Then microprobe sections were taken adjacent to subsamples earmarked for XRD-RIM and chemical analyses. XRD-RIM and chemical analyses were obtained on aliquots of the same homogeneous powder.

XRD-RIM modes were obtained at SDSM&T utilizing preparation and X ray diffraction techniques discussed at length by Davis [1980, 1984, 1986], Davis and Johnson [1982, 1986], and Davis et al. [1986]. This method for determining quantitative modes includes the creation of an aerosol from a finely pulverized sample, followed by collection of the randomly oriented particles on a glass fiber substrate. Direct beam X ray transmission measurements were completed on both blank and loaded filters using CuKα radiation to provide mass absorption coefficients. This procedure [Davis, 1986] provides a check on the composition determined by the XRD-RIM procedure via comparison with computed sample mass absorption from either the elemental or compound matrix. Each filter was mounted on a circular spinner mount of a Norelco diffractometer and scanned at 1/2° 2θ min^{-1}. Radiation was CuKα raised to 40 kV, 20 mA, with β component removed by a graphite monochromator. Intensities were theta-compensated and corrected prior to data reduction for transparency and matrix effects and for variable beam coverage. These intensities I_i were then combined with reference constants κ_i in the relation

$$W_j = \left[\frac{\kappa_j}{I_j} \Sigma \frac{I_i}{\kappa_i} \right]^{-1} \quad (1)$$

where W_j is the weight fraction of component j.

All the W_i sum to unity; the relative weight proportions of all components are correct regardless of the presence of unidentified components or amorphous components present. In the latter case the quantity of amorphous components may be determined from mass absorption measurements [Davis and Johnson, 1986].

Computer processing of the intensity data leading to the solution of (1) includes a formal variance error propagation algorithm. Errors from the balance weighing operations, transmission measurements, reference constant measurements, intensity measurements (including count-rate statistics), and estimated errors in

TABLE 1. Samples Used in Study

Index	Sample
1	476.0
2	613.2
3	905.6
4	918.7
5	918.7
6	959.2
7	1293.7A
8	1293.7B
9	1424.2
10	1425.9
11	1699.3
12	1699.4
13	1841.0
14	1984.3
15	1984.3
16	1984.6
17	1984.9
18	2097.3
19	2227.0
20	2300.7
21	2301.3
22	2355.9
23	2356.1
24	2480.6
25	2484.7
26	2559.0
27	2683.0
28	2819.2
29	2819.3
30	2887.7A
31	2887.7B
32	2887.7C
33	2954.8
34	2954.8
35	3020.0-3021.2 Shale
36	3020.0-3021.2 EP

Index for Tables 2 and 3.
Indexed to depth in meters.

mass absorption from natural chemical species variations are all included in the method. Variance error in the component weight percent for individual mineral phases is as follows: quartz = 2-7, K-feldspar = 0.9-9, plagioclase = 0.2-4, chlorite = 0.3-5, illite = 6-12, biotite = 0.1-5, epidote = 0.5-4, calcite = 2-9, pyrite = 0.03-0.3, actinolite = 0.6-2, sphene = 0.2. Multiple analyses (m = 5) of samples indicate reproducibility equal to a standard deviation of between 0.4 and 3.7. The modal data derived from XRD-RIM have statistical errors equivalent to or lower than standard thin section point counting techniques. Interpretation of reproducibility tests reported by Chayes and Fairbairn [1953] indicates that the volume percentages of the major mineral could be determined by point counting techniques to within approximately 5% of the amount present. Due to the fine-grained character of many of the Salton Sea samples used in this study, this error for standard point counting technique will be large if it can be done at all.

We emphasize that the XRD-RIM technique does not discriminate between authigenic and allogenic grains of the same mineral phase. Discrimination must be made with an optical microscope or SEM. In addition, unlike optical modal analysis, which calculates mineral abundances by volume, XRD-RIM modal results are presented in weight percent.

Chemical analyses of subsamples of sample powders were obtained by X ray fluorescence (XRF), atomic absorption spectroscopy (AA), inductively coupled argon plasma spectroscopy (ICP), and flame emission spectroscopy (FE). A total of 28 major, minor, and trace elements for 29 samples were analyzed at Battelle Pacific Northwest Laboratories by energy-dispersive X ray fluorescence using pressed disks of rock powder. Major element analyses for three samples and error evaluations of XRF analyses were obtained by AA, FE, and ICP at SDSM&T. Sample solutions for these analyses were prepared using a modified lithium metaborate dissolution technique [Medlin et al., 1969] and a multiacid dissolution technique in pressurized teflon digestion vessels. In all whole rock analyses at both Battelle and SDSM&T, U.S. Geological Survey standards BCR-1, AGV-1, G2, and GSP1 were used to monitor accuracy and precision. CO_2 and H_2O were estimated based on the modal abundances of carbonate and hydrous mineral phases as determined by XRD-RIM. Mineral compositions were determined with a MAC-5 electron microprobe (SDSM&T), operated at an acceleration voltage of 15 kV and a sample current of 10 nA. Natural mineral standards were used. Data were reduced using the Bence and Albee [1968] method.

Petrography and Mineral Chemistry

Samples collected for this study contain authigenic minerals which range in grain size from <1 to >100 μm. Emphasis was placed on the sediments with an average grain size of <10 μm to illustrate the effectiveness of the combined XRD-RIM and XRF analysis and to provide quantitative petrological-mineralogical data for a suite of very fine grained lithologies in the core from this drill site. Several coarser grained sandstone samples adjacent to the shales were selected for comparison. Vein assemblages are not represented in this sample suite, although several samples were adjacent to a vein system. In addition to the characteristic sediments and their altered equivalents, epidote- or carbonate-rich pods were also studied (2887.7, 2484.7, 1984.7, and 1156.2 m).

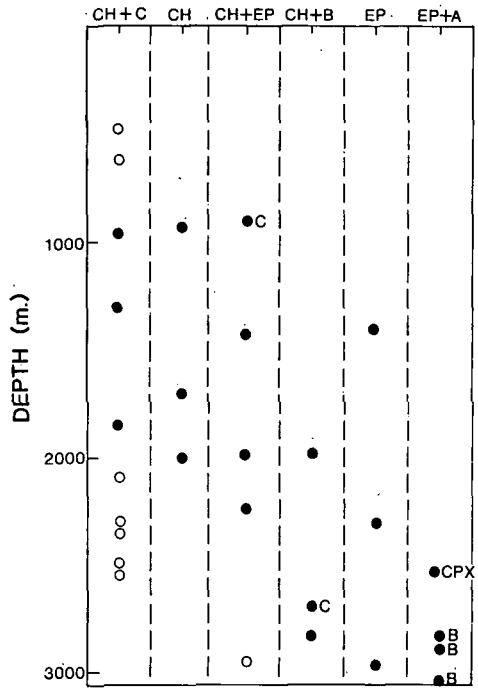

Fig. 1. Distribution of mineral assemblages downhole. CH-C, calcite-chlorite assemblages; CH, chlorite assemblages; CH-EP, chlorite + epidote assemblages; CH+B, chlorite + biotite assemblages; EP, epidote assemblages; EP-A, epidote + actinolite assemblages. Open circles are assemblages with illite. C, assemblages with calcite (not including CH-C); B, assemblages with biotite; CPX, assemblages with clinopyroxene.

Seven mineral assemblages have been identified in this sample suite: (1) chlorite + calcite + quartz + plagioclase ± K-feldspar ± illite between 476 and 2559 m, (2) chlorite + quartz + plagioclase + K-feldspar between 918.7 and 1984.3 m, (3) chlorite + epidote + quartz ± plagioclase ± calcite ± K-feldspar ± illite ± magnetite between 905.6 and 2954.8 m, (4) chlorite + biotite ± calcite + quartz + plagioclase + K-feldspar between 2700.0 and 2819.2 m, (5) epidote + quartz ± plagioclase between 1424.2 and 2954.8 m, (6) epidote ± actinolite + quartz ± biotite ± chlorite ± plagioclase ± K-feldspar ± anhydrite between 2819.3 and 3021.2 m and (G) epidote + clinopyroxene + actinolite + quartz at 2484.7 m. Distribution of assemblages downhole are illustrated in Figure 1. The modal abundance and compositional characteristics of each phase in our sample suite is presented below.

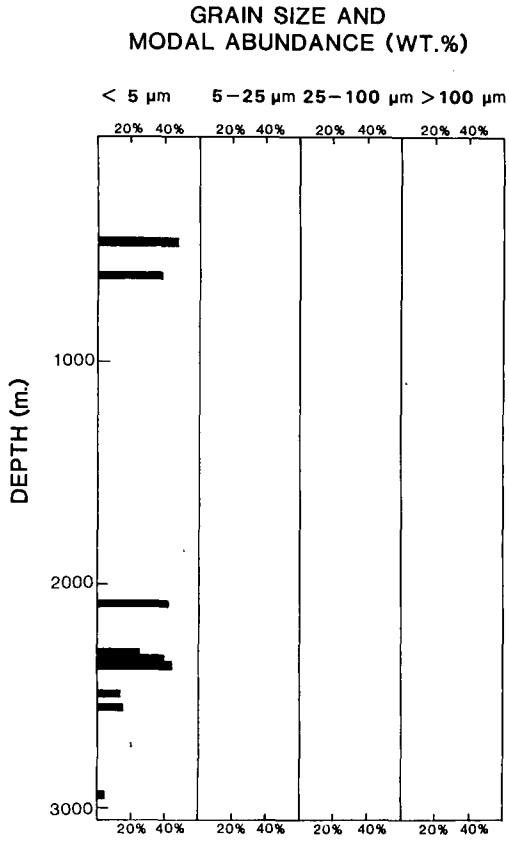

Fig. 2. Distribution and modal abundance of illite. Grain size refers to grain size of illite.

Illite

Illite was observed to be the dominant dioctahedral phyllosilicate in the sample suite. Glycol treatment of the samples demonstrated a lack of a significant amount of smectite, although Donaghe and Peacor [1987] observed mixed layer illite/smectite at depths less than 1222 m. The illite occurs only in samples with an average grain size of less than 5 μm, and its modal abundance ranges up to 48.9 wt % (Figure 2). Illite is present in the shallowest sample of this suite (48.90 wt %) and is observed down to 2954.8 m (4.0 wt %).

Potassium Feldspar

Potassium feldspar occurs in the sample suite from 476.0 to 3021.2 m in abundances up to 52.2 wt % (Figure 3). It has been observed in sediments with a range of grain sizes, although in the fine-grained (<10 μm) samples it only becomes a dominant phase at depths greater than 1676.4 m. In most of the sediments with grain size less than 5 μm, the modal abundances of potassium feldspar and illite vary inversely (compare Figures 2 and 3).

The composition of the potassium feldspar shows limited downhole variation, ranging from Or_{90} to Or_{98} (Figure 4). Typical analyses of potassium feldspar are presented in Table 3. More intriguing is the systematic decrease with depth of Si-Al ordering in of selected potassium feldspars (Figure 5). It must be emphasized that the X-ray diffraction data from which the structural state information was derived do not discriminate between allogenic and authigenic feldspar. The structural state information, therefore, is an average for the allogenic-authigenic feldspar mixture derived from broadened 204 and 060 peaks. This systematic increase in ΔAl-Si disorder with depth suggests that either disorder of allogenic feldspar is being increased with depth or, more probably, higher proportions of disordered authigenic potassium feldspar are being added to the assemblage. Similar variations in structural state have been observed by McDowell [1986] at other Salton Sea sites.

Plagioclase

The modal abundance of plagioclase in the sample suite ranges from 0 wt % to approximately 58 wt % (Table 2). Samples with plagioclase are consistently epidote-rich (24.6-83.1 wt %) indicating derivation from a carbonate-rich sediment. Typical analyses of plagioclase are presented in Table 3. The composition of plagioclase is nearly end-member albite at depths less than 1828.8 m (Figure 4). At depths greater than 1828.8 m the plagioclase is more calcic. At depths exceeding 2865.1 m, plagio-

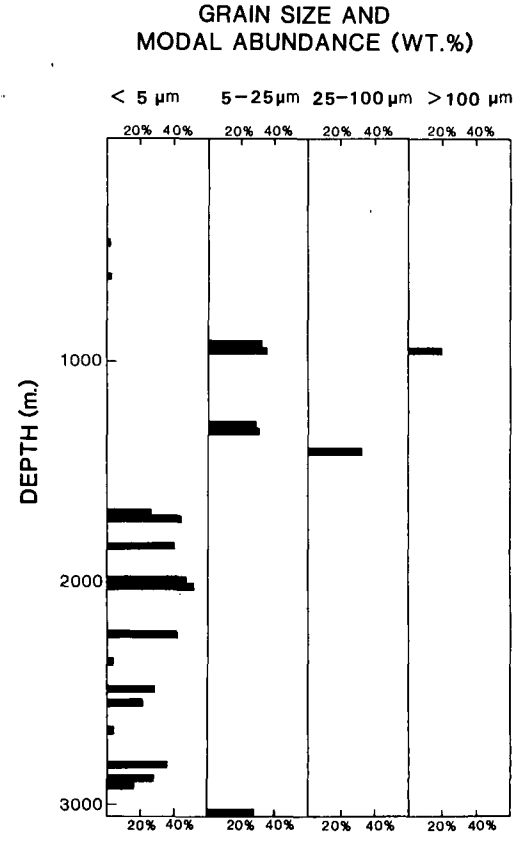

Fig. 3. Distribution and modal abundance of potassium feldspar. Grain size refers to grain size of potassium feldspar.

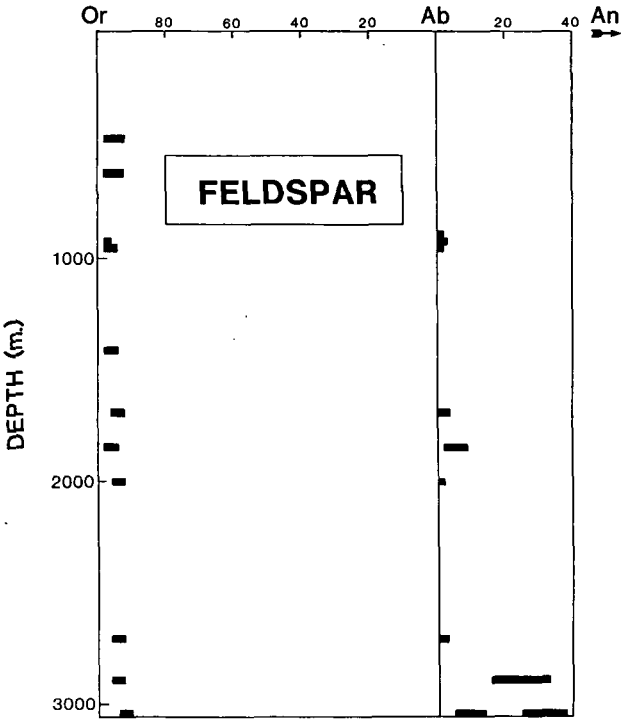

Fig. 4. Composition of feldspars.

clase displays some compositions more calcic than An_{20}. In samples below the 3017.5-m level, a three-feldspar assemblage was observed: potassium feldspar (~Or_{91}), albite-sodic oligoclase (~An_{5-14}) and calcic oligoclase-andesine (An_{25-37}).

Calcite

Calcite occurs in a wide range of grain sizes (<5 to > 200 μm) from the shallowest sample (476 m) to 2683.0 m (Figure 6). Up to 17.2 wt % calcite has been documented in the sample suite, although higher modal calcite in the sediments is indicated by the lithologic core logs [Mehegan et al., 1986]. Calcite commonly occurs with chlorite and to a lesser extent with epidote (905.6 m) and biotite (2683.0 m). It has not been observed to occur with actinolite or diopside.

Chlorite

Chlorite occurs in chlorite + calcite + illite assemblages at shallow depths (476.0 m), and although sparse, it is associated with biotite and epidote + biotite + actinolite-bearing assemblages at depths between 2743.2 and 3021.2 m. Between 476.0 and 2743.2 m the modal abundance of chlorite shows considerable variation (Figure 7). Within this range chlorite can compose up

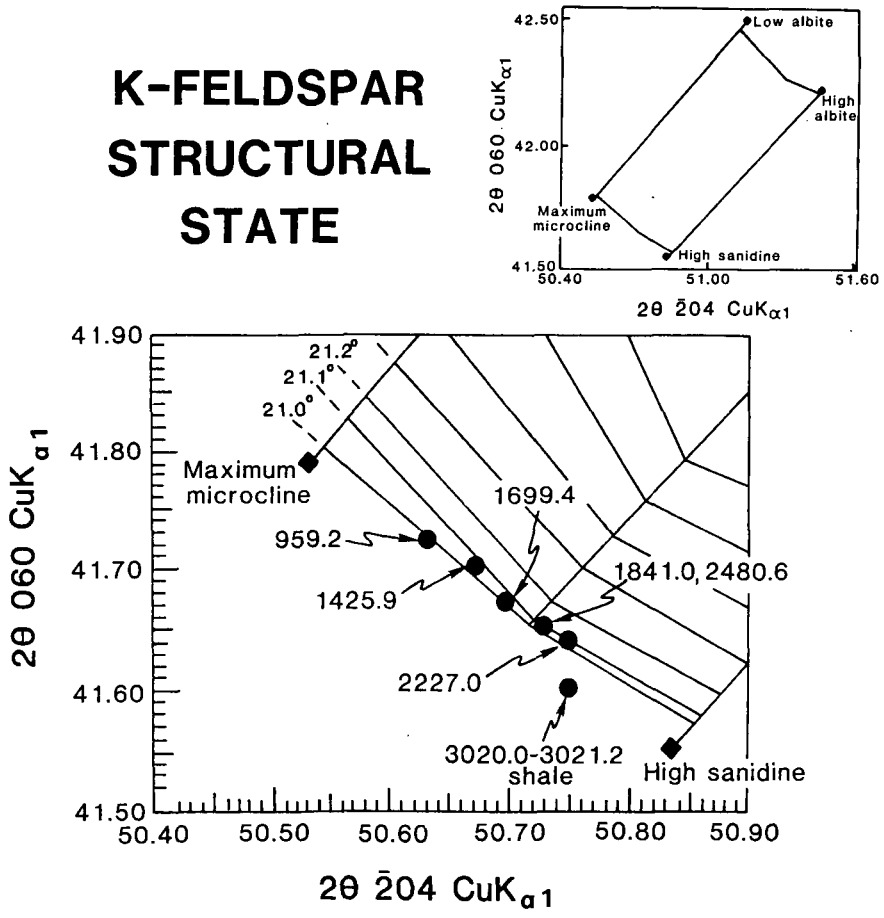

Fig. 5. Bulk K-feldspar structural state represented in a plot of 2θ 060 $CuK_{\alpha 1}$ versus 2θ 204 $CuK_{\alpha 1}$.

TABLE 2. Modes of Samples From Salton Sea Core

	1	2	3	4	5	6	7	8	9	10	11	12	13	14	15	16	17	18
Illite	48.9	37.5	—	—	—	—	—	—	—	—	—	—	—	—	—	—	—	42.7
Chlorite	14.4	13.1	1.4	35.9	15.7	5.5	2.7	4.8	—	4.2	27.0	23.4	13.8	16.7	20.4	2.5	5.3	7.8
Calcite	10.0	17.2	3.3	—	—	1.5	7.8	11.2	—	—	—	—	5.1	—	—	—	—	15.1
Anhydrite	—	—	—	—	—	—	—	—	—	—	—	—	—	—	—	—	—	—
Epidote	—	—	2.5	—	—	—	—	—	75.5	9.7	—	—	—	—	—	24.6	22.0	—
Sphene	—	—	—	—	—	—	—	—	—	—	—	—	—	—	—	—	—	—
Biotite	—	—	—	—	—	—	—	—	—	—	—	—	—	—	—	0.9	—	—
Actinolite	—	—	—	—	—	—	—	—	—	—	—	—	—	—	—	—	—	—
Diopside	—	—	—	—	—	—	—	—	—	—	—	—	—	—	—	—	—	—
Quartz	22.0	24.5	64.6	30.8	32.2	68.7	48.3	35.4	15.6	52.4	30.0	11.6	21.3	18.0	11.6	69.8	71.0	22.8
Plagioclase	2.3	4.7	27.5	9.7	15.0	3.0	10.9	11.8	—	1.4	15.2	17.9	21.3	17.0	15.8	—	—	10.5
K-feldspar	2.2	2.7	—	33.1	36.2	6.2	30.0	35.4	—	31.1	25.9	45.7	38.3	48.2	52.2	—	—	—
Magnetite	—	—	—	—	—	—	—	—	—	—	—	—	—	—	—	2.1	1.7	—
Pyrite	0.2	0.3	0.6	0.4	0.5	0.2	1.3	1.5	8.9	1.2	1.9	1.4	0.2	—	—	—	—	1.0
Halite	—	—	—	—	0.6	—	—	—	—	—	—	—	—	—	—	—	—	—

	19	20	21	22	23	24	25	26	27	28	29	30	31	32	33	34	35	36
Illite	—	26.4	—	40.5	46.7	14.0	—	17.7	—	—	—	—	—	—	4.0	—	—	—
Chlorite	25.6	18.6	—	13.0	13.9	10.8	—	7.8	14.7	4.7	—	—	—	—	10.3	—	0.5	—
Calcite	—	3.6	—	17.2	12.4	9.3	—	4.5	12.0	—	—	—	—	—	—	—	—	—
Anhydrite	—	—	—	—	—	—	—	—	—	—	17.0	—	—	—	—	—	—	—
Epidote	4.6	—	28.9	—	—	—	53.0	—	—	—	72.2	3.7	83.1	18.2	6.7	13.8	4.4	38.2
Sphene	—	—	1.2	—	—	—	—	—	—	—	—	—	—	—	—	—	—	1.5
Biotite	—	—	—	—	—	—	—	—	0.4	5.6	1.3	17.9	2.7	22.7	—	—	5.8	—
Actinolite	—	—	—	—	—	—	4.0	—	—	—	8.9	1.2	5.5	3.9	—	—	5.0	12.6
Diopside	—	—	—	—	—	—	41.6	—	—	—	—	—	—	—	—	—	—	—
Quartz	12.1	25.1	70.0	16.3	17.7	15.7	1.4	21.8	46.5	14.0	0.7	0.8	8.8	10.3	21.3	32.6	27.5	47.6
Plagioclase	15.6	26.1	—	10.4	8.5	21.5	—	26.0	20.8	38.1	—	7.2	—	28.2	57.8	53.6	28.0	—
K-feldspar	42.1	—	—	2.5	—	27.3	—	21.8	5.4	36.3	—	9.4	—	16.7	—	—	28.6	—
Magnetite	—	—	—	—	—	—	—	—	—	—	—	—	—	—	—	—	—	—
Pyrite	—	0.2	—	—	0.8	1.2	—	0.2	0.1	1.3	—	—	—	—	—	—	—	—
Halite	—	—	—	—	—	—	—	—	—	—	—	—	—	—	—	—	—	—

TABLE 3a. Representative Analyses of Minerals From the SSSDP Well: Feldspar

	6	6	35	35	35
SiO_2	64.18	68.02	63.89	68.82	59.79
Al_2O_3	19.12	20.01	18.97	19.32	25.93
Fe_2O_3	0.00	0.08	0.14	0.00	0.20
CaO	0.02	0.21	0.03	0.45	6.84
Na_2O	0.36	11.55	0.81	11.90	7.71
K_2O	16.52	0.11	15.26	0.27	0.26
Total	**100.20**	**99.98**	**99.10**	**100.76**	**100.73**
Si	2.966	2.973	2.975	2.991	2.644
Al	1.042	1.031	1.036	0.988	1.351
Total	**4.008**	**4.004**	**4.011**	**3.979**	**3.995**
Ca	0.000	0.010	0.000	0.020	0.323
Na	0.032	0.977	0.073	0.014	0.660
K	0.974	0.003	0.904	1.002	0.014
Total	**1.006**	**0.990**	**0.977**	**1.036**	**0.997**

to 36 wt % of the altered sediment. At depths greater than 2743.2 m chlorite never exceeds 11 wt % in this sample suite.

The composition of chlorite (Table 3) varies considerably. The Fe/(Fe+Mg) ratio varies from approximately 0.50 to 0.45 at relatively shallow depths to approximately 0.23 to 0.33 near the base of the drill hole (Figure 8). This apparent systematic variation in chlorite composition with depth appears, however, to reflect bulk composition rather than metamorphic grade (Figure 9).

Epidote

Unlike the associated vein mineral assemblages, epidote occurs sparingly in the authigenic mineral assemblages down to depths of greater than 1371.6 m (Figure 10). At shallower depths, epidote occurs primarily in low abundance (2.5 wt %) in the sediments with an average grain size of greater than 50 μm. At depths greater than 1371.6 m and in finer-grained sediments (<25 μm), the epidote in the calcium-rich lithologies can exceed 70%.

Typical analyses of epidote are shown in Table 3. The variation in the ratio $Fe^{3+}/(Fe^{3+}+Al)$ in the epidotes from this sample suite is shown in Figure 11. In the samples analyzed for this study, $Fe^{3+}/(Fe^{3+}+Al)$ varies from 0.40 to 0.18. There appears to be no systematic variation in epidote composition with depth. This could, however, be partially disguised by the dependency of initial epidote crystallization on grain size/pore space. While the epidote in sediments with grain size >50 μm shows a possible decrease in $Fe^{3+}/(Fe^{3+}+Al)$, the epidote in sediments with grain size <25 μm shows no or limited variation in $Fe^{3+}/(Fe^{3+}+Al)$ over an interval of 1066.8 m. The variation in $Fe^{3+}/(Fe^{3+}+Al)$ within individual samples is more systematic.

Epidotes in vein assemblages have higher $Fe^{3+}/(Fe^{3+}+Al)$ than the sediments they cut. In addition, in large discrete epidote grains in veins (1984.3 m), $Fe^{3+}/(Fe^{3+}+Al)$ increases from core to rim. However, in discrete epidote grains in the sediments (1425.9, 2954.8, and 3020-3021.2 m EP), $Fe^{3+}/(Fe^{3+}+Al)$ decreases from core to rim. Irregular masses of epidote show irregular variation in the $Fe^{3+}/(Fe^{3+}+Al)$ within individual samples. Different lithologies at the same depth can have epidote with identical compositions. As an example, sample 3020.0-3021.2 m shale ($Fe_2O_3/(Fe_2O_3+Al_2O_3)$ = 0.23, CaO = 4.10 wt %, 4.4 wt % epidote) and sample 3020.0-3021.2 m EP ($Fe_2O_3/(Fe_2O_3+Al_2O_3)$ = 0.43, CaO = 15.0 wt %, 38.2 wt % epidote) both have epidote compositions with $Fe^{3+}/(Fe^{3+}+Al)$ of approximately 0.30. Bird et al. [1987] observed an increase in the extent of Fe^{3+} ordering in the M(3) site of epidote with

TABLE 3b. Analyses for Chlorite

	1	2	6	11	11	13	26	33	35
SiO_2	32.05	31.85	28.78	30.25	27.33	27.13	30.13	29.49	31.59
TiO_2	0.10	0.08	0.05	0.07	0.09	0.05	0.07	0.06	0.14
Al_2O_3	21.83	21.38	20.31	19.75	19.85	23.00	22.25	19.31	19.50
FeO	17.00	19.50	22.77	18.20	20.21	21.40	13.52	13.49	16.90
MnO	0.13	0.77	0.71	0.47	0.55	0.34	0.11	0.19	0.17
MgO	15.90	13.10	15.34	16.61	18.09	16.43	19.21	24.22	16.98
CaO	0.13	0.11	0.07	0.10	0.12	0.11	0.90	0.05	0.16
Na_2O	0.14	0.27	0.13	0.14	0.83	0.07	0.49	0.02	0.25
K_2O	0.85	0.85	0.00	1.23	0.09	0.00	0.25	0.56	1.61
Total	**88.13**	**87.91**	**88.16**	**86.82**	**87.16**	**88.53**	**86.93**	**87.39**	**87.30**
Si	3.168	3.208	2.956	3.093	2.830	2.752	2.982	2.922	3.180
Al	0.832	0.792	1.044	0.907	1.170	1.248	1.018	1.078	0.820
Total	**4.000**	**4.000**	**4.000**	**4.000**	**4.000**	**4.000**	**4.000**	**4.000**	**4.000**
Fe	1.407	1.640	1.956	1.554	1.748	1.817	1.119	1.117	1.422
Mn	0.012	0.067	0.062	0.043	0.050	0.027	0.009	0.015	0.012
Mg	2.339	1.967	2.351	2.531	2.793	2.485	2.837	3.576	2.548
Al	1.709	1.746	1.416	1.472	1.251	1.504	1.964	1.175	1.494
Ti	0.009	0.006	0.003	0.006	0.009	0.070	0.003	0.003	0.008
Total	**5.476**	**5.426**	**5.788**	**5.606**	**5.851**	**5.903**	**5.932**	**5.886**	**5.484**
Ca	0.012	0.012	0.012	0.012	0.012	0.008	0.093	0.003	0.015
Na	0.024	0.048	0.024	0.024	0.162	0.011	0.093	0.003	0.047
K	0.107	0.109	0.000	0.160	0.012	0.000	0.028	0.069	0.204
Total	**0.143**	**0.169**	**0.036**	**0.196**	**0.186**	**0.019**	**0.214**	**0.075**	**0.266**

TABLE 3c. Analyses for Epidote

	10	10	15	15	15	36	36
SiO_2	38.90	39.26	37.75	37.15	38.09	37.86	38.04
TiO_2	0.24	0.04	0.06	0.23	0.11	0.04	0.03
Al_2O_3	18.55	20.52	24.30	22.68	25.41	21.43	21.88
FeO	19.24	16.79	13.37	15.66	12.08	16.17	14.04
MnO	0.20	0.01	0.51	0.00	0.34	0.14	0.10
MgO	0.06	0.02	0.11	0.05	0.14	0.09	0.26
CaO	22.10	21.88	22.73	23.17	22.64	23.31	23.46
Total	**99.29**	**98.52**	**98.83**	**98.94**	**98.81**	**99.04**	**97.81**
	core	rim	vein core	vein rim		core	rim
Si	3.105	3.121	2.975	2.951	2.983	3.010	3.043
Al	--	--	0.025	0.049	0.017	--	--
Total	**3.105**	**3.121**	**3.000**	**3.000**	**3.000**	**3.010**	**3.043**
Al	1.745	1.923	2.233	2.076	2.329	2.010	2.064
Fe^{3+}	1.154	1.003	0.793	0.935	0.712	0.968	0.846
Total	**2.899**	**2.926**	**3.026**	**3.011**	**3.041**	**2.978**	**2.910**
Mn	0.014	0.000	0.033	0.000	0.024	0.010	0.005
Mg	0.010	0.000	0.019	0.010	0.009	0.010	0.029
Ti	0.014	0.002	0.002	0.014	0.007	0.002	0.002
Ca	1.889	1.863	1.918	1.970	1.901	1.988	2.010
Total	**1.927**	**1.865**	**1.972**	**1.994**	**1.941**	**2.010**	**2.046**

increasing depth. This contrasts with the Si-Al ordering observed in the K-feldspar.

Biotite

Only minor amounts of biotite (<1 wt %) have been observed at depths shallower than 2804.2 m (1984.6 m and 2683.0 m). These biotites, however, may be allogenic in nature. High modal abundances of biotite (>20 wt %) occur at depths greater than 2804.2 m and in sediments with an average grain size of less than 10 μm. In coarse sediments the biotite content is less than 6.1 wt % (Figure 12).

TABLE 3d. Analyses for Biotite and Actinolite

	28	35	35	31
SiO_2	36.68	37.31	38.10	54.44
TiO_2	2.68	0.25	2.80	0.07
Al_2O_3	18.58	15.15	16.02	4.07
FeO	15.18	15.30	15.81	7.14
MnO	0.12	0.20	0.22	0.47
MgO	13.10	15.33	11.71	20.04
CaO	0.00	0.00	0.00	10.70
Na_2O	0.06	0.12	0.08	0.10
K_2O	9.32	10.36	10.07	1.14
Total	**95.72**	**94.02**	**94.81**	**98.17**
Si	2.716	2.844	2.870	7.596
Al	1.284	1.156	1.130	0.404
Total	**4.000**	**4.000**	**4.000**	**8.000**
Ti	0.149	0.014	0.158	0.008
Al	0.338	0.206	0.291	0.267
Fe	0.939	0.975	0.996	0.838
Mn	0.009	0.014	0.014	0.059
Mg	1.446	1.740	1.313	4.167
Total	**2.881**	**2.949**	**2.772**	**5.339**
Ca	0.000	0.000	0.000	1.602
Na	0.009	0.018	0.009	0.034
K	0.881	1.008	0.969	0.201
Total	**0.890**	**1.026**	**0.978**	**1.837**

Biotite is 28, 35, and 35; actinolite is 31.

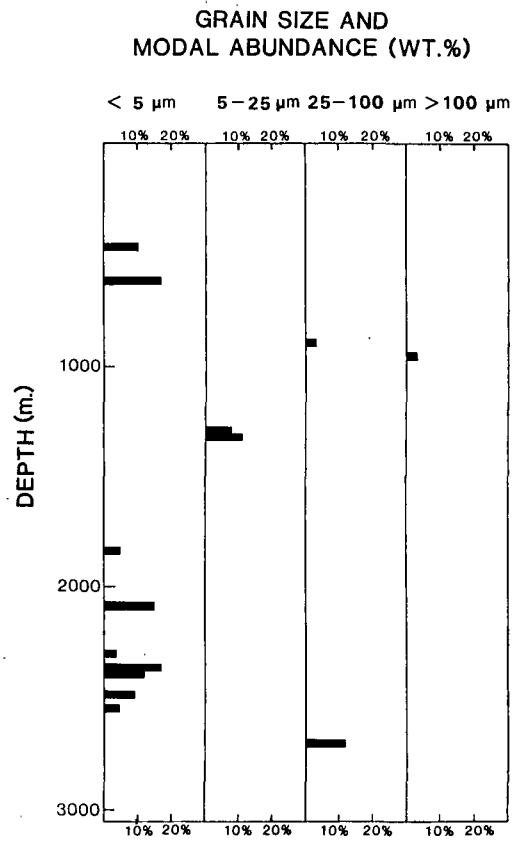

Fig. 6. Distribution and modal abundance of calcite. Grain size refers to grain size of calcite.

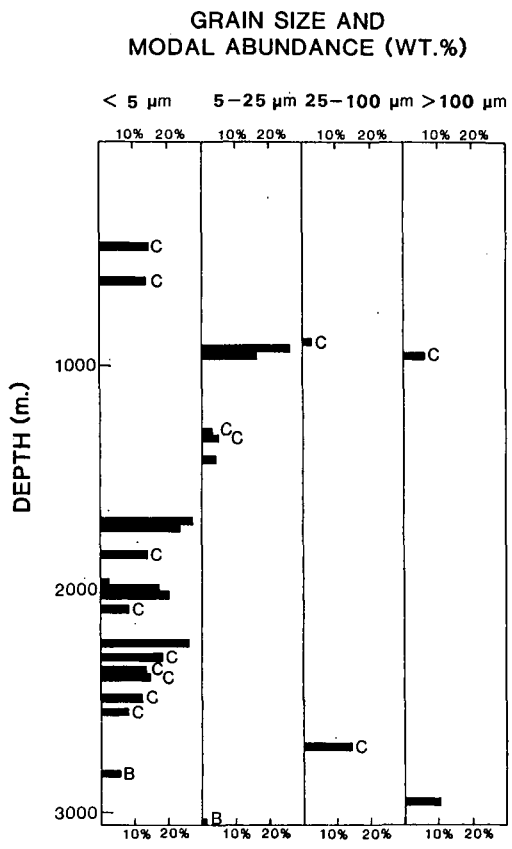

Fig. 7. Distribution and modal abundance of chlorite. C, calcite-bearing assemblages; B, biotite-bearing assemblages. Grain size refers to grain size of chlorite.

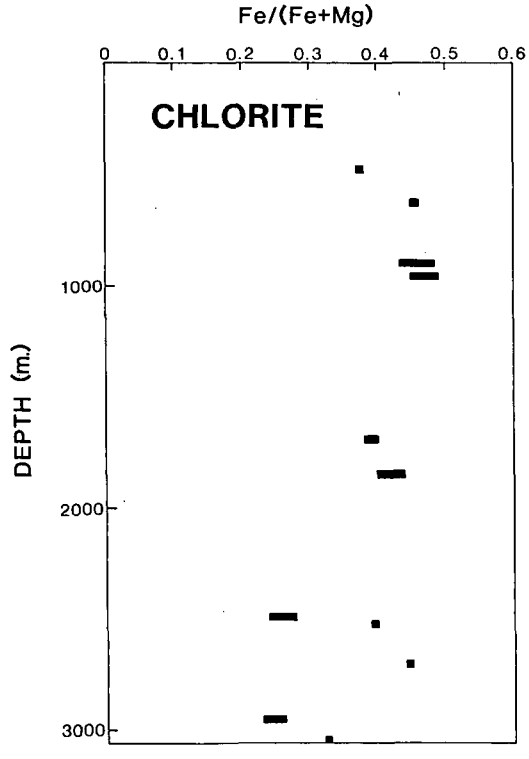

Fig. 8. Downhole variation in the Fe/(Fe+Mg) in chlorite.

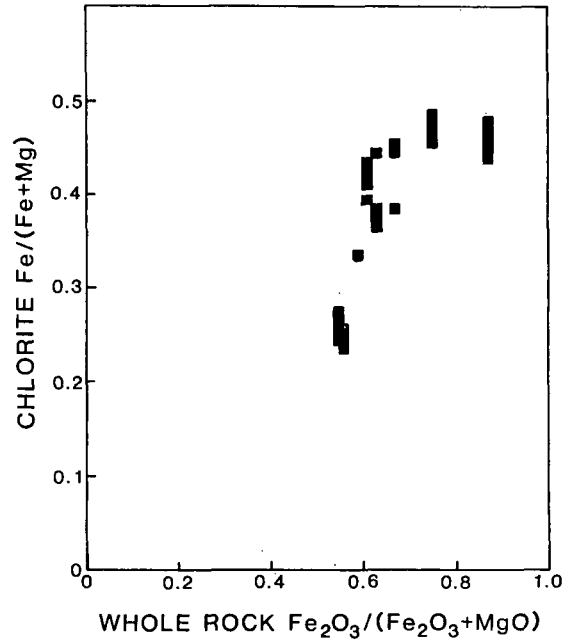

Fig. 9. Relationship between Fe/(Fe+Mg) in chlorite and the $Fe_2O_3/(Fe_2O_3+MgO)$ in the whole rock.

Fe/(Fe+Mg) in biotite ranges from 0.20 to 0.47. Variation in Fe/(Fe+Mg) with depth between 2743 and 3048 m is illustrated in Figure 13. Sample 2887.7 shows two composition populations for biotite. The Fe-poor biotite (which also has high Si and lower ^{IV}Al and ^{VI}Al) may be an allogenic biotite unequilibrated with the alteration mineralogy. Typical analyses of biotite are presented in Table 3.

Actinolite

Actinolite first occurs in the sample suite in epidote + clinopyroxene pods at 2484.7 m. The surrounding shale (2355.9, 2356.1, 2480.6, 2559.0, and 2683.0 m) is calcite-bearing, and actinolite is not observed. Actinolite occurs in both epidote pods and associated altered shale and sandstone at depths greater than 2743.2 m. The modal abundance of actinolite is presented in Figure 14.

Microprobe analyses and preliminary SEM observations indicate that the actinolite may consist of patchy intergrowths of actinolite + hornblende (3020.0-3021.2 m EP). Such assemblages were observed by Cho et al. [1987] at depths of 3120 m. In addition, Yau et al. [1986] noted the association of amphibole and pyriboles in other Salton Sea drill sites. Of the available amphibole analyses obtained from the sample suite only the actinolite analyses proved satisfactory based on the site occupancy criteria of Robinson et al. [1982]. A typical analysis is presented in Table 3. The actinolite exhibits very low degrees of A-site and ^{IV}Al substitution (Figure 15). In addition, the Fe/(Fe+Mg) ratio ranges from approximately 0.18 to 0.22 between 2743.2 and 2895.6 m to approximately 0.31 to 0.35 between 2987.0 and 3048 m (Figure 15).

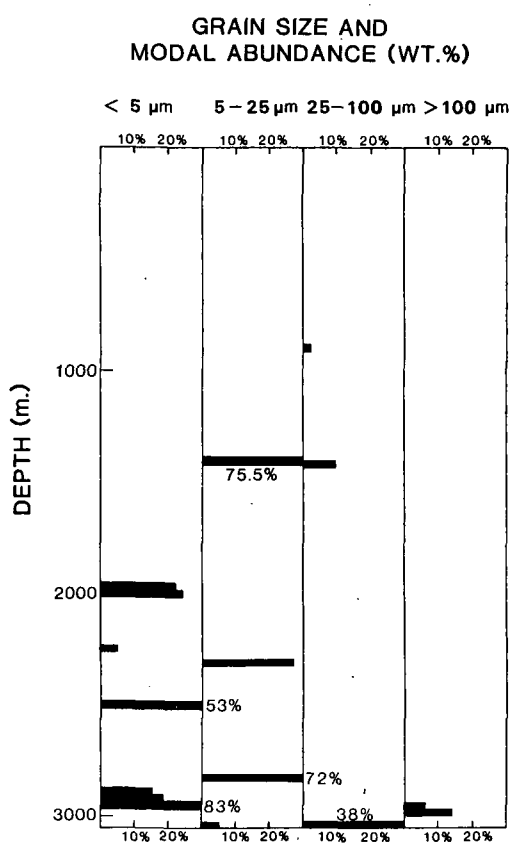

Fig. 10. Distribution and modal abundance of epidote. Grain size refers to grain size of epidote.

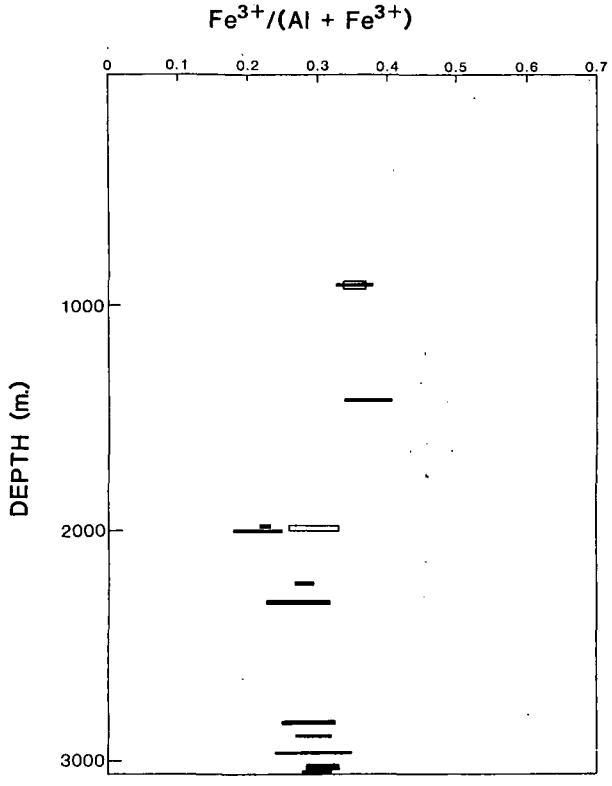

Fig. 11. Downhole variation in $Fe^{3+}/(Al+Fe^{3+})$ in epidote. Solid lines are epidote in sediment. Open lines are epidote in associated veins.

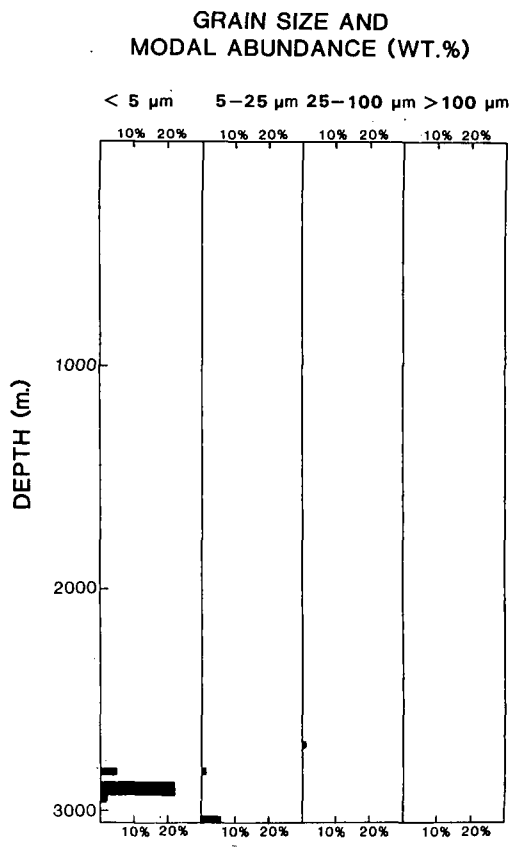

Fig. 12. Distribution and modal abundance of biotite. Grain size refers to grain size of biotite.

Whole Rock Chemistry

The major, minor, and trace element chemistry of this sample suite is presented in Table 4. Overall, the samples show a wide range in bulk rock chemistry. Comparisons of similar lithologies, however, show a much more limited compositional range. As an example, shales with an average grain size of less than 10 μm and containing low abundances of Ca-bearing minerals (i.e. calcite and epidote) have bulk compositions with SiO_2 = 56-62 wt %, Al_2O_3 = 13.4-16.9 wt %, CaO = 1.25-2.05 wt %, Nb = 13.1-15.9 ppm, Rb = 120-205 ppm, Sr = 110-250 ppm, and Zr = 140-170 ppm.

Correlation analyses relating mineralogy to bulk rock composition show a high degree of correlation (correlation coefficient greater than

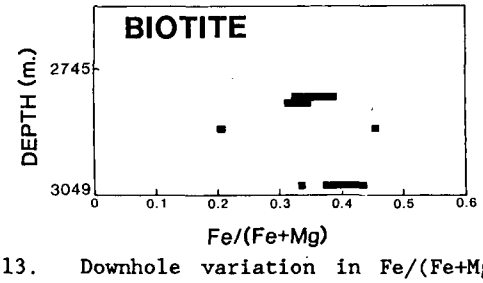

Fig. 13. Downhole variation in Fe/(Fe+Mg) in biotite.

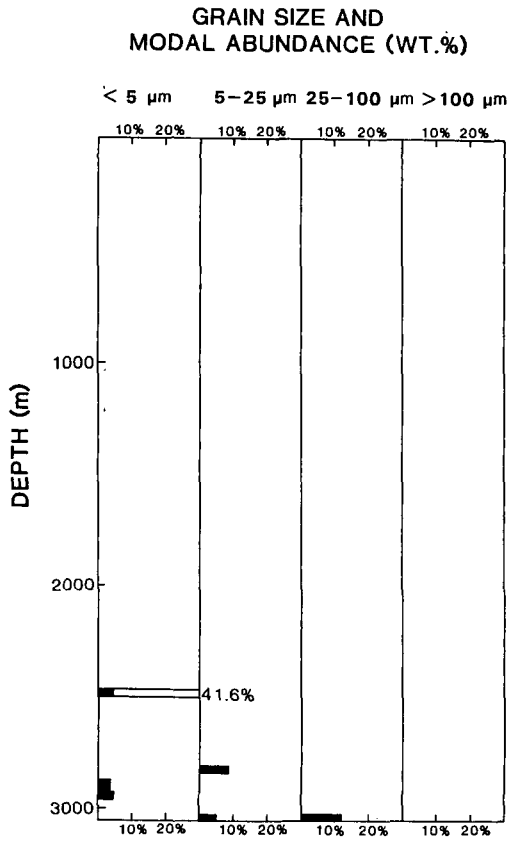

Fig. 14. Distribution and modal abundance of actinolite. Open line is modal abundance of clinopyroxene. Grain size refers to grain size of actinolite.

0.75) for the following: (1) quartz with SiO_2 (+), Al_2O_3 (-), MgO (+), (2) potassium feldspar with K_2O (+), (3) calcite (between 476.0 and 2,683.1 m) with CaO and CO_2, and (4) epidote (between 2653.1 and 3021.2 m) with CaO and Fe_2O_3. Elements of particular interest which show a high degree of correlation (correlation coefficient) are (1) Cl and Br, (2) V and Ga, (3) Rb and K_2O, (4) SiO_2 and MgO, (5) SiO_2 and Ga, and (6) Zn and Nb.

Discussion

General Discussion

The distribution of authigenic minerals in this sample suite and in other SSSDP studies [Donaghe and Peacor, 1987; Bird et al., 1987; Kramer and McDowell, 1987; Cho et al., 1987] essentially define three distinct metamorphic zones in the California State 2-14 well: chlorite-calcite zone, biotite zone, and actinolite zone (also referred to as clinopyroxene zone). Similar authigenic mineral zones have been reported from the Magmamax and Elmore wells [Muffler and White, 1969; McDowell and Elders, 1980]. As the reactions defining the authigenic mineral assemblage probably occur through the dissolution of reactant and the precipitation of products [Yau et al., 1986], the abundances of pore space-fracture systems and fluid composition are critical to the initiation and progress of a reaction. In addition, the original bulk composition and grain size of the sediment is intimately involved in the initiation and progress of a reaction.

Many of the authigenic mineral-producing reactions defined in the sediments in the Salton Sea geothermal area have been based primarily on textural relationships in the metasandstones and semiquantitative and qualitative optical and X ray diffraction estimates of the modal mineralogy. A major objective of this study was to complement these previous investigations by comparing the variation in quantitative modal mineralogy of a series of shales with similar bulk compositions to define further the mineral reactions responsible for the authigenic mineral assemblages in our sample suite. The form of reactions calculated in this manner, although disguising the actual dissolution-precipitation processes, does account for the observed mineral assemblages. These reactions, quantitative mineral assemblages, and whole rock chemistries can then be used to evaluate the influence of bulk rock characteristics (i.e., grain size, composition) on mineral reactions. In addition, geochemical modifications of the sediments observed by McDowell [1987] can be evaluated in the light of bulk composition and mineral reactions.

Variations in the Modal Mineralogy of Selected Bulk Compositions

The mineral assemblage of four different bulk compositions were compared. Muffler and White [1969] and Yau et al. [1986] suggested that many of the mineralogical transformations within the Salton Sea sediments only require that the system

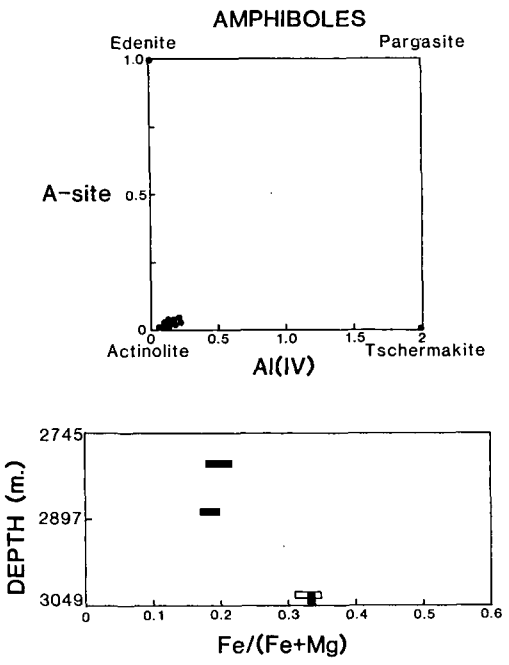

Fig. 15. (a). Composition of amphiboles plotted in A-site versus Al(IV). (b). Fe/(Fe+Mg) in amphibole.

TABLE 4. Chemical Analyses of Samples From Salton Sea Core

	1	2	3	4	5	6	7	8	10	11	12	13	14	15	16	18
SiO_2	55.0	51.0	80.3	60.3	63.0	81.2	63.5	64.9	75.9	62.0	56.0	59.0	58.5	59.0	69.8	51.6
TiO_2	0.63	0.60	0.20	0.94	0.45	0.21	0.64	0.53	0.40	0.65	0.65	0.61	0.70	0.70	0.60	0.60
Al_2O_3	16.6	14.1	6.0	13.5	13.5	5.0	12.5	12.4	8.6	13.4	16.9	14.5	16.5	16.9	10.0	15.5
Fe_2O_3+	5.2	4.8	1.6	7.5	5.4	2.1	2.8	2.3	4.3	7.6	6.5	4.3	4.0	4.3	7.1	4.5
MnO	0.11	0.26	0.05	0.27	0.22	0.08	0.08	0.06	0.07	0.16	0.13	0.08	0.10	0.10	0.13	0.06
MgO	3.00	2.60	0.22	2.80	1.80	0.70	1.40	1.10	0.62	3.60	3.10	2.75	2.70	2.70	2.05	3.00
CaO	4.90	7.80	2.00	1.40	1.35	2.10	5.40	5.50	2.83	1.32	1.25	4.00	1.80	2.05	9.10	8.00
Na_2O	0.75	1.00	3.20	2.00	2.20	0.80	2.00	1.80	0.64	2.10	2.50	2.65	2.00	2.25	0.25	1.70
K_2O	3.91	4.10	0.60	5.87	7.00	2.96	6.70	6.70	4.70	5.20	9.40	6.25	9.20	8.80	0.70	3.60
H_2O*	5.98	4.82	0.15	3.95	1.73	0.61	0.30	0.53	0.63	2.97	2.57	1.52	1.84	2.24	0.75	4.70
CO_2*	4.35	7.48	1.44	—	—	0.65	3.39	4.87	—	—	—	2.22	—	—	—	6.57
SO_3	0.11	0.12	0.85	0.19	0.39	0.14	1.8	1.1	1.93	1.82	1.70	<0.07	<0.07	<0.07	<0.07	1.10
Cl	0.09	0.15	0.05	0.82	0.56	0.48	0.26	0.12	0.22	0.30	0.14	0.17	0.31	0.24	0.30	0.05
Total	**100.63**	**98.83**	**96.66**	**99.54**	**97.60**	**97.03**	**100.77**	**101.91**	**100.84**	**101.12**	**100.84**	**98.05**	**97.65**	**99.28**	**100.78**	**100.98**
As	7.8	4.9	1.8	3.7	<2.0	2.1	21.0	17.6	4.4	92	12	2.7	4.2	3.2	6.9	13.3
Ba	460	520	130	1200	930	540	990	1300	1120	1900	1900	1000	177	440	<10	1000
Br	<1	<1	<1	7.7	4.1	3.1	<1	<1	2.1	2.2	2.4	<1	2.0	2.2	3.6	<1
Ce	80	70	26	23	60	40	60	23	43	25	80	73	61	42	51	50
Cr	45	50	74	120	85	50	60	75	70	135	80	60	80	80	140	100
Cu	26.6	11	19.3	10.3	11.6	10.5	13.0	14.5	11.6	26.6	13.5	29.1	160.0	20.0	16.7	90
Ga	19.6	19.0	7.4	14.1	10.7	4.0	9.0	8.5	8.5	14.4	12.0	19.0	16.1	16.0	15.2	19.4
La	61	37	23	36	40	20	41	34	28	30	40	47	49	23	40	35
Mo	<2	<2	<2	<2	2	79	<2	2.3	3.2	12.8	4.5	2.7	3.0	<2	3.5	2.2
Nb	40	15	270	23	8	6	14.6	16.7	140	16.2	13.1	41.8	15.1	15.9	51.1	19.3
Ni	28	18	11	31	25	14	23	18	19	50	50	40	34	32	51	28
Pb	13.6	11.7	4.5	11.0	14.0	7.6	21.0	11.7	6.3	25.5	8.2	5.1	4.6	6.0	<3	20.0
Rb	200	200	11.7	170	200	60	175	180	91	120	190	165	205	200	63.3	160
Sr	80	135	40	100	110	45	350	370	230	150	110	160	250	240	430	450
U	<7	7.7	<3	<6	<6	<3	8.6	<7	<3	<6	<6	7.2	<6	<6	<3	<6
V	130	120	<20	90	<40	<30	80	50	<30	<40	65	80	100	70	80	110
Y	30.4	27.0	14.3	34.0	31.0	13.0	28.0	23.0	19.0	23.4	16.2	27.0	32.5	28.5	30	26.1
Zn	73	93	580	180	145	52	230	46	39	140	100	75	86	84	95	80
Zr	160	155	140	375	130	170	220	255	200	170	140	165	160	150	210	130

TABLE 4. (continued)

	19	20	21	22	23	24	26	27	28	29	30	31	32	33	34	35	36
SiO_2	57.2	56.0	68.0	50.7	51.0	52.4	57.5	62.1	57.0	36.2	50.3	44.2	51.4	67.1	71.5	63.9	59.9
TiO_2	0.6	0.6	0.5	0.6	0.6	0.6	0.6	0.4	0.65	0.44	0.59	0.49	0.60	0.41	0.17	0.60	0.53
Al_2O_3	16.2	16.5	11.6	15.8	16.0	14.6	16.8	10.1	17.4	11.0	16.5	18.5	16.3	13.3	12.0	13.9	10.0
Fe_2O_3	7.2	4.7	7.5	4.5	5.6	6.1	4.2	4.9	4.1	12.4	5.4	10.2	5.8	2.7	3.6	4.3	11.4
MnO	0.17	0.08	0.10	0.06	0.06	0.08	0.06	0.09	0.04	0.18	0.13	0.21	0.12	0.03	0.04	0.03	0.10
MgO	4.10	2.90	0.25	3.30	3.70	4.90	2.60	2.90	3.90	5.24	9.65	3.23	8.98	2.10	0.20	3.10	2.65
CaO	1.85	5.88	12.60	7.60	6.15	6.30	4.60	7.30	5.00	21.0	6.92	21.0	7.87	2.30	5.60	4.10	15.0
Na_2O	2.50	2.70	0.16	2.00	1.55	2.30	3.00	2.35	3.30	0.40	1.90	0.16	1.76	6.35	4.60	2.75	0.16
K_2O	6.32	3.10	0.09	3.40	3.60	3.71	3.60	1.10	4.10	0.30	5.13	0.78	4.93	0.62	0.15	4.62	0.07
H_2O*	2.90	4.42	0.53	5.08	5.73	2.45	2.45	1.63	0.74	1.53	0.81	1.71	1.31	1.61	0.25	0.95	0.47
CO_2*	—	1.57	—	7.48	5.39	4.05	1.96	5.22	—	—	—	—	—	—	—	—	—
SO_3	<0.07	<0.07	<0.1	<0.07	1.0	3.3	0.15	<0.07	3.61	10.40	Nd	Nd	Nd	1.1	0.29	<0.06	<0.10
Cl	0.74	0.04	0.08	0.03	0.03	0.02	0.04	0.12	0.02	0.91	Nd	Nd	Nd	0.10	0.04	0.07	0.07
Total	**99.78**	**98.49**	**101.41**	**100.62**	**100.41**	**100.81**	**97.56**	**98.21**	**99.86**	**100.00**	**97.33**	**100.48**	**99.07**	**97.72**	**98.44**	**98.32**	**100.35**
As	<2	<2	28.4	8.2	11.9	16.2	19.0	5.9	29.4	16.8				<2	3.2	2.8	16.0
Ba	1640	510	21	510	510	900	30	280	1050	<10				200	710	900	36
Br	7.5	<1	<1	<1	<1	2.3	<1	1.3	<1	5.1				1.5	<1	<1	<1
Ce	54	74	50	75	75	63	35	40	72	61				80	<20	60	80
Cr	100	65	110	70	70	90	60	80	80	110				80	85	100	110
Cu	9.3	26.5	10.5	8.8	16.4	43.0	24.0	16.3	10.0	11.0				6.8	10.0	19.0	18.0
Ga	15.2	20.0	21.2	20.6	20.9	21.1	19.0	13.4	17.4	20.0				11.0	15.0	14.2	16.2
La	34	56	27	45	35	32	31	28	45	25				44	<20	22	58
Mo	<2	<2	6.1	<2	<2	5.8	<2	3.3	1.8	22.0				2.3	2.6	3.5	12.9
Nb	20.9	18.4	13.2	14.0	14.0	17.5	27.8	11.4	18.7	11.2				18.8	8.8	15.6	15.3
Ni	25	31	8	34	35	46	34	31	45	15.1				27	10	45	29
Pb	11.1	6.0	10.7	5.3	18.1	11.5	5.3	3.9	5.7	9.1				8.4	7.9	11.4	16.0
Rb	150	120	5.8	150	160	130	115	22	160	14.1				18.3	3.8	140	2.6
Sr	230	360	410	470	380	540	300	230	400	550				320	370	310	250
U	<6	8.2	<3	<6	<6	<6	<6	<3	<6	7.6				<3	<3	14	<3
V	50	100	100	130	120	110	130	40	95	100				40	45	95	80
Y	23.0	32.0	22.0	27.0	28.0	28.0	33.0	21.1	30.0	24.5				28.0	26.1	30.0	32
Zn	180	67	16	100	110	69	63	59	31.4	89				21.0	8.0	25.5	29.1
Zr	125	145	175	130	130	121	130	210	155	100				310	90	240	370

+ Total Fe calculated as Fe_2O_3.

* H_2O and CO_2 calculated from modal mineralogy in Table 2. For CO_2, calcite = 43.5%. For H_2O, illite = 9%; chlorite = 11%; epidote = 1.87%, biotite = 4%, amphibole = 2% and sphene = 0.7%.

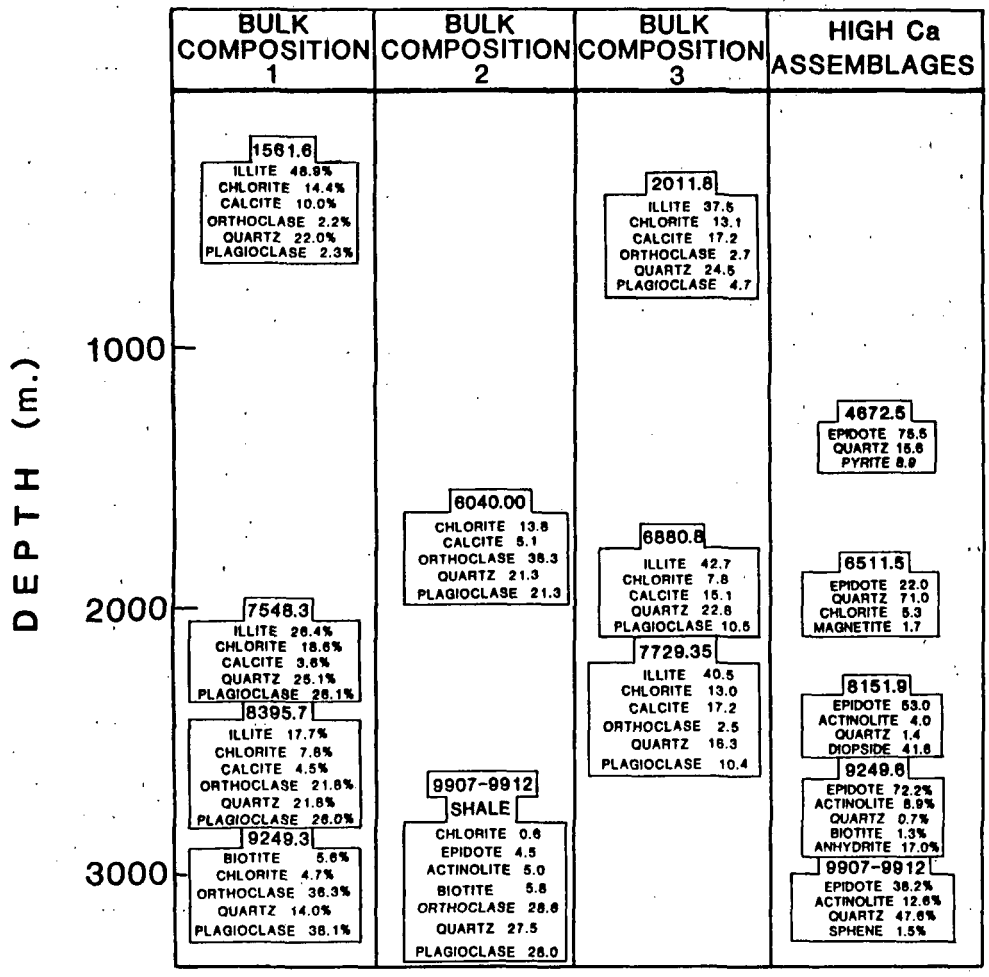

Fig. 16. Variations in selected bulk compositions with depth.

be open to H_2O and CO_2. Volatile-free bulk compositions were calculated as an approximate correction for volatile loss-gain and volume change. Other reactions proposed by Muffler and White [1969] suggest that there may be an exchange of Fe^{3+} between the brines and sediments, thereby modifying the sediment composition. In addition to normalization due to volatile loss, similar bulk compositions were selected by evaluating variations in refractory trace elements [Winchester and Floyd, 1976; Cann, 1975; Hart et al., 1974]. It would be expected that refractory elements such as Y and Zr would increase with volume loss. Unsystematic variations would suggest that the variation in Y and Zr in the original sediment exceeds the increases brought about by volume loss. In addition, the Y/Zr ratio should remain constant during such loss and should be useful in identifying similar bulk compositions.

Variations in the mineral assemblages with depth in the four selected bulk compositions are shown in Figure 16. Bulk composition 1 (BC1) which includes samples 476, 2300.7, 2559.0, and 2819.2 m is representative of a series of fine-grained shales with the following bulk chemical characteristics: SiO_2 = 55.0-57.5 wt %, Al_2O_3-16.5-17.4 wt %, $Fe_2O_3/(Fe_2O_3 + MgO)$ = 0.51-0.63, CaO = 4.60-5.88 wt %, K_2O = 3.10-4.10 wt %, TiO_2 = 0.60-0.65 wt % and Y/Zr - 0.19-0.25. Sample 476 m deviates from the other three samples with a lower Na_2O (0.75 wt % compared to 2.70-3.30 wt %) which is reflected in the modal abundance of plagioclase. Three distinct variations are observed in the modal mineralogy: (1) With increasing depth, the potassium feldspar/(potassium feldspar + illite) ratio increases from 0.04 in 476 m to 0.55 in 2559.0 m before illite disappears from the assemblage in 2819.2 m. The relationship between illite and potassium feldspar may reflect original lithologic differences, or the potassium feldspar may be a product of a reaction involving the breakdown of illite. The increase in the degree of Si-Al disorder in the potassium feldspar with depth may be related to the latter. Similar inverse relationships between illite and potassium feldspar were not observed by Muffler and White [1969], nor was this reaction observed by optical or XRD evaluation of the much coarser grained sandstones in this study or previous studies. (2) Calcite is not present in the assemblage in 2819.2 m. The near constant CaO in 2819.2 m relative to the other samples may reflect an increase in the anorthite content in plagioclase. (3) The chlorite abundance increases from 476 to 2300.7 m, then decreases, corresponding to the first appearance of biotite (2819.2 m).

Calculations illustrating differences between

TABLE 5. Mineralogical Differences Between Samples of Bulk Composition 1

	Illite	Calcite	Chlorite	K-feldspar	Quartz	Plagioclase	Biotite
476.0	49.0	10.0	14.4	2.2	22.1	2.3	0.0
2300.7	26.5	3.6	18.6	0.0	25.1	26.1	0.0
Δg	-22.5	-6.4	+4.2	-2.2	+3.0	+23.8	0.0
Δm	-0.027	-0.064	+0.006	-0.008	+0.050	+0.091	0.0
2300.7	26.5	3.6	18.6	0.0	25.1	26.1	0.0
2559.0	17.8	4.5	7.8	21.9	21.9	26.1	0.0
Δg	-8.7	+0.9	-10.8	+21.9	-3.2	0.0	0.0
Δm	-0.011	+0.009	-0.017	0.079	0.053	0.000	0.000
2559.0	17.8	4.5	7.8	21.9	21.9	26.1	0.0
2819.2	0.0	0.0	4.8	36.7	14.2	38.6	5.7
Δg	17.8	-4.5	-3.0	+14.8	-7.7	+12.5	5.7
Δm	-0.022	-0.045	-0.005	+0.053	-0.128	+0.048	+0.012

Modes represent grams of mineral per 100 grams of sample (Δg, difference in grams and Δm = Δg/molecular weight of mineral). Reactions (R1a) and (R1b) are calculated to account for these differences.

samples are given in Table 5. Possible reactions to account for these differences are:

(R1a) calcite + albite + illite = plagioclase + K-feldspar + SiO_2 + CO_2 + H_2O

(R1b) illite + chlorite = biotite + K-feldspar + H_2O + SiO_2

The exchange of Fe^{3+} between the fluid and the sediment and the liberation into the fluid of a proportion of the Ca [Muffler and White, 1969] are not included in these reactions. These exchanges would undoubtedly affect the composition of the plagioclase (R1a) and biotite (R1b). The extent of Ca loss and Fe gain is uncertain, as the chemical data (Table 4) do not appear to indicate a systematic relationship among depth, Fe enrichment, and Ca depletion in sediment of similar lithologies. Refractory trace elements Nb, Zr, Y, and Ti do not show systematic variations with mineral assemblage change suggesting that the original variation in trace element content of the sediment exceeds the concentration changes brought about by alteration.

Bulk composition 2 (BC2), which includes samples 1841.0 m and 3020.0-3021.2 m shale is a shale with the following bulk chemical characteristics: SiO_2 = 59.0-63.9 wt %; Al_2O_3 = 13.9-14.5 wt %, $Fe_2O_3/(Fe_2O_3 + MgO)$ = 0.58-0.61, CaO = 4.0-4.1 wt %, K_2O = 4.6-6.2 wt %, TiO_2 = 0.60-0.61 wt %, Na_2O = 2.65-2.75 wt % and Y/Zr = 0.13-0.16. The primary differences between BC2 and BC1 are reflected in Al_2O_3 and CaO. Mineralogical differences between the two samples reflect the breakdown of chlorite + calcite assemblages and the stability of epidote + actinolite + biotite assemblages. Reactions for these differences in mineral assemblage (see Table 6) are

(R2a) 5 K-feldspar + 3 chlorite + 4 calcite = 2 epidote + 5 biotite + $3SiO_2$ + $4CO_2$ + $4H_2O$

(R2b) 3 chlorite + 10 calcite + 21 SiO_2 = 3 actinolite + 2 epidote + 8 H_2O + 10 CO_2

Increases in trace element concentrations of Zr and Y (165-240, 27-30 respectively), suggest a decrease in volume. This is also suggested by the difference in volume between reactants and products in reactions (R2).

Bulk composition 3 (BC3), which includes samples 613.2, 2097.3, and 2355.9 m is a shale with the following bulk chemical characteristics: SiO_2 = 50.7-51.6 wt %, Al_2O_3 14.1-15.8 wt %, $Fe_2O_3/(Fe_2O_3 + MgO)$ = 0.58-0.62, CaO = 7.6-8.0 wt %, K_2O = 3.4-4.1 wt % and Y/Zr = 0.17-0.21. Throughout this depth and temperature range, the mineral assemblages in BC3 show little variation except that which may be attributed to original differences in lithology. The variability in the potassium feldspar/(potassium feldspar + illite) ratio and the modal abundance of chlorite observed in BC1 from 476 to 2559 m are not observed in BC3. This may be attributed either to differences in the reactivity of the bulk composition or special relations to fracture systems.

The high-CaO assemblages represented in Figure 16 actually include a wide range of bulk compositions which either have high concentrations of CaO or essentially consist of quartz + epidote assemblage (i.e., 1984.7 m). These assemblages occur as either epidote pods (1424.2, 1984.9, 2484.7, and 2887.7 m) or associated with fracture systems (3020.0-3021.2 m EP). Epidote

TABLE 6. Mineralogical Differences Between Samples of Bulk Composition 2

	Chlorite	Calcite	K-feldspar	Epidote	Actinolite	Biotite	Quartz	Plagioclase
1841.0	13.8	5.1	38.4	0.0	0.0	0.0	21.4	21.3
3020.0-3021.2 shale	0.6	0.0	28.6	4.5	5.0	5.8	27.5	28.0
Δg	-13.2	-5.1	-9.8	+4.5	+5.0	+5.8	+6.1	+6.7
Δm	-0.020	-0.051	-0.035	+0.009	+0.006	+0.013	+0.102	+0.026

Modes represent grams of mineral per 100 grams of sample reactions (R2a) and (R2b).

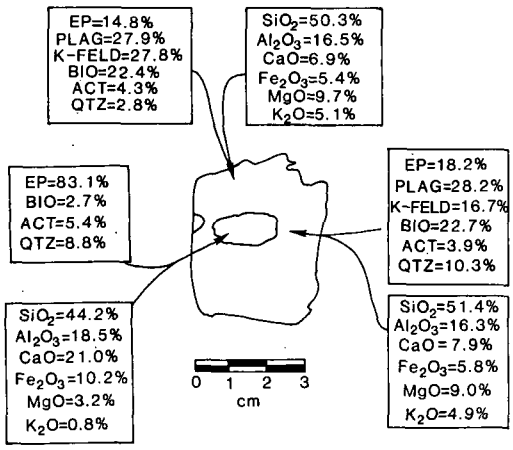

Fig. 17. Chemical and mineralogical variations in sample 2887.7.

is the dominant authigenic mineral in all the high-CaO assemblages. Epidote ± chlorite assemblages common in the shallow portions of the well are replaced by epidote + actinolite ± diopside assemblages at depths greater than 2400 m. The actinolite-bearing assemblages occur in these bulk compositions prior to their development in the surrounding shale (compare 2484.7 to 2559.0 m), although at depths greater than 2800 m, actinolite-bearing assemblages occur in both high- and intermediate-Ca bulk compositions.

The modal and bulk compositional differences between epidote pods and the surrounding sediment in sample 2887.7 m are illustrated in Figure 17. The epidote pods consistently have higher CaO contents and $Fe_2O_3/(Fe_2O_3 + MgO)$ and lower K_2O contents. These are reflected primarily in the modal abundances of epidote and biotite.

The simple epidote + quartz assemblages (1424.2 and 2301.3 m) may be derived from calcite + quartz + "clay component" assemblages by the reaction:

(R3) $$\underset{\text{calcite}}{8CaCO_3} + \underset{\text{clay component}}{3(Fe,Al)_4Si_4O_{10}(OH)_8}$$

$$= 4\ \underset{\text{epidote}}{Ca_2(Fe,Al)_3Si_3O_{12}(OH)} + 10H_2O + 8\ CO_2$$

Although the reaction is appropriate for observed assemblages, it ignores rather complex reactions involving the clay minerals such as montmorillonite-mixed layer clay-illite reactions. It also simplifies the probable Al^{3+}-Fe^{3+} exchange between fluids and sediments by incorporating that exchange in the clay and epidote formulae as $(Fe, Al)_3$. The reaction is essentially identical to that of Muffler and White [1969], excluding the K-bearing components. In addition, these epidote assemblages occur well within the calcite-chlorite zone and not at the high limit of the calcite-chlorite zone [Muffler and White 1969; Ferry, 1986]. The reaction also results in a minimum of 35% volume reduction in particular bulk compositions.

Compared to the epidote assemblage, the epidote + chlorite assemblages (1984.9 m) occur in sediments with higher bulk $(Fe_2O_3 + MgO)/(Fe_2O_3 + MgO + Al_2O_3)$. Assemblages are derived from such sediments by a combination of reaction (R3) and chlorite-producing reactions proposed by Muffler and White [1969], McDowell and Elders [1980], and Zen and Thompson [1974]. Whereas the epidote + quartz assemblage appears to be stable over a wide temperature range in the borehole, the actinolite and clinopyroxene assemblages form at the expense of the epidote + chlorite assemblages. On the basis of the observed assemblages in the high-Ca sediments and mineral chemistries, actinolite- and clinopyroxene-forming reactions are reaction (R2b)

$$\underset{\text{chlorite}}{3(Fe_3Mg_2Al_{0.33}Fe^{3+}_{0.67})(AlSi_3)O_{10}(OH)_8}$$

$$+ \underset{\text{calcite}}{10CaCO_3} + \underset{\text{quartz}}{21SiO_2} =$$

$$\underset{\text{actinolite}}{3Ca_2(Fe_3Mg_2)Si_8O_{22}(OH)_2} + \underset{\text{epidote}}{2Ca_2Fe^{3+}Al_2Si_3O_{12}(OH)} +$$

$$8H_2O + 10CO_2$$

and

(R4)

$$\underset{\text{chlorite}}{3(Fe_{2.5}Mg_{2.5})(Fe_{0.67}Al_{0.33})AlSi_3O_{10}(OH)_8}$$

$$+ \underset{\text{calcite}}{19CaCO_3} + \underset{\text{quartz}}{27SiO_2}$$

$$= \underset{\text{clinopyroxene}}{15Ca(Fe_{0.5}Mg_{0.5})Si_2O_6} + 11H_2O + 19CO_2$$

$$+ \underset{\text{epidote}}{2Ca_2FeAl_2Si_3O_{12}(OH)}$$

Yau et al. [1986] suggested an additional clinopyroxene-forming reaction:

(R5) $$\underset{\text{tremolite}}{Ca_2Mg_5Si_8O(OH)_2} + \underset{\text{calcite}}{3CaCO_3} + \underset{\text{quartz}}{2SiO_2}$$

$$= \underset{\text{diopside}}{5CaMgSi_2O_6} + H_2O + 3CO_2$$

Reactions (R2b), (R4) and (R5) are consistent with textural observations made in this study on selected metasandstones and by Yau et al. [1986].

Using reaction (R5) and the Mg end-member analogs to reaction (R4), Yau et al. [1986] concluded that the formation of actinolite and clinopyroxene required low X_{CO2} conditions at temperatures observed in the Salton Sea borehole. This agrees with the chemographic interpretation of Cho et al. [1987], and calculated F_{CO2} by Helgeson [1968] and Bird and Norton [1981]. Reactions (R2-R5) involve decarbonation which produces fluids with $X_{CO2} > 0.44$. The contrast between X_{CO2} produced by these reactions and the composition of the fluid in equilibrium with the sediments [Helgeson, 1968; Bird and Norton, 1981; Cho et al, 1987; Yau et al., 1986] indicates relatively extensive interaction between even the fine-grained shale (<10 μm grain size; porosities of 2.5% ± 1.9% (calcite-chlorite zone) and 4.1% ±

4.6% (biotite zone) [Noblet and McDowell, 1987]) and fluid [Ferry, 1986].

Geochemical Modification of the Sediments

McDowell [1987] observed in Magmamax and Elmore wells extensive leaching of Mn, Zn, and Cu in the sediments metamorphosed to biotite zone conditions. The mudstones at higher grades in the SSSDP well were observed to be similar in metal content to the low-grade mudstones. Comparison of the trace element content of high-grade to low-grade sediments of the selected bulk compositions (BC1, BC2, BC3) and coarser-grained samples illustrates some systematic variation in trace elements. Those variations are shown in Table 7. In the shales with grain size <5 μm, with increasing depth there are systematic decreases in Cu, Mn, Cl, and Zn; systematic increases in Cr, Ni, and Sr; and variable changes (dependent upon bulk composition) in As and Fe_2O_3. Unlike the observations made on other cores [Muffler and White, 1969] there appears to be no systematic enrichment of Fe in these assemblages. In the sandstone there is a systematic increase in Cr and Sr and a systematic decease in Br, Cl, Mn, and Zn. The decrease in Mn, Zn, and Cu in these sediments resulting from leaching particularly within the biotite and actinolite zones appears to be typical of observations in the interior of the Salton Sea geothermal area [McDowell, 1987]. Differences in the thermal profile between California State 2-14 well and Magmamax-Elmore wells may indicate that the extensive leaching observed in the latter two wells may occur at greater depth not penetrated by the California State 2-14 Well. Of particular interest is the substantial increase in Sr with degree of alteration/metamorphism. Normalized to Ca, the Ca/Sr ratio decreases from 450 to 300 in upper calcite-chlorite zone sediments to less than 150 in the biotite and actinolite zone sediments. This relative Sr enrichment indicates differences in the exchange of Sr and Ca between fluids and sediments.

TABLE 7. Downhole Compositional Variation in Selected Bulk Compositions

	Bulk Composition 1				Bulk Composition 2			Bulk Composition 3			Sandstones			
	476.0	2300.7	2559.0	2819.2	1841.0	3020.0-3021.2		613.2	2097.3*	2355.9	959.2	1425.9	2683.0	2954.8
					Shale									
As	7.8	<2	19	29.4	2.7	2.8		4.9	13.3	8.2	2.1	4.4	5.9	<2	3.2
Br	<2	<2	<2	<2	<2	<2		<2	<2	<2	79	3.2	3.3	2.3	2.6
Cl	0.09	0.04	0.04	0.02	0.17	0.07		0.15	0.05	0.03	0.48	0.22	0.12	0.10	0.04
Cr	45	65	60	80	60	100		50	100	70	50	70	80	80	85
Cu	26.6	26.5	24.0	10.0	29	19		11	90	8.8	10.5	11.6	16.3	6.8	10
Fe_2O_3	5.2	4.7	4.2	4.1	4.3	4.3		4.8	4.5	4.5	2.1	4.3	4.9	2.7	3.6
Mn	0.11	0.08	0.06	0.04	0.08	0.03		0.26	0.06	0.06	0.08	0.07	0.09	0.03	0.04
Ni	28	31	34	45	40	45		18	28	34	14	19	31	27	10
Sr	80	360	300	400	260	310		135	450	470	45	230	230	320	370
Ca/Sr	438	117	110	89	110	94		413	127	162	334	171	317	51	108
Zn	73	67	63	31.4	75	25.5		93	80	100	52	39	59	21	8

*High pyrite content.

Summary

In summary, seven authigenic mineral assemblages have been observed in the SSSDP core: (1) chlorite + calcite, (2) chlorite, (3) chlorite + epidote, (4) chlorite + biotite, (5) epidote, (6) epidote + actinolite, and (7) epidote + diopside + actinolite. The depths at which important minerals are either stable or metastable [Bird et al., 1987], as suggested by this suite of samples, are

Chlorite + calcite	476.0-2559.0 m
Epidote	below 905.6 m
Illite	476.0-2954.8 m
Biotite	below 2770 m
Actinolite	below 2484.7 m
Clinopyroxene	below 2484.7 m

Mineral chemistries exhibit a wide range of variation in this sample suite although bulk composition appears to be the most important variable. The Fe/(Fe+Mg) ratio in chlorite, and possibly biotite, varies systematically with bulk compositional variation within individual

samples. Epidote in vein assemblages has a higher $Fe^{3+}/(Fe^{3+}+Al)$ than the epidote in the adjacent sediments. In the veins, epidote $Fe^{3+}/(Fe^{3+}+Al)$ increases from core to rim, whereas in the sediments $Fe^{3+}/(Fe^{3+}+Al)$ in discrete grains, epidote decreases from core to rim. In the feldspars, K-feldspar (Or_{90-96}) becomes increasingly disordered with depth, plagioclase becomes more calcic in the biotite and actinolite zones, and three-feldspar assemblages were observed in samples below 2800 m.

Numerous reactions (reactions (R1)-(R5)) are consistent with the downhole variations in modal mineralogy for a wide range of bulk compositions. Several epidote-forming reactions occur at various temperature conditions which correspond to the first appearance of epidote (reaction (R3)), the first appearance of biotite (reaction (R2A)), the first appearance of clinopyroxene (reaction (R4)), and the first appearance of actinolite (reaction (R2b)). The metastable nature of epidote-producing reactions in the lower portion of the chlorite-calcite zone has been suggested by Bird et al. [1987]. Mixed volatile reactions, associated with the decarbonation of calcite and the dehydration of chlorite and actinolite, produced fluids with $X_{CO2} > 0.44$. The contrast between X_{CO2} produced by fluids and the X_{CO2} in equilibrium with the sediments indicates relatively extensive interaction between fluid and the fine-grained shales. This interaction also resulted in the leaching of Cu, Zn, and Mn and the enrichment of Sr, Ni, and Cr in the sediments. This chemical exchange, however, does not appear to be as extensive as in other wells at the same horizon in the interior of the geothermal field [McDowell, 1987].

Acknowledgments. We are grateful to V. Jensen, G. Duke, P. Papike, and C. Larive for their assistance in the preparation of this manuscript and resolving analytical problems. The authors also wish to thank Dennis Nielson, W. Elders and H.C. Helgeson for their thoughtful and constructive reviews. This research was funded by Department of Energy grant DE-FG01-85-ER13407 (C.K. Shearer and J.J. Papike).

References

Andes, J. P., and M. A. McKibben, Thermal and chemical history of mineralized fractures in cores from the Salton Sea scientific drilling project, Eos Trans. AGU, 68, 439, 1987.

Bence, A. E., and A. L. Albee, Emperical correction factors for the electron microanalysis of silicates and oxides, J. Geol., 76, 382-403, 1968.

Bird, D. K., and D. L. Norton, Theoretical prediction of phase relations among aqueous solutions and minerals: Salton Sea geothermal system, Geochim. Cosmochim. Acta, 45, 1479-1493, 1981.

Bird, D. K., M. Cho, C. J. Janik, J. G. Liou, and L. J. Caruso, Compositional, structural and isotopic properties of epidote in California State 2-14 well, Salton Sea, geothermal system, Eos Trans. AGU, 68, 454, 1987.

Campbell, A. C., J. M. Edmond, T. S. Bowers, C. I. Measures, M. K. Palmer, and E. T. Brown, Geochemistry of Salton Sea Scientific Drilling Project hydrothermal fluids and comparisons to Red Sea brines, Eos Trans. AGU, 68, 439, 1987.

Cann, J. R., Rb, Sr, Y, Zr, Nb in some ocean-floor basaltic rocks, Earth Planet. Sci. Lett., 27, 211-218, 1975.

Caruso, L. J., D. K. Bird, M. Cho and J. G. Liou, Mineralized fractures in SSSDP well 2-14 core samples, Eos Trans. AGU, 68, 445, 1987.

Chayes, F., and H. W. Fairbairn, A test of the precision of thin-section analysis by point counter, Am. Mineral., 36, 704-712, 1951.

Cho, M., J. G. Liou, and D. K. Bird, Prograde phase relations in the California State 2-14 well meta-sandstone, Salton Sea geothermal field, Eos Trans. AGU, 68, 445, 1987.

Davis, B. L., "Standardless" x ray diffraction quantitative analysis, Atm. Environ., 14, 217-220, 1980.

Davis, B. L., Reference intensity quantitative analysis using thin-layer aerosol samples. Adv. X ray Anal., 27, 339-348, 1984.

Davis, B. L., A tubular aerosol suspension chamber for the preparation of powder samples for x ray diffraction analysis. Powd. Diff., 1, 240-243, 1986.

Davis, B. L., and L. R. Johnson, On the use of various filter substances for quantitative particulate analysis by x ray diffraction, Atm. Environ., 16, 273-282, 1982.

Davis, B. L., and L. R. Johnson, The use of mass absorption in quantitative x ray diffraction analysis, Adv. X ray Anal., 30, 333-342, 1987.

Davis, B. L., L. R. Johnson, and T. Mebrahtu, X ray quantitative analysis of coal by the reference intensity method, Powd. Diff., 1, 244-255, 1986.

Donaghe, L. L., and D. R. Peacor, Textural and mineralogic transitions in SSSDP argilaceous sediments, Eos Trans. AGU, 68, 454, 1987.

Elders, W.A., and J.H. Sass, The Salton Sea Scientific Drilling Project, J. Geophys. Res. this issue.

Ferry, J. M., Reaction progress: A monitor of fluid-rock interaction during metamorphic and hydrothermal events, in Fluid-Rock Interactions During Metamorphism, edited by J.V. Walter and Wood, B.J., pp. 60-88, Springer-Verlag, New York. 1986.

Hart, S. R., A.J. Erlank, and E. J. D. Kable, Sea-floor basalt alteration: Some chemical and Sr isotopic effects, Contrib. Mineral. Petrol., 44, 219-230, 1974.

Helgeson, H. C., Geologic and thermodynamic characteristics of the Salton Sea geothermal system, Am. J. Sci., 266, 129-166, 1968.

Janik, C. J., H. Shigeno, T. Cheatham, and A. H. Truesdell, Gas geothermometers applied to separated steam from December 1985 flow test of the SSSDP well, Eos Trans. AGU, 68, 440, 1987.

Keith, T. E. C., L. J. P. Muffler and M. Cremer, Hydrothermal epidote formed in the Salton Sea geothermal system, California, Am. Mineral., 53, 1635-1644, 1968.

Kendall, C., Petrology and stable isotope geochemistry of three wells in the Buttes area of Salton Sea Geothermal Field, Imperial Valley, California, MS thesis, University of California, Riverside, IGPP Rep. No. 76/17, 211 pp.

Kramer, R. S., and S. D. McDowell, Mineral

chemistry of altered sandstone from borehole IID2, Salton Sea geothermal field, CA, Eos Trans. AGU, 68, 445, 1987.

McDowell, S. D., and M. O. McCurry, Active metamorphism in the Salton Sea Geothermal Field, California, Geol. Soc. Am. Abstr. with Progr., 9, 1088, 1977.

McDowell, S. D., Composition and structural state of coexisting feldspars, Salton Sea geothermal field, Mineral. Mag., 50, 75-34, 1986.

McDowell, S. D., The Salton Sea scientific drill hole in context, Eos Trans. AGU, 68, 444, 1987.

McDowell, S. D., and W. A. Elders, Authigenic layer silicate minerals in borehole Elmore 1, Salton Sea geothermal field, California, U.S.A., Contrib. Mineral. Petrol., 74, 293-310, 1980.

McDowell, S. D., and W. A. Elders, Allogenic layer silicate minerals in borehole Elmore #1, Salton Sea geothermal field, California, Am. Mineral., 68, 1146-1159, 1983.

Medlin, J. H., N. H. Suhr, and J. B. Bodkin, Atomic absorption analysis of silicates employing $LiBO_2$ fusion, At. Absorpt. Newsl., 8, 25-29, 1969.

Mehegan, J. M., C. T. Herzig, and R. M. Sullivan, Visual core descriptions, Salton Sea Scientific Drilling Project California State 2-14 well., Inst. of Geophys. and Planet. Phys., Univ. of Calif., Riverside, 1986.

Muffler, L. J. P, and D. W. White, Active metamorphism of upper Cenozoic sediments in the Salton Sea geothermal field and the Salton Sea Trough, southeastern California, Geol. Soc. Am. Bull., 80, 157-182, 1969.

Noblet, L. A., and S. D. McDowell, Petrophysical measurements of core from the Salton Sea drill hole, Eos Trans. AGU, 68, 434, 1987.

Robinson, P., F. S. Spear, J. C. Schumacher, J. Laird, C. Klein, B. W. Evans, and B. L. Doolan, Phase relations of metamorphic amphiboles: Natural occurrence and theory, in Reviews in Minerology, vol. 9B, edited by D. R. Veblen and P. H. Ribbe, pp. 1-227, Mineralogical Society of America, Washington, D.C., 1982.

Sass, J. H., J. D. Hendrichs, S. S. Priest, and L. C. Robison, Temperature and heat flow in the State 2-14 well, Salton Sea Scientific Drilling Program, Eos Trans. AGU, 68, 454, 1987.

Valette-Silver, N.J., F. Tera, R. L. Watters, J. Klein, and R. Middleton, ^{10}Be and trace element chemistry in the Salton Sea geothermal system, Eos Trans. AGU, 68, 439, 1987.

Williams, A. E., Chemical and isotopic variations and the distribution of brines across the Salton Sea geothermal field, California, Eos Trans. AGU, 68, 438, 1987.

Winchester, J. A., and P. A. Floyd, Geochemical magma type discrimination: Application to altered and metamorphosed basic igneous rocks, Earth Planet. Sci. Lett., 28, 459-469, 1976.

Yau, Y., D. R. Peacor, and E. J. Essene, Occurrences of wide-chain Ca-pyriboles as primary crystals in the Salton Sea Geothermal Field, California, U.S.A., Contrib. Mineral. Petrol., 94, 127-134, 1986.

Zen, E. A., and A. B. Thompson, Low grade regional metamorphism: Mineral equilibrium relations, Annu. Rev. Earth Planet. Sci., 2, 179-212, 1974.

B. L. Davis, J. J. Papike, C. K. Shearer, and S. B. Simon, South Dakota School of Mines and Technology, Rapid City, SD 57701.

J. C. Laul, Battelle, Pacific Northwest Laboratories, Richland, WA 99352.

(Received August 10, 1987;
revised May 4, 1988;
accepted May 24, 1988.)

JOURNAL OF GEOPHYSICAL RESEARCH, VOL. 93, NO. B11, PAGES 13,123–13,133, NOVEMBER 10, 1988

Epidote-Bearing Veins in the State 2-14 Drill Hole: Implications for Hydrothermal Fluid Composition

L. J. CARUSO, D. K. BIRD, M. CHO,[1] AND J. G. LIOU

Department of Geology, Stanford University, Stanford, California

Epidote-bearing veins in State 2-14 drill core from 900 to 2960 m depth were examined using backscattered electron microscopy and electron probe microanalysis to characterize the mineralogy, parageneses, texture, and composition of vein minerals. In order of decreasing abundance, minerals in epidote-bearing veins are pyrite, calcite, K-feldspar, quartz, anhydrite, hematite, chlorite, Fe-Cu-Zn sulfides, actinolite, titanite, and allanite. The downhole distribution of minerals in epidote-bearing veins (+ pyrite and quartz) varies as a function of depth and includes : (1) calcite above ~2000 m, (2) K-feldspar between 1700 and 2745 m, (3) anhydrite between 2195 and 2745 m, (4) hematite ± sulfides above 2773 m, and (5) actinolite below ~2890 m. Where present, K-feldspar was the first mineral to precipitate in veins followed by epidote. In all other veins, epidote was the earliest vein mineral to form. Calcite, quartz, anhydrite, hematite, and sulfides were paragenetically later. Compositional zoning, common in most vein epidotes, is typically symmetric with Al-rich cores and Fe^{3+}-rich rims. The minimum mole fraction of $Ca_2Fe_3Si_3O_{12}(OH)$ (X_{Ps}) in vein epidotes decreases systematically with increasing depth from ~0.33 at 906 m to ~0.21 at 2900 m, and the maximum X_{Ps} at any given depth is greater than 0.33. Thermodynamic analyses of phase relations among vein-filling minerals and aqueous solutions at depths near 1867 m and 300°C indicate that the modern reservoir fluid in the Salton Sea geothermal system is in equilibrium with calcite + hematite + quartz + epidote (X_{Ps} = 0.33) ± anhydrite. The predicted fugacity of CO_2 (~14 bars) for the modern Salton Sea brine is in close agreement with the calculated value of f_{CO_2} for the 1867 m production fluid. Theoretical phase diagrams in the system CaO-K_2O-Fe_2O_3-Al_2O_3-SiO_2-H_2O-O_2-S_2-CO_2 demonstrate that the mineralogies and mineral parageneses recorded in epidote-bearing veins and the observed variations in Al-Fe^{3+} content of vein epidotes may result from only minor changes in the fugacity of CO_2, O_2, and S_2 of the geothermal fluid.

INTRODUCTION

Recent petrological, geochemical, and numerical modeling studies of active and fossil geothermal systems document the physiochemical characteristics of hydrothermal fluid circulation associated with the emplacement and cooling of igneous intrusions [*Forester and Taylor,* 1976; *Taylor and Forester,* 1979; *Norton and Taylor,* 1979; *Ferry,* 1976, 1979, 1985; *Elders et al.,* 1984]. Hydrothermal fluid flow controls the transport of chemical components and the nature of fluid-rock interaction which may lead to the formation of ore deposits [*Cathles,* 1981; *Norton,* 1982]. Numerical analogs of magma-hydrothermal systems demonstrate that permeability is the most significant parameter controlling the size and duration of hydrothermal fluid circulation [*Norton and Knight,* 1977; *Fehn et al.,* 1978; *Norton,* 1984]. Fractures represent the primary pathways for the reactive aqueous solutions in these systems. Active and fossil geothermal systems are characterized by a history of multiple fracturing and fracture sealing by mineral precipitation, which can act as an effective barrier to fluid flow [*Batzle and Simmons* 1976; *Norton and Knapp,* 1977; *Elders,* 1982; *Caruso and Simmons,* 1979; *Bird et al.,* 1986]. The time-space variation in fracture width due to vein mineralization is important in controlling the spatial and temporal changes in porosity and permeability in geothermal systems.

Despite the obvious importance of fracturing and fracture-related mineralization in geothermal systems, relatively few studies have specifically addressed these processes. This is a consequence of the type of drill hole samples from geothermal areas which are usually drill cuttings, <1 cm in maximum dimension, that preserve only incomplete portions of veins. In addition, crosscutting relations among veins are generally not observed. These factors make the determination of vein mineral parageneses and the relative ages among vein sets difficult or impossible. However, core samples from the State 2-14 drill hole in the Salton Sea geothermal system are not subject to these shortcomings and thus provide an unique opportunity to study mineralized fractures in an active geothermal system. The State 2-14 well, drilled by the Salton Sea Scientific Drilling Project to 3200 m, recovered more than 225 m of core [*Herzig and Mehegan,* 1987; *Herzig et al.,* this issue].

Recent studies of mineralized fractures in metasediments from the State 2-14 well [*Andes and McKibben,* 1987] and from other wells in the Salton Sea geothermal system [*McKibben and Elders,* 1985] have emphasized fracture-controlled ore mineralization. These studies identified two types of sulfide-bearing veins: (1) an early sulfide (including pyrrhotite) + carbonate ± silicate (± epidote) vein system and (2) a later hematite + silicate (including epidote) + sulfide ± sulfate vein system. They conclude that the chemistry of the hydrothermal fluids associated with sulfide vein mineralization evolved from reduced (early type 1 veins) to more oxidized (late type 2 veins), possibly in response to an influx of oxidized, meteoric fluids associated with repeated fracturing of the metamorphosed sediments.

[1]Now at Department of Earth and Space Sciences, University of California, Los Angeles.

Paper number 7B7111.
0148-0227/88/007B-7111$05.00

Most active geothermal systems in which measured or paleotemperatures exceed 200-250°C contain epidote as a major hydrothermal calc-silicate mineral [*Bird et al.*, 1984]. Epidote is the most abundant and widespread mineral in veins intersected by the State 2-14 drill hole and is a common secondary matrix mineral in State 2-14 metasandstones [*Cho et al.*, 1987, this issue; *Bird et al.*, this issue]. In this study we (1) document the textures, mineralogies, and parageneses of well-preserved epidote-bearing veins from the State 2-14 drill core, (2) describe compositional variations and zoning patterns in the vein epidotes, and (3) use thermodynamic analysis of phase relations among vein minerals to evaluate the effects of hydrothermal fluid composition on vein mineralogy and parageneses and on the composition of vein epidotes. These observations on epidote-bearing veins in the State 2-14 drill hole build upon previous theoretical studies of the chemistry of nonstoichiometric hydrothermal minerals. [*Bird and Helgeson*, 1980, 1981; *Bird and Norton*, 1981; *Rose and Bird*, 1987].

Geological Background

The State 2-14 well is located near the southeast end of the Salton Sea in the Salton Trough, a structural depression associated with an active continental rift environment marking the tectonic boundary of the North American and Pacific plates. *Elders and Sass* [1987, this issue] give locations and physical details of the drill hole. Excellent reviews of the geology, geophysics, and reservoir characteristics of the Salton Sea geothermal system are presented by *Younker et al.* [1982] and *Elders and Cohen* [1983]. Since the Pliocene, sedimentation in the Salton Trough has been characterized by fine-grained fluvial-deltaic sediments and associated evaporitic and lacustrine deposits derived from the Colorado River system. In response to recent volcanism and active faulting, these terrigenous sediments have undergone a complex history of active metamorphism, fracturing, hydrothermal alteration, and vein mineralization [*Schiffman et al.*, 1985]. High temperatures (>360°C) and hypersaline brines (>200,000 ppm total dissolved solids) are causing incipient silicate, sulfide, and oxide mineralization [*White et al.*, 1961; *Helgeson*, 1967; *Skinner et al.*, 1967; *Muffler and White*, 1969; *White*, 1981; *McDowell and Elders*, 1983; *McKibben and Elders*, 1985].

Decarbonation of calcareous sediments is associated with prograding thermal fronts in the Salton Sea system as described by *Muffler and White* [1968, 1969] and *Ferry* [1986]. In the upper ~200 m of the Salton Sea geothermal system, CO_2-rich sandstone aquifers were mined by shallow drill holes for making dry ice between 1934 and 1954. Carbon dioxide in these shallow aquifers was formed by decarbonation reactions associated with the development of the Salton Sea magma-hydrothermal system within the calcareous sediments of the Colorado River delta [*Muffler and White*, 1968]. At temperatures between ~150° and 200°C, dolomite reacts with kaolinite to produce chlorite, calcite, and CO_2, and at temperatures between 300° and 325°C, CO_2 is liberated by reactions associated with the breakdown of calcite ± chlorite ± K-feldspar and the formation of epidote ± biotite [*Muffler and White*, 1969; *McDowell and Elders*, 1983; *Cho et al.*, 1987, this issue].

Methods of Investigation

Fifty samples collected from 13 epidote-bearing vein sets from the State 2-14 drill core were examined (Table 1). Because individual samples were generally <15 cm in length, only short segments of mineralized fractures could be studied in detail using the analytical techniques described below. Sample depths range from 900 to 2900 m; host rock lithology includes sandstone, siltstone, and shale. The general structure, lithology, characteristics of mineralized fractures, and secondary mineralogy of State 2-14 drill core are described by *Mehegan et al.* [1986], *Herzig and Mehegan* [1987] and *Herzig et al.* [this issue]. Metamorphic mineralogy, the composition of metamorphic minerals, and their associated phase relations in State 2-14 metasediments are presented by *Cho et al.* [1987, this issue] and *Shearer et al.* [1987].

Polished, 100-μm-thick sections were prepared for each sample; thicker polished sections minimize the production and enhancement of microcracks [*Richter and Simmons*, 1977]. In addition, each sample was epoxy impregnated in an attempt to reduce plucking of delicate minerals present in fractures. The polished sections were examined with a petrographic microscope and with a scanning electron microscope equiped with a high-resolution backscattered electron (BSE) detector and an energy dispersive X ray (EDX) spectrometer. The detector has a spatial resolution of 100 Å and an atomic number resolution of approximately 0.1. The applications of BSE imaging and EDX analysis to this study are (1) characterization of vein morphology, (2) identification and determination of complex textures among fracture-filling minerals, (3) detection of compositional variation in individual vein minerals, and (4) qualitative determination of the chemical composition of microscopic and submicroscopic (less than 1 μm) grains.

Epidote compositions were determined with an automated JEOL 733A electron microscope, using a 3- or 10-μm beam size, a 15-kV accelerating voltage and a 15-nA beam current. Natural diopside, kaersutite, and spessartine were used as standards. The *Bence and Albee* [1968] method was applied for matrix corrections.

Characteristics of Epidote-Bearing Veins

Vein Morphology

Vertical to subvertical fractures containing epidote are widespread in the State 2-14 drill core from depths below 900 m. However, their relative abundance is highly variable. In some core sections, only a few, widely spaced, subparallel fractures are observed. Other sections (e.g., the depth interval 1415-1427 m and at 2773 m) contain multiple sets of closely spaced fractures that intersect to form small, irregular blocks which were locally rotated and recemented resulting in the formation of elongate vugs up to 2 cm in the maximum dimension (Figure 1*b*). Several narrow (<1 m long) zones at 1417, 1426, and 2883 m (adjacent to a mafic dike) are characterized by brecciation, intense alteration, and pervasive fracture-controlled mineralization. Vein density generally decreases progressively away from these zones.

The morphology of epidote-bearing veins is variable and somewhat dependent on the lithology and pore structure of

TABLE 1. Mineralogy, Paragenesis, and Host Rock Lithology of Epidote-Bearing Veins in the State 2-14 Drill Core

Depth,	Rock[a]	Vein Minerals[b]											
m	Type	Ep	Py	Cc	Qtz	Ksp	Anh	Chl	Hm	Sfd	Act	Ttn	Aln
906	ss	1	*	2					*	*			
1415	slt	1	+	2	+			*	*	*			
1427	ss	1	*	3	2			*	2	*			
1699	sh	2	*	3	+	1		*	+	*			
1984	slt	1	2	*	*				*	2			
2061	ss	+	+		*					*			
2195	sh	2	+			1	3		*				
2560	sh	2	+	*		1				+			
2619	ss	+			+		+						
2745	slt	2	3		+	1	3	+	3	*		+	+
2773	ss	1	2		+			+	+	+			
2889	ss	+	*		*						+		
2955	ss	+						*			+		

Numbers and pluses from this study ; asterisks from *Mehegan et al.*, [1986]. Where apparent, relative ages of mineral are specified by numbers (1 represents the earliest vein mineral; 2 and 3 are progressively later). Minerals with ambiguous or indeterminant paragenesis are denoted by plus.

[a] ss, metasandstone; slt, metasiltstone; sh, metashale.

[b] See text for mineral abbreviations.

the host rock. Veins in metasandstone are generally arcuate, range in width from 10 μm to 3.0 cm, and usually contain some open space (Figure 1*b*). Individual fractures are continuous for only short distances (less than a few tens of centimeters) and commonly terminate on other fractures forming an interconnected network. Vein apertures may vary from 100 μm to 1 cm over a distance of only a few centimeters. Crack branching is common. Veins hosted in metasiltstones and metashales are typically straight, more uniform in width, and usually filled completely with secondary minerals (Figure 1*a*). Individual veins may be continuous for distances of up to 5 m. Fracture widths range from 10μm to a few millimeters. Narrow subsidiary microcracks locally bifurcate from the primary fractures.

Euhedral crystals of epidote and other minerals commonly grow across fractures forming mineral bridges (Figure 2) which may help to prevent the fractures from closing mechanically. Because fracture-bridging minerals were not broken or disrupted during coring or sample preparation, measured fracture widths represent "in situ" values. The porosity created by partial filling of fractures by epidote (e.g., Figure 2) provided pathways for hydrothermal fluids that produced paragenetically later vein minerals, which locally overgrow or partially replace earlier fracture-lining epidote and K-feldspar (Figure 3).

Vein Mineralogy and Paragenesis

The mineralogy and paragenesis of epidote-bearing veins examined in this study are summarized in Table 1. In order of decreasing abundance, minerals identified in epidote-bearing veins are pyrite (Py), calcite (Cc), K-feldspar (Ksp), quartz (Qtz), anhydrite (Anh), hematite (Hm), chlorite (Chl), Fe-Cu-Zn sulfides (Sfd, mostly chalcopyrite), actinolite (Act), titanite (Tnt), and allanite (Aln, a rare earth element (REE)-rich epidote). With the exception of pyrite, which has been observed to occur in all but one of the epidote fracture sets, the downhole distribution of modally abundant minerals in epidote-bearing veins is restricted to depth intervals as follows: (1) calcite above ~2000 m, (2) K-feldspar between 1700 and 2745 m, (3) anhydrite between 2195 and 2745 m, (4) hematite ± sulfides above 2773 m, and (5) actinolite below ~2890 m.

At depths shallower than 2000 m, calcite and pyrite are the most common fracture-filling minerals to occur with epidote in veins. Hematite, quartz, sulfides, and K-feldspar are present in minor amounts. The assemblage Ep + Cc is rare below 2000 m. However the maximum depth of occurrence of calcite in veins without epidote is 2683 m [*Mehegan et al.*, 1986]. In all epidote-bearing veins containing calcite, epidote was the first mineral to precipitate, and calcite was always paragenetically later. Epidote occurs as euhedral crystals growing on the walls of fractures or as mineral aggregates incorporated in the later calcite (Figure 3*a*) and less frequently in hematite. Microbrecciation of vein-lining epidote is evidenced by broken crystal fragments now enclosed within calcite (Figure 3*a*). Later calcite veins commonly crosscut and offset earlier veins filled with epidote and other vein minerals. The assemblage Ep + Hm + Cc + Qtz is common in veins from a highly fractured and mineralized zone at 1427 m (Figure 3*b*). Hematite forms as aggregates of fibrous crystals enclosed in calcite. Quartz occurs as elongate euhedral crystals, many of which bridge the fracture.

Vein K-feldspar first appears at 1700 m. It occurs in metashale-hosted veins as <100 μm euhedral to subhedral crystals lining the fracture wall (Figure 3*c*). Epidote euhedra are either intergrown with this K-feldspar or incorporated in later vein-filling calcite. The surfaces of K-feldspar crystals in contact with calcite are usually irregular and embayed, suggesting that local dissolution of K-feldspar occurred during the calcite-forming event.

Veins in metasediments between 2000 and 2746 m are filled primarily with one or more of the following minerals: epidote, K-feldspar, and anhydrite. Also present are lesser amounts of quartz, pyrite, hematite, calcite, chlorite, and Fe-Cu-Zn sulfides and trace quantities of titanite and allanite (Table 1). Veins from 2195 and 2745 m (Figures 3*d* and 3*e*) exemplify the textures and mineral parageneses in typical epidote-mineralized veins from 2000 to 2746 m depth.

K-feldspar was the first mineral to form in metasandstone-

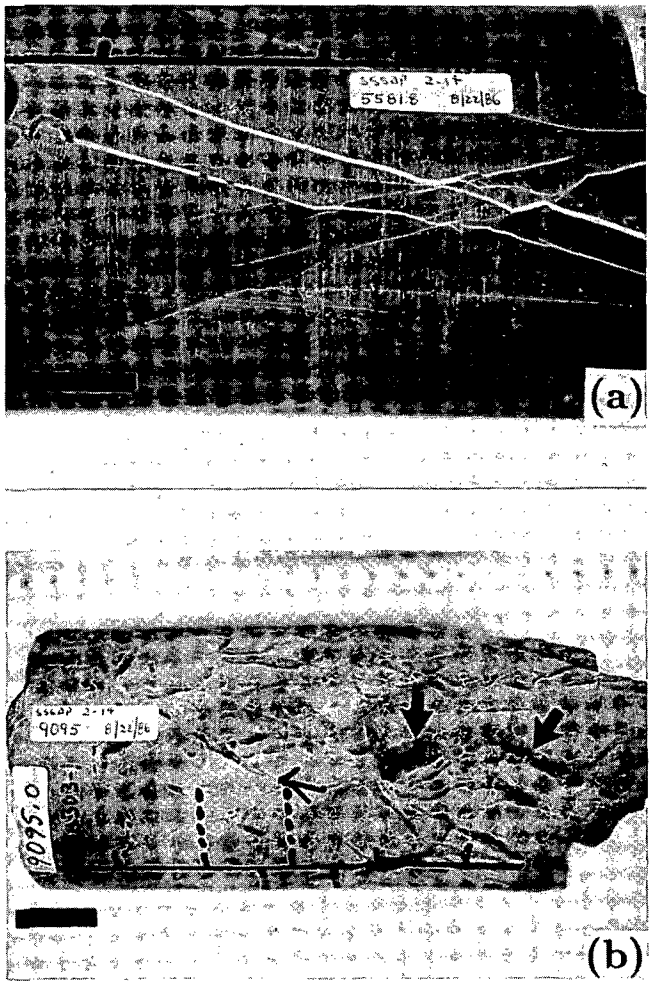

Fig. 1. Macroscopic morphological characteristics of epidote mineralized fractures in State 2-14 drill core. Scale bars are 30 mm. (*a*) Epidote and calcite sealed veins in a metasiltstone at a depth of 1984 m. Vein widths are generally uniform. Note the bifurcating nature of this mineralized fracture. (*b*) Metasandstone from 2773 m contains abundant open fractures lined with pyrite, epidote, and quartz. The latter two minerals cannot be distinguished at this scale. Note the wide variation in vein width. Arrows mark the location of elongate vugs which occur in abundance in this section of the core.

and metashale-hosted veins at a depth of ~2195 m. It occurs along the entire length of most veins and commonly seals many sections of individual fractures. Epidote occupies the discontinuous pore space in the central portion of the fractures. These pores are from 10 μm to several mm long and are uniformly lined with sawtooth-shaped K-feldspar crystals projecting out from the veins walls (Figure 3*d*). In places, later anhydrite replaces vein epidote. The degree of replacement is highly variable. Open space in the central portion of these K-feldspar-bearing veins is completely filled with either anhydrite or epidote. Usually, anhydrite replaces only a portion of the earlier epidote. This paragenesis of Ksp→ Ep→ Anh is shown in Figure 3*d*. Dissolution of K-feldspar by later anhydrite-saturated fluids is evidenced by the irregular and pitted surface of K-feldspar crystals adjacent to anhydrite and by the subangular pores along the Ksp-Anh interfaces (Figure 3*d*). In contrast, the contacts between epidote and K-feldspar are sharp, commonly interlocking, and devoid of open space.

Two mineralogically distinct vein sets occur in metasediments from 2745 m. The older fractures are filled with Ep + Hm and one or more of the following minerals: K-feldspar, quartz, chlorite, pyrite, titanite, and allanite. Where present in these earlier veins, K-feldspar was the first mineral to form, followed by epidote. In portions of these veins where K-feldspar is absent, epidote was the earliest vein mineral. K-feldspar and epidote are commonly intergrown with quartz and hematite (Figure 3*e*). The modal abundance of hematite varies from a few randomly dispersed, fibrous crystals in narrow veinlets to abundant, bladelike, microscopic ($< 10\mu$m) crystals intergrown with epidote in wider veins. The latter texture is evidence that epidote and hematite coprecipitated. Later anhydrite-filled veins extend from anhydrite-rich metasandstone layers into adjacent metashale layers where they have wedge-shaped terminations. These veins crosscut, offset, or terminate against earlier epidote-bearing veins (Figure 3*f*), and epidote is locally replaced by anhydrite where these two vein sets intersect. These relations indicate that the anhydrite-bearing veins are younger than veins filled with epidote.

At depths below 2746 m, epidote is the most abundant and paragenetically the earliest mineral to precipitate in fractures and may occur with quartz, pyrite, actinolite, and chlorite. Epidote euhedra up to several millimeters long line the walls of many fractures; segments of some fractures are sealed with massive epidote. Later minerals (including pyrite, chlorite, and actinolite) coat and locally fill cavities lined with epidote. Euhedral crystals of epidote, quartz, and pyrite form mineral bridges across partially open, metasandstone-hosted fractures. At depths below 2773 m, veins filled with epidote only are common.

Vein Epidote Compositions

The major nonstoichiometry of epidote solid solution results from Fe^{3+} and Al substitution in its octahedral sites. Compositional variation in vein epidotes from State 2-14 metasediments is summarized in Table 2; the downhole variation in epidote compositions as a function of host

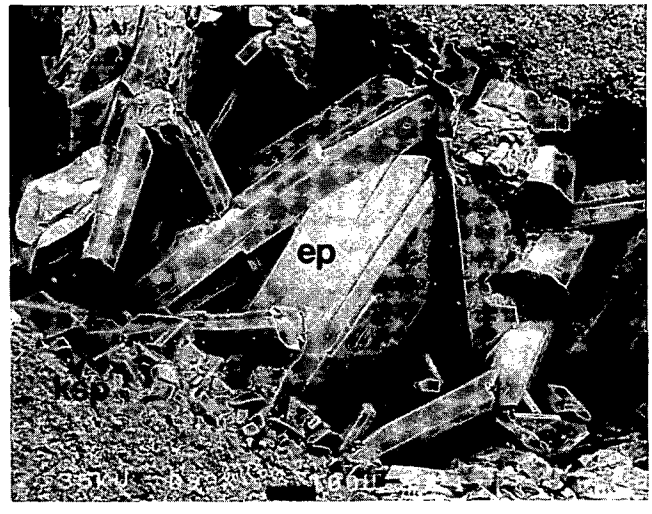

Fig. 2. Secondary electron image of euhedral epidote (Ep) growing across an open fracture. Suhedral K-feldspar (Ksp) crystals occur along the fracture wall. Host rock is a metasiltstone. Dark regions represent open space. Sample depth is 2195 m. Scale bar is 100 μm .

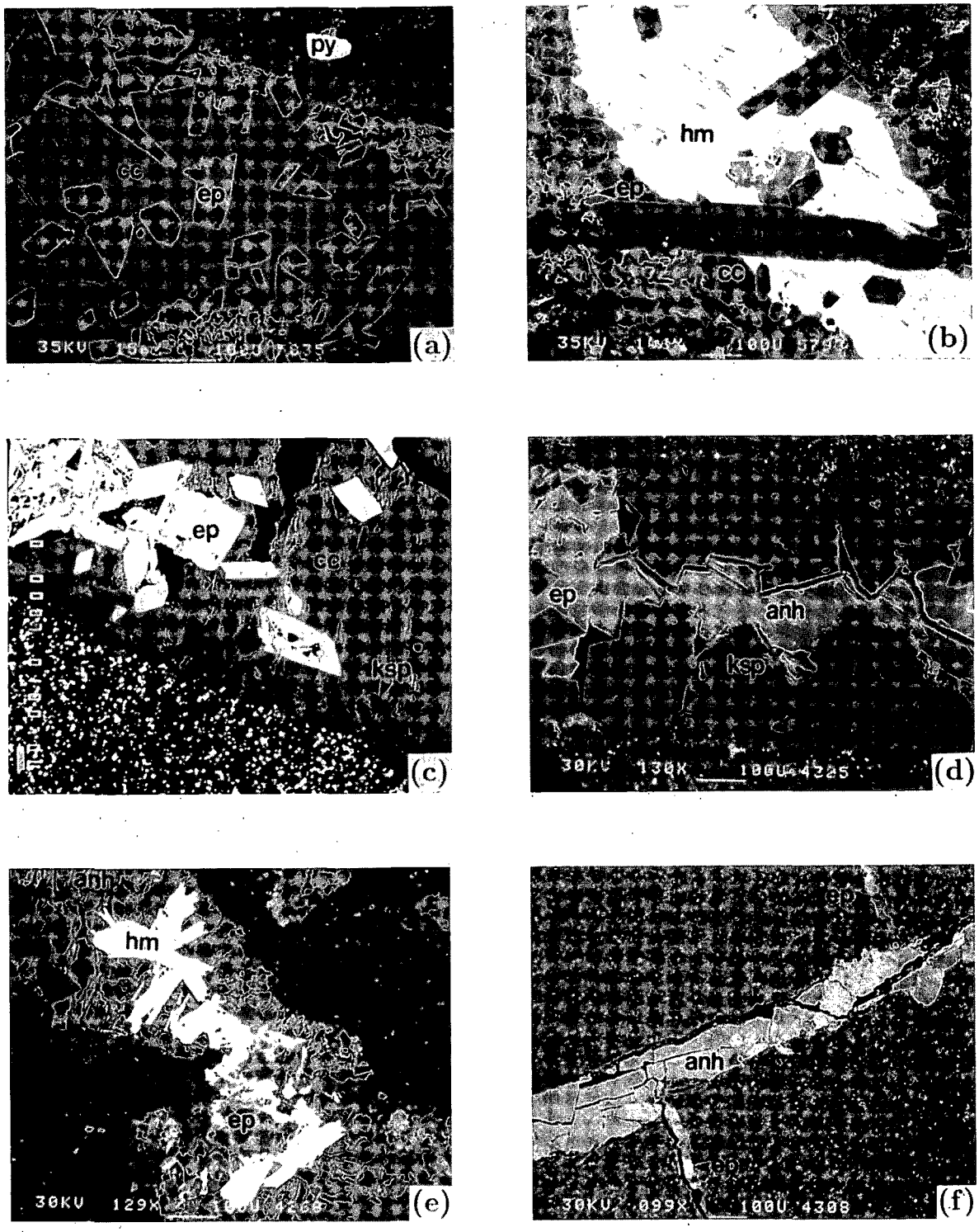

Fig. 3. Backscattered electron images of representative textures and parageneses among minerals in epidote-bearing veins in the State 2-14 drill hole. (*a*) Epidote (Ep) + calcite (Cc) sealed vein in metasiltstone. Epidote euhedra line the vein wall. Many are broken and enclosed in the later calcite. Sample depth is 1415 m. Scale bar is 100 μm. (*b*) Hematite (Hm) + epidote (Ep) + calcite (Cc) + quartz (qtz) vein in meta-sandstone. The f_{CO_2} of the hydrothermal fluid can be estimated using thermochemical data for this vein assemblage (see discussion). Sample depth is 1427 m. Scale bar is 100 μm. (*c*) Segment of K-feldspar (Ksp) + epidote (Ep) + calcite (Cc) filled fracture. K-feldspar crystals line the vein wall. Epidote euhedra are enclosed in calcite and are intergrown with K-feldspar. Host rock is a metasiltstone at depth of 1984 m. The bright grains in the matrix are pyrite. Scale bar is 100 μm. (*d*) Portion of a vein sealed with K-feldspar (Ksp), epidote (Ep) and anhydrite (Anh). First, subhedral K-feldspar crystals formed along both vein walls and grew inward perpendicular to the wall. Then epidote filled the interior of the vein. Finally, anhydrite partially replaced epidote. The host rock is metasiltstone. Sample depth is 2195 m. The scale bar is 100 μm. (*e*) Epidote (Ep) + K-feldspar (Ksp) + hematite (Hm) + anhydrite (Anh) vein. K-feldspar was the earliest vein mineral followed by epidote. Anhydrite occurs replacing epidote. Quartz (dark) is also present in this vein. Sample depth is 2745 m. Scale bar is 100 μm. (*f*) The spatial relationship between the epidote-bearing (Ep) and anhydrite (Anh) fracture sets can be seen in this micrograph. Early Ep + Ksp + Chl vein is offset by a later anhydrite-filled vein. Host rock is a metashale. Sample depth is 2745 m. The scale bar is 100 μm.

TABLE 2. Iron Content of Vein Epidotes in the State 2-14 Drill Core

Depth, m	$X_{Ca_2Fe_3Si_3O_{12}(OH)}$ Fe-Poor Zone		Intermediate Zone		Fe-Rich Zone		Associated Mineralogy
	Mean	Range	Mean	Range	Mean	Range	
906			0.36[a]	0.34-0.40			Cc±Hm±Py
1415	0.30	0.28-0.33	0.34	0.33-0.35	0.37	0.36-0.40	Cc±Hm±Py
1427			0.38[a]	0.35-0.40			Cc+Hm+Qtz
1699	0.29	0.26-0.31			0.36	0.33-0.40	±Cc±Ksp±Hm
1984	0.27	0.25-0.29			0.30	0.29-0.33	Py±Cc±Qtz
2061	0.25	0.24-0.26			0.33	0.30-0.36	±Py±Qtz
2195	0.28	0.25-0.32			0.37	0.33-0.41	Ksp±Anh±Hm
2560	0.26	0.23-0.28			0.32	0.29-0.36	Ksp±Cc
2619	0.29	0.27-0.30			0.34	0.32-0.36	±Anh±Qtz
2745	0.32	0.26-0.34			0.39	0.36-0.40	Ksp+Hm±Anh±Py
2773	0.27	0.23-0.29			0.33	0.32-0.35	Py±Qtz
2889	0.27	0.21-0.29			0.34	0.33-0.34	±Py±Qtz±Act
2955	0.25	0.21-0.27			0.30	0.28-0.31	±Act

Zoned epidotes are subdivided into broad compositional domains (Fe-poor, intermediate, and Fe-rich) which correspond to regions of different brightnesses identified with BSE imaging (e.g., see Figure 5). Calculation of the mean composition is based on a minimum of 10 analyses.

[a] Zoning not recognized in vein epidotes from this depth.

rock lithology is shown in Figure 4. The mole fraction of $Ca_2Fe_3Si_3O_{12}(OH)$ (X_{Ps}) in vein epidote ranges from 0.21 to 0.41. The minimum Fe^{3+} content of vein epidotes generally decreases with increasing depth from X_{Ps} ~0.33 at 906 m to $X_{Ps} \sim 0.21$ at 2900 m (Figure 4); the maximum X_{Ps} is > 0.33 at any given depth. Vein epidotes do not show the same minima and maxima observed in the compositions of metasandstone epidotes as a function of depth [see *Bird et al.*, 1987, this issue]. No obvious correlation is apparent between epidote composition and host rock lithology, as shown in Figure 4. The composition of vein epidotes appears to be related to the associated vein mineralogy, parageneses, depth (i.e., downhole temperature), and fluid composition (discussed in the following section). In hematite-bearing assemblages, epidotes tend to be more Fe-rich (Table 2). A qualitative correlation may exist between the modal increase in vein anhydrite at depths from 2195 to 2745 m and the slight increase in the Al content of epidote with increasing depth.

Compositional zoning, common in most vein epidote crystals, is defined by variations in X_{Ps} or, to a lesser degree, in REE content. The zoning pattern is generally systematic, from core to rim (Figure 5). Crystal cores are Al-rich, whereas their rims are enriched in Fe^{3+} and in contact with later vein minerals including calcite, anhydrite, and hematite. This compositional zoning accounts for the bimodal and, in one case, trimodal distribution of epidote

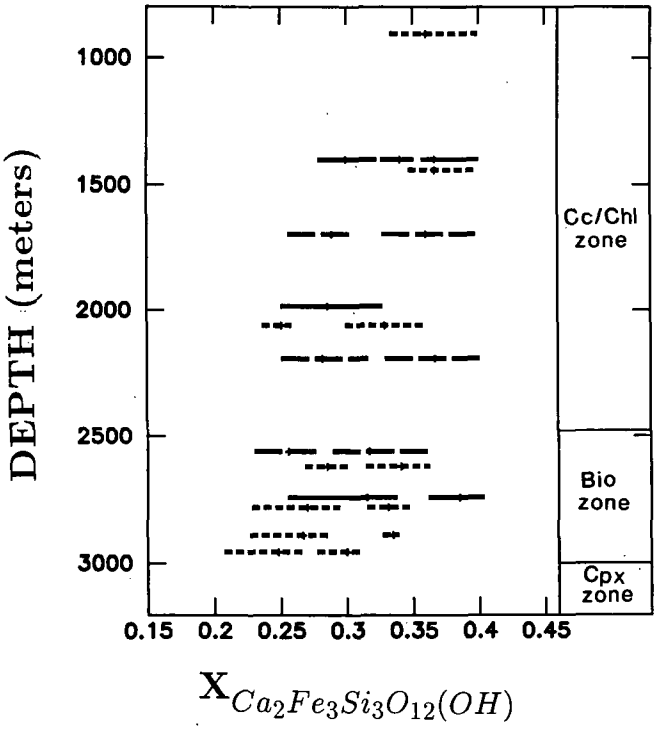

Fig. 4. Vein epidote compositions as a function of depth in the State 2-14 drill hole. Host rock lithology is given by different line types : (1) solid line, metasiltstone, (2) long dashed line, metashale, and (3) short dashed line, metasandstone. The breaks in lines correspond to separate data sets represented by the mean (ticmarks) and range in X_{Ps} compositions presented in Table 2 . Metamorphic zones from *Cho et al.* [1987, this issue].

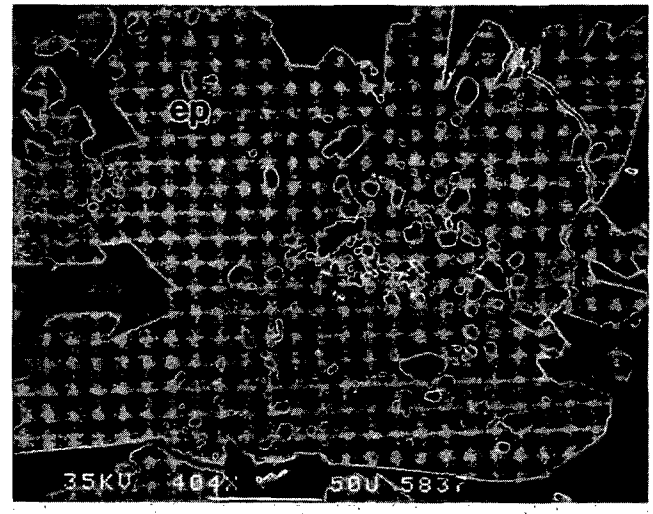

Fig. 5. Backscattered electron image showing compositional zoning in vein epidotes. The Al-rich core (dark) is rimmed by Fe-rich epidote (light). Microscopic inclusions of cassiterite (light grains) occur in the core. Later calcite (Cc) encloses epidote. Sample depth is 1415 m. Scale bar is 50 μm.

compositions presented in Figure 4. In some grains of epidote, more complex zoning patterns are apparent.

THERMODYNAMIC ANALYSIS OF VEIN MINERAL PHASE RELATIONS

An understanding of the extent to which equilibrium is obtained among vein minerals and hydrothermal solutions is essential for adequate description and interpretation of mineral paragenesis and chemical mass transfer associated with fracture sealing in geothermal systems. The preservation of mineralized veins in drill core and the availability of hydrothermal fluids from the State 2-14 drill hole at 1867 m depth enable comparison of predicted and observed phase relations. Phase diagrams presented below illustrate the effects of the activity of aqueous species (a_i), and the fugacities (f_i) of CO_2, O_2, and S_2 on the stability relations of the vein-filling minerals.

Thermodynamic analysis of phase relations involving epidote of variable composition requires provision for exchange of octahedral Fe^{3+} and Al. Equations and data describing the activities of the $Ca_2FeAl_2Si_3O_{12}(OH)$ (epidote) and $Ca_2Al_3Si_3O_{12}(OH)$ (clinozoisite) components of epidote solid solution are given by *Bird and Helgeson* [1980]. For epidote, the mixing model explicitly accounts for the temperature dependence of substitutional order-disorder of Fe^{3+} and Al in the M1 and M3 octahedral sites. Ideal mixing of Fe^{3+} and Al is assumed in a single octahedral site in prehnite and in the two octahedral sites of grandite garnet for the iron-rich compositions considered here. Unit activity is adopted for quartz, K-feldspar, hematite, calcite, anhydrite, and muscovite. Thermodynamic data for minerals and aqueous solutions are from *Helgeson et al.* [1978, 1981] and *Helgeson and Kirkham* [1974*a*, *b*, 1976]. All diagrams are constructed at 300°C , which represents the approximate temperature of the geothermal fluid from the 1867 m production zone *Sass et al.*, [1987, this issue].

Phase relations in the system CaO-K_2O-Fe_2O_3-Al_2O_3-SiO_2-H_2O-H_2SO_4-CO_2 are shown in Figure 6 at 300°C and 86 bars as a function of log $a_{Ca^{2+}}/a^2_{H+}$ and log a_{K+}/a_{H+} in an aqueous phase in equilibrium with quartz where a_{H_2O} = 1. Figures 6*a* and 6*b* illustrate phase relations involving epidote of X_{Ps} = 0.27 and X_{Ps} = 0.33, respectively, projected onto the log $a_{Ca^{2+}}/a^2_{H+}$ - log a_{K+}/a_{H+} plane. These compositions correspond to the average values of Fe-poor and Fe-rich domains in zoned epidotes (Table 2). The minimum value of $a_{Ca^{2+}}/a^2_{H+}$ in a fluid in equilibrium with epidote and quartz is constrained by the stability field of hematite according to the reaction

$$6Ca_2FeAl_2Si_3O_{12}(OH) + 8H^+ \rightleftharpoons 4Ca_2Al_3Si_3O_{12}(OH) + 3Fe_2O_3 + 4Ca^{2+} + 6SiO_2 + 5H_2O \quad (1)$$

Saturation of the fluid phase with respect to calcite and anhydrite, represented by the reactions

$$CaCO_3 + 2H^+ \rightleftharpoons Ca^{2+} + CO_2 + H_2O \quad (2)$$

$$CaSO_4 \rightleftharpoons Ca^{2+} + SO_4^{2-} \quad (3)$$

are given in terms of f_{CO_2} and log $a_{SO_4^{2-}} \cdot a^2_{H+}$, respectively, on the right-hand side of the phase diagrams in Figure 6. The dashed line in Figure 6 represents the calcite saturation for f_{CO_2} of 14 bars. This value was calculated using the gas and brine analyses measured in the December 1985 flow test

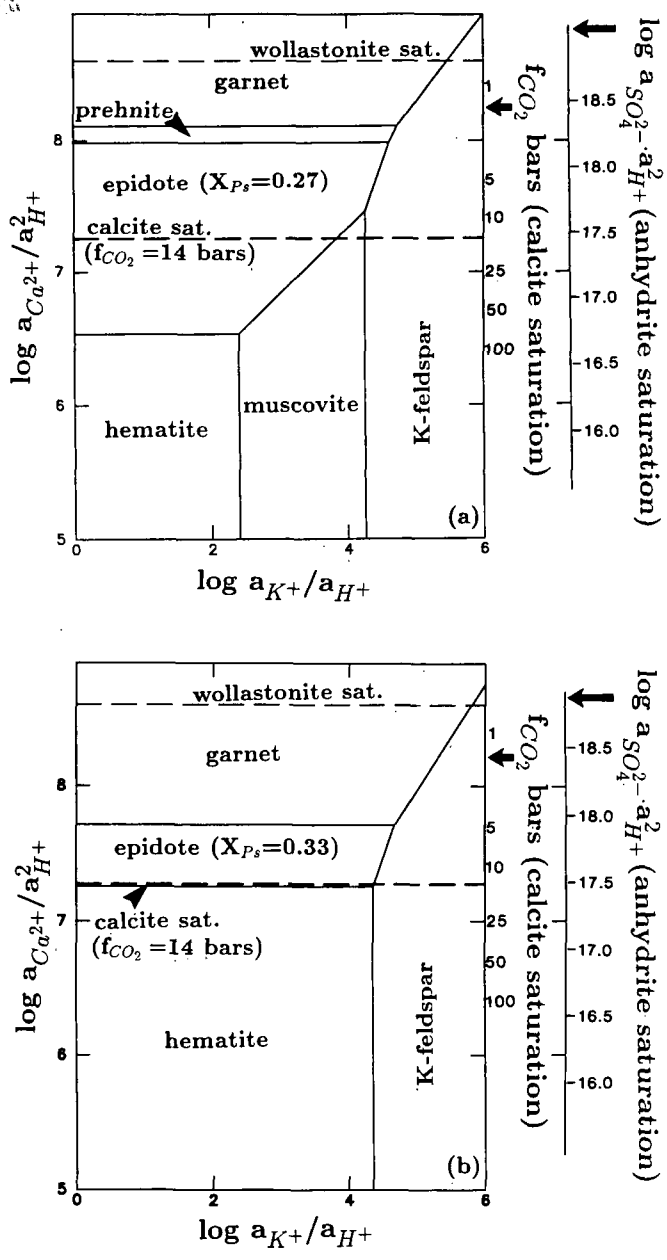

Fig. 6. Logarithmic activity-activity diagrams for the system CaO-Al_2O_3-K_2O-Fe_2O_3-SiO_2-H_2O- H_2SO_4-CO_2, at 300°C and pressure corresponding to liquid-vapor equilibrium of H_2O (86 bars) where a_{H_2O} = 1, and a_{SiO_2} = quartz saturation. Phase relations involving epidote with a composition corresponding to X_{Ps} = 0.27 and 0.33 are given in Figures 6*a* and 6*b*, respectively. Calcite saturation in the 1867 m discharge fluid is represented by the bold dashed line. See text for further discussion.

at 1867 m [*Janik et al.*, 1987] together with the experimentally determined solubility data and fugacity coefficients of [*Drummond*, 1981] for CO_2 in a 6.7 molal equivalent NaCl solution. To account for the high salinity of the Salton Sea brines, phase relations were also determined using values for a_{H_2O} of 0.8 and 0.9; it can be shown that this causes no appreciable change in the phase diagram topologies presented in Figure 6.

As shown in Figures 6*a* and 6*b*, increasing the Fe content of epidote, as represented by zoning in State 2-14 epidotes (e.g., Figure 5), causes epidote to be stable over a narrower range of log $a_{Ca^{2+}}/a^2_{H+}$ values and stabilizes the assem-

blage K-feldspar + epidote + hematite in accord with the decrease and eventual disappearance of the intervening stability field of muscovite above $X_{Ps} \simeq 0.31$. The paragenesis of Ksp→Ep (e.g., see Figures 3*c*, 3*d*, and 3*e*) is consistent with an isobaric, isothermal decrease in a_{K+}/a^2_{H+} relative to $a_{Ca^{2+}}/a^2_{H+}$ in the geothermal fluid. Calcite precipitation in veins, which everywhere occurred later than K-feldspar + epidote, might have happened either in response to an increase in f_{CO_2} or in $a_{Ca^{2+}}/a^2_{H+}$ or to some combination of both. In a similar way, the precipitation of anhydrite, which also postdates K-feldspar and epidote in veins, may have resulted from an increase in $a_{Ca^{2+}}/a^2_{H+}$ or from an increase in the $a_{SO_4^{2-}}$ of the fluid or from some combination of these two variables. A decrease in *p*H would favor precipitation of anhydrite preferentially to calcite as shown by the reaction

$$CaCO_3 + 2H^+ + SO_4^{2-} \rightleftharpoons CaSO_4 + CO_2 + H_2O \quad (4)$$

Dissolution of K-feldspar by calcite- or anhydrite-saturated fluids, as evidenced by the corroded and embayed character of K-feldspar in contact with these later vein minerals (Figure 3*d*), demonstrates that these late fluids were not in local equilibrium with K-feldspar. It should be noted in Figure 6*a* that for $f_{CO_2} = 14$ bars, calcite cannot coexist with aluminuous epidote and hematite if $X_{Ps} < 0.33$.

The absence of prehnite, a common hydrothermal calc-silicate mineral in epidote-bearing geothermal systems [*Bird et al.*, 1984], may be attributed to the f_{CO_2} of the hydrothermal fluid which is too high to stabilize prehnite. For equilibria involving epidote with an X_{Ps} content of 0.27 at 300°C (Figure 6a), prehnite is stable for values of $f_{CO_2} < 3$ bars, which is significantly less than the calculated f_{CO_2} of 14 bars in the reservoir fluid at 1867 m and 300°C. Other geochemical parameters of the fluid which may also be responsible for the absence of prehnite include f_{O_2} [*Cho et al.*, 1987, this issue] and Fe^{3+} to H^+ ion activity ratio [*Rose and Bird*, 1987].

The vein assemblage of epidote, hematite, calcite, and quartz occurs at depths from 900 to 2000 m in the State 2-14 drill hole (Figure 3*b*), where temperatures range from ~250 to 300°C. Local equilibria among these vein minerals are represented in Figure 7 as a function of temperature, X_{Ps} in epidote, and log $a_{Ca^{2+}}/a^2_{H+}$ and log f_{CO_2} in the fluid phase. The solid curves in Figure 7 delineate equilibrium among epidote, hematite, quartz, and an aqueous fluid (reaction (1)) for a range of X_{Ps} values, and the dashed curves denote equilibrium of the fluid with calcite (reaction (2)) as a function of f_{CO_2}. In Figure 7, the solid circle denotes the temperature (300°C) and f_{CO_2} (14 bars) of the fluid in the State 2-14 drill hole at 1867 m. The modern brine appears to be in local equilibrium with hematite, quartz, calcite, and epidote with a composition of $X_{Ps} = 0.33$. This is consistent with the observed zoning patterns in vein epidotes where the rims are typically Fe-rich and in contact with later calcite (Figure 5) and hematite. Hematite, calcite, and quartz in equilibrium with a more aluminous epidote (e.g., $X_{Ps} <$ 0.27) would require unreasonably high f_{CO_2} values for the geothermal fluid (>50 bars at temperatures > 280°C) as shown in Figure 7. *McKibben and Elders* [1985] and *Charles et al.*, [1987] also reported that the fluids in the Salton Sea geothermal system are in local equilibrium with hematite + silicate-bearing assemblages.

Phase relations illustrated in Figure 7 indicate that compositional variations in vein epidotes might result from

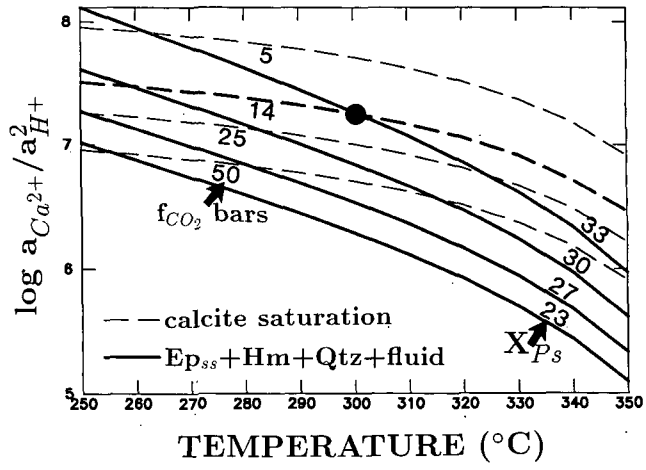

Fig. 7. Log $a_{Ca^{2+}}/a^2_{H+}$ - temperature (degrees Celsius) diagram for the system CaO-Al_2O_3-K_2O-Fe_2O_3-SiO_2-H_2O-CO_2, at 300°C and 86 bars where $a_{H_2O} = 1$, and a_{SiO_2} = quartz saturation. Equilibria for the reaction (1) as a function of X_{Ps} of epidote is denoted by the solid lines. The dashed lines show calcite saturation as a function of f_{CO_2}; the bold dashed line represents values of log $a_{Ca^{2+}}/a^2_{H+}$ and temperature required for calcite saturation when the $f_{CO_2} = 14$ bars, i.e., the value of the production fluid at 1867 m. The predicted value of f_{CO_2}, defined by the assemblage Ep (X_{Ps}=0.33) + Hm + Cc + fluid, coincides with that of the geothermal fluid at 300°C (denoted by the solid circle). See text for further discussion.

isothermal fluctuations in the f_{CO_2} of the fluid associated with decarbonation reactions in the host metasediments or with the formation of secondary calcite in other parts of the geothermal system. If the observed Al-Fe^{3+} zoning in epidotes occurred in local equilibrium with hematite + calcite + quartz, then it can be inferred from Figure 7 that epidote growth occurred due to either an increase in temperature at approximately constant f_{CO_2} or to a decrease in f_{CO_2} at constant or decreasing temperature.

Phase relations in the system CaO-K_2O-Fe_2O_3-Al_2O_3-SiO_2-H_2O-CO_2-O_2-S_2 are presented in Figure 8 at 300°C and 86 bars as a function of log f_{S_2} and log f_{O_2}. Equilibrium among epidote, anhydrite, quartz, and an aqueous solution in the presence of hematite (reaction (5)) and pyrite (reaction (6)) can be represented by the reactions

$$6Ca_2FeAl_2Si_3O_{12}(OH) + 2S_2 + 6O_2 \rightleftharpoons 4Ca_2Al_3Si_3O_{12}(OH) + 3Fe_2O_3 + 4CaSO_4 + 6SiO_2 + H_2O \quad (5)$$

$$6Ca_2FeAl_2Si_3O_{12}(OH) + 8S_2 + \tfrac{3}{2}O_2 \rightleftharpoons 4Ca_2Al_3Si_3O_{12}(OH) + 6FeS_2 + 4CaSO_4 + 6SiO_2 + H_2O \quad (6)$$

respectively. The bold lines in Figure 8 denote computed values of f_{O_2} and f_{S_2} for these reactions and for epidote compositions of $X_{Ps} = 0.27$ and 0.33. Calcite-anhydrite equilibrium according to the reaction

$$2CaSO_4 + 2CO_2 \rightleftharpoons 2CaCO_3 + S_2 + 3O_2 \quad (7)$$

is plotted as a function of f_{CO_2} (long dashed lines). The short dashed lines are metastable extensions of reaction (6) for the conditions of $f_{CO_2} = 14$ bars and calcite saturation. Note that for a f_{CO_2} value equivalent to the 1867 m production fluid (14 bars), calcite saturation in the fluid phase (reaction (7)) closely corresponds to equilibrium with the

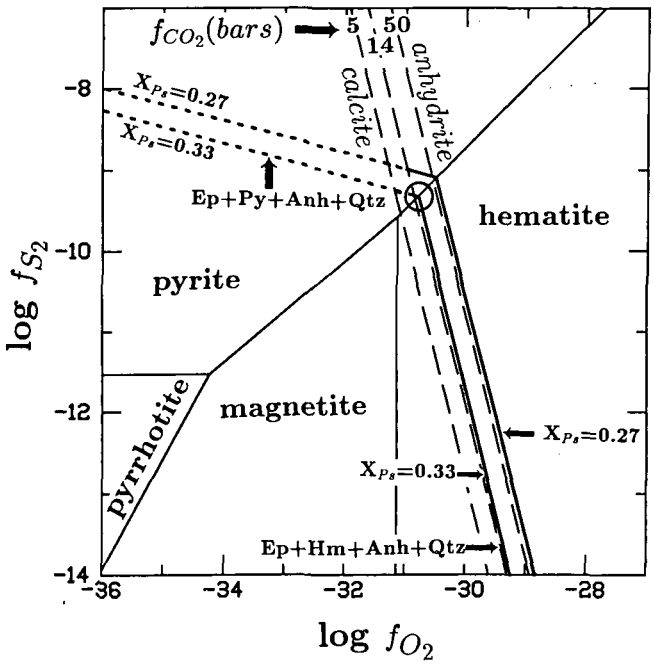

Fig. 8. Log f_{O_2} - log f_{S_2} diagram for the system CaO-Al_2O_3-K_2O-Fe_2O_3-SiO_2-H_2O-CO_2-O_2-S_2 at 300°C and 86 bars showing the stabilty field of the Fe sulfides and oxides. Ep + Hm + Anh + Qtz + fluid equilibrium (reaction (5)) and Ep + Py + Anh + Qtz + fluid equilibrium (reaction (6)) are plotted for epidote compositions of X_{Ps} = 0.27 and 0.33 (bold lines). The long dashed lines denote calcite-anhydrite equilibrium (reaction (7)) as a function of f_{CO_2} of the aqueous fluid. Metastable extensions of reaction (6) for conditions of f_{CO_2} = 14 bars and calcite saturation are represented by the short dashed lines. The log f_{O_2} and log f_{S_2} condition corresponding to calcite saturation in the fluid phase and the assemblage of epidote (X_{Ps} = 0.33) hematite, anhydrite, pyrite, and quartz is denoted by the open circle. See text for further discussion.

assemblage hematite + anhydrite + quartz ± pyrite + epidote with a composition of X_{Ps} = 0.33. This composition is similar to the rims of zoned vein epidotes. As in Figure 7, it can be seen in Figure 8 that equilibrium among the above phases and a more aluminous epidote (X_{Ps} =0.27), similar to the cores of zoned vein epidotes, would require unreasonably high f_{CO_2} values. The log f_{O_2} of ~-30.5 for the asssemblage of Hm + Anh + Ep (X_{Ps} = 0.33) + Qtz ± Py, denoted by the open circle in Figure 8, is in close agreement with a calculated log f_{O_2} of the Salton Sea brines in the Magmamax 2 drill hole reported by *McKibben and Elders* [1985]. As shown in Figure 8, increasing f_{O_2} of the hydrothermal fluid at constant f_{S_2}, temperature, and pressure results in a decrease in the iron content of epidote in equilibrium with hematite, anhydrite, and quartz. This occurs due a decrease in the calcium to hydrogen ion activity ratio in the fluid in equilibrium with the assemblage Ep + Hm + Anh + Qtz with increasing f_{O_2}. However, for the assemblage epidote + quartz in the absence of hematite and anhydrite, an increase in f_{O_2} increases X_{Ps} in epidote [*Liou*, 1973; *Bird and Helgeson*, 1981]. Phase relations among State 2-14 vein minerals presented in Figure 8 demonstrate that the composition of epidote, as well as its phase relations with calcite, anhydrite, hematite, and pyrite, are sensitive to small variations in f_{O_2}, f_{S_2}, and f_{CO_2}.

CONCLUSIONS

Epidote-bearing veins occur throughout the State 2-14 drill hole below 900 m and usually contain one or more of the following minerals: pyrite, calcite, K-feldspar, quartz, anhydrite, and hematite. Also present are minor amounts of chlorite, actinolite, Fe-Cu-Zn sulfides, titanite, and allanite. Minerals in epidote-bearing veins which are restricted to certain depth intervals include (1) calcite above ~2000 m, (2) K-feldspar from 1700 to 2745 m, (3) anhydrite from 2195 to 2745 m, and (4) actinolite below ~2890 m. Where present, K-feldspar was the first mineral to form in veins followed by epidote. In K-feldspar-absent veins, the first mineral to precipitate was epidote. Quartz, hematite, and sulfides are always paragenetically later. Calcite or anhydrite was the last vein mineral to form. Epidotes are typically zoned with Fe-rich rims and Al-rich cores. The mole fraction of $Ca_2Fe_3Si_3O_{12}(OH)$ of vein epidotes ranges from 0.21 to 0.41. In vein epidotes the maximum X_{Ps} is greater than 0.33 at any given depth; the minimum X_{Ps} generally decreases with increasing depth from ~0.33 at 906 m to ~0.21 at 2900 m.

Thermodynamic analyses of phase relations among minerals common to epidote-bearing veins indicates that the modern Salton Sea brines represented by the 1867 m production fluid appears to be in equilibrium with Fe-rich epidote (X_{Ps} = 0.33), hematite, calcite and quartz. The production fluid is not in equilibrium with Fe-poor epidote (X_{Ps} = 0.27) + Hm + Cc + Qtz. These results are consistent with the observations that the epidotes from the production zone are Fe-rich (X_{Ps} = 0.32 from *Bird et al.*, [1987, this issue]) and that the rims of zoned vein epidotes are Fe-rich and in contact with later vein minerals including calcite and hematite. The predicted value of f_{CO_2} (14 bars) for the modern Salton Sea brine in equilibrium with Ep (X_{Ps}) + Hm + Qtz + Cc is in close agreement with the calculated value of f_{CO_2} for the 1867-m reservoir fluid. This study demonstrates that variations in Al-Fe^{3+} content of epidotes may result from only minor changes in f_{CO_2}, f_{O_2}, and f_{S_2} of the fluid phase. Variations in one or more of these parameters may determine the parageneses of minerals in epidote-bearing veins and the extent of isothermal compositional zoning in vein epidotes from State 2-14 drill core reported in this paper and by *Bird et al.*, [1987, this issue])

Acknowledgments. We thank W. A. Elders, J. Mehegan, and others at University of California, Riverside for their assistance and cooperation in our investigation of the State 2-14 drill core. Helpful suggestions and assistance from N. Rose, C. Janik, and H. Hreggvidsdottir during the course of this research are gratefully acknowledged. Reveiws by C. M. Manning, P.B.L. Browne, T. Bowers, and W.A. Elders improved the quality of this manuscript. We are indebted to Prof. Gene Simmons of the Massuchusetts Institute of Technology for the use of his electron microscope facility. Electron probe microanalysis was performed at the Center for Materials Research at Stanford University. The research was funded by National Science Foundation grant NSF-EAR-84-18147.

REFERENCES

Andes, J., and M. A., McKibben, Thermal and chemical history of mineralized fractures in cores from the Salton Sea Scientific Drilling Project, (abstract), *Eos Trans. AGU, 68*, 439, 1987.

Batzle, M. L., and G. Simmons, Microfractures in rocks from two geothermal areas, *Earth Planet. Sci. Lett., 30*, 71-93, 1976.

Bence, A. E., and A. L. Albee, Empirical correction factors for the electron microanalysis of silicates and oxides, *J. Geol., 76*, 382-403, 1968.

Bird, D. K., and H. C. Helgeson, Chemical interaction of aqueous solutions with epidote-feldspar mineral assemblages in geologic systems, I, Thermodynamic analysis of phase relations in the system CaO-FeO-Fe_2O_3-Al_2O_3-SiO_2-H_2O-CO_2, *Am. J. Sci., 280,* 907-941, 1980.

Bird, D. K., and H. C. Helgeson, Chemical interaction of aqueous solutions with epidote- feldspar mineral assemblages in geologic systems, II, Equilibrium constraints in metamorphic/geothermal processes, *Am. J. Sci., 281,* 576-614, 1981.

Bird, D. K., and D. L. Norton, Theoretical predictions of phase relations among aqueous solution and minerals: Salton Sea geothermal system, *Geochim. Cosmochim. Acta, 45,* 1479-1493, 1981.

Bird, D. K., P. Schiffman, W. A. Elders, A. E. Williams, and S. D. McDowell, Calc-silicate mineralization in active geothermal systems, *Econ. Geol., 79,* 671-695, 1984.

Bird, D.K., R. D. Rogers, and C. M. Manning, Mineralized fracture systems of the Skaergaard Intrusion, East Greenland, *Medd. Gronl., 16,*, 68 pp., 1986.

Bird, D. K., M. Cho, C. J. Janik, J. G. Liou, and L. J. Caruso, Compositional, structural, and isotopic properties of epidote in California State 2-14 well, Salton Sea geothermal system, (abstract), *Eos Trans. AGU, 68,* 454, 1987.

Bird, D. K., M. Cho, C. J. Janik, J. G. Liou, and L. J. Caruso, Compositional, order/disorder, and stable isotope characteristics of Al-Fe epidote, State 2-14 drill hole, Salton Sea geothermal system, *J. Geophys. Res.,* this issue.

Caruso, L.J., and G .Simmons, Uranium and microcracks in a 1000 meter core, Redstone, New Hampshire, *Contrib. Mineral. Petrol., 90,* 1-17, 1985.

Cathles, L.M., Fluid flow and genesis of hydrothermal ore deposits. *Econ. Geol., 75th Anniversary Volume,* 424-457, 1981.

Charles, R., D. R., Janecky, and F., Goff, Thermodynamic analysis of chlorite-bearing assemblage stability from the 1866 m aquifer, Salton Sea Scientific Drilling Project, (abstract), *Eos Trans. AGU, 455,* 68, 1987.

Cho, M., J. G. Liou, and D. K. Bird, Prograde phase relations in the California State 2-14 well meta-sandstones, Salton Sea geothermal field, (abstract), *Eos Trans. AGU, 68,* 445, 1987.

Cho, M., J. G. Liou, and D. K. Bird, Prograde phase relations in the State 2-14 well metasandstones, Salton Sea geothermal field, California, *J. Geophys. Res.,* this issue.

Drummond, S. E., Boiling and mixing of hydrothermal fluids: Chemical effects on mineral precipitation, Ph.D. thesis, Pa. State Univ., University Park, 1981.

Elders, W. A., Determination of the fracture history in geothermal reservoirs through the study of minerals, Fractures in Geothermal Reservoirs, *Geothermal Resources Council Spec. Rept., 12,* 65-70, 1982.

Elders, W. A., and L. H. Cohen, The Salton Sea geothermal field, California, as a near-field analog of a radioactive waste repository in salt, Battelle Mem. Inst., Office of Nucl. Waste Isol., *BMI/ONWI-513,* 139 p., Columbus, Ohio, 1983.

Elders, W. A., and J. H. Sass, An overview of the SSSDP, (abstract), *Eos Trans. AGU, 68,* 438, 1987.

Elders, W. A., and J. H. Sass, An overview of the SSSDP, *J. Geophys. Res.,* this issue.

Elders, W. A., D. K. Bird, A. E. Williams, and P. Schiffman, Hydrothermal flow regime and magmatic heat source of the Cerro Prieto geothermal system, Baja California, Mexico, *Geothermics, 13,* 27-47, 1984.

Fehn, U., L. M. Cathles, and H. D. Holland, Hydrothermal convection and uranium deposits in abnormally radioactive plutons, *Econ. Geol., 73,* 1556-1566, 1978.

Ferry, J. M., P, T, f_{CO_2}, and f_{H_2O} during metamorphism of calcareous sediments in the Waterville-Vassalboro area, south-central Maine, *Contrib. Mineral. Petrol., 57,* 119-143, 1976.

Ferry, J. M., Reaction mechanisms, physical conditions, and mass transfer during hydrothermal alteration of mica and feldspar in granitic rocks from south-central Maine, USA, *Contrib. Mineral. Petrol., 68,* 125-139, 1979.

Ferry, J.M., Hydrothermal alteration of Tertiary igneous rocks from the Isle of Skye, northwest Scotland, I, Gabbros, *Contrib. Mineral. Petrol., 91,* 264-282, 1985.

Ferry, J. M., Reaction progress: A monitor of fluid-rock interaction during metamorphism and hydrothermal events, in *Fluid-Rock Interaction During Metamorphism,* edited by J. V. Walter and B. J. Wood, *Adv. Phys. Geochem.*, vol. 5, pp. 60-88, Springer-Verlag, New York, 1986.

Forester, R.W. and Taylor, H.P., ^{18}O-depleted igneous rocks from the Tertiary complex of the Isle of Mull, Scotland, *Earth Planet. Sci. Lett., 32,* 11-17, 1976.

Helgeson, H. C., Solution chemistry and metamorphism, *Researches in Geochemistry,* vol. 2, edited by P. H. Abelson, pp. 362-404, John Wiley, New York, 1967.

Helgeson, H. C., and D. H. Kirkham, Theoretical prediction of the thermodynamic behavior of aqueous electrolytes at high pressures and temperatures, I, Summary of the thermodynamic/electrostatic properties of the solvent, *Am. J. Sci., 274,* 1089-1198, 1974*a*.

Helgeson, H. C., and D. H. Kirkham, Theoretical prediction of the thermodynamic behavior of aqueous electrolytes at high pressures and temperatures, II, Debye-Huckel parameters for activity coefficients and relative partial molal properties, *Am. J. Sci., 274,* 1199-1261, 1974*b*.

Helgeson, H. C., and D. H. Kirkham, Theoretical prediction of the thermodynamic behavior of aqueous electrolytes at high pressures and temperatures, III, Equations of state for aqueous species at infinite dilution, *Am. J. Sci., 276,* 97-240, 1976.

Helgeson, H. C., J. M. Delaney, H. W. Nesbitt, and D.K. Bird, Summary and critique of the thermodynamic properties of rock-forming minerals, *Am. J. Sci., 278,* 229, 1978.

Helgeson, H. C., D. H. Kirkham, and G. C. Flowers, Theoretical predictions of the thermodynamic behavior of aqueous electrolytes at high pressures and temperatures, IV, Calculations of activity coefficients, osmotic coefficients and apparent molal and standard and relative partial molal properties to 5 kb and 600°C, *Am. J. Sci., 281,* 1249-1516, 1981.

Herzig, C. T., and J. M. Mehegan, The lithostratigraphy of the Colorado River delta in the active SSGF pull-apart basin, California (abstract), *Eos Trans. AGU, 68,* 444, 1987.

Herzig, C. T., J. M. Mehegan, and C. E. Stelting, Lithostratigraphy of the State 2-14 borehole: Salton Sea Scientific Drilling Project, *J. Geophys. Res.,* this issue.

Janik, C. L., H. Shigeno, T. Cheatam, and A. H. Truesdell, Gas geothermometers applied to separated steam from the December 1985 flow test of the SSSDP well, (abstract) *Eos Trans. AGU, 68,* 440, 1987.

Liou, J. G., Synthesis and stability relations of epidote, $Ca_2Al_2FeSi_3O_{12}(OH)$. *J. Petrol., 14,* 381-413, 1973.

McDowell, S. D., and W. A. Elders, Allogenic layered silicate minerals in borehole Elmore #1, Salton Sea geothermal system, California, *Am. Mineral., 68,* 1146-1159, 1983.

McKibben, M. A., and W. A. Elders, Fe-Zn-Cu-Pb mineralization in the Salton Sea Geothermal System, Imperial Valley, California, *Econ. Geol., 80,* 539-559, 1985.

Mehegan, J. M., C. T. Herzig, and R. M. Sullivan, Salton Sea Scientific Drilling Project, California State 2-14 well: Visual core descriptions, vols. 1 and 2, *Rep. UCR/IGPP-86/1,* Univ. of Calif., Riverside, 1986.

Muffler, L. J. P., and D. E. White, Origin of CO_2 in the Salton Sea geothermal system, southern California, USA, *Proc. Int. Geol. Congress,* 23rd, 185-194, 1968.

Muffler, L. J. P., and D. E. White, Active metamorphism of upper Cenozoic sediments in the Salton Sea geothermal field and Salton Trough, southeastern California, *Geol. Soc. Am. Bull., 80,* 157-182, 1969.

Norton, D. L., Fluid and heat transport phenomena typical of copper-bearing plutons environments, southeastern Arizona, *Advances in Geology of Porphyry Copper Deposits, Southwestern North America,* edited by S. R. Titley, pp. 59-72, University of Arizona Press, Tucson, 1982.

Norton, D.L., Theory of hydrothermal systems, *Annu. Rev. Earth Planet. Sci., 12,* 155-177, 1984.

Norton D. L., and R. Knapp, Transport phenomena in hydrothermal systems, the nature of porosity, *Am. J. Sci., 277,* 913-936, 1977.

Norton D. L., and J. Knight, Transport phenomena in hydrothermal systems, cooling plutons, *Am. J. Sci., 277,* 937-981, 1977.

Norton, D.L. and H.P. Taylor, Quantitative simulation of hydrothermal systems of crystallizing magma on the basis of transport theory and oxygen isotope data: an analysis of the Skaergaard intrusion, *J. Petrol., 20,* 421-486, 1979.

Richter, D., and G. Simmons, Microcracks in crustal igneous rock:

Microscopy, *The Earth's Crust, Geophys. Monogr. Ser.*, vol. 20, edited by J. Heacock, pp. 149-180, Washington, D. C., 1977.

Rose, N. M., and D. K. Bird, Prehnite-epidote phase relations in the Nordre Aputiteq and Kruuse Fjord layered gabbros, East Greenland, *J. Petrol., 28,* 1193-1218, 1987.

Sass, J. H., J. D. Hendricks, S. S. Priest, and L. C. Robinson, Temperature and heat flow in the state 2-14 well, Salton Sea Scientific Drilling Project (abstract), *Eos Trans. AGU, 68,* 454, 1987.

Sass, J. H., S. S. Priest, L. E. Duda, C.C. Carson, J. D. Hendricks, and L. C. Robinson, Thermal regime of the state 2-14 well, Salton Sea Scientific Drilling Project, *J. Geophys. Res.*, this issue.

Schiffman, P. D., D. K. Bird, and W. A. Elders, Hydrothermal mineralogy of calcareous sandstones from the Colorado River delta in the Cerro Prieto geothermal system, Baja California, Mexico, *Mineral. Mag., 49,* 435-449, 1985.

Shearer, C. K., J. J. Papike, S. B. Simon, B. L. Davis, F. J. Rich, and J. C. Laul, Progress of mineral reactions: Variations in the modal mineralogy, mineral chemistry and bulk chemistry of the SSSDP core (abstract), *Eos Trans. AGU, 68,* 446, 1987.

Skinner, B. J., D. E. White, H. J. Rose, and R. E. May, Sulfides associated with the Salton Sea geothermal brine, *Econ. Geol., 62,* 316-330, 1967.

Taylor, H. P. and R. W., Forester, An oxygen isotope study of the Skaergaard intrusion and its country rocks: A description of a 55-m.y. old fossil hydrothermal system, *J. Petrol., 20,* 355-419, 1979.

White, D. E., Active geothermal systems and hydrothermal ore deposits, *Econ. Geol., 75th Anniversary Volume,* 392-423, 1981.

White, D. E., E. T. Anderson, and D. K. Grubbs, Geothermal brine well-mile-deep drill hole may tap ore-bearing magmatic water and rocks undergoing metamorphism, *Science, 139,* 919-922, 1961.

Younker, L. W., P. W. Kasameyer, and J. D. Tewhey, Geological, geophysical, and thermal characteristics of the Salton Sea geothermal field, California, *J. Volcanology Geotherm. Res., 12,* 221-258, 1982.

D. K. Bird, L. J. Caruso, and J. G. Liou, Department of Geology, Stanford University, Stanford, CA 94306.

M. Cho, Department of Earth and Space Sciences, University of California, Los Angeles, CA 90024.

(Received August 5, 1987;
accepted February 17, 1988.)

JOURNAL OF GEOPHYSICAL RESEARCH, VOL. 93, NO. B11, PAGES 13,135–13,144, NOVEMBER 10, 1988

Compositional, Order/Disorder, and Stable Isotope Characteristics of Al-Fe Epidote, State 2-14 Drill Hole, Salton Sea Geothermal System

D.K. BIRD AND M. CHO[1]

Department of Geology, Stanford University, Stanford, California

C.J. JANIK

U. S. Geological Survey, Menlo Park, California

J.G. LIOU AND L.J. CARUSO

Department of Geology, Stanford University, Stanford, California

Epidote ($Ca_2Fe_3Si_3O_{12}(OH)$-$Ca_2Al_3Si_3O_{12}(OH)$) is a common hydrothermal mineral in metasediments and veins at depths >900 m in the State 2-14 drill hole of the Salton Sea geothermal system. The mole fraction of $Ca_2Fe_3Si_3O_{12}(OH)$ in epidotes (X_{ps}) from this drill hole ranges from 0.11 to 0.42, and complex compositional zoning of octahedral Fe^{3+} and Al is typical within single grains. With increasing depth there is an overall, but irregular, decrease in the Fe^{3+} content of epidotes in metasandstones. In most samples, vein epidotes are more Fe^{3+}-rich and exhibit a wider compositional range than metasandstone epidotes from the same depth. Octahedral Fe^{3+} in the M(1) sites in four epidotes, evaluated by ^{57}Fe Mössbauer spectroscopy, ranges from 7.5 ± 1.7% to 11.4 ± 1.5% of the total iron. The most ordered epidote formed in veins at 2618 m in the biotite zone. This epidote has an ordering parameter (σ=1-2$X_{Fe^{3+},M(1)}$) of 0.85 ± 0.03 which corresponds to a calculated state of equilibrium order/disorder at ~390° ± 60°C, in close agreement with the probable downhole temperature of ~340°C, Two epidote samples from the chlorite + calcite zone (1420 m, ~265°C; 1867 m, ~300°C) are more disordered, corresponding to calculated states of equilibrium order/disorder of >450°C, These data suggest that the analyzed epidotes from the chlorite + calcite zone are in a metastable state of substitutional order/disorder. The measured value of $\delta D_{epidote}$ from 1420 m is -96°/₀₀ , which is 5-6°/₀₀ lighter than epidotes from 1867 m ($\delta D_{epidote}$= -90°/₀₀), 2227 m ($\delta D_{epidote}$= -91°/₀₀), and 2618 m ($\delta D_{epidote}$= -90 °/₀₀). When compared to the reservoir fluid from the December 1985 flow test, the derived fractionation of hydrogen isotopes between epidote and the geothermal brine is -19°/₀₀ at 1867 m and ~340°C. This value is in accord with published experimental hydrogen isotope fractionations between iron-rich epidote and aqueous electrolyte solutions. Therefore, considering the complexity of the Salton Sea brine, the isotopic temperature is similar to the inferred downhole temperature.

INTRODUCTION

Hydrothermal metmorphism of Colorado River delta sediments in the Gulf of California rift system has produced systematic mineral zoning that can be related to subsurface temperature and the circulation of hydrothermal solutions. The largest geothermal system in this region is located near the southern end of the Salton Sea and is characterized by high temperatures (>350°C at ~2 km depth), by high-salinity hydrothermal solutions (>200,000 ppm total dissolved solids), and by a positive residual Bouguer gravity anomaly with ~20 mGal closures [*Elders et al.*, 1972]. The gravity anomaly is due in part to thermal metamorphism and metasomatism of the sedimentary basin fill by a magma-hydrothermal system that is forming modally abundant, high-density secondary minerals such as epidote (ρ=3.3-3.6 g/cm^3) and pyrite (ρ=5.0 g/cm^3). In this geothermal system, epidote is one of the most abundant secondary minerals at >1 km depths and >250°C, [*White, et al.*, 1961; *Helgeson*, 1967, 1968; *Keith, et al.*, 1968; *Muffler and White*, 1969].

In addition to its occurrence in the Salton Sea geothermal system, epidote is a common secondary mineral formed during hydrothermal alteration and low to medium grades of regional metamorphism of a wide variety of igneous, metamorphic, and sedimentary rocks. Detailed petrologic observations, hydrothermal experiments, and theoretical calculations have documented the dependence of epidote stability on bulk composition, temperature, and pressure and have demonstrated that Fe^{3+}-Al exchange in epidote is a sensitive function of cation to hydrogen ion activity ratios, *p*H, and the fugacities of CO_2 and O_2 of the fluid phase [*Ramberg*, 1949; *Rosenqvist*, 1952; *Harpum*, 1954; *Miyashiro and Seki*, 1958; *Fyfe*, 1960; *Kretz*, 1963; *Chatterjee*, 1967; *Seki*, 1972; *Strens*, 1965; *Holdaway*, 1972; *Liou*, 1973, 1983; *Best*, 1977; *Bird and Helgeson*, 1980, 1981; *Cavaretta et al.*, 1982; *Shikazono*, 1984; *Schiffman et al.*, 1985; *Rose and Bird*, 1987; *Caruso et al.*, 1987, this issue]. Complex compositional zoning, parageneses, and textures on the scale of petrographic thin sections are typical of many natural epidotes, and it is these features that makes interpretation of possible local equilibrium assemblages difficult to ascertain. Wide variations in the distribution of Fe^{3+} and Al between coex-

[1]Now at Department of Earth and Space Sciences, University of California, Los Angeles.

Paper number 88JB03238.
0148-0227/88/88JB-03238$05.00

isting epidote, grandite garnet, and/or prehnite suggest that metastable phase relations are commonly preserved during hydrothermal processes [e.g., *Tazaki*, 1983; *Bird et al.*, 1984, 1986; *Rose and Bird*, 1987].

The exchange of octahedral Fe^{3+}-Al in epidote is further complicated by intracrystalline substitutional order/disorder in the M(1) and M(3) octahedral sites. Although Fe^{3+} is preferentially ordered into the octahedral M(3) site of epidote, several of the natural and all of the synthetic epidotes analyzed by *Dollase* [1973] have 7-14% of their total Fe^{3+} in the smaller octahedral M(1) site. The temperature dependence of octahedral substitutional order/disorder in epidote has been predicted by *Bird and Helgeson* [1980] from experimental observations reported by *Liou* [1973] and *Dollase* [1973]; however, the extent to which the octahedral ordering state of natural epidotes approximates the equilibrium intracrystalline site distributions is at present unknown.

Epidote is also known to have unusual hydrogen isotope concentrations in that D is concentrated in epidote relative to other coexisting hydrous minerals in fossil hydrothermal systems [*Sheppard and Taylor*, 1974; *Forester and Taylor*, 1977; *Taylor and Forester*, 1979]. Experimental studies by *Graham and Sheppard* [1980], *Graham et al.* [1980], and *Graham* [1981] suggest that hydrogen isotope exchange between epidote and aqueous solutions is rapid relative to other hydrous silicates, that the closure temperature for the exchange is ~200°C, and that the equilibrium D content of epidote is dependent on temperature and the chemistry of the coexisting aqueous electrolyte solution.

The compositional, structural, and isotopic properties of epidote, described above, affect the way petrologists predict the physical-chemical conditions of epidote formation based on geologic observations, experimental measurements, and theoretical calculations. In this paper we report on the variations of Fe^{3+} and Al content of epidotes from metasandstones and veins throughout the core samples of the State 2-14 drill hole, and on the degree of octahedral order/disorder and stable isotope compositions of four epidote concentrates. These observations on the crystal-chemical and stable isotopic properties of epidote from an active geothermal system will assist in evaluating experimental and theoretical studies of epidote formation in geologic systems. The location and characteristics of the State 2-14 drill hole of the Salton Sea Scientific Drilling Project are described in *Elders and Sass* [1987, this issue].

Phase Relations

Epidote is found as a common secondary mineral at depths >900 m within the State 2-14 drill hole samples. It first appears as replacement of interstitial carbonate cement and as fine-grained clots in shales and argillaceous siltstones. In metasandstones, epidote occurs as fine-grained crystals that line or partially fill interstitial pores and as partial replacement of detrital feldspars and lithic clasts. With increasing depth and temperature, epidote and other secondary minerals become larger and more equant, developing an equigranular fabric where the hydrothermal and detrital minerals are approximately the same size. The distribution of the secondary minerals in metasandstones from the State 2-14 drill hole is summarized in Figure 1 and is given in detail by *Cho et al.* [1987, this issue]. Characteristic assemblages, including epidote, quartz, and albite, are (1) chlorite + K-feldspar, or phengitic muscovite + calcite for the chlorite + calcite zone (~900-2480 m); (2) biotite + chlorite + K-feldspar ± anhydrite, or biotite + actinolite ± chlorite for the biotite zone (2480-3000 m); and (3) salite + actinolite ± biotite ± oligoclase ± actinolitic hornblende for the clinopyroxene zone (3000-3180 m).

In many of the fracture systems penetrated by the drill hole, epidotes form up to 3-mm-long crystals lining fracture walls, filling veins, or overgrowing vein K-feldspar. Associated secondary minerals in the fractures include varied assemblages of K-feldspar, quartz, calcite, anhydrite, pyrite, hematite and trace amounts of Fe-Cu-Pb-Zn sulfides [*Mehegan et al.*, 1986; *Andes and McKibben*, 1987; *Caruso et al.*, 1987, this issue]

Major Element Composition

Compositions of several hundreds of epidote grains throughout the State 2-14 drill hole were determined by electron microprobe techniques (see *Cho et al.*, [this issue] for details) to evaluate the characteristics and variations in the exchange of octahedral Fe^{3+} and Al. Minor amounts of rare earth element (REE)-rich epidotes (allanite) locally coexist with the epidotes studied. The analyzed epidotes contain mean concentrations of less than several weight percent of Mn, Mg, and REE and can thus be closely approximated by the binary ($Ca_2Fe_3Si_3O_{12}(OH)$-$Ca_2Al_3Si_3O_{12}(OH)$) (see Table 1 for representative analyses).

Compositional variations associated with Fe^{3+} and Al exchange in epidotes from metasandstones and veins are summarized in Table 2 and Figure 1. Epidotes are typically zoned with Fe^{3+}-rich rims and Al-rich cores (Figure 2). The mole fraction of $Ca_2Fe_3Si_3O_{12}(OH)$ (X_{ps}) in all the analyzed epidotes ranges from 0.11 to 0.42. The most Fe^{3+} epidotes occur in the metasandstones at ~900 m (Figure 1). With increasing depth in the chlorite + calcite zone, the mean Fe^{3+} content of matrix epidotes decreases, with local minima at ~1220 m and ~2480 m (Figure 1*b*). Near the transition from the chlorite + calcite to biotite zones, the values of X_{ps} in metasandstone epidotes increase from ~0.15-0.29 at ~2479 m to ~0.29-0.35 at ~2620 m. Actinolitic hornblende first appears as a secondary phase in the metasandstones near the X_{ps} minimum at ~3100 m.

In most of the samples studied, vein epidotes exhibit a wider range in Fe^{3+}-Al exchange and are more Fe^{3+}-rich when compared to the metasandstone epidotes from the same depth throughout the drill hole (Figure 1). Some of the vein epidotes have distinct compositional discontinuities that are associated with Al-rich cores and Fe^{3+}-rich rims, and the most Fe^{3+}-rich epidotes occur in veins that contain hematite. In vein epidotes, the minimum X_{ps} decreases from ~0.33 at 906 m to ~0.21 at 2900 m, and the maximum X_{ps} is >0.33 at any one depth throughout the drill hole samples.

As in regional metamorphic rocks described by *Miyashiro and Seki* [1958], epidotes found at the lowest temperatures in the State 2-14 drill hole are restricted to Fe^{3+}-rich compositions, and there is, in general, an increase in the Al content of epidotes with increasing temperature. The increase of X_{ps} in metasandstone epidotes associated with an increase in modal biotite and a decrease in modal calcite that marks the transition between the chlorite + calcite zone and biotite zone (2479-2620 m) has also been reported in drill hole samples elsewhere in the Salton Sea [*McDowell and*

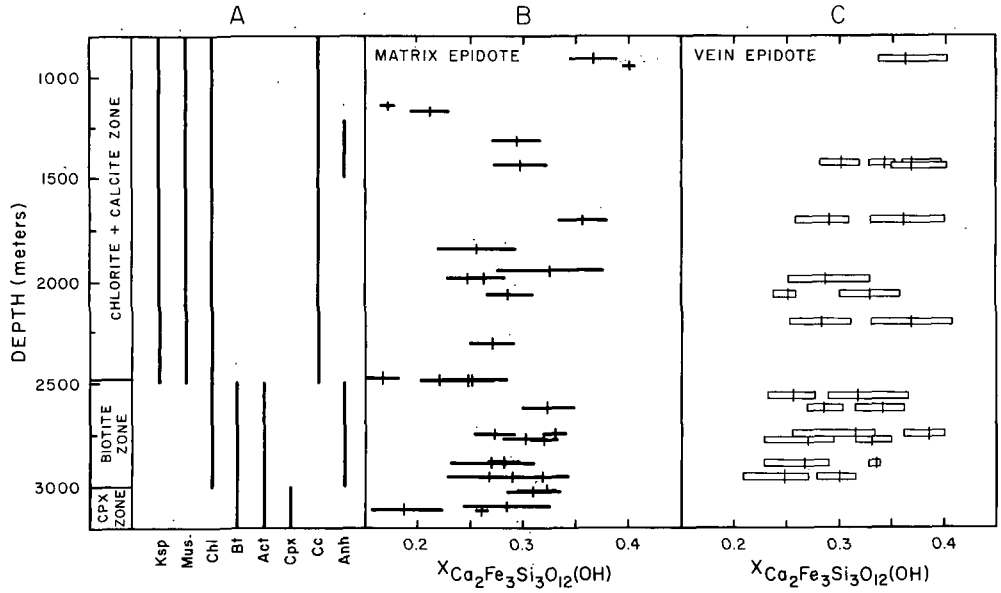

Fig. 1. Generalized distributions of secondary minerals in metasandstones and epidote compositions in metasandstone matrices and veins as a function of depth in the State 2-14 drill hole. (*a*) Phase relations include epidote, albite, and quartz (see *Cho et al.*, this issue). (*b*) The mean and one standard deviation of epidote compositions in metasandstones (see Table 2). (*c*) The mean and range in vein epidote compositions. *Caruso, et al.* [this issue] give details on vein epidote compositions and phase relations. Ksp, K-feldspar; Mus, muscovite; Chl, chlorite; Bt, biotite; Act, actinolite; Cpx, clinopyroxene; Cc, calcite; Anh, anhydrite.

McCurry, 1977] and Cerro Prieto geothermal systems [*Bird et al.*, 1984].

Mineral Separates

Five epidote concentrates were prepared from core samples at four depths for Mössbauer and stable isotope studies.

TABLE 1. Major Element Compositions of Epidotes

	Sample Depth, m			
	1420	1867	1867	2618
SiO_2	37.69	37.89	37.43	37.34
TiO_2	0.05	0.04	0.10	0.02
Al_2O_3	22.22	22.63	20.55	20.48
Fe_2O_3[a]	13.79	13.73	17.56	17.28
MnO	0.18	0.22	0.21	0.13
MgO	0.07	0.05	0.04	n.d.[b]
CaO	22.38	23.48	23.18	22.74
Total	96.38	98.04	99.07	97.98
	Cations per 12.5 Anhydrous Oxygens			
Si	3.048	3.021	2.995	3.013
Ti	0.003	0.003	0.006	0.001
Al	2.118	2.127	1.938	1.948
Fe^{3+}	0.839	0.824	1.057	1.049
Mn	0.012	0.015	0.014	0.009
Mg	0.008	0.006	0.005	0.000
Ca	1.939	2.006	1.986	1.967
Sum	7.967	8.002	8.001	7.987
X_{Fe}	0.284	0.279	0.353	0.350

The compositions of epidotes were analyzed by electron microprobe. See *Cho et al.* [this issue] for further details on analytical conditions.

[a]Total Fe as Fe_2O_3.

[b]Not detected.

These samples are described below, and histograms of analyzed X_{ps} in each separate are given in Figure 3.

1. Vein epidote from the chlorite + calcite zone at 1420 m occurs in medium to dark gray finely laminated metasiltstone containing abundant phyllosilicates and quartz together with minor pyrite porphyroblasts. Thin (<0.02 mm thick) quartz (±epidote) veinlets are crosscut by thicker (0.5-1 mm thick) epidote-rich veins. Epidotes that formed massive aggregates of coarse-grained, short, prismatic crystals were separated from the latter vein type. Associated phases in these epidote veins include quartz, hematite, and calcite.

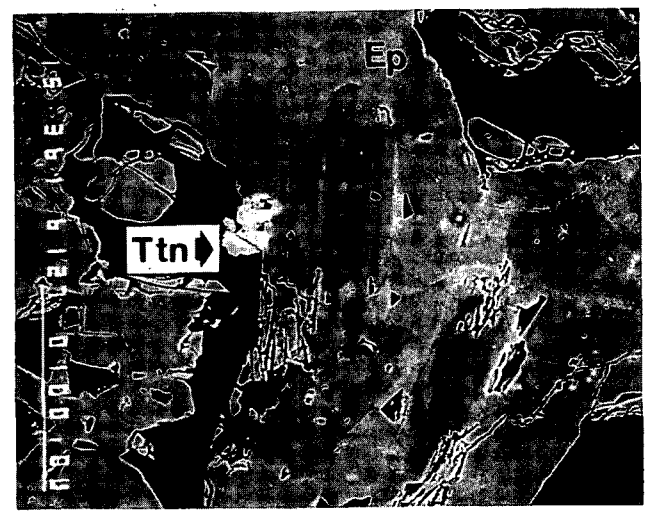

Fig. 2. Backscattered electron image of zoned epidote in rock chip ejected during production test at 1867 m. The Al-rich cores of the epidotes (dark) are rimmed by Fe^{3+}-rich epidote (light). Minor titanite (Ttn) coexists with epidote in this sample. Epidote compositions are given in Figure 3 and Table 1. The scale bar is 100 μm.

TABLE 2. Iron Content of Epidotes in Metasandstones, State 2-14 Drill Hole

Sample Depth, m	X_{ps}[a] (average±1σ)	Number of analyses	Comments[b]
		Chlorite-Calcite Zone	
905.5	36.42 ± 2.24	14	+Cc+Ab(0-1)
939.7	39.75 ± 0.59	4	
1158.7	22.10 ± 1.72	14	+Cc+Ab+Olig
1223.9	16.67 ± 1.17	7	+Cc+Ab(1-4)
1235.4	21.04 ± 2.39	10	+Cc+Ab+Olig
1305.8	29.19 ± 2.29	23	+Cc+Ab(0-2)
1426.5	29.59 ± 2.54	20	+Ab(tr.)
1699.1	35.46 ± 2.27	7	+Ab(tr.), Hm in vein
1839.6	25.51 ± 3.69	24	+Cc
1867.0	32.10 ± 5.29	31	production zone
1983.4	26.15 ± 1.98	7	+Cc+Ab
1983.7	24.62 ± 1.92	28	+Ab(?)
2061.2	28.54 ± 1.98	17	+Ab(0-2)
2301.0	26.95 ± 2.08	23	+Cc+Ab+Olig
2478.8	16.53 ± 2.15	26	+Cc+Sl+Py
		Biotite Zone	
2483.0	25.05 ± 3.37	20	+Ab
2483.5	21.96 ± 1.85	19	+Ab (1-10)
2485.5	24.69 ± 2.37	28	+Anh
2616.6	32.31 ± 2.26	15	+Ab (0-1)
2617.6	32.43 ± 2.46	10	+Ab (0-2)
2620.0	32.31 ± 1.67	10	+Ab
2745.2	33.02 ± 1.09	13	+Anh+Ab
2745.5	27.34 ± 1.94	9	+Anh
2772.1	30.15 ± 2.09	8	
2772.6	31.97 ± 1.23	11	+Ab (0-1)
2884.2	28.19 ± 1.40	19	+Ab (0-1)
2887.7	27.00 ± 2.45	6	+Cc
2887.8	26.96 ± 3.93	14	+Ab (1-3)
2955.0	26.80 ± 3.99	15	+Ab (1-5)+Olig (11-17)
2955.2	31.92 ± 2.42	16	+Ab (1-10)+Anh
2955.8A	31.92 ± 2.42	16	+Ab (0-2, 8)
2955.8B	28.95 ± 3.61	21	+Ab (0-3)
		Clinopyroxene Zone	
3019.5	31.28 ± 1.76	18	
3026.5	30.97 ± 2.46	13	chips, +Ab
3096.6	28.51 ± 4.11	22	chips, +Ab, Olig
3118.0	18.73 ± 3.67	10	chips, +Ab, Olig
3118.0	26.13 ± 0.54	4	Ep-only chip

[a] X_{ps} denotes mole fraction of $Ca_2Fe_3Si_3O_{12}(OH)$

[b] Parenthetical numbers denote mole fractional $CaAl_2Si_2O_8$ in plagioclase: Ab, albite; Anh, anhydrite; Cc, calcite; Ep, epidote; Hm, hematite; Sl, sphalerite; and Olig, oligoclase.

2. Two separates of epidote from the chlorite + calcite zone at 1867 m are designated as 1867A and 1867B. During the December 1985 flow test, numerous epidote-rich rock chips, up to ~5 cm across, were ejected from a high-permeability zone near this depth. Many of the rock specimens consist of abundant (up to 95%) euhedral and subhedral epidote crystals ranging from ~0.5 to 1.3 mm in length. Some chips contain abundant specular hematite. Minor phases are fine-grained hematite, pyrite, chlorite, and titanite. Traces of allanite occur in some of the samples. Epidote crystals are interlocked to form a network with up to ~20% porosity in some samples. Most epidote grains are Fe^{3+}-rich, but some are zoned with an Al-rich core (Figure 3). Textural relations between the metasediments and the secondary phases suggest that the ejected samples were derived from an area of intense metasomatic alteration associated with a fracture zone in the metasediments.

3. Vein epidote from the chlorite + calcite zone at 2227 m occurs in dark to pale green-gray interbedded fine-grained metasandstones and metasiltstones that contain abundant quartz, K-feldspar, and albite in the matrix. Euhedral epidote with minor quartz and anhydrite occurs in the veins and in irregularly spaced cavities. In some cavities, epidote is partially replaced by anhydrite. Epidote crystals range from 1 to ~3 mm in length.

4. Vein epidote from the biotite zone at 2618 m occurs in light green, medium-grained massive metasandstone containing abundant disseminated epidote (±pyrite) crystals in irregular porous veinlike structures. The hand sample is extensively recrystallized to an equigranular hornfels. It consists mainly of quartz and albite ($An_{0.3-1.5}$) with minor amounts of epidote and titanite. Epidote constitutes less than 5% by volume of the metasandstone; it is variable in grain size (0.01-0.1mm), anhedral in form (both granular

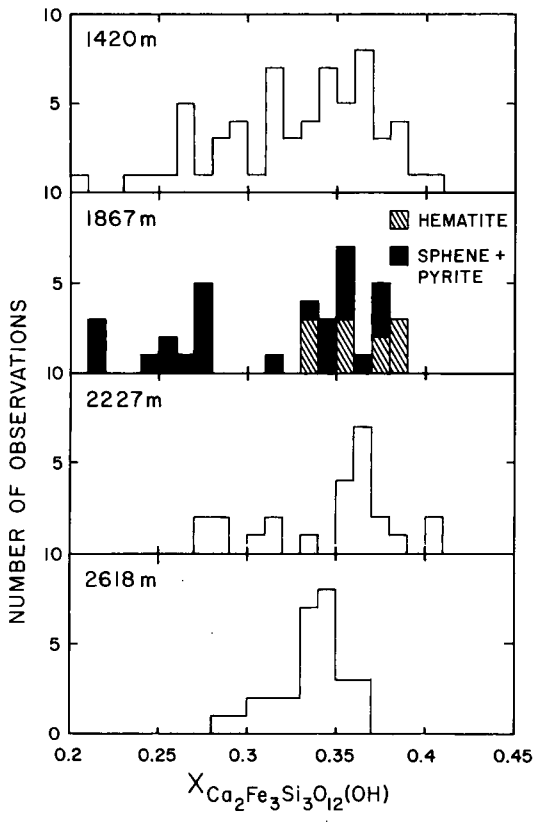

Fig. 3. Histograms of $X_{Ca_2Fe_3Si_3O_{12}(OH)}$ in epidote samples used for Mössbauer and isotope analyses. The two types of shading of the 1867 m data denote phases coexisting with the analyzed epidotes.

and fine prismatic), and irregularly zoned. Epidote becomes modally abundant in the metasandstones adjacent to the veins. Euhedral vein epidotes, from which separates were taken, are up to 1 mm long and line fracture walls together with quartz and minor amounts of anhydrite.

Although the equilibrium downhole temperatures in the State 2-14 drill hole are not known at present, the following temperatures were approximated for the present study from the temperature data presented by *Elders and Sass* [1987, this issue] and *Sass et al.* [1987, this issue]: 1420 m, ~265° ± 25°C, 1867 m, ~300° ± 25°C, 2227 m, ~320° ± 25°C, and 2618 m, ~340° ± 25°C.

Order/Disorder

Epidote ($Ca_2Fe_3Si_3O_{12}(OH)$ - $Ca_2Al_3Si_3O_{12}(OH)$) exhibits a limited range of intracrystalline substitutional order/disorder of Al and Fe^{3+} in the M(1) and M(3) octahedral sites [*Dollase*, 1973]. Fe^{3+} is preferentially partitioned into the largest and most distorted M(3) site, and up to ~14% of the total Fe^{3+} has been reported in the smaller M(1) site in epidotes synthesized from oxide mixtures at ~620°-686°C, at 5 kbar. Figure 4 shows the distribution of Fe^{3+} in the M(1) and M(3) sites reported by *Dollase* [1973] for natural and synthetic epidotes and a natural epidote that was heated at 650°C at 3 kbar for 28 days. Order/disorder in epidote can be represented in terms of the intracrystalline reaction,

$$Fe^{3+}_{M(3)} + Al_{M(1)} = Fe^{3+}_{M(1)} + Al_{M(3)}$$

which represents substitution among Fe^{3+} and Al cations in the M(1) and M(3) sites in the epidote structure. Thermodynamic analysis of distribution coefficients for this reaction reported by *Dollase* [1973] and epidote-feldspar-garnet compositions and phase relations reported by *Holdaway* [1972], *Liou* [1973], and *Best* [1977], together with the approximation of ideal mixing of Al and Fe^{3+} in the M(1) and M(3) sites in epidote, suggest that epidote is ~20% disordered at ~800°C, but nearly ordered at 25°C, [*Bird and Helgeson*, 1980]. The solid curves in Figure 4 denote isotherms of equilibrium substitutional order/disorder predicted by Bird and Helgeson [1980].

Octahedral order/disorder in epidote concentrates from a vein at 1420 m, two samples of the ejected rock chips at 1867 m, and a vein at 2618 m were evaluated by ^{57}Fe Mössbauer spectroscopy. Examples of the spectra are given in Figure 5; the Mössbauer spectra and regression data are outlined in Table 3. As suggested by *Dollase* [1973], the spectra were evaluated in terms of two closely spaced doublets, the large outer doublets representing $Fe^{3+}_{M(3)}$ and smaller inner doublets representing $Fe^{3+}_{M(1)}$ Considering the total iron in epidote to be Fe^{3+}, the percentage of Fe^{3+} in the M(1) site ranges from 7.5 ± 1.7% to 11.4 ± 1.5% in the analyzed epidotes; the most disordered epidotes occur in the chlorite + calcite zone (Table 3). Note in Table 3 that the spectra for epidote at 1420 m were fit in two ways: (1) a four-peak analysis assuming all the iron as Fe^{3+} (1420A, see also Figure 6*a*), and (2) a five-peak analysis which considers the presence of Fe^{2+} in the epidote structure (1420B). In the latter

TABLE 3*a*. Parameters of Mössbauer Spectra for State 2-14 Epidotes

Sample[a] Depth, m	Γ, mm/s	Cauchy Fraction[b]	Fe^{3+} in M(3) Isomer Shift,[c] mm/s	Fe^{3+} in M(3) Quadrupole Splitting, mm/s	Fe^{3+} in M(3) Area	Fe^{3+} in M(1) Isomer Shift, mm/s	Fe^{3+} in M(1) Quadrupole Splitting, mm/s	Fe^{3+} in M(1) Area	Fe^{2+} Area
1420A	0.35	0.824	0.176	2.041	0.888 (16)	0.120	1.518	0.112 (16)	-
1420B	0.35	0.765	0.176	2.042	0.855 (17)	0.062	1.666	0.103 (17)	0.041
1867A	0.35	0.721	0.135	2.027	0.912 (9)	0.078	1.455	0.088 (9)	-
1867B	0.34	0.928	0.136	2.034	0.886 (15)	0.091	1.567	0.114 (15)	-
2618	0.36	0.739	0.128	2.028	0.925 (17)	0.079	1.518	0.075 (17)	-

[a] All samples analyzed at Center for Material Research, Stanford University. Samples 1420A and 1420B represent fit of the same spectra using four-peak and five-peak analysis, respectively.
[b] Fraction of spectra fit with Lorentzian line shape.
[c] Relative to ^{57}Fe in Pd.

TABLE 3*b*. Goodness of Fit Parameters

Sample Depth, m	Rms X	Misfit	Δ Misfit
1420A	1.09	0.00671	0.00122
1420B	0.95	0.00510	0.00104
1867A	1.16	0.00281	0.00041
1867B	1.52	0.00399	0.00046
2618	1.04	0.00409	0.00073

From Ruby [1973].

case, ~4% of the total iron may be Fe^{2+}, which changes the peak areas representing the distribution of Fe^{3+} in the M(1) site by ~1% when compared to the fit for 1420A.

The percentages of total Fe^{3+} in the M(1) and M(3) sites are shown in Figure 6 as a function of depth. Although variations are small and data limited, Figure 6 illustrates a decrease in the Fe^{3+} content of the M(1) site in epidote with increasing depth and temperature. The most disordered epidotes (1420 and 1867 m) also exhibit the widest range in X_{ps} (Figure 2) and are associated with hydrothermal hematite. In Figure 4, octahedral site distributions can be compared with equilibrium isotherms reported by *Bird and Helgeson* [1980]. Vein epidote in the biotite zone (2618 m) has an ordering parameter $\sigma = 1 - 2X_{Fe^{3+},M(1)}$, (see *Bird and Helgeson*, [1980]) of 0.85 ± 0.03. This corresponds to an equilibrium state of order/disorder at ~390° ± 25°C, which is in close agreement with the probable downhole temperature of ~340° ± 25°C. The chlorite + calcite zone epidotes from 1420 and 1867 m, where inferred downhole temperatures are 265°C and 300°C, respectively, are more disordered, corresponding to equilibrium ordering states between 450°-600°C (Figure 4). These observations on four epidote concentrates suggest that vein and replacement epidotes from the chlorite + calcite zone are in a metastable state of order/disorder, whereas the vein epidote in the biotite zone closely approximates an equilibrium distribution of octahedral Fe^{3+} and Al.

Stable Isotope Composition

Measured values of δD and $\delta^{18}O$ for epidote separates described above are presented in Table 4 and Figure 7. Values of $\delta D_{epidote}$ = -91 to -90 and $\delta^{18}O_{epidote}$ = +2.0 to 2.7°/₀₀ are characteristic of the analyzed epidotes at 1867, 2227, and 2618 m; at 1420 m, $\delta D_{epidote}$ is -96°/₀₀. The isotope composition of the geothermal brine at 1867 m (δD = -73 and $\delta^{18}O$ = +2.3°/₀₀) shown in Figure 7 was calculated from measured isotope compositions of separated steam and brine from the December 1985 flow test (C. J. Janik and A. H. Truesdell, personal communication, 1987). Oxygen iso-

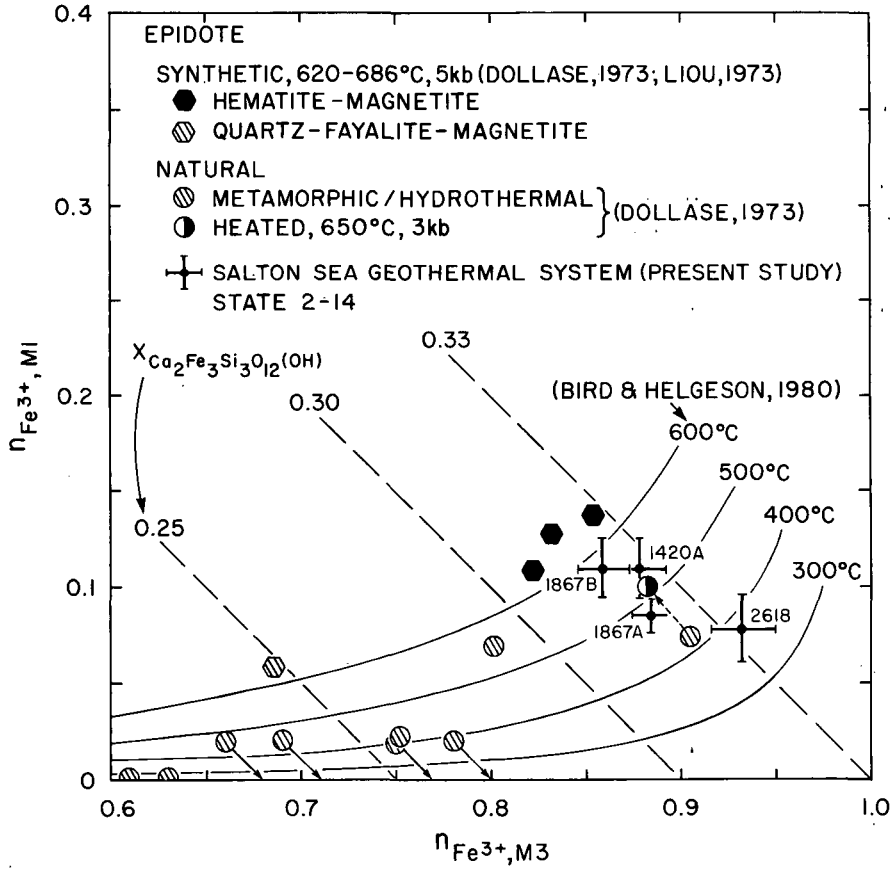

Fig. 4. Observed (symbols) and theoretical (solid curves) distribution of Fe^{3+} in the M(1) and M(3) sites in epidote reported as atoms (n) per 12.5 anhydrous oxygens. The site distributions of the State 2-14 epidotes are plotted using their mean compositions calculated from the data in Figure 2: 1420 m, X_{ps} = 0.328; 1867 m, X_{ps} = 0.323; 2618 m, X_{ps} = 0.336; Small solid arrows denote possible ranges in the ordering state, and the small dashed arrow shows the amount of disordering during heating of the epidote sample for 28 days [*Dollase*, 1973].

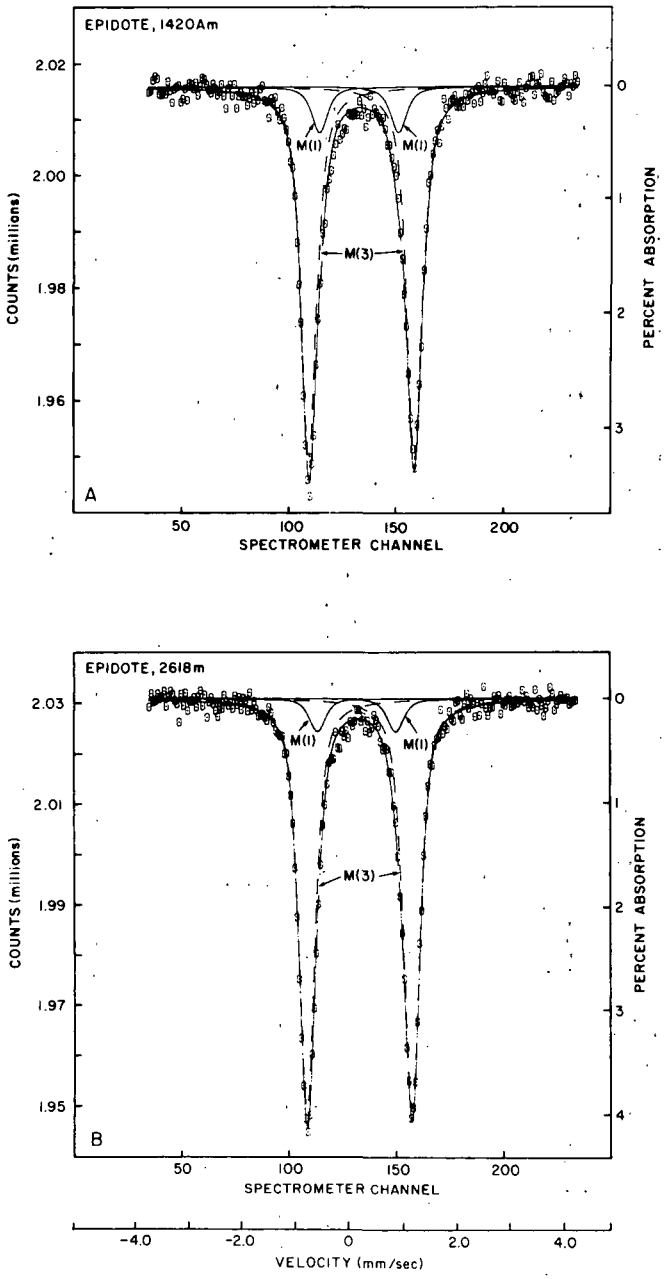

Fig. 5. Mössbauer spectra of epidotes at 1420 and 2618 m. Open symbols denote experimental observations; the curve through the spectra denotes the sum of the areas representing Fe^{3+} in the M(3) site (dashed curves) and in the M(1) sites (solid curves).

tope fractionation between epidote and geothermal brine is ~0 °/₀₀ at 1867 m and ~300°C; hydrogen isotope fractionation, as represented by 1000 ln $\alpha_{epidote-solution}$ [see *O'Neil*, 1986], is equal to -19°/₀₀. The latter value is plotted in Figure 8 where it can be compared to experimental and geothermal hydrogen isotope fractionations between epidote and aqueous electrolyte solutions reported by *Graham et al.* [1980] and *Graham and Sheppard* [1980]. It can be seen in Figure 8 that there is close agreement among the measured epidote-geothermal brine H-D fractionations from the State 2-14, IID-1, and IID-2 drill holes in the Salton Sea geothermal system. Note that these three measured hydrogen isotope fractionations are decreased by ~14-17°/₀₀ relative to the experimentally determined fractionations between epidote and pure water, and that these measurements are in general accord with the experimental hydrogen isotope fractionation curves between epidote and complex electrolytes, such as seawater. After taking into account the salinity of the Salton Sea geothermal brine (e.g., *Williams*, [1987]; *Thompson and Fournier* [this issue]), these measured fractionations suggest that the isotopic temperatures are close to the probable downhole temperatures.

TABLE 4. Isotopic Compositions of Epidote, State 2-14 Drill Hole

Sample Depth, m	$\delta D_{epidote}$	$\delta^{18}O_{epidote}$
1420	-96	na
1867	-90	2.0
2227	-91	2.7
2618	-90	2.1

Analyses are given in per mil relative to SMOW; na, not analyzed.

The $\delta D_{epidote}$ at 1420 m in the State 2-14 drill hole is 5-6°/₀₀ lighter than epidotes at 1867, 2227, and 2618 m. Geothermal reservoir fluids were not sampled from an interval near the epidote at 1420 m, which precludes direct eval-

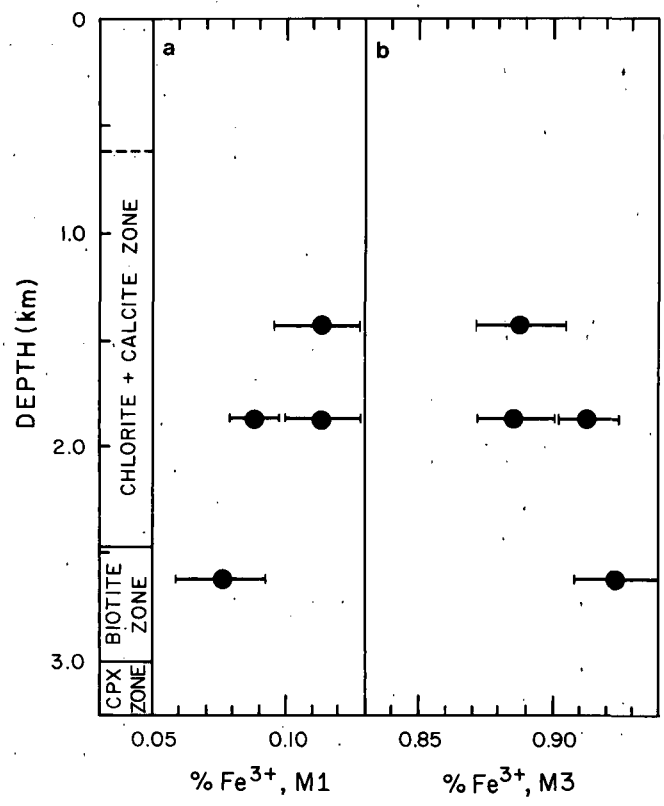

Fig. 6. Distribution of mineral zones in metasandstones, and the percent Fe^{3+} in (*a*) the M(1) and (*b*) M(3) sites in epidote. Data points for octahedral site distributions are calculated assuming $Fe_{total} = Fe^{3+}$. See Table 3.

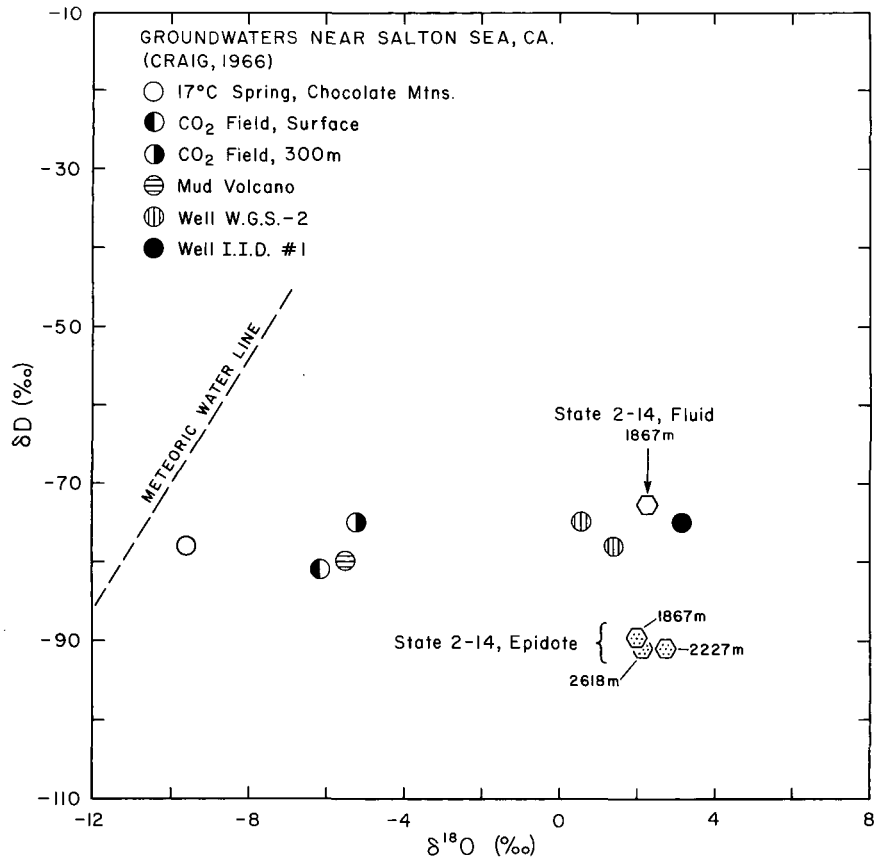

Fig. 7. Isotopic properties of aqueous solutions and epidotes from the Salton Sea geothermal system. Isotopic composition of State 2-14 fluids is calculated using measured isotopic compositions of separated steam and brine from December 1985 flow test at 1867 m (C. J. Janik and A. H. Truesdell, personal communication, 1987).

uation of the observed variation in $\delta D_{epidote}$. The lighter value for $\delta D_{epidote}$ at 1420 m may be related to isotopic and salinity stratification of the geothermal reservoir fluids that have been documented by *Williams* [1987], A. E. Williams and M. A. McKibben (unpublished manuscript, 1988), and *McKibben et al.* [1988] in their analysis of well waters from over 40 drill holes in the Salton Sea geothermal system.

Concluding Remarks

Interpretation of processes responsible for the epidote paragenesis in the Salton Sea geothermal system, as well as in other geologic environments, requires an understanding of (1) the dependence of epidote composition on changes in temperature, pressure, and chemical potential of thermodynamic components, (2) the extent to which metastable compositions and substitutional order/disorder occur in epidote and associated secondary phases, and (3) the rate of epidote-forming reactions as a function of the local transport of thermal energy and mass in the hydrothermal system. From our preliminary evaluation of the complex compositional, paragenetic, textural, and structural characteristics of epidote, it is apparent that the sensitivity of these properties to variations in the thermodynamic and transport characteristics of magma-hydrothermal systems makes cause-and-effect relations difficult to ascertain. Systematic study of epidotes and hydrothermal fluids from the Salton Sea and other active geothermal systems contributes to our understanding of such relations.

Observations presented above suggest that there are significant variations in the extent of Fe^{3+}-Al exchange and lesser variations in the degree of substitutional order/disorder and hydrogen isotope contents of vein and replacement epidotes formed in the upper ~2600 m of the Salton Sea geothermal system near the State 2-14 drill hole. The inferred metastable states of ordering in epidotes (see above), in alkali feldspars [*Bird and Norton,* 1981; *McDowell,* 1986], and in sericites [*Bird and Norton,* 1981] suggest that nonequilibrium ordering states are typical of many hydrothermal minerals formed in the upper ~1.5-2 km of this geothermal system. Perhaps variations in temperature and in the flux and composition of hydrothermal fluids during the evolution of the geothermal system led to conditions that favor rapid formation of metastable disordered secondary phases in and near the high-permeability fracture systems. The available data on δD for the geothermal reservoir fluids do not allow definitive interpretation of the observed variations in $\delta D_{epidote}$ as a function of depth, temperature, or composition of the hydrothermal solutions. The measured H-D fractionation between epidote and the geothermal brine at 1867 m and ~300°C is, however, consistent with *Graham and Sheppard*'s [1980] experimental observations of smaller fractionations in systems with saline electrolyte solutions relative to systems with pure water.

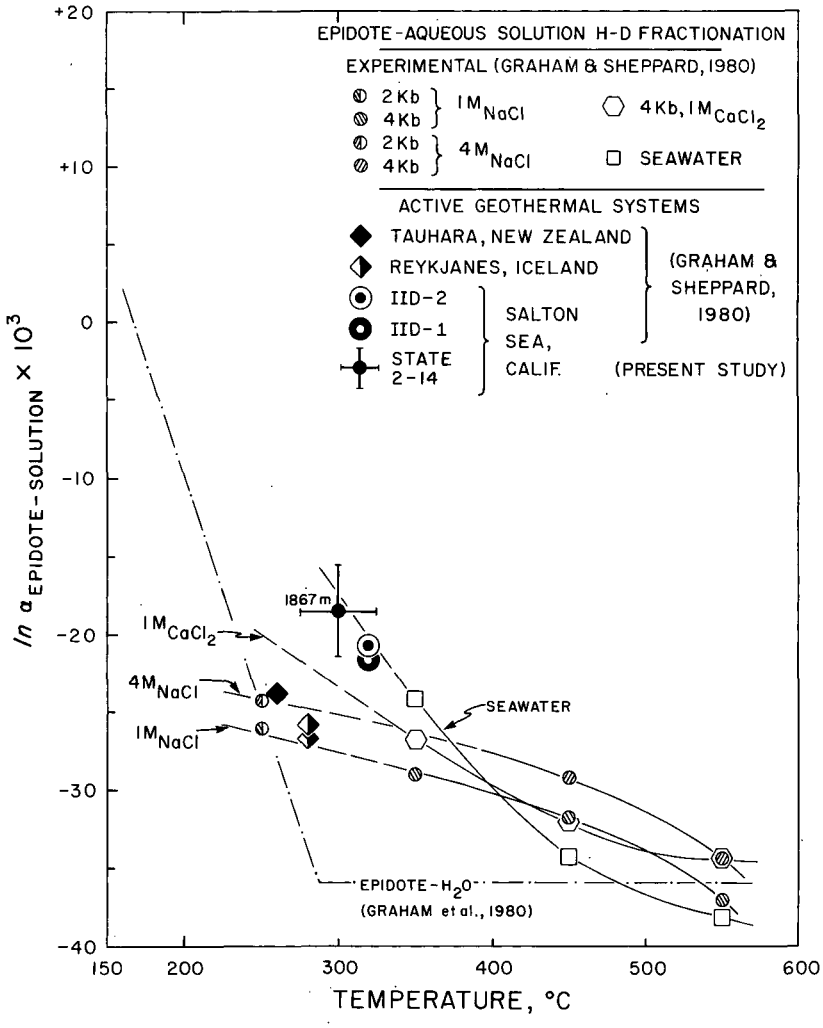

Fig. 8. Experimental and calculated values of 1000 ln $\alpha_{epidote-solution}$ as a function of temperature. Error bars for the State 2-14 drill hole at 1867 m correspond to an analytical uncertainty of ± 2 °/oo in $\delta D_{epidote}$ and $\delta D_{solution}$ and ± 25°C in the downhole temperature. See text.

Acknowledgments. We thank W. A. Dollase and G. Waychunas and J. R. O'Neil, respectively, for allowing use of their laboratories to conduct the the Mössbauer and isotope analyses. L. Adami, C. Ross, M. Stairs, and D. White provided technical assistance in these analyses. We also thank J. Goldsmith, M. Donato, and W. Carothers for helpful reviews of the manuscript. This research was supported by National Science Foundation grant EAR-84-18147.

REFERENCES

Andes, J., and M. A., McKibben, Thermal and chemical history of mineralized fractures in cores from the Salton Sea Scientific Drilling Project (abstract), *Eos Trans. AGU, 68*, 439, 1987.

Best, N.F., Experimental studies of greenschist facies metamorphism of basic rocks, PhD. dissertation, Univ. of Edinburgh, 1977.

Bird, D. K., and H. C. Helgeson, Chemical interaction of aqueous solutions with epidote-feldspar mineral assemblages in geologic systems, I, Thermodynamic analysis of phase relations in the system CaO-FeO-Fe_2O_3-Al_2O_3-SiO_2-H_2O-CO_2, *Am. J. Sci., 280*, 907-941, 1980.

Bird, D. K., and H. C. Helgeson, Chemical interaction of aqueous solutions with epidote-feldspar mineral assemblages in geologic systems, II, Equilibrium constraints in metamorphic/geothermal processes, *Am. J. Sci., 281*, 576-614, 1981.

Bird, D. K., and D. L. Norton, Theoretical predictions of phase relations among aqueous solution and minerals: Salton Sea geothermal system, *Geochim. Cosmochim. Acta, 45*, 1479-1493, 1981.

Bird, D. K., P. Schiffman, W. A. Elders, A. E. Williams, and S. D. McDowell, Calc-silicate mineralization in active geothermal systems, *Econ. Geol., 79*, 671-695, 1984.

Bird, D.K., R. D. Rogers, and C. M. Manning, Mineralized fracture systems of the Skaergaard Intrusion, East Greenland, *Medd. Gronl., 16*,, 68 pp., 1986.

Caruso, L.J., D.K. Bird, M. Cho, and J.G. Liou, Epidote mineralized fractures in SSSDP well 2-14 core samples (abstract), *Eos Trans. AGU, 68*, 445, 1987.

Caruso, L.J., D.K. Bird, M. Cho, and J.G. Liou, Epidote-bearing veins in the State 2-14 drill hole: Implications for hydrothermal fluid composition, *J. Geophys. Res.*, this issue.

Cavaretta, G., G. Gianelli, and M. Puxeddu, Formation of authigenic minerals and their use as indicators of the physicochemical parameters of the fluid in the Larderello-Travele geothermal field, *Econ. Geol., 77*, 1071-1084, 1982.

Chatterjee, N.D., Experiments on the phase transition calcite + wollastonite + epidote = grossular-andradite$_{ss}$ + CO_2 + H_2O, *Contrib. Mineral. Petrol., 14*, 114-122, 1967.

Cho, M., J. G. Liou, and D. K. Bird, Prograde phase relations in the California State 2-14 well meta-sandstones, Salton Sea geothermal field (abstract), *Eos Trans. AGU, 68*, 445, 1987.

Cho, M., J. G. Liou, and D. K. Bird, Prograde phase relations in the State 2-14 well metasandstones, Salton Sea geothermal field, California, *J. Geophys. Res.*, this issue.

Craig, H., Isotopic composition and origin of the Red Sea and Salton Sea geothermal brines, *Science, 154,* 1544-1547, 1966.

Dollase, W.A, Mössbauer spectra and iron distribution in the epidote-group minerals, *Z. Kristallogr., 138,* 41-63, 1973.

Elders, W. A., and J. H. Sass, An overview of the SSSDP (abstract), *Eos Trans. AGU, 68,* 438, 1987.

Elders, W. A., and J. H. Sass, An overview of the SSSDP, *J. Geophys. Res.,* this issue.

Elders, W.A., R.W. Rex, T. Meidav, P.T. Robinson, and S. Biehler, Crustal spreading in southern California, *Science, 178,* 15-24, 1972.

Forester, R. W., and H. P. Taylor, Jr., $^{18}O/^{16}O$, D/H, and $^{13}C/^{12}C$, studies of the Tertiary igneous complex of Skye, Scotland, *Am. J. Sci., 277,* 136-177, 1977.

Fyfe, W.S., Stability of epidote minerals, *Nature, 187,* 497, 1960.

Graham, C.M., Experimental hydrogen isotope studies, III, Diffusion of hydrogen in hydrous minerals, and stable isotope exchange in metamorphic rocks, *Contrib. Mineral. Petrol., 76,* 216-228, 1981.

Graham, C.M., and S.M.F. Sheppard, Experimental hydrogen isotope studies, II, Fractionation in the systems epidote-NaCl-H_2O, epidote-$CaCl_2$-H_2O and epidote-seawater, and the hydrogen isotope compositions of natural epidotes, *Earth Planet. Sci. Lett., 49,* 237-251, 1980.

Graham, C.M., S.M.F. Sheppard, and T.H.E. Heaton, Experimental hydrogen isotope studies, I, Systematics of hydrogen isotope fractionation in the system epidote-H_2O, zoisite-H_2O, and AlO(OH)-H_2O, *Geochim. Cosmochim. Acta, 44,* 353-364, 1980.

Harpum, J. R., Formation of epidote in Tanganyka, *Geol. Soc. Am. Bull., 65,* 1075-1092, 1954.

Helgeson, H. C., Solution chemistry and metamorphism, *Researches in Geochemistry,* vol. 2, edited by P. H. Abelson, pp. 362-404, John Wiley, New York, 1967.

Helgeson, H.C., Geologic and thermodynamic characteristics of the Salton Sea geothermal system, *Am. J. Sci., 267,* 129-166, 1968.

Holdaway, M.J., Thermal stability of aluminum-iron epidote as a function of f_{O_2} and iron content, *Contrib. Mineral. Petrol., 36,* 307-340, 1972.

Keith, T.E.C., L.J.P. Muffler, and M. Creamer, Hydrothermal epidote in the Salton Sea geothermal system, California, *Am. Mineral., 53,* 1644-1653, 1968.

Kretz, R., Note on some equilibria in which plagioclase and epidote participate, *Am. J. Sci., 261,* 973-982, 1963.

Liou, J. G., Synthesis and stability relations of epidote, $Ca_2Al_2FeSi_3O_{12}(OH)$. *J. Petrol., 14,* 381-413, 1973.

Liou, J.G., Occurrences, compositions and stabilities of some Ca-Al hydrous silicates in low-grade metamorphic rocks, *Mem. Geol. Soc. China, 5,* 47-66, 1983.

McDowell, S. D., Composition and structural state of coexisting feldspars, Salton Sea geothermal field, *Mineral. Mag., 50,* 75-84, 1986.

McDowell, S.D., and M. McCurry, Active-metamorphism in the Salton Sea geothermal field, California: Mineralogical and mineral chemical changes with depth and temperature in sandstone (abstract), *Geol. Soc. Am., Abstr. Programs, 9,* 1088, 1977.

McKibben, M.A., A.E. Williams, W.A. Elders, and C.S. Eldridge, Saline brines and metallogenesis in a modern sediment-filled rift: The Salton Sea geothermal system, California, U.S.A., *Appl. Geochem.,* in press, 1988.

Mehegan, J. M., C. T. Herzig, and R. M. Sullivan, Salton Sea Scientific Drilling Project, California State 2-14 well: Visual core descriptions, vols. 1 and 2, *Rep. UCR/IGPP-86/1,* Univ. of Calif., Riverside, 1986.

Miyashiro, A., and Y. Seki, Enlargement of the composition field of epidote and piemontite with rising temperature, *Am. J. Sci., 256,* 423-430, 1958.

Muffler, L. J. P., and D. E. White, Active metamorphism of upper Cenozoic sediments in the Salton Sea geothermal field and Salton Trough, southeastern California, *Geol. Soc. Am. Bull., 80,* 157-182, 1969.

O'Neil, J.R., Terminology and standards, Stable Isotopes in High Temperature Geological Processes, edited by J.W. Valley, H.P. Taylor, Jr. and J.R. O'Neil, *Rev. in Mineral., 16,* 561-570, 1986.

Ramberg, H., The facies classification of rocks: A clue to the origin of quartzofeldspathic massifs and veins, *J. Geol., 57,* 18-54, 1949.

Rose, N. M., and D. K. Bird, Prehnite-epidote phase relations in the Nordre Aputiteq and Kruuse Fjord layered gabbros, East Greenland, *J. Petrol., 28,* 1193-1218, 1987.

Rosenqvist, I. Th., The metamorphic facies and the feldspar minerals, *Arbok Univ. Bergen, Naturvetensk. Ser., 1952(4),* 108, 1952.

Ruby, S.L., Why Misfit when you already have X^2? in *Mössbauer Effect Methodology,* vol. 8, edited by I. J. Gruverman and C. W. Siedel, pp. 263-276, Plenum, New York, 1973.

Sass, J. H., J. D. Hendricks, S. S. Priest, and L. C. Robinson, Temperature and heat flow in the State 2-14 well, Salton Sea Scientific Drilling Project (abstract), *Eos Trans. AGU, 68,* 454, 1987.

Sass, J. H., S. S. Priest, L. E. Duda, C.C. Carson, J. D. Hendricks, and L. C. Robinson, Thermal regime of the state 2-14 well, Salton Sea Scientific Drilling Project, *J. Geophys. Res.,* this issue.

Seki, Y., Lower-grade stability limit of epidote in light of natural occurences, *Geol. Soc. Japan J., 78,* 405-413, 1972.

Schiffman, P. D., D. K. Bird, and W. A. Elders, Hydrothermal mineralogy of calcareous sandstones from the Colorado River delta in the Cerro Prieto geothermal system, Baja California, Mexico, *Mineral. Mag., 49,* 435-449, 1985.

Sheppard, S.M.F., and H.P. Taylor, Jr., Hydrogen and oxygen isotope evidence for the origins of water in the Boulder batholith and the Butte ore deposits, Montana, *Econ. Geol. 69,* 926-946, 1974.

Shikazono, N., Compositional variations in epidote from geothermal areas, *Geochem. J., 18,* 181-187, 1984.

Strens, R.G., Stability-relations of Al-Fe epidotes, *Mineral. Mag., 35,* 464-475, 1965.

Taylor, H. P. and R. W., Forester, An oxygen isotope study of the Skaergaard intrusion and its country rocks: A description of a 55-m.y. old fossil hydrothermal system, *J. Petrol., 20,* 355-419, 1979.

Tazaki, K., Andradite garnet in altered basalt from Borup Fjord, Ellesmere Island, Northwest Territories, *Current Research, 83-1B,* Geol. Surv. of Can., pp. 237-242, 1983.

Thompson, J. M. and R. O. Fournier, Chemistry and geothermometry of brine produced from the Salton Sea Scientific Drill Hole, Imperial Valley, CA, *J. Geophys. Res.,* this issue.

White, D. E., E. T. Anderson, and D. K. Grubbs, Geothermal brine well-mile-deep drill hole may tap ore-bearing magmatic water and rocks undergoing metamorphism, *Science, 139,* 919-922, 1961.

Williams, A.E., Chemical and isotopic variations and the distribution of brines across the Salton Sea geothermal field, California (abstract), *Eos Trans. AGU, 68,* 438, 1987.

D. K. Bird, L. J. Caruso, and J. G. Liou, Department of Geology, Stanford University, Stanford, CA 94306.

M. Cho, Department of Earth and Space Sciences, University of California, Los Angeles, CA 90024.

C. J. Janik, U. S. Geological Survey, 345 Middlefield Road, MS 910, Menlo Park, CA 94025.

(Received July 20, 1987;
revised April 1, 1988;
accepted July 12, 1988.)

JOURNAL OF GEOPHYSICAL RESEARCH, VOL. 93, NO. B11, PAGES 13,145–13,157, NOVEMBER 10, 1988

Chemographic and Thermodynamic Analysis of the Paragenesis of the Major Phases in the Vicinity of the 6120-Foot (1866 m) Flow Zone, California State Well 2-14

R. W. CHARLES, D. R. JANECKY, AND FRASER GOFF

Los Alamos National Laboratory, Los Alamos, New Mexico

M. A. MCKIBBEN

University of California, Riverside, California

The major phases found in the vicinity of the 1866m flow zone are K-feldspar, epidote, pyrite, hematite, and chlorite. These are found to exist in primarily four, two-phase assemblages, the dominant being K-feldspar + pyrite, epidote + pyrite, epidote + hematite, and chlorite + pyrite. Complete reaction relations among these isobaric isothermal divariant phase assemblages oriented in log f_{O_2} - pH space are compatible with stable growth at 300°C. Sensitivity of reaction relations to total sulfur, temperature, pressure, and thermodynamic values is investigated. The aqueous fluid sampled at 1866 m is out of equilibrium with the more reducing phase assemblages lying stratigraphically above and below the flow zone as well as pyrite-bearing assemblages in the flow zone and shows aspects of mixing with other, hotter, flow zones. High concentrations of CO_2 may indicate contribution to the fluid of CO_2 from hotter portions of the system. Low total sulfur and high total iron are due to possible gas loss during down hole sampling and reaction of the fluid with well casing and lost circulation materials.

INTRODUCTION

The Salton Trough is an extensional basin 4–5 m.y. old with general structure defined as sediments consisting of up to 3 km of Plio-Pleistocene basin fill from the ancestral Colorado River in isostatic equilibrium with underlying gabbroic material [*Lachenbruch et al.*, 1985]. The trough is the onland extension of the East Pacific Rise with active rifting and seismisity. The high-temperature, metal-bearing, hypersaline brines of the Salton Sea geothermal system have attracted significant attention as an active analog of ore deposit systems and as an exploitable geothermal resource [*White* 1963; *Skinner et al.*, 1967; *Helgeson*, 1968; *McKibben and Elders*, 1985]. Many wells have been drilled in the Salton Trough for commercial geothermal exploitation, and studies of drill cuttings and bulk fluid samples have provided a broad base of information. However, many aspects of the system have remained obscured, in part due to the lack of access for core recovery, fluid sampling from carefully defined flow zones, and other scientific experiments. The Salton Sea Scientific Drilling Project (SSSDP) [*Sass and Elders*, 1986], as part of the thermal regimes portion of the National Continental Scientific Drilling Program, has provided the initial opportunity for such experiments.

The first major lost circulation zone encountered in the SSSDP California State well 2-14 occurred at 1866 m (SSSDP quarterly, March 1986). Samples of rocks and fluids from this zone provide a unique opportunity to examine water-rock equilibria and reactions critical to issues of geothermal energy and mineral extraction. Our objective in the present communication is to use the major mineral phase compositions and assemblages to define the metasomatic conditions of the aquifer zone at 1866 m and to examine the relationship to the sampled aqueous fluid. This study builds upon previous studies of ore mineralogy and mineral paragenesis by *White* [1963], *Skinner et al.* [1967], *Helgeson* [1968], *Bird and Norton* [1981], *McKibben and Elders* [1985], A. W. Williams and M. A. McKibben (A brine interface in the Salton Sea geothermal system, California: Fluid geochemical and isotopic distribution, submitted to *Journal of Geophysical Research*, 1987, hereinafter referred to as submitted manuscript, 1987), M. A. McKibben et al. (Metamorphosed Plop-Pleistocene evaporites and the origins of hypersaline brines in the Salton Sea geothermal system, California, submitted to *Economic Geology*, 1987, hereinafter referred to as submitted manuscript, 1987).

PETROLOGY AND MINERALOGY

Stratigraphy in the region of the first produced lost circulation zone (1866 m) was determined from cores taken above and below the zone and from rock fragments ejected from the well during the flow test in December 1985. Rock cores in the interval 1837–1843 m consisted of a mudstone with some epidote, quartz, and trace pyrite. The next core was taken in the interval 1984–1987 m after the well was deepened beyond the 1866 m flow zone. It yielded a gray claystone with minor epidote. Nitrogen stimulation and initiation of flow from the well resulted in rock samples being ejected from the interval between these corings. Rock samples from this interval were collected by Goff from ejecta blasted out the blooie line. These showed a sequence

Paper number 7B7133.
0148-0227/88/007B-7133$05.00

TABLE 1. Observed Phase Compositions

	Composition
Chlorite	$Na_{0.07(1)}Ca_{0.05(1)}Mn_{0.06(1)}Mg_{2.75(35)}\ Fe_{1.96(5)}Al_{1.14(6)}Si_{2.87(22)}Al_{1.13}O_{10}(OH)_8$
Epidote	$Ca_{1.94(8)}Mg_{0.01(1)}Mn_{0.02(1)}Fe^{+3}_{0.94(14)}Al_{2.01(17)}Si_{3.02(10)}O_{12}(OH)$
Pyrite	FeS_2
Hematite	Fe_2O_3
K-feldspar	$K_{0.90(5)}Na_{0.12(2)}Si_{2.98(5)}Al_{1.02(2)}O_8$

(top to bottom) of indurated gray to black mudstone, epidote rock, and flow zone rock and the reverse with stratigraphic depth. The gross mineralogy of hydrothermal minerals in both core and rock fragment samples indicates greenschist facies metamorphism [*Turner*, 1968].

The mudstone contains obvious pyrite and epidote. Epidote occupies a greater percentage of the rock volume as the flow zone is approached stratigraphically. Samples from the flow zone consisted of rounded lumps of epidote-pyrite and epidote-specular hematite rock. In general, grain sizes are coarser than the mudstone. Epidote, pyrite, and hematite are not observed in the same rock fragment. Scanning electron microscope and powder X-ray diffraction examination of the rocks revealed other phases. In addition to those mentioned above, the mudstone contains major K-feldspar and quartz with trace apatite, sphene, zircon, chlorite, and albite. Epidote rock fragments consist primarily of epidote and quartz. Platey chlorite can be seen in vugs bounded by quartz. Rock fragments from the aquifer zone are consistently composed of three phases (epidote, pyrite, and hematite) in two phase assemblages. The phase assemblages observed were epidote + pyrite and epidote + specular hematite.

The major phase compositions were analyzed by electron microprobe (Table 1). Quartz, pyrite, and hematite were essentially end-member in composition. K-feldspar is a mixture of primarily K-feldspar and albite with the average composition $Or_{90}Ab_{10}An_0$. Chlorite and epidote were found to be variable solid solutions. Chlorite was found primarily in the mudstone and contained low alkali and subequal amounts of magnesium and iron. There were no systematic variations in chlorite composition. Epidote composition was generally close to $Ps_{33}Cz_{67}$. It was found throughout the sequence and showed small variations in iron content which was not examined in detail. Iron content in this study is greater than that observed in well Elmore 1.: 0.05 to 0.25 $X_{Ca_2Fe_3^{+3}Si_3O_{12}(OH)}$ [*McDowell and McCurry*, 1977].

FLUID CHEMISTRY

Two analyses of the fluid chemistry in the SSSDP well are presented in Table 2. The values of *Michels* [1986a, 1986*b*] were determined from surface samples obtained during the flow test in late December 1985. The values listed represent corrected analyses for samples collected from four sequential orifice plates in the flow line. Water and gas samples were collected from separate points at each orifice plate. Flowing temperatures at the orifice plates varied from 235° to 164°C and pressures were as high as 31.0 bars gauge. Subsurface temperature at 1866 m is 298°C [*Goff et al.*, 1987]. The *p*H of flashed, cooled brine at the first orifice plate is approximately 5.3, while the density varied from 1.21 to 1.22 g/cm^3.

The values of SS-21A (corrected) were determined from an in situ sample collected just after the March 1986 flow test (Goff, et al., 1987). The sample filled a gas-tight, downhole sampling tool lowered to a depth of 3110 m at a temperature of 351°C and a pressure of 295.6 bars absolute. A significant fraction of the fluid extracted from the 3110-m zone originated in overlying flow zones as high as 1866 m by communication outside the casing annulus of the poorly cemented liner. Gas was collected quantitatively from the sampling tool at the surface by use of a special gas extraction system. The *p*H and Eh of the degassed brine at 33°C are 5.3 and -32 mV, respectively. The density of the degassed brine at 25°C was 1.178 g/cm^3. All fluid samples collected during the March 1986 flow test were contaminated with drilling fluids. This is best observed in the Ba content of the fluid. To estimate the fluid composition at 1866 m, corrections were made based on assumptions of mixing behavior of the fluids and on isotopic composition of flashed brine and surface steam (c.o. Grigsby et al., unpublished manuscript, 1988).

The two analyses of the 1866 m fluid listed in Table 2 are very compatible (within 2.5% in Cl content and 2–10% for other elements). The biggest difference is in silica content. It is our opinion that the silica value of *Michels* [1986*b*] is too low due to possible precipitation of silica from hypersaline brine during flashing in the well bore and two-phase flow in the flow line. The silica content of SS-21A (corrected) is more consistent with experimental data on silica solubility in hypersaline NaCl solutions at high temperature [*Fournier, et al.* 1982].

CHEMOGRAPHICS FOR THE 1866 M AQUIFER

The determination of chemical potentials for this flow zone will involve the use of local equilibrium. The potential nets yield information about the state of disequilibrium in any natural system. Examination of thin sections and hand specimens yields a reasonable sequence of local assemblages that can be tested against known or supposed fluid compositions, thermodynamic properties, and chemographic relations. For other examples, see *Zen* [1974] and *Charles et al.* [1986]. The question asked is: How do observed phase assemblages relate to one another in potential space?

Determination of phase assemblages

Petrographic observation of the rock fragments yields the important phase assemblages. These consist dominantly of mineral pairs. Definition of observed phase assemblages can be to some extent subjective. These ejected fragments may not be entire phase assemblages but are useful as a starting point in the determination of relevant

TABLE 2a. Fluid Composition

Brine	In Situ Sample SS-21A[a]	Estimated Composition (1866 m) SS-21A (Corrected)[b]	*Michels* [1986][c]
SiO_2	743	774	384
Ba	1554	200[d]	198
Ca	27700	29900	26780
Mg	14.5	38[e]	37
Sr	409	450	407
Na	51710	57250	52750
K	17090	18920	16620
Li	225	250	192
NH_4	242	268	330
Fe	1410	1560	1535
Mn	1260	1400	1390
$HCO_{3_t}^-$	106	117	—
$HCO_{3_{tot}}^-$ [f]	—	2325	—
Cl	142600	157600	153540
Br	103	114	—
$SO_4^=$	3.3	7.4[g]	—
B	267	296	255
Cs	14	16	—
F	30	33	—
I	9	10	—
Pb	121	134	97
Rb	95	105	—
Zn	524	580	510
Ag	4.0	4.5	
As	7.7	8.5	
Cd	2.7	3.0	

*Amount detected was <1 for elements Al, Au, Co, Cr, Hg, Mo, Ni, Sb, Se, Sn, Ta, Te, Th, Ti, U, and W.
[a]C. O. Grigsby et al. (unpublished manuscript, 1988).
[b]Assumes sample SS-21A is diluted by 10.7% with drilling fluid.
[c]Average of two brine analyses.
[d]Estimate based on evaluation of "uncontaminated" samples.
[e]Estimate based on ratio of Mg/Cl during first flow test.
[f]Sum of $HCO_{3_t}^-$ and CO_2 as HCO_3^-.
[g]Estimate based on ratio of $SO_4^=/Cl^-$ during first flow test.

natural assemblages. We are employing a more conservative approach in that major mineral phases must be observed in contact or at least in close (micron scale) proximity without exhibiting reaction relations. *Bird and Helgeson* [1981] takes a much broader view and consider epidote + K-feldspar + K-mica + calcite + quartz as an assemblage. This may not strictly be correct as these minerals form a system of distinct combinations of two determining phases. Taking the aquifer first, epidote + pyrite and epidote + hematite are two phase assemblages consisting of pairs of minerals in intimate contact suggesting equilibrium. While the construct presented here is useful in visualizing the overall system, all assemblages are assumed to be fluid present and may allow communication (and possible local equilibrium) with other solid phases not in intimate contact. Later in the discussion, some trace phases predicted to be supersaturated in the observed fluid will be added to the initially two-phase, fluid present, assemblages. Moving stratigraphically from the aquifer, epidote + quartz is the dominant phase assemblage with less common epidote + pyrite. The mudstone contains a number of phases: K-feldspar, albite, epidote, chlorite, quartz, sphene, apatite, and zircon. The pyrite and K-feldspar are seen in intimate association. Void fillings contain chlorite, pyrite, and epidote. For the mudstone, then, the assemblage K-feldspar + pyrite appears important and possibly epidote + pyrite, chlorite + pyrite, and chlorite + epidote as well. The other phases are indifferent to reactions be-

TABLE 2b. Gas Composition

Gas	SS-21A[a]	Estimated Composition (1866 m) This Study[b]	*Michels* [1986][c]
CO_2	1440	1594	1664
H_2S	3.35	3.71	7.01
NH_3	0.072	0.090	—
H_2	14.16	15.7	—
N_2	15.64	17.3	—
CH_4	29.33	32.5	—

[a]C. O. Grigsby et al. (unpublished manuscript, 1988).
[b]Assumes sample SS-21A is diluted by 10.7% with drilling fluid.
[c]Average of two brine analyses.

TABLE 3. Chemographic System

Invariant Assemblages	Univarant Assemblages[a]	Divariant Assemblages[b]
CEHK [P]	4Ksp + Hem → 2Epi	CE EH HK KP
CEHP [K]	Hem → 2Py	CH EK
EHKP [C]	4Ksp + Py → 2Epi	CK EP
CHKP [E]	2Ksp + 2py → Chl	CP
CEKP [H]	Chl + 2Ksp → 2Epi	
	Chl → Epi + Py	
	Chl → $\frac{1}{2}$Hem + Epi	
	Chl → 2Ksp + Hem	

Ksp = K = K-feldspar $KAlSi_3O_8$, Hem = H = Hematite Fe_2O_3, Py = P = Pyrite FeS_2, Epi = E = Epidote $Ca_2Al_2Fe^{+3}Si_3O_{12}(OH)$, Chl = C = Chlorite $Mg_3Fe_2Al_2Si_3O_{10}(OH)_8$

[a]Balanced reaction relations in terms of determining inert components. Complete reaction relations are presented after distribution of species calculations at appropriate log f_{O_2} and pH in a later section.

[b]HP is a univarant assemblage with the compositional degenerecy of hematite and pyrite in this multivarient net.

tween these major phases. See Table 4 and the appendix for the principal reaction relations.

Chemical potential net

Taking the flow zone and its environment as a whole, the system can be described with a minimum of 14 components: SiO_2, Al_2O_3, K_2O, Na_2O, CaO, MgO, FeO, P_2O_5, TiO_2, ZrO_2, H_2O, S_2, Cl, and O_2. Table 2 shows even more possible components. The objective is to define the determining inert components in such a way as to agree with the phase rule for invariant, variant, and divariant situations [see *Korzhinskii*, 1959, pp. 96–107). *Helgeson* [1968] states the basin is closed with respect to a number of these components (MgO, CaO, K_2O, Na_2O, Al_2O_3, SiO_2, H_2O, CO_2, O_2, and possibly FeO). This may be true basin wide but based on the number of two-phase solid assemblages, the geochemistry may, at least on the local level, be open to a number of components. Using these components as the framework for major phases observed at 1866 m, Na_2O is an indifferent component; H_2O, CO_2, CaO, O_2, and K_2O are variable mobile components; SiO_2 is an excess component; and MgO and FeO are isomorphous components. This leaves FeO + MgO and Al_2O_3 as the two determining inert components. The 14 components listed above may also be reduced in the same manner. If we consider H_2O, K_2O, CaO, S_2, Cl, and O_2 as variable mobile components; Na_2O as an indifferent component, SiO_2 as an excess component (not necessarily true in the aquifer, where a_{SiO_2} may be less than 1); ZrO_2, TiO_2, and P_2O_5 trace or indifferent components; and finally MgO and FeO as isomorphous components, we are left with two determining inert components: (FeO + MgO) and Al_2O_3. This analysis conforms to the general relationship (fluid present) for a system in divariant equilibrium. Divariant assemblages with more than two phases will include the trace phases and may be considered as overlays on this multisystem where each trace phase adds an additional component (i.e., chalcopyrite, Cu): number of phases = number of components.

For conditions of quartz saturation and aqueous fluid present conditions, the phases which determine reaction relations are K-feldspar, hematite, pyrite, epidote, and chlorite. Albite, zircon, sphene, and other minor phases are indifferent to these reactions. The chemographic system thus defined is a multisystem of one negative degree of freedom, with 10 possible divariant fields, 10 univariant lines, and five invariant points (Table 3). Because of the compositional degeneracy (pyrite and hematite contain only one inert component in the current system), only eight univariant reactions will exist (Table 3). An unoriented connected net, showing all of these relations (Figure 1) allows relative relations of all of the phase assemblages along the pseudobinary bulk composition to be examined.

The net may be oriented in chemical potential space. Reaction relations between the observed phases are sensitive to redox, pH, activities of sulfur, potassium, magnesium, and calcium. For example,

Ksp + Hem ⇌ Epi:

$$4Ksp + Hem + 4Ca^{+2} + 3H_2O \rightleftharpoons 6Q + 4H^+ + 2Epi + 4K^+$$

Ksp + Chl ⇌ Epi:

$$2Ksp + Chl_{35} + 0.325O_2 + 4Ca^{+2} \rightleftharpoons 2.65H_2O + 3Q + 2Epi + 2K^+ + 3Mg^{+2}$$

Py ⇌ Hem:

$$Py + 2H_2O + 3.75O_2 \rightleftharpoons 4H^+ + 2SO_4^{-2} + 0.5Hem$$

See Table 4 and the appendix for other examples. See Tables 3 and 4 for abbreviations. Oxygen fugacity, pH, and sulfur fugacity will be used to examine the phase equilibria. Chemical potential diagrams allow more efficient manipulation of the connected nets to identify logical orientations and morphologies. The two net variants for the Salton Sea system of interest here are shown in Figure 2. These show the incompatibility of the [C] and [E] invariant assemblages (i.e., only one may be stable) for a given set of physical and chemical parameters.

THERMODYNAMIC DATA AND CONVENTIONS

Aqueous components

Transformation of the chemical potential nets into log f_{O_2} versus pH coordinates requires that we account for solution specie activities in the hypersaline brines of the Salton Sea. This involves accounting for both activity coefficients and formation of complex species.

Calculated molal concentrations of dissolved species reflect the concentrated nature of the Salton Sea geothermal fluids:

m_i=((mg/kg)/(GFW)(1000))(1000/(1000-TDS/1000))

where TDS is total dissolved solids, m_i is molal concentration of component i, GFW is gram formula weight.

A value of 0.88 is used for a_{H_2O} extrapolated from *Helgeson* [1969] and *Pitzer et al.* [1983]. Numbers for solvation need to be known for $a_{H_2O} << 1$ [*Hemley et al.*, 1977; *Walther and Helgeson*, 1980]. As reliable numbers are not available and because a_{H_2O} is not $<< 1$, problems with solvation are not considered further in this study.

In the present study, because the axes of the diagrams are not formulated in terms of activity ratios (see the treatment of *Bird and Norton* [1981]), activity coefficients must be estimated for the brine. While a variety of models have been proposed for activity relations in brines [e.g., *Pitzer*, 1973; *Harvie and Weare*, 1980], none are yet applicable to complex multicomponent brines such as exist in the Salton Sea geothermal system. Thus we have chosen the simplified method of *Lindsay* [1980] for approximating activity coefficients as outlined by *McKibben and Elders* [1985]. Briefly stated, the nonideality of the fluid is assumed to be solely due to stoichiometric ionic strength effects. Activity and hence activity coefficients are calculated based upon the stoichiometric activity coefficient of Cl^- and the charge of the species of interest:

$$a_i = (\gamma_{st}^{|z|})^{|z|} m_i$$

where γ_{st} is the stoichiometric activity coefficient of Cl^- (approximately 0.16) a_i is the activity of species *i*, *z* is charge, and m_i is molality of species *i*. Stoichiometric ionic strength is 6.25. A distribution of species calculation at near neutral *p*H (5.5) shows less dissociation for a calculated ionic strength of about 4.75. The γ_{st} for Cl^- is approximately 0.16 at I=4.75. Thus, for example, the activity coefficient for a monovalent complex is 0.16 and for a divalent complex, 6.55×10^{-4}, at 300°C. Activity coefficients for neutral species are calculated from the data of *Drummond* [1981]: $\gamma_{H_2S} = 2.22$ and $\gamma_{H_2CO_3} = 3.19$ at 300°C and 6 molar NaCl.

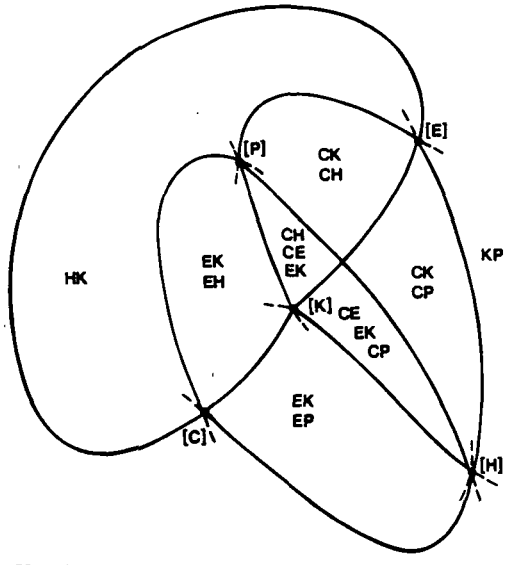

Fig. 1. Unoriented connected net revealing all possible divariant relationships in the 1866 m zone. C, chlorite; E, epidote; K, kspar; H, hematite; and P, pyrite where, for instance, CH is the chlorite-hematite present divariant field.

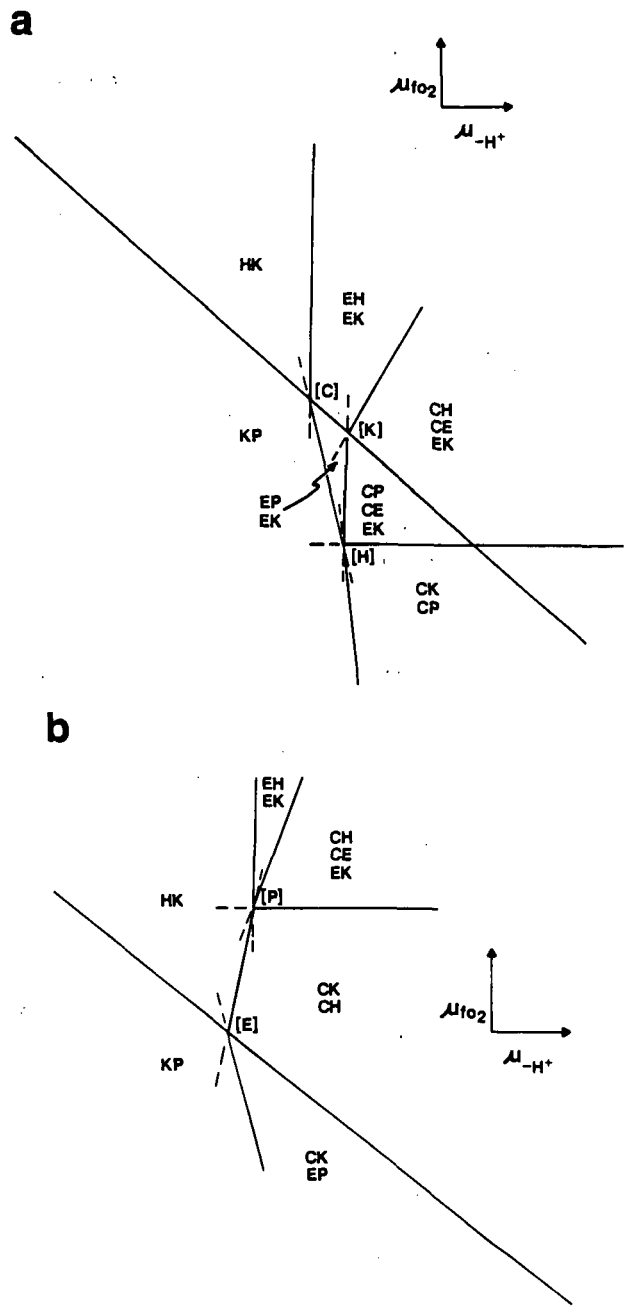

Fig. 2. The two possible net variants generated by orienting Figure 1 plotted in chemical potential space ($\mu_{f_{O_2}}$ - μ_{-H+}) space. See Figure 1 for abbreviations.

Accounting for complex species involves the use of activity coefficients as defined above, and a set of dissociation constants for the complex species to free ions. Dissociation constants for aqueous species (Table 4) used in this work were taken from the data base of *Janecky* [1982] and *Janecky and Seyfried* [1983, 1984]. Variations in these constants due to pressure were calculated using an isodielectric approach [*Helgeson*, 1969; *Janecky and Seyfried*, 1983].

Mineral Thermodynamic Data

Mineral dissolution constants were calculated using the SUPCRT code and data from *Helgeson et al.* [1978], *Helgeson and Kirkham* [1974a,b; 1976], *Helgeson et al* [1981],

TABLE 4. Dissociation Constants

	P = 86 bar T = 300°C	250 bar 300°C
I Aqueous Reactions		
$H_2S \rightarrow H^+ + HS^-$	-8.96	-8.61
$HS^- + 2O_2 \rightarrow H^+ + SO_4^=$	51.69	53.66
$HSO_4^- \rightarrow H^+ + SO_4^=$	-6.39	-6.08
$S^= + H^+ \rightarrow HS^-$	12.89	12.60
$2H_2O \rightarrow H_{2(aq)} + 2O_{2(g)}$	-37.56	-38.83
$H_2O \rightarrow H^+ + OH^-$	-10.86	-10.78
$Fe^{+3} + \frac{1}{2}H_2O \rightarrow H^+ + \frac{1}{2}O_2 + Fe^{+2}$	1.05	0.80
$CaOH^+ + H^+ \rightarrow Ca^{+2} + H_2O$	7.65	7.74
$MgOH^+ + H^+ \rightarrow Mg^{+2} + H_2O$	5.77	5.83
$H_2CO_3 \rightarrow H^+ + HCO_3^-$	-8.61	-8.45
$CO_3^= + H^+ \rightarrow HCO_3^-$	12.15	11.98
$CH_{4(aq)} + 2O_{2(g)} \rightarrow H_2O + H^+ + HCO_3^-$	56.84	58.70
II Solid Phase Reactions		
$Hem + 4H^+ \rightarrow 2Fe^{+2} + 2H_2O + \frac{1}{2}O_2$	-9.56	-9.14
$Mt + 6H^+ \rightarrow 3Fe^{+2} + \frac{1}{2}O_2 + 3H_2O$	-6.58	-5.95
$Py + H_2O \rightarrow \frac{1}{2}O_2 + 2HS^- + Fe^{+2}$	-34.64	-34.04
$Po + H^+ \rightarrow Fe^{+2} + HS^-$	-7.03	-6.63
$Qz \rightarrow SiO_{2(aq)}$	-2.01	-1.97
$Ksp + 4H^+ \rightarrow 2H_2O + K^+ + Al^{+3} + 3SiO_{2(aq)}$	-3.46	-2.91
$Epi + 12H^+ \rightarrow 2Ca^{+2} + Fe^{+2} + \frac{1}{4}O_2 + 3SiO_{2(aq)} + 6.5H_2O + 2Al^{+3}$	0.76	2.21
$Cp + H^+ + .5H_2O \rightarrow Fe^{++} + 2HS^- + Cu^+$	-31.70	-31.04
$Bn + 3H^+ + .5H_2O \rightarrow Fe^{++} + 5Cu^+ + 4HS^- + .25O_2$	-70.38	-69.11
$CC + H^+ \rightarrow Ca^{++} + HCO_3^-$	-2.22	-1.85
$Chl_0 + 16H^+ \rightarrow 3Mg^{+2} + 2Fe^{+2} + 2Al^{+3} + 3SiO_{2(aq)} + 12H_2O$	12.66	14.55
$Chl_{35} + 16H^+ \rightarrow 3Mg^{+2} + 2Fe^{+2} + 2Al^{+3} + 3SiO_{2(aq)} + 11.65H_2O + 0.175O_2$	6.87	8.78
$Wal\ I + 12H^+ \rightarrow 6Mg^{+2} + 4SiO_{2(aq)} + 10H_2O$	26.29	27.61
$Wal\ II + 16H^+ \rightarrow 5Mg^{+2} + 2Al^{3+} + 3SiO_{2(aq)} + 12H_2O$	16.95	18.84
$Wal\ III + 16H^+ \rightarrow 5Fe^{+2} + 2Al^{+3} + 3SiO_{2(aq)} + 12H_2O$	8.92	10.79
$Wal\ IV + 14H^+ \rightarrow 7Fe^{+2} + 3SiO_{2(aq)} + 11H_2O + \frac{1}{2}O_{2(g)}$	0.47	1.96
$Wal\ V + 12H^+ \rightarrow 4Al^{+3} + 4SiO_{2(aq)} + 10H_2O$	-10.26	-8.63
$Wal\ VI + 16H^+ \rightarrow 5Fe^{+2} + 2Al^{+3} + 3SiO_{2(aq)} + 11.5H_2O + \frac{1}{4}O_{2(g)}$	-1.08	0.82

See also nomenclature at bottom of Table 3. Mt, magnetite; Po, Pyrhotite; Qz, quartz; Cp, chalcopyrite; Bn, Bornite; CC, Calcite; Chl_0, Chlorite with 0 mol % Ferric iron; Chl_{35}, Chlorite with 35 mol % Ferric iron; Wal I-VI, Chlorite and end members [after *Walsche*, 1986].

and H. C. Helgeson (personal communication of updates and corrections to the data). Chlorite solid solution dissolution constants are calculated after the method of *Walshe* [1986] for zero and 35 mol % ferric iron content more appropriate for Salton Sea chlorites. Epidote is calculated as $Ps_{33}Cz_{67}$. Dissociation constants are taken directly from SUPCRT. All mineral dissolution reactions used in this work were written in terms of completely dissociated

aqueous species. In particular, dissolved silica was used in chlorite dissolution reactions, rather than quartz as used by *Walshe* [1986].

PHASE EQUILIBRIA IN THE CURRENT SALTON SEA SYSTEM

The estimated fluid composition of the 1866 m flow zone may be compared against the observed phase assemblages as a test of compatibility. Aquifer temperature is approximately 300°C and $\Sigma S = 0.0003$ m. The minimum hydrostatic pressure for one-phase aqueous fluid is about 86 bars at 300°C ($a_{H_2O} = 1$). This pressure is slightly different when $a_{H_2O} = 0.88$ (approximately 70 bars) but is not deemed to be important for the calculations, as will be shown in a later section along with calculations for higher pressures.

Phase compositions used in the calculations are similar to those shown in Table 1. Chlorite is approximated as $Mg_3Fe^{+2}_{1-x}Fe^{+3}_xAl_2Si_3O_{12}(OH)_{8-x}O_x$. Na and Ca are not considered and Mn is added to Mg. Calculated values for ferric iron after *Walshe* [1986] are about 35 mol % of the total iron ($x = 0.35$). Epidote is very nearly $Ca_2Al_2Fe^{+3}Si_3O_{10}(OH)$ with all iron calculated as ferric. Pyrite and hematite are considered to be pure phases. Activity of K-feldspar is presumed to equal 1 because microprobe analyses appear to be a mixture not a solid solution of albite and K-feldspar. Thermodynamic quantities for the K-feldspar are presumed to be similar to those for adularia.

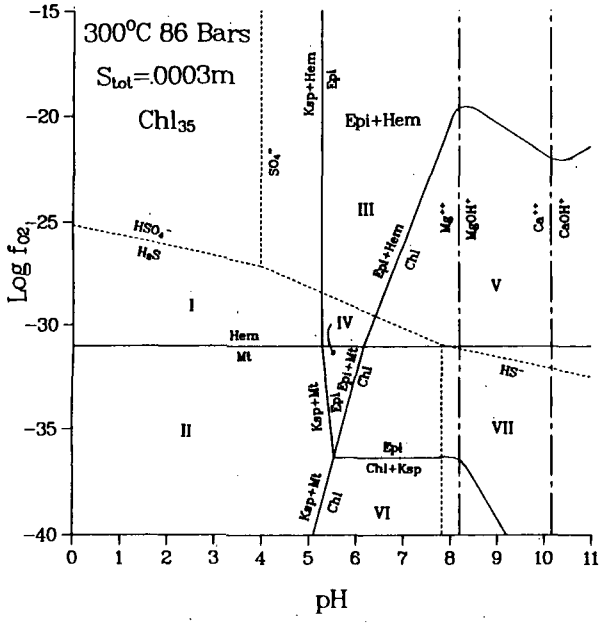

Fig 3.a. Log f_{O_2} - pH predominance diagram at $T = 300°C$, $\Sigma S = 0.0003$ m, quartz saturation, $P = 86$ bars. Abbreviations are described in Tables 3 and 4. The ferric iron content of the chlorite is calculated at 35 mol %. Only the observed Hem + Epi divariant field is labelled. All possible divariant assemblages are shown as follows I, Ksp + Hem; II, Ksp + Mt; III, Epi + Hem, Epi + Ksp; IV, Epi + Mt, Epi + Ksp; V, Chl + Hem, Chl + Epi, Epi + Ksp; VI, Chl + Ksp, Chl + Mt; VII, Chl + Mt, Chl + Epi, Epi + Ksp.

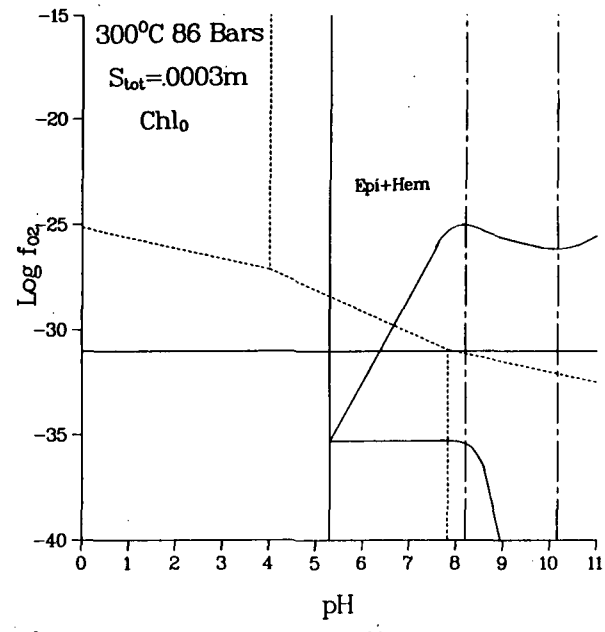

Fig. 3b. Reaction relations with 0 mol % ferric iron in chlorite.

Calculations indicate the net variant shown in Figure 2a is the relevant one in real space. The phase equilibria presented there are oriented in a log f_{O_2} versus *p*H predominance diagram shown in Figure 3. Species dominance is rarely intuitive in this system. Actual distribution of species calculations were used to determine dominance throughout the development presented here. These calculations were particularly useful in regions where several species were subequal in calculated concentration. Reaction relations show the dominant species participating. Others may not be materially relevant. At 300°C, K^+ is dominant over KCl by about 2 to 1 ($K^+ = 0.45$ m, KCl = 0.21 m) at this concentration of chloride. Also, $Ca^{+2} = 0.90$ m and the most abundant chloride specie, $CaCl^+ = 0.12$ m (Calculated by Janecky after *Berndt* [1987]). NaCl is dominant over Na^+, but Na is indifferent to the reaction relations considered herein. The calculated molalities of K^+, etc., are used in the following numerical analyses. Complete phase assemblage information which is bulk composition dependent is presented for each labeled sector as shown. The reaction hematite $\rightleftharpoons$ $1/6O_2 + 2/3$ magnetite divides the system into hematite- and magnetite-bearing assemblages. Magnetite was never observed in this study; consequently, the possible additional assemblages chlorite + K-feldspar and epidote + K-feldspar are relevant only above the horizontal line representing this reaction relation in the presence of excess iron oxide. Chlorite + epidote is shown to be relatively more reducing and, at lower f_{O_2}, more alkaline than epidote + hematite. The reaction relations between the observed assemblages epidote + hematite and chlorite + epidote are:

*p*H > 10.09:

$$1/2\text{Hem} + \text{Epi} + 3Mg(OH)^+ + 3.15H_2O \rightleftharpoons H^+ + 2Ca(OH)^+ + 0.325O_2 + \text{Chl}_{35}$$

*p*H 8.21 to 10.09:

$$1/2\text{Hem} + \text{Epi} + 3Mg(OH)^+ + 1.15H_2O + H^+ \rightleftharpoons 2Ca^{+2} + 0.325O_2 + \text{Chl}_{35}$$

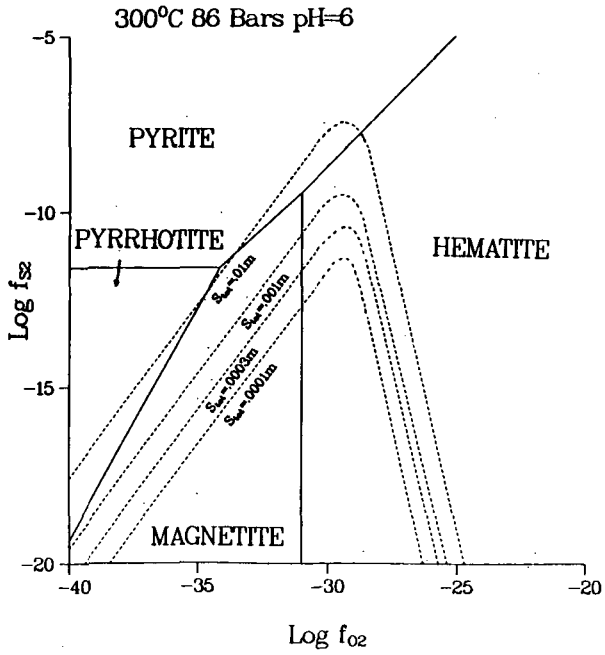

Fig. 4a. Isobaric-isothermal log f_{S_2} - log f_{O_2} at 300°C, 86 bars, and pH = 6. Fe-S phase relations are contoured with respect to sulfur concentration. S_{tot} = 0.0003 m is the concentration taken from Table 2.

pH 6.17 to 8.21:

$$1/2Hem + Epi + 3Mg^{+2} + 4.15H_2O \rightleftharpoons 2H^+ + 2Ca^{+2} + 0.325O_2 + Chl_{35}$$

Use of 35 mol % ferric iron does not have a very critical effect upon the phase equilibria. Figures 3a and 3b shows the chlorite present reactions with both 35 mol % and 0 mol % ferric iron. Decrease in the ferric iron content greatly decreases the chlorite bearing assemblages divariant field only at very high f_{O_2} and high pH while slightly increasing the size of the chlorite bearing divariant fields at low f_{O_2}. The former conditions are unreasonable for most natural systems.

Reaction relations for the chlorite$_{35}$ bearing reactions in addition to the ones given above are:

$$Chl_{35} + 0.242O_2 + 2Ca^{+2} + 2H^+ \rightleftharpoons 1/3Mt + Epi + 4.15H_2O + 3Mg^{+2}$$

$$Chl_{35} + 3Q + 0.159O_2 + 4H^+ + 2K^+ \rightleftharpoons 2/3Mt + 2Ksp + 5.65H_2O + 3Mg^{+2}$$

$$Chl_{35} + 2Ksp + 4Ca^{+2} + 0.325O_2 \rightleftharpoons 2Epi + 3Q + 2.65H_2O + 2K^+ + 3Mg^{+2}$$

$$Chl_{35} + 2Ksp + 4Ca^{+2} + 0.3250_2 + 0.35H_2O \rightleftharpoons 2Epi + 3Q + 3H^+ + 3Mg(OH)^+ + 2K^+$$

Similar reaction relations are generated for Chl_0 (see the appendix). Perhaps the most important observation is that no pyrite-bearing assemblages are stable anywhere on the diagram.

In a dynamic hydrothermal system, such as found in the Salton Sea reservoir, one may expect important chemical and physical parameters to change as the system evolves. Changes in pressure, temperature, and fluid chemistry, particularly ΣS, may be important and can be examined with the diagrams. If the sulfides grew at 300°C, what other conditions must prevail? Figure 4a is contoured with respect to total sulfur at 300°C and pH = 6. The observed total sulfur content from the 1866 m flow zone is 0.0003 m. Clearly, sulfur content must be greatly in excess of 0.0003 m for pyrite to be stable. The point where the pyrite field, expanding from the left in Figure 3, impinges upon the isobaric-isothermal reaction relation K-feldspar + hematite = epidote at a pH of 5.29 and log f_{O_2} = -28.42 will yield a minimum ΣS for any epidote + pyrite field. This minimum value in this case is ΣS = 0.003m, or 10 times the observed value.

Thus far, calculations have been at steam saturation. Pressure increases could change the positions of the univariant relations. The isobaric-isothermal diagram in Figure 4b (250 bars) shows slightly less sulfur is required to stabilize pyrite at constant pH. The reaction K-feldspar + hematite = epidote occurs at a pH of 5.42 at 300°C and 250 bars. The minimum ΣS for any epidote + pyrite field in this case is about 0.0031 m. Clearly, ΣS > 0.003 m is needed to create any reasonable field for epidote + pyrite stability regardless of pressure.

Changes in temperature will produce similar results. Calculations at higher temperatures at constant ΣS show a decrease in the stability of pyrite, while lower temperature increases the stability of pyrite with respect to oxides. Temperatures below 300°C are probably unwarranted as fluid inclusions of the Type 2 assemblages from M. A. McKibben et al. (submitted manuscript, 1987) extrapolated to 1866 m yield temperatures of about 305°C.

DISCUSSION

We have established the sensitivity of the phase relations to changes in fluid composition (ΣS), pressure, and temperature. Reasonable variations in these quantities and relationships with stability of observed assemblages must now be examined.

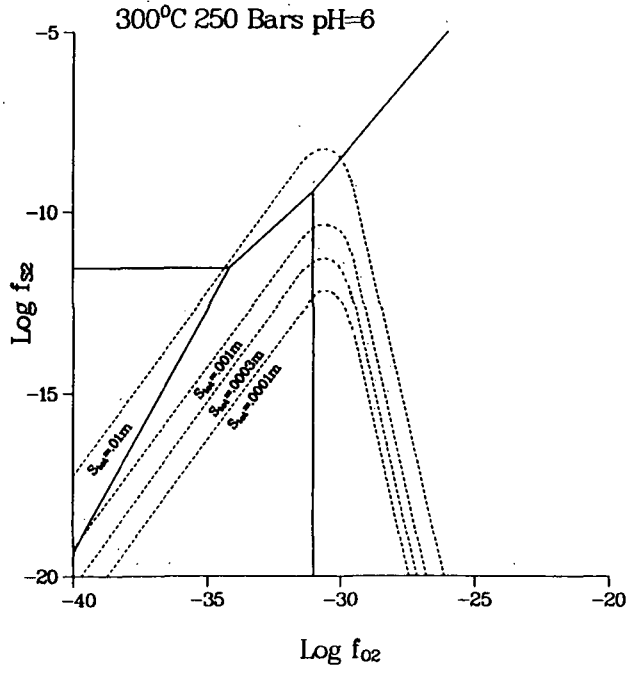

Fig. 4b. Phase relations at 250 bars.

TABLE 5. Total Sulfur Concentration for Other Salton Sea Wells

Well	ΣS Molality	Reference
State 2–14	0.0003	this study
Sportsman No. 1	0.0005	*Palmer* [1975]*
I.I.D. No. 1	0.0007	*Skinner et al.* [1967]
I.I.D. No. 2	0.0012	*Helgeson* [1968]
State No. 1	0.0012	*Helgeson* [1968]
Sinclair No. 4	0.0013	*Palmer* [1975]*

*Not known to be corrected for steam loss.

Measured total sulfur in State 2-14 is 0.0003 m although A. E. Williams and M. A. McKibben (submitted manuscript, 1987) presented a higher value (0.0009 m). Table 5 compares the lower value with sulfur concentrations measured by other investigators in other Salton Sea wells. *Helgeson* [1968] chose a mean value of $f_{S_2} = 10^{-10}$. Other measured sulfur concentrations range from roughly two to four times that observed in State 2-14. Solutions were sampled during flow tests in all cases except State 2-14 where both flow sampling and downhole sampling was involved. However, calculations clearly show that an increase in total sulfur to above 0.003 m at 86 bars and 300°C will be necessary to stabilize pyrite + epidote to any significant extent in the system. The reason for such a discrepancy is not altogether clear, although drilling activities and sampling procedures may cause significant affects. Sulfur loss due to drilling activities may be attributed to reaction of sulfide with the metal liner or precipitation of sulfate by reaction with drilling fluids. Sulfate concentration in equilibrium with anhydrite in a State 2-14 composition solution is approximately 0.002 m (G. K. Bayhurst and D. R. Janecky, unpublished experimental data, 1988). Sulfide might also be lost during flow sampling; however, a gas-tight sample was obtained from State 2-14 with a downhole sampler which contained similar low total sulfur concentration but may represent mixtures of several flow zones. Thus, while there are sufficient reasons to question the sampled concentrations, no direct way to identify or quantify such losses exists.

Measured total carbonate, another volatile, is 0.052 m which fits well within the range shown by *Helgeson* [1968]: well I.I.D. 2, 0.016 m and well State 1, 0.16 m. However, *Bird and Norton* [1981] have shown a gradient in f_{CO_2} in Salton Sea reservoirs with temperature and depth. Their value for f_{CO_2} at 300°C is about 2.5 atm at 300°C. Because the downhole sample (SS-21, Table 2) was collected at 3110 m, it may show a fluid signature corresponding to this deeper horizon. *Bird and Norton* [1981] estimated f_{CO_2} at 350°C for Elmore 1 to be of the order of 20 atm based on calculations defining the chlorite + calcite and biotite zones with respect to temperature and f_{CO_2}. For these reasons, a value of 0.03 m as ΣC will be used in our calculations, rather than 0.052 m.

Measured well pressure at total depth is 295.6 bars absolute. Using a gradient of 0.0968 atm^{-1}/m (*Helgeson*, 1968], the predicted value at 3110 m is 301 atm. At 1866 m the predicted pressure is 181 atm, well above the vapor pressure at $a_{H_2O} = 0.88$ (≈70 bars).

Errors in the thermodynamic data may also be a problem. As an example, for the reaction,

$$Py + 2H_2O + 3.75O_2 \rightleftharpoons 4H^+ + 2\,SO_4^{-2} + 0.5Hem$$

at 86 bars, 300°C, log K = 73.52. The minimum change in log K to stabilize a pyrite + epidote field (ΣS = 0.0003m, *p*H = 5.29) would be a decrease in log K to about 71.45. Because we are dealing with log quantities, this is a very large change and probably unwarranted. The minimum change in the activity coefficient of sulfate to produce a similar effect would be about a 1000% increase (7×10^{-3} versus 6.55×10^{-4}).

If the thermodynamic values are sufficiently accurate, we have established increased total sulfur and pressure above vapor saturation are required to stabilize pyrite at 300°C. In Figure 5 we have recalculated the equilibria considered in Figure 3a at 250 bars and ΣS = 0.005 m. Pyrite, chalcopyrite, and bornite have been added to the relations. Balanced reaction relations may be found in the appendix. All possible divariant fields are shown in the Figure 5 caption. Under these conditions a significant pyrite + epidote field appears. While it is not strictly correct to use Figure 5 to quantify *p*H and redox changes as one progresses stratigraphically from the mudstone to the flow zone rock because possibly temperature and additional compositional axes are necessary to yield a more complete picture, a simple figure like Figure 5 is useful to predict some trends in local equilibrium for the more complex system. The hematite + epidote-bearing assemblages are more oxidizing than K-feldspar + pyrite, epidote + pyrite, and chlorite + pyrite and this assemblage occurs at a lower *p*H than chlorite + epidote and chlorite + pyrite.

The assemblages containing pyrite + epidote and hematite + epidote are located in a very restricted region of *p*H and log f_{O_2}. Figure 6 shows a portion of this region with the addition of calcite relations. From Figure 6 it is chemographically and thermodynamically possible to produce phase assemblages calcite free, as is observed in our samples. These are assemblages K-feldspar + pyrite + chalcopyrite, epidote + hematite + chalcopyrite, and epidote + pyrite + chalcopyrite (III, VIII, and IX in Figure 6). A small increase in *p*H adds calcite to these assemblages (IIIa, VIIIa, IXa on Figure 6). One can see, at 300°C, chalcopyrite and calcite may be added to many of the phase assemblages shown in Figure 5. Calcite was not found in the rock fragments that we examined. This may be due to the violent nature of sample extraction. Calcite is not a common phase in other, similar, veins (M. A. McKibben et al., submitted manuscript, 1987), and chalcopyrite is also relatively rare. The thermodynamics of K-mica were ignored in the detailed calculations. K-mica (muscovite) will appear below a *p*H of about 4.9, not affecting conclusions drawn from Figure 6. While the width of some

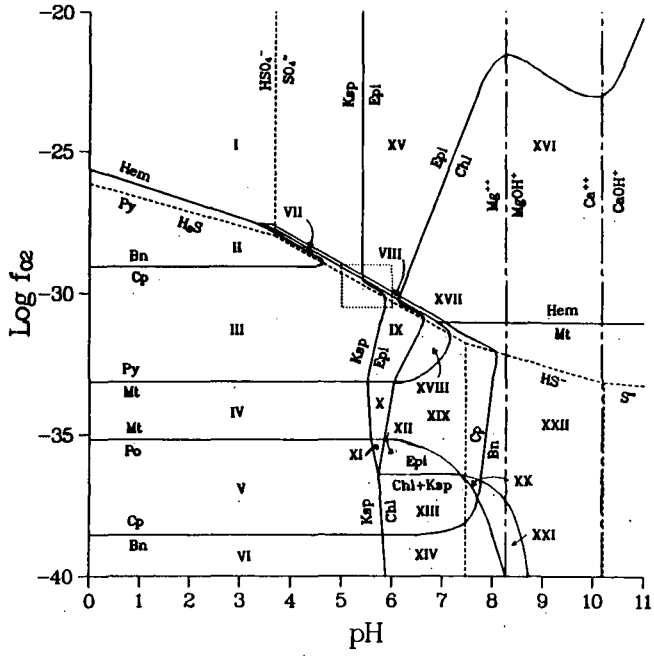

Fig. 5. Isobaric-isothermal log f_{O_2} - pH diagram of phase relations at 300°C, S_{tot} = 0.005 m, P_{tot} = 250 bars. Chl = Chl_{35}. Chalcopyrite relations have been added. The dotted rectangle in the center is expanded in Figure 7. For complete reaction relations see the appendix. The possible divariant fields depending upon bulk composition are I, Ksp + Hem + Bn; II, Ksp + Py + Bn; III, Ksp + Py + Cp; IV, Ksp + Mt + Cp; V, Ksp + Po + Cp; VI, Ksp + Po + Bn; VII, Ksp + Hem + Cp; VIII, Epi + Hem + Cp, Epi + Ksp + Cp; IX, Epi + Py + Cp, Epi + Ksp + Cp; X, Epi + Mt + Cp, Epi + Ksp + Cp; XI, Epi + Po + Cp, Epi + Ksp + Cp; XII, Chl + Po + Cp, Epi + Ksp + Cp, Chl + Epi + Cp; XIII, Chl + Po + Cp, Chl + Ksp + Cp; XIV, Chl + Po + Bn, Chl + Ksp + Bn; XV, Epi + Hem + Bn, Epi + Ksp + Bn; XVI, Chl + Hem + Bn, Epi + Ksp + Bn; XVII, Chl + Hem + Cp, Chl + Epi + Cp, Epi + Ksp + Cp; XVIII, Chl + Py + Cp, Chl + Epi + Cp, Epi + Ksp + Cp; XIX, Chl + Hem + Cp, Chl + Epi + Cp, Epi + Ksp + Cp; XX, Chl + Mt + Cp, Chl + Ksp + Cp; XXI, Chl + Mt + Bn, Chl + Ksp + Bn; XXII, Chl + Mt + Bn, Chl + Epi + Bn, Epi + Ksp + Bn.

fields on these diagrams is only a few tenths of a pH unit and less and thus may not be significant given the inherent errors in thermodynamic parameters, the observed assemblage information is closely consistent with that predicted by phase stability. The phase assemblages are of the type 2 variety described by M. A. McKibben et al. (submitted manuscript, 1987). The phase equilibria clearly show the growth of K-feldspar-, epidote-, and chlorite-bearing assemblages occur over a wide variety of conditions at 300°C. Pyrrhotite may appear at low f_{O_2} and occasionally does appear in their type 1 assemblages. Oxidation and sulfur transport may yield stable hematite bearing assemblages. *Skinner et al.* [1967] maintain hematite occurs in "association" with pyrite and quartz. M. A. McKibben et al. (submitted manuscript, 1987) show several pyrite + epidote and hematite + epidote-bearing assemblages and one pyrite + hematite + epidote-bearing assemblage. The latter may occur near the isothermal isobaric univariant reaction hematite ⇌ pyrite at approximately log f_{O_2} = -29.7 and pH = 5.6 which is close to the estimated values (log f_{O_2} = -30 and pH = 5.4) calculated by *McKibben and Elders* [1985] at 300°C. The appearance of authogenic chlorite intergrown with hematite and pyrite (M. A. McKibben et al., submitted manuscript, 1987) would occur at slightly more akaline pH's in the vicinity of the hematite ⇌ pyrite reaction (pH >6, Figure 5).

If the isobaric-isothermal univariant assemblage epidote + pyrite + hematite (± chalcopyrite) represents the stable phase assemblage in equilibrium with present-day fluids, sulfur must have been lost during sampling or due to the drilling operations. Such shifts in solution composition and sulfur transport could also be accomplished by convection as suggested by *Helgeson* [1968], but would have to have occurred relatively recently. The relatively thin sedimentary sequence overlying a heterogeneous heat source requires a set of small convection cells [*Lauchenbruch et al.*, 1985], which could be moved significantly as a result of small changes in the nature of the heat source. *Michels* [1986*b*] stated the brines are too dense to convect, disagreeing with the convection hypothesis. The observation which fits all data most closely may be a combination of factors discussed in detail in this section. In order to observe stable pyrite-bearing assemblages at 300°C, one or a combination of the following must obtain: ΣS must be above 0.003 m or adjustment of the thermodynamic values used in the calculations.

Some aspect of human intervention are displayed in Figure 7. Plotted are solubilities of several phases of import to the Salton Sea system. The hatched area represents the phase assemblages hematite + epidote and pyrite + epidote (both ± chalcopyrite) which correspond to redox and pH conditions in the vicinity of the flow zone at

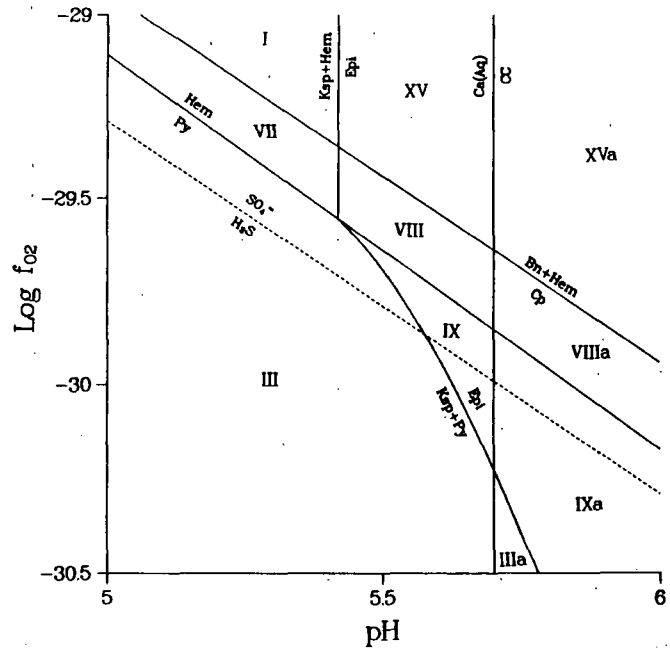

Fig. 6. Expanded portion of Figure 5 showing the relationship between Hem + Epi and Py + Epi fields. Calcite relations are added. XVa, VIIIa, etc., are simply VX, VIII, etc., of Figure 5 with calcite added to each assemblage.

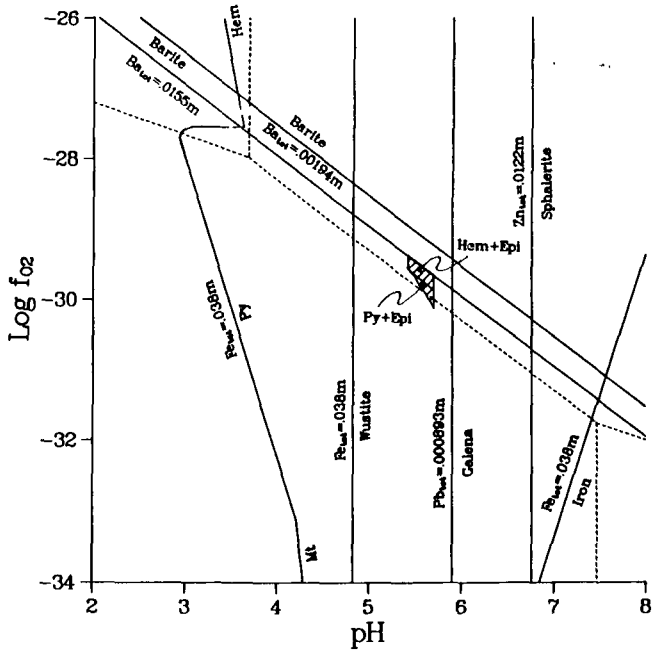

Fig. 7. Isobaric-isothermal log f_{O_2} - pH diagram showing saturation with respect to various phases based upon observed fluid compositions. See text for details. The hatched region in the Hem + Epi and Py + Epi region in Figure 7. No solid-solid relations are plotted. Dashed curves represent sulfur speciation as shown previously.

1866 m. Clearly, the flow zone is well supersaturated with respect to pyrite at the observed iron concentration of 0.038 m. For comparison wustite and metallic iron solubilities are also shown. The fluid is supersaturated with respect to wustite but well undersaturated with respect to metallic iron. Any iron-bearing casing is metastable in this system. The solubility of barite is contoured for observed concentration (0.0155 m) and concentration corrected for the addition of drilling muds (0.00194 m). The latter shows undersaturation with respect of barite, while the former is saturated with barite under conditions found near the flow zone. The observed concentrations of Pb (0.000893 m) and Zn (0.0122 m) are undersaturated with respect of galena and sphalerite. Sulfates are not considered. Acanthite saturates well to the right of this diagram. Dominant species in these latter cases are $PbCl_4^{-2}$, $ZnCl_4^{-2}$, and $AgCl_4^{-3}$ species in this high chloride system.

CONCLUSIONS

Chemographic and thermodynamic analysis of solid phases and aqueous fluid taken from the 1866 m flow zone in State well 2-14 are generally consistent with the growth of the major phase assemblages at 300°C at pressures above vapor saturation. Conditions in the region of the flow-zone are about pH = 5.6, log f_{O_2} = -29.7, and ΣS above 0.003 m. We have examined the effects of total dissolved sulfur, temperature, pressure, and varying thermodynamic values. Fluid sampling in this very difficult environment shows the effects of mixing of more than one flow zone, reaction of the fluid with the metal liner, and reaction with drilling fluids. It seems likely that low dissolved sulfur is due to reaction with lost circulation materials, metal liner, and possible fractionation during sampling. Although the amount of this loss is ambiguous, a reasonable value for ΣS is about 0.003 m–0.005 m. Observed CO_2 is incompatible with the flow zone mineral assemblages due to communication with deeper flow zones. A partial pressure of 2.5 bars [*Bird and Norton*, 1981] appears appropriate. Aqueous iron is very high due to liner dissolution. Barium seems saturated with respect to barite. The system is well undersaturated with respect to galena, sphalerite, and acanthite. Distribution of species calculations indicate chloride is the dominant complexing ligand for some metals (Pb, Zn, Ag, Na, and Fe) but is subordinate in other metals (Ca, Mg, Ba, and K).

Major phase assemblages are K-feldspar + pyrite, epidote + pyrite, epidote + hematite, and chlorite + pyrite. All assemblages may contain calcite and chalcopyrite. Phase assemblages lying stratigraphically above and below the aquifer are more reducing than is compatible with sampled fluid. The fluid shown in Table 2 is in equilibrium with hematite-bearing assemblages at 300°C. Transport of sulfur from the system cannot be ruled out but seems unlikely.

APPENDIX: SOME REACTIONS USED IN THE CALCULATIONS

See text for mineral abbreviations.

Reaction:

$Py + 2H_2O + 3.75O_2 = 2H^+ + 0.5Hem + 2HSO_4^-$
$Py + 2H_2O + 3.75O_2 = 4H^+ + 2SO_4^= + 0.5\ Hem$
$Py + 2H_2O = 0.5Hem + 2H_2S + 0.25O_2$
$Py + H_2O = H^+ + 0.5O_2 + HS^- + Po$
$Py + H_2O = H_2S + 0.5O_2 + Po$
$3Py + 6H_2O + 11O_2 = 12H^+ + 6SO_4^= + Mt$
$3Py + 6H_2O = 6H^+ + O_2 + 6HS^- + Mt$
$3Py + 6H_2O = 6H_2S + O_2 + Mt$
$Mt + 3H^+ + 3HS^- = 3Po + 1/2O_2 + 3H_2O$
$Mt + 3H_2S = 0.5O_2 + 3Po + 3H_2O$
$Hem = 0.167O_2 + 0.667Mt$
$5Cp + 2H_2O = O_2 + 2H_2S + Bn + 4Po$
$5Cp + 2H_2O = O_2 + 2H^+ + 2HS^- + Bn + 4Po$
$5Cp + 6H_2O = 0.333O_2 + 6H^+ + 6HS^- + Bn + 1.333Mt$
$5Cp + 6H_2O + 11.667O_2 = 12H^+ + 6SO_4^= + Bn + 1.333Mt$
$5Cp + 6H_2O + 12O_2 = 12H^+ + 6SO_4^= + 2Hem + Bn$
$5Cp + 5H_2O + 12O_2 = 6H^+ + 6HSO_4^- + 2Hem + Bn$
$5Cp + 2HSO_4^- + 2H^+ = 3O_2 + 2H_2O + 4Py + Bn$
$5Cp + O_2 + 2H_2S = Bn + 4Py + 2H_2O$
$CC + 2H^+ = Ca^{2+} + H2CO3$
$12H^+ + 6Qz + 2Epi + 4K^+ + 4SO_4^= = 4Ksp + 2Py + 7H_2O + 4Ca^{2+} + 7.5O_2$
$8H^+ + 0.5O_2 + 4HS^- + 6Qz + 2Epi + 4K^+ = 4Ksp + 2Py + 7H_2O + 4Ca^{2+}$
$4H^+ + 0.5O_2 + 4H_2S + 6Qz + 2Epi + 4K^+ = 4Ksp + 2Py + 7H_2O + 4Ca^{2+}$
$4H^+ + 6Qz + 2Epi + 4K^+ = 4Ksp + 3H_2O + 2/3Mt + 4Ca^{2+} + 0.167O_2$
$2H_2S + 4H^+ + 6Qz + 2Epi + 4K^+ = 4Ksp + 5H_2O + 2Po + 0.5O_2 + 4Ca^{2+}$
$2HS^- + 6H^+ + 6Qz + 2Epi + 4K^+ = 4Ksp + 5H_2O + 2Po + 0.5O_2 + 4Ca^{2+}$

$6Qz + 4H^+ + 2Epi + 4K^+ = 4Ksp + Hem + 4Ca^{2+} + 3H_2O$

$Chl_0 + 2H^+ + 2Ca^{2+} + 0.5O_2 = 4.5H_2O + 3Mg^{2+} + 0.5Hem + Epi$

$Chl_0 + 0.25O_2 + 3H^+ + HS^- + 2Ca^{2+} = Po + 5.5H_2O + 3Mg^{2+} + Epi$

$Chl_0 + 0.25O_2 + HS^- + 2Ca^{2+} = 2.5H_2O + Po + 3Mg(OH)^+ + Epi$

$Chl_0 + 0.5O_2 + 2Ca(OH)^+ + H^+ = 3.5H_2O + 3Mg(OH)^+ + 0.5Hem + Epi$

$Chl_0 + 0.5O_2 + 2Ca^{2+} = 1.5H_2O + 3Mg(OH)^+ + H^+ + 0.5Hem + Epi$

$Chl_0 + 2H^+ + 2Ca^{2+} + 0.417O_2 = 4.5H_2O + 0.333Mt + Epi + 3Mg^{2+}$

$Chl_0 + 2Ca^{2+} + 0.25O_2 + 2H^+ + H_2S = Po + 5.5H_2O + 3Mg^{2+} + Epi$

$Chl_0 + 2Ca^{2+} + 2H^+ + 2H_2S + 0.75O_2 = 6.5H_2O + Epi + Py + 3Mg^{2+}$

$Chl_0 + 2Ca^{2+} + 6H^+ + 2SO_4^{=} = 3.25O_2 + 6.5H_2O + 3Mg^{2+} + Py + Epi$

$Chl_0 + 2H_2S + 2K^+ + 4H^+ + 3Qz = 2Po + 8H_2O + 3Mg^{2+} + 2Ksp$

$Chl_0 + 4H^+ + 3Q + 2K^+ + 0.333O_2 = 6H_2O + 0.667Mt + 2Ksp + 3Mg^{2+}$

$Chl_0 + 2Ksp + 4Ca^{2+} + 0.5O_2 = 3H_2O + 3Mg^{2+} + 2Epi + 2K^+ + 3Q$

$Chl_0 + 2Ksp + 4Ca^{2+} + 0.5O_2 = 3Qz + 3Mg(OH)^+ + 3H^+ + 2Epi + 2K^+$

$Chl_0 + 2Ksp + H^+ + 4Ca(OH)^+ + 0.5O_2 = 3Qz + 4H_2O + 3Mg(OH)^+ + 2Epi + 2K^+$

$Chl_0 + 4H^+ + 2H_2S + 3Qz + 2K^+ = 2Po + 3Mg^{2+} + 2Ksp + 8H_2O$

$Chl_0 + 4H^+ + 4H_2S + 3Qz + O_2 + 2K^+ = 3Mg^{2+} + 2Py + 2Ksp + 10H_2O$

$Chl_0 + 0.417O_2 + 2Ca(OH)^+ + H^+ = 3.5H_2O + 3Mg(OH)^+ + Epi + 0.333Mt$

$Chl_0 + 0.417O_2 + 2Ca^{2+} + 2H^+ = 4.5H_2O + 3Mg^{2+} + Epi + 0.333Mt$

$Chl_0 + 0.417O_2 + 2Ca^{2+} = 1.5H_2O + H^+ + 3Mg(OH)^+ + Epi + 0.333Mt$

$Chl_0 + 2K^+ + 3Qz + 4H^+ + 0.333O_2 = 3Mg^{2+} + 0.667Mt + 2Ksp + 6H_2O$

$Chl_{35} + 2Ca^{2+} + 0.325O_2 + 2H^+ = 4.15H_2O + Epi + 0.5Hem + 3Mg^{2+}$

$Chl_{35} + 0.075O_2 + H_2S + 2Ca^{2+} + 2H^+ = 5.15H_2O + Po + Epi + 3Mg^{2+}$

$Chl_{35} + 0.242O_2 + 2Ca(OH)^+ + H^+ = 3.15H_2O + 0.167Mt + 3Mg(OH)^+ + Epi$

$Chl_{35} + 0.242O_2 + 2Ca^{2+} = 1.15H_2O + 0.333Mt + Epi + 3Mg(OH)^+ + H^+$

$Chl_{35} + 0.325O_2 + 2Ca(OH)^+ + H^+ = 3.15H_2O + 3Mg(OH)^+ + 0.5Hem + Epi$

$Chl_{35} + 0.575O_2 + 2H_2S + 2Ca^{2+} + 2H^+ = Py + Epi + 3Mg^{2+} + 6.15H_2O$

$Chl_{35} + 0.325O_2 + 2Ca^{2+} = 1.15H_2O + 0.5Hem + Epi + 3Mg(OH)^+ + H^+$

$Chl_{35} + 2Ca^{2+} + 0.242O_2 + 2H^+ = 4.15H_2O + Epi + 0.667Mt + 3Mg^{2+}$

$Chl_{35} + 2Ca^{2+} + 2SO_4^{=} + 6H^+ = Py + Epi + 3Mg^{2+} + 6.15H_2O + 3.425O_2$

$Chl_{35} + 2Ca^{2+} + 4H^+ + 0.575O_2 + HS^- = Py + Epi + 3Mg^{2+} + 6.15H_2O$

$Chl_{35} + 2Ca^{2+} + 0.075O_2 + HS^- + 3H^+ = 3Mg^{2+} + 5.15H_2O + Po + Epi$

$Chl_{35} + 2Ca^{2+} + 0.075O_2 + HS^- = 2.15H_2O + Po + Epi + 3Mg(OH)+$

$Chl_{35} + 4H^+ + 3Q + 2K^+ + 0.159O_2 = 5.65H_2O + 0.667Mt + 2Ksp + 3Mg^{2+}$

$Chl_{35} + 4H^+ + 3Q + 2H_2S + 2K^+ = 0.174O_2 + 2Po + 7.65H_2O + 2Ksp + 3Mg^{2+}$

$Chl_{35} + 4Ca^{2+} + 0.325O_2 + 2Ksp = 2.65H_2O + 2K^+ + 2Epi + 3Q + 3Mg^{2+}$

$Chl_{35} + 4Ca^{2+} + 0.325O_2 + 2Ksp + 0.35H20 = 3H^+ + 3Mg(OH)^+ + 2K^+ + 2Epi + 3Q$

$Chl_{35} + 4H^+ + 3Q + 4H_2S + 2K^+ 0.826O_2 = 9.65H_2O + 2Py + 2Ksp + 3Mg^{2+}$

$12H^+ + 4HS^- + 6Qz + 4K^+ + Chl_{35} = 4Ksp + 15.3H_2O + 4Po + 0.35O_2 + 6Mg^{2+}$

$8H^+ + 4H_2S + 6Qz + 4K^+ + Chl_{35} = 4Ksp + 15.3H_2O + 4Po + 0.35O_2 + 6Mg^{2+}$

$2.65H_2O + 3Q + 2Epi + 2K^+ + 3Mg^{2+} = Chl_{35} + 2Ksp + 0.325O_2 + 4Ca^{2+}$

$6H^+ + 6Mg(OH)^+ + 2\ Epi + 4K^+ + 6Qz = 2Chl_{35} + 4Ksp + 8Ca^{2+} + 1.7H_2O$

Acknowledgments. This work was funded by a grant from the Office of Basic Energy Sciences, US Department of Energy and Institutional Supporting Research at Los Alamos. We acknowledge the assistance of G. Bayhurst for some of the phase identification and analysis. We are also grateful to P. Rogers for many helpful discussions concerning phase equilibria and calculations dealing with concentrated brines. Reviews by R. Fournier, W. Elders, and especially P. Barton, Jr., greatly improved the interpretations of rock-water relations in this complex and hostile environment.

REFERENCES

Berndt, M. E., Experimental and theoretical constraints on the origin of mid-ocean ridge geothermal fluids, PhD thesis, Univ. of Minn. at Minneapolis St. Paul, 1987.

Bird, D. K., and H. C. Helgeson, Chemical interaction of aqueous solutions with epidote-feldspar mineral assemblages in geologic systems, II, Equilibrium constraints in metamorphic/geothermal processes, *Am. J. Sci., 281*, 576-614, 1981.

Bird, D. K., and D. L. Norton, Theoretical prediction of phase relations among aqueous solutions and minerals: Salton Sea geothermal system, *Geochim. Cosmochim. Acta, 45*, 1479-1493, 1981.

Charles, R. W., R. J. Vidale Buden, and F. Goff, An interpretation of the alteration assemblages at Sulphur Springs, Valles Caldera, New Mexico, *J. Geophy. Res., 91*, 1887-1898, 1986.

Drummond, S. E., Jr., Boiling and mixing of hydrothermal fluids: Chemical effects on mineral precipitation, Ph.D. thesis, 381 pp., Pa. State Univ., University Park, 1981.

Fournier, R. O., R. J. Rosenbauer, and J. L. Bischoff, The solubility of quartz in aqueous sodium chloride solution at 350°C and 180 to 500 bars, *Geochim. Cosmochim. Acta, 46*, 1975-1978, 1982.

Goff, F., L. Shevenell, C. O. Grigsby, and B. Dennis, Downhole fluid sampling at the SSSDP California State 2-14 well, Salton Sea, California, *Informal Rep.* LA-11052-OBES, 35 pp., Los Alamos Natl. Lab., Los Alamos, NM., 1987.

Harvie, C. E., and J. H. Weare, The prediction of mineral

solubilities in natural waters: The Na-K-Mg-Ca-Cl-SO_4-H_2O system from zero to high concentration at 25°C, *Geochim. Cosmochim. Acta, 48*, 981-997, 1980.

Helgeson, H. C., Geologic and thermodynamic characteristics of the Salton Sea geothermal system, *Am. J. Sci., 266*, 129-166, 1968.

Helgeson, H. C., Thermodynamics of hydrothermal systems at elevated temperatures and pressures, *Am. J. Sci., 267*, 729-804, 1969.

Helgeson, H. C., and D. H. Kirkham, Theoretical prediction of the thermodynamic behavior of aqueous electrolytes at high pressures and temperatures, I, Summary of the thermodynamic/electrostatic properties of the solvent, *Am. J. Sci., 274*, 1089-1198, 1974a.

Helgeson, H. C., and D. H. Kirkham, Theoretical prediction of the thermodynamic behavior of aqueous electrolytes at high pressures and temperatures, II, Debye-Hückel parameters for activity coefficients and relative partial molal properties, *Am. J. Sci., 274*, 1199-1261, 1974b.

Helgeson, H. C., and D. H. Kirkham, Theoretical prediction of the thermodynamic behavior of aqueous electrolytes at high pressures and temperatures, III, Equation of state for aqueous species at infinite dilution, *Am. J. Sci., 276*, 97-240, 1976.

Helgeson, H. C., J. M. Delany, H. W. Nesbitt, and D. K. Bird, summary and critique of the thermodynamic properties of rock-forming minerals, *Am. J. Sci., 278-A*, 1-220, 1978.

Helgeson, H. C., D. H. Kirkham, and G. C. Flowers, Theoretical prediction of the thermodynamic behavior of aqueous electrolytes at high pressures and temperatures, IV, Calculation of activity coefficients, osmotic coefficients, and apparent molal and standard and relative partial molal properties to 600°C and 5 kb, *Am. J. Sci., 281*, 1249-1516, 1981.

Hemley, J. J., J. W. Montoya, D. R. Shaw, and R. W. Luce, Mineral equilibria in the MgO-SiO_2-H_2O system: II. talc-antigorite-forsterite-anthophyllite-enstatite stability relations and some geologic implications in the system, *Am. J. Sci., 277*, 353-383, 1977.

Janecky, D. R., Serpentinization of peridotite within the oceanic crust: Experimental and theoretical investigations of seawater-peridotite interaction at 200°C and 300°C, 500 bars, Ph.D. dissertation, 244 pp., Univ. of Minn. at Minneapolis, St. Paul, 1982.

Janecky, D. R., and W. E. Seyfried, Jr., The solubility of magnesium hydroxide sulfate hydrate in seawater at elevated temperatures and pressures, *Am. J. Sci., 283*, 831-860, 1983.

Janecky, D. R., and W. E. Seyfried, Jr., Formation of massive sulfide deposits on oceanic ridge crests: Incremental reaction models for mixing between hydrothermal solutions and seawater, *Geochim. Cosmochim. Acta, 48*, 2723-2738, 1984.

Korzhinskii, D. S., *Physicochemical Basis of the Analysis of the Paragenesis of Minerals*, 142 pp., Consultants Bureau, Inc., New York, 1959.

Lauchenbruch, A. H., J. H. Sass, and S. P. Galanis, Jr., Heat flow in southernmost California and the origin of the Salton Trough, *J. Geophys. Res., 90*, 6709-6736, 1985.

Lindsay, W. T., Jr., Estimation of concentration quotients for ionic equilibria in high temperature water: The model substance approach, *Proc. Int. Water Conf. Eng. Soc. West Pa., 41st*, 284-294, 1980.

McDowell, S. D., and M. O. McCurry, Active metamorphism in the Salton Sea Geothermal Field, California, *Geol. Soc. Am. Abstr. Programs, 9*, 1088, 1977.

McKibben, M. A., and W. A. Elders, Fe-Zn-Cu-Pb mineralization in the Salton Sea geothermal system, Imperial Valley, California, *Econ. Geol., 80*, 539-559, 1985.

Michels, D. E., A chemical method for measuring steam quality in two-phase flowlines, *Trans. Geotherm. Resour. Counc., 10*, 437-442, 1986a.

Michels, D. E., SSSDP fluid compositions at first flow test of State 2-14, *Trans. Geotherm. Resour. Counc., 10*, 461-465, 1986b.

Palmer, T. D., Characteristics of geothermal wells located in the Salton Sea geothermal field, Imperial County, California, *Rep. UCRL-51976*, Lawrence Livermore Natl. Lab., Livermore, Calif., 1975.

Pitzer, K. S., Thermodynamics of electrolytes, I, Theoretical basis and general equations, *J. Phys. Chem., 77*, 268-285, 1973.

Pitzer, K. S., D. J. Bradley, P. S. Z. Rogers, and J. C. Peiper, Thermodynamics of high temperature brines, paper presented at American Society for Testing and Materials Symposium, Honolulu, Hawaii, April 5, 1979.

Pitzer, K. S., J. C. Peiper, and R. H. Bussey, Thermodynamic properties of aqueous sodium chloride solutions, *Rep. LBL-15512*, 138 pp, Lawrence Berkeley Lab., Berkeley, Calif., 1983.

Sass, J. H., and W. A. Elders, Salton Sea Scientific Drilling Project: Scientific program, *Trans. Geotherm. Res. Counc., 10*, 473-478, 1986.

Skinner, B. J., D. E. White, H. J. Rose, Jr.,and R. E. Mays, Sulfides associated with the Salton Sea geothermal brine, *Econ. Geol., 62*, 316-330, 1967.

Turner, F. J., *Metamorphic Petrology*, 403 pp., McGraw-Hill, New York, 1968.

Walshe, J. L., A six-component chlorite solid solution model and the conditions of chlorite formation in hydrothermal and geothermal systems, *Econ. Geol., 81*, 681-703, 1986.

Walther, J. V., and H. C. Helgeson, Description and interpretation of metasomatic phase relations at high pressures and temperatures, 1, Equilibrium activities of ionic species in nonideal mixtures of CO_2 and H_2O, *Am. J. Sci., 280*, 575-606, 1980.

White, D. E., The Salton Sea geothermal brine, an ore-transporting fluid (abstract), *Min. Eng., 15*, 60, 1963.

Zen, E.-A., Prehnite- and pumpellyite-bearing mineral assemblages, west side of the Appalachian metamorphic belt, Pennsylvania to Newfoundland, *J. Petrol., 15*, 197-242, 1974.

R. W. Charles and D. R. Janecky, Los Alamos National Laboratory, INC-7, MS-J514, Los Alamos, NM 87545.

Fraser Goff, Los Alamos National Laboratory, ESS-1, MS-D462, Los Alamos, NM 87545.

M. A. McKibben, Tunell Economic Geology Laboratory, Department of Earth Sciences and Geothermal Resources Program, Institute of Geophysics and Planetary Physics, University of California, Riverside, CA 92521.

Received September 21, 1987;
revised April 6, 1988;
accepted May 18, 1988.)

JOURNAL OF GEOPHYSICAL RESEARCH, VOL. 93, NO. B11, PAGES 13,159-13,164, NOVEMBER 10, 1988

FLUID INCLUSIONS IN SALTON SEA SCIENTIFIC DRILLING PROJECT CORE: PRELIMINARY RESULTS

Edwin Roedder[1] and Kevin W. Howard[2]

U.S. Geological Survey, Reston, Virginia

Abstract. Fluid inclusions (191) in calcite, quartz, K-feldspar, and epidote from ≈1-mm veinlets in cores and well cuttings from 604-2560 m homogenize from 217° to >500°C and vary widely in salinity, suggesting a complex history of fluids surrounding these samples. No daughter minerals were seen, and no clathrates were recognized on freezing. Vapor-rich inclusions under pressure, presumably containing CO_2 and/or CH_4, were found from a wide range of depths, suggesting that effervescence has occurred. Low-salinity fluids (1.2 -4.0 wt % NaCl eq) were present as deep as 1939 m. The data can be explained by a combination of processes such as thermal metamorphism of evaporites and other sediments and mixing of water from metamorphic dehydration reactions with partly evaporated Colorado River water.

Introduction

Although there have been extensive studies of the geochemistry of geothermal fluids and of the mineralogy of the cores from geothermal bores, relatively few studies have been made of fluid inclusions from such environments [e.g., Roedder, 1984, pp.494-501]. This is unfortunate because the fluid inclusions represent samples of the fluids that were present when the host minerals grew, and hence they can provide valuable evidence on the changes in the hydrothermal system with time. If the inclusion hosts are relatively recent in origin, primary or secondary inclusions in them can provide true measures of field temperature during the drilling, thus avoiding the difficult problem of establishment of equilibrium temperature in the drill hole after the thermal shock of drilling [Sass et al., this issue]. If the inclusion hosts formed in the past, the inclusions provide a record to compare with present-day temperatures and compositions.

The Salton Sea Scientific Drilling Program (SSSDP) well, State 2-14, in the Salton Sea geothermal area, California, penetrated to a depth of 3.22 km, where temperatures of 355° ± 10°C were measured; the borehole produced alkali chloride brines containing more than 25 wt % of total dissolved solids [Elders and Sass, this issue]. In this preliminary study we examined fluid inclusions in small subcores from 16 depths. Fifteen samples were from the chlorite-calcite metamorphic zone, and one sample was from the biotite metamorphic zone in the well [Cho et al., 1987]. The data obtained help to constrain the possible physical and chemical processes that have occurred in these metamorphic zones.

Samples and Procedures

Most of the samples studied were subcores, drilled out of the main cores recovered, that were approximately 2 cm in diameter and ≤ 4 cm long; in addition, some well cuttings were used. Each subcore was selected on the basis of the presence of a crosscutting veinlet, and inclusion studies were on minerals in such veinlets. The veinlets are seldom >1 mm in thickness. The samples are from 16 depths between 604 m (1983 ft) and 2560 m (8399 ft). One or more doubly polished plates 0.1-0.3 mm thick were cut from each core, perpendicular to the veinlet.

After petrographic examination, microthermometric determinations were made on selected inclusions. The small amount of material in the thin veins, and the small size of most inclusions, unfortunately limited the study to a relatively few selected inclusions (191) that were large enough for the measurements to be made (≥ 10 μm diameter). The selected inclusions were mainly in calcite, but some were studied in quartz, potassium feldspar, and epidote. Some inclusions could be reasonably assigned a primary or pseudosecondary origin [Roedder, 1984], and some were obviously secondary, but approximately one quarter could not be assigned a specific origin with any confidence. Most fluid inclusions found were two-phase aqueous liquid plus vapor; no daughter minerals or liquid CO_2 phases were seen. These inclusions were mainly liquid-rich, containing ≈ 20% vapor, but a few two-phase vapor-dominant inclusions, and a few monophase vapor inclusions were found in many samples, throughout most of the depth range.

The temperatures of homogenization (Th), of melting of last ice (Tm), and of eutectic melting (Te) [Roedder, 1984] were all determined on each selected inclusion that permitted such determinations, using a U.S. Geological Survey gas-flow heating/freezing stage [Werre et al., 1979]. (Th, sometimes with a correction for pressure, provides the temperature of growth or fracture healing of the host mineral; Tm provides a measure of the salinity of the fluid; and Te provides qualitative information on the possible major solute species.) Calibrations were made at the melting points of Zn (419.58°C), $K_2Cr_2O_7$ (398°C), Sn (231.97°C), and CO_2 (-56.6°C). Some

---

[1]Now at Department of Earth and Planetary Sciences, Harvard University, Cambridge, Massachusetts.

[2]Now at Energetics, Incorporated, Columbia, Maryland.

Paper number 7B7110.
0148-0227/88/007B-7110$05.00

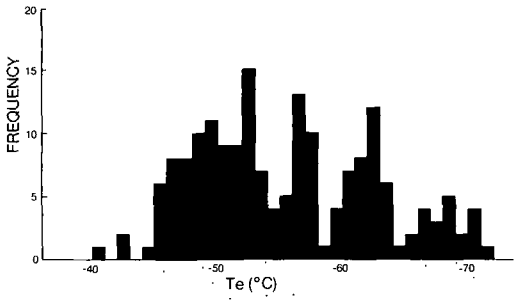

Fig. 1. Histogram of the temperature of eutectic melting, Te, for individual runs on 56 inclusions in Salton Sea drill core samples. The average is ≈ -55°C.

inclusions were tested for noncondensable gases on a crushing stage [Roedder, 1970]. As many of the inclusions are less than optimum, the microthermometric data are less precise than normally obtained but are believed to fall within the following uncertainties in terms of reproducibility: Th ± 5°C, Tm ± 0.5°C, Te ± 5°C. Data from the inclusions that leaked during measurement were discarded.

Results

Te, temperature of eutectic melting. Te values ranged from -40° to -72°C and averaged ≈ -55°C (Figure 1). For a variety of reasons, Te values are, at best, only approximations. In addition to the observational uncertainty of ±5°C, these data are almost certainly biased toward values that are too high (i.e., too warm), perhaps by a number of degrees Celsius above the true eutectic point [Roedder and Howard, 1988]. Even so, the values obtained are so low that major amounts of ions other than $Na^+ + Cl^-$ (± K^+) must be present. Only a few geologically reasonable ions can result in eutectic melting of -50°C or lower [Roedder, 1984, p. 249]. The most likely is Ca^{++}, which, along with Na^+ and Cl^-, shows Te at -52°C. Addition of Li^+ and Fe^{++} or Fe^{+++} chlorides will yield an even lower eutectic, but no data are available on the six-component system $NaCl$-$CaCl_2$-$LiCl$-$FeCl_2$-$FeCl_3$-H_2O. Analyses of fluids from the borehole show 1385 ppm Mn [McKibben, et al., 1988a] and as much as 1580 ppm Fe [Grigsby, et al., 1987]. McKibben et al. [1988a] have shown that the state of oxidation of the brines has changed with time, so both Fe^{++} and Fe^{+++} are possible. If the Fe is ferric, it is equivalent to ≈ 5000 ppm $FeCl_3$, which may well be adequate by itself, without the other trace constituents, to produce recognizable eutectic melting at the temperatures found.

Tm, temperature of last melting of ice. The values for Tm ice (Figure 2) ranged from -0.7 to -29.4°C. The former corresponds to a salinity of 1.2 wt % NaCl eq. The later is near the estimated metastable eutectic halite-ice (≈ -28°C), and as hydrohalite is very sluggish to form, it is relatively easy to obtain the metastable assemblage [Roedder, 1984], but we believe that the temperature agreement is probably fortuitous, in view of the abundant Te evidence for the presence of solutes other than NaCl. As seen in Figure 2, the Tm values cover the entire salinity range with only a few small gaps that may merely represent insufficient sampling. We found no discernible difference between Tm ice for the liquid phase in vapor-rich inclusions and adjacent liquid-rich inclusions.

Th, temperature of homogenization. Th ranges from a minimum of 208° to >500°C (the upper limit of the stage), but most samples fall in the range 240°-340°C (Figure 2). In terms of a Th versus Tm plot (Figure 2) the data cluster erratically; at this preliminary stage we do not know how much of this clustering is simply a result of inadequate sampling. The Th of four vapor-rich inclusions, homogenizing in the vapor phase, ranges from 427° to >500°C (Figure 3).

Crushing stage. Samples of calcite from 604, 920, 1294, 1701, and 2560 m (1983, 3017, 4245, 5582, and 8399 ft) were tested for noncondensable gases on the crushing stage. All inclusions (mostly secondary but some primary) tested contained noncondensable gases which expanded on crushing to completely fill the inclusions. Liquid-dominant inclusions contained roughly 20% vapor by volume and, on crushing, filled with vapor, indicating a vapor pressure of ≈ 5 atm [Roedder, 1970]. In some inclusions (604 and 2560 m) the evolved gases dissolved almost instantly and completely in the mounting oil, as would be expected for hydrocarbon gases such as CH_4; in others, even at the same sample depths, the gases dissolved much more slowly and might be CO_2.

Discussion and Interpretation

It would be premature to speculate greatly on the significance of these preliminary data. The available data also are too limited in both number of samples and suitable inclusions to reliably correlate any of the measured parameters with inclusion origin or host mineral. However, a few comments are appropriate.

Vapor-rich inclusions. The coexistence of vapor-rich or monophase vapor inclusions and liquid-rich ones in most samples from 604 to 2226 m (1983 to 7302 ft) suggests that at the time these inclusions were trapped, two fluid phases were present. This could mean effervescence of a gas phase, such as CO_2 or CH_4, or simple boiling of a single component (i.e., a steam phase). Boiling is not likely, as Th for the liquid-rich inclusions is generally below that necessary for boiling, even under hydrostatic conditions [Haas, 1971] (Figure 3), and the liquid in the vapor-rich inclusions has salinities similar to those of nearby liquid-rich inclusions. Because these inclusions contain gases under pressure >> 1 atm at room temperature, the term effervescence is more appropriate than "boiling," and Muffler and White [1968] report modern CO_2 mudpots near the State 2-14 well. As the crushing-stage tests showed that the gas in these vapor-rich inclusions varied widely in its solubility in oil, we suggest that some are CH_4-rich, some CO_2-rich, and some contain a mixture of both gases. If the gas were all CO_2, the data of Sasada et al. [1986] suggest that the minimum concentration would be ≈ 0.15 mol %, but the crushing data show that at least some inclusion gases are very low in CO_2. Data on Th, pCO_2, composition of the brines, and vein mineralogy might permit calculation of pH, but unfortunately, these various data cannot be correlated with each other at present.

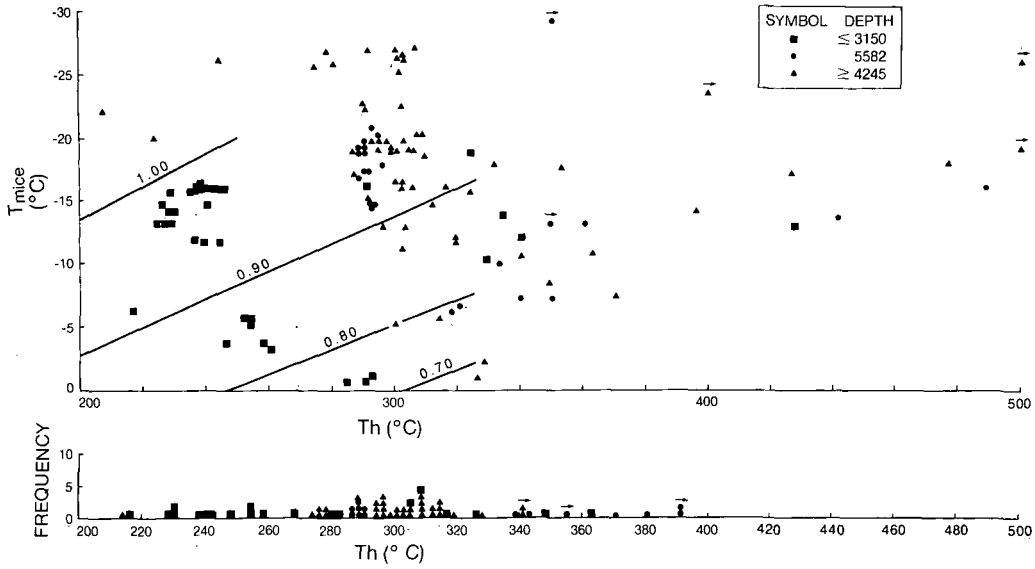

Fig. 2. Plot of temperature of homogenization (Th) versus temperature of last melting of ice (Tm ice) for the 123 inclusions on which both values could be obtained. At bottom is a histogram of Th for 68 additional inclusions on which only Th could be determined. The three symbols used categorize the data in three depth ranges: "3150" = ≤ 960 m; "5582" = 1701 m ; "4245" = ≥ 1291 m. Lines of equal density for vapor-saturated fluids in the system NaCl-H_2O [Haas, 1976] are also shown. Arrows indicate minimum Th values due to decrepitation or poor optics.

The variation in the composition of the gases in the inclusions might be expected in view of the changes in the state of oxidation of the fluids with time as evidenced by the ore-vein mineralogy [McKibben and Elders, 1985; McKibben et al., 1988a].

It is likely that the few liquid-rich inclusions with very high Th values represent the trapping of a small amount of a vapor phase along with the liquid phase, just as the few vapor-rich inclusions, which also have high Th values, have probably trapped some liquid along with vapor. As a consequence of the probability of such heterogeneous trapping, the high Th values in both groups are considered invalid. There is no way of determining which high values in Figure 2 are invalid, but many of the extremely high values can probably be assigned to this status and discarded from further geothermometric consideration. However, such inclusions may still be useful for constraining fluid composition and pressure at the time of trapping.

Th vs depth. In Figure 3 we plot the available Th and Tm data against sample depth, along with other data. From this diagram, and the data above, the following points should be noted:

1. The bulk of the Th values, both for primary and secondary inclusions, are rather close to the present well temperature. This can be variously interpreted: either the inclusions were trapped rather recently, or the rock temperatures have not changed much, or both. Another possibility is that the bulk of the inclusions, formed in some earlier environment, have reequilibrated under the present well conditions. It has long been known that some inclusions will reequilibrate or stretch (i.e., increase their internal volume) by generally invisible deformation of the walls if the internal pressure exceeds the external pressure sufficiently [e.g., Roedder, 1984, pp. 70 and 257]. Soft minerals such as calcite may be expected to stretch more readily than hard minerals, and Prezbindowski [1987] has shown experimentally that natural calcite cements do stretch easily. However, the small deviations of the major clusters of our data from present well temperature and the apparent concordance of data from relatively strong minerals such as quartz, K-feldspar, and epidote with those from weak calcite seem to preclude any extensive reequilibration in the Salton Sea samples. It is unfortunate that most of the optically good fluid inclusions in these samples are in calcite.

2. Th values at 604 m (1983 ft) exceed the well temperature by ≈ 70°C, suggesting that temperatures have dropped in this region since these inclusions were trapped. Circulation of cooler surface water is the most plausible explanation, and McKibben et al. [1988a] have shown that an interface between different salinity fluids has moved vertically in the State 2-14 area.

3. Five inclusions, three primary and two secondary, show Th far below well temperature. These discrepant data are not readily explicable. In other geological environments, such low values might be ascribed to necking down [Roedder, 1984, p. 19], but in this environment the rock is still at high temperature, so necking down would have occurred under essentially isothermal conditions, at the temperature of trapping, and hence should have no effect on Th. Similarly, these inclusions should have developed high internal pressures at ambient well temperatures and decrepitated, or at least reequilibrated. They may represent artifacts from some unusual conditions during drilling or sampling.

4. Unlike the inclusion data from many

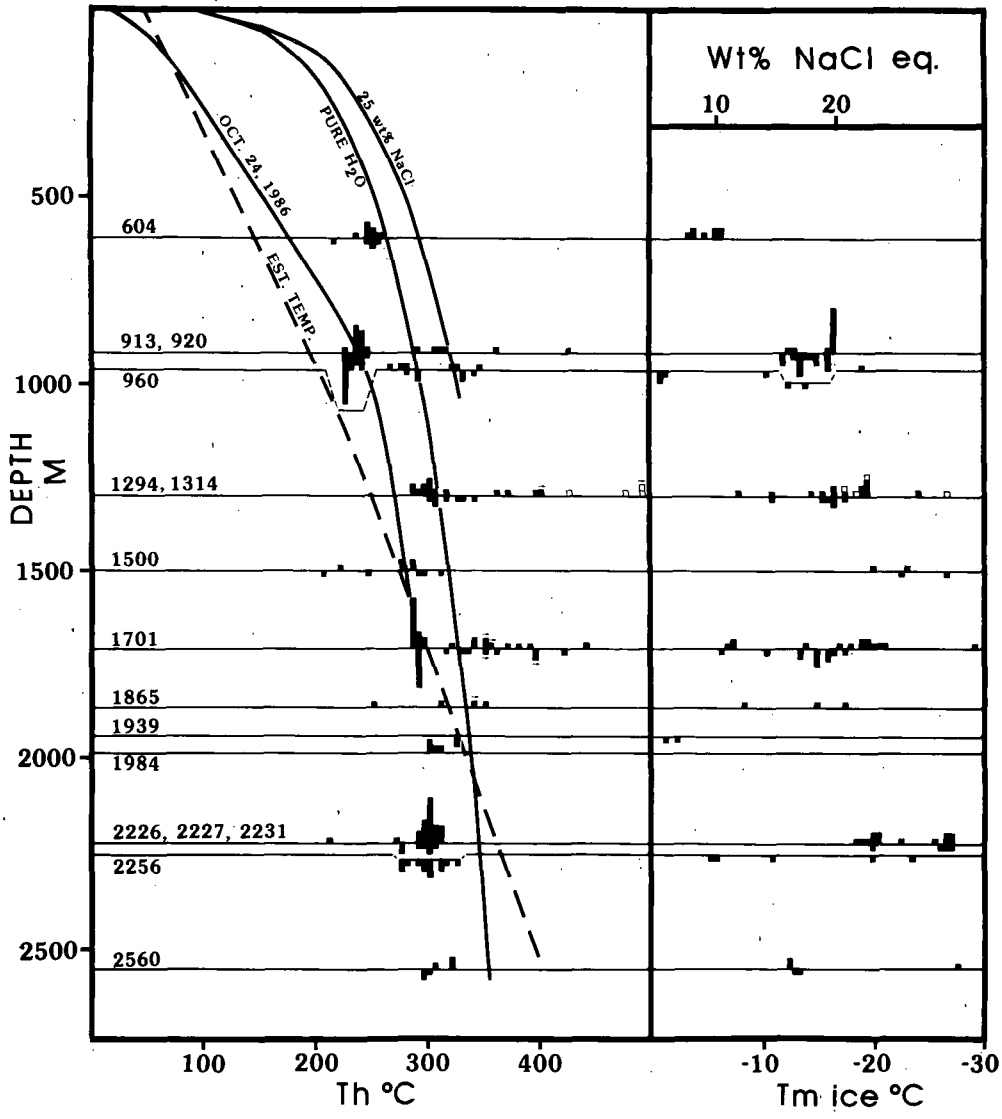

Fig. 3. Plot of Th and of Tm (and equivalent NaCl) of inclusions versus sample depth. The estimated temperature profile was drawn before the start of drilling [U.S. Department of Energy, 1986]; the "October 24, 1986" curve refers to the downhole measurements made at that date, after almost complete thermal recovery from the drilling operation [Sass et al., this issue]. The boiling curves for pure H_2O and 25 wt % NaCl are from Haas [1971]. Inclusions presumed to be primary are plotted above the sample depth line; secondary inclusions are plotted below. Some closely associated sample depths have been composited for clarity. The four open squares represent inclusions homogenizing in the vapor phase. Arrows indicate minimum values due to decrepitation or poor optics.

metallic ore deposits, including those from fossil geothermal areas [Roedder, 1984, p. 496], in these samples, the secondary inclusions show ranges of Th values that are very similar to those of the primary inclusions from the same depth. This similarity is expectable in an active geothermal system that has been nearly isothermal since the original vein filling.

5. To obtain the temperature of trapping from Th, a correction must be added if the ambient pressure was greater than the vapor pressure of the fluid. The maximum correction for pressure, for the sample from 2560 m (8399 ft), assuming lithostatic load and 25 wt % NaCl, would be +55°C [Potter, 1977]. However, at least some inclusions seemed to have formed from effervescing solutions, conditions which would require no pressure correction, and shut-in pressure measurements in the well show hydrostatic, not lithostatic pressures [McKibben et al., 1988b].

Tm vs depth and Th. 1. Although highly saline fluids (i.e., Tm of -20°C or lower) are present in most deep samples ≥ 1294 m (4245 ft), perhaps in part from the dissolution and metamorphism of evaporites [McKibben et al., 1988b], none were found in the shallower samples 604-960 m (1983-3150 ft). Presumably, the shallower samples have had greater opportunity for dilution by surface waters, or never were highly saline. Williams [1987] has reported that brines with low total dissolved solids (i.e., <10

wt %) now overlie hypersaline brines in several parts of the geothermal field.

2. Although these highly saline fluids occur in most samples from ≥ 1294 m, most of the primary fluid inclusions at these depths are significantly less saline (i.e., Tm of -10° to -20°C). The wide range of salinity at any given depth on Figure 3 contrasts with the results that Andes and KcKibben [1987] found for ore-bearing veins and is almost certainly an indication of a real variation in salinity with time at that given depth and not an artifact of measurement.

3. The fluids sometimes varied significantly in salinity even during the growth of a given crystal within a 1-mm vein but changed little, if at all, in temperature. Such variations require significant differences in the origin or history of the fluids passing this point in the vein, but the processes yielding the variation cannot be specified at present.

4. Clustering of data points on a Tm-Th plot (Figure 2) could be simply a result of inadequate sampling but also could suggest that there have been incursions of fluids with specific temperature-salinity characteristics, as have been reported in numerous geothermal areas.

5. The low-salinity fluids (i.e., Tm above -10°C, corresponding to ≤ 14 wt % NaCl eq) are particularly significant. Those found at 604 m (1983 ft) might simply represent a deep incursion of relatively fresh surface water. However, the very low salinity inclusions, with Tm ice in the range 0.7-2.4 (i.e., salinities of 1.2-4.0 wt % NaCl eq (Figure 3)) from as deep as 1938 m (6360 ft), require a special explanation. Although secondary, all five of these inclusions have Th in the range 285°-328°C. Perhaps the simplest explanation would involve fresh water from the dehydration of gypsum [McKibben, et al., 1988b], but gypsum would have decomposed long before the rock reached these temperatures. Perhaps other metamorphic dehydration reactions are involved, however, and mixing of such water might also be involved in the origin of the inclusion fluids of intermediate salinity.

6. These hot, low-salinity fluids would be less dense than adjacent high-salinity fluids at similar temperatures. The densities of mixed-solute fluids at elevated temperatures are unknown, but those for the pure system NaCl-H_2O can be used for a first approximation. From the data of Haas [1976] for NaCl-H_2O (Figure 2), 300°C vapor-saturated fluids, with salinities of 2.84 and 25 wt % NaCl, have a density contrast of 0.233 g/cm^3 (densities of 0.744 and 0.977 g/cm^3, respectively). Such density contrasts should result in rapid convection, but the evidence that they must have coexisted suggests that permeabilities, both through the beds and through the fractures, were probably low. An unlikely alternative would involve a gravitationally stable density gradient that changed with time as earlier fluids were replaced with new ones. Oakes and Williams [1987] reported similar variations in fluid densities in other Salton Sea wells.

Conclusions

The inclusion data reported here show that calcite, quartz, K-feldspar, and epidote from veinlets in the State 2-14 core grew from saline fluids of a composition and temperature generally similar to those encountered now in the well, even though the trapping occurred at some unknown earlier time. The common occurrence of variable vapor/liquid ratios and the presence of noncondensable gases in vapor-rich inclusions suggest that effervescence (CO_2 and/or CH_4?) occurred over a range of depths. The variation in salinity and temperature of homogenization, however, suggest that a variety of processes have been involved in the history of any given inclusion fluid. The possible processes, which have already been proposed by other SSSDP workers on the basis of other lines of evidence (e.g., other papers in this special section), include local igneous intrusions, fracturing of deep overpressured zones, and mixing of water from metamorphic dehydration reactions with partly evaporated Colorado River water, modified chemically by a series of mineralogical changes resulting from thermal metamorphism of the original evaporites and other sediments to a metamorphic chlorite-calcite-greenschist facies rock.

Acknowledgements. We are most indebted to W.A. Elders for his perseverance in organizing the SSSDP project and to M.A. McKibben for sample selection. We are also indebted to M.S. Guffanti and H.E. Belkin (USGS), W.A. Elders and M.A. McKibben (University of California, Riverside), F.M. Haynes (Exxon), and J.R. Kyle (University of Texas at Austin) for helpful reviews.

References

Andes, J.P., Jr., and M.A. McKibben, Thermal and chemical history of mineralized fractures in cores from the Salton Sea Scientific Drilling project (abstract), Eos Trans. AGU, 68, 439, 1987.

Cho, M., J.G. Liou, and D.K. Bird, Prograde phase relations in the California State 2-14 well meta-sandstones, Salton Sea geothermal field (abstract), Eos Trans. AGU, 68, 445, 1987.

Elders, W.A., and J.H. Sass, The Salton Sea Scientific Drilling Project, J. Geophys. Res., this issue.

Grigsby, C.O., F. Goff, L. Shevenell, J. Archuleta, J. Cruz, P.E. Trujillo, D. Counce, and G.K. Bayhurst, Downhole fluid sampling and analytical data for SSSDP well, Salton Sea, California (abstract), Eos Trans. AGU, 68, 454, 1987.

Haas, J.L., Jr., The effect of salinity on the maximum thermal gradient of a hydrothermal system at hydrostatic pressure, Econ.Geol., 66, 940-946, 1971.

Haas, J.L., Jr., Thermodynamic properties of the coexisting phases and thermochemical properties of the NaCl component in boiling NaCl solutions, U.S. Geol. Surv. Bull. 1421B, 71 pp., 1976.

McKibben, M.A., and W.A. Elders, Fe-Zn-Cu-Pb mineralization in the Salton Sea geothermal system, Imperial Valley, California, Econ.Geol., 80, 539-559, 1985.

McKibben, M.A., J.P. Andes, Jr., and A.E. Williams, Active ore-formation at a brine interface in metamorphosed deltaic-lacustrine sediments: The Salton Sea geothermal system, California. Econ.Geol., in press, 1988a.

McKibben, M.A., A.E. Williams, and S. Okubo, Metamorphosed Plio-Pleistocene evaporites and the origins of hypersaline brines in the Salton Sea geothermal system, California: Fluid inclusion evidence, Geochim. Cosmochim. Acta 52, 1047-1056, 1988b.

Muffler, L.J.P., and D.E. White, Origin of CO_2 in the Salton Sea geothermal system, southeastern California, USA, Proc. Int. Geol.Congress, 23rd, 185-194, 1968.

Oakes, C.S., and A.E. Williams, Fluid inclusion, stable isotope, and chemical evidence for fluid mixing in the Salton Sea geothermal field, California, paper presented at Conference on Amer. Current Research on Fluid Inclusions, Program and Abstracts, Socorro, N. M., Jan. 5-7, 1987.

Potter, R.W., II, Pressure corrections for fluid-inclusion homogenization temperatures based on the volume properties of the system NaCl-H_2O, J. Res. U.S. Geol. Surv., 5, 603-607, 1977.

Prezbindowski, D.R., Experimental stretching of fluid inclusions in calcite--Implications for diagenesis studies, Geology, 15, 333-336, 1987.

Roedder, E., Application of an improved crushing microscope stage to studies of the gases in fluid inclusions, Schweiz. Mineral. Petrogr. Mitt., 50(1), 41-58, 1970.

Roedder, E., Fluid Inclusions, Rev. Mineral. vol. 12, 644 pp., Mineralogical Society of America, Washington, D.C., 1984

Roedder, E., and K.W. Howard, Taolin Zn-Pb-fluorite deposit, People's Republic of China: An example of some problems in fluid inclusion research on mineral deposits, J. Geol. Soc. London, 145, 163-174, 1988.

Sasada, M., E. Roedder, and H.E. Belkin, Fluid inclusions from drill hole DW-5, Hohi geothermal area Japan: Evidence of boiling and procedure for estimating CO_2 content, J. Volcanol. Geotherm. Res., 30, 231-251, 1986.

Sass, J.H., S.S. Priest, L.E. Duda, C.C. Carson, J.D. Hendricks, and L.C. Robison, Thermal regime of the State 2-14 well, Salton Sea Scientific Drilling Project, J. Geophys.Res., this issue.

U.S. Department of Energy, Salton Sea Scientific Drilling Program 5th quarterly progress report (Oct.-Dec. 1985), FY 1986, Washington, D.C., March 1986.

Werre, R.W. Jr., R.J. Bodnar, P.M. Bethke, and P.B. Barton, Jr., A novel gas-flow fluid inclusion heating/freezing stage (abstract), Geol. Soc. Am. Abstr. Programs, 11, 539, 1979.

Williams, A.E., Chemical and isotopic variations and the distribution of brines across the Salton Sea geothermal field, California (abstract), Eos Trans. AGU, 68, 438-439, 1987.

K.W. Howard, Energetics, Inc., 9210 Route 108, Columbia, MD 21045.

E. Roedder, Department of Earth and Planetary Sciences, Harvard University, Cambridge, MA 02138

(Received August 5, 1987;
accepted February 17, 1988.)

JOURNAL OF GEOPHYSICAL RESEARCH, VOL. 93, NO. B11, PAGES 13,165–13,173, NOVEMBER 10, 1988

Chemistry and Geothermometry of Brine Produced From the Salton Sea Scientific Drill Hole, Imperial Valley, California

J. M. THOMPSON AND R. O. FOURNIER

U.S. Geological Survey, Menlo Park, California

The December 29–30, 1985, flow test of the State 2-14 well, also known as the Salton Sea Scientific drill hole, produced fluid from a depth of 1865–1877 m at a reservoir temperature of 305° ± 5°C. Another flow test at a depth of 3170 m produced brine contaminated by drilling fluid and diesel oil. Therefore we focus on the first flow test. Samples were collected at five different flashing pressures. The brines are Na-Ca-K-Cl-type waters with very high metal and low SO_4 and HCO_3 contents. Compositions of the flashed brines were normalized relative to the 25°C densities of the solutions, and an ionic charge balance was achieved by adjusting the Na concentration. The composition of the preflashed reservoir fluid was calculated using enthalpy-chloride relations applied to the normalized and charge-balanced brines. The calculated total dissolved solids in the preflashed reservoir fluid ranges from about 24.8 wt %, assuming insignificant thermal losses from the erupting fluid before sampling, to 26.0 wt %, assuming a 10% enthalpy loss by conduction of thermal energy through casing and surface piping. The preferred total dissolved solids of the reservoir fluid is 25.05 wt %. The calculated specific density of the preflashed reservoir fluid at 305°C and 1870 m depth ranges from 0.9980 (no thermal loss prior to sampling) to 1.0107 ± 0.0023 g cm^{-3} (10% thermal loss). Of the various cation geothermometers that are now in common use, the Na-K-Ca method gives a temperature (310°C) closest to the measured temperature (305°C) in the production horizon. Calculated Na/K geothermometer temperatures, using equations suggested by different investigators, range from 326° to 364°C. The Mg/K^2 method gives a temperature of about 350°C, Mg/Li^2 about 282°, and Na/Li 395°–418°C.

INTRODUCTION

To date, two flow tests have been conducted to characterize the reservoir conditions and fluids encountered by the State 2-14 well, the Salton Sea Scientific drill hole (SSSDH). This hole was drilled with funds administered by the Department of Energy on land controlled by the Kennecott Copper Corporation. The first flow test was conducted on December 29–30, 1985, when the total depth was 1898 m and the estimated formation temperature at the bottom of the hole was 305° ± 5°C [*Sass et al.*, 1987]. Brine was produced from the first permeable zone (about 1865-1877 m) that was encountered after setting casing to a depth of 1829 m. Little drilling fluid had been lost to the portion of the formation that was flow tested, and the produced liquid was clear with no visual trace of drilling mud 2 hours after the start of the flow test. The second flow test, March 20–21, 1986, was conducted under much less favorable conditions when the hole had a depth of 3170 m and a liner was suspended to a depth of 3089 m. Brine, contaminated by drilling fluid and diesel oil, was produced during this flow test, and the test had to be terminated before the contamination was flushed from the system. Therefore we focus on the first flow test. The results presented here differ from those previously presented [*Thompson and Fournier*, 1987] because of an inadvertent comingling of data in milligrams per liter and milligrams per kilogram.

PHYSICAL CONDITIONS AT THE TIME OF SAMPLING

The apparatus used for collecting liquid and gas samples at different flashing pressures during flow testing of the SSSDH has been described by Michels [*1986a*] and is shown schematically in Figure 1. The sampling spool, shown in Figure 1, was located several tens of meters downstream from the wellhead. A mixture of brine and steam flowed from the wellhead through the sampling spool where it passed through a series of pressure-reducing orifice plates into sections of pipe equipped with traps and sampling ports (SP3–SP6) designed to sample brine or steam (Figure 1). Brine samples were collected at successively lower pressures and temperatures (greater fractions of flashed steam) from all the regularly available sampling ports (SP3, SP4, SP5, and SP6). In addition, the Kennecott Copper Corporation kindly allowed us to sample brine from a sampling port (SP2) that they had installed near the wellhead. We used a small, portable cyclone separator to ensure complete separation of brine and steam while sampling at port 2.

Approximate locations of pressure gauges (P1–P8) and thermal wells for in-line temperature measurements (T1–T8) are shown in Figure 1. The temperatures and pressures at which samples were collected are given in Table 1 and shown in Figure 2. For reference, boiling-point curves for pure water and aqueous solutions containing 25 and 30 wt % NaCl also are shown. Note that the temperature-pressure conditions measured near SP3–SP6 are within the expected range for boiling brines containing 25–30 wt % dissolved salt and small partial pressures of noncondensible gas, mainly CO_2 (calculated maximum about 1.2 bars at SP3 and 0.2 bars at SP6), in the steam fractions. In contrast, the temperature-pressure condition at SP2, measured during the December 29, 1985, flow test, plots slightly to the high-pressure side of the boiling-point curve of pure water. This result cannot be ascribed to instrumental error because different pressure and temperature measuring instruments installed upstream (wellhead and P1, T1) and downstream (P8, T8) from SP2 also gave the same readings, about 235°C and 32.5 Bars (S. S. Priest, written communication, 1987).

The pressure readings at the various ports give the sums of the partial pressures of steam plus all other gases (predominantly CO_2) at those measurement points. Therefore the pressure measured at a given temperature is expected to be some-

Paper number 7B7117.

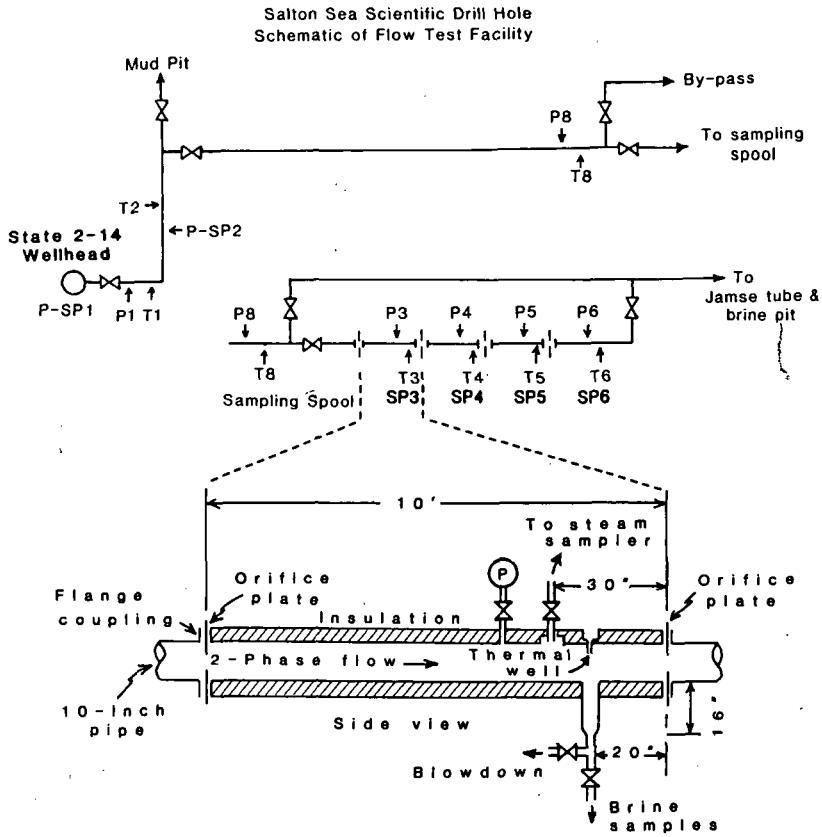

Fig. 1. Schematic diagram of surface piping, pressure and temperature measurement points (P1–P8 and T1–T8, respectively), fluid and gas sampling spool, and sampling ports (SP2–SP6) used during the December 29–30, 1985, and March 21, 1986, flow tests of the State 2-14 scientific drill hole.

what higher than the vapor pressure of water for the particular salinity of the solution. However, this effect is not large enough to explain the observed pressures between the wellhead and the sampling spool. For an initial concentration of 0.1664 wt % CO_2 dissolved in the reservoir fluid prior to flashing [*Michels*, 1986*b*] and taking account of CO_2 salting-out effects owing to the high salinity [*Ellis and Golding*, 1963], the calculated initial partial pressure of CO_2 at 305°C prior to flashing is 37.1 bars. During movement of the fluid up the well, the mass fraction of steam increased, the volume of the gas phase expanded, and the CO_2/H_2O ratio in the steam decreased markedly. After flashing to the temperature measured at P2, the calculated partial pressure of CO_2 is only 1.9 bars. Subtracting 1.9 bars from the measured pressure yields a corrected steam pressure of 30.6 bars, which is equal to the vapor pressure of pure water at 235°C [*Keenan et al.*, 1969]. In contrast, the expected vapor pressure of a 25 wt % brine at 235°C is less than 23 bars (Figure 2). One of us [*Fournier*, 1987*a*] concluded that nonequilibrium three-phase flow (brine plus dilute water plus steam) occurred within the piping up to the point of entry into the sampling spool. Others have come to the same conclusion (GeothermEx, written communication, 1986). Evidently, small thermal losses during flow of the fluid up the well and along the surface piping resulted in condensation of a small amount of steam. The resulting very dilute condensate water tended to float on top of the brine, rather than mix with it, because of the significantly different specific densities of the two liquids (about 0.82 g cm^{-3} for the condensate and >1.00 g cm^{-3} for the brine). Therefore the liquid sample collected from port 2 could have been a mixture of brine and a small amount of dilute liquid water. The dilute liquid water fraction appears to have disappeared (probably by flashing) when the fluid passed through the orifice plate at the inlet to the port 3 sampling chamber. In contrast to the above, during the March 21, 1986, flow test when the well was discharged at a greater flow rate than during the December 29–30, 1985, flow test, the measured pressure and temperature near port 2 were appropriate for brine-steam equilibrium (shown by the triangle in Figure 2) with no indication of a dilute liquid water phase.

Sampling and Analytical Procedures

Five samples of brine were collected at each sampling port: (1) a raw, unfiltered sample (500 mL), (2) a diluted (1:5), raw, unfiltered sample (500 mL), (3) a raw unfiltered, acidified sample (250 mL), (4) a diluted (1:4), raw, unfiltered, acidified sample (250 mL), and (5) a diluted (1:3), raw, unfiltered sample for the determination of silica. The brine samples that were acidified were collected directly into bottles containing acid, without filtration of the sample prior to acidification. This was done to prevent loss of calcium that might have precipitated as a carbonate during the lengthy collection process and to minimize precipitation of iron that occurred as a result of oxidation. To prevent separation of steam from brine after a sample emerged from the sampling port, each sample was passed through a stainless steel tube immersed in an ice bath so that it was chilled to less than 80°C before emerging at atmospheric pressure. Determinations for alkalinity, specific gravity, and total dissolved solids (TDS) were made immedi-

TABLE 1. Analytical Results for Brines Collected During the December 29, 1985, Flow Test of the State 2-14 Well

	Port 2	Port 3	Port 4	Port 5	Port 6
Hour	~1930	1600–1610	1626–1633	1805–1815	1640–1650
Temperature, °C	235	221	189	164	154
Pressure, bars	32.5	19	9.5	5	3.5
Density (weight)	1.222	1.236	1.245	1.252	1.261
Density (hydrometer)	1.225	1.241	1.246	1.252	1.263
pH	5.47	5.44	5.06	3.08	3.89
SiO_2*	322	340	428	251	236
Fe*	1,430	1,640	1,630	1,890	. . .
Mn*	1,730	1,830	2,050	2,150	. . .
Ca*	36,100	38,600	40,900	42,500	43,200
Mg*	42.6	46.5	49.5	52.6	51.9
Sr*	495	545	580	586	590
Ba*	234	271	187	219	184
Na*	57,100	62,300	60,300	62,700	69,500
K*	18,800	20,000	20,300	21,800	22,600
Li*	241	250	270	286	281
Rb*	132	139	156	155	161
Cs*	42	43	49	46	47
Zn*	547	610	625	614	634
Cu*	6.0	8.2	8.6	8.7	9.4
HCO_3*	217	187	78	0	0
SO_4*	0	0	0	0	0
Cl*	170,800	186,200	185,100	190,000	196,800
F*	17	15	19	12	15
B*	530	411	420	437	528
Sum, wt %	28.84	31.32	31.30	32.36	33.44
TDS (measured), wt %	29.23	30.27	34.00(?)	32.22	33.33
Sum anions, equivalents	4.75	5.15	5.18	5.40	5.76
Sum cations, equivalents	4.81	5.25	5.22	5.36	5.55
Cl/Na†	2.99	2.99	3.07	3.03	2.83
Cl/K†	9.09	9.31	9.12	8.72	8.71
Cl/Ca†	4.73	4.82	4.53	4.47	4.56
Cl/Mg†	4,010	4,000	3,740	3,610	3,790
Cl/Li†	708	744	685	664	700
Ca/Na†	0.63	0.62	0.68	0.68	0.62
Ca/K†	1.92	1.92	2.01	1.95	1.91
Ca/Mg†	847	830	826	808	832
Ca/Li†	149	154	151	148	153

*In milligrams per kilogram.
†By weight.

ately upon return to Menlo Park, California. The TDS were determined by evaporation of a known volume and weight of brine at 180°C, using the method described by *Fishman and Friedman* [1985]; chloride was determined by the mercurimetric method [*Fishman and Friedman*, 1985]. Copper and lead were determined by atomic absorption spectrometry in an air-acetylene flame at 325 and 217 nm, respectively. Specific gravity (density) was determined by two methods, by weighing of a known volume of liquid and by hydrometer. For the weight method we modified the procedure reported by *Fishman and Friedman* [1985]: 25 mL of distilled water were transferred into a preweighed evaporating dish and weighed to calibrate the pipet volume; then, using the same pipet, 25 mL of each brine were transferred into a separate preweighed evaporating dish and weighed. The specific gravity was calculated from weight of brine/weight of distilled water, assuming equal volumes. ERTCO ASTM Specific Gravity, plain form hydrometers were used, having subdivisions of 0.0005 g cm^{-3} and a range of 0.050 g cm^{-3}. All other constituents were determined using the methods reported by *Thompson* [1985].

Analytical Results and Balancing of Charges

The results of the chemical analyses are shown in Table 1. The differences between the sums of the cation and anion charges shown in Table 1 are not large, considering the many potential sources of error that are present in the collection and analysis of dissolved constituents in brines containing over 25 wt % TDS. The brines are Na-Ca-K-Cl-type waters with extremely high metal contents (Fe, Mn, Zn, Pb) and very low SO_4 and HCO_3. During the flow test some dissolved silica precipitated in the flow line as a consequence of flashing of steam and cooling, but no indication of salt precipitation was found upstream or within the sampling apparatus after the flow test. The variations in the ratios of dissolved constituents shown in Table 1 appear to be mainly the result of analytical uncertainty and not precipitation of salts before or after sampling, as there are no systematic changes going from the most dilute to the most concentrated samples (port 2 to port 6).

The first step in calculating the composition of the preflashed reservoir fluid was to derive an internally consistent

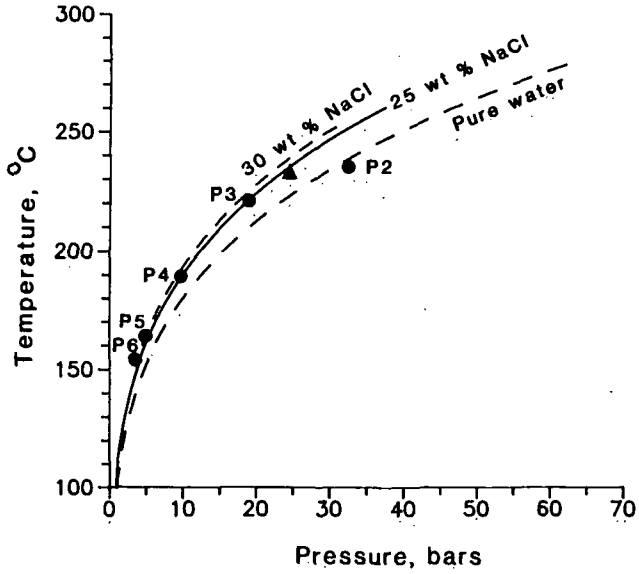

Fig. 2. Temperature-pressure diagram showing conditions at the sampling ports (numbered circles) during the December 29, 1985, flow test. The triangle is for port 2 during the March 21, 1986, flow test. Also shown are the boiling-point curves for pure water and for 25 and 30 wt % NaCl solutions.

data set of brine compositions obtained from the various sampling ports that were also consistent with the densities of these brines cooled to 25°C. The analytically determined values for dissolved Ca and K systematically increase with increasing density of the solution, but those for Na and Cl do not (Table 1). Also, ratios of calcium to other dissolved constituents were found to be generally more consistent than ratios involving other elements, and cation ratios involving sodium were found to be the least consistent of those calculated. Therefore the analytical results for K, Mg, Li, and Cl were normalized relative to Ca, and then the concentration of Na required to balance the ionic charges was calculated. The next step was to calculate the densities of the normalized and charge-balanced compositions for comparison with the measured densities at 25°C.

The densities of the brines at 25°C were calculated using a model that is applicable for brines that are composed predominantly of NaCl, KCl, and $CaCl_2$ [*Potter and Haas*, 1978]. In that model the measured density of the brine, d_b, is related to the composition of the brine as follows:

$$d_b = d_N + (d_K - d_N)f_K + (d_C - d_N)f_C \quad (1)$$

where d_N, d_K, and d_C are the densities of pure solutions of NaCl, KCl, and $CaCl_2$, respectively, at the molality of the total chloride in solution, and f_K and f_C are the mole fractions of chloride present in the brine as KCl and $CaCl_2$, respectively. Densities of the pure chloride solutions of the three salts were taken from *Potter and Brown* [1976, 1977] and *Potter and Clynne* [1976]. Density data for KCl at 25°C extend only to about 5 m solutions, so densities of more concentrated solutions in the range 5.0-5.8 m were obtained by extrapolation, using a plot of chloride molality versus the difference in density between KCl and NaCl for solutions of the same molality with respect to chloride. Above 4 m chloride that plot is close to a straight line, and a straight-line extrapolation was used (Figure 3). Departure of the KCl curve in Figure 3 from a straight line in the 5–6 molal chloride range should affect the final calculated density of the Salton Sea brine by less than 0.0002 g cm^{-3}. The calculated densities of the normalized and charge-balanced brines at 25°C from the sampling ports SP2–SP6 are 1.221, 1.237, 1.252, 1.262, and 1.266, respectively. The agreement with measured densities (Table 1) is generally good. The exclusion of iron and other dissolved constituents from the density model is not likely to have made a significant difference, even though they constitute about 2 wt % of the brine, because extra sodium compensated in great part for their not being included in the computations. This compensation was accomplished by using sodium to bring the cation charges into balance with the anion charge.

Finally, complete agreement between the measured and calculated densities was obtained by making minor adjustments to the calcium concentrations and renormalizing other ions relative to calcium until a charge-balanced solution was obtained with a calculated density that agreed with measured densities. The final preferred brine compositions are shown in Table 2. The results are only slightly different from the analytical values shown in Table 1.

Calculated Composition of Reservoir Fluid Prior to Flashing

The preflashed composition of a fluid can be determined graphically using enthalpy-dissolved constituent diagrams [*Fournier*, 1979*a*]. The method requires knowledge of the initial fluid enthalpy in the reservoir (obtained from the reservoir temperature and approximate initial TDS of the fluid), the enthalpies of the boiling liquids at the point of collection, and the brine composition after flashing at a given pressure. Initial reservoir fluid compositions can be estimated with or without assumed thermal losses by conduction prior to sampling. In contrast, *Michels* [1986*a*, *b*] used a method based on chloride and CO_2 in coexisting brine and steam at different confining pressures to determine steam quality and the preflashed composition of the reservoir fluid without assuming an initial reservoir temperature. It will be seen subsequently that our cal-

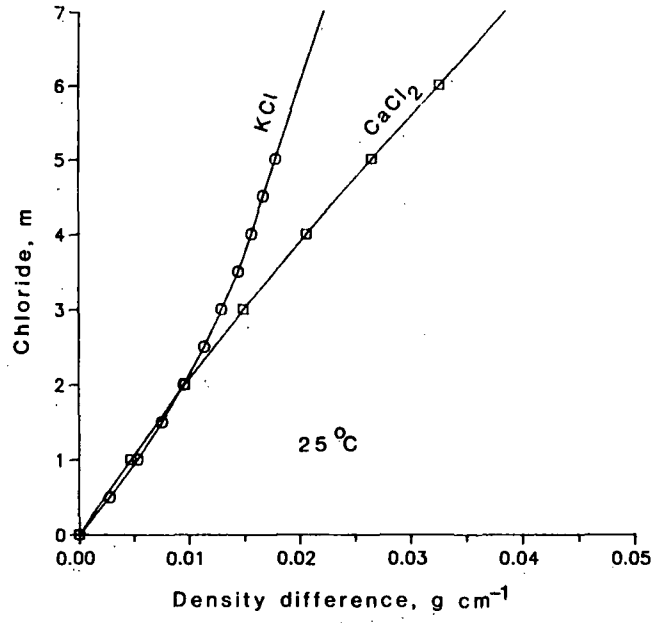

Fig. 3. Molal chloride versus the density difference between $CaCl_2$ and NaCl at 25°C, with data points shown by squares, and between KCl and NaCl, with data points shown by circles.

TABLE 2. Smoothed and Charge-Balanced Compositions of Brines Collected During the December 29, 1985, Flow Test of the State 2-14 Well

	Port 2	Port 3	Port 4	Port 5	Port 6
Calculated density, g cm^{-3}	1.221	1.237	1.252	1.262	1.266
Ca, mg/kg	36,100	38,200	39,800	41,000	42,400
Mg, mg/kg	44.6	47.3	49.2	50.7	52.4
Na, mg/kg	54,400	57,600	60,000	61,700	63,900
K, mg/kg	18,900	20,000	20,800	21,400	22,200
Li, mg/kg	241	255	265	273	283
Cl, mg/kg	165,000	174,500	181,800	187,000	193,600
Total wt %*	27.5	29.0	30.2	31.1	32.2

*Total dissolved solids may be as much as about 0.5 wt % greater owing to other dissolved constituents.

culated results and those of *Michels* [1986*a*, *b*] are in good agreement.

The fractures supplying fluid during the December 29–30, 1985, flow test were close to the bottom of the well where the formation temperature is estimated to be 305 ± 5°C [*Sass et al.*, 1987]. According to *Michels* [1986*a*] the enthalpy, HB, of a brine (in Btu/lb of brine) at its boiling point is given by

$$\mathrm{HB} = 0.36(F)^{1.16}[\exp_{10}(-0.006Nn) \quad (2)$$

where F is temperature in Fahrenheit, N is the wt % NaCl in a simple brine, and n is the multiplier that relates a mixed brine of N wt % TDS and a simple brine with the same N value. For the simple system NaCl-water in which $n = 1$, equation (1) becomes

$$H = 0.837(1.8t + 32)^{1.16} \times 10^{-0.006N} \quad (3)$$

where H is enthalpy in joules per gram and t is temperature in degrees Celsius. Using (3), the calculated enthalpies of 20–30 wt % NaCl solutions at 150°–225°C range from about 9 to 0% higher than corresponding enthalpies of a synthetic Salton Sea brine published by *Helgeson* [1968].

Figure 4 is an enthalpy-chloride diagram constructed using enthalpies derived from equation (3) and chloride values (shown as circles) from Table 2. Data points representing brines collected from the various sampling ports are labeled P2–P6. The range in enthalpies of the steam phases coexisting with the brines sampled at the various sampling ports is shown by points S2 and S6 in Figure 4. These estimated enthalpies of steam coexisting with the brine range from about 70 to 80 J/g higher than those of steam in equilibrium with pure water at the same temperature. The chloride of the initial unflashed reservoir fluid should lie along the line connecting a particular flashed liquid with its coexisting steam, such as line P6–S6 in Figure 4. However, because the Salton Sea brine contains significant amounts of salts other than NaCl, the value of n in (2) is not unity, and (3) gives calculated enthalpies of Salton Sea brines that are slightly in error, with the largest errors at higher salinities (most flashed brines). If corrections had been made for the differences in enthalpy of the actual brines compared to NaCl solutions with the same TDS, the positions of the brines and steam-brine tie lines, such as P6–S6 in Figure 4, would be very slightly rotated using the enthalpy of the coexisting steam as a focal point. The difference in enthalpy of steam in equilibrium with the actual brine compared to a NaCl solution with the same TDS is likely to be small. The net result of calculating enthalpies of Salton Sea brines using a NaCl-H_2O model is that the calculated enthalpy of the initial reservoir fluid is likely to be slightly in error, but the calculated chloride value for the preflashed reservoir fluid is likely to be about the same.

The calculated enthalpy of a 305°C solution that contains NaCl in the expected range, about 24.4–26.0 wt % (14.8–15.8 wt % chloride) varies from about 962 to 943 J/g. For the P6–S6 tie line in Figure 4 the initial reservoir fluid plots at 955 J/g and 14.96 wt % Cl (point R6) when insignificant thermal losses prior to sampling are assumed. Except for P2, other flashed chloride-steam pairs give initial reservoir chloride concentrations ranging from about 14.7 to 15.0 wt % and average 14.89. Point P2 yields a calculated reservoir chloride of 14.52 wt %. That value appears to be anomalously low, probably because of incorporation of dilute water during sampling (nonequilibrium three-phase flow, as previously discussed). The calculated composition of the initial preflashed reservoir fluid with 14.89 wt % Cl is given in Table 3, sample A.

At the time of sampling, temperatures and pressures measured at the surface had attained a steady state, and the above calculations were made with the assumption that thermal losses during flow up the well and through the surface piping prior to entering the sampling spool were not significant. However, if the interpretation is correct that condensation of steam during flow up the well and through the surface piping resulted in nonequilibrium three-phase flow involving a small amount of dilute condensate water that did not readily mix

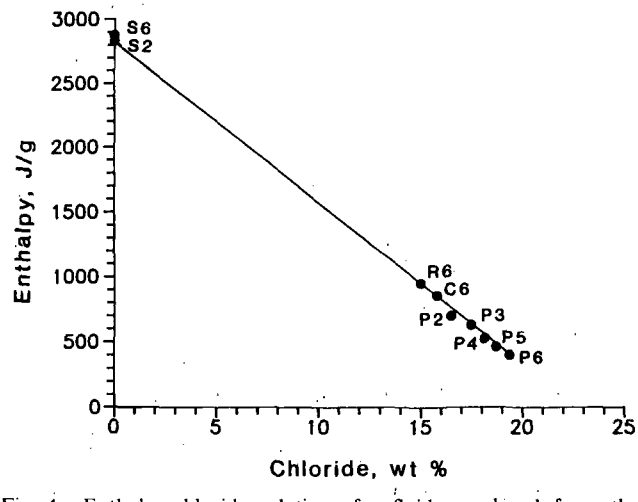

Fig. 4. Enthalpy-chloride relations for fluids produced from the State 2-14 well. Additional explanation in text.

TABLE 3. Calculated Preflash Concentrations of Selected Elements in Brine From a Depth of 1829–1898 m in the State 2-14 Well, December 1985 Flow Test

	Sample				
	A Dec. 29	B Dec. 29	C Dec. 29	D Dec. 29	E Dec. 30
SiO_2,* mg/kg	808	776	803	793	795
Ca, mg/kg	31,600	33,200	31,900	27,100	26,500
Mg, mg/kg	39.1	41.0	39.4	37	36
Na, mg/kg	50,600	53,100	50,900	52,800	52,700
K, mg/kg	16,500	17,300	16,700	16,700	16,500
Li, mg/kg	211	221	212	193	190
Cl, mg/kg	148,900	156,100	150,000	153,400	153,700
Total dissolved solids, wt %	24.86†	26.25†	25.05†	25.54	25.46

A, this study, assumed no thermal losses; B, this study, assumed 10% thermal losses; C, this study, reservoir fluid with density = 1 g cm^{-3}; D, reported by *Michels* [1986*b*]; E, reported by *Michels* [1986*b*].

*Calculated by the method of *Fournier* [1983].

†TDS may be as much as about 0.5 wt % greater owing to other dissolved constituents.

with the much denser brine, effects of thermal losses must be considered. The effect of a conductive loss of enthalpy on the relations shown in an enthalpy-chloride diagram (e.g., Figure 4) is to move the calculated preflashed reservoir chloride to a lower concentration. We have calculated the effect of a 10% decrease in enthalpy (95.5 J/g) within the erupting fluid by conduction of heat through the casing and surface piping, although it is unlikely that this large a thermal loss occurred during the interval when sampling occurred. For the P6-S6 tie line in Figure 4 the initial chloride in the reservoir fluid plots at C6 for an assumed 10% enthalpy loss by conduction. For all the brines sampled, with 10% assumed thermal loss by conduction, the calculated chloride concentrations in the preflashed reservoir fluid range from about 15.5 to 15.7 wt %, and average 15.61 wt %. The calculated composition of this average initial preflashed reservoir fluid with 15.61 wt % Cl is given in Table 3, sample B.

The uncertainty in TDS for the compositions shown for samples A and B in Table 3 is about ±1 wt %. In addition, the TDS could be as much as 0.5 wt % greater than the totals shown because of the presence of other dissolved constituents that are not listed, such as iron, manganese, and zinc. However, as previously discussed, adding in these ionic species requires a corresponding decrease in sodium. According to our analyses and calculations the actual composition of the preflashed reservoir fluid should be between those given by samples A and B, and probably closer to A. The agreement with the reservoir fluid composition calculated by Michels [1986*b*] is very good.

Density of Brine in the Reservoir at 305°C

The density of the brine in the reservoir prior to flashing is of considerable interest in regard to developing models of heat and mass transfer within the hydrothermal system. During drilling, the mud weight required to just balance the pore fluid pressure at a depth of 1879 m indicated a pore fluid density very close to 1 g cm^{-3} (J. H. Sass, personal communication, 1986). No downhole pressure measurements were made at that depth, and downhole fluid sampling was unsuccessful, so the only available check on the pore fluid density is by calculation, using the preflashed composition of the brine sampled at the surface. This calculation was carried out using the density model of *Potter and Haas* [1978], densities of the pure chloride solutions of the three salts from *Potter and Brown* [1976, 1977] and *Potter and Clynne* [1976], and the brine compositions shown in Table 3. In that calculation, however, corrections had to be made for conditions slightly beyond the range of the available density data for the pure salts. Densities of aqueous solutions of KCl at temperatures in the 200°–400°C range extend only to about 4 m, so densities of more concentrated solutions in the range 4.0–5.8 m were obtained by extrapolation, using a plot of chloride molality versus the difference in density of KCl and NaCl for solutions of the same molality with respect to chloride, as was described previously for the calculation carried out at 25°C. At 300°C that plot and a similar plot for $CaCl_2$, instead of KCl, yield straight lines (Figure 5). Also, density data for both KCl and $CaCl_2$ are available only at the vapor pressures of the solutions, and density data for $CaCl_2$ are not available above 300°C. Therefore densities of the preflashed reservoir fluid were calculated at 300°C and the vapor pressure of the solution, and those results were then multiplied by factors to correct for the slightly increased temperature and pressure actually present in the reservoir. The correction factors were obtained by assuming that the changes in density caused by increased temperature and pressure were proportional to the changes in density caused by similar increases in temperature and pressure in the pure NaCl system. The temperature correction factor that was used required multiplication of the density calculated at 300°C and the vapor pressure of the solution by 0.995, and the pressure correction factor required multiplication by 1.019. These corrections for temperature and pressure act in opposite directions, and the combined correction factor requires multiplication by 1.014. The exclusion of iron and other dissolved constituents from the density model is not likely to have made a significant difference for reasons previously discussed.

Calculated densities of preflashed reservoir fluids produced from the SSSDH at a depth of 1865–1877 m and a temperature of 305°C are shown in Table 4. The reservoir fluids published by *Michels* [1986*b*] yield densities very close to 1 g cm^{-3}. Our average reservoir fluid, calculated with the assumption that there was insignificant thermal loss prior to

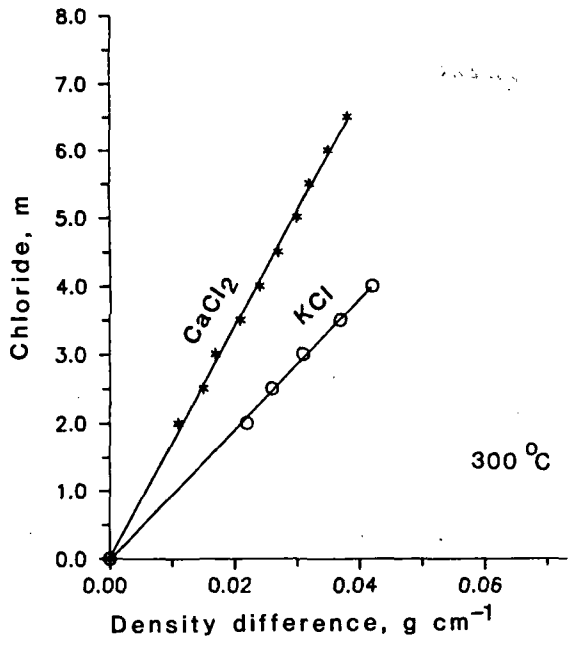

Fig. 5. Molal chloride versus the density difference between $CaCl_2$ and NaCl at 300°C, with data points shown by stars, and between KCl and NaCl, with data points shown by circles.

sampling, yields a density of 0.9980 ± 0.0023 g cm^{-3}, and the average reservoir fluid calculated with the assumption of 10% thermal loss yields a density of 1.0107 ± 0.0023 g cm^{-3}. The errors associated with not taking account of small amounts of other constituents in the brines, such as iron and manganese, and assuming a model based on pure NaCl to correct for pressures greater than the vapor pressure of the solution and a temperature of 305°C instead of 300°C, will cause the calculated density to be slightly on the low side. Therefore the chemical data favor reservoir fluid densities of about 1 g cm^{-3} or greater at a depth of 1870 m.

If isochemical conditions prevailed above about 2 km and the brine at a depth of 1.8 km had a density of 1 g cm^{-3}, the brine at the top of the system at a depth of 1 km and a temperature of 275°C would have a specific density of about 1.02–1.03 g cm^{-3}. That high a fluid density in the shallow part of the system would not be consistent with free convection driven by the influx of cold dilute water at the sides of the system. However, a fluid density of 1 g cm^{-3} at a depth of 1.8 km is consistent with a double-diffusive model that provides a mechanism for efficiently transferring heat by convection from the bottom to the top of the hydrothermal system while maintaining vertical and horizontal salinity gradients [*Fournier*, 1987*b*, 1988]. In the double-diffusive model of the Salton Sea geothermal system a series of thin convection cells are present that contain hot brines at slightly different temperatures and salinities but having similar densities that are close to unity [*Fournier*, 1987*b*, 1988]. These convection cells are in approximate pressure equilibrium with cold water at the sides of the hydrothermal system. Our calculated composition of the reservoir fluid having a density of 1 g cm^{-3} at 305°C at a depth of 1.8 km is given in Table 3, sample C.

The fluid mechanical behavior resulting in double-diffusive convection was first studied experimentally by *Stommel* [1962] and described by *Turner and Stommel* [1964]. *Huppert and Turner* [1981] provided an excellent summary of double-diffusive convective processes within bodies of liquid, and experiments by *Griffiths* [1981] have shown that double-diffusive convection cells may develop in porous media when hot saline waters underlie more dilute cooler waters. The important parameters that lead to the establishment of a double-diffusive convection system are the contrasting rates of transport of heat and salt across a boundary layer separating cooler less saline water above from hotter more saline water below. Both heat and salt are transported through the interface solely by molecular diffusion. Thermal input from below into the deeper more saline water causes it to become less dense than the overlying less saline water and convection is initiated. Upward movement of the more saline water continues until a slight cooling increases its density to the point when buoyancy is no longer a driving force. When the thermal boundary layer ahead of the convecting region reaches a critical Rayleigh number, it too becomes unstable, and a second layer forms above the first. Eventually, many individual salinity layers form and convection is sustained by a more rapid vertical

TABLE 4. Calculation of Specific Density of Preflashed Brine at 305°C at a Depth of 1865–1877 m in the State 2-14 Well

	Sample			
	A Dec. 29	B Dec. 29	C Dec. 29	D Dec. 30
d_K-d_N	0.0590	0.0629	0.0603	0.0602
d_C-d_N	0.0328	0.0350	0.0335	0.0335
f_K	0.101	0.101	0.0987	0.0973
f_C	0.376	0.376	0.3125	0.3050
d_N	0.9660	0.9774	0.9698	0.9696
$(d_K$-$d_N)f_K$	0.0060	0.0064	0.0060	0.0059
$(d_C$-$d_N)f_C$	0.0123	0.0132	0.1047	0.1022
Sum	0.9843	0.9970	0.9862	0.9857
PT correction	× 1.0139	× 1.0139	× 1.0139	× 1.0139
Density at 305°C	0.9980	1.0108	0.9999	0.9994

The notation is the same as in the text. A, this study, assumed no thermal losses; B, this study, assumed 10% thermal losses; C, reported by *Michels* [1986*b*]; D, reported by *Michels* [1986*b*].

TABLE 5. Calculated Temperatures of Last Water-Rock Equilibrium, Using Various Cation Geothermometers

Geothermometer	Reference	Dec. 29*	Dec. 29†	Dec. 30†
Na/K	*Arnórsson et al.* [1983]	331°C	327°C	326°C
Na/K	*Fournier* [1979*b*]	345	341	339
Na/K	*Giggenbach* [1986]	349	345	345
Na/K	*Truesdell* [1976]	364	358	355
Na-K-Ca	*Fournier and Truesdell* [1973]	310	311	310
Na/Li	*Fouillac and Michard* [1981]	418	396	395
Mg/Li^2	*Kharaka and Mariner* [1988]	285	281	281
Mg/K^2	*Giggenbach* [1986]	348	351	350

*This study.
†Reported by *Michels* [1986*b*].

transport of heat relative to salt. For the situation in which there are horizontal as well as vertical temperature and salinity gradients, individual double-diffusive convection cells should be bounded on the sides by other convection cells that have slightly different salinities and temperatures.

GEOTHERMOMETRY OF THE RESERVOIR FLUID

Temperatures of brine-rock chemical equilibration prior to flashing were calculated using a variety of cation geothermometers. The results are shown in Table 5. The temperatures calculated using our preferred reservoir fluid, sample C, Table 3, give essentially the same results as the data reported by *Michels* [1986*b*]. The Na-K-Ca method of *Fournier and Truesdell* [1973] appears to give the most reliable results, 310°–311°C compared to a measured temperature of 305° ± 5°C. Calculated Na/K temperatures range from 326° to 364°C, depending on the equation that is used [*Arnórsson et al.*, 1983; *Fournier*, 1979*b*; *Giggenbach*, 1986; *Truesdell*, 1976], the Mg/K^2 method [*Giggenbach*, 1986] gives about 350°C, and the Mg/Li^2 method [*Kharaka and Mariner*, 1988] gives 281°–285°C. The Na/Li method [*Fouillac and Michard*, 1981] gives results that are much too high, 395°–418°C. Silica geothermometry is not appropriate because of loss of significant amounts of silica from solution prior to sampling. The calculated concentration of silica in the reservoir fluid prior to flashing is 790–800 mg/kg, using the method of *Fournier* [1983], and TDS ranging from 25.2 to 25.7, and fluid density equal to 1 g/cm^3 at 305°C.

CONCLUSIONS

The preflashed reservoir fluid, according to this study, contains about 24.8 wt % TDS if calculated with the assumption that there was insignificant thermal loss before sampling and about 26.0 wt % TDS if there was 10% thermal loss. Our preferred value for the TDS of the reservoir fluid is about 25.0 wt % (sample C, Table 3). These values might be increased by up to 0.5 wt %, depending on adjustments for various trace elements, such as iron and manganese, that were not included in the charge-balancing and density models. Our calculated preflashed reservoir fluid is in good agreement with that reported by *Michels* [1988*b*]. The main difference between the two studies is that slightly less Na and more Ca were found in the present study than were reported by *Michels* [1986*b*]. Of the various cation geothermometers, the Na-K-Ca method gives temperatures closest to the apparent temperature of the reservoir supplying brine during the December 1985 flow test of the State 2-14 well. Accurately determined densities of brines composed predominantly of $NaCl$-$CaCl_2$-KCl can be used to check analytical results and resolve inconsistencies in ionic charge balances.

Acknowledgments. D. E. Michels designed the sampling apparatus and coordinated the sampling efforts of many groups before and during the flow test. His enthusiastic help is gratefully acknowledged. We also thank the Kennecott Copper Corporation for kindly allowing us to use their sampling port to obtain a fluid sample at a higher temperature and pressure than was possible at the regular sampling ports. The manuscript was critically reviewed by Yousif K. Kharaka, Donald E. White, A. F. White, and Donald E. Michels.

REFERENCES

Arnórsson, S., E. Gunnlaugsson, and H. Svavarsson, The chemistry of geothermal waters in Iceland, III, Chemical geothermometry in geothermal investigations, *Geochim. Cosmochim. Acta*, *47*, 567–577, 1983.

Ellis, A. J., and R. M. Golding, The solubility of carbon dioxide above 100°C in water and sodium chloride solutions, *Am. J. Sci.*, *261*, 47–60, 1963.

Fishman, M. J., and L. C. Friedman (Eds.), Methods for determination of inorganic substances in water and fluvial sediments, Techniques of Water Resources Investigations of the United States Geological Survey, Book 5, Chapter A1, *U.S. Geol. Surv. Open File Rep.*, *85-495*, 709 pp., 1985.

Fouillac, C., and G. Michard, Sodium/lithium ratios in water applied to geothermometry of geothermal reservoirs, *Geothermics*, *10*, 55–70, 1981.

Fournier, R. O., Geochemical and hydrologic considerations and the use of enthalpy-chloride diagrams in the prediction of underground conditions in hot-spring systems, *J. Volcanol. Geotherm. Res.*, *5*, 17–34, 1979*a*.

Fournier, R. O., A revised equation for the Na/K geothermometer, *Trans. Geotherm. Resour. Counc.*, *3*, 221–224, 1979*b*.

Fournier, R. O., A method of calculating quartz solubility in aqueous sodium chloride solutions, *Geochim. Cosmochim. Acta*, *47*, 579–586, 1983.

Fournier, R. O., Nonequilibrium three-phase flow during testing of the Salton Sea Scientific drill hole—Implications regarding interpretation of fluid inclusions in natural hydrothermal systems (abstract), *Eos Trans. AGU*, *68*, 1537, 1987*a*.

Fournier, R. O., Double-diffusive convective control of salinities within the Salton Sea hydrothermal system (abstract), *Eos Trans. AGU*, *68*, 628, 1987*b*.

Fournier, R. O., Double-diffusive convection as a mechanism for transferring heat and mass within the Salton Sea geothermal brine, *Proceedings Thirteenth Workshop on Geothermal Reservoir Engineering*, Stanford University, Stanford, Calif., in press, 1988.

Fournier, R. O., and A. H. Truesdell, An empirical Na-K-Ca geothermometer for natural waters, *Geochim. Cosmochim. Acta*, *37*, 515–525, 1973.

Giggenbach, W. F., Graphical techniques for the evaluation of water/rock equilibration conditions by use of Na, K, Mg, and Ca-contents of discharge waters, paper presented at 8th New Zealand Geothermal Workshop, Univ. of Auckland Geotherm. Inst., 1986.

Griffiths, R. W., Layered double-diffusive convection in porous media, *J. Fluid Mech., 102*, 221–248, 1981.

Helgeson, H. C., Geologic and thermodynamic characteristics of the Salton Sea geothermal system, *Am. J. Sci., 226*, 129–166, 1968.

Huppert, H. E., and J. S. Turner, Double-diffusive convection, *J. Fluid Mech., 106*, 299–329, 1981.

Keenan, J. H., F. G. Keys, P. G. Hill, and J. G. Moore, *Steam Tables*, International Edition, Metric Units, 162 pp., John Wiley, New York, 1969.

Kharaka, Y. K., and R. H. Mariner, Chemical geothermometers and their application to formation waters from sedimentary basins, in *Thermal History of Sedimentary Basins*, edited by N. D. Naeser and T. H. McCollon, pp. 99–117, Society of Economic Paleontologists and Mineralogists, Tulsa, Okla., 1988.

Michels, D. E., A chemical method for measuring steam quality in two-phase flow lines, *Trans. Geotherm. Resour. Counc., 10*, 437–442, 1986*a*.

Michels, D. E., SSSDP fluid compositions at first flow test of State 2-14, *Trans. Geotherm. Resour. Counc., 10*, 461–465, 1986*b*.

Potter, R. W., II, and D. L. Brown, The volumetric properties of vapor-saturated aqueous potassium chloride solutions from 0° to 400°C based on a regression of the available data, *U.S. Geol. Surv. Open File Rep., 76-243*, 5 pp., 1976.

Potter, R. W., II, and D. L. Brown, The volumetric properties of aqueous sodium chloride solutions from 0° to 500°C at pressures up to 2000 bars based on a regression of the available data, *U.S. Geol. Surv. Bull., 1421-C*, 36 pp., 1977.

Potter, R. W., II, and M. A. Clynne, The volumetric properties of vapor saturated aqueous calcium chloride solutions from 0° to 300°C based on a regression of the available data, *U.S. Geol. Surv. Open File Rep., 76-365*, 5 pp., 1976.

Potter, R. W., II, and J. L. Haas, Models for calculating density and vapor pressure of geothermal brines, *J. Res. U.S. Geol. Surv., 6*, 247–257, 1978.

Sass, J. H., J. D. Hendricks, S. S. Priest, and L. C. Robison, Temperatures and heat flow in the State 2-14 well, Salton Sea Scientific Drilling Program (abstract), *Eos Trans. AGU, 68*, 454, 1987.

Stommel, H., Examples of mixing and self-stimulated convection on the S, T diagram (in Russian), *Okeanologiya, 2*, 205–209, 1962.

Thompson, J. M., Chemistry of thermal and nonthermal springs in the vicinity of Lassen Volcano National Park, *J. Volcanol. Geotherm. Res., 25*, 81–104, 1985.

Thompson, J. M., and R. O. Fournier, Geothermometry and chemistry of the Salton Sea brine, California (abstract), *Eos Trans. AGU, 68*, 454, 1987.

Truesdell, A. H., Summary of section III, geochemical techniques in exploration, in *Proceedings of 2nd United Nations Symposium on Development and Use of Geothermal Resources*, vol. 1, pp. 1iii–1xxix, U.S. Government Printing Office, Washington, D. C., 1976.

Turner, J. S., and H. Stommel, A new case of convection in the presence of combined vertical salinity and temperature gradients, *Proc. Natl. Acad. Sci. U.S.A., 52*, 49–53, 1964.

R. O. Fournier and J. M. Thompson, U.S. Geological Survey, 345 Middlefield Road, MS 910, Menlo Park, CA 94025.

(Received August 10, 1988;
accepted February 16, 1988.)

JOURNAL OF GEOPHYSICAL RESEARCH, VOL. 93, NO. B11, PAGES 13,175-13,186, NOVEMBER 10, 1988

THE KINETICS OF RADIOISOTOPE EXCHANGE BETWEEN BRINE AND ROCK IN A GEOTHERMAL SYSTEM

Douglas E. Hammond, Jeffrey G. Zukin[1] and Teh-Lung Ku

Department of Geological Sciences, University of Southern California, Los Angeles

Abstract. A wide range of isotopes in the ^{238}U, ^{235}U, and ^{232}Th decay chains was measured in geothermal brines collected from two production zones at 1898 and 3220 m in the Salton Sea *Scientific Drilling Project well*. *High* concentrations of radium, radon, and lead isotopes are generated and maintained by the input of these isotopes from solid phases into brine by both recoil and leaching processes, by the high chloride content of the brine which complexes radium and lead, and by the apparent absence of suitable unoccupied adsorption sites. In contrast, uranium, thorium, actinium, bismuth, and polonium isotopes all have low concentrations due to their efficient sorption from brine to rock. Measurements of short-lived isotopes in these decay series yield insights regarding the mechanisms controlling radioisotope exchange, and they permit estimation of rates of brine-rock interaction. For example, the $^{228}Ac/^{228}Ra$ activity ratio of 0.2 in brines indicates that the mean residence time of actinium in solution before sorption onto solid surfaces is less than 2.5 hours. If molecular diffusion to fracture walls limits the rate of actinium sorption, the maximum width of the larger fractures in which sampled brine resides is 1-2 cm. However, the mean width of fractures must be only 1-2 μm, in order to account for the recoil input of ^{223}Ra. The ratios of radium isotopes in the brine provide information about the mechanisms of recoil and leaching in transferring radium from rock to brine. Brine/rock concentration ratios $[(dpm/g)_b/(dpm/g)_r]$ of radium isotopes increase with increasing half-life, so that ^{223}Ra (11 days) = 0.05-0.09, ^{228}Ra (5.8 years) = 0.26-0.40, ^{226}Ra (1600 years) = 0.45-0.97. Two mechanisms could explain this dependence on half-life: (1) input of radium by the alpha recoil process occurs in microfractures and pore spaces, but the rate of diffusion down microfractures is so slow that it diminishes the effect of recoil input of the shorter-lived isotopes to the larger fractures where the brine sampled resides, or (2) weathering and leaching of radium from solid phases occurs on time scales comparable to the half-lives of ^{228}Ra and ^{226}Ra. The second mechanism is more likely because the $^{212}Pb/^{224}Ra$ activity ratios are within 20% of the value predicted by a simple recoil model with negligible adsorption, indicating that recoil input of ^{212}Pb (10.6-hour half-life) is not limited by diffusion. This model permits the rates of chemical exchange between brine and rock to be estimated. These rates indicate the mean residence times of lead and radium in solution are about 30 years, and the residence time of radium in associated solid phases is about 2000 years. The estimated uncertainty in these residence times is about a factor of 2.

Introduction

Uranium 238, uranium 235, and thorium 232 decay to stable isotopes of Pb through a series of shorter-lived intermediate daughters (Figure 1). In a closed system these daughters grow into secular equilibrium with their parents, so that the daughter/parent activity (disintegration) ratio becomes unity. However, groundwater and geothermal waters are not closed systems but interact with the solid phases that they contact. Because of the different geochemical properties of the intermediate isotopes in each chain, significant radioactive disequilibria often exist in these waters and sometimes in solid phases associated with them. Both thermodynamic and kinetic factors play a role in creating and maintaining these disequilibria, and a number of workers have discussed these factors. Langmuir and his colleagues have provided recent reviews of the thermodynamic properties governing the behavior of uranium, thorium, and radium in natural waters [Langmuir, 1978; Langmuir and Herman, 1980; Hsi and Langmuir, 1985; Langmuir and Riese, 1985; Langmuir and Melchior, 1985]. Others have focused on physical factors, such as recoil during alpha decay [Tanner, 1964; Krishnaswami et al., 1982; Laul et al., 1985; Petit et al., 1985; Davidson and Dickson, 1986; and others], migration of nuclides along microfractures and grain boundaries [Rama and Moore, 1984], and the possible preferential emplacement of uranium-bearing phases along grain boundaries [Krishnaswami and Seidemann, 1988].

Studies of uranium and thorium series disequilibria are of value for several reasons. First, the behavior of actinides and their daughters in thermal saline waters and their associated rocks is pertinent to the management of radioactive waste, as a natural analog study of near-field conditions of radioactive waste repositories in salt [Elders and Moody, 1985]. Second, while studies of saturation states of minerals can give insights to possible mineral alterations [Langmuir and Melchior, 1985], the radioisotope disequilibria observed in fluid and solid phases are useful for estimating rates of brine-rock chemical interaction. Third, radioactive disequilibria may be useful for estimating parameters of geologic interest in hydrothermal systems, such as brine flow rates, fracture sizes, and ages of vein deposits

[1]Now at Dames and Moore, Goleta, California

Paper number 88JB03243.
0148-0227/88/88JB-03243$05.00

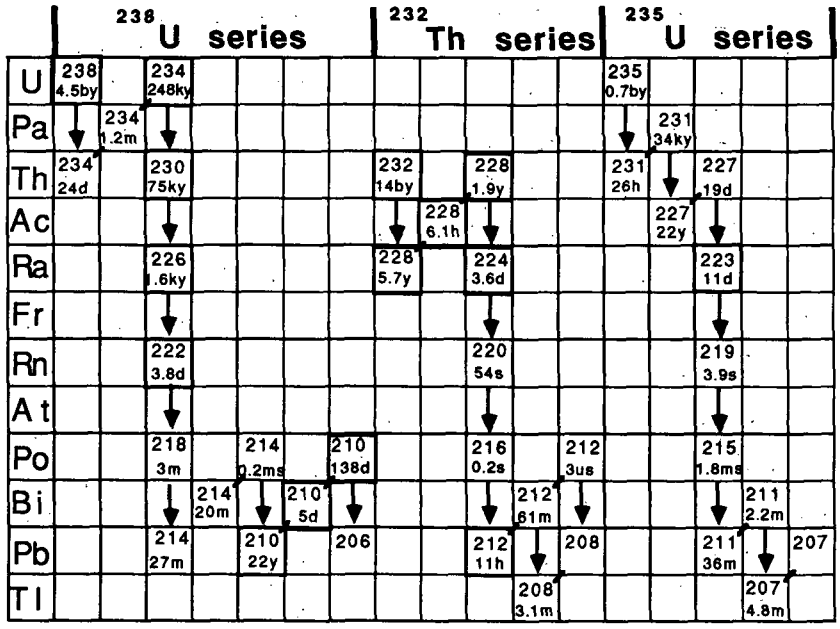

Fig. 1. The uranium and thorium decay series. Isotopes measured in this study are bordered by heavy lines. The mass number and half-life for each isotope are given. Vertical arrows indicate alpha decays, and short diagonal bars indicate beta decays.

[Zukin et al., 1987; Sturchio and Binz, 1988]. The Salton Sea Scientific Drilling Project (SSSDP) well has provided a unique opportunity to study the in situ behavior of the naturally occurring U-Th series radionuclides in deep geothermal brines.

The Salton Sea geothermal field (SSGF) (Figure 2) is one of a number of geothermal fields existing in the Salton Trough, a broad structural depression that is partially filled with Pliocene to Recent sediments. The depression is thought to be an actively growing rift margin dominated by leaky transform faulting in tensional zones or rhombochasms [Elders and Biehler, 1975]. The transform zones have been associated with the intrusion of mafic and silicic dikes and sills into the upper sedimentary section. These intrusions produce high geothermal heat flow in the region and drive an active geothermal circulation [Helgeson, 1968; Kasameyer et al., 1984; Newmark et al., 1986; and others]. Boreholes drilled in the SSGF have produced brines with a bimodal distribution of total dissolved solids (TDS). The brine chemistry is discussed elsewhere [Helgeson, 1968; Williams, 1987; Elders and Sass, this issue]. Briefly, a cooler (in situ temperature <260°C), lower-salinity (less than 10% TDS) fluid overlies a hotter, more saline brine (TDS=19-28%; T=260°-300°C). Brines sampled in this study are from the deeper fluid and are highly concentrated in Na (53,000 ppm), Cl (154,000 ppm), Ca (27,000 ppm), and K (16,500 ppm), containing approximately 25% TDS [Michels, 1986]. They are enriched in heavy metals, including Fe (1550 ppm), Mn (1400 ppm), Zn (500 ppm), Pb (95 ppm), and Ag, and contain small amounts of SO_4^{2-} (110 ppm), H_2S (7 ppm), and CO_2 (1700 ppm). The deep brine may have originated from the inflow of Colorado River water [Coplen, 1976], followed by the dissolution of lacustrine evaporite deposits [Helgeson, 1968; Elders and Cohen, 1983; McKibben et al., 1988].

Previous work concerning the behavior of actinides and their daughters in hydrothermal environments includes measurements of several isotopes made in hot springs [Mazor, 1962; Wollenberg, 1975; Cowart and Osmond, 1976], measurements of radon and uranium in geothermal production wells [Belin, 1959; D'Amore, 1975; Stoker and Kruger, 1975; Kraemer, 1981; Kraemer and Kharaka, 1986; etc.], and measurements of uranium and thorium in hydrothermally altered rocks [Wollenberg and Flexser, 1986; Sturchio et al., 1987]. Submarine hydrothermal waters emanating from the East Pacific Rise have been analyzed for uranium [Michard et al., 1983; Krishnaswami and Turekian, 1982; Chen et al., 1986], thorium [Chen et al., 1986], and lead, radium, radon, and polonium isotopes [Kim and Finkel, 1980; Chung et al., 1981; Dymond et al., 1983; Turekian and Cochran, 1986]. However, little work has been done on short-lived isotopes in brines, and few measurements have been made on both brines and their associated solid phases, primarily because of the difficulties in obtaining in situ samples. These problems have been partially overcome by Zukin [1986] and Zukin et al. [1987], who studied a wide range of isotopes at several locations in the SSGF and discussed their general in situ behavior in some detail. This article presents results of isotope measurements in the SSSDP brines, compares these results to those in other parts of the SSGF, and presents models interpreting these results in terms of fracture geometry and brine-rock interaction processes. The discussion presented will focus on short-lived isotopes, including ^{228}Ac, ^{224}Ra, ^{223}Ra, and ^{212}Pb, which turn out to

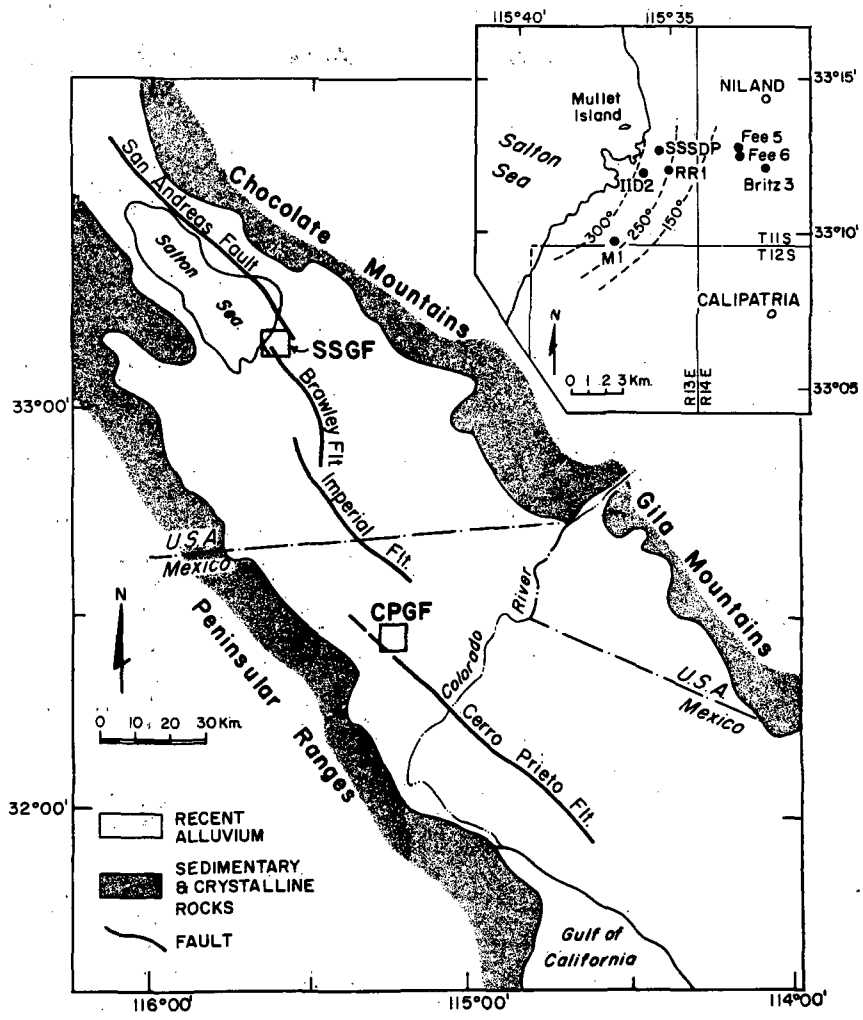

Fig. 2. Map of the Salton Trough showing the geologic setting of two geothermal fields, the SSGF and the CPGF (Cerro Prieto geothermal field). The inset shows the location of the SSSDP and other boreholes that we have studied in the SSGF. The dashed lines show isotherms at 914 m estimated by Elders and Cohen [1983].

be key isotopes for determining the mechanisms and rates of brine-rock interaction.

Methods

Details regarding the drilling and plumbing system used to produce fluid from the well are described elsewhere [Michels, 1986]. Brines were produced from two zones in the well, during separate flow tests. The first sampling occurred when the well was 1898 m deep on December 29-30, 1985, with production presumed to come from a fracture zone near the bottom. The second set of samples was collected when the well was 3220 m deep on March 20-21, 1986, with production also originating primarily near the bottom. Because the volume of brine that could be produced during each flow test was limited by the size of a pit built to receive water discharged from the well, only 4000 m^3 could be produced during each test. Measurements of major constituents and stable isotopes suggest that for the first test this brine volume was sufficient to clear the well of fluids introduced during drilling. However, the second flow test showed evidence that the fluid produced contained 5-10% of contaminant material introduced during the drilling operation [Sturtevant and Williams, 1987]. Our measurements of radioisotopes in the brine should not be noticeably influenced by such contamination, except perhaps for isotopes of U and Th that are present in relatively low concentrations. Another possible complication is that sulfate contamination from drilling fluids may have caused some barite to precipitate during the mixing of brine and drilling fluid, and this barite may have scavenged some radium from solution. While we think this effect should be small, it cannot be evaluated. Thus the radium concentrations measured during the second flow test are lower limits, but measured ratios of radium isotopes should be accurate.

A steel pipe was attached to the wellhead to transport brine and steam to a cooling tower before its discharge into the waste pit. The pipe was fitted with a series of sampling ports separated by orifice plates, providing different pressures and temperatures for sampling the two-phase flow. Sample ports were constructed so

that either brine or steam could be withdrawn from the flow line. Previous work at other SSGF sites has shown that radium and lead concentrations in the brine are not strongly influenced by the flash process [Zukin et al., 1987]. Therefore different locations in this flow line should yield equivalent samples, at least for Ra and Pb. Brine samples were collected by allowing hot brine to flow through a cooling coil immersed in an ice-water bath into a polyethylene container filled partially with dilute HCl. Samples were not filtered, so measurements of uranium and thorium may be upper limits due to possible contamination with particulates transported in the brine [Zukin et al., 1987]. Gas samples for ^{222}Rn analysis were collected by allowing steam to flow through a cooling coil where condensation occurred, and the remaining noncondensable gas fraction was passed into a glass bottle fitted with inlet and outlet tubes. Analyses for isotopes in the brine were carried out as described by Zukin et al. [1987], with some modifications. The CO_2 fraction in the gas sample was measured using gas chromatography, and the radon fraction was measured using alpha scintillation techniques. The brine radon concentration was then calculated from the measured Rn/CO_2 ratio and in situ CO_2 concentration [Michels, 1986]. Radium 223 was determined from gammas emitted by its short-lived daughters ^{219}Rn and ^{211}Pb at 401 and 405 keV from the $BaSO_4$ precipitate collected for analysis of ^{228}Ra and ^{224}Ra (about 300 mL brine used). The ^{210}Bi and ^{210}Po results are upper limits, based on an analysis for ^{210}Po made about 0.5 days after sample collection. The ^{210}Bi was calculated assuming that no ^{210}Po was present initially, while the ^{210}Po value was calculated assuming that no ^{210}Bi was present initially.

When more than one sample was taken for analysis of a constituent, the results given represent the average, weighted by the uncertainty of individual analyses. All uncertainties quoted are ± 1σ, derived from counting statistics. Data have been corrected for evaporative losses (5-15%) prior to collection, based on estimates of the flash fraction for different sample ports [Michels, 1986]. Results are reported as isotope activities (disintigration rate) in the brine in situ.

Results and Discussion

Geochemistry of U/Th-series isotopes in hydrothermal waters. Our results (Table 1 and Figure 3) for the SSSDP brines generally corroborate those reported previously for saline hydrothermal systems. The measurements obtained are similar to those of Zukin et al. [1987], and consequently, this discussion will include only a brief summary of the geochemistry of uranium and thorium series isotopes in saline, reducing hydrothermal waters. The first and second flow tests have similar concentrations for most isotopes, with the exception of uranium and radium isotopes which had lower concentrations for SSSDP-2 (Table 1). Because of the possible effects of contamination described above, we will not attempt to interpret these differences, although they may be real. The concentrations of uranium and thorium are quite low, and the $^{234}U/^{238}U$ ratio is also low in comparison to most groundwaters [Osmond et al., 1983]. The low uranium concentration suggests that uranium is in the +4 valence, and the low uranium isotope ratio indicates either that uranium exchanges rapidly between brine and rock [Wollenberg, 1975; Cowart,

TABLE 1. Uranium and Thorium Series Isotopes in the SSSDP Brine Samples

Isotope	SSSDP-1		SSSDP-2	
	dpm/kg	n	dpm/kg	n
^{238}U	0.071(4)	1	0.033(4)	2
^{234}U	0.077(5)	1	0.038(4)	2
^{230}Th	0.043(6)	1	<0.020	1
^{226}Ra	2190(80)	2	1060(50)	2
^{222}Rn	2130(150)	2	2600(1400)	3
^{210}Pb	3260(125)	2	3220(80)	2
^{210}Bi	<740	1	<1370	1
^{210}Po	<0.95	1	<2.8	2
^{232}Th	0.007(4)	1	<0.007	1
^{228}Ra	1120(60)	2	720(40)	4
^{228}Ac	250(170)	1	150(90)	1
^{228}Th	0.58(4)	1	0.41(3)	2
^{224}Ra	1010(60)	2	540(30)	4
^{212}Pb	2250(280)	1	1440(140)	1
^{223}Ra	6(31)	2	11(7)	4

Data have been corrected to preflash conditions, based on temperature and pressure at the sample port. The first flow test was carried out at 1898 m and the second at 3220 m. The analytical uncertainties in the last digits (±1σ from counting statistics) are shown in parentheses, and the numbers of samples analyzed are given as n. If more than one analysis was made, averages were weighted by the analytical uncertainties in each measurement.

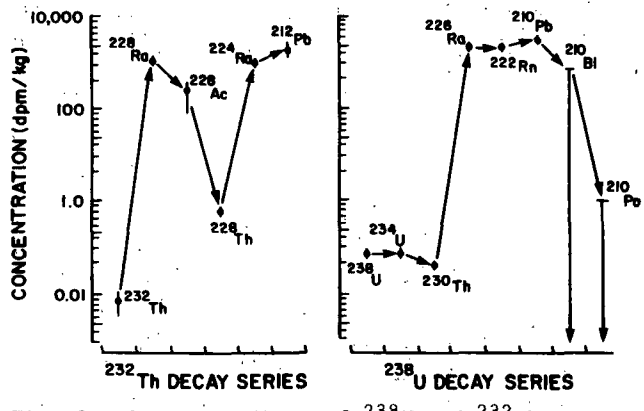

Fig. 3. Concentrations of ^{238}U and ^{232}Th decay series isotopes measured in the SSSDP well (SSSDP-1; December 1985; well depth 1898 m). Note that the vertical axis is logarithmic. Arrows indicate movement down the decay chain. The ^{210}Bi and ^{210}Po data are upper limits. Rapid exchange of isotopes between brine and rock is required to create the extreme disequilibria observed for short-lived isotopes. These results are typical for SSGF wells.

TABLE 2. Radium Concentrations (as Activities) Observed at Different Times During SSSDP Flow Tests

Sample	Date	Local Time	^{226}Ra, dpm/kg	$\frac{^{228}Ra}{^{226}Ra}$	$\frac{^{224}Ra}{^{228}Ra}$	$\frac{^{223}Ra}{^{226}Ra}$
SSSDP-1 -4	Dec. 29, 1985	1600	2040(90)	--	--	--
SSSDP-1-14	Dec. 29, 1985	1710	2450(120)	0.51(1)	0.93(3)	0.017(27)
SSSDP-1-18	Dec. 30, 1985	~1200	--	0.51(1)	--	-0.001(15)
Average			2190(80)	0.51(1)	0.93(3)	0.003(18)
SSSDP-2-26	Mar. 20, 1986	2210	--	0.64(1)	0.74(2)	0.020(27)
SSSDP-2-28	Mar. 21, 1986	0850	--	0.70(1)	0.74(2)	0.025(13)
SSSDP-2-37	Mar. 21, 1986	1120	1150(60)	0.75(2)	0.77(2)	0.002(9)
SSSDP-2-45	Mar. 21, 1986	1210	1020(50)	0.64(1)	0.77(2)	0.008(16)
Average			1060(50)	0.68(1)	0.76(2)	0.010(13)

Uncertainties in the last digits ($\pm 1\sigma$, derived from counting statistics) are given in parentheses. Averages are weighted means.

1980] or that measurements are biased by incorporation of rock fragments in samples [Zukin et al., 1987]. In the latter case, uranium concentrations would be even lower than those listed in Table 1. In contrast, radium concentrations (in activity units) are 10^3-10^4 times greater than those of their parents. These high concentrations must be maintained by input from surrounding solid phases. The persistence of radium in solution, in contrast to radium behavior in low-salinity, oxygenated groundwater, may reflect the stability of the $RaCl^+$ complex, which constitutes 70% of the dissolved radium present in 350°C SSGF brines [Langmuir and Riese, 1985]. The high radium concentrations may also reflect a displacement of Ra^{2+} from adsorption sites by either Ca^{2+} or H^+ [Tanner, 1964; Kraemer and Reid, 1984; Langmuir and Melchior, 1985]. However, brines sampled from 6 different wells in the SSGF have shown a fourfold range in ^{226}Ra while chloride and alkaline earth (Ca^{2+}, Sr^{2+}, Ba^{2+}) concentrations have varied by less than 20% [Zukin, 1986]. This suggests that occupation of adsorption sites by alkaline earths is not the primary variable controlling Ra^{2+} behavior in this system. In situ pH has not yet been rigorously calculated, but depends primarily on the CO_2 concentration. While the two brines with highest CO_2 also have the highest ^{226}Ra, the correlation for all six wells is far from perfect, indicating that a variable other than pH must also be important [Zukin, 1986]. The ^{226}Ra concentrations appear to be correlated with elements forming sulfides, Fe and Zn, but we cannot say at this time whether Fe and Zn influence Ra or whether another parameter influences all three of these elements. Herczeg et al. [1988] have found a similar correlation between Ra^{2+} and Fe^{2+}, and they suggested that the absence of manganese dioxide adsorption sites in reducing environments such as this one may be a primary variable affecting radium behavior. Radon concentrations have an activity comparable to, or slightly greater than, those of its parent ^{226}Ra, suggesting that dissolved radium greatly exceeds both adsorbed radium and that located within recoil range of solid surfaces [Laul et al. 1985; Zukin et al. 1987]. ^{210}Pb and ^{212}Pb concentrations are also high, again reflecting the importance of chloride complexing at high temperature. Some daughters of these isotopes (^{228}Ac, ^{228}Th, ^{210}Po) are much lower in concentration, reflecting the low solubilities of these elements and their rapid sorption from solution. The measurements of ^{228}Ac are of particular interest as they indicate that the majority of this isotope must be sorbed within its 9-hour mean life. In summary, in SSGF brines, radium, radon and lead are quite soluble while uranium, thorium, actinium, bismuth, and polonium have much lower solubilities.

Several samples were collected for radium analyses at different times during the flow test, and the isotope ratios observed are of interest (Table 2). The $^{224}Ra/^{228}Ra$ ratio was uniform during each flow test, although the ratio observed for the second test differed from that of the first. The lack of a change in this ratio during the 14 hours of the second test (Table 2) indicates that the values of less than one that were observed here and in the nearby Fee wells [Zukin et al., 1987] were not a transient effect due to initiation of flow but must reflect steady state in situ values. Formation water should have $^{224}Ra/^{228}Ra > 1.17$ if alpha recoil is the only mechanism for radium input [Krishnaswami et al., 1982; Davidson and Dickson, 1986]. If the system is in a dynamic equilibrium, the low ratios (<1) observed here must reflect the importance of one or more of the following effects: (1) weathering of solids, which effectively increases the activity of longer-lived isotopes (^{228}Ra) relative to short-lived isotopes (^{224}Ra), (2) growth of crystals that incorporate ^{228}Th to depths comparable to the recoil range, so that the fraction of ^{224}Ra recoiled into solution from the sorbed ^{228}Th is less than the 50% expected, or (3) recoil input that is limited by slow diffusion down microfractures. The variation in $^{228}Ra/^{226}Ra$ ratios observed during the second flow test exceeds analytical error (Table 2), but the cause of this variation is not apparent. It is possible

that flow from multiple zones with different ratios of radium isotopes occurred during the second test, and the relative contributions from these zones varied with time.

Rates of brine-rock Interaction. A general equation can be written to express the rate of change in concentration of a radioactive isotope dissolved in a volume of brine with constant density:

$$\frac{dC}{dt} = P_b + P_r + P_w + P_d - \lambda C - S_a - S_p - L \quad (1)$$

where

- C concentration in brine, atoms/g;
- t time, s;
- P_b production from decay of parent dissolved in brine, atoms/g s;
- P_r input from rock to brine by alpha recoil, atoms/g s;
- P_w input from rock to brine by weathering and leaching, atoms/g s;
- P_d desorption from rock surfaces to brine, atoms/g s;
- λ decay constant, s^{-1};
- S_a adsorption from brine to rock surfaces, atoms/g s;
- S_p sorption from brine by incorporation into precipitates, atoms/g s;
- L loss of isotope by diffusion or advection, atoms/g s.

All terms for production (P) and sorption (S) are written per unit mass of brine. This equation is simplistic in the sense that it treats all mineral phases as a single homogeneous entity. Given sufficent time, one expects the system to attain a state of dynamic equilibrium, so that dC/dt= 0. Different isotopes can be used to estimate unknown terms and give information such as brine residence time, rates of sorption of reactive elements from brines, or exchange rates between brine and solid phases. A similar formulation has been used by Krishnaswami et al. [1982] to describe behavior of short-lived isotopes in groundwater.

Zukin et al. (1987) previously used a modified form of equation (1) to estimate the residence time of brine in the geothermal fluid by constructing a material balance for ^{226}Ra. They obtained drill cuttings from Fee 5, a deep drill hole about 5 km from the SSSDP site (Figure 2), and found them to have an 8% deficiency of ^{226}Ra, so that the sum $(P_r + P_w + P_d - S_a - S_p)$ could be evaluated by estimating porosity. L was parameterized by combining effects of diffusion and advection in a box model formulation so that

$$L = (C-C_i)/T_b \quad (2)$$

where C_i is the concentration of radium in inflowing water (in atoms per gram) and T_b is the residence time of brine in the field (in seconds). By assuming C_i = 0 and measuring P_b and λC, T_b was found to be 100-1000 years, with a best estimate of 350 years. Zukin et al. [1987] calculated a similar material balance for ^{18}O that indicated the age of the geothermal field is 10,000-40,000 years with a best estimate of 16,000 years.

TABLE 3. Average Isotopic Ratios and Fracture Characteristics Estimated from $^{228}Ac/^{228}Ra$ Ratios

	SSSDP-1	SSSDP-2
$\frac{^{210}Pb}{^{226}Ra}$	1.49(9)	2.23(9)
$\frac{^{212}Pb}{^{224}Ra}$	2.23(30)	2.66(30)
$\frac{^{228}Ra}{^{226}Ra}$	0.51(1)	0.68(1)
$\frac{^{224}Ra}{^{228}Ra}$	0.93(3)	0.75(1)
$\frac{^{223}Ra}{^{226}Ra}$	0.003(12)	0.010(6)
$\frac{^{228}Ac}{^{228}Ra}$	0.22(15)	0.21(12)
T_a, hours	2.5	2.4
$2x_o$, cm	2.5	2.4

Uncertainties in the last digits ($\pm 1\sigma$, derived from counting statistics) are given in parentheses.

Because T_b is long relative to the mean time required for isotope exchange (to be calculated subsequently), Ra, Pb, and presumably several other dissolved constituents should be locally derived, as Doe et al. [1966] and White [1981] have previously argued from measurements of stable Pb and Sr isotopes.

In the present study we will apply equation (1) to derive: (1) the rate constant for adsorption of an insoluble element produced by radioactive decay of a soluble parent, and (2) the rate constants for dissolution and precipitation of phases containing radium. For case 1, we consider the adsorption of ^{228}Ac, the daughter of ^{228}Ra. For ^{228}Ac, P_w and S_p are assumed to be zero because its half-life (6.1 hours) is so short that negligible time is available for leaching or precipitation. P_r for ^{228}Ac should also be zero because the recoil energy available in beta decay is small. We assume that diffusive and advective transport of ^{228}Ac and desorption are negligible (i.e., $L=P_d=0$) and that adsorption is a first-order process so that

$$S_a = k_1 C \quad (3)$$

where k_1 is the constant for adsorption (s^{-1}).

Equation (1) can be rearranged to calculate the mean residence time of ^{228}Ac in solution before sorption, T_a, from

TABLE 4. Relative Inputs of Radium Isotopes to the Brines via the Proposed Mechanisms, Recoil, and Dissolution

	^{224}Ra	^{223}Ra	^{228}Ra	^{226}Ra
Half-life, years	0.0145	0.0451	5.75	1600
e_i	0.96	1.00	0.80	1.00
Recoil input, %	100	100	49	0.5
Leaching input, %	<1	<1	51	99.5

Calculations assume that solid phases have $^{238}U/^{235}U$ activity ratio = 21.4, ^{238}U = 2.64 dpm/g, ^{232}Th = 2.81 dpm/g, $^{226}Ra/^{238}U$ = 0.9, $^{228}Ra/^{232}Th$ = 1.0, and $^{224}Ra/^{232}Th$ = 1.0, based on analyses from a nearby well, Fee 5 [Zukin et al., 1987]. The brine data used are those of the SSSDP-1 sample; ^{226}Ra = 2.19 dpm/g, $^{223}Ra/^{226}Ra$ = 0.017, and $^{228}Ra/^{226}Ra$ = 0.51.

$$T_a = \frac{1}{k_1} = \frac{1}{\lambda}\left\{\frac{R}{1-R}\right\} \quad (4)$$

where $R = \lambda C/P_b$, the $^{228}Ac/^{228}Ra$ activity ratio in the brine. R values (Table 3) were similar for the two flow tests. The value for T_a of 2.5 hours should be an upper limit because P_d is probably greater than zero. This is larger than the upper limit of 1.2 hours estimated by Zukin et al. [1987] for ^{228}Ac in brine for the neighboring Fee 6 well. Undoubtedly, k_1 and T_a depend on brine chemistry, surface chemistry, fracture geometry, and temperature, but the results illustrate the potential for rapid interaction between the brines and solid phases. The use of this result to estimate an upper limit for fracture width will be discussed later. One other significance of this result is that isotopes with half-lives that are long compared to T_a should be nearly in equilibrium with regard to adsorption-desorption. This equilibrium can be written as

$$\bar{C} = KC \quad (5)$$

where $\bar{C}$ is the concentration of adsorbed isotope in the system, expressed per unit mass of brine, K is the dimensionless partition coefficient for the brine-rock system, and C is the concentration of isotope in brine. A material balance for adsorbed atoms requires that

$$\lambda\bar{C} = S_a - P_d \quad (6)$$

Case 2, estimation of rate constants for the chemical exchange of radium between brine and rocks, can be treated by considering the effect of recoil on the addition of radium isotopes to the brine. It is well known that alpha recoil transports isotopes from solids into the surrounding fluid, although quantitative assessment is hampered by the difficulty in estimating the surface area per unit volume of fluid that is available for recoil input. We assume that the recoil input for each Ra isotope to a brine is proportional to the activity of its decay chain progenitor (^{232}Th, ^{238}U, or ^{235}U) in the adjoining rock, so that for Ra isotope i,

$$(P_r)_i = e_i \, E \, A'_r \quad (7)$$

where e_i is the recoil efficiency of i, relative to that for ^{223}Ra, E is the efficiency of recoil for input of ^{223}Ra from solid phases into solution, and A'_r is the progenitor activity in rock (atoms/g s). Krishnaswami et al. [1982] have proposed this approach using ^{222}Rn to normalize recoil efficiency. They considered the distribution of successive decay chain daughters due to the effect of recoil in a crystal contacting water. They made the following assumptions: (1) the distribution of progenitor in the crystal is homogeneous initially, (2) fractures receiving recoiled daughters are wide relative to the recoil distance, (3) insoluble daughters may be adsorbed to surfaces so that a subsequent decay can cause the atom to be recoiled back into the crystal, (4) daughters residing in the crystal do not migrate due to processes other than alpha recoil, and (5) atoms dissolved in the water are not recoiled into the crystal. The situation in saline brines is somewhat different from that in the dilute groundwater Krishnaswani et al. [1982] considered, because of the high concentrations of radium and lead in the SSGF brines. Consequently, the relative values of recoil efficiency for each isotope are slightly different in this case. Values for e_i (in equation (7)) in the SSGF were estimated by graphical integration of the concentration profiles calculated by Krishnaswami et al. [1982, Figure A2] for successive isotopes in each decay chain, taking into account the adsorption behavior of each. Results for radium isotopes are listed in Table 4, normalized to ^{223}Ra rather than ^{222}Rn because virtually all ^{223}Ra in solution should be introduced by recoil. Most ^{222}Rn in this brine is produced by decay of dissolved ^{226}Ra, in contrast to the situation in dilute groundwater.

One test of the accuracy of this approach is to consider the $^{212}Pb/^{224}Ra$ ratio in brine. These isotopes are both short-lived and soluble; their concentrations in brine should not be influenced

much by dissolution or precipitation processes, so that P_w and S_p approach zero. The decay intermediates between these isotopes are so short-lived (Figure 1) that they should remain in solution because insufficient time is available for their sorption. Equations (1), (5), (6), and (7) can be combined, so that at steady state,

$$P_b + e_i E A'_r - \lambda (1 + K) C = 0 \quad (8)$$

For radium, P_b is negligible, and K must be very small because of the similarity in ^{222}Rn and ^{226}Ra concentrations. With these assumptions, equation (8) can be written for each isotope and used to calculate the activity ratio in solution:

$$\frac{^{212}Pb}{^{224}Ra} = \frac{1 + \frac{e_{212}}{e_{224}}}{(1 + K_{Pb})} \quad (9)$$

which should be 2.8, if K_{Pb} is also negligible. The observed $^{212}Pb/^{224}Ra$ ratios are slightly lower, 2.2-2.7 (Table 3). The closeness of these values suggests that adsorption of lead from SSGF brines is small and recoil supplies most of these isotopes to the brine. Furthermore, the recoil input of these isotopes must not be significantly slowed by diffusion along microfractures.

Addition of radium isotopes to the brine by weathering and leaching processes should depend on the abundance of atoms in solid phases, and therefore we assume that

$$P_w = k_w A_r/\lambda \quad (10)$$

where A_r is the isotope activity in rocks (atoms/kg s), k_w is the rate constant for weathering and leaching (s^{-1}), and λ is the decay constant of isotope (s^{-1}). The effectiveness of adding isotopes by weathering and leaching depends on the ratio k_w/λ. This ratio increases with increasing half-life, so that the weathering supply may exceed the recoil supply for longer-lived isotopes. This mechanism can create $^{224}Ra/^{228}Ra$ ratios less than 1 in the brine, which the recoil model cannot produce.

Uptake of radium by incorporation in authigenic minerals is assumed to occur as a first order process so that

$$S_p = k_2 C \quad (11)$$

where k_2 is the rate constant for uptake in crystalline phases (s^{-1}). For all radium isotopes, P_b approaches zero, because thorium is insoluble in these brines. If incoming brine has low radium concentrations ($C_i = 0$), equation (1) for Ra at steady state can be combined with equations (2), (7), (10) and (11) to obtain

$$e_i E A'_r + \frac{k_w A_r}{\lambda} - (k_2 + \lambda + \frac{1}{T_b})C = 0 \quad (12)$$

^{238}U and ^{232}Th concentrations have been found to be closely correlated in rocks from the nearby Fee 5 borehole (Zukin et al., 1987). Radium 226 was found to be about 8% deficient in these rocks, but other shorter-lived radium isotopes should be in secular equilibrium with their parents. Lithologies for the SSSDP site are similar to those at Fee 5, and thus we assume that the solid phase chemistry at the two sites is similar. Therefore three unknowns remain in equation (12): E, k_w, and k_2. They can be calculated by solving simultaneously three material balance equations for three radium isotopes with different half-lives.

The importance of the recoil input relative to the weathering input must increase as the half-life decreases. Thus it is desirable to choose radium isotopes with a wide range of half-lives for this calculation, and ^{226}Ra, ^{228}Ra, and ^{223}Ra fulfill this requirement. Although the measurements of ^{223}Ra have a large uncertainty, this isotope is preferred to ^{224}Ra because the latter has a soluble grandparent (^{228}Ra) whose migration may complicate the recoil input of ^{224}Ra in some way not predicted by the model. It is important to note that although ^{226}Ra and ^{223}Ra have equivalent positions in their respective decay chains (Figure 1), the $^{223}Ra/^{226}Ra$ ratio in the brine is no more than 30% of the production ratio of these isotopes in solid phases (Table 3). This observation indicates that either most ^{226}Ra is supplied by weathering and leaching processes or the recoil input of Ra isotopes is important but the isotopes have to diffuse through microfractures and nannopores into the large fractures. Because of the large uncertainty in the $^{223}Ra/^{226}Ra$ ratio, the upper limit of 0.017 for this ratio was used in the calculation. Simultaneous solution of the three material balances (equation (12)) for these radium isotopes indicated that k_2 is approximately equal to k_w, both having values of about 0.03 yr^{-1}. Data for SSSDP-1 were used for this calculation because of the possible effect of drilling-fluid contamination in SSSDP-2. If the measured value of ^{223}Ra is used in the calculation rather than the upper limit, the rate constants k_2 and k_w are larger, about 0.08 yr^{-1}. Thus the mean time for Ra in solution to precipitate in minerals ($T_p = 1/k_2$) is about 13-33 years. The mean time to leach radium from solid phases (T_{wRa}) can also be estimated from this calculation if the porosity of the system is known. This leaching time will be simply the mass of radium in the solid phase ($M_r A_r/\lambda$), divided by the flux into solution ($k_w M_b C$):

$$T_{wRa} = \frac{M_r}{M_b} \frac{A_r}{\lambda C} \frac{1}{k_w} \quad (13)$$

where M_r is the mass of rock and M_b is the mass of brine. Porosity estimates vary with lithology, with sandstones having ϕ = 5-10% and shales having almost no porosity [Paillet and Morin, this issue]. Shales are about twice as abundant as sandstones, so a reasonable estimate for porosity is about 3%. Equation (13) predicts that the mean time required to leach radium from solids is about 2000 years. If k_w for ^{210}Pb is the same as that for radium and adsorption is negligible ($K_{Pb} = 0$), equation (1) may be used to calculate k_2 for Pb. The result of this calculation indicates T_p for Pb to be 15-45 years, depending on the value used for k_w.

A rough test of this model is calculate the $^{224}Ra/^{228}Ra$ ratio in the brine. From equation (12), this ratio is calculated to be 0.77, comparable to the observed ratios of 0.75 and 0.93. This agreement indicates that ^{228}Ra

migration apparently does not invalidate the assumptions and that the factor causing the $^{224}Ra/^{228}Ra$ ratio in these brines to be less than 1 is the importance of chemical weathering in leaching radium from solid phases. The relative importance of recoil inputs, calculated as $P_r/(P_r + P_w + P_b)$, is such that virtually all input of the two short-lived radium isotopes (^{223}Ra and ^{224}Ra) is by the recoil process, while ^{228}Ra and ^{226}Ra are supplied more rapidly by weathering and leaching than by recoil (Table 4).

One possible problem with these calculations is that if thorium and uranium reside in different phases that have different rates of leaching, k_w for ^{228}Ra and ^{224}Ra would be different from k_w for ^{226}Ra and ^{223}Ra. Another possible problem is that the e_i values may depend on half-life. The model assumed that this brine, sampled from the large fractures, has the same isotopic composition as that in the small fractures and pore spaces which receives most of the recoil input. Rama and Moore [1984] showed that some difference may exist because diffusion along microfractures and mannopores may be a necessary step in allowing recoiled atoms to enter groundwater systems. However, their study focused on ^{220}Rn (50-s half-life) and may not be applicable to isotopes with longer half lives. Also, Krishnaswami and Seidemann [1988] have reported recently that the postulated microfractures may not be prevalent in some rock types. At this time, we cannot completely clarify the role of the microfractures and distinguish their effects from those of possible rapid weathering and leaching, but the observation discussed earlier that the $^{212}Pb/^{224}Ra$ ratio is very close to that predicted by the direct recoil model suggests that the recoil input of isotopes into microfractures reaches the large fractures within a few hours.

Fracture width in the SSGF. As shown earlier, ^{228}Ac, a short-lived daughter of ^{228}Ra, is rapidly sorbed onto solid phases. It is possible that sorption onto fracture walls is limited by the time required for ^{228}Ac to migrate from the site of decay to the fracture wall. The width of fractures forming the main conduits for the brine that we sampled may be calculated from $^{228}Ac/^{228}Ra$ activity ratios, based on the following assumptions. If it is assumed that ^{228}Ac is adsorbed only on fracture walls, that fracture dimensions are large relative to their opening width, and that transport of Ac occurs only by molecular diffusion, the equation describing ^{228}Ac behavior in a fracture is

$$\frac{\partial C}{\partial t} = P_b - \lambda C + D\frac{\partial^2 C}{\partial x^2} = 0 \qquad (14)$$

where

P_b decay rate of ^{228}Ra in brine;
C concentration of ^{228}Ac in brine;
λ ^{228}Ac decay constant;
D in situ molecular diffusivity;
x distance perpendicular to the fracture wall.

Zukin (1986) has assumed that La^{3+} is a chemical analog of Ac^{3+} and estimated D for Ac at 300°C from the Stokes-Einstein relation, the temperature dependence of ion mobility derived by Nigrini [1970] and the viscosity-temperature relation of

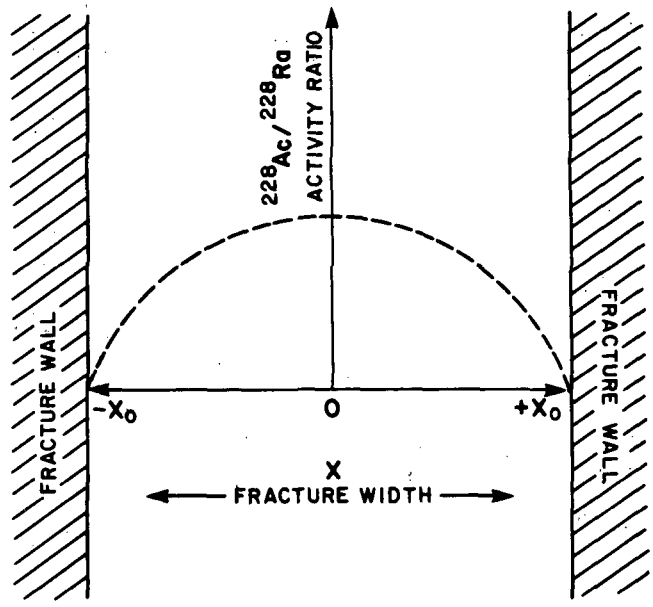

Fig. 4. A model for the ^{228}Ac distribution (dashed curve) in SSGF reservoir fractures whose widths are $2x_o$. Actinium 228 is assumed to be transported by molecular diffusion, and its activity is assumed to be zero at the fracture boundaries.

Salvinien and Brun [1964]. If adsorption of Ac is very strong, the concentration of ^{228}Ac at the fracture wall is negligible. Equation (14) can be solved to obtain the concentration profile shown in Figure 4, by applying the boundary conditions that $dC/dx=0$ at $x=0$ and $C=0$ at $x=x_o$. The solution can be integrated to find the $^{228}Ac/^{228}Ra$ activity ratio:

$$\frac{\lambda C^*}{P_b} = 1 - \frac{1}{a}\left(\frac{e^a - e^{-a}}{e^a + e^{-a}}\right) \qquad (15)$$

where C^* is the average measured ^{228}Ac in brine, $a = x_o(\lambda/D)^{1/2}$, and x_o is the fracture half width. From the measured ratio, x_o can be found by iteration or graphically. This dimension should be considered an upper limit, because we have not firmly established the assumption that the ^{228}Ac concentration is zero at fracture walls and because some sorption may occur on walls of smaller fractures connected to the main ones. Fractures for the SSSDP site appear to be 2-3 cm in width, with an uncertainty of about a factor of 2 (Figure 5 and Table 3). $^{228}Ac/^{228}Ra$ measurements in Fee 6 were <0.12 and may provide an upper limit for the ^{228}Ac at fracture boundaries. If this is the case, equations (14) and (15) could be modified and the data point in Figure 5 would shift to $^{228}Ac/^{228}Ra = 0.10\pm0.15$, equivalent to a fracture width of 1 ± 1 cm. The largest fractures present probably supply most of the brine sampled, and these estimates are comparable to vein widths observed in drill cores.

Many spaces much smaller than centimeter-sized fractures must also be present in order to allow for the recoil input of ^{223}Ra. If this isotope is homogeneously distributed in the rock, the mean surface area of the fracture system per unit

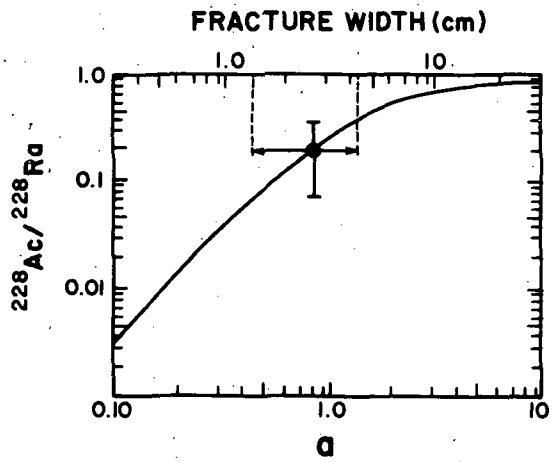

Fig. 5. Graphical solution of the average $^{228}Ac/^{228}Ra$ activity ratio in a fracture versus nondimensionalized crack width (lower scale). The concentration profile is assumed to be that shown in Figure 4. The upper scale indicates width based on the estimated Ac diffusivity for these brines of 8×10^{-5} cm^2/s.

volume of brine (SA) can be calculated from

$$SA = \frac{E}{\alpha r}\left(\frac{\rho_b}{\rho_r}\right) \quad (16)$$

where

E recoil efficiency for $^{223}Ra = \lambda C/A'_r$;
ρ density of rock or brine, g/cm^3;
α constant depending on position in the decay chain;
r recoil range, cm.

The recoil range for ^{223}Ra is estimated to be 0.1 μm, α is about 0.3 for ^{223}Ra [Krishnaswami et al., 1982], and (ρ_b/ρ_r) is about 0.5. Zukin et al. [1987] found ^{238}U = 2.64 dpm/g in rocks from neighboring Fee 5, so that ^{235}U = 0.119 dpm/g. If ^{223}Ra = 10 dpm/kg (Table 1), E = 0.08 so that equation (16) yields SA = 1.4 μm^{-1}. If this surface area is provided by planar microfractures, their mean width must be 1.5 μm. Thus, while most of the brine sampled resides in the large fractures, most of the isotope exchange must go on in small fractures. This observation has been made previously in other systems using ^{222}Rn balances [Tanner, 1964; Rama and Moore, 1984; etc.]. However, if uranium-bearing phases are located preferentially on grain boundaries as Krishnaswami and Seidemann [1988] have suggested, or if fracture geometry is not planar, this estimate of fracture width will be too small.

Conclusions

The behavior of uranium and thorium series isotopes in brines from the SSSDP well is very similar to that in expected in a high-tmperature, high-salinity brine. Uranium, thorium, actinium, bismuth, and polonium are all relatively insoluble, indicating their rapid sorption from solution. In contrast, radium, lead, and radon are all found in high concentrations. These high concentrations reflect the importance of weathering, leaching, and recoil inputs of these elements into brine from adjacent solid phases, complexing of lead and radium by chloride which helps keep these elements in solution, and the lack of suitable unfilled adsorption sites capable of removing these elements from solution.

Measurements of short-lived isotopes in these decay series demonstrate the rapid exchange that may occur between brine and solid phases. The deficiency of ^{228}Ac in brine relative to its parent, ^{228}Ra, indicates that the average time required for adsorption of actinium from the brine to solid surfaces is less than 2.5 hours. If the adsorption process for actinium is limited by the time required to diffuse through the brine to the fracture wall where the concentration of this element is assumed to be negligible, large fractures that contain brine at this site are estimated to be 2.5 cm or less in width. However, consideration of the surface area required to provide the recoil input of ^{223}Ra indicates that mean fracture widths in this system have dimensions of 1-2 μm. If alpha recoil directly into fractures is the only process adding radium into solution, the observed $^{223}Ra/^{226}Ra$ and the $^{224}Ra/^{228}Ra$ ratios should be greater than or equal to those in rocks. Observed ratios are lower, indicating that either (1) the recoil input is dependent on the isotope half-life because it is limited by the rate of diffusion through microfractures and nannopores, or (2) weathering and leaching are so rapid that most of the ^{226}Ra and ^{228}Ra are added to the brine by these processes. The $^{212}Pb/^{224}Ra$ ratio is consistent with the value predicted by the direct recoil model, favoring possibility 2. The direct recoil model can be used to estimate the mean removal time of radium and lead atoms from brines to minerals to be approximately 30 yrs. If the porosity of the system is 3%, the mean time radium isotopes reside in solid phases is about 2000 years. These calculated values are probably accurate within a factor of 2.

There are very few estimates of rates of brine-rock interaction rates in any system. The models presented above, though highly simplified, demonstrate the usefulness of U/Th series isotopes for estimating the time scales of brine-rock interaction, fluid residence times, and fracture widths. These are parameters of fundamental interest for understanding the genesis of hydrothermal deposits and the transfer of heat and material through a geothermal field. They are also valuable in predicting the possible migration rate of radioactive waste.

Acknowledgements. This project could not have been carried out without the assistance of Wilf Elders, Don Michels, and Al Williams in designing and executing field work. Their comments have also provided valuable insight into the nature of hydrothermal systems. Careful reviews by K. Turekian and an anonymous reviewer greatly improved the manuscript. In addition, we thank K. G. Knauss, S. Krishnaswami, J. C. Laul, M. Smith, and B. Leslie for stimulating discussions. Sue Turnbow and Desser Moton patiently typed this manuscript. Financial support for this work was provided by Battelle Memorial Institute subcontract E512-08300 to University of California, Riverside (W. Elders as principal investigator), under their contract

DE-AC02-83CHI 0140 with the Department of Energy. National Science Foundation grant EAR-8804735 has partially supported the manuscript preparation.

References

Belin, R. E., Radon in the New Zealand geothermal regions, Geochim. Cosmochim. Acta, 16, 181-191, 1959.

Chen, J. H., G. J. Wasserburg, K. L. Von Damm, and J. M. Edmond, The U-Th-Pb systematics in hot springs on the East Pacific Rise at 21°N and Guaymas Basin, Geochim. Cosmochim. Acta, 50, 2467-2479, 1986.

Chung, Y., R. Finkel, and K. Kim, Hydrothermal ^{210}Pb on the East Pacific Rise at 21°N, EOS Trans. AGU, 62, 913, 1981.

Coplen, T., Cooperative geochemical resource assessment of the Mesa Geothermal System, final report contract 14-06-300-2497, 106, pp., U.S. Dep. of the Inter., Bur. of Reclam., Washington, D.C., 1976.

Cowart, J. B., The relationship of uranium isotopes to oxidation/reduction in the Edwards carbonate aquifer of Texas, Earth Planet. Sci. Lett., 48, 277-283, 1980.

Cowart, J. B., and J. K. Osmond, Dissolved uranium series nuclides in geothermal waters, Geol. Soc. Am. Abstr. Programs, 8, 823, 1976.

D'Amore, F., Radon-222 survey in Larderello geothermal field, Italy (Part 1), Geothermics, 4, 96-108, 1975. Davidson, M. R., and B. C. Dickson, A porous flow model for steady state transport of radium in groundwater, Water Resour. Res., 22, 34-44, 1986.

Doe, B. L., C. E. Hedge, and D. E. White, Preliminary investigation of the source of lead and strontium in deep geothermal brines underlying the Salton Sea geothermal area, Econ. Geol., 61, 462-483, 1966.

Dymond, J., R. Cobler, L. Gordon, P. Biscaye and G. Mathieu, ^{226}Ra and ^{222}Rn contents of Galapagos Rift hydrothermal waters -- The importance of low temperature interactions with crustal rocks, Earth Planet. Sci. Lett., 64, 417-429, 1983.

Elders, W. A., and S. Biehler, Gulf of California rift system and its implication for the tectonics of western North America, Geology, 3, 85-87, 1975.

Elders, W. A., and L. W. Cohen, The Salton Sea geothermal field, California, as a near-field natural analog of a radioactive repository in salt, Tech. Rep. BMI/ONWI 513, 1465 pp., Battelle Mem. Inst., Columbus, OH, 1983.

Elders, W. A., and J. B. Moody, The Salton Trough geothermal field as a natural analog for the near-field in a salt high-level nuclear waste repository, in Scientific Basis for Nuclear Waste Management, v. 8, edited by C. E. Jantzen, S. A. Stone, and R. Ewing, pp. 565-572, Materials Research Society, Pittsburgh, 1985.

Elders, W. A. and J. Sass, The Salton Sea Scientific Drilling Project, J. Geophys. Res., This issue.

Helgeson, H. C., Geologic and thermodynamic characteristics of the Salton Sea geothermal system, Am. J. Sci., 266, 129-166, 1968.

Herczeg, A. L., H. J. Simpson, R. F. Anderson, R. M. Trier, G. G. Mathieu, and B. L. Deck, Uranium and radium mobility in groundwaters and brines within the Delaware basin, southeastern New Mexico, USA, Chem. Geol., 72, 181-196, 1988.

Hsi, C.-K. D., and D. L. Langmuir, Adsorption of uranyl onto ferric oxyhydroxides: Application of the surface complexation site-binding model, Geochim. Cosmochim. Acta, 49, 1931-1941, 1985.

Kasameyer, P. W., L. W. Younker, and J. M. Hanson, Development and application of a hydrothermal model for the Salton Sea geothermal field, California, Geol. Soc. Am. Bull., 95, 1242-1252, 1984.

Kim, K., and R. Finkel, Radioactivities on 21°N hydrothermal system, EOS Trans. AGU, 61, 995, 1980.

Kraemer, T. F., ^{234}U and ^{238}U concentrations in brine from geopressured aquifers for the northern Gulf of Mexico basin, Earth Planet. Sci. Lett., 56, 210-216, 1981.

Kraemer, T. F., and Y. K. Kharaka, Uranium geochemistry in geopressured-geothermal aquifers of the U.S. Gulf Coast, Geochim. Cosmochim. Acta, 50, 1233-1238, 1986.

Kraemer, T. F., and D. F. Reid, The occurrence and behavior of radium in saline formation water of the U.S. gulf coast region, Isot. Geosci., 2, 153-174, 1984.

Krishnaswami, S., and D. E. Seidemann, Comparative study of ^{222}Rn, ^{40}Ar, ^{39}Ar, and ^{37}Ar leakage from loss from rock and minerals: Implications for the role of nannopores in gas transport through silicates, Geochim. Cosmochim. Acta, 52, 655-658, 1988.

Krishnaswami, S., and K. K. Turekian, ^{238}U, ^{226}Ra and ^{210}Pb in some vent waters of the Galapagos spreading center, Geophys. Res. Lett., 9, 827-830, 1982.

Krishnaswami, S., W. C. Graustein, K. K. Turekian, and J. F. Dowd, Radium, thorium and radioactive lead isotopes in groundwaters: Applications to the in situ determination of adsorption-desorption rate constants and retardation factors, Water Resour. Res., 18, 1633-1675, 1982.

Langmuir, D., Uranium solution-mineral equilibria at low temperatures with applications to sedimentary ore deposits, Geochim. Cosmochim. Acta, 42, 547-569, 1978.

Langmuir, D., and J. S. Herman, The mobility of thorium in natural waters at low temperatures, Geochim. Cosmochim. Acta, 44, 1753-1766, 1980.

Langmuir, D., and D. Melchoir, The geochemistry of Ca, Sr, Ba, and Ra sulfates in some deep brines from the Palo Duro Basin, Texas, Geochim. Cosmochim. Acta, 49, 2423-2432, 1985.

Langmuir, D., and A. C. Reise, The thermodynamic properties of radium, Geochim. Cosmochim. Acta, 49, 1593-1601, 1985.

Laul, J. C., M. R. Smith, and N. Hubbard, Behavior of natural uranium, thorium and radium isotopes in the Wolfcamp brine aquifers, Palo Duro Basin, Texas, Mater. Resour. Soc. Proc., 44, 475-482, 1985.

Mazor, E., Radon and radium content of some Israeli water sources and a hypothesis on underground reserviors of brines, oils and gases in the Rift Valley, Geochim. Cosmochim. Acta, 26, 706-786, 1962.

McKibben, M. A., A. E. Williams, and S. Okubo, Metamorphosed Plio-Pleistocene evaporites and the origins of hypersaline brines in the Salton Sea geothermal system, California: Fluid inclusion evidence, Geochim. Cosmochim. Acta, 52, 1047-1056, 1988.

Michard, A., F. Albarede, G. Michard, J. F. Minster, and J. L. Charlou, REE and U concentrations in high temperature hydrothermal waters from the East Pacific Rise at 13°N, EOS Trans. AGU, 64, 333, 1983.

Michels, D. E., SSSDP fluid composition at first flow of State 2-14, Trans. Geotherm. Resour. Counc., 10, 461-465, 1986.

Newmark, R. L., P. W. Kasameyer, L. W. Younker, and P. C. Lysne, Research drilling at the Salton Sea geothermal field, California: The shallow thermal project, EOS Trans. AGU, 67, 698-707, 1986.

Nigrini, A., Diffusion in rock alteration systems, I, Prediction of limiting equivalent ionic conductances at elevated temperatures, Am. J. Sci., 269, 65-91, 1970.

Osmond, J. K., J. B. Cowart, and M. Ivanovich, Uranium isotopic disequilibrium in groundwater as an indicator of anomalies, Int. J. Appl. Radiat. Isot., 34, 283-308, 1983.

Paillet, F. L., and R. H. Morin, Analysis of geophysical well logs obtained in the State 2-14 borehole, Salton Sea geothermal area, California, J. Geophys. Res., this issue.

Petit, J. C., Y. Langevin, and J. C. Dran, $^{234}U/^{238}U$ disequilibrium in nature: Theoretical reassessment of the various proposed models, Bull. Mineral., 108, 745-753, 1985.

Rama, and W. S. Moore, Mechanism of transport of U-Th series radioisotopes from solids into ground water, Geochim. Cosmochim. Acta, 48, 395-399, 1984.

Salvinien, J., and B. Brun, Mesure des coefficients de self diffusion des constituants (ions et solvant) de solutions salines entre de larges limites de concentrations, C. R. Hebd. Seances Acad. Sci., 259, 565-567, 1964.

Stoker, A. K., and P. Kruger, Radon in geothermal reservoirs, in Second U.N. Symposium on the Development and Use of Geothermal Resources, San Francisco, pp. 1797-1803, Lawrence Berkeley Laboratory, University of California, Berkeley, 1975.

Sturchio, N. C., and C. M. Binz, Uranium-series age determination of calcite veins, VC-1 drill core, Valles caldera, New Mexico, J. Geophys. Res., 93, 6097-6102, 1988.

Sturchio, N. C., C. M. Binz, and C. H. Lewis II, Thorium-uranium disequilibrium in a geothermal discharge zone at Yellowstone, Geochim. Cosmochim. Acta, 51, 2025-2034, 1987.

Sturtevant, R. G., and A. E. Williams, Oxygen isotopic profiles of the State 2-14 geothermal well: Evidence for a complex thermal history, EOS Trans. AGU, 68, 445, 1987.

Tanner, A. B., Radon migration in the ground: a review: in The Natural Radiation Environment, edited by J. A. S. Adams and W. M. Lowder, pp. 161-190, University of Chicago Press, Chicago, Ill., 1964.

Turekian, K. K., and J. K. Cochran, Flow rates and reaction rates in the Galapagos rise spreading center hydrothermal system as inferred from $^{228}Ra/^{226}Ra$ in vesicomyid clam shells, Proc. Natl. Acad. Sci. U.S.A., 83, 6241-6244, 1986.

White, D. E., Geothermal systems and hydrothermal ore deposits, in Econ. Geol., 75th Anniv., 392-423, 1981.

Williams, A. E., Chemical and isotopic variations and the distribution of brines across the Salton Sea geothermal field, California, EOS Trans. AGU, 68, 438, 1987.

Wollenberg, H. A., Radioactivity of geothermal systems, in Second U. N. Symposium on the Development and Use of Geothermal Resources, San Francisco, pp. 1283-1292, Lawerence Berkeley Laboratory., University of California, Berkeley, 1975.

Wollenberg, H. A., and S. Flexser, Contact zones and hydrothermal systems as analogues to repository conditions, Chem. Geol., 55, 345-359, 1986.

Zukin, J. G., Uranium and thorium series isotopes in the Salton Sea geothermal field, southeastern California--Their application in determining the rates of brine-rock interaction and radionuclide transport, M.S. thesis, 156 pp., Univ. of South. Calif., Los Angeles, 1986.

Zukin, J. G., D. E. Hammond, T.-L. Ku, and W. A. Elders, Uranium-thorium series isotopes in brines and reservoir rocks from two deep geothermal well holes in the Salton Sea geothermal field, southeastern California, Geochim. Cosmochim. Acta, 51, 2719-2731, 1987.

D. E. Hammond and T.-L. Ku, Department of Geological Sciences, University of Southern California, Los Angeles, CA 90089.

J. G. Zukin, Dames and Moore, 175 Gremona Drive, Coleta, CA 93117.

(Received October 13, 1987;
revised July 11, 1988;
accepted July 12, 1988.)

SECTION C

Reprint from ECONOMIC GEOLOGY, VOLUME 83, 1988.

McKibben, M.A., Andes, J.P., and Williams, A.E., "Active Ore Formation at a Brine Interface in Metamophosed Deltaic Lacustrine Sediments: The Salton Sea Geothermal System, California," pp 511-523.

Economic Geology
Vol. 83, 1988, pp. 511-523

Active Ore Formation at a Brine Interface in Metamorphosed Deltaic Lacustrine Sediments: The Salton Sea Geothermal System, California

MICHAEL A. MCKIBBEN,

Tunell Economic Geology Laboratory, Department of Earth Sciences, and Geothermal Resources Program, Institute of Geophysics and Planetary Physics, University of California, Riverside, California 92521

JERRY P. ANDES, JR., AND ALAN E. WILLIAMS

Geothermal Resources Program, Institute of Geophysics and Planetary Physics, University of California, Riverside, California 92521

Abstract

The Salton Sea geothermal system is an area of active hydrothermal metamorphism of Pliocene to Pleistocene deltaic, lacustrine, and evaporitic sediments deposited in a modern continental rift zone. Temperatures up to 365°C, hypersaline metalliferous brines with up to 26 wt percent total dissolved solids and active base metal ore formation accompany low-pressure greenschist and amphibolite facies metamorphism at depths less than 3.2 km. Drill cores recovered by the Salton Sea Scientific Drilling Project shed new light on the nature and origin of ore formation in the eastern portion of the Salton Sea geothermal system.

Base metal ore mineralization occurs in vertical fractures that comprise the major form of fluid permeability at 1 to 3 km in the modern geothermal system. Type 1 veins are dominated by carbonate, contain pyrrhotite and other sulfides, are completely sealed, and occur in wall rock showing minimal alteration. Fluid inclusion data indicate that they were deposited under a thermal gradient much higher than that now found in the eastern part of the system. Type 2 veins are dominated by silicates and hematite, are permeable, and occur in wall rocks showing pervasive chloritization and epidotization. Fluid inclusion data indicate that they are forming now from the geothermal brines under the modern thermal gradient.

Fluid inclusions record an apparent steep, progressive salinity increase in the vein systems in the upper 2 km of the system. However, fluid production data from Salton Sea geothermal wells indicate that reduced, metalliferous hypersaline brine averaging 23 wt percent total dissolved solids is overlain by more oxidized, metal-poor fluid averaging 5 wt percent total dissolved solids. A sharp interface exists between the fluids at 1 to 2 km, paralleling the 250°C isothermal surface.

A model is developed for type 2 vein ore formation involving mixing at the interface between the two fluids. Magmatic intrusion induces fracturing, heating, and the expulsion of reduced connate fluids to cause early type 1 vein mineralization. Following the rising thermal front, deep hypersaline brine rises diapirically and mixes with overlying fluids in vertical fractures transecting the ascending interface, forming type 2 veins. The hypersaline brine rises to a level of density-temperature stabilization, causing pervasive greenschist metamorphism of the host sediments. The diapir then begins to cool and descend. Shallow, oxidized brine is drawn in as the hypersaline brine descends, promoting late-stage hematite in type 2 veins. The eastern Salton Sea geothermal system presently appears to be in this latter mode of cooling and retrograde brine descent.

Ore formation in the system is caused by the coincidence of transaxial entry of a major river into an active rift zone, deposition of metal-bearing deltaic sediments to form a closed-basin sedimentary environment, episodic lacustrine evaporite formation, and injection of heat and elements by rift-related magmatic intrusions at depth. The presence of an upwelling brine diapir in the system may be analogous to conditions immediately prior to the exhalation of metalliferous fluids that formed stratiform Fe-Zn-Pb-Cu sulfide and oxide deposits in paleorift zone environments.

Introduction

THE Salton Sea geothermal system is well known for its high temperatures, hypersaline brines, and active ore deposition (White et al., 1963; Skinner et al., 1967; Helgeson, 1968; McKibben and Elders, 1985). New drill cores recovered by the Salton Sea Scientific Drilling Project have allowed us to improve dramatically our understanding of ore mineralization in this system. In this paper we report our mineralogic and fluid inclusion studies of ore-mineralized veins in cores from drilling project well,

0361-0128/88/801/511-13$2.50

California State 2-14. Our results allow us to expand and improve upon our previous study of ore mineralization (McKibben and Elders, 1985). In conjunction with new data on brine chemistry and distribution in the Salton Sea system (Williams and McKibben, 1988), we propose a model for ore formation involving interaction between an upwelling hypersaline brine diapir and overlying lower salinity fluids in this sediment-hosted geothermal system.

Salton Sea Geothermal System

The Salton Sea geothermal system is located in the Salton trough of southern California (Fig. 1), an active continental rift zone forming the landward extension of the Gulf of California-East Pacific Rise spreading system (Elders et al., 1972; Elders, 1979). The Colorado River presently enters the east margin of the rift near Yuma and is prograding its delta south toward the Gulf of California (Fig. 1). The delta has filled the rift as it has opened, isolating the northern part of the Salton trough from the gulf for the past 4 m.y. (Elders, 1979; Winker and Kidwell, 1986). A large brackish lake, Lake Cahuilla, has formed and evaporated several times in the northern trough since the Pleistocene. The modern Salton Sea formed in 1905 when spring floods damaged an irrigation canal, diverting the Colorado River north into the old Salton Sink salina

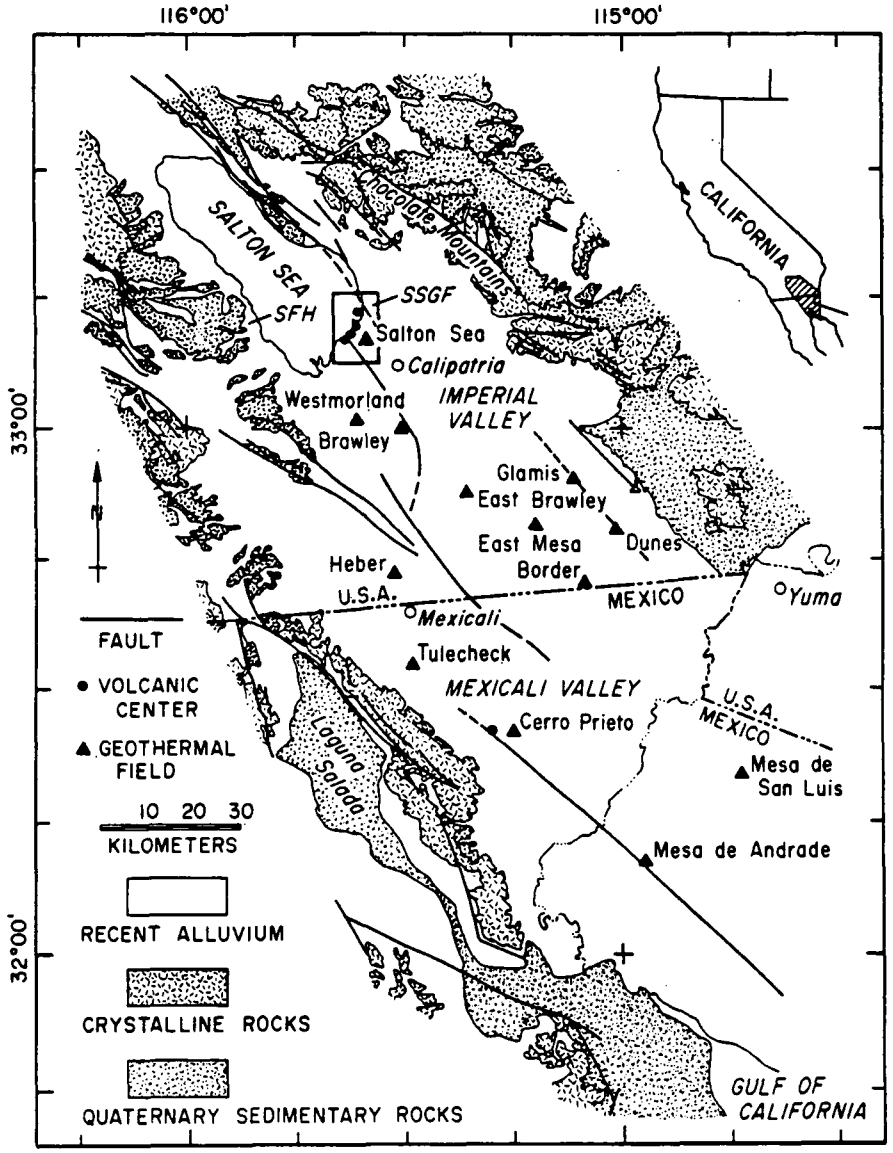

FIG. 1. Generalized geologic map of the Salton trough, showing the locations of active geothermal fields and young igneous extrusions. The Colorado River enters the trough near Yuma (dashed-dotted line) and presently meanders south to the Gulf of California. SSGF = Salton Sea geothermal field, SFH = San Felipe hills.

for two years. Arnal (1961) estimated that this flooding event dissolved 114 million metric tons of salt that had accumulated from previous dry lake stages. The long history of the northern Salton trough as a closed, evaporative basin has been responsible for the high salinities of the geothermal brines (see discussions by McKibben et al., 1987, 1988).

The Salton Sea geothermal system is located at the south end of the Salton Sea in the Imperial Valley and is associated with an arc of five Quaternary rhyolite domes (Helgeson, 1968; Muffler and White, 1969). It is the locus of positive gravity and magnetic anomalies and exhibits high heat flow. Recent summaries of petrologic and geochemical data from the system were given by McDowell and Elders (1980, 1983), Elders and Cohen (1983), McDowell and Paces (1985), McKibben and Elders (1985), and McKibben et al. (1987). The sedimentary rocks penetrated by geothermal wells in the system are mainly Pliocene to Pleistocene fluvial and lacustrine deltaic deposits derived from the Colorado River. Temperatures up to 365°C and hypersaline Na-Ca-K-Cl brines with total dissolved solids up to 26 wt percent are encountered at depths of 2 to 3 km. The deltaic sediments are progressively metamorphosed with depth, largely to hornfels containing greenschist facies mineral assemblages: actinolite-quartz-epidote-biotite-andradite (Muffler and White, 1969; McDowell and Elders, 1980, 1983). The deepest rocks recovered from the Salton Sea Scientific Drilling Project well contain 2-amphibole assemblages that mark the transition from greenschist to amphibolite facies at 3-km depth (Cho et al., 1988).

Because of the high temperatures and high metal contents of the brines, White et al. (1963) first suggested that they represented magmatic fluids. Later, isotopic studies of brine and rock indicated that the water in the brines was largely meteoric in origin (Craig, 1966, 1969; White, 1968, 1981). Williams and McKibben (1988) have shown that there are actually two chemically and isotopically distinct geothermal fluids in the system: deep hypersaline metamorphic brines and shallow lower salinity fluids. Either fluid may owe its origin to different fossil lake waters that were derived from fossil Colorado River waters and/or from fossil rainfall. Rex (1985) has proposed that the deep hypersaline brine reservoir extends over an area of 1,000 km^2 in the Imperial Valley. It normally lies below 4-km depth in nonthermal areas but rises to depths as shallow as 1 km in the Salton Sea system due to heating.

The hypersaline nature of the system brines has been attributed to the dissolution of shallow nonmarine evaporites by meteoric waters (White, 1968; Rex, 1972, 1983, 1985). Concentration solely by evaporation of Colorado River water (Helgeson, 1968) is untenable on the basis of stable isotope data (Craig, 1969; Williams and McKibben, 1988). White (1968) suggested that local rainwaters dissolved shallow lacustrine evaporites, whereas Rex suggested that cold ground waters dissolved halite that had accumulated in the old Salton Sink from evaporation of ancient Lake Cahuilla. The latter hypothesis is consistent with Arnal's (1961) observations on halite dissolution during formation of the Salton Sea. Recently, McKibben et al. (1988) demonstrated that high salinities are derived in part by the dissolution of NaCl during hydrothermal metamorphism of lacustrine evaporites at 1-km depth (≃300°C). Such evaporites are more common in Salton Sea host rocks than has been recognized previously. Geochemical and isotopic data for the brines and evaporites indicate that marine waters have not played a significant role in generation of the evaporites or brines (McKibben et al., 1987).

Isotopic data indicate that most of the Pb and Sr in the brines is leached from the host sediments (Doe et al., 1966). XRF analyses of shales indicate that they undergo progressive losses of Pb, Sn, Mn, Zn, and Cu with increasing depth at temperatures above 250°C (McDowell and Bornhorst, 1985; McDowell, pers. commun., 1987). Thus, metamorphism and leaching by the saline reservoir brines have effectively stripped the host rocks of their original detrital metal content. McKibben and Elders (1985) demonstrated that base metal transport in the brines can be accounted for by chloride complexing.

Skinner et al. (1967) and McKibben and Elders (1985) described ore mineralization from the Salton Sea system, based mainly on studies of drill cuttings. McKibben and Elders (1985) classified the occurrences into strata-bound diagenetic Fe sulfides, Fe-Zn-Cu-Pb sulfides in hydrothermal veins, and metamorphic Fe sulfide porphyroblasts. Vein ore mineralization was particularly abundant at depths of 900 to 1,500 m in the wells River Ranch 1 and Magmamax 2 (Fig. 2). On the basis of fluid-mineral equilibria calculations, they concluded that the modern hypersaline brines were interacting with a relatively oxidized porous vein assemblage containing quartz, pyrite, epidote, and hematite. A second nonporous vein assemblage containing calcite and sulfides was assumed to be older. However, their studies were limited by a lack of large-scale textural information on veins and did not include comprehensive fluid inclusion data. Thus, a mechanism for ore formation was not firmly established.

The origin and mechanism of transport of the sulfur occurring in vein sulfides remains to be established. Based on replacement textures, McKibben and Elders (1985) speculated that biogenic sedi-

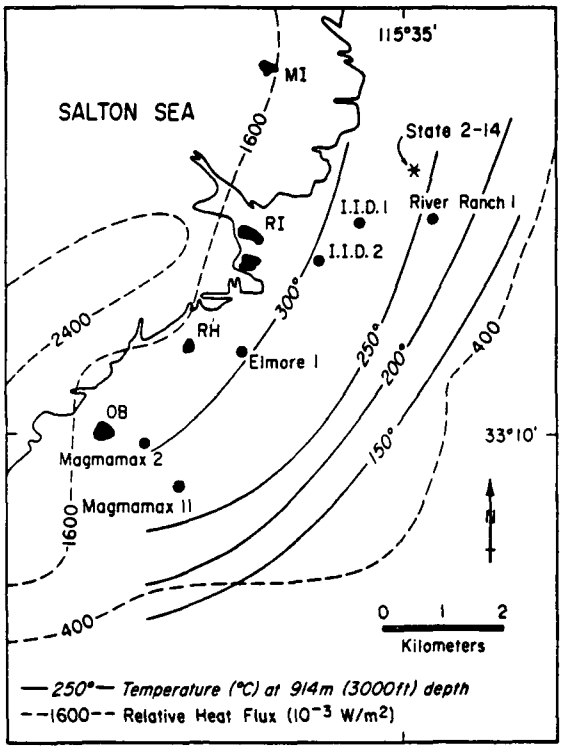

FIG. 2. Map of the Salton Sea geothermal field, showing locations of the geothermal wells discussed in the text. Measured subsurface temperatures increase progressively toward the arc of Quaternary volcanic domes. Rhyolite extrusions: OB = Obsidian Butte, RH = Rock Hill, RI = Red Island, MI = Mullet Island. Modified from McKibben and Elders (1985).

mentary sulfides in the host rocks were a major source of reduced sulfur for hydrothermal vein ore mineralization. However, subsequent sulfur isotope studies indicate that replacement of sedimentary sulfide is not a major source of sulfur for vein sulfides. Injection of magmatic sulfide and/or ≈50 percent reduction of SO_4 derived from evaporitic anhydrite in the host sediments seem to be required to produce the consistent zero per mil $\delta^{34}S$ values that characterize the vein sulfides (McKibben, 1986; McKibben et al., 1986; McKibben and Eldridge, in prep.).

Salton Sea Scientific Drilling Project Well, California State 2-14

The Salton Sea Scientific Drilling Project well, California State 2-14 (S2-14), located in the eastern part of the Salton Sea system (Fig. 2), was drilled to a depth of 3,201 m (Sass and Elders, 1986). Drill cuttings and 221 m of core were recovered. A summary of the well lithology is given by Herzig et al. (1988). The interbedded deltaic lacustrine sediment types, progressive metamorphic mineral zones, and vein mineralization are similar to nearby wells previously described from the system (Muffler and White, 1969; McDowell and Elders, 1980, 1983; McKibben and Elders, 1985), particularly River Ranch 1. Two zones of fluid flow were sampled in well S2-14, at depths of 1,870 and 3,201 m. Each zone produced hypersaline brines. The third column in Table 1 lists a chemical analysis of brine from the 1,870-m zone, which produced fluid having a reservoir temperature of 305°C. (The fluid from the 3,201-m zone was contaminated by drilling fluids but was chemically very similar to that encountered at 1,870 m). During flow testing of the 1,870-m zone, rock fragments containing porous epidote-hematite-pyrite vein assemblages were ejected from the flow line (Charles et al., 1988). The significance of these ejecta is discussed below.

Attempts to sample shallow (<1 km) fluids in well S2-14 were not made. However, shallow fluids have been recovered from other nearby wells in the system (Williams and McKibben, 1988); the second column in Table 1 lists an analysis of a typical shallow, lower salinity geothermal fluid. As discussed

TABLE 1. Analyses of Typical Shallow, Low-Salinity Geothermal Fluid and Deep, Hypersaline Geothermal Brine from Wells (B-1R, S2-14) in the Eastern Part of the Salton Sea Geothermal System

Constituent	Shallow (well B-1R)	Deep (well S2-14)
Na	15,000	52,700
Ca	2,500	26,500
K	2,500	16,500
Fe	86	1,550
Mn	60	1,390
Zn	11	506
SiO_2	255	>475
Sr	112	405
NH_4	103	336
B	92	253
Ba	45	194
Li	55	190
Pb	3	95
Mg	54	36
Cu	nd	6
Cd	nd	2
As	nd	5
Cl	31,000	154,000
Br	24	99
SO_4	53	110
H_2S	nd	7
CO_2	10,100	1,660
Total dissolved solids	62,100	257,000
Flow zone depth	950 m	1,870 m
Flow zone temperature	240°C	305°C

Data from Williams and McKibben (1988) and Williams (unpub.); concentrations in ppm; concentrations of Ba and SO_4 may be too high due to contamination by drilling fluids; analyses have been corrected for steam loss during flashing to yield true downhole concentrations; nd = no data

below, we conclude that mixing between the two fluid types is an important mechanism for vein ore mineralization.

Mineralized Fractures

Eight major zones of vertical to near-vertical fractures containing ore minerals were encountered in well S2-14 cores. The strike azimuth of the veins in these fractures is unknown because the cores are unoriented, but their vertical dip is consistent with the horizontal orientation of the axis of least principal stress in a tensional rift environment such as the Salton trough. At depths greater than ≃1 km in the Salton Sea geothermal system, geothermal fluid production intervals in wells generally coincide with such vertical fracture zones.

Photographs of representative cores recovered from the fracture zones are shown in Figure 3. The veins cut a variety of lithologies, including conglomerates, shales, siltstones, and sandstones. Alteration envelopes are rarely visible due to the pervasive host-rock metamorphism, but thin disseminated areas of carbonate, silicate, hematite, and pyrite sometimes surround veins. Transmitted- and reflected-light studies were made of polished samples from the eight vertical fracture zones. The depth range and mineral paragenesis of each of these zones are given in Table 2; more detailed descriptions are given in Andes (1987).

Based on textures, mineralogy, and fluid inclusion data, the eight vertical fracture zones can be divided into the two general types outlined in Table 3. Type 1 veins are completely filled by minerals, dominated by calcite, and occur in wall rock that exhibits carbonate cementation but minimal epidote-chlorite alteration. Figure 4A–D shows examples of typical textures in this vein type. Silicates (epidote, adularia) were precipitated first, followed

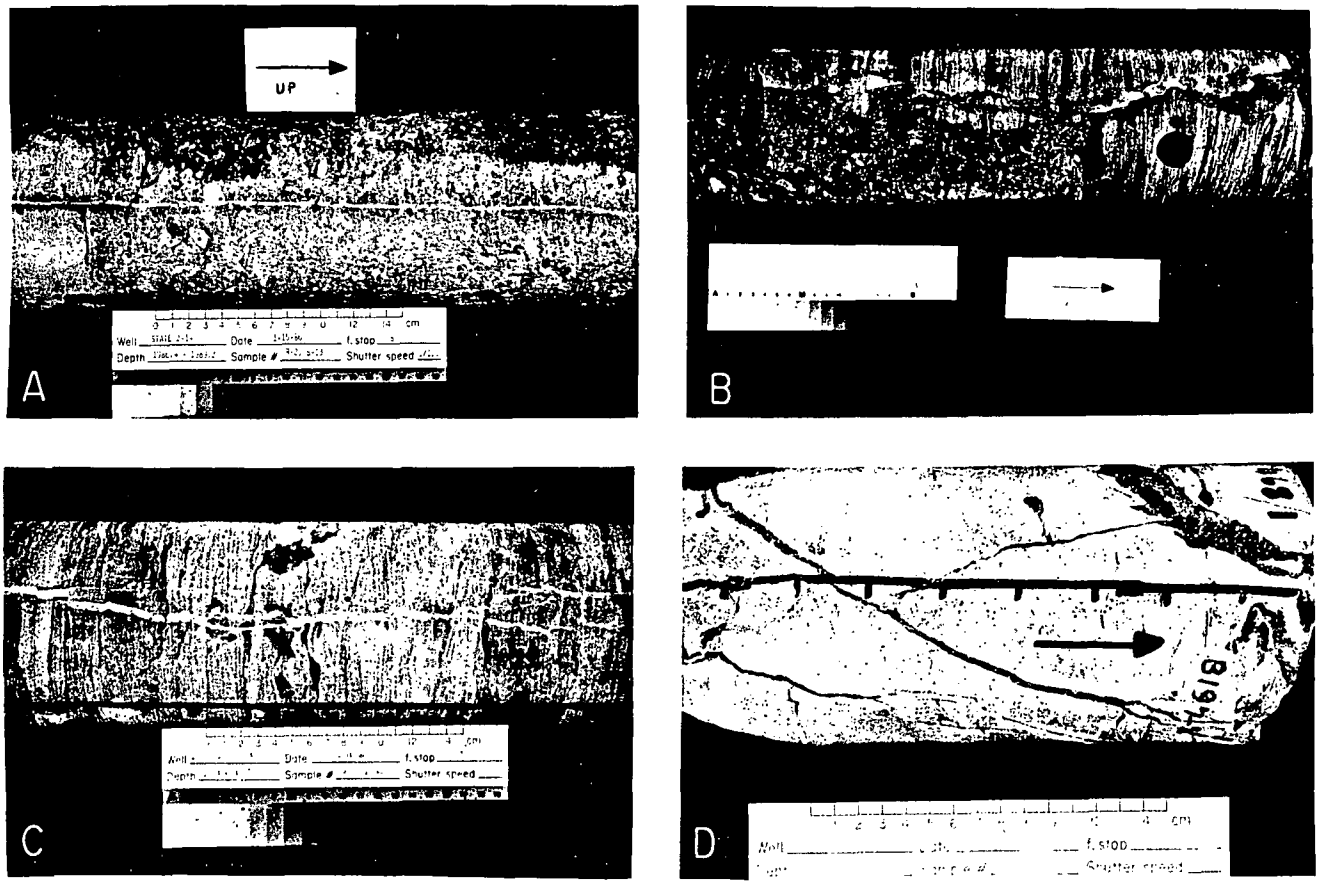

FIG. 3. Photographs of mineralized veins in 12-cm-diam cores from Salton Sea Scientific Drilling Project well, California State 2-14. A. Type 1 vertical carbonate vein in cemented conglomerate and mudstone, 602 m. B. Type 2 vertical open fracture in crossbedded chloritized and epidotized sandstone and shale, 914 m. The fracture contains mainly chalcopyrite, calcite, and epidote. C. Type 1 vertical carbonate vein in laminated siltstone, 1,286 m. Dark grains in vein are mainly sphalerite. D. Type 2 subvertical open fractures in cemented sandstone, 1,419 m. The fracture contains mainly specular hematite and epidote.

TABLE 2. Vertical Fracture Zones in Cores from the Well S2-14

Zone	Depth (m)	Type	Paragenesis[1]
1	601–603	1	ep (5) + ad (3), cc (85), py (2), sph (3), cpy (2) + gn (<1)
2	908–916	2	qz (9) + ep (60), cc (20), py (3), cpy (5) + gn (1) + sph (<1), hm (2)
3	1,286–1,288	1	ep (5), ank (2), cc (90) + sph (3) + cpy (<1) + po (<1)
4	1,407–1,430	2	ep (90), qz (1), cc (4), py (1) + cpy (1), hm (3)
5	1,689–1,690	2	ep (65), chl (15), cc (4) + ad (2) + qz (2) + py (1) + cpy (1) + hm (10)
6	2,465–2,466	1	cc (92), po (6), anh (2)
7	2,756	2	py (65) + qz (35)
8	2,856–2,857	2	cc (90), ad (3) + spn? (2), py (5)

[1] Paragenesis lists the mineral phases in order of precipitation in vein, earliest to latest, separated by commas; minerals that precipitated simultaneously are listed with plus signs; numbers in parentheses are volume percents of minerals in veins

Abbreviations: ad = adularia, anh = anhydrite, ank = ankerite, cc = calcite, chl = chlorite, cpy = chalcopyrite, ep = epidote, gn = galena, hm = hematite, po = pyrrhotite, py = pyrite, sph = sphalerite, spn = sphene

TABLE 3. Summary of Characteristics for Vein Types 1 and 2

Characteristic	Type 1 (early) veins	Type 2 (modern) veins
Dominant mineralogy	Carbonate	Silicate, oxide
Porosity	Low	High
Redox-sensitive minerals	Pyrrhotite	Hematite
Fluid inclusion temperatures	Higher than present temperature	Same as present temperature
Wall-rock alteration	Minimal: carbonate cementation	Major: epidote, chlorite

by calcite, and finally by base metal sulfides. Sulfides are generally deposited in the order pyrite, sphalerite, chalcopyrite, galena. The presence of pyrrhotite in vertical fracture zones 3 and 6 (Fig. 4C) implies a relatively low fluid oxidation state during vein deposition. Sphalerite color is strongly zoned from light cores to dark rims, suggestive of changing fluid chemistry during precipitation (Fig. 4A and D). Energy dispersive probe analyses of sphalerite yield compositions from 1 to 22 mole percent FeS.

Type 2 veins are only partly filled by minerals and occur in wall rock that exhibits pervasive alteration to epidote and chlorite. Fresh euhedral crystals project into open pore spaces. Figure 4E–H shows examples of typical textures in this vein type. Silicates (epidote, quartz) were precipitated first, followed by calcite, then by sulfides (mainly pyrite and chalcopyrite), and finally by hematite. Hematite often replaces sulfides (Fig. 4D), sometimes preferentially at the contacts between different sulfide minerals. Evidently fluid conditions became progressively oxidizing in the late stages of vein deposition. Some segments of veins locally contain nearly 100 percent hematite (Fig. 3D). Compositional data on vein epidotes are reported by Caruso et al. (1988); they note that epidotes in hematite-bearing veins tend to have higher Fe contents.

FIG. 4. Photomicrographs of mineral textures in veins from Salton Sea Scientific Drilling Project well, California State 2-14. A. Transmitted light view of a type 1 vein, 602 m (Fig. 3A). Parallel calcite (cc) veins, separated by dark selvage of wall rock, contain flattened masses of sphalerite (sp). Sphalerite is color zoned with dark rims. Tiny crystals of epidote and adularia line the vein walls. Width of figure is 0.5 mm. B. Transmitted light view of primary (?) fluid inclusions in sphalerite from a type 1 vein, 602 m (Figs. 3A and 4A). Width of figure is 0.15 mm. C. Reflected light view of a type 1 vein, 1,286 m (Fig. 3C). Blebs of pyrrhotite (po) are sandwiched between calcite (cc) and sphalerite (sp). Width of figure is 0.13 mm. D. Transmitted light view of a type 1 vein, 1,287 m (Fig. 3C). Color-zoned sphalerite with opaque rim in calcite. Width of figure is 0.25 mm. E. Reflected light view of a type 2 vein, 914 m (Fig. 3B). Vein wall lined with epidote (ep). Nucleus of pyrite (py) surrounded and partially replaced (triangular patches) by chalcopyrite (cp). (Almost all of the chalcopyrite crystals in this vertical fracture zone contain nuclei of pyrite in their cores.) Width of figure is 0.25 mm. F. Reflected light view of a type 2 vein, 914 m (Fig. 3B). Former pyrite nucleus in chalcopyrite (cp) is completely replaced by late-stage hematite (hm). Specular hematite spray grew into open space at left. Width of figure is 0.5 mm. G. Reflected light view of a type 2 vein, 1,413 m (similar to Fig. 3D). Late-stage specular hematite (hm) envelopes quartz (qz) and calcite (cc). Width of figure is 0.5 mm. H. Transmitted light view of secondary (?) fluid inclusions in calcite from a type 2 vein, 914 m. Width of figure is 0.15 mm.

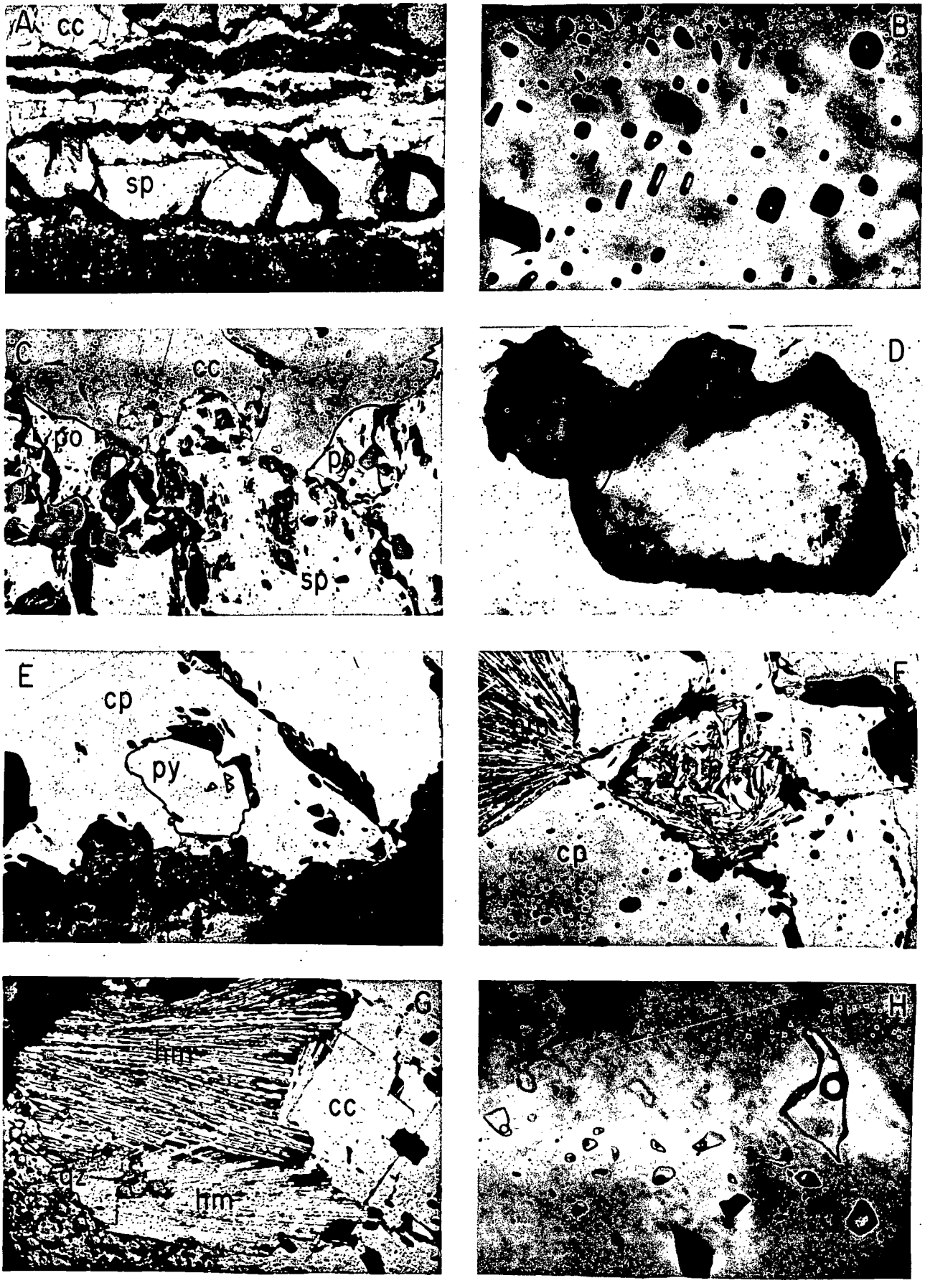
A
cc
sp
B
C
cc
po
po
sp
D
E
cp
py
F
cp
G
hm
cc
qz
hm
H

Unfortunately, no examples of crosscutting relationships between type 1 and 2 veins were observed in the cores, probably because the scattered cores represent less than 7 percent of the drilled interval. However, we believe that the type 2 veins are younger, for several reasons. Texturally, the vertical fracture zones with type 2 veins appear to represent modern, open fracture systems that are presently interacting with the geothermal reservoir brines. This is also supported by the fact that fragments of porous reservoir rocks ejected during well S2-14 flow zone tests were type 2 in character (epidote-pyrite-hematite), as mentioned above. Additionally, fluid-mineral equilibria calculations indicate that the modern brines are near equilibrium with the type 2 vein assemblage epidote-chlorite-pyrite-hematite (McKibben and Elders, 1985; Charles et al., 1988; Caruso et al., 1988). Finally, the fluid inclusion data presented below also support the inference that type 2 veins are younger.

Fluid Inclusion Data

Freezing and heating measurements were made on ≃200 fluid inclusions in calcite, sphalerite, and quartz from vertical fracture zones 1, 2, 3, 4, and 7; detailed descriptions are given in Andes (1987). Examples of the inclusions are shown in Figure 4B and H. All of the inclusions measured were two phase and liquid dominated; a few vapor(?)-rich or empty inclusions were found in zones 1, 3, and 4, but they showed no detectable phase changes upon freezing or heating. They may have leaked during sample polishing. Eutectic melting temperatures for the fluid inclusions had an average value of −52°C, as expected on the basis of the Na-Ca-K-Cl-dominated nature of modern brines (Table 1).

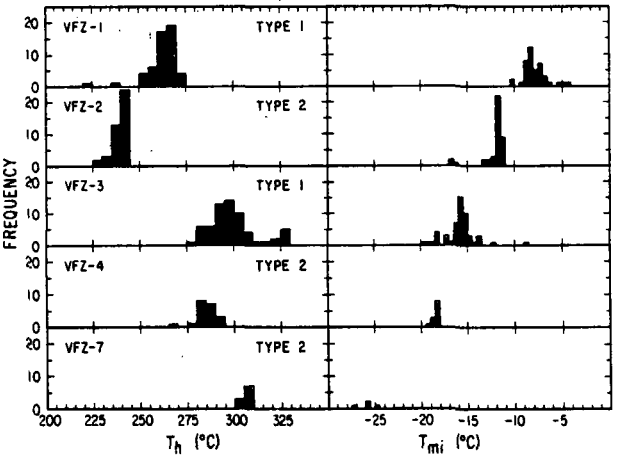

FIG. 5. Histograms showing homogenization temperatures (T_h) and final ice melting temperatures (T_{mi}) measured on fluid inclusions in vertical fracture zones (VFZ) 1, 2, 3, 4, and 7.

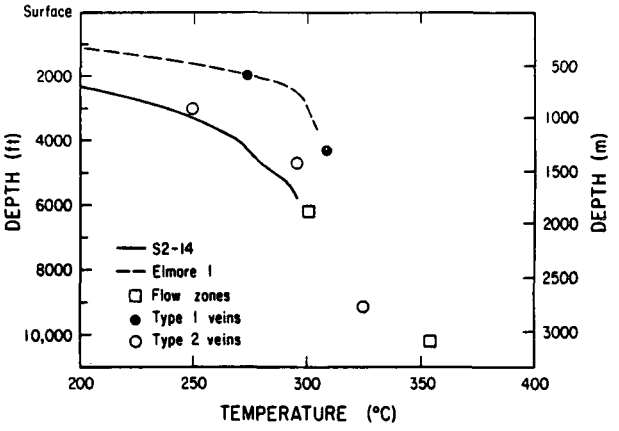

FIG. 6. Plot of mean fluid inclusion trapping temperature versus depth, based on data in Figure 5. Homogenization temperatures were corrected to trapping temperatures by assuming hydrostatic pressure at depth, because most flow zones in Salton Sea geothermal wells exhibit near-hydrostatic shut-in pressures. The dashed line shows a temperature profile from well Elmore 1 (Helgeson, 1968) located near the hot, central part of the modern system. The solid line shows the modern temperature profile measured downhole in well S2-14 (Sass et al., 1987).

Fluid temperatures and salinities

Fluid inclusion homogenization temperatures and ice melting temperatures are shown in Figure 5. There were no systematic differences in T_h and T_{mice} between inclusions interpreted as primary or secondary. Figure 6 shows a summary plot of mean trapping temperature versus depth based on the data in Figure 5. This figure provides evidence for thermal and temporal differences between the vertical fracture zones with type 1 or type 2 veins, because the fluid inclusion trapping temperatures define two different temperature profiles. The temperatures of the fracture zones with type 1 veins fall along a high-temperature gradient similar to that now found only in wells from the hot central part of the modern Salton Sea geothermal system, such as Elmore 1. The temperatures of the fracture zones with type 2 veins and the two flow tests fall along a more moderate temperature gradient that is identical to the modern downhole temperature measurements in this peripheral part of the system.

From the fluid inclusion and textural data, we conclude that the type 1 vein fracture zones represent an early vein system formed when the part of the geothermal system penetrated by State 2-14 was as hot as the central part of the modern system is now. This vein system is presently sealed and is not interacting with the modern brines. The type 2 vein fracture zones represent an open vein set that is forming now from the modern brines under a moderate temperature gradient. Therefore, the upper 2 km of this part of the geothermal system

appears to have cooled by as much as 100°C since formation of the type 1 vein fracture zones. Recent oxygen isotope studies of authigenic carbonates from State 2-14 support this interpretation of a high paleogeothermal gradient (Sturtevant and Williams, 1987). We next discuss the relation between modern brine distribution and type 2 vein mineralization.

Mineralization at a Brine Interface

Figure 7 shows a plot of mean fluid inclusion salinity versus depth, based on the data in Figure 5. Also shown are the total dissolved solids of brines analyzed from the two S2-14 flow-zone tests. One might conclude from this figure that the salinity of fluids existing within the type 1 and 2 vein systems increased progressively with depth in the upper 2 km but became constant at greater depths. However, well production data indicate that two distinctly different geothermal fluids exist in the modern Salton Sea geothermal system, separated by a sharp interface (Williams and McKibben, 1988). Figure 8 is a histogram of the salinities of fluids from 62 wells in and near the geothermal system, showing that geothermal fluids are bimodal in salinity: shallow fluids contain less than 11 wt percent total dissolved solids (avg 5%), whereas deep brines contain greater than 17 wt percent total dissolved solids (avg 23%). No individual flow zones produce brines with intermediate salinities, although a few wells produce mixed fluid from multiple depths (Fig. 8). This bimodality is also reflected in the two representative fluid analyses given in Table 1, having 6 and 26 wt percent total dissolved solids, respectively. The shallow fluids have much lower metal contents than the deep brines, because they have lower salinities and a higher oxidation state (Williams and McKibben, 1988).

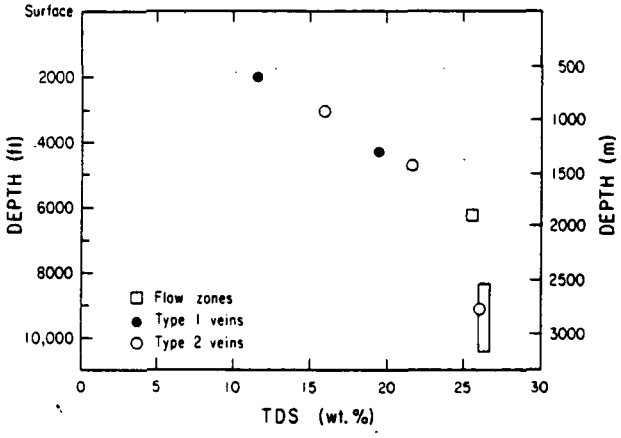

FIG. 7. Plot of mean equivalent total dissolved solids (wt%) versus depth for vein fluid inclusions, based on data from Figure 5 and the two flow zone fluids. Equivalent total dissolved solids (TDS) of the inclusion fluids were determined by treating them as $NaCl$-$CaCl_2$-H_2O equivalent fluids with a molal ratio of $NaCl/CaCl_2$ equal to the molal ratio of $(NaCl + KCl)/CaCl_2$ in typical Salton Sea geothermal system hypersaline brines (e.g., Table 1). This $NaCl/CaCl_2$ ratio yields a binary section through the ternary $NaCl$-$CaCl_2$-H_2O system that can be used to calculate total dissolved solids from $T_{m_{ice}}$, analogous to determining total dissolved solids from $T_{m_{ice}}$ in the $NaCl$-H_2O system (Roedder, 1984). The exact depth of origin of fluids during the second flow test is uncertain, but the rectangle encompasses the possible range. An approximate corrected total dissolved solids amount for the contaminated fluid was determined by Michels (1986).

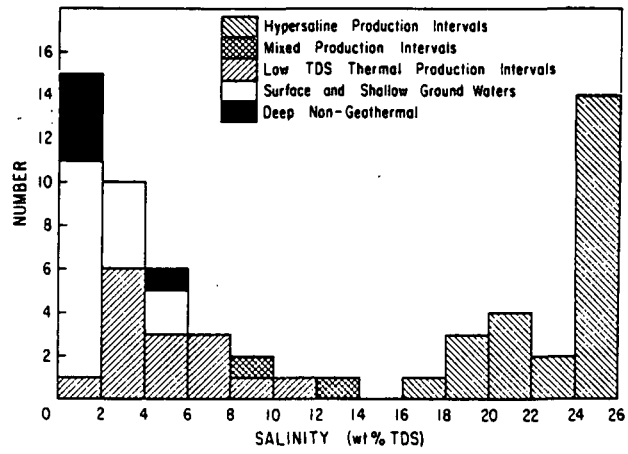

FIG. 8. Histogram showing salinity of fluids produced from 62 wells in the Salton Sea geothermal system and surrounding area (modified from Williams and McKibben, 1988). Geothermal brines are bimodal in their salinity distribution, with shallow brines less than 12 wt percent and deep brines more than 16 wt percent. A few wells produced mixed fluids from multiple depths.

Williams and McKibben (1988) demonstrated that a relatively sharp subhorizontal interface between the two fluid types exists within the modern geothermal system. Figure 9 shows the data for geothermal fluids in Figure 8 plotted as salinity versus depth, segregated according to geographic location across the geothermal field. The interface is shallowest in the center of the field; its depth varies systematically across the field, generally paralleling the 250°C isothermal surface.

Within the eastern portion of the geothermal system where well S2-14 is located, the brine interface occurs at a depth of 900 to 1,500 m. Comparison with the data in Figure 7 indicates that it is over this same depth range that the fluid inclusions of type 2 veins record a sharp salinity gradient, with salinities that are intermediate between the bimodal salinities of the production brines. This apparent salinity gradient recorded by inclusions must be the result of transient mixing between the two fluid types rather than of a static brine stratification. We conclude that the abundant vein ore minerals found over this interfacial depth range in well S2-14 were

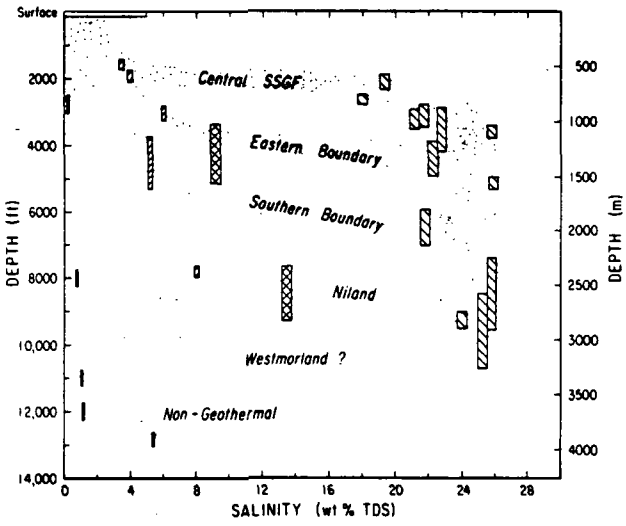

FIG. 9. Plot of salinity versus depth for geothermal fluids from wells in Salton Sea geothermal field (SSGF) and surrounding area, based on data in Figure 8 (modified from Williams and McKibben, 1988). Key to symbols is the same as in Figure 8. Stippled bands group shallow and deep fluid production zones according to geographic location in the geothermal field, effectively illustrating the changing depth of the inferred brine interface across the geothermal field. Niland is located immediately northeast of the SSGF.

precipitated at the interface between the two fluid types, trapping fluids with intermediate salinities due to advective or diffusional mixing. Abundant vein ore mineralization also occurs at this depth in nearby wells (e.g., River Ranch 1, McKibben and Elders, 1985). The active seismicity and magmatism in the geothermal system provide a favorable environment for episodic fracturing and fluid mixing.

Discussion

We propose that type 1 and 2 veins formed during a cycle of heating, upwelling, cooling, and descent of a hypersaline brine diapir that is also responsible for the pervasive greenschist facies metamorphism of the Salton Sea geothermal system host rocks. Rex (1985) has proposed that a deep hypersaline brine reservoir extends over an area of 1,000 km^2 in the Imperial Valley, built up over time by downward percolation of partially evaporated lake waters and ground waters that had redissolved salina salt formed in the closed Salton basin. Dissolution of buried evaporites also has increased the salinity of basin fluids (McKibben et al., 1988). Occurring at depths of more than 4 km in nonthermal areas, the hypersaline brine rises to depths as shallow as 1 km in the geothermal system due to heating. Heating is caused by rift-related magmatic intrusion and seismicity at depth in the Salton trough, expressed at the surface by the arc of rhyolite domes. Intrusive diabase dikes or sills were encountered at the base of well S2-14 (Elders, 1987) and are found at depth in other geothermal wells in the Salton trough (Browne and Elders, 1976; Elders and Cohen, 1983).

A model for heating, upwelling, and mixing of fluids in the Salton Sea geothermal system is shown in Figure 10. Prior to magmatic intrusion, hypersaline brine lies at depths greater than 4 km as suggested by Rex (1985). Rift-related magmatism causes fracturing, heating, and the expulsion of reduced connate fluids in the sediments, resulting in formation of calcite-dominated type 1 veins. CO_2 loss results in sulfide deposition, and carbonate cementation around the veins seals off the local wall rocks from further alteration. Following behind the rising thermal front, the hypersaline brine wells up through the reservoir rocks, perhaps with further heating and fracturing caused by additional intrusions. Type 2 mineralization occurs in fractures at the ascending fluid interface due to eddy mixing between unlike fluids; cooling, dilution, and slight oxidation of hypersaline brine cause sulfide deposition. The hypersaline brine rises to a point of density-temperature stabilization and equilibrates with the wall rock that it has infiltrated, resulting in pervasive epidote-chlorite metamorphism of sediments. It then begins to cool and descend. Late-stage hematite mineralization occurs in type 2 veins during brine descent as shallower, oxidized fluid is drawn in, permeating rocks that had equilibrated with the hypersaline brine at its maximum ascent. This late-stage cooling is consistent with the fluid inclusion temperature data in Figure 6.

This model for the formation of a hypersaline brine diapir in the Salton Sea geothermal system is supported by Hele-Shaw laboratory analogue experiments on the heating of salinity-stratified fluids (Henley and Thornley, 1979). As a diapiric interface rises, fluids convect separately and in opposite directions as shown in Figure 10, promoting mixing at the interface due to eddy currents. Although local variations in permeability and porosity will certainly result in complications, the simple model is applicable to a reservoir that is a fractured porous medium on a large scale.

If our model is accurate, then it also has important implications for the interpretation of fluid inclusion data in fossil hydrothermal systems and ore deposits formed by repetitive brine upwelling in paleoenvironments similar to the Salton Sea system. During long periods of seismic and magmatic quiescence between intrusive events, fluid types equilibrate with their host rocks in a steady state configuration. Hypersaline brine lies at depth well below the level of interface mineralization. Fluid inclusions may not be trapped during these long-term periods of passive water-rock equilibration, due to slow crystal

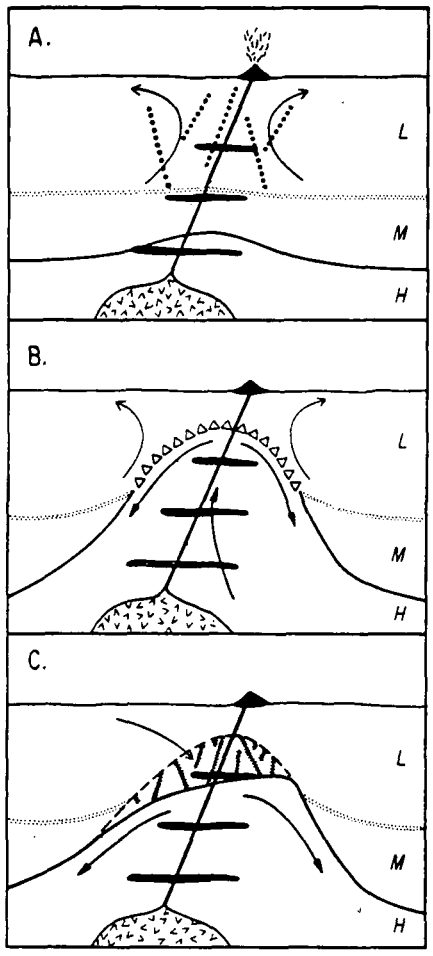

FIG. 10. Schematic cross-sectional cartoon of our model for mineralization by brine upwelling and mixing in the Salton Sea geothermal system (SSGS). Arrows indicate directions of fluid movement. Prior to magmatic intrusion, hypersaline brine (H) lies at depths greater than 5 km, overlain by moderate-salinity (M) and low-salinity (L) fluids. A. Intrusion causes fracturing, heating, and the expulsion of reduced connate fluids, forming type 1 veins (large dotted lines). B. Following the rising thermal front, an ascending diapir of hypersaline brine interacts with and displaces moderate- and low-salinity fluids, forming type 2 mineralization in fractures that transect the rising fluid interface (triangles). Eddy mixing occurs at the fluid interface due to counter-rotation of the fluids (Henley and Thornley, 1979). Hypersaline brine rises to a maximum density-stabilized depth, pervasively altering the invaded host rocks to greenschist facies assemblages. C. Upon cooling, the brine diapir begins to descend, drawing in cooler, oxidized waters and forming late-stage hematite in the type 2 veins (hatchured lines). The Salton Sea geothermal system appears to be in this latter mode of retrograde brine descent at the present time.

growth rates. However, during periodic magmatic intrusion and seismic fracturing, hypersaline brine ascends and nonsteady state mixing with shallower fluids occurs in newly opened fractures. Abundant fluid inclusions are trapped in vein minerals due to rapid, nonequilibrium crystal growth. The majority of fluid inclusions in veins thus preserve intermediate salinities generated during transient mixing phenomena rather than end-member fluid compositions. Therefore, fluid inclusion data from the mineralized zone should be interpreted cautiously when reconstructing the long-term fluid configuration in fossil hydrothermal systems formed in environments similar to the Salton Sea geothermal system.

Ore formation in the Salton Sea geothermal system is caused by a coincidence of several geologic and tectonic factors: entry of a major river into an active rift zone, deposition of metal-bearing deltaic sediments to form a closed-basin sedimentary environment, evaporation leading to saline lake waters and episodic evaporite formation, and injection of heat and elements by rift-related magmatic intrusions at depth (McKibben et al., 1987). These processes lead to leaching of metals and salt from the deltaic host sediments and the formation of hot hypersaline brines and hydrothermal ore minerals.

It is important to bear in mind that the Salton Sea system is geologically a very young feature. Although the vein ore mineralization is currently subeconomic, it may be an ore deposit in the making. Repetition through time of our proposed cycle of intrusion, heating, brine upwelling, cooling, and descent could eventually deposit several generations of vein ore minerals in sufficient quantities to form an economic ore deposit.

It is also interesting to speculate on what would happen if the metalliferous hypersaline brine in the Salton Sea system were suddenly vented onto the sediment surface by rapid heating or tectonic processes. If vented onto the floor of an anoxic, H_2S-laden lake, a massive stratiform exhalative sulfide deposit might be formed. The Salton Sea geothermal system and Salton trough thus have potential applications to modeling the formation of strata-bound ore deposits formed in paleorift zone environments, such as the Zambian copper belt, McArthur River, Mount Isa, Sullivan, White Pine, etc. (e.g., Annels, 1984; Cluzel and Guilloux, 1986; Raybould, 1978; Williams, 1978). However, the modern Salton Sea is relatively well mixed and aerobic. Venting of the hypersaline brine into such a lake might result instead in formation of a stratiform deposit containing metal oxides as well as sulfides. Perhaps the Salton Sea geothermal system and Salton trough can be viewed as a potential analogue for rift environments where exhalative processes resulted in the formation of iron-formations or even Olympic Dam-type deposits (Roberts and Hudson, 1983).

Because the Salton Sea system is an active example of well-characterized mineralization forming by mixing of two fluids whose chemistry is known, it

provides an ideal candidate for testing and refining geochemical codes for fluid-mineral interaction and reaction progress. We are beginning such modeling efforts, with the goal of reproducing the observed vein parageneses. However, modeling of speciation and activity coefficients in the Salton Sea geothermal system brines is made difficult due to their very saline nature. Only a few water molecules are available per ion in the hypersaline brine!

Conclusions

1. Two types of vertical mineralized fracture zones are present in the eastern portion of the Salton Sea geothermal system penetrated by the S2-14 drill hole: an early, sealed carbonate-dominated vein set (type 1) containing relatively reduced assemblages, and a modern, open silicate-oxide-dominated vein set (type 2) containing relatively oxidized assemblages.

2. Fluid inclusion data indicate that type 1 veins were deposited at relatively high temperatures similar to temperatures that are now found only in the hot central part of the geothermal system to the southwest. Type 2 veins were deposited at lower temperatures that agree with those presently measured downhole. These relations require that the upper 2 km of the system has cooled by as much as 100°C in this peripheral part of the system.

3. Fluid inclusions in veins record an apparent steep gradient in salinity from 900 to 1,500 m, with salinity relatively constant below 1,500 m. The depth of the steep fluid inclusion salinity gradient corresponds exactly to the depth of a sharp interface between shallow, relatively low salinity geothermal fluids and deep, hypersaline geothermal brines inferred from well production data (Williams and McKibben, 1988). Therefore, the vein fluid inclusions are recording mixing between fluid types in vertical fracture systems that transect the brine interface.

4. The abundance of active vein ore mineralization at the depth of this fluid interface indicates that mixing between the two fluid types is a major mechanism for ore deposition in the Salton Sea system. A model for ore formation is proposed, involving thermal upwelling of a hypersaline brine diapir due to magmatic intrusion and seismic fracturing. Heating and expulsion of reduced connate fluids causes formation of the type 1 veins. Following the thermal front, upwelling reduced hypersaline brine reacts with shallower wall rocks and fluids, forming type 2 veins in fractures by mixing at the ascending fluid interface. The hypersaline brine then cools and descends, drawing in cold, oxygenated surface fluids and forming late-stage hematite in type 2 veins. Efforts are currently underway to model this mixing process using geochemical computer codes.

5. Because fluid inclusions in hydrothermal veins in the Salton Sea geothermal system are more likely to record transient, nonsteady state mixing phenomena rather than long-term steady state water-rock equilibration, fluid inclusion data must be used cautiously in interpreting the compositions of end-member fluids in fossil hydrothermal systems formed in environments similar to the Salton Sea system.

Acknowledgments

This study was funded by a U. S. Department of Energy-Office of Basic Energy Science grant DE-FG03-85ER13408 to M.A.M. as part of the multiagency Salton Sea Scientific Drilling Project. We thank W. A. Elders, Salton Sea Scientific Drilling Project chief scientist, for making it possible for so many diverse scientists to participate in the project in spite of seemingly infinite political, bureaucratic, and scientific hurdles. Our ideas on geothermal processes would not have developed and evolved without his perspective and insight. Comments by two *Economic Geology* reviewers resulted in many improvements to the final version of the paper, as did discussion of our ideas with R. W. Henley. Much of the petrographic and fluid inclusion data were collected by J.P.A. in fulfillment of the requirements for a Master of Science degree. Invaluable assistance in field and laboratory work was provided by Jim Mehegan, Pete Collier, Charlie Oakes, and Jose Abreu. Linda Jankov provided expert assistance with photography and drafted all of the figures. This is report 87/27 of the Institute of Geophysics and Planetary Physics, University of California, Riverside.

July 24, November 19, 1987

REFERENCES

Andes, J. P., Jr., 1987, Mineralogic and fluid inclusion study of ore-mineralized fractures in drillhole State 2-14, Salton Sea Scientific Drilling Project: Unpub. M.Sc. thesis, Riverside, Univ. California, 125 p.

Annels, A. E., 1984, The geotectonic environment of Zambian copper-cobalt mineralization: Geol. Soc. London Jour., v. 141, p. 279–289.

Arnal, R., 1961, Limnology, sedimentation, and micro-organisms of the Salton Sea, California: Geol. Soc. America Bull., v. 72, p. 427–478.

Browne, P. R. L., and Elders, W. A., 1976, Hydrothermal alteration of diabase, Heber geothermal field, Imperial Valley, California [abs.]: Geol. Soc. America Abstracts with Programs, v. 8, p. 793.

Caruso, L. J., Bird, D. K., Cho, M., and Liou, J. G., 1988, Epidote-mineralized fractures in the CS 2-14 well: Implications on hydrothermal fluid composition: Jour. Geophys. Research, in press.

Charles, R. W., Janecky, D. R., Goff, F., and McKibben, M. A., 1988, Chemographic and thermodynamic analysis of the parageneses of the major phases in the vicinity of the 6120 ft (1866 m) flow-zone, California State well 2-14: Jour. Geophys. Research, in press.

Cho, M., Liou, J. G., and Bird, D. K., 1988, Prograde phase rela-

tions in the California State 2-14 well meta-sandstones, Salton Sea geothermal field: Jour. Geophys. Research, in press.
Cluzel, D., and Guilloux, L., 1986, Hydrothermal character of the Shaba Cu-Co-U mineralization [abs.]: Canadian Mineralogist, v. 24, p. 182.
Craig, H., 1966, Isotopic composition and origin of the Red Sea and Salton Sea geothermal brines: Science, v. 154, p. 1544–1548.
—— 1969, Discussion: Source fluids for the Salton Sea geothermal system: Am. Jour. Sci., v. 267, p. 249–255.
Doe, B. R., Hedge, C. E., and White, D. E., 1966, Preliminary investigation of the source of lead and strontium in deep geothermal brines underlying the Salton Sea geothermal area: ECON. GEOL., v. 61, p. 462–483.
Elders, W. A., 1979, The geological background of the geothermal fields of the Salton trough, *in* Elders, W. A., ed., Geology and geothermics of the Salton trough: Riverside, Univ. California, Campus Museum Contr. 5, p. 1–19.
—— 1987, Igneous rocks in the SSSDP well and in the Salton trough [abs.]: Am. Geophys. Union Trans., v. 68, p. 446.
Elders, W. A., and Cohen, L. H., 1983, The Salton Sea geothermal field, California, as a near-field natural analog of a radioactive waste repository in salt: Columbus, Ohio, Battelle Memorial Inst., Office Nuclear Waste Isolation, BMI/ONWI-513, 139 p.
Elders, W. A., Rex, R. W., Meidav, T., Robinson, P. T., and Biehler, S., 1972, Crustal spreading in southern California: Science, v. 178, p. 15–24.
Helgeson, H. C., 1968, Geologic and thermodynamic characteristics of the Salton Sea geothermal system: Am. Jour. Sci., v. 266, p. 129–166.
Henley, R. W., and Thornley, P., 1979, Some geothermal aspects of polymetallic massive sulfide formation: ECON. GEOL., v. 74, p. 1600–1612.
Herzig, C. T., Mehegan, J. M., and Stelting, C. E., 1988, Lithostratigraphy of an active pull-apart basin: Salton Sea Scientific Drilling Project: Jour. Geophys. Research, in press.
McDowell, S. D., and Bornhorst, L. E., 1985, Geochemical changes during geothermal alteration of shale, Salton Sea geothermal field [abs.]: Am. Geophys. Union Trans., v. 66, p. 1144.
McDowell, S. D., and Elders, W. A., 1980, Authigenic layer silicate minerals in borehole Elmore 1, Salton Sea geothermal field, California, U. S. A.: Contr. Mineralogy Petrology, v. 74, p. 293–310.
—— 1983, Allogenic layer silicate minerals in borehole Elmore #1, Salton Sea geothermal field, California: Am. Mineralogist, v. 68, p. 1146–1159.
McDowell, S. D., and Paces, J. B., 1985, Carbonate alteration minerals in the Salton Sea geothermal system, California, USA: Mineralog. Mag., v. 49, p. 469–479.
McKibben, M. A., 1986, Hydrothermal sulfide minerals in the Salton Sea geothermal system, Imperial Valley, California: Stanford Univ. Pub., Geol. Sci., v. 20, p. 161–164.
McKibben, M. A., and Elders, W. A., 1985, Fe-Zn-Cu-Pb mineralization in the Salton Sea geothermal system, Imperial Valley, California: ECON. GEOL., v. 80, p. 539–559.
McKibben, M. A., Williams, A. E., Elders, W. A., and Eldridge, C. S., 1986, Metamorphosed Plio-Pleistocene evaporites and the origins of sulfur and salinity in the Salton Sea geothermal brines [abs.]: Am. Geophys. Union Trans., v. 67, p. 1258.
McKibben, M. A., Williams, A. E., Elders, W. A., and Eldridge, C. S., 1987, Saline brines and metallogenesis in a modern sediment-filled rift: The Salton Sea geothermal system, California, U. S. A.: Appl. Geochemistry, v. 2, p. 563–578.
McKibben, M. A., Williams, A. E., and Okubo, S., 1988, Metamorphosed Plio-Pleistocene evaporites and the origins of hypersaline brines in the Salton Sea geothermal system, California: Fluid inclusion evidence: Geochim. et Cosmochim. Acta, v. 52, p. 1057–1067.
Michels, D. E., 1986, SSSDP fluid composition at first flow of State 2-14: Geothermal Resources Council Trans., v. 10, p. 461–465.
Muffler, L. J. P., and White, D. E., 1969, Active metamorphism of upper Cenozoic sediments in the Salton Sea geothermal field and the Salton trough, southeastern California: Geol. Soc. America Bull., v. 80, p. 157–182.
Raybould, J. G., 1978, Tectonic controls on Proterozoic stratiform copper mineralization: Inst. Mining Metallurgy Trans., v. 87, sec. B, p. B79–B86.
Rex, R. W., 1972, Cooperative investigation of geothermal resources in the Imperial Valley area and their potential value for desalting of water and other purposes: U. S. Dept. Interior, Bur. Reclamation, Final Rept. Contract 14-06-300-2194, 267 p.
—— 1983, The origin of the brines of the Imperial Valley, California: Geothermal Research Council Trans., v. 7, p. 321–324.
—— 1985, Temperature-chlorinity balance in the hypersaline brines of the Imperial Valley, California, *in* Stone, C., ed., 1985 International symposium on geothermal energy: Davis, California, Geothermal Resources Council, p. 351–356.
Roberts, D. E., and Hudson, G. R. T., 1983, The Olympic Dam copper-uranium-gold deposit, Roxby Downs, South Australia: ECON. GEOL., v. 78, p. 799–822.
Roedder, E., 1984, Fluid inclusions: Rev. Mineralogy, v. 12, 644 p.
Sass, J. H., and Elders, W. A., 1986, Salton Sea Scientific Drilling Project: Scientific program: Geothermal Research Council Trans., v. 10, p. 473–478.
Sass, J. H., Hendricks, J. D., Priest, S. S., and Robison, L. C., 1987, Temperatures and heat flow for the State 2-14 well, Salton Sea Scientific Drilling Program [abs.]: Am. Geophys. Union Trans., v. 68, p. 454.
Skinner, B. J., White, D. E., Rose, H. J., Jr., and Mays, R. E., 1967, Sulfides associated with the Salton Sea geothermal brine: ECON. GEOL., v. 62, p. 316–330.
Sturtevant, R. G., and Williams, A. E., 1987, Oxygen isotopic profiles of the State 2-14 geothermal well: Evidence for a complex thermal history [abs.]: Am. Geophys. Union Trans., v. 68, p. 445.
White, D. E., 1968, Environments of generation of some base-metal ore deposits: ECON. GEOL., v. 63, p. 301–335.
—— 1981, Active geothermal systems and hydrothermal ore deposits: ECON. GEOL. 75TH ANNIV. VOL., p. 392–423.
White, D. E., Anderson, E. T., and Grubbs, D. K., 1963, Geothermal brine well: Mile-deep drill hole may tap ore-bearing magmatic water and rocks undergoing metamorphism: Science, v. 139, p. 919–922.
Williams, A. E., and McKibben, M. A., 1988, A brine interface in the Salton Sea geothermal system, California: Fluid geochemical and isotopic distribution: Riverside, Univ. California, rept. 87/31, 40 p.
Williams, N., 1978, Studies of the base metal sulfide deposits at McArthur River, Northern Territory, Australia: I. The Cooley and Ridge deposits: ECON. GEOL., v. 73, p. 1005–1035.
Winker, C. D., and Kidwell, S. M., 1986, Paleocurrent evidence for lateral displacement of the Pliocene Colorado River delta by the San Andreas fault system, southeastern California: Geology, v. 14, p. 788–791.

SECTION D

Reprints selected from GEOTHERMAL RESOURCES COUNCIL TRANSACTIONS, VOLUME 12, 1988.

Herzig, C.T., and Elders, W.A., "Probable Occurrence of the Bishop Tuff in the Salton Sea Scientific Drilling Project Borehole, Salton Sea Geothermal System, California," pp 115-120.

McKibben, M.A., Eldridge, C.S., and Williams, A.E., "Sulfur and Base Metal Transport in the Salton Sea Geothermal System," pp 121-125.

Williams, A.E., "Delineation of a Brine Interface in the Salton Sea Geothermal System, California," pp 151-157.

PROBABLE OCCURRENCE OF THE BISHOP TUFF IN THE SALTON SEA SCIENTIFIC DRILLING PROJECT BOREHOLE, SALTON SEA GEOTHERMAL SYSTEM, CALIFORNIA

Charles T. Herzig and Wilfred A. Elders

Institute of Geophysics and Planetary Physics
University of California
Riverside, California 92521

ABSTRACT

In spite of extensive drilling, the age of the geothermal systems in the Salton Trough and the rocks in which they occur is poorly known. The chemical composition of a silicic tuff recovered in the State 2-14 research borehole of the Salton Sea Scientific Drilling Project suggests that it is correlative with the Durmid Hill tuff cropping out 25 km NE. In turn, both of these volcanic rocks appear to be deposits of the Bishop Tuff, erupted 0.7 Ma ago from the Long Valley caldera of central California. If the age of the State 2-14 tuff is 0.7 Ma, its occurrence at a depth of 1704 m indicates a combined sedimentation and subsidence rate of 2.4 mm/yr for this part of the Salton Sea Geothermal System during this time interval, and that the Plio-Pleistocene boundary should occur at a depth of about 3.8 km in this region of the Salton Trough.

INTRODUCTION

Age control is very poor for the sedimentary rocks in the subsurface within the geothermal fields of the Salton Trough, an active rift zone lying between the San Andreas Fault system to the north and the Gulf of California to the south (Elders, et al, 1972) (Figure 1). Ingle (1982) tentatively assigned the Plio-Pleistocene boundary to a depth of about 2000 m in the Cerro Prieto geothermal field (Figure 1) based on microfossils. North of the international border, van de Kamp (1973) reported ^{14}C ages for gastropods and wood fragments from the near-surface. However, extrapolating these age data deeper in the subsurface may not be very useful, because the short-term sedimentation and subsidence rates in the Salton Trough are probably not constant over millions of years due to the episodic nature of sedimentation in this arid region (van de Kamp, 1973). Thus, we are examining materials from the subsurface which could be dated to serve as: (a) time-stratigraphic markers yielding information about the long-term sedimentation and subsidence rates in the Salton Trough; (b) markers for structural correlation within the geothermal fields and with the rocks at the surface around the margins of the Salton Trough; (c) constraints on the depths at which the boundaries between epochs, such as the Plio-Pleistocene, occur.

The 3.22-km-deep research borehole, (California) State 2-14, of the Salton Sea Scientific Drilling Project (SSSDP), drilled into the active Salton Sea Geothermal System (SSGS), provided cores and cuttings of sedimentary rocks, and of three occurrences of igneous rocks (Figure 2) (Elders and Sass, 1988). The sedimentary rocks recovered, partly altered to greenschist and lower amphibolite facies mineral assemblages, consist dominantly of lacustrine shale units up to 100 m thick, with interbedded fluvial-deltaic sandstones and pebbly mudstones ranging in thickness from a few cm to 10 m (Figure 2) (Herzig, et al, 1988). Based upon the lithologies and stratigraphic occurrence of the (meta)sedimentary rocks observed, the rocks are correlated with the Plio-Pleistocene, Borrego-Brawley Formation (Babcock, 1969; 1974; Dibblee, 1954).

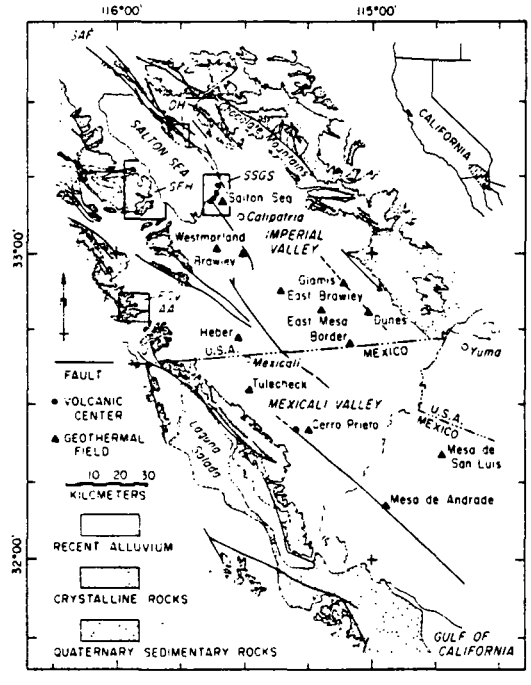

Figure 1. Generalized map showing the major tectonic features in the region of the Salton Trough. AA: Alverson andesite; DH: Durmid Hill; FCV: Fish Creek-Vallecito; J: Jacumba; SAF: San Andreas Fault; SFH: San Felipe Hills; SSGS: Salton Sea Geothermal System.

The three intervals of igneous rocks penetrated in the SSSDP borehole include a silicic tuff cored at 1704 m depth; and two altered sills of diabase at 2880 and 2896 m depth (Herzig and Elders, in review). The sills may be high-level occurrences of the new oceanic crust believed to be forming beneath the Salton Trough (Fuis et al, 1984). The silicic tuff has trace element compositions which suggest that it may be a deposit of the Bishop Tuff, erupted from the Long Valley caldera of central California 0.7 Ma ago (Izett, et al, 1970; Borchardt, et al, 1972; Hildreth, 1979).

Deposits of the Pleistocene Bishop Tuff, a chemically and petrographically distinctive ash flow tuff, have been identified as far east as Nebraska (Izett, et al, 1970; Borchardt, et al, 1972). Merriam and Bischoff (1975) suggested that a silicic ash deposit at Durmid Hill in the Salton Trough (Figure 1) is correlative with the Bishop Tuff. The certain identification of this time-stratigraphic unit in the subsurface of the SSGS would provide an important age constraint for this region of the Salton Trough. The purpose of this note is to present petrographic and geochemical data which suggest that the silicic tuff at 1704 m depth in the State 2-14 borehole is correlative with the Durmin Hill tuff, and that both are in turn deposits of the Bishop Tuff.

PETROLOGY

The altered tuff from the State 2-14 borehole is extremely homogeneous and lacks primary depositional structures, a feature differentiating it from the metasedimentary rocks. Based on its wireline characteristics, the light grey to buff-colored silicic tuff may be up to a meter thick, but only 0.25 m of its lower contact with the metasedimentary rocks was cored. It is composed of feldspar and quartz grains, < 0.07 to 0.15 mm in size, within a microcrystalline groundmass too fine to identify optically. Quartz grains consist dominantly of clear, fractured bipyramids of obvious volcanic origin. However, some quartz present appears to be reworked grains derived from underlying sediments. Crystals of chlorite replace primary biotite. Opaque minerals are scarce. Volcanic glass has not been observed either optically or by x-ray diffraction, however, the textures of the microcrystalline groundmass suggest it is most likely devitrified and altered glass.

The cored interval of tuff is cut by subvertical, millimeter-wide fractures, which are sealed with epidote and adularia deposited from hydrothermal fluids which circulated through the fractures. Minor amounts of authigenic epidote and sphene occur in the groundmass, and plagioclase has been partially replaced by adularia.

GEOCHEMISTRY

Table 1 shows the chemical composition of the silicic tuff from the SSSDP borehole compared to

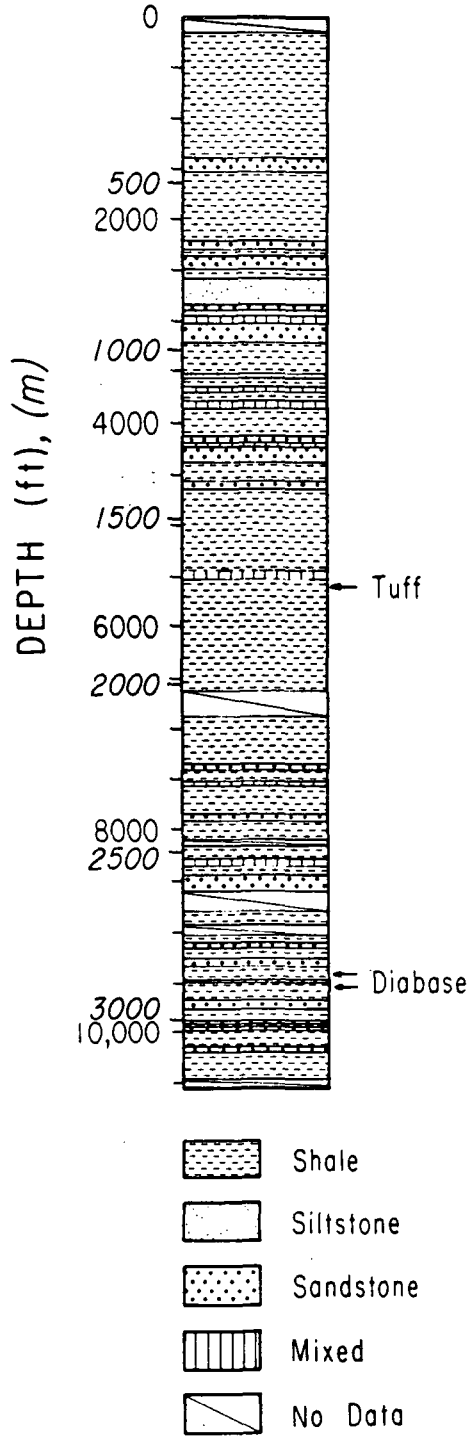

Figure 2. Simplified lithostratigraphic column of the State 2-14 research borehole showing the stratigraphic position of the silicic tuff and the diabase sills.

some unaltered tuffs. These include the nearest known outcrop of tuff to the State 2-14 well, the Durmid Hill tuff (Babcock, 1969; 1974), occurring 25 km to the northeast (Figure 1), and the Bishop Tuff, Green Mountain ash, and Pearlette-like ash. The latter three silicic ashes are the deposits of the three major rhyolitic volcanic centers active during the Pleistocene in the western United States (Izett, et al, 1970; Borchardt, et al, 1972; Hildreth, 1979). The materials erupted from these volcanic centers are clearly distinguishable from each other by their petrographic and chemical properties. The State 2-14 and Durmid Hill silicic tuffs are compared with these three, unique ashes because the latter represent the deposits of the possible sources for the tuffs in the Salton Trough. Each differs to such a degree in their petrographic and chemical characteristics that the eruptive center of the State 2-14 and Durmid Hill tuffs may be fingerprinted.

The abundances of oxides, such as SiO_2 and Al_2O_3, are similar among the nine rocks. However, the State 2-14 tuff is enriched in TiO_2, MgO, K_2O, and iron oxides in comparison to the tuffs from the Durmid Hill and elsewhere. We believe that the enrichment of these oxides in the State 2-14 tuff reflects the formation of secondary, hydrothermal minerals, such as sphene, chlorite, adularia, and pyrite, respectively.

The trace elements, Sr and Ba, are strongly enriched in the State 2-14 tuff in comparison to Durmid Hill and other tuffs (Table 1), also reflecting the hydrothermal alteration of the subsurface rock. Other trace elements, such as Zr, Sc, Cr and Ni appear to be slightly enriched and Rb appears slightly depleted in the State 2-14 tuff in comparison to the unaltered tuffs.

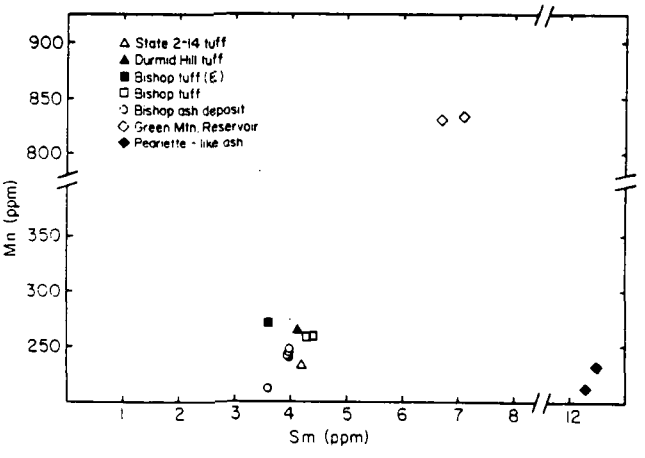

Figure 3. Variation diagram of Mn versus Sm for the silicic ash flow tuffs. Diagram after Borchardt, et al, (1972). Additional data not shown in Table 1 from Borchardt, et al, (1972).

Borchardt, et al (1972) used discriminant function analysis to determine that Mn and Sm were the most useful elements for distinguishing chemically between the Bishop, Green Mountain Reservoir, and Pearlette-like ashes. A plot of Mn versus Sm for the State 2-14 and Durmid Hill tuffs, and the other rocks listed in Table 1 is therefore shown in Figure 3. The similarity of the Mn and Sm abundances of the State 2-14 and Durmid Hill tuffs and of the Bishop ash units is obvious. However, because the manganese concentration in the hydrothermal brines of the SSGS is around 1000 ppm, the Mn abundance of the State 2-14 tuff may have been changed by hydrothermal alteration. However, the tight clustering of the State 2-14 tuff with the Bishop Tuff units suggests here that the change in Mn composition has been slight. As will be discussed below, the rare earth elements also support this assertion.

The chondrite-normalized, rare earth element (REE) patterns of the State 2-14 tuff, and of the other tuffs discussed above are shown in Figure 4. The REE pattern of the State 2-14 tuff and that of the Durmid Hill tuff closely resemble each other, and apart from a slight difference in Eu depletion, also resemble the patterns of the Bishop ash flow tuff units. The reported differences in the size of the Eu anomalies could in part be due to the use of different analytical techniques between this and earlier studies. Another possibility explaining the small differences in Eu depletion and the REE patterns is that small amounts of local detrital materials were incorporated into the bedded ash deposits.

DISCUSSION

The Durmid Hill tuff was identified by Merriam and Bischoff (1975) as a deposit of the Bishop ash. They based this correlation upon the presence of biotite phenocrysts in the Durmid tuff, considered to be diagnostic of the Bishop ash (Izett, et al, 1970), and the similar Rb-Sr-Zr abundances. The Rb, Sr, and Zr compositions of the Durmid Hill sample analyzed during this study, along with the abundances of Mn and Sm, and the rare earth elements, are similar to those of the Bishop ash flow tuffs (Table 1). Thus our petrographic and geochemical data support the correlation of the Durmid Hill tuff with the Bishop ash, as suggested earlier by Merriam and Bischoff (1975).

As far as we are aware, the State 2-14 tuff is the first core of pyroclastic rock reported from the subsurface in the Salton Trough. It is likely that tuffs have been overlooked in drill cuttings from other geothermal wells due to their textural similarity to arenitic siltstones. Dating of the State 2-14 tuff is difficult because of its altered nature. However, if it can be correlated with its volcanic source, it could be a useful time-stratigraphic marker.

Because hydrothermal alteration has recrystallized the groundmass of the State 2-14 tuff,

correlation based on petrography and texture is not very easy. However, the presence of chlorite porphyroblasts, believed to be replacing biotite phenocrysts, is consistent with it being the Bishop Tuff. Although hydrothermal alteration has changed some of the major element, Sr, and Ba abundances in the State 2-14 tuff; we believe that the Mn, Sm and other REE abundances represent its primary composition. The concentrations of these elements in the State 2-14 tuff is very similar to that of both the Durmid Hill and Bishop Tuffs, and differs strongly from the other pyroclastic rocks shown in Table 1. Furthermore, the REE pattern of the State 2-14 tuff is nearly identical to that of the Durmid Hill tuff, and both are very similar to the REE patterns of the Bishop ash flow tuffs, with only minor differences in Eu content. These patterns clearly differ from the REE patterns of the other pyroclastics with which they were compared.

Though not shown here, a comparison of the geochemistry of the silicic tuff in the State 2-14 borehole with the rhyolites of the Salton Buttes and dacites of the Cerro Prieto volcanoes (Robinson, et al, 1976; Reed, 1984) (Figure 1), indicates that the State 2-14 tuff cannot be a deposit derived from the volcanoes. Furthermore, given its depth of occurrence, the State 2-14 tuff must be much older than the volcanoes.

CONCLUSION

The geochemical data presented here permits correlation between the State 2-14 and Durmid Hill tuffs, which, in turn, are believed to be deposits of the Bishop Tuff, derived from the Long Valley caldera of central California. This implies that the tuff at 1704 m depth in the State 2-14 research borehole is 0.7 Ma old, and the rate of sedimentation and subsidence in this part of the SSGS would have averaged approximately 2.4 mm/yr for 0.7 Ma. Extrapolating this rate deeper would imply that the Plio-Pleistocene boundary in the SSGS should occur at a depth of approximately 3.8 km, i.e., 600 m deeper than the depth reached by the State 2-14 borehole.

ACKNOWLEDGMENTS

This investigation was supported by NSF grant EAR-8502402 as part of the Salton Sea Scientific Drilling Project, a research drilling project supported by the U.S. Dept. of Energy, the U. S. Geological Survey, and the U.S. National Science Foundation. We thank Linda Jankov who drafted the figures and P. Collier who prepared the thin sections for this study. J.M. Mehegan helped with the interpretation of the geochemistry of the State 2-14 tuff. This paper is UCR/IGPP Report # 88/29.

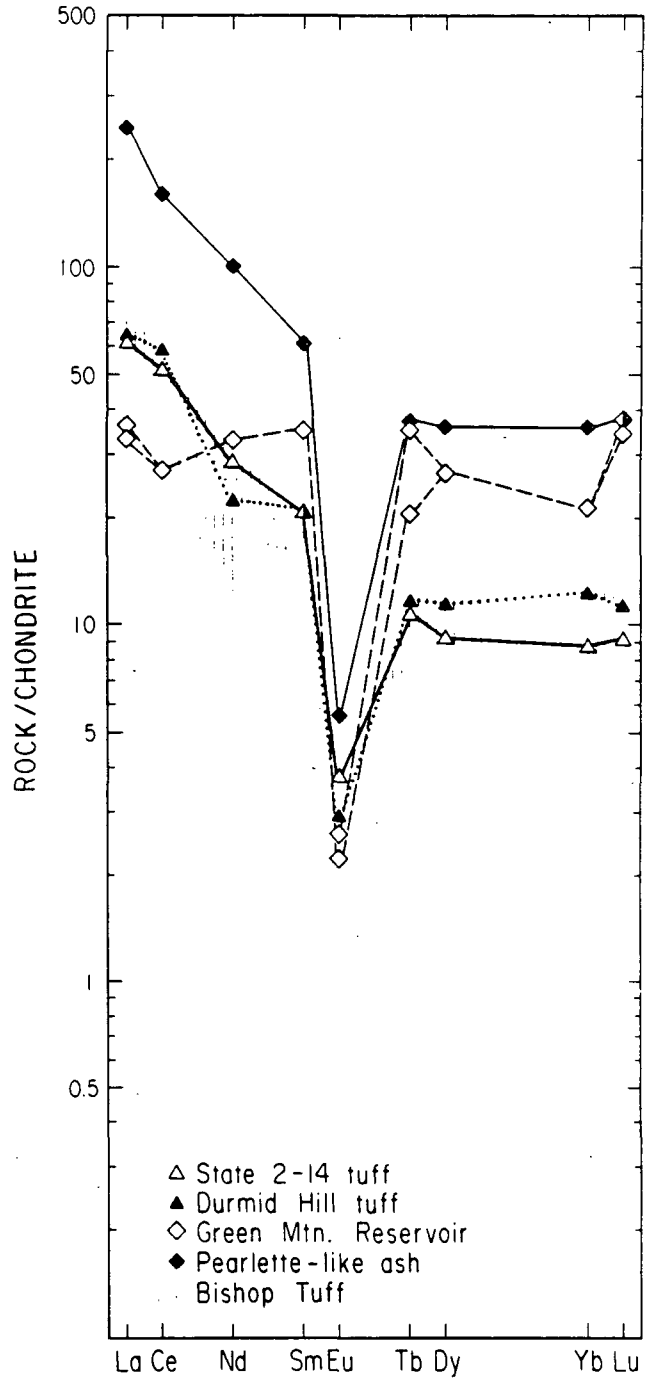

Figure 4. Chondrite-normalized, rare earth element diagram for the silicic ash flow tuffs (normalizing factors from Nakamura, 1974).

Table 1. Whole rock analyses of the State 2-14 and Durmid Hill Tuffs and the Bishop Tuff, Green Mountain Reservoir Ash, and a Pearlette-like Ash.

Sample:	St2-14	DH	Bishop T.[1] (E)	Bishop Ashes[2,3] 3	7	10	G. M. R.[2,3] 12	13	Pear. A.[2,3] 14
SiO_2	74.60	73.81	77.4	72.8	73.2	73.1	71.5	71.5	72.1
TiO_2	0.14	0.07	0.07	0.07	0.07	0.08	0.03	0.07	0.12
Al_2O_3	12.18	12.53	12.3	12.4	11.5	12.1	13.2	13.3	11.7
Fe_2O_3	0.62	0.88							
FeO	0.98	0.38	0.7*	0.7*	0.6*	0.7*	0.4*	0.4*	1.2*
MgO	1.39	0.09	0.01	0.04	0.04	0.08	0.07	0.08	0.02
CaO	0.38	0.43	0.45	0.41	0.42	0.46	0.69	0.67	0.49
Na_2O	3.16	4.14	3.9	3.30	3.28	2.73	3.48	3.50	2.44
K_2O	5.67	3.55	4.8	5.05	4.86	4.59	4.45	4.13	6.11
P_2O_5	0.03	<0.01	0.01	NA	NA	NA	NA	NA	NA
LOI	1.03	2.72		3.98	4.31	4.08	4.68	4.61	3.89
Total	100.18	98.61	99.64	98.75	98.28	97.92	98.50	98.26	98.07
La	20	21	19	17	18	27	11	12	81
Ce	45	51	45	34	31	47	23	23	139
Nd	18	<14	17	20	8	15	21	20	65
Sm	4.21	4.13	3.6	4.0	3.9	3.6	7.1	6.7	12.5
Eu	0.29	0.23	0.05	0.03	0.03	0.10	0.20	0.17	0.46
Tb	0.51	0.56	0.57	0.44	0.37	0.40	1.66	0.97	1.73
Dy	3.14	4.03	3.7	4.1	3.7	3.1	9.2	9.4	12.3
Yb	1.91	2.68	2.6	1.4	1.5	1.3	4.7	4.7	8.0
Lu	0.31	0.38	0.37	0.49	0.45	0.39	1.27	1.18	1.28
Rb	124	169	190	169	153	145	286	267	213
Sr	179	10	<10	8	12	18	18	20	<8
Zr	94	86	85	76	88	75	63	88	177
Ba	1055	84	<10	51	68	106	119	204	179
Mn	233	265	270	249	244	213	834	831	232
Th	19.0	20.9	20.5	19.0	17.9	16.3	14.0	13.7	30.3
U	5.58	7.29	6.5	7.1	6.9	5.8	15.9	14.2	6.7
Hf	4.2	3.8	4.2	3.6	3.3	3.2	4.6	4.5	7.6
Ta	2.6	2.7	2.1	2.1	2.0	1.7	5.4	5.2	3.6
Sc	3.4	2.9	3.0	2.6	2.4	2.2	9.09	8.69	1.40
Cr	4	2	3.0	1.1	2.1	1.9	3.8	2.9	3.0
Ni	6	<5	<3	NA	NA	NA	NA	NA	NA
Zn	36	29	38	NA	NA	NA	NA	NA	NA

Notes: DH: Durmid Hill; G. M. R.: Green Mountain Reservoir; Pear. A.: Pearlette-like ash. Bishop Tuff, (E): Early unit of the Bishop Tuff[1]. Bishop ash bed localities[2,3]: 3: Pleistocene lake beds, Lake Tecopa, Inyo County, Ca.; 7: Harpole Mesa Fm, Grand County, Utah; 10: Ash bed in alluvium, Nuckolls County, Nebraska; 12: Pleistocene deposits, Montrose County, Colo.; 13: Pleistocene deposits, Summit County, Colo.; 14: Type locality of Sappa Fm., Harlan County, Nebraska. Major element analyses of St2-14 and DH samples by ICP; precision stated in Kroneman, et al, (1984). Trace element and REE analyses of St2-14 and DH samples during this study by INAA (Minor, et al, 1981; Garcia, et al 1982). NA: not analyzed. *: total iron as FeO. LOI: Loss on ignition. Major oxides in weight per cent. Trace elements in ppm. References: 1: Hildreth (1979); 2: Izett, et al, (1970); 3: Borchardt, et al, (1972).

REFERENCES

Babcock, E.A., 1969, Structural geology and geophysics of the Durmid area, Imperial Valley, California (Ph. D. dissertation), Riverside, Univ. of California, 145 pp.

Babcock, E.A., 1974, Geology of the northeast margin of the Salton Trough, Salton Sea, California, Geol. Soc. Amer. Bull., v. 85, p. 321-332.

Borchardt, G.A., Aruscavage, P.J., and H.T. Millar, Jr., 1972, Correlation of the Bishop ash, a Pleistocene marker bed, using instrumental neutron activation analysis, J. Sed. Pet., v. 42, p. 301-306.

Dibblee, T.W., 1954, Geology of the Imperial Valley region, California: in Jahns, R.H. (ed.), Geology of California, Chapter 2: Geology of the natural provinces, Calif. Div. Mines Bull., v. 170, p. 21-28.

Elders, W.A., Rex, R., Meidev, T., Robinson, P.T., and S. Biehler, 1972, Crustal spreading in southern California, Science, v.178, p. 15-24.

Elders, W.A., and J. Sass, 1988, The Salton Sea Scientific Drilling Project: Its Scientific Significance: J. Geophys. Res., (in press).

Fuis, G.S., Mooney, W.D., Healy, J.H., McMechan, G.A., Lutter, W.J., 1984, A seismic refraction survey of the Imperial Valley, California: J. Geophys. Res., v. 89, p. 1165-1189.

Garcia, S.R., Hensley, W.K., Denton, M.M., and M.A. Fuka, 1982, An automated multidetector system for instrumental neutron activation analysis of geological and environmental materials: in Atomic and nuclear methods in fossil energy research, Filby, R.H., Carpenter, B.S., and R.C. Ragiani (eds.), p. 133-140.

Herzig, C.T., and W.A. Elders, Igneous rocks of the State 2-14 research borehole: Salton Sea Scientific Drilling Project: J. Geophys. Res., (in review).

Herzig, C.T., Mehegan, J.M., and C.E. Stelting, 1988, Lithostratigraphy of the State 2-14 borehole: Salton Sea Scientific Drilling Project: J. Geophys. Res., (in press).

Hildreth, W., 1979, The Bishop Tuff: evidence for the origin of compositional zonation in silicic magma chambers, Geol. Soc. Amer. Special Paper 180, p. 43-75.

Ingle, J., 1982, Microfaunal evidence of age and depositional environments of the Cerro Prieto section (Plio-Pleistocene), Baja California, Mexico: Report LBL-13897, Lawr. Berk. Lab., Berkeley, Ca.

Izett, G.A., Wilcox, R.E., Powers, H.A., and G.A. Desborough, 1970, The Bishop ash bed, a Pleistocene marker bed in the western United States, Quat. Res., v. 1, p. 121-132.

Kroneman, R.L., Yorgason, K.R., and J.N. Moore, 1984, Preferred methods of analysis for chemical tracers in moderate- and high-temperature geothermal environments, Earth Science Lab., UURI (DOE/ID/12079-128; ESL-84001-TR).

Merriam, R., and J.L. Bischoff, 1975, Bishop ash: A widespread volcanic ash extended to southern California, J. Sed. Pet., v. 45, p. 207-211.

Minor, M.M., Hensley, W.K., Denton, M.M., and S.R. Garcia, 1981, An automated activation analysis system, Radioanal. Chem., v. 70, p. 459.

Nakamura, N., 1974, Determination of REE, Ba, Fe, Mg, Na and K in carbonaceous and ordinary chondrites, Geochim. Cosmo. Acta, v. 38, p. 757-775.

Reed, M.J., 1984, Relationship between volcanism and hydrothermal activity at Cerro Prieto, Mexico, Geoth. Res. Counc., Trans., v. 8, p. 217-221.

Robinson, P.T., Elders, W.A., Muffler, L.J.P., 1976, Quaternary volcanism in the Salton Sea geothermal field, Imperial Valley, California, Geol. Soc. Amer. Bull., v. 87, 347-360.

van de Kamp, P.C., 1973, Holocene continental sedimentation in the Salton Basin, California: A reconnaissance, Geol. Soc. Amer. Bull., v. 84, p. 827-848.

SULFUR AND BASE METAL TRANSPORT IN THE SALTON SEA GEOTHERMAL SYSTEM

Michael A. McKibben[1], C. Stewart Eldridge[2], and Alan E. Williams[1]

[1]Geothermal Resources Program, Institute of Geophysics and Planetary Physics, University of California, Riverside, California, 92521 USA

[2]Geology Department, and Research School of Earth Sciences, Australian National University, G.P.O. Box 4, Canberra, A.C.T. 2601, Australia

ABSTRACT

Sulfur isotope data demonstrate that H_2S in the SSGS brines is generated by partial hydrothermal reduction of SO_4^{2-} derived from dissolution of lacustrine sulfate minerals in the host sediments. No magmatic input of sulfur is indicated. SO_4^{2-} reduction is promoted by interaction of the sediments with an upwelling diapir of Fe^{2+}–rich hypersaline brine. Base metals are carried in the brines as the chloride complexes $PbCl_3^-$, $ZnCl_2^0$, $CdCl_2^0$, $CuCl_3^{2-}$, and $MnCl_2^0$. Fe is probably carried as both $FeCl_3^-$ and $FeCl_4^-$ complexes. Vein sulfide precipitation within the reservoir occurs during brine dilution and oxidation at an interface between the hypersaline brines and overlying, more oxidized lower–salinity fluids.

INTRODUCTION

The hypersaline reservoir brines of the SSGS are very deficient in sulfur relative to metals, so that the availability of reduced sulfur remains the major limitation on sulfide deposition in the reservoir (Skinner at al., 1967). In order to identify sulfur sources and more accurately model metal transport in the SSGS reservoir brines, we have conducted a systematic investigation of the sulfur isotopic variations in minerals and hydrothermal fluids from this active ore–forming geothermal system. These studies have been made possible by new drillcores provided by the Salton Sea Scientific Drilling Project (Elders and Sass, 1988). We have also determined the nature of the complexes transporting base metals in the brines, allowing more accurate calculation of metal sulfide solubilities in brines.

SULFUR ISOTOPE STUDIES

A few early $\delta^{34}S$ values of $\simeq 0$ permil for vein sulfides and pipe scales tentatively suggested a magmatic origin for the reduced sulfur in the brines (White, 1968). However, significant amounts of metamorphosed lacustrine evaporites, rich in $CaSO_4$, are now known to be present in the SSGS host rocks at 1–3 km depth (Herzig et al., 1988; McKibben et al., 1988a; Osborn et al., 1988). This occurrence adds another possible mechanism of generating reduced sulfur for ore genesis: hydrothermal reduction of evaporite–derived SO_4.

We have performed 46 conventional analyses and 219 SHRIMP (Eldridge et al., 1987) analyses of $\delta^{34}S$ for sulfide and sulfate minerals in host rock sediments, veins, and igneous rocks. Fourteen samples of aqueous H_2S and SO_4 were collected from flow–tests of 9 geothermal wells and analyzed for $\delta^{34}S$. The results and interpretation summarized here are being published in more detail elsewhere (McKibben and Eldridge, 1988).

Stratiform gypsum and anhydrite

Sulfate minerals in the deltaic–lacustrine host sediments range from disseminated stratabound crystals and nodules in mudstones to stratiform bedded accumulations of evaporitic gypsum and anhydrite (McKibben and Elders, 1985; McKibben et al., 1988b; Herzig et al., 1988). The $\delta^{34}S$ data lie chiefly between 0 and 20 permil with a mean for all sulfate analyses of 10 permil (Figure 1), compositions that are consistent with those found in lacustrine evaporites precipitated from sulfate derived from continental sources. Sulfate input into the Salton Basin has been dominated largely by Colorado River water, but punctuated by variable contributions from local streams and storm runoff from the mountain ranges surrounding the Salton Trough.

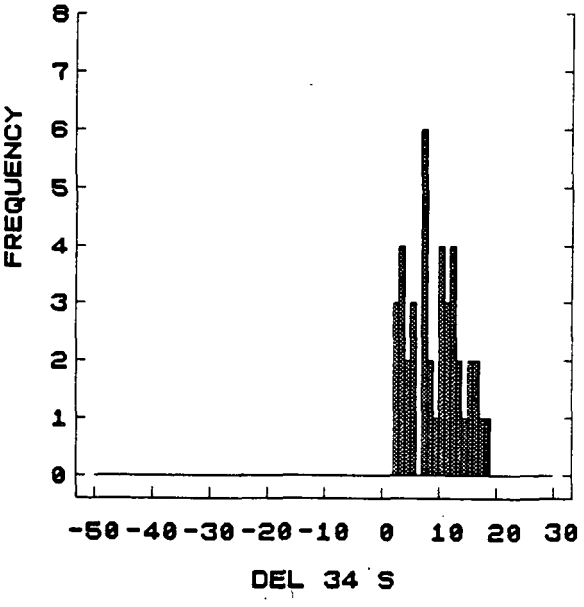

FIGURE 1. Histogram of $\delta^{34}S$ values for sedimentary anhydrite in the SSGS host sediments. Mean is 10 permil.

Pyrite in sediments

Pyrite typically occurs as framboids (5–50μm), cubes (5–100 μm), and rarely as pyritohedrons (up to 0.1 mm) in stratiform diagenetic layers and lenses that may locally comprise up to a few volume percent of a sample of sediment (McKibben and Elders, 1985). In general these pyrites are isotopically light, ranging widely from –48 to 6 permil (Figure 2). The mean isotopic composition of pyrite in sediments (≃–10 permil) indicates that the kinetic fractionation effect for the biogenic reduction of SO_4 in the lacustrine sediments was generally around 20 permil (k_1/k_2 of Ohmoto and Rye (1979) = 1.020).

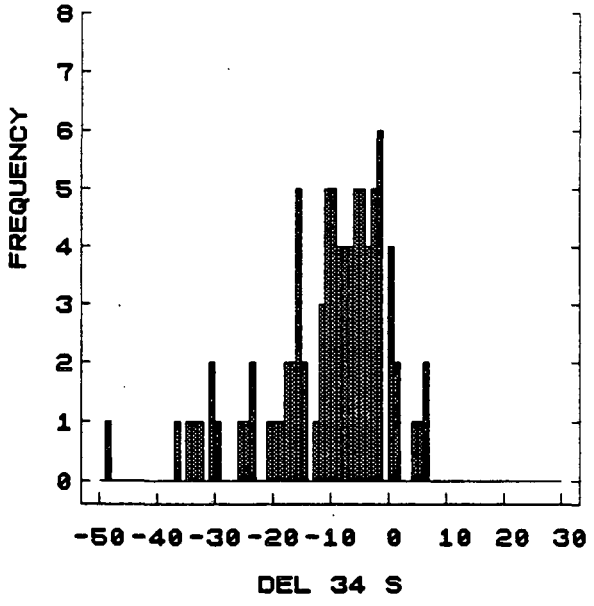

FIGURE 2. Histogram of $\delta^{34}S$ values for sedimentary pyrite in the SSGS host sediments. Mean is –10 permil.

Sedimentary anhydrite–pyrite isotopic fractionation

The apparent sulfur isotopic fractionation between intergrown sedimentary anhydrite and pyrite can be quite variable (Figure 3). The comparison of measured Δ values with those expected at equilibrium illustrates that there has been no consistent movement toward equilibrium isotope partitioning between sulfate and sulfide in the Pleistocene and younger sediments at temperatures up to 350°C, implying that the isotopic compositions of stratiform sulfate and sulfide still reflect those of the initial shallow lacustrine depositional environment.

Pyrite in igneous rocks

An altered diabase sill and its lower contact zone were cored at a depth of 2.9 km in the well S2–14 (Elders, 1987; Herzig and Elders, 1988). Brecciated metasediments and stringers of diabase within the contact zone contain abundant secondary pyrite crystals. The pyrite in the diabase stringers replaces plagioclase phenocrysts and groundmass. Pyrite is also found as coarse–grained cubes in hydrothermal veins that clearly cut and post–date the main mass of the diabase sill. The $\delta^{34}S$ values of all of these pyrites (–7 to 2 permil) fall entirely within the range

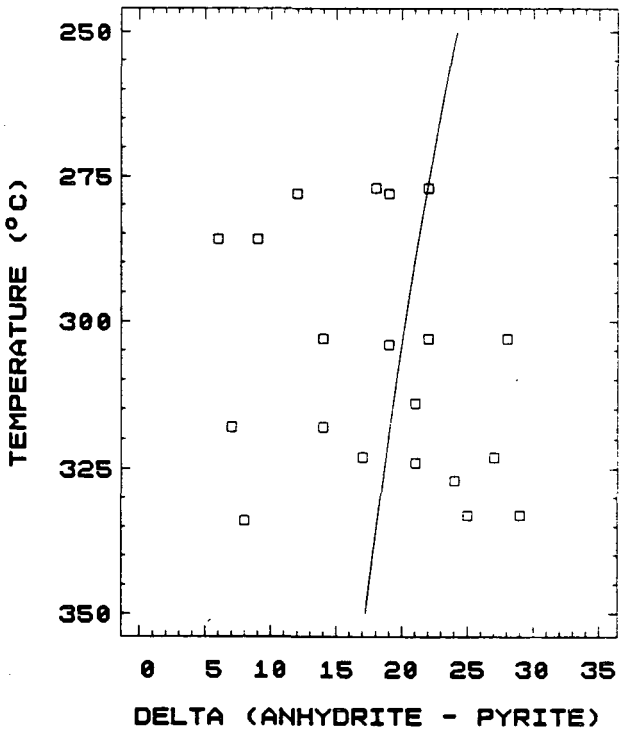

FIGURE 3. Plot of S isotopic fractionation between intergrown sedimentary anhydrite and pyrite (Δ) versus measured downhole temperature. Curve is for equilibrium SO_4–H_2S fractionation from Ohmoto and Lasaga (1982).

noted for the vein mineralization (see below), indicating that the sill is overprinted by later hydrothermal events.

Vein sulfides

Vein mineralization in the SSGS is most abundant in the depth interval 2000–5000 ft (610–1524 m) (McKibben et al., 1988a). With the exception of one vein, vein sulfides have a fairly limited range of sulfur isotopic compositions from –9 to 9 permil, with a mean of ≃0 permil (Figure 4). Variation in the $\delta^{34}S$ values of the vein sulfides probably reflects some variability in the source of sulfide, the redox state of the brine, or possibly the metal/sulfide ratio of the fluid.

In those samples containing both hydrothermal and sedimentary pyrite, the hydrothermal pyrite does not have isotopic values shifted significantly toward the very light sedimentary compositions. Therefore, the sulfur–poor, metal–rich brines are <u>not</u> deriving reduced sulfur from leaching of sedimentary sulfides in the host rocks.

Fluid precipitates and pipe scales

There are two types of SSGS fluids, recognizable by their differing salinities and chemistries, which appear to be density–stratified (McKibben et al., 1987, 1988a; Williams and McKibben, 1988). They are referred to as the deep hypersaline brines, which have measurable amounts of both H_2S (10–15 ppm) and SO_4 (5–120 ppm), and the shallow lower–salinity geothermal fluids, which do not generally contain measurable amounts of H_2S and often have high SO_4 contents (500–2000 ppm). The

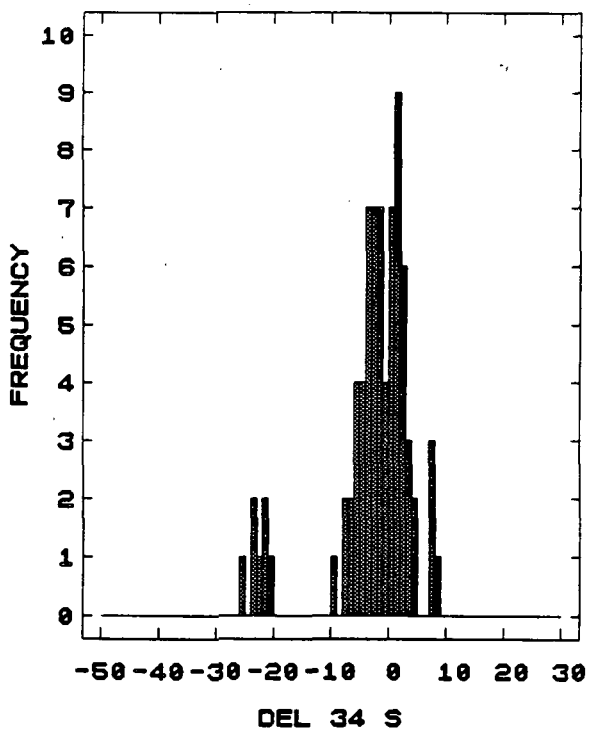

FIGURE 4. Histogram of $\delta^{34}S$ values for veins sulfides in the SSGS. Mean of the main population is 0 permil.

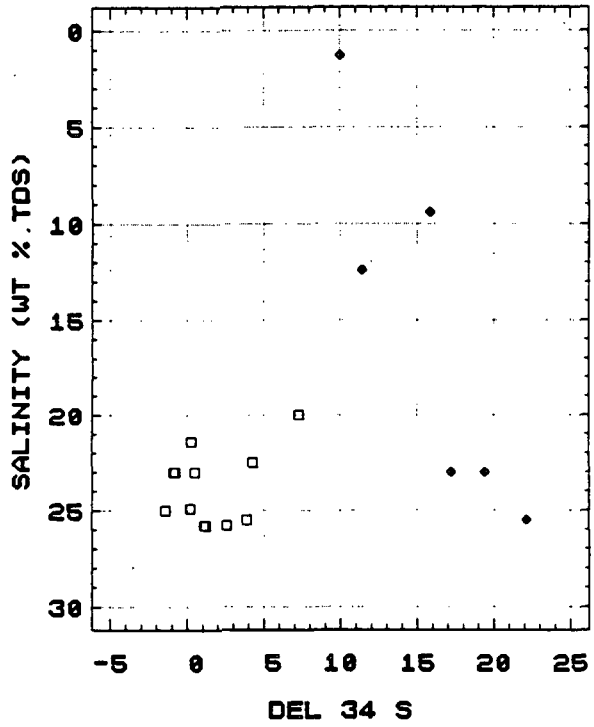

FIGURE 5. Plot of $\delta^{34}S$ values for aqueous SO_4^{2-} (solid diamonds) and aqueous H_2S (open squares) versus flash–corrected salinity for SSGS reservoir fluids.

subhorizontal interface between the two fluid types generally coincides with the domal shape of the 250°C isotherm in the SSGS (Williams and McKibben, 1988), which varies in depth from 2000–5000 ft (606–1515 m) across the geothermal field. Figure 5 shows $\delta^{34}S$ values of H_2S and SO_4 samples from these fluids plotted versus reservoir fluid salinity.

The total range (6–22 permil) in $\delta^{34}S$ values for aqueous SO_4 is significantly greater than that found for H_2S (–1.4 to 7.3 permil). The highest values for SO_4^{2-} (17–22 permil) are from the deep hypersaline brines (>20 wt % TDS) and the lower values for SO_4^{2-} (9–16 permil) are from shallow lower–salinity fluids (<10 wt % TDS) or from well–bore mixtures of low–salinity and hypersaline fluids produced from multiple flow–zones over large uncased intervals in wells (Williams and McKibben, 1988). The $\delta^{34}S$ values of SO_4 generally appear to increase with increasing salinity (and temperature) as the fluid interface is approached and crossed (Figure 5).

Comparison of the isotopic compositions of aqueous SO_4 and sedimentary anhydrite (Figures 5 and 1) shows that the maximum $\delta^{34}S$ value of the SO_4 from the deep hypersaline brines exceeds that of any anhydrite found by 3 permil and is enriched in ^{34}S relative to the mean anhydrite value (10 permil) by 12 permil.

Paired samples of fluid H_2S and SO_4 were collected from hypersaline flow–zones in three wells:

Well	Sample	Salinity	Temp	$\delta^{34}S$	Δ
1	steam H_2S	25.5 wt %	310°C	3.9 ‰	
	fluid SO_4	25.5	310	22.1	18.2
2	steam H_2S	23.0	299	–0.9	
	fluid SO_4	23.0	299	17.2	18.1
3	steam H_2S	23.0	300	0.5	
	steam H_2S	23.0	300	–0.8	
	fluid SO_4	23.0	300	19.4	19.5

The reservoir temperatures of all three brines fell within 300–310°C and differences in isotopic composition between reduced and oxidized sulfur species was remarkably consistent at 18–20 permil.

The observed sulfur isotopic fractionation between aqueous H_2S and SO_4 in the deep hypersaline brines agrees very well with the experimentally determined equilibrium fractionation (19–20 permil, Ohmoto and Lasaga, 1982) for dilute solutions. Therefore, the equilibrium sulfur isotopic fractionation between reduced and oxidized aqueous sulfur species is not strongly affected by the very high salinities of these brines at this temperature. It is not surprising that equilibrium has been attained, as the residence times for brines in the SSGS appear to be 10^2 to 10^3 years (Zukin et al., 1987) whereas only 140 days would be required to establish equilibrium for Salton Sea reservoir brine conditions (McKibben and Elders, 1985; Ohmoto and Lasaga, 1982).

Sources of aqueous sulfate and sulfide

The similarity between the mean $\delta^{34}S$ values of SO_4 in low–salinity geothermal fluids and sedimentary gypsum and anhydrite (≈10 permil) is consistent with the notion that SO_4 in these shallow fluids is derived directly from

dissolution of sedimentary sulfate. However, the contrast between $\delta^{34}S$ values for sedimentary sulfates and SO_4 in the deep hypersaline brines (≈20 permil) suggests that simple dissolution of stratiform anhydrite is not likely to be the sole process influencing the isotopic composition of aqueous SO_4 in the deep brines. The ^{34}S enrichment of aqueous SO_4 in the deep hypersaline brines must reflect high temperature partial reduction of SO_4 dissolved from stratiform anhydrite in the deeper parts of the hydrothermal system.

This hypothesis can be evaluated using the mass balance (Ohmoto, 1986):

$$\delta^{34}S_{\Sigma S} = \delta^{34}S_{H_2S} + \Delta_{SO_4-H_2S}\,(R/(1+R))$$

where R is the mole ratio of sulfate and sulfide in solution. For conditions of 300°C applicable to the SSGS reservoir brines, the resulting values of $\delta^{34}S_{\Sigma S}$ average 10 permil, in perfect agreement with the mean $\delta^{34}S$ value for sedimentary anhydrite in the host sediments. SO_4 derived from dissolution of anhydrite in the reservoir rocks (≈ 10 permil) therefore could have undergone ≈ 50% reduction to yield H_2S (≈ 0 permil) and ^{34}S–enriched SO_4 (≈ 20 permil) in the deep hypersaline brines.

The deep hypersaline reservoir brines are rich in Fe and Mn (1000–2000 ppm each) and have high Fe/Zn+Pb and H_2S/SO_4 ratios relative to the overlying less saline fluids, implying that these deep brines have a relatively reduced oxidation state (McKibben et al., 1987; Williams and McKibben, 1988). Therefore, interaction of these reduced thermally–upwelling brines with the reservoir of evaporitic SO_4 in the host sediments could promote reduction and H_2S generation. Replacement of sedimentary anhydrite by epidote and amphibole has been observed in the SSGS (Osborn et al., 1988), implying that reactions of the type:

$$2CaSO_4 + 8Fe^{2+} + 3H_4SiO_4 + 4.5H_2O =$$

$$Ca_2Fe_3Si_3O_{12}OH + 2.5Fe_2O_3 + 18H^+ + SO_4^{2-} + H_2S$$

may be responsible for partial hydrothermal SO_4 reduction to generate H_2S. Such a reaction is consistent with the epidote–hematite paragenesis of veins (McKibben et al., 1988a).

In addition to variations caused by different degrees of SO_4 reduction, fluctuations in the isotopic composition of aqueous H_2S and hence of vein sulfides (i.e., 0±9 permil) could conceivably have been generated by several processes. Partial reduction of anhydrite sulfate along with dissolution of some intergrown diagenetic sulfide could result in a fluid with $\delta^{34}S$ values less than 0 permil. Fluid H_2S isotopic compositions could also be made either more positive or negative during vein sulfide precipitation if the fluid contained more metals than sulfur. Precipitation of sulfides could then significantly reduce the H_2S content of the fluid, making it isotopically lighter if pyrite were precipitated or isotopically heavier if galena were precipitated (Ohmoto, 1986). Local reduction of aqueous SO_4^{2-} or partial oxidation of H_2S to sulfanes at the site of deposition (fluid interface) could also produce the observed $\delta^{34}S$ variations in vein sulfides.

METAL TRANSPORT

Few experimental data exist to evaluate the speciation and thermodynamics of metal chloride complexes in saline fluids at elevated temperatures appropriate for the SSGS. Therefore, it is necessary to determine such information empirically. Our database from the Salton Sea geothermal system includes a series of 44 nearly isothermal (≈300°C) Na–Ca–K–Cl brine analyses covering a range of total chloride concentrations from 3–6 molal (Williams and McKibben, 1988). In such brines only 4–9 water molecules exist per ion, and the low dielectric constant of water further reduces the degree of ionization. Consequently, the predominant metal chloride species in these brines should be neutral or high ligand number chloride complexes.

Published thermodynamic data on alkali chloride solutions indicate that activity coefficients remain relatively constant at high salinities at elevated temperatures. Therefore, isothermal plots of log total metal molality versus log total chloride molality will yield slopes corresponding to the mean ligand number of the metal chloride complexes, assuming that a single mineral controls a given metal's solubility and that pH and mH_2S remain relatively constant over the salinity range.

From such plots we have determined the mean ligand numbers for several metal chloride complexes in the Salton Sea brines (McKibben and Williams, 1988). For Zn, our data yield a mean ligand number of 2.1 (Figure 6), in excellent agreement with the lower–salinity experimental data of Ruaya & Seward (1986) and Bourcier & Barnes (1987). Similar determinations for all base metals indicate that the dominant chloride complexes are: $PbCl_3^-$, $ZnCl_2^0$, $CdCl_2^0$, $CuCl_3^{2-}$, and $MnCl_2^0$. Fe data are complicated by the presence of both Fe^{2+} and Fe^{3+} in the brines, yielding a mean ligand number of 4.4. This implies that Fe is carried by mixtures of $FeCl_3^-$ and $FeCl_4^-$ complexes.

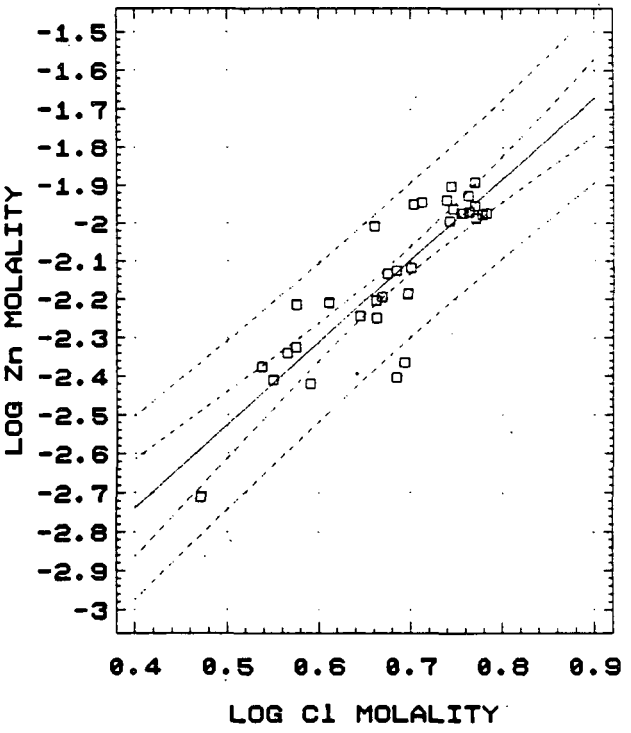

FIGURE 6. Regression of log total Zn molality versus log total Cl molality for SSGS hypersaline brines (≈300°C). Slope is 2.1, indicating that $ZnCl_2^0$ complex is dominant.

These empirical speciation data allow more accurate calculation of metal sulfide solubilities in the SSGS brines, with obvious applications to scaling problems.

Vein mineral precipitation mechanisms

Sulfide vein mineralization is most concentrated at depths of 2000–5000 ft (610–1524 m) which happens to be the interval occupied by the interface between an upwelling hypersaline brine diapir and overlying lower–salinity fluids (McKibben et al., 1987, 1988a; Williams and McKibben, 1988). This interval is also a zone of abundance of evaporitic sulfate occurrences (Figure 1). Coincidence of the brine interface and abundance of vein mineralization suggests that the main mechanism involved in ore mineral precipitation is simple cooling and dilution of the H_2S– and metal–bearing hypersaline brine. H_2S, derived chiefly from partial reduction of sedimentary anhydrite at depth, could rise with the hot brines and be precipitated as sulfides during destabilization of metal chloride complexes at the fluid interface. This process could also be enhanced though partial reduction of sulfate contained in the shallow low–salinity fluids, due to interaction with Fe^{2+} in the reduced hypersaline brines. Precipitation by partial oxidation of H_2S to sulfanes (S_2^{2-} in pyrite, S_3^{2-} in chalcopyrite) at the fluid interface could also account for some of the $\delta^{34}S$ variations of the vein sulfides.

Acknowledgements This research was supported by DOE grant DE–FG03–85ER13408 and NSF grant EAR–8617430 to M.A.M.

REFERENCES

Bourcier, W. L., and Barnes, H. L., 1987, Ore solution chemistry VII. Stabilities of chloride and bisulfide complexes of zinc to 350°C; Econ. Geol., 82, 1839–1863.

Elders, W. A., 1987, Igneous rocks in the SSSDP well and in the Salton Trough [abstr.]: EOS Trans. AGU, v. 68, p. 446.

Elders, W. A., and Sass, J. H., 1988, The Salton Sea scientific drilling project: its scientific significance: in press, Jour. Geophys. Res.

Eldridge, C. S., Compston, W., Williams, I. S., Walshe, J. L., and Both, R. A., 1987, In situ microanalysis for $^{34}S/^{32}S$ ratios using the ion microprobe SHRIMP: Int. Jour. Mass Spectr. Ion Processes, v. 76, p. 65–83.

Herzig, C. T., and Elders, W. A., 1988, Igneous rocks in the State 2–14 research borehole, Salton Sea scientific drilling project, California, U.S.A.: in review, Jour. Geophys. Res.

Herzig, C. T., Mehegan, J. M., and Stelting, C. E., 1988, Lithostratigraphy of an active pull–apart basin: Salton Sea Scientific Drilling Project: in press, Jour. Geophys. Res.

McKibben, M. A., and Elders, W. A., 1985, Fe–Zn–Cu–Pb mineralization in the Salton Sea geothermal system, Imperial Valley, California: Econ. Geol., v. 80, p. 539–559.

McKibben, M. A., and Eldridge, C. S., 1988, Sulfur isotopic variations among minerals and fluids in the Salton Sea geothermal system: a SHRIMP ion microprobe and conventional study; in review, American Journal of Science.

McKibben, M. A., and Williams, A. E., 1988, Empirical determinations of metal chloride complex speciation in saline hydrothermal fluids; in prep.

McKibben, M. A., Williams, A. E., Elders, W. A., and Eldridge, C. S., 1987, Saline brines and metallogenesis in a sediment–filled rift: the Salton Sea geothermal system, California: Appl. Geochem., v. 2., p. 563–578.

McKibben, M. A., Andes, J. P. Jr., and Williams, A. E., 1988a, Active ore–formation at a brine interface in metamorphosed deltaic–lacustrine sediments: the Salton Sea geothermal system, California: Econ. Geol., v. 83, no. 3 (in press).

McKibben, M. A., Williams, A. E., and Okubo, S., 1988b, Metamorphosed Plio–Pleistocene evaporites and the origins of hypersaline brines in the Salton Sea geothermal system, California: fluid inclusion evidence: Geochim. et Cosmochim. Acta, v. 52., p. 1057–1067.

Ohmoto, H., 1986, Stable isotope geochemistry of ore deposits: in Valley, J. W., Taylor, H. P., Jr., and O'Neil, (Eds.), 1986, Stable Isotopes in High Temperature Geological Processes: Min. Soc. Am., Rev. in Min., Vol. 16, p. 491–560.

Ohmoto, H., and Lasaga, A. C., 1982, Kinetics of reactions between aqueous sulfates and sulfides in hydrothermal systems: Geochim. et Cosmochim. Acta, v. 46, p. 1727–1746.

Ohmoto, H., and Rye, R. O., 1979, Isotopes of Sulfur and Carbon, in Barnes, H. L. (Ed.), Geochemistry of Hydrothermal Ore Deposits: Ch. 10, Wiley–Interscience.

Osborn, W. L., McKibben, M. A., and Williams, A. E., 1988, Formation, diagenesis and metamorphism of lacustrine sulfates under high geothermal gradients in an active continental rift zone (abstract); Geol. Soc. America, Ann. Mtg., Denver (submitted).

Ruaya, J. R., and Seward, T. M., 1986, The stability of chlorozinc (II) complexes in hydrothermal solutions up to 350°C; Geochim. et Cosmochim. Acta, v. 50, p. 651–662.

Skinner, B. J., White, D. E., Rose, H. J., Jr., and Mays, R. E., 1967, Sulfides associated with the Salton Sea geothermal brine: Econ. Geol., v. 62, p. 316–330.

White, D. E., 1968, Environments of generation of some base–metal ore deposits: Econ. Geol., v. 63, p. 301–335.

Williams, A. E., and McKibben, M. A., 1988, A brine interface in the Salton Sea geothermal system, California: fluid geochemical and isotopic distribution: in review

Zukin, J. G., Hammond, D. E., Ku, T–L, and Elders, W. A., 1987, Uranium–thorium series radionuclides in brines and reservoir rocks from two deep geothermal boreholes in the Salton Sea geothermal field, southeastern California: Geochim. et Cosmochim. Acta, v. 51, p. 2719–2732.

Geothermal Resources Council, TRANSACTIONS, Vol. 12, October 1988

DELINEATION OF A BRINE INTERFACE IN THE SALTON SEA GEOTHERMAL SYSTEM, CALIFORNIA

Alan E. Williams

Geothermal Resources Program
Institute of Geophysics and Planetary Physics
University of California, Riverside, CA 92521, U.S.A.

ABSTRACT

Fluids in the Salton Sea Geothermal System (SSGS) cluster into two distinct populations in terms of their salinity. The hot, hypersaline brine for which the SSGS is known, is overlain by a cooler (<260°C) fluid with distinctly lower salinity. Both types of fluid are produced from closely spaced production intervals in geothermal wells, indicating that a sharp salinity interface exists over much of the field. Sedimentary features are typically cross–cut by the fluid interface, which parallels the elongate dome–like thermal structure of the SSGS. The fluid interface occurs in portions of the reservoir where temperatures are ≈260°C. Hypersaline brines have densities of approximately 1.0 gm/cm^3, while the low TDS fluids have densities as low as .85 gm/cm^3. The stable, density–stratified interface implied by the data should act as a barrier to convective heat and mass transfer in the SSGS, isolating the hypersaline reservoir from overlying dilute fluids.

INTRODUCTION

The Salton Sea Geothermal System (SSGS) has been the focus of a great deal of interest, both commercial and scientific, since high temperature brines were first encountered during drilling in 1958. Located at the southeastern end of the Salton Sea in southern California (Fig. 1), the SSGS is one of many active geothermal fields located within the Salton Trough.

Brines from the SSGS typically have high total dissolved solids, and are rich enough in dissolved metals to be considered ore–forming fluids (White et al., 1963; Skinner et al., 1967). During early investigations, a few examples of "unusual", lower salinity production fluids were also reported (Helgeson, 1968; Muffler and White, 1969; Rex, 1971). Rex (1971, 1985) proposed a southward–dipping interface between dilute Salton basin fluids and the deep, hypersaline SSGS geothermal brines. Helgeson (1968), on the other hand, felt that the "unusual" IID #3 well data were most likely an analysis of brine contaminated with drilling fluid. The subsequent production of similar, low salinity geothermal fluids from 18 other SSGS wells now indicates that such fluids are a real and significant component of the exploitable SSGS.

The development of a detailed, three–dimensional picture of fluid distribution in the SSGS has, however, been hampered by limited data on shallow fluids and by poor constraints on producing intervals (flow zones). Here, we have made an effort to interrelate all information available (including previously unpublished data) to constrain the published production and chemical data. We have also obtained well–controlled samples and production information from recent commercial, exploration and scientific drilling projects in the SSGS area. At present, our chemical data–base consists of information concerning 60 production intervals in 40 geothermal wells drilled into the SSGS and analyses of 9 geothermal surface manifestations (mud pots and warm springs). The thermal well intervals range in depth from approximately 200 meters to greater than 3500 m and are distributed over an area of the SSGS exceeding 200 km^2 (Fig. 1).

In this paper we perform a first order summary of this data–base in order to focus on field–wide distributions of chemical, thermal and other physical parameters critical to our understanding of the SSGS as a whole.

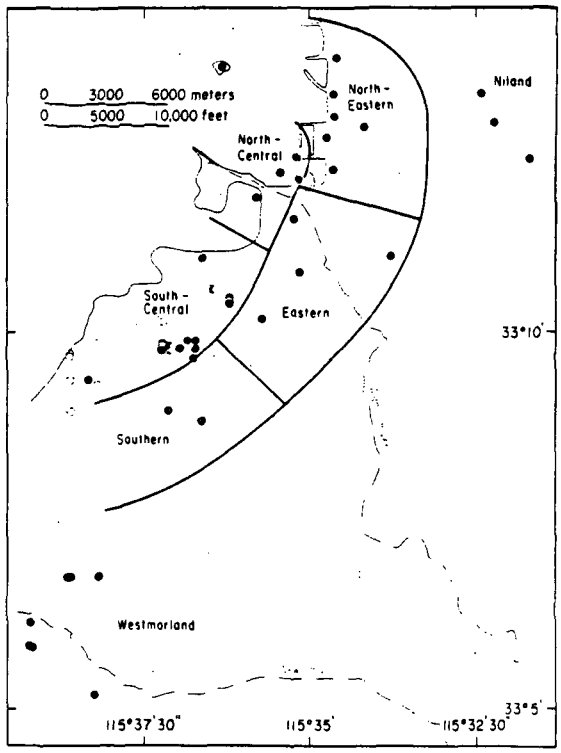

FIGURE 1. Map of the SSGS.

SALINITY

Total dissolved solids (TDS) values of fluids from 60 geothermal production intervals in the high temperature wells of the SSGS have been compiled and illustrated as a histogram (Fig. 2). Where possible, chemical analyses were corrected for production induced steam and gas loss, to yield reservoir compositions, using direct measurements of brine and steam production rates. In cases where this information was not available, approximate steam corrections were made on the basis of other available data such as reservoir temperature, production depth, well–head pressure–temperature conditions, chemical geothermometry and data from adjacent wells.

In the salinity histogram (Fig. 2), geothermal production intervals have been divided into three classifications: "hypersaline", "mixed" and "low TDS". Subdivision into the two primary categories (hypersaline ; low TDS) was made strictly on the basis of the bimodal character of this histogram. Consequently, the low TDS category contains fluids (up to 13 wt% TDS) that in other geothermal systems would be considered quite high in salinity.

Seven mixed production intervals denoted on Figure 2 separate the clusters of hypersaline and low TDS data points. These intervals were identified as mixed, not because of their intermediate salinity but because of independent evidence for the inflow of different fluids from more than one producing horizon within the open or perforated interval. In one well, (the Britz #3, drilled by Republic Geothermal Inc.) fluids having approximately 8 wt% and 24 wt% TDS were produced simultaneously from different horizons separated by less than 300 m depth (Williams and Oakes, 1986). In several other commercial wells with open intervals of only a few hundred meters, mixing between hypersaline brines and fluids of less than 10 wt% TDS have also been deduced from production fluid changes during extended or multiple flow tests.

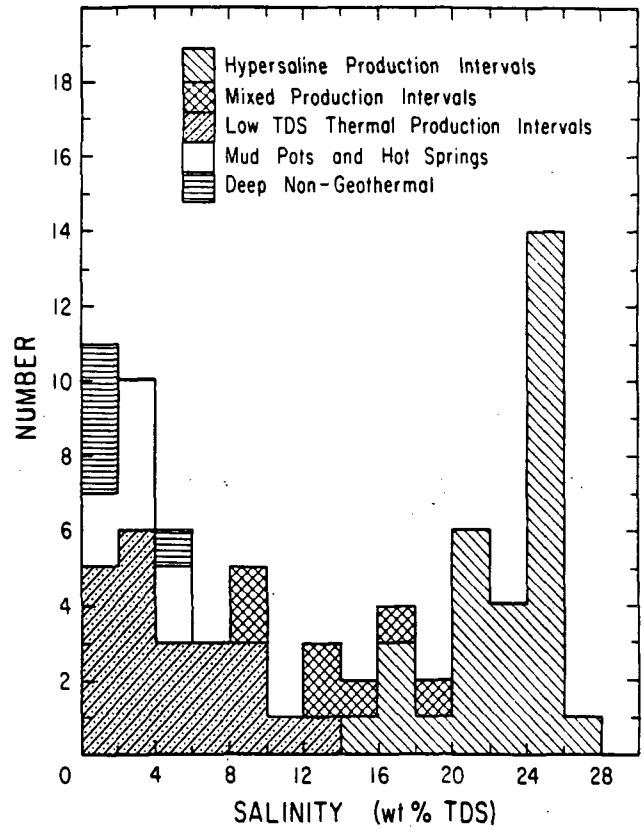

FIGURE 2. Histogram of SSGS fluid salinities.

TABLE 1. Examples of flash–corrected fluid analyses.

	HYPERSALINE					LOW T.D.S.			
	SSSDP Well, State 2-14								
	Test 1	Test 2[d]	Test 3[e]	Commercial Well #11	Commercial Well #10	Woolsey[f] Well #1	Commercial Well #5	I.I.D.[g] Well #3	Commercial Well #1
Na	53,000 ppm	54,800	54,300	46,200	41,400	25,000	15,000	10,600	4,800
Ca	27,400	28,500	27,800	22,800	20,900	11,000	2,520	1,130	117
K	16,700	17,700	17,000	12,500	11,800	5,000	2,480	1,250	297
Fe	1,560	1,710	1,550	582	969	65	86	0.7	25
Mn	1,450	1,500	1,450	801	855	NA	60	6.4	ND
SiO_2[c]	>461	>588	>847	>336	>404	NA	>255	>120	102
Zn	518	507	574	321	323	NA	11	ND	ND
Sr	411	421	420	376	345	513	112	85	10
B	257	271	262	204	197	NA	92	100	32
Ba	203	353[b]	262	183	156	NA	45	3	0.7
Li	194	209	193	157	152	93	55	40	9
Mg	33	49	54	19	33	NA	54	74	24
Pb	100	102	87	69	67	NA	2.6	ND	ND
Cu	5.9	6.8	3.0	NA	2	NA	ND	ND	ND
Cs	2.2	2.3	2.3	NA	1.4	NA	ND	ND	ND
NH_4^+	333	330	NA	339	341	NA	103	321	NA
Cl^-	151,000	157,500	152,300	128,000	116,000	85,000	31,000	19,700	6,900
Br^-	99	111	111	95	78	NA	24	15	10
CO_2[a]	1,600	1,580	NA	1,100	5,500	NA	10,000	NA	NA
H_2S	15	10	NA	15	20	NA	NA	NA	NA
$SO_4^=$	65	53	~141	~100	53	NA	53	621	440
TDS	~25.6%	~26.5	~25.7	~21.4	~20.0	~ 12.7	~6.2	~3.5	~1.3

(a) Volumetric measurement of total non-condensible gas.
(b) Probable contamination from drilling fluid.
(c) Silica values low due to precipitation prior to and during sampling.
(d) Concentrations corrected for ~5% dilution by drilling fluid.
(e) Short clean-out flow, some contamination
(f) Needham et al. 1980
(e) Muffler and White, 1969

FLUID CHEMICAL COMPOSITIONS

As recognized in early SSGS studies involving geothermal fluids of both hypersaline and low TDS affinities (Helgeson, 1968; Muffler and White, 1969; Rex, 1971), these fluids have quite different chemical characteristics (Table 1). Hypersaline brines are typically Na–Ca–K chloride solutions having molar cation ratios of approximately 0.68: 0.20: 0.12, respectively. High concentrations of Fe, Mn, Zn, Sr and other constituents are typical in these brines (Table 1). Low TDS fluids on the other hand, are relatively NaCl dominated (Table 1) with molar Na–Ca–K typically >0.77:<0.15:<0.09, and have drastically lower concentrations of dissolved metals.

As examples, we have listed (Table 1) fluid analyses from (1) three separate deep flow intervals in the SSSDP well S2–14, (2) data from two shallower commercial wells producing hypersaline fluid of slightly lower TDS, and (3) analyses from four wells producing low TDS fluids spanning the range of salinity from less than 2 wt% to 13 wt% TDS. It is obvious that Mn, Zn and particularly Fe concentrations in these fluids drop off drastically due to the decrease in chloride complexing at lower salinities.

DISTRIBUTION OF SSGS FLUID TYPES

The salinity of fluids from the 60 geothermal production intervals has been plotted against their production depth in Figures 3a and 3b. On these depth vs. salinity diagrams, it is apparent that fluids having salinity greater than 23 wt% are produced only from deep (greater than 1 km) production intervals. This relationship implies an upper limit to the high salinity SSGS reservoir which deserves more complete three–dimensional examination. For this purpose we have differentiated wells in our data–base into seven categories based on their location within the geothermal system (Fig. 1). Within each of these regions, multiple production intervals exist which provide constraints on the depth of the interface between the hypersaline geothermal brines and the low TDS thermal fluids. In order to provide approximate salinity profiles for the SSGS reservoir in various regions, we have produced depth versus salinity diagrams showing data subdivided as to region (Figs. 3a and 3b). We have distinctively shaded data from production intervals located in the Central, Southern and Niland regions of the field on Figure 3a, and those from Northern–Northeastern and Westmorland regions on Figure 3b.

The shallow, sharp decrease in salinity illustrated by data from wells in the Central Regions implies a ≃500 m depth for the interface. Hypersaline fluids produced from within 500 m of this interface show significantly lower salinities than those produced from depths greater than 1 km. This gradient in salinity approaching the interface provides constraints on processes of fluid mixing across it. Convection induced turbulence and diffusive processes should both tend to soften the sharp interface with time.

A similar, abrupt and well constrained interface is illustrated by the data from the Northern and Northeastern regions as seen on Figure 3b. In these areas of the SSGS however, the interface depth is slightly greater than 1.0 km. Fewer data points are present to accurately constrain the shape of salinity profiles in the other regions of the SSGS. The interface most likely occurs at depths of approximately 1.5 km in the Southern Region and 2.5 km in the Niland Region. The poorest constraints exist in the Westmorland Region where only low TDS production was observed to depths greater than 2.5 km indicating an interface depth probably on the order of 3.0 km. Data from a series of production zones in non–geothermal (petroleum exploration) wells outside of the SSGS (Rex, 1971) indicate low TDS fluids at depths of at least 4.0 km (Fig. 3a).

Salinity profiles for all regions of the SSGS (Figs. 3a, 3b) show very sharp increases in salinity (interfaces with gradients of more than 200 ppm TDS/meter) over rather narrow depth intervals (approximately 500 m). The depth to this interface increases away from the central regions of the SSGS, reaching 2.5 km in the Niland region and probably 3 km near Westmorland. The apparent dip of this brine interface toward the south was recognized by Rex as early as 1971 and became an important part of his model of the SSGS (Rex, 1985). In contrast to that model, involving southward and downward flow of salt rich brines, our data indicates that the interface becomes deeper in <u>all</u> directions away from the hot, central SSGS. In the immediate area of the SSGS, the topology of the inferred brine interface can be examined by contouring the depth to the high salinity gradient portion of the reservoir salinity profiles in each region of the SSGS where constraints exist. Such contouring indicates that the fluid interface roughly coincides with the elongate domal shape of the SSGS thermal anomaly.

RELATION TO STRATIGRAPHY AND STRUCTURE

A sharp fluid interface in the SSGS could be produced by several mechanisms. These include the effects of impermeable structures or stratigraphic barriers which could separate aquifers, thereby limiting the upward convection of the deep geothermal fluid. Such impermeable barriers have long been considered responsible for the thermal profiles of SSGS wells (Helgeson, 1968; Randall, 1974; Kasameyer et al., 1984). In these studies, a thick sequence of unconsolidated lacustrine muds was viewed as a lithologic "cap" to the upward circulation of hot brines. Recently acquired well logs from a large number of commercial production, injection and exploration wells in several regions of the SSGS have permitted us to test this assertion by accurately correlating lithologic units in localized areas. These correlations permit the definition of both sedimentary and structural features as well as the inference of their control on hydrothermal circulation.

We have presented a representative cross section across a boundary region of the SSGS as Figure 4. Lithologic units and two normal faults were recognized and were easily correlated between wells with the use of electric well log information. Production interval, temperature and salinity information from the wells in this region are illustrated in Figure 4b.

It is apparent from comparison of Figures 4a and 4b that the thermal and fluid salinity distributions are not strongly controlled by stratigraphic features. It is very important to note that, in contrast to popular models of the thermal structure of the SSGS, thermal gradients in this and several other boundary regions of the field are <u>not</u> limited by a sedimentary or structural "cap".

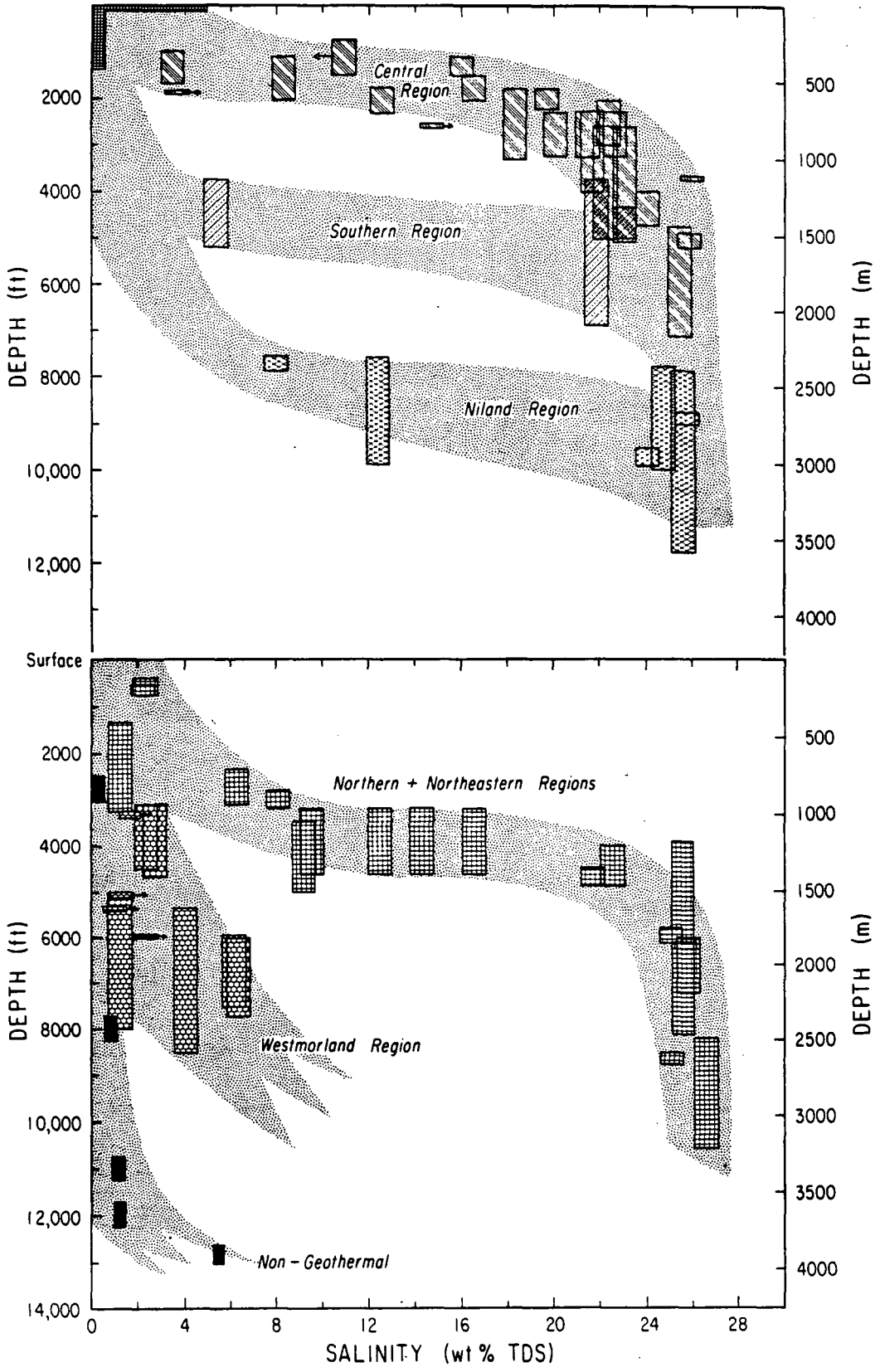

FIGURE 3. Salinity vs. depth plots for geothermal production intervals in different regions of the SSGS.

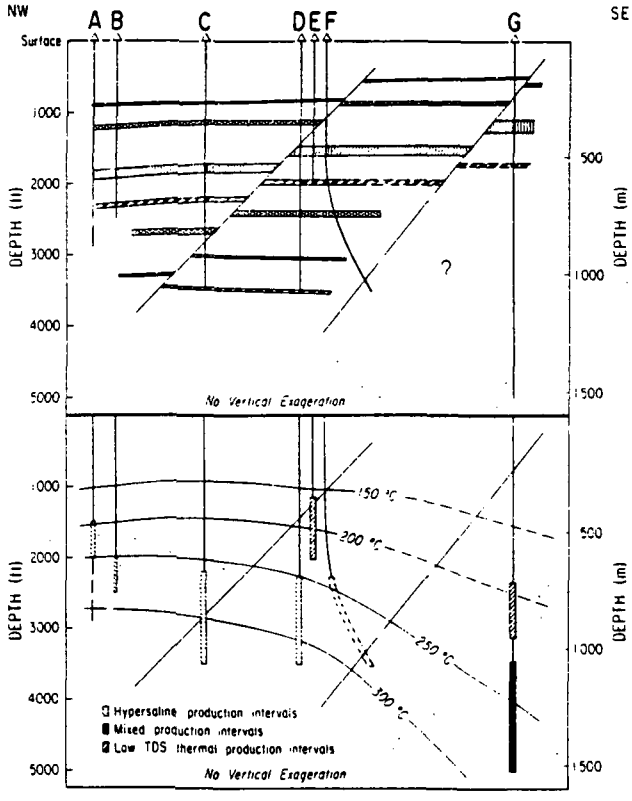

FIGURE 4. Cross section in the SSGS:
(a) Structure and stratigraphy.
(b) Temperature and salinity.

THERMAL CONTROL OF THE INTERFACE

As implied by the correlation between the topologies of the brine interface and the thermal distribution, fluid salinity in SSGS production intervals correlates closely with the temperature of the reservoir in that production interval. On a temperature versus salinity plot (Fig. 5), SSGS reservoir fluids indicate a rather sharp discontinuity between low TDS fluids, produced from reservoirs at temperatures lower than 260°C, and hypersaline brines, typically produced from regions of higher temperature. A few examples of hypersaline production at lower temperatures are, however, observed. Examples for which well–bore mixing is implied lie between the clusters of low temperature, low TDS and high temperature, hypersaline data points on Figure 5, as expected for a mixing process.

The close coherence of the inferred brine interface and the thermal distribution of the SSGS argue for some physical connection between the two phenomena. Although it is obvious that low salinity (and consequently lower density) fluids will tend to float on top of higher density hypersaline brines, development of a sharp interface coincident with the 250–260°C isothermal surface is not straightforward.

DEVELOPMENT OF A BRINE DIAPIR

Data concerning 60 geothermal production intervals in 40 SSGS wells indicates the presence of a rather sharp salinity gradient (brine interface) separating the hypersaline reservoir from overlying low TDS thermal fluids. Rex (1985) describes a hypersaline pool with a sharp upper boundary as forming from low to moderate temperature dissolution of primarily NaCl salina deposits left in the Salton Trough sediments by multiple flooding–evaporation cycles of ancient Lake Cahuilla (Waters, 1983; McKibben et al., 1988a). These salt brines, due to their high density (1.1 to 1.2 gm/cm^3) would descend through any available vertical permeability to pond at the base of the permeable section. It is conceivable that if this downward flow occurred in localized channels rather than by percolation, a sharp salinity interface could be produced. As mentioned previously, the presence of such a density stabilized interface would act as a barrier to mass and energy transfer by convection, permitting relatively long term isolation of fluids in this brine pool.

Once a sharp, density stabilized fluid interface is developed in the Salton basin, the evolution of a locally heated region to form a feature similar to the domal SSGS is conceptually straightforward (Figure 6). We have adopted the term diapir to describe this feature because the interface itself tends to dome upward, displacing or piercing through shallower fluid aquifers while maintaining its sharp salinity contrast.

When locally heated by shallow magmatic activity (Herzig and Elders, 1988), convection within the brine pool may be stimulated or enhanced. This localized convection will produce a concentration of heat transfer to a section of the interface above the upwelling fluid (Fig. 6a). Since this heat cannot be convected across the interface, a localized, high, conductive thermal gradient is produced,

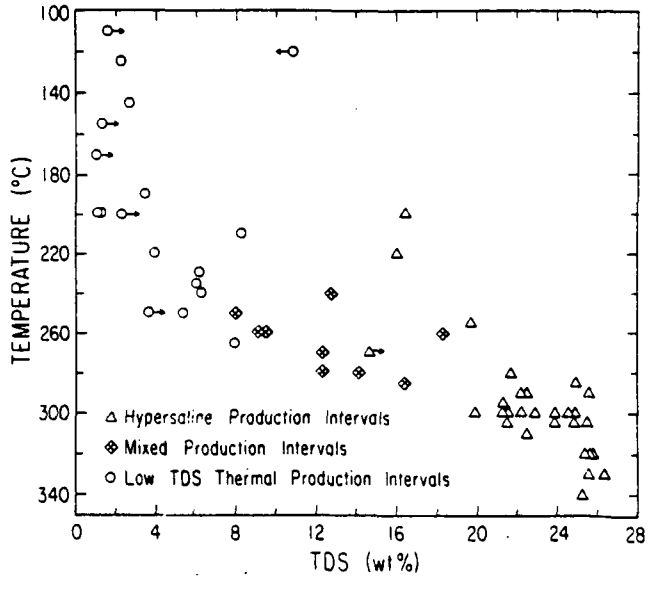

FIGURE 5. Salinity vs. temperature plot.

possibly forming a convective regime in the overlying dilute fluids. If, due to high permeability in the overlying strata, fluid pressures are roughly hydrostatic with respect to cool, dilute fluids elsewhere in the basin, hypersaline fluids will advect upward once they reach the temperature at which their density becomes < 1.0 gm/cm^3. For fluids of more than 20 wt% TDS, this temperature is slightly greater than 260°C.

Although convection may be occurring both in the hypersaline brines and in the overlying dilute fluids, the upward movement of the interface itself should be controlled by the rate of conductive heat transfer across it. When sufficient heat has been conducted across the interface to raise the temperature of the immediately adjacent overlying rock, the heated brines will be able to move upward, displacing the overlying hydrostatic fluid column. When heat transfer to the interface by convection in the hypersaline reservoir exceeds that away from the interface by dilute fluid convection, the interface will tend to rise (Fig. 6b). If heat input decreases, the interface will slowly recede (Fig.6c), despite continued convection both within the hypersaline diapir and in the dilute fluids.

Diapir–like interface behaviors identical to those postulated for the evolution of the SSGS (Figure 6) have been produced by laboratory Hele–Shaw simulations (Henley and Thornley, 1979). Their Figure 6 illustrates how a salinity differential of about 1 % NaCl was sufficient to produce isolated counter–rotating convection cells in saline and dilute fluids separated by an interface which remained quite sharp throughout the experiment. Upon increased heating from below, the interface rose upward in a manner identical to that proposed for SSGS development.

McKibben et al. (1987, 1988b) provide evidence for ore–forming processes which can be explained by the advancement and recession of the SSGS brine interface. In addition, fluid inclusion evidence indicates processes of fluid displacement and mixing near brine interfaces. Williams and Oakes (1986) and show fluid inclusion evidence (from the Niland region of the SSGS) for the displacement of dilute fluids by hypersaline brines under nearly isothermal conditions. McKibben et al. (1987; 1988b), on the other hand, show the effects of displacing a hot, reducing brine with a cooler, oxidizing fluid during a recession of the SSGS interface in the region near to the SSSDP well, State 2–14.

Although our brine interface observations and the diapir model of the SSGS are only qualitative descriptions of processes which should occur in a density stratified reservoir, constraints provided by models similar to these must be incorporated if realistic quantitative models describing the evolution and dynamics of the SSGS are to be generated.

CONCLUSIONS

Our observations indicate that geothermal fluids from the Salton Sea Geothermal System are distinctly bimodal with respect to their salinities. Most fluids are of either hypersaline (between 20 and 27 wt% total dissolved solids) or of low TDS (less than 10 wt% TDS) character. Wells producing fluids of intermediate salinity are relatively rare and can often be shown to be artificial mixtures of fluids produced simultaneously from different flow zones in the well bore.

A rather sharp (a few hundred meters thick) interface appears to separate the deeper, hypersaline brine from the less dense, low TDS fluid. In regions where adequate information is available, the fluid interface appears discordant with both stratigraphic and structural features. The topology of this interfacial surface mimics the elongate, domal form of the SSGS thermal anomaly and roughly coincides with the 260°C isothermal surface. The close concordance of the thermal and salinity features of the SSGS indicates a causative link, probably through density stratification and its control of convective fluid transport. It appears likely that heated saline fluids can convect upward only until they reach hydrodynamic equilibrium with the cool, dilute, hydrostatic fluid column of the Salton Trough. Convecting fluids as well as heat are unable to cross this density stabilized interface except by

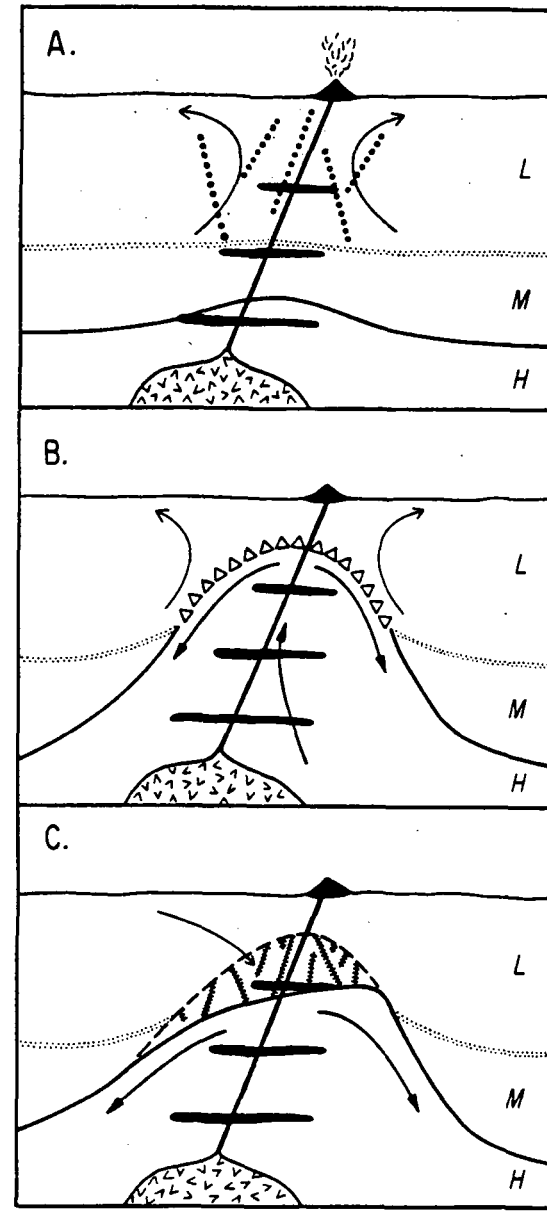

FIGURE 6. Model of SSGS brine diapir (McKibben et al., 1988b).

diffusive (conductive) processes or by local turbulent mixing across the interface. This conductive control of the heat and mass fluxes out of the deep SSGS reservoir is an important constraint on any qualitative or quantitative model of the system.

Diffusive and turbulent mixing processes across such interfaces may prove to be important precipitation mechanisms concentrating the sulfide, oxide, silicate, sulfate and carbonate mineralization observed in the Salton Sea Geothermal System and in hydrothermal ore deposits.

ACKNOWLEDGEMENTS

Information contained in this paper is a summary of a data base generated and/or collected by the UCR Geothermal Resources Program of the Institute of Geophysics and Planetary Physics. The authors gratefully acknowledge support from NSF grant EAR–8502404 (A.E.W.), DOE grant DE–FG03–85ER13408 (M.A.McKibben), NSF grant EAR–8303557 (W.A.Elders,P.I.) and Battelle contract E512–08300 (W.A.Elders, P.I.). Republic Geothermal Inc., Magma Power Co., Dow Chemical U.S.A., Kennecott Corp., and Bechtel International deserve our greatest thanks for providing personal communications, access to critical information, opportunities to obtain well controlled samples and information from recent drilling projects and for permission to publish much of the information acquired. This is report number 88/25 of the Geothermal Resources Group of IGPP/UCR.

REFERENCES

Helgeson H.C. (1968) Geologic and thermodynamic characteristics of the Salton Sea geothermal system. Amer. J. Sci. 266, 129–166.

Henley R.W., and Thornley P. (1979) Some geothermal aspects of polymetallic massive sulfide formation. Econ. Geol. 74, 1600–1612.

Herzig C.T. and Elders W.A. (1988) Igneous rocks in the State 2–14 research borehole, Salton Sea Scientific Drilling Project California, U.S.A. J. Geophys. Res. (submitted).

Kasameyer P.W., Younker L.W. and Hanson J.M. (1984) Development and application of a hydrothermal model for the Salton Sea geothermal field, California. Geol. Soc. Amer. Bull. 95, 1242–1252.

McKibben M.A., Williams A.E. and Okubo S. (1988a) Metamorphosed Plio–Pleistocene evaporites and the origins of hypersaline brines in the Salton Sea geothermal system, California: fluid inclusion evidence. Geochim. Cosmochim. Acta. 52, 1057–1067.

McKibben M.A., Andes J.P. Jr. and Williams A.E. (1988b) Active ore–formation at a brine interface in metamorphosed deltaic–lacustrine sediments: The Salton Sea Sea geothermal system, California. Econ. Geol. 83, (in press).

McKibben M.A., Williams A.E., Elders W.A. and Eldridge C.S. (1987) Saline brines and metallogenesis in a sediment filled rift: The Salton Sea geothermal system, California. Applied Geochem. 2, 563–578.

Muffler L.J.P. and White D.E. (1969) Active metamorphism of upper Cenozoic sediments in the Salton Sea geothermal field and the Salton Trough, southeastern California. Geol. Soc. Amer. Bull. 80, 157–182.

Needham P.B. Jr., Riley W.D., Conner G.R. and Murphy A.P. (1980) Chemical Analyses of Brines from Four Imperial Valley, Ca., Geothermal Wells. Soc. Petrol. Eng. J., April, p. 105–112.

Randall W. (1974) An analysis of the subsurface structures and stratigraphy of the Salton Sea geothermal anomaly, Imperial Valley, California. Ph.D. Dissertation, Univ. California, Riverside, 94 p.

Rex R.W. (ed.) (1971) Cooperative geological geophysical–geochemical investigations of geothermal resources in the Imperial Valley area of California. Final Report, U.S. Dept. Interior, Bureau of Reclam., 153 p.

Rex R.W. (1985) Temperature–chlorinity balance in the hypersaline brines of the Imperial Valley, California. In International Symposium on Geothermal Energy, Geothermal Resources Council, (ed. C. Stone) pp. 351–356.

Skinner B.J., White D.E., Rose H.J. Jr. and Mays R.E. (1967) Sulfides associated with the Salton Sea geothermal brine. Econ. Geol. 62, 316–330.

Waters M.R. (1983) Late Holocene Lacustrine chronology and archaeology of ancient Lake Cahuilla, California. Quatern. Res. 19, 373–387.

White D.E., Anderson E.T. and Grubbs D.K. (1963) Geothermal brine well—mile deep drill hole may tap ore–bearing magmatic water and rocks undergoing metamorphism. Science 129, 919–922.

Williams A.E. and Oakes C.S. (1986) Isotopic and chemical variations in hydrothermal brines from the Salton Sea geothermal field, California. Int'l Symp. Water–Rock Interaction, Reykjavik, Int'l Assoc. Geochem. Cosmochem., 5th, 633–636.